AGARD CONFERENCE PROCEEDINGS No 35

AGARD CP No 35

AGARD

ADVISORY GROUP FOR AEROSPACE RESEARCH & DEVELOPMENT

7 RUE ANCELLE 92 NEUILLY-SUR-SEINE FRANCE

Transonic Aerodynamics

★

SEPTEMBER 1968

NORTH ATLANTIC TREATY ORGANIZATION

AGARD Conference Proceedings No. 35

NORTH ATLANTIC TREATY ORGANIZATION

ADVISORY GROUP FOR AEROSPACE RESEARCH AND DEVELOPMENT

(ORGANISATION DU TRAITE DE L'ATLANTIQUE NORD)

TRANSONIC AERODYNAMICS

Copies of papers presented at a Specialists' Meeting of the
Fluid Dynamics Panel of AGARD held in
Paris, France, 18-20 September 1968.

The material in this publication has been produced directly from copy supplied by each author.

Printed by Technical Editing and Reproduction Ltd
Harford House, 7-9 Charlotte St. London. W. 1.

SUMMARY

The last major international meeting on "Transonic Aerodynamics" was the "Symposium Transsonicum" held in Aachen in 1962. Since that time there have been considerable developments in this field, for both military and civilian applications, in a number of NATO countries and it was felt that sufficient information had been accumulated to justify a Specialists' Meeting on this topic. It was planned to hold this meeting on 18-20 September in Paris at the Ecole Nationale Supérieure de l'Aéronautique.

Members of the Program Committee were:

M.R.Legendre, France (Chairman), Prof.S.Erdmann, Netherlands, Dr.D.Küchemann, U.K., Dr.J.Lukasiewicz, U.S.A., Prof.A.Naumann, Germany, and Prof.B.H.Goethert, U.S.A. (Co-opted member).

These proceedings contain a collection of the papers presented at this meeting, the purpose of which was to review and discuss the practical methods available for the study of flows around airplanes flying at subsonic speeds at which local supersonic regions appear.

The collection of papers emphasizes various calculation methods, experimental studies on profiles, with or without viscosity effects, and wing-body interference, to present a good cross-section of the state-of-the-art and to provide guidance for further research and development in this field.

Contributions have come from five NATO countries.

533.6.011.3

RESUME

Depuis 1962, où s'était tenu à Aix-la-Chapelle le "Symposium Transsonicum", aucune réunion internationale importante n'avait été consacrée à l'Aérodynamique Transsonique. Pourtant, depuis cette date, des réalisations considérables, intéressant à la fois les activités civiles et militaires, avaient été accomplies dans ce domaine par un certain nombre de pays de l'OTAN et l'on estima que la somme d'informations accumulées à ce sujet justifiait l'organisation d'une Réunion de Spécialistes. C'est ainsi que prit naissance l'idée de la réunion qui s'est déroulée à Paris, à L'Ecole Nationale Supérieure de l'Aeronautique du 18 au 20 Septembre 1968.

Le Comité du Programme chargé de sa réalisation se composait des membres suivants:

M.R.Legendre, France (Président), Prof.S.Erdmann, Pays-Bas, Dr.D.Küchemann, Grande-Bretagne; Dr.J.Lukasiewicz, U.S.A., Prof.A.Naumann, Allemagne et le Prof.B.H.Goethert, U.S.A. (admis par cooptation).

Ce compte-rendu rassemble les exposés présentés à cette réunion, dont l'objectif était de passer en revue et d'examiner les méthodes pratiques dont on dispose à l'heure actuelle pour étudier les écoulements autour d'avions volant aux vitesses subsoniques où apparaissent des régions supersoniques locales.

Ces exposés, fruit du travail de cinq pays de l'OTAN, sont consacrés en particulier aux diverses méthodes de calcul, aux études expérimentales sur les profils, avec ou sans effets de viscosité, et aux interférences voilure-fuselage. Ils donnent un bon aperçu de l'état actuel de la technologie dans ce domaine et contiennent des données permettant d'orienter les recherches et développements futurs.

Cinq pays de l'OTAN ont donné leur contribution.

CONTENTS

	Page
SUMMARY	iii
RESUME	iv

	Reference
TRANSONIC SHOCK-FREE FLOW, FACT OR FICTION? (INTRODUCTORY PAPER) by G.Y.Nieuwland and B.M.Spee	1
LAX-WENDROFF DIFFERENCE SCHEME APPLIED TO THE TRANSONIC AIRFOIL PROBLEM by R.E.Singleton	2
INVISCID SUPERCRITICAL AIRFOIL THEORY by R.Magnus, W.Gallaher and H.Yoshihara	3
APPLICATION OF THE CHARACTERISTICS TO THE NUMERICAL COMPUTATION OF A STEADY COMPRESSIBLE FLOW by P.Carrière and C.Capelier	4
TIME DEPENDENT CALCULATION OF THE FLOW ABOUT AIRFOILS IN A TRANSONIC FREESTREAM by D.MacKenzie and G.Moretti	5
SUPERCRITICAL TRANSONIC AIRFOIL DESIGN FROM PRESCRIBED VELOCITY DISTRIBUTION by M.S.Cahn, H.R.Wasson and J.R.Garcia	6
ANALOGY DETERMINATION OF WING PROFILES IN TRANSONIC FLOW by F.Rigault	7
DIGITAL DETERMINATION OF SUB-CRITICAL WING PROFILES BY THE HODOGRAPH METHOD by P.Bevière	8
AN EXPERIMENTAL INVESTIGATION OF UNSTEADY TRANSONIC FLOW BY HIGH-SPEED INTERFEROMETRIC PHOTOGRAPHY by G.Meier and W.Hiller	9
THEORY OF VISCOUS TRANSONIC FLOW - A SURVEY by M.Sichel	10
THE INTERACTION BETWEEN LOCAL EFFECTS AT THE SHOCK AND REAR SEPARATION by H.H.Pearcey, A.B.Haines and J.Osborne	11

Reference

THE PREDICTION OF AEROFOIL PRESSURE DISTRIBUTIONS FOR SUB-CRITICAL VISCOUS FLOWS
by R.C.Lock, B.J.Powell, C.C.L.Sells and P.G.Wilby — 12

EXPERIMENTAL RESEARCH ON SUPERCRITICAL WING PROFILES
by M.Vincent de Paul — 13

LEADING-EDGE SUPERSONIC VELOCITY PEAKS AND THE DETERMINATION OF THE VELOCITY DISTRIBUTION ON AN AEROFOIL IN A SONIC STREAM
by N.Thompson and P.G.Wilby — 14

AN APPROACH TO THE DESIGN OF THE THICKNESS DISTRIBUTION NEAR THE CENTER OF AN ISOLATED SWEPT WING AT SUBSONIC SPEED
by M.M.Freestone — 15

FACTORS AFFECTING THE CHOICE OF A THREE-DIMENSIONAL SWEPT WING DESIGN FOR HIGH SUBSONIC SPEEDS
by A.B.Haines — 16

AN APPROXIMATE METHOD FOR THE DETERMINATION OF THE PRESSURE DISTRIBUTION ON WINGS IN THE LOWER CRITICAL SPEED RANGE
by T.E.Labrujere, W.Loeve and J.W.Slooff — 17

THE AERODYNAMIC DESIGN AND TESTING OF A LIFTING SWEPT WING BODY CONFIGURATION WITH SHOCK FREE WING FLOW AT M = 1.2
by J.Bridgewater, S.O.Han and H.Kramer — 18

WING-BODY INTERFERENCE AT SUPERSONIC SPEEDS
by K.Stewartson and D.A.Treadgold — 19

EXPERIMENTAL INVESTIGATION OF WING BODY INTERFERENCES IN THE MACH NUMBER RANGE FROM 0.5 to 2.0
by W.Schneider — 20

EFFECT OF REYNOLDS NUMBER AND BOUNDARY-LAYER TRANSITION LOCATION ON SHOCK-INDUCED SEPARATION
by J.A.Blackwell — 21

WIND TUNNEL EXPERIMENTS ON THE INTERFERENCE BETWEEN A JET AND A WING AT SUBSONIC SPEEDS
by J.A.Bagley — 22

SOME PROBLEMS OF TRANSONIC FLOW FOR ENGINE NACELLES OF AIRBUS TYPE AIRCRAFT
by G.Meauze and J.Leynaert — 23

SOME NEW RESULTS ON STEADY TWO-DIMENSIONAL TRANSONIC FLOW
by K.Oswatitsch — 24

Transonic shock-free flow, fact or fiction ?

by G.Y. Nieuwland and B.M. Spee

National Aerospace Laboratory NLR, Amsterdam, Netherlands

Summary

It has to be realized that such terms as physical significance and stability, used in the transonic controversy, have different connotations from the engineering, mathematical and physical point of view.

The conclusions that have been obtained from an experimental study on quasi-elliptical aerofoil sections may be said to constitute the relevance of transonic potential flow in the engineering sense. These conclusions are :

- the agreement between experiment and theory can in principle be made arbitrarily good by eliminating model imperfections and boundary layer effects;
- the shock-free design condition is embedded in, and can be reached in a stable manner from, the neighbouring conditions where shock waves are present.

The only legitimate way to discuss the physical significance of potential flow solutions from the mathematical point of view is to exhibit such solutions as the limit of solutions of the unsteady compressible Navier-Stokes equations for $Re \rightarrow \infty$, $t \rightarrow \infty$. Morawetz's non-existence theorems for transonic potential flow have therefore very limited physical content, they are rather concerned with the computability of such flows.

From a physical point of view, arguments for the instability of transonic potential flows against time dependent disturbances have been advanced by Kuo and others. These arguments disregard a stabilizing effect on acoustic wave propagation in the flow, essentially dependent on its two-dimensional nature. This stability mechanism for unsteady disturbances in a shock-free transonic flow is demonstrated.

It can be claimed, in spite of earlier criticism, that the use of potential flow theory in the transonic region is, both mathematically and physically, as respectable, as it is anywhere else in aerodynamics.

Notation

c	-	propagation speed of small disturbance
c_o	-	stagnation value of c
J	-	determinant of rate of strain tensor $\nabla \bar{q}$
M	-	Mach number q/c
n	-	curvilinear coordinate normal to streamline
q	-	flow velocity
$\bar{q}$	-	flow velocity vector
$\bar{r}$	-	unit vector normal to wave front
s	-	curvilinear coordinate along streamline
$\bar{t}$	-	unit vector tangential to wave front
α	-	wave front inclination with respect to velocity vector
γ	-	specific haats ratio
θ	-	flow angle
ω	-	wave front local rate of turning

Transonic shock-free flow, fact or fiction ?

by G.Y. Nieuwland x) and B.M. Spee x)

National Aerospace Laboratory NLR, Amsterdam, Netherlands.

1 Historical introduction.

In his preface to the Symposium Transsonicum (Aachen 1962, ref.1), Oswatitsch explains that " ... Those concerned with the transonic controversy are split in two camps with different points of view. Rigorous proofs which could settle the controversy have not yet been found".

There is not much point in attempting a documented reconstruction of the two positions involved, but it is probably fair to state the most widely held one as follows :

1) The basic assertion was, that experimentally only transonic flows involving shock waves were found, at least when a well developed supersonic region was present, say for M_{loc} max > 1.1.
2) Theoretically, examples of transonic potential flows can be constructed, exhibiting shock free recompression from the supersonic flow region back to subsonic flow speed. However, if 1) was true, one had to suppose that these solutions were unstable in some sense.
3) For this instability, two complementary explanations were given. The first explanation was sought in the mathematical fact, that a transonic potential flow solution, if it exists for some particular aerofoil shape, can be blown up by an arbitrarily small perturbation of the part of the contour bounding the supersonic region (Busemann, ref.2; Morawetz, ref.3). Secondly, the argument was advanced that the development in time of a perturbed transonic potential flow around a fixed profile would be unstable, as upstream running perturbations would increase exponentially with time in the supersonic recompression region of the flow (Kuo, ref.4; Werner, ref.5). Both these arguments conveyed the suggestion of the collapse of a potential flow solution into the supposedly standard, stable, transonic flow solution with a shock.

Against this often rather agressively held position, the defenses put up by the other camp were, one feels, rather weak; as it now turns out, perhaps unnecessarily so. While the opponents gradually left their trenches to partake in more fashionable activities than the at that time rather out-moded transonic aerodynamics, the whole picture was changed by Pearcey and his group at the NPL. Having first experimentally sorted out the highly complex viscous phenomena in the transonic speed range (see ref.6), he next evolved the concept of the "peaky" pressure distribution" (ref.7), and showed that in fact, a for all practical purposes shock free transonic flow could experimentally be realised.

The first opportunity of systematically confronting transonic potential theory and experiment for aerofoil flows, came with the development of the theory of quasi-elliptical aerofoils at NLR (refs. 8, 9).

As a survey of the existing experimental information has very recently been given (ref. 10), we will here restrict to pointing out the main facts. The purpose of the present paper is to demonstrate that the fundamental theorems on the mathematical "non-existence" of transonic potential flow due to Busemann and Morawetz, together with some recently discovered facts about the time dependent stability aspects, and the experimental data now available, provide on the level of present day knowledge a consistent physical picture of transonic flow in the high subsonic speed range. In our opinion this means that at any rate the old "transonic controversy" can be regarded as definitively settled.

---

x) Senior Research Engineer, Aerodynamics Division.

2 Experimental facts.

Although now several examples of theoretical solutions for the transonic potential flow around lifting quasi-elliptical aerofoils are available, the experimental evidence is at present entirely based on symmetrical aerofoils. The reason is simply that these were much earlier available. This is, however, not at all a serious limitation, as long as the aim is a basic investigation of the stability of the shock-free supersonic region. As the transonic effects are purely local, one would not expect to miss anything worthwile this way. From an experimental point of view, the symmetrical flow has important benefits. The absence of large wall interference and boundary-layer effects on circulation makes the interpretation of the experimental results easier and more reliable.

Two examples will be discussed. The aerofoil shape, theoretical design pressure distribution and shape of the sonic line are given in fig.1a, b. These examples were taken from the collection of ref.11, and are designated as (0.1-0.675-1.6) and (0.115-0.75-1.2). The first one is a 16 % thick aerofoil with design Mach number M_∞ = 0.745, having a peaky pressure distribution with a maximum local Mach number M_{max} = 1.47. The other is 11 % thick and has a peaky pressure distribution with a secondary expansion just in front of the suction peak, the design Mach number being M_∞ = 0.806 and the maximum local Mach number M_{max} = 1.26.

Fig.2a, b shows the comparison between theory and experiment at the design condition for the 16 % thick aerofoil. In fig. 2a the pressure is plotted against the chordwise distance measured from the leading edge, in fig. 2b against the aerofoil ordinate normal to the chord. The experimental design Mach number is somewhat higher (0.002) than the theoretical value, in accordance with the estimated blockage effect in the wind tunnel.

The discrepancies between experiment and theory are due to model imperfections and boundary layer effects. The slight underexpansion in the supersonic region, leading to a very weak shock wave, is caused mainly by a small laminar separation bubble at 8 % chord, free transition being at 12 %.

Fig.3 shows a shadowgraph picture of the flow around the 16 % thick aerofoil at the design condition, with the theoretical shape of the sonic line drawn in. The shadowgraphs were obtained with a short duration spark exposure that arrests upstream-moving disturbances. The distrubances form sharp pressure fronts at these speeds.

The appearance of laminar separation bubbles is a consequence of the relatively low Reynolds number (2.10^6) of the tests. These separations would undoubtedly disappear at full-scale Reynolds numbers. The only way to avoid separation effects in the wind tunnel is by fixing the transition point of the boundary layer. This, however, has an unfavourable effect on the agreement between theory and experiment. The transition strip generally disturbs the flow by generating a weak shock wave.

A still better agreement between theory and experiment has been found for the 11 % thick aerofoil, as shown in fig. 4a, b for a Mach number which is considerably higher than the design Mach number. The reason for the very good agreement in this particular case is the absence of separation. For Mach numbers close to the design value there is a relatively large separation bubble in the laminar boundary layer. At slightly higher Mach numbers, however, this separation bubble disappears. The agreement leaves little to be desired. On the basis of pressure plots and optical observations, the flow is really shock-free.

Having thus settled the design case, the next question of interest is the sensitivity of these flows, more generally their off-design behaviour. Fig. 5 demonstrates the development of shocks both below and above the design point for the 11 % thick aerofoil. The relevant shadowgraphs are given in fig. 6a, b and c. These data show the shock-free design condition embedded in a family of flows involving shock waves. Similar results have been obtained for small variations in angle of incidence.

From these data, and also from the response of the flow to things like transition strips, one can get the impression of a great sensitivity of these flows. In a sense, of course, this is true. Yet in another sense, the flows are rather insensitive. In fig. 7 the dependence of the drag coefficient on Mach number is given for the 16 % thick aerofoil, which shows that although there are shocks in off-design conditions, the wave drag remains negligible in a rather large interval. In fact, this 16 % thick aerofoil has a higher drag rise Mach number than the 12 % thick NACA 0012 aerofoil.

The following conclusions may said to constitute "physical significance" of the transonic potential flow solutions in the engineering sense.

1. The differences between experiment and theory are due to model imperfections and boundary layer effects. The results suggest that the theoretical potential flow can be approached arbitrarily close if these effects are eliminated.
2. The shock-free design condition is embedded in, and can be reached in a stable manner from, the neighbouring conditions involving shocks. In a usefully large interval of conditions, the wave drag remains negligible.

3 Mathematical problems.

Having reviewed this experimental material, it is perhaps useful to spend a few remarks on the interpretation of the famous Morawetz theorems, which have been regarded as providing the key to a physical understanding of these flows.

Very roughly, the content of one of these theorems is as follows. Consider a given transonic potential flow solution describing a profile flow, for instance a quasi-elliptical aerofoil flow. This solution can also be regarded as the solution of a boundary value problem for the equations for plane compressible potential flow, with the given aerofoil shape and the free stream as boundary conditions. Next, perturb the profile contour by an arbitrarily small amount in the supersonic region, and Morawetz proves that now no solution to the boundary value problem exists. In contrast to the subsonic flow case, a transonic potential flow is "not continuously dependent on the boundary data".

From the physical point of view, we must side with Busemann et al., and conclude - on the principle that nature does not jump - that the boundary value problem in potential flow theory is not a physically adequate model for a real transonic flow. In other words, the basic assumption of strict irrotationality makes the transonic flow too rigid a fabric to be smoothed around an arbitrary shape. But we must own the other side, that we cannot logically reverse this conclusion in the sense that if we try to model a given theoretical solution in a wind tunnel, the resulting type of flow is necessarily drastically different. The results of the last section show that this is not the case.

If, however, we had to discuss the physical significance of potential flow solutions in the strict mathematical sense, as opposed to the engineering sense of "adequate" agreement between theory and experiment, we would have to study viscous compressible flow solutions in the limit $Re \longrightarrow \infty$, and also the unsteady variant of these in the limit $t \longrightarrow \infty$. The problem would be to investigate under what conditions these solutions would have a potential flow as the limiting case. This problem is far beyond the power of the available mathematical methods, even for incompressible flow; therefore the physical significance of potential flow solutions at any flow speed is at the moment in the strict sense, an entirely open problem.

If, for a moment, we would be allowed to venture into the realm of science fiction, and speculate what at some distant future date the physical significance of transonic potential flow solutions might look like, we would get something as follows. In accordance with Morawetz' theorems, we would expect that in general, no transonic irrotational flow limit would exist for a viscous solution as $Re \longrightarrow \infty$, except for a very special set of isolated "admissible" contours, which would admit a potential flow limit at one particular Mach number each. If then we could prove, that for such Mach numbers the discrepancy between a viscous flow solution and a transonic potential flow solution could be made arbitrarily small for Re sufficiently large and an aerofoil shape sufficiently near an "admissible" one, we would have obtained a mathematical concept of physical significance which would cover todays experimental data.

Returning to fact rather than fiction, we must conclude that the import of Morawetz's theorem is computational rather than physical, as it states the impossibility of constructing transonic flow solutions for a given aerofoil by posing a direct boundary value problem in the physical plane for the equations for potential flow. Accordingly, the potential flows around quasi-elliptical aerofoils were mathematically defined in a quite different, inverse way; alternatively, modern developments of numerical methods for the direct problem do not make use of the equations for potential flow but include simulated viscosity terms. In conclusion we might say that the problem of the physical significance of transonic potential flow solutions is in the mathematical sense essentially an open problem, but not (at the moment) a controversial one.

4 Unsteady aspects.

A second line of argument against the physical existence of shock free transonic flows was based on the supposed unstability of these flows as a result of unsteady waves moving upstream into the supersonic region. This argument was developed by Kuo (ref.4), and also mentioned by Holder (ref.6). In its briefest outline, the argument was that such waves, when superimposed on a steady shock free basic flow could move upstream as long as the local steady flow speed was subsonic, but as they entered the region of supersonic local flow speeds would necessarily come to a standstill, coalesce, and interact with the basic flow until a stationary shock wave was formed.

It is clear from the experiments discussed in section 2 that this does not, in fact, happen, but we can also give a simple physical explanation why it does not.

Let us first perform a numerical, or rather graphical, experiment. We take a transonic quasi-elliptical aerofoil flow, and at time $t = 0$, generate an acoustic pulse at the trailing edge. Knowing the velocities in the outer flow field, we can easily construct by Huygens' principle, the development in time of the wave front moving locally at a sonic relative speed. The picture we get in this way is sketched in fig.8. What happens is that the wave front, in the gradient field of the basic flow, turns over in such a way, that on entering the supersonic region, the wave front is everywhere inclined at an angle with the local flow velocity larger than the local characteristic angle. This means that the component of the flow velocity normal to the wave front is everywhere smaller than the sonic value, and so the wave front moves locally as if in a subsonic flow. Far from coming to a standstill, the wave moves upstream with respect to a stationary observer, at an even faster rate in the supersonic region than in the subsonic part downstream.

Now this is only one particular case, and we can ask whether this property holds generally. A simple analysis shows that the answer is in the affermative. Let $\bar{q}$ be the local velocity vector, c the local velocity of sound, and $\bar{t}$ and $\bar{r}$ unit vectors tangential and normal to the wave front. The local rate of turning ω of the wave front can be expressed as

$$\omega = \text{grad } c \cdot \bar{t} + \bar{t} \cdot \nabla\bar{q} \cdot \bar{r} \tag{1}$$

If now we express the rate of strain tensor $\nabla\bar{q}$ in a local reference frame along and normal to the streamline, we have

$$\nabla\bar{q} = \begin{pmatrix} q_s & q_n \\ q\theta_s & q\theta_n \end{pmatrix}, \tag{2}$$

with q and θ as local velocity and flow angle. In irrotational and isentropic flow we have the equations for continuity and irrotationality in this frame :

$$\begin{aligned} (1 - M^2)\, q_s + q\theta_n &= 0 \\ q_n - q\theta_s &= 0 \end{aligned} \tag{3}$$

The local propagation speed of the wave is

$$c' = c\,(1 - M\sin\alpha\,), \tag{4}$$

where α is the angle of the wave front with respect to the local velocity vector, and the local speed of sound is connected with q by :

$$\frac{q^2}{2} + \frac{c^2}{\gamma - 1} = \frac{c_o^2}{\gamma - 1} \;. \tag{5}$$

Now if a wave front would be stationary, we would have $c' = 0, \omega = 0$. The first of these relations means, of course, that the wave front is aligned along a characteristic. To see whether in that case also $\omega = 0$ is possible, we substitute the relation $c' = 0$ in eq.(1), and using eqs (2), (3), (4), (5) we obtain :

$$\omega = -\frac{q\theta_s}{M^2}\left(2 - \frac{3-\gamma}{2}M^2\right)\left(1 - \frac{q_n}{q\theta_s}\sqrt{M^2 - 1}\right). \tag{6}$$

If we have $\omega > 0$, this means that the wave front is rotating into the "safe" direction, i.e. the interval of wave angles in which the local velocity component normal to the wave front is subsonic (fig.9). Now it follows that $\omega > 0$ obtains if

$$\theta_s < 0 \, , \tag{7a}$$

$$M^2 < \frac{4}{3 - \gamma} \, , \tag{7b}$$

$$\frac{q_s}{q\theta_s} < \frac{1}{\sqrt{M^2-1}} \, . \tag{7c}$$

Condition (7a) expresses convexity of the aerofoil in the supersonic region, (7b) says that the local Mach number should be smaller than 1.58 for $\gamma = 1.4$, and expression (7c) means that the Jacobian of the hodograph transformation

$$J = \frac{\partial (u,v)}{\partial (x,y)} < 0 \, ,$$

and this is always the case in the class of analytic hodograph flows(ref.9,App.C)and we could at most have $J = 0$ at an isolated point of the contour of a general aerofoil.

We have then, that the waves are locally always turning into the safe direction, and some further reflection (ref.12) shows this to mean, that all unsteady waves must traverse the supersonic region in a finite time. This turning effect of disturbance waves was disregarded in Kuo's semi-one-dimensional instability arguments, and is in fact the reason why these two-dimensional flows behave differently from the stability point of view than one-dimensional diffuser flows do.

We would like to add one remark on condition (7b). Laitone (ref.1) has conjectured, that $M = 2\,(3 - \gamma)^{-\frac{1}{2}}$ would be the maximum possible local speed in a transonic flow. It is easy to see (ref.12) that a transonic flow with a higher local Mach number is unstable against unsteady disturbances, and so these cannot physically be realised. On the other hand we have as yet not been able to prove that such flows cannot be found, although for quasi-elliptical aerofoils the record stands today not higher than $M_{max} = 1.54$.

5 Conclusion.

Shock-free transonic flow : fact or fiction ? The answer depends obviously on one's definition of what is "shock-free". Probably nobody would care to deny, that in every real transonic flow, shock phenomena could be detected if scrutinised closely enough.

From the engineer's point of view, however, much more interesting is the fact, that agreement between potential flow theory and experiment can be obtained within all practical limits, if the experiment is conducted with sufficient care. Moreover, the flow changes into off-design conditions in an entirely smooth and stable way, and the wave drag remains negligible in a promisingly large interval of neighbouring conditions.

From the mathematician's point of view, the problem would be to decide what sense transonic potential flow solutions could be regarded as an asymptotic limit of solutions of the equations for viscous compressible flow. Unfortunately, it looks as if this problem will remain open for some considerable time.

From the physicist's point of view, the essential difference between the stability behaviour of transonic one-dimensional, and a two-dimensional flow has been clarified, so that we now can understand how a "shock free" flow stays alive.

6 References.

1. Oswatitsch, K.(ed.) — Symposium Transsonicum, IUTAM Symposium, Aachen 1962. Berlin (1964).

2. Busemann, A. — The nonexistence of transonic potential flow, in : M.H. Martin (ed.), Fluid dynamics, New York (1953).

3. Morawetz, C.S. — On the non-existence of continuous transonic flows past profiles II. Comm.Pure Appl.Math. vol 10, pp.107-131 (1957).

4. Kuo, Y.H. — On the stability of two-dimensional smooth transonic flows. Journ.Aer.Soc. vol.18, pp. 1-6 (1951).

5. Werner, W. — Instabilität stoszfreier transonischer Profilströmungen. ZAMM, vol 41, pp.448-458 (1961).

6. Holder, D.W. — Transonic flow past two-dimensional aerofoils. J.R.Aero.Soc., vol 68, pp.501-516 (1964).

7. Pearcey, H.H. — The aerodynamic design of section shapes for swept wings; in : Advances in Aeronautical Sciences, vol 3, London (1962).

8. Nieuwland, G.Y. — Theoretical design of shock-free, transonic flow around aerofoil sections, in : J. Bradbrooke et al. (eds.), Aerospace Proceedings 1966, London (1967).

9. Nieuwland, G.Y. — Transonic potential flow around a family of quasi-elliptical aerofoil sections.NLR-TR T.172 (1967).

10. Spee, B.M. — Experimental verification of shock-free transonic flow around quasi-elliptical aerofoil sections. Lecture presented at 6th ICAS-Congress, Munich, Sept.1968.

11. Boerstoel, J.W. — A survey of symmetrical transonic potential flows around quasi-elliptical aerofoil sections.NLR-TR T.136 (1967).

12. Spee, B.M. — On the stability of two-dimensional transonic flows. NLR-TN T.182

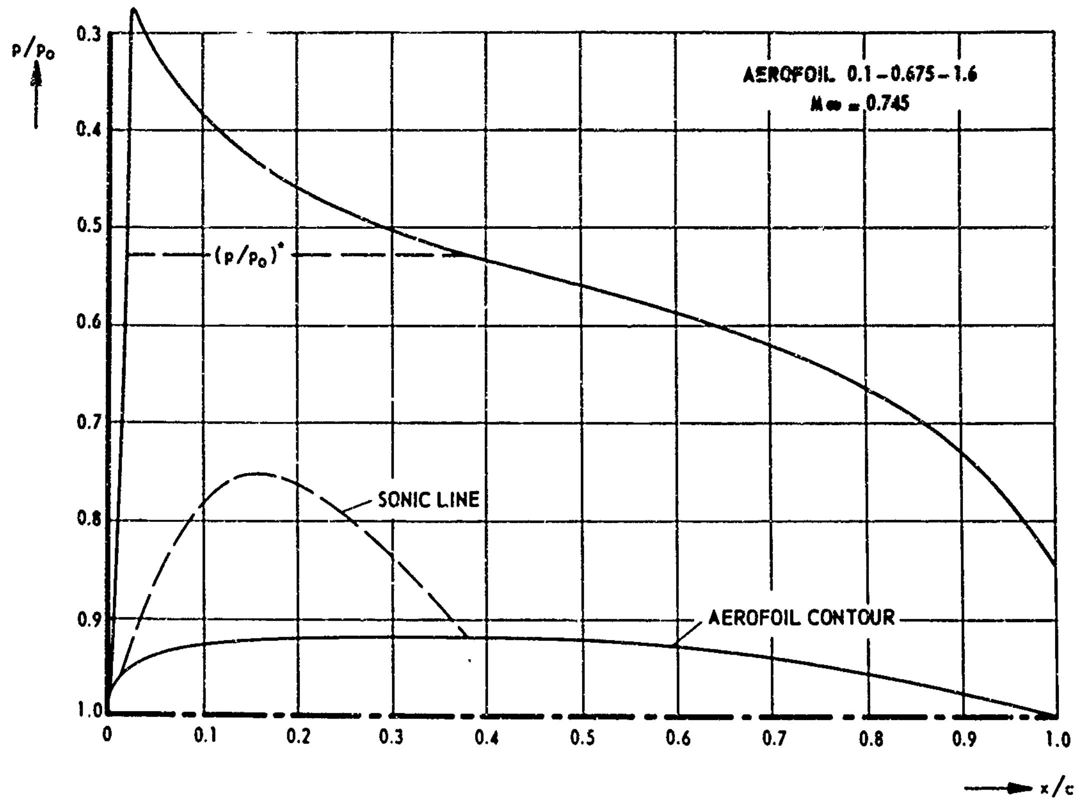

a) aerofoil 0.1-0.675-1.6

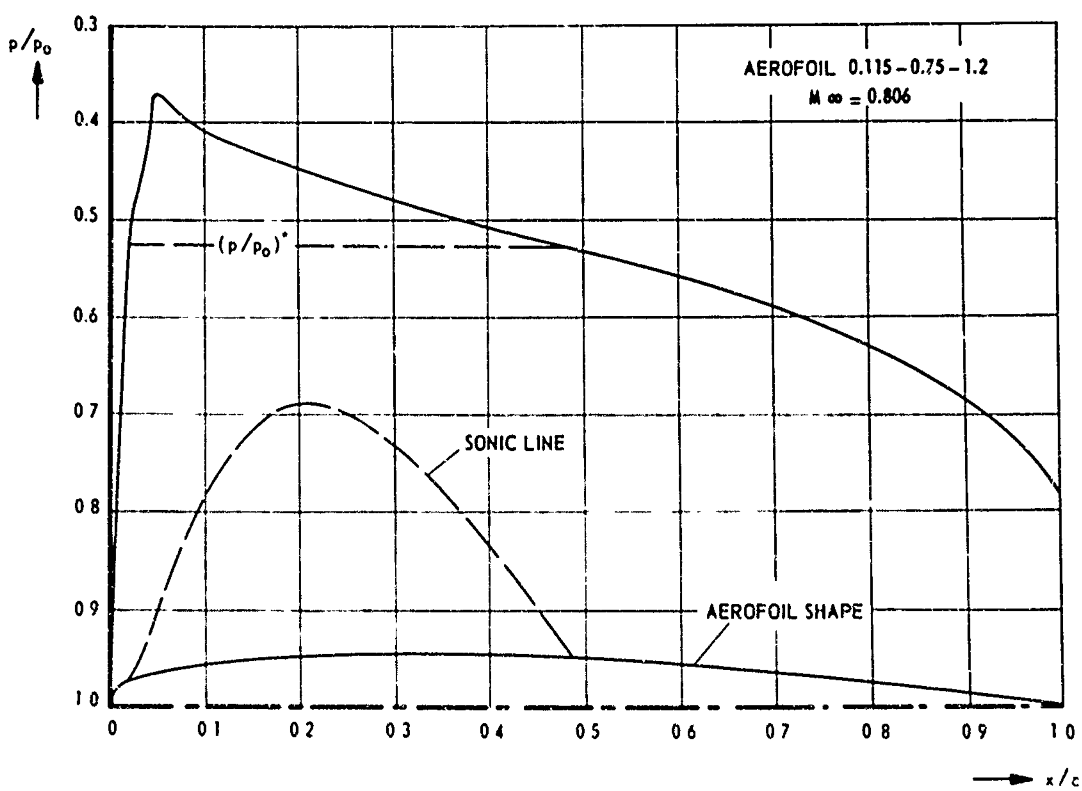

b) aerofoil 0.115-0.75-1.2

Fig.1 Transonic potential flow around quasi-elliptical aerofoil.

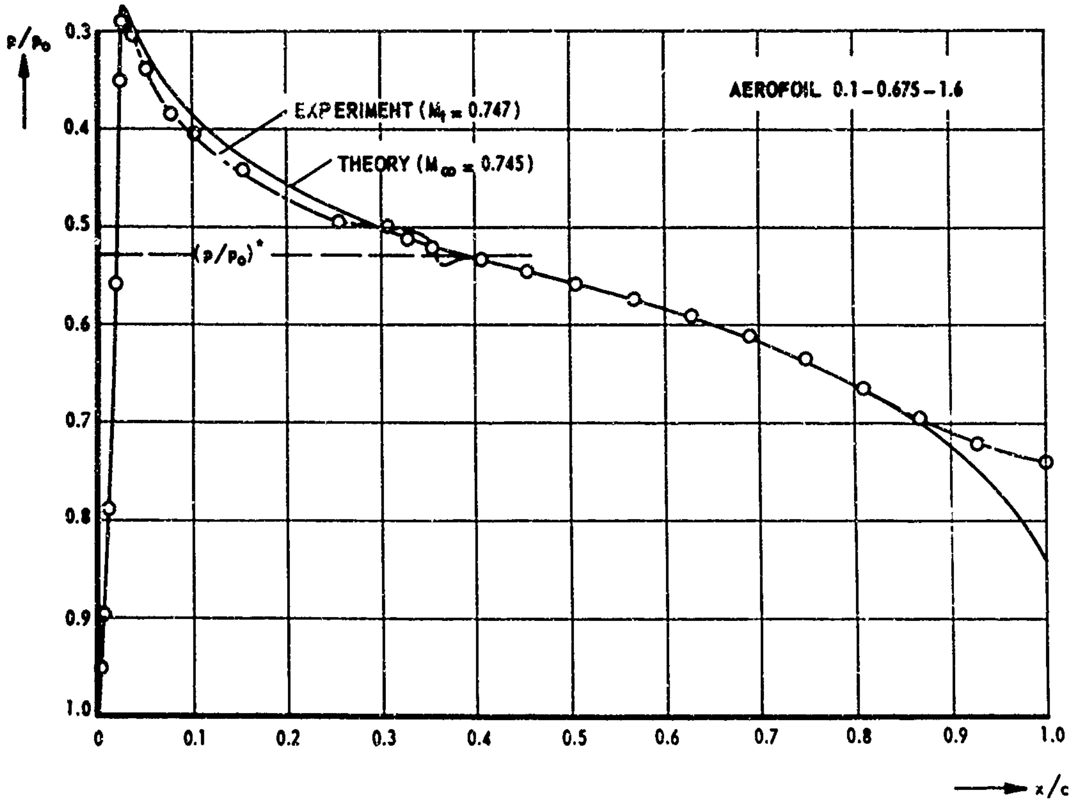

a) pressure distribution versus x/c

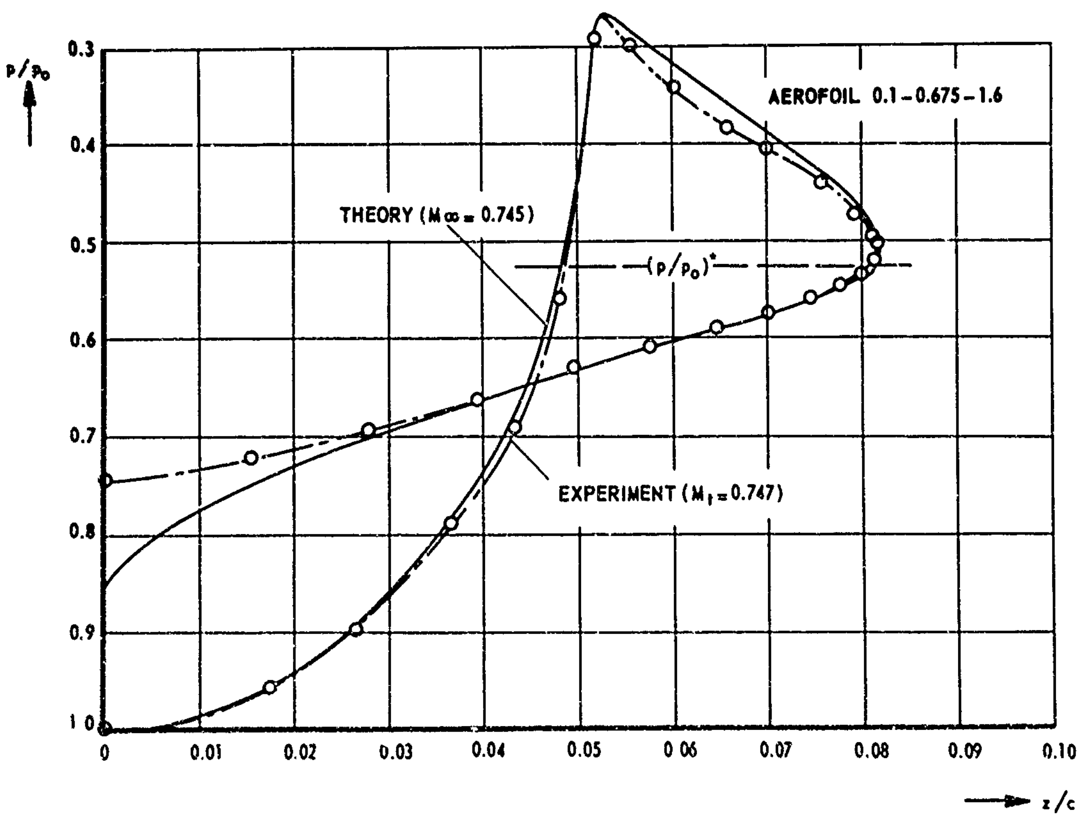

b) pressure distribution versus z/c

Fig.2 Comparison between theory and experiment, aerofoil 0.1-0.675-1.6.

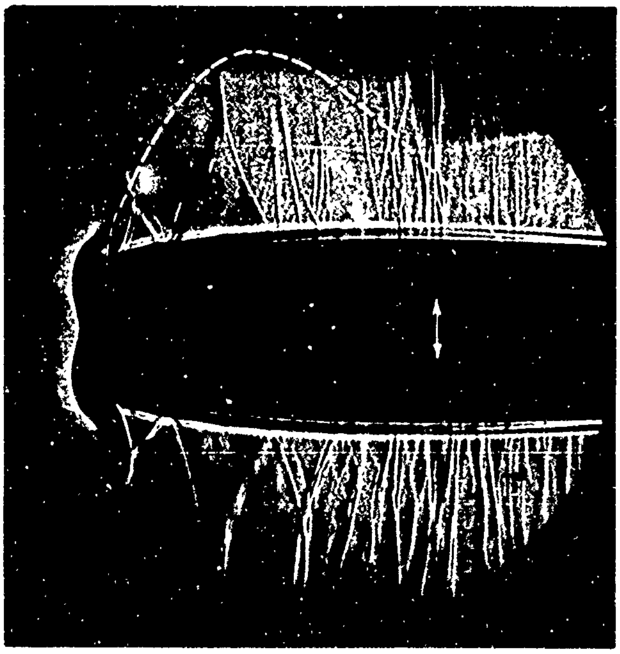

Fig.3 Shadowgraph of flow around aerofoil 0.1-0.675-1.6, design condition.

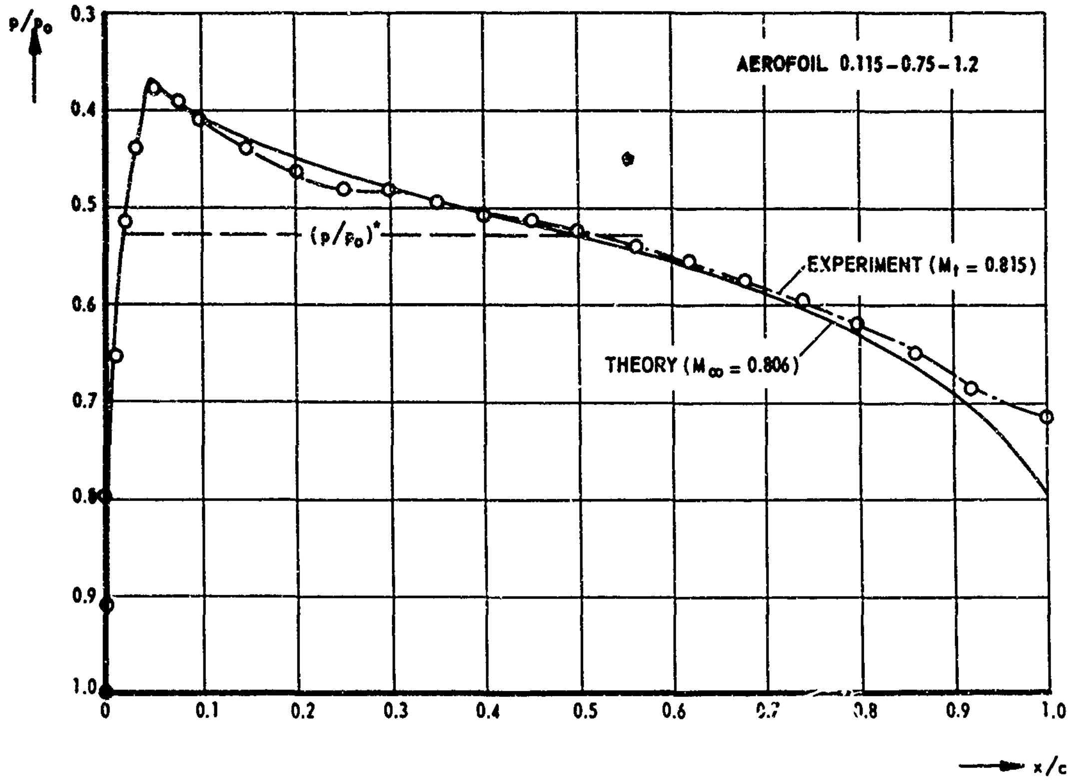

a) pressure distribution versus x/c

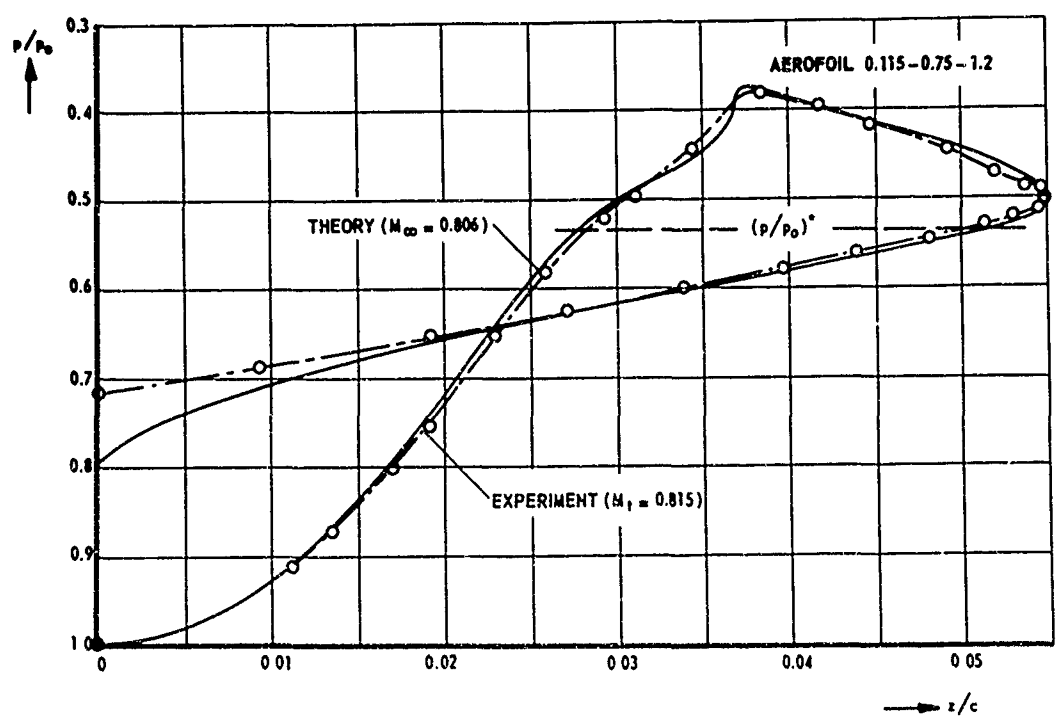

b) pressure distribution versus z/c

Fig.4 Comparison between theory and experiment, aerofoil 0.115-0.75-1.2.

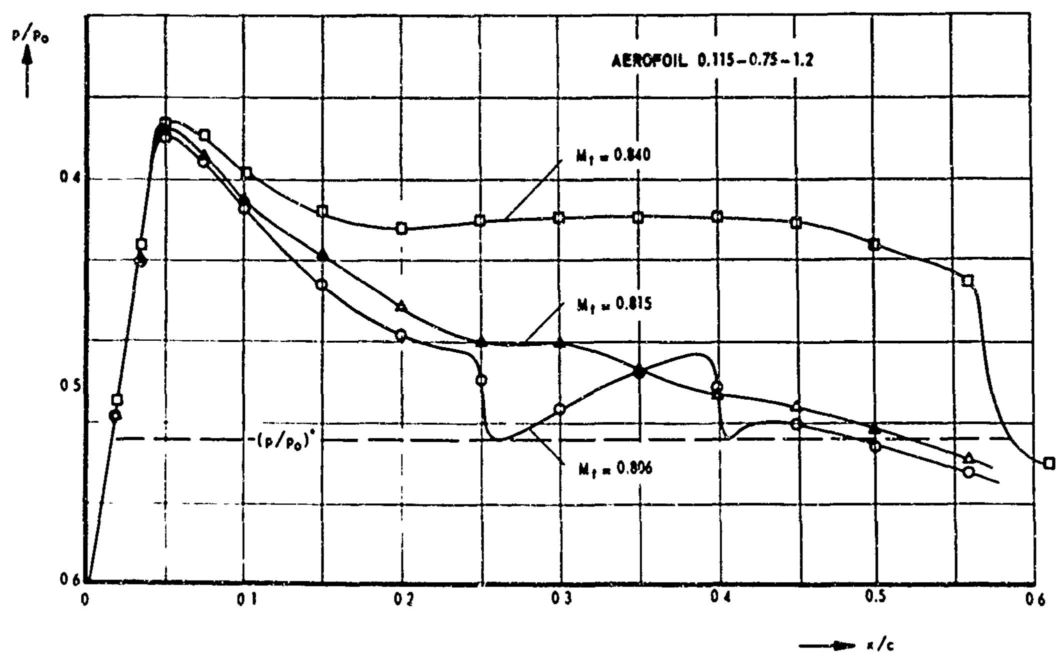

Fig.5 Shock development in off-design conditions, pressure distribution, aerofoil 0.115-0.75-1.2.

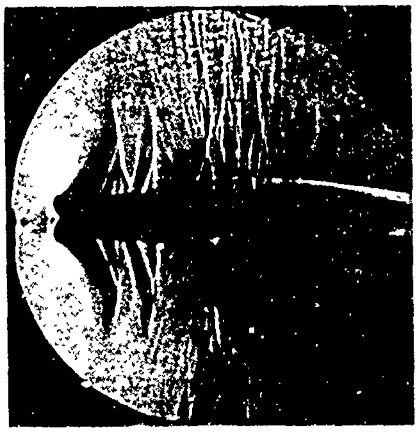

a) M_t = 0.806

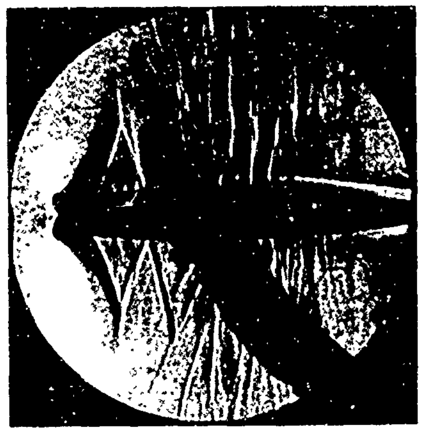

b) M_t = 0.815

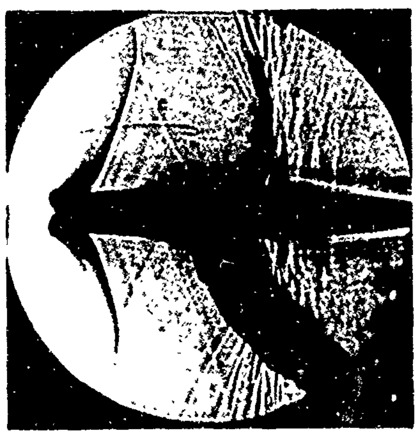

c) M_t = 0.840

Fig.6 Shock development in off-design conditions, shadowgraphs aerofoil 0.115-0.75-1.2.

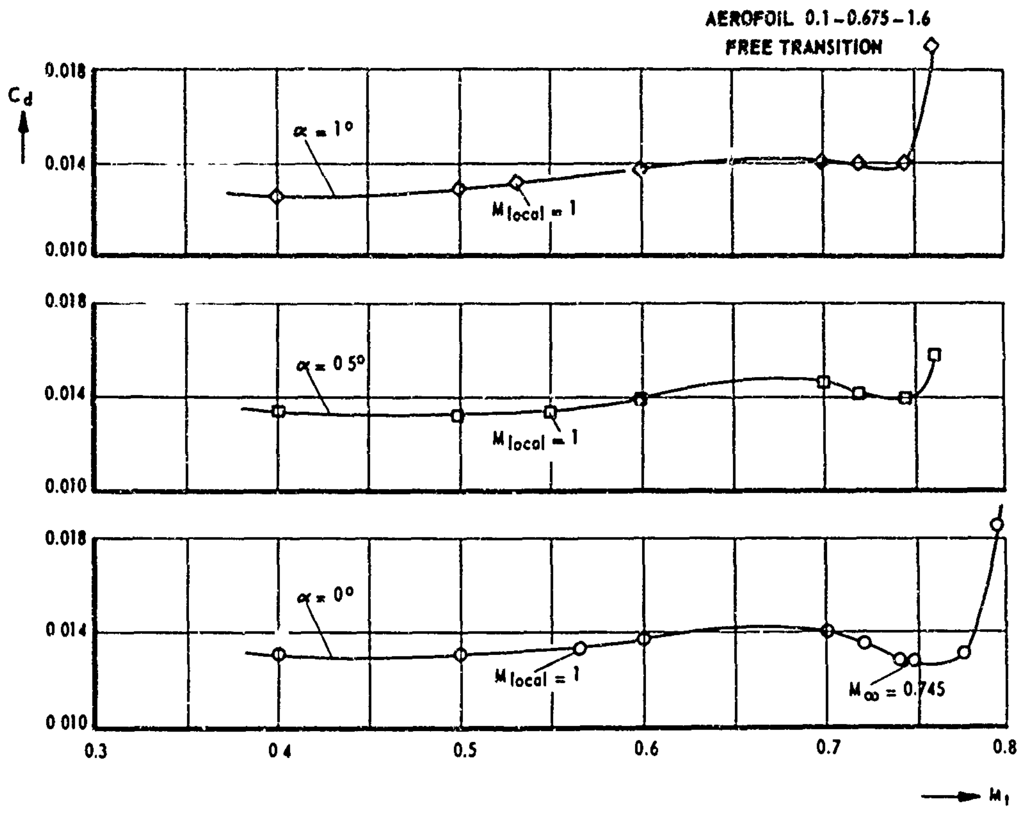

Fig.7 Drag characteristics aerofoil 0.1-0.675-1.6.

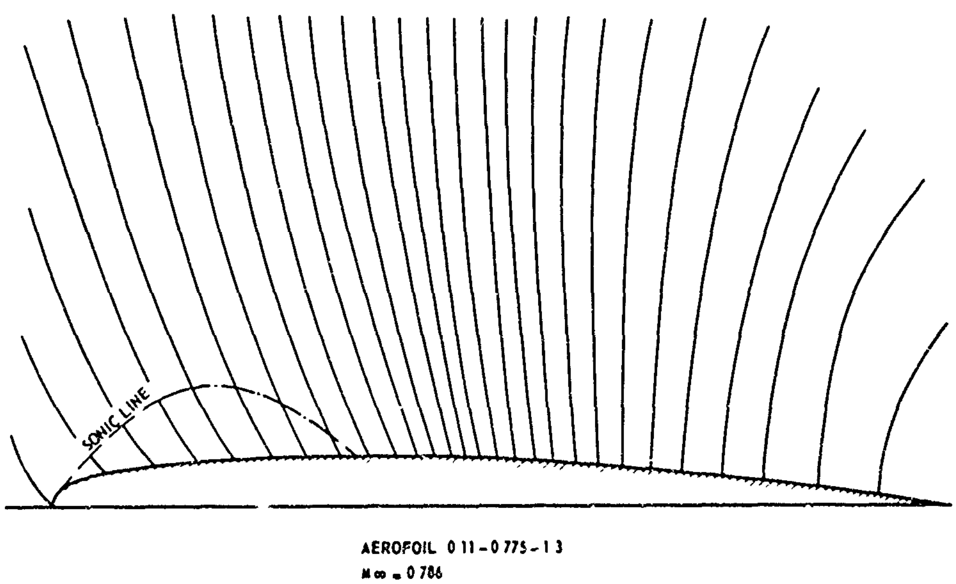

Fig.8 Acoustic wave propagation in transonic potential flow.
Wave front constructed at constant time intervals.

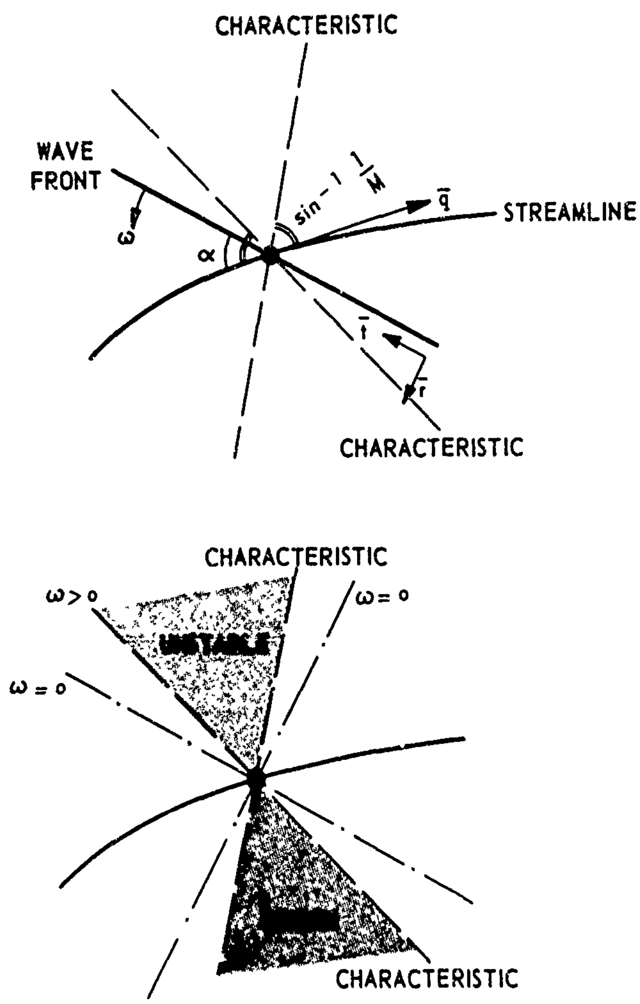

Fig.9 Acoustic wave propagation in locally supersonic region.
Turning effect on wave front.

Lax-Wendroff Difference Scheme Applied to the Transonic Airfoil Problem

Robert E. Singleton

Lockheed-Georgia Company, Marietta, Georgia

Summary

A numerical method is developed for solving the unsteady-flow equations for the flow of a nonconducting, inviscid gas around an arbitrary profile. The governing equations are differenced by a two-step, Lax-Wendroff scheme, and steady-state solutions are sought in the limit of long times. Boundary conditions are numerically prescribed and the Lax-Wendroff method is shown to give near-steady-state, subsonic Mach number distributions after a few hundred time steps. The method gave results for transonic flow with a shock wave for the one case considered. This matter is being further investigated with a more accurately given airfoil. The procedure requires large computer memory and long computer runs.

Lax-Wendroff Difference Scheme Applied to the Transonic Airfoil Problem+

Robert E. Singleton*

Lockheed-Georgia Company, Marietta, Georgia

I. Introduction

The mathematical complexities associated with the transonic potential flow over arbitrary profiles are well known; however, the usefulness of a successful method continues to inspire researchers to look for methods of solution. One heretofore unexplored possibility is to circumvent some of the mathematical complexities by bringing the tremendous capabilities of modern high-speed computers to bear on the problem. This paper attempts to accomplish this task by developing a numerical procedure for the transonic potential flow over a non-lifting, arbitrary profile to be solved on a high-speed computer.

The governing equations describing the conservation of mass, momentum and energy for the unsteady flow of an inviscid, nonconducting gas are written in divergence-free form. By retaining the unsteady terms, these partial differential equations remain hyperbolic, even when the flow is of a mixed type containing both supersonic and subsonic regions. The steady-state solution is sought asymptotically as time approaches infinity. This procedure is also desirable because the shock-wave relations are contained as a special case of the governing equations, provided weak solutions are allowed. Consequently, the shock wave is considered as part of the solution and not as a predetermined interior boundary. To mention a few references, Godunov et al.(1), Burstein(2), and Bohachevsky et al.(3) have all developed this procedure for two-dimensional, supersonic, blunt-body flows. Thommen(4) has treated the viscous supersonic flow over a flat plate using this approach, Burstein(5) has studied supersonic flow in a constricted channel, and Thommen and D'Attore(6) apply this technique to three-dimensional supersonic flow fields. Quite recently, Yoshihara(7) reported successful results for the transonic flow with shock waves over a circular-arc profile.

Apparently the application of unsteady numerical methods for generating steady-state solutions is quite wide, and this paper is concerned with the application of this technique to blunt, two-dimensional non-lifting profiles. The geometry of the profile is chosen to be one of Nieuwland's(8) isentropic compression profiles found by using the hodograph method. The governing equations are differenced by a modified two-step Lax-Wendroff difference scheme which is quite similar to the scheme used by Thommen(4). The boundary conditions at the airfoil surface are satisfied by a multiple reflection technique, and the boundary conditions at the outer edge of the mesh were adjusted to allow unsteady effects to pass through.

The following sections of this paper describe first the actual formulation of the equations and techniques to be used. Secondly, the preliminary results are given and the indicated modifications to the program are discussed. The next section deals with the final results obtained and the final section gives the conclusions from this research.

II. Formulation of the Method

The coordinates for the chosen airfoil section are given to the nearest one thousandth by Nieuwland(8) who also gave the Mach number distribution over this airfoil, found by using the hodograph method. A Cartesian coordinate system is used, with all lengths made dimensionless with the airfoil chord length. The front stagnation point of the airfoil is located at $x = 3.8$, $y = 3.0$. The calculation grid is distributed in the area $1 \leq x \leq 7.6$, $3.0 \leq y \leq 4.96$. Since the airfoil is symmetric and non-lifting, only the upper surface of the airfoil is considered. Thus, the calculation grid extends 1.96 chord lengths normal to the airfoil and 2.8 chord lengths in front of and behind the airfoil. Although the choice of mesh size is a difficult decision to make prior to the calculations, it was decided to let $\Delta x = 0.06$ for $1 \leq x \leq 7.6$, $\Delta y = 0.04$ for $3.0 \leq y \leq 3.08$, $\Delta y = 0.06$ for $3.08 \leq y \leq 3.20$, and $\Delta y = 0.08$ for $3.20 \leq y \leq 4.96$. This initial choice for the grid has 2,997 points. The Courant-Friedrichs-Levy condition for stability as derived from linearized analysis gives a guide for establishing the time step. It is easy to show that if

$$\frac{\Delta t}{\Delta} \leq \frac{M_\infty}{1+M_{max}}\left[1+\frac{\gamma-1}{2}M_\infty^2\right]^{-\frac{1}{2}} ,$$

where $\Delta \equiv \Delta x$ or Δy, M_{max} = maximum local Mach number, M_∞ = freestream Mach number, then the Courant-Friedrichs-Levy condition is certainly satisfied. Recognizing that this requirement for stability can serve only as a guide to nonlinear problems, a Δt of .008 was chosen such that the above condition would be generously satisfied for reasonable values of M_∞, M_{max}, γ and Δ.

+This paper resulted from work sponsored by Aerospace Research Laboratories, Office of Aerospace Research, United States Air Force under Contract AF 33(615)-5397.

*Scientist, Lockheed Georgia Research Laboratory; Lecturer, School of Aerospace Engineering, Georgia Institute of Technology.

The governing equations of motion are next considered by letting c = chord length of airfoil, ρ' = gas density, u', v' = gas velocity components, E' = internal plus kinetic energies per unit volume, $m' = \rho' u'$, $n' = \rho' v'$. Then by defining dimensionless variables

$$x' = cx\,,\; y' = cy\,,\; m' = \rho_\infty U_\infty m\,,\; n' = \rho_\infty U_\infty n\,,\; u' = U_\infty u\,,\; v' = U_\infty v$$

$$p' = \rho_\infty U_\infty^2 p\,,\; \rho' = \rho_\infty \rho\,,\; E' = \rho_\infty U_\infty^2 E\,,\; t' = \frac{c}{U_\infty} t\,,$$

the conservation of mass, momentum, and energy for an inviscid, nonconducting gas can be written

$$W_t = F_x + G_y$$

where the subscript denotes differentiation and W, F, and G are vectors defined by

$$W = \begin{bmatrix} \rho \\ m \\ n \\ E \end{bmatrix} ; \quad F(W) = \begin{bmatrix} -m \\ \frac{\gamma-3}{2}\frac{m^2}{\rho} - (\gamma-1)E + \frac{\gamma-1}{2}\frac{n^2}{\rho} \\ -\frac{mn}{\rho} \\ -\frac{\gamma E m}{\rho} + \frac{\gamma-1}{2}\frac{m^3 + mn^2}{\rho^2} \end{bmatrix} ; \quad G(W) = \begin{bmatrix} -n \\ -\frac{nm}{\rho} \\ \frac{\gamma-3}{2}\frac{n^2}{\rho} - (\gamma-1)E + \frac{\gamma-1}{2}\frac{m^2}{\rho} \\ -\frac{\gamma E n}{\rho} + \frac{\gamma-1}{2}\frac{n^3 + nm^2}{\rho^2} \end{bmatrix} .$$

These partial, nonlinear, differential equations are differenced by the two-step Lax-Wendroff method to obtain a second-order accurate difference scheme. This scheme is similar to those difference schemes given by Thommen(4) and Burstein(2) and is given below. Let $W^k_{i,j} = W(t + k\Delta t, x + i\Delta x, y + j\Delta y)$, then

$$W^{k+\frac{1}{2}}_{i\pm\frac{1}{2},j} = \frac{1}{2}\left(W^k_{i,j} + W^k_{i\pm1,j}\right) + \frac{\Delta t}{2}\,\frac{F^k_{i\pm1,j} - F^k_{i,j}}{x_{i\pm1} - x_i} + \frac{\Delta t}{4}\,\frac{\left(G^k_{i,j+1} + G^k_{i\pm1,j+1} - G^k_{i,j-1} - G^k_{i\pm1,j-1}\right)}{y_{j+1} - y_{j-1}}$$

$$W^{k+\frac{1}{2}}_{i,j\pm\frac{1}{2}} = \frac{1}{2}\left(W^k_{i,j} + W^k_{i,j\pm1}\right) + \frac{\Delta t}{2}\,\frac{G^k_{i,j\pm1} - G^k_{i,j}}{y_{j\pm1} - y_j} + \frac{\Delta t}{4}\,\frac{\left(F^k_{i+1,j} + F^k_{i+1,j\pm1} - F^k_{i-1,j} - F^k_{i-1,j\pm1}\right)}{x_{i+1} - x_{i-1}}$$

$$W^{k+1}_{i,j} = W^k_{i,j} + 2\Delta t\,\frac{F^{k+\frac{1}{2}}_{i+\frac{1}{2},j} - F^{k+\frac{1}{2}}_{i-\frac{1}{2},j}}{x_{i+1} - x_{i-1}} + 2\Delta t\,\frac{G^{k+\frac{1}{2}}_{i,j+\frac{1}{2}} - G^{k+\frac{1}{2}}_{i,j-\frac{1}{2}}}{y_{j+1} - y_{j-1}} .$$

The physical boundary conditions are that uniform flow conditions exist far from the airfoil, and the normal velocity on the airfoil is zero. However, since the grid system is finite and the flow field is unsteady, the boundary conditions around the outer edge of the mesh system are not well defined. Along the incoming boundary, $x = 1$, $3.0 \le y \le 4.96$, the flow is specified as uniform, freestream flow. Although this specification of the boundary condition does not allow for unsteady effects, results of the calculation showed that only very small disturbances reached the forward boundary, and these small disturbances apparently caused no problems.

Along the upper boundary, $1 \le x \le 7.6$, $y = 4.96$, it was first specified that $m = 1$, and the other three variables were determined by backward linear interpolation in the y-direction. It was thought that, in this manner, the freestream pressure would be maintained along the upper boundary. However, the results of several long-time runs indicated that unsteady effects were not getting through the upper boundary but were propagating back into the flow field near the airfoil and causing a divergence there. By specifying a backward linear interpolation in the y-direction on m also, this problem was eliminated. The boundary conditions on the downstream boundary $x = 7.6$, $3.0 \le y \le 4.96$ were set by backward linear interpolation in the x-direction on all variables. The line of symmetry was specified by symmetrically reflecting ρ, m, and E and antisymmetrically reflecting n across the line $1 \le x \le 7.6$, $y = 3.0$.

The application of boundary conditions along general curved surfaces is always a difficult problem in numerical analysis. The curved airfoil surface of interest here is no exception, but considerable effort was exerted to devise a suitable scheme based on the reflection principle. To illustrate the technique, a mesh point which lies outside the airfoil but with a neighboring mesh point, either a Δx or Δy away, lying inside the airfoil is considered. The current value of the vector W at the outside point is denoted W_0, and likewise the current value of the vector W at the inside point is denoted W_i. The line joining the inside and outside points cuts the airfoil surface at a unique point where the slope is dY/dx. The distance from this point on the airfoil surface to the outside mesh point is denoted by L_1 and the distance from this point to the inside mesh point is denoted by L_2. The W_i is determined as a function of W_0 by requiring that the linear interpolation for the velocity normal to the airfoil surface at the point of intersection on the airfoil surface be zero. The values for the velocity tangential to the airfoil surface at the intersection point on the airfoil as well as ρ and E are taken as being the same as the corresponding values at the outside point. These conditions are satisfied by setting

$$W_i = \begin{bmatrix} 1 & 0 & 0 & 0 \\ 0 & \dfrac{1-\frac{L_2}{L_1}\left(\frac{dY}{dx}\right)^2}{1+(dY/dx)^2} & \dfrac{\frac{dY}{dx}\left(1+\frac{L_2}{L_1}\right)}{1+(dY/dx)^2} & 0 \\ 0 & \dfrac{\frac{dY}{dx}\left(1+\frac{L_2}{L_1}\right)}{1+(dY/dx)^2} & \dfrac{\left(\frac{dY}{dx}\right)^2-\frac{L_2}{L_1}}{1+(dY/dx)^2} & 0 \\ 0 & 0 & 0 & 1 \end{bmatrix} W_0$$

This technique requires the calculation of the airfoil slope, dY/dx, at the intersection point. At first, this was accomplished by looking in the given coordinate table, finding the nearest two points on either side of the intersection point and calculating the slope from this linear approximation. Later the procedure was modified as will be described in the next section. Also, since several outside mesh points can share the same inside mesh point, multiple storage capability at each inside point must be allowed for.

It was assumed that initial conditions could be arbitrarily chosen subject to compatibility with the boundary conditions. The first calculations which were performed were done with uniform, freestream flow specified at all interior points of the mesh, i.e.

$$W^0_{i,j} = \begin{bmatrix} 1 \\ 1 \\ 0 \\ \frac{1}{2} + \frac{1}{\gamma(\gamma-1)M_\infty^2} \end{bmatrix}$$

Since the equations are independent of the Mach number, the initial conditions and the boundary conditions on the incoming boundary are the only places where the Mach number enters the calculations.

III. Preliminary Results

Having written a computer program for the above equations together with their boundary and initial conditions, computations were carried out first on an IBM 7094 computer and then later with a Univac 1108. A long-time run of 250 time steps was made with $M_\infty = 0.704$ and a $\Delta t = .008$. The results for the surface Mach number distribution are shown in Figure 1 along with a plot of the airfoil surface. The calculations diverge at K = 250 at x = 4.54, as results at earlier values of K demonstrate.

In view of the results of Burstein[2], it was perhaps not surprising that the calculations did diverge, as Burstein showed that one might suspect instabilities to occur in the vicinity of stagnation points and sonic lines. Since Burstein used a pseudo-viscous term to achieve stability in his case, a similar effort was made for the present case. To damp oscillations which might be generated, an artificial viscosity, tailored after Burstein's model, was developed and added to the basic difference scheme. However, the inclusion of the pseudo-viscous term did not prevent the divergence of the resultant calculations. Moreover, a wide variety of values for the rate of increase of damping, the maximum value of the damping, and the time step were tried with little improvement in the results.

At this point, it was suspected that the divergent character was perhaps a result of very poor accuracy in the transonic range coupled with very crude initial conditions. To study this idea, a long-time run of 800 time steps was made with zero viscosity for $M_\infty = 1/2$. Figure 2 shows the results to be converging to a subsonic solution; however, some oscillations or "wiggles" appear in the Mach number distribution.

The results obtained for $M_\infty = 0.5$ at $K = 800$ were then modified by letting

$$\left[E^{800}_{i,j}\right]_{M_\infty=.5} \frac{\left[\frac{1}{2} + \frac{1}{\gamma(\gamma-1)M_\infty^2}\right]_{M_\infty=.6}}{\left[\frac{1}{2} + \frac{1}{\gamma(\gamma-1)M_\infty^2}\right]_{M_\infty=.5}} = \left[E^{0}_{i,j}\right]_{M_\infty=.6}$$

for all i and j, and then these results are used as initial conditions for $M_\infty = 0.6$. After a few hundred time steps of calculations, the results were similarly modified to get initial conditions for $M_\infty = .656$ and then similarly for $M_\infty = 0.707$. Figure 3 shows that this approach to the transonic regime yields better results than before; however, it also appears that the oscillations which appeared in the subsonic distribution grow to substantial amounts at transonic speeds and thus prohibit any meaningful results.

In order to get better results, several modifications to the existing computer program were made. First, the calculations demonstrated an inability of the existing mesh size to resolve the flow field accurately in the vicinity of rapid flow changes, i.e., the nose region. Consequently, the mesh was made more dense over the front half of the airfoil by inserting eight more vertical lines between $x = 3.82$ and $x = 4.30$, which resulted in 224 additional mesh points. The method of representing the airfoil by linear interpolation between given tabular points was examined by comparing the resulting airfoil ordinates and slopes with the theoretical ordinates and slopes given by Nieuwland. The ordinates and slopes calculated by the computer program were found to be accurate to the nearest hundredth, while Nieuwland's theoretical values were given to the nearest thousandth. Hence, the computer program was modified to do fifth order polynomial interpolation for the airfoil ordinates and slopes were computed from this interpolation polynomial. This procedure gave ordinates and slopes at least as accurate as Nieuwland's data.

Next, attention was given to the numerical problem of determining the dependent variables at non-mesh points from information given at the mesh points. For example, if the Mach number is given at the mesh points close to the airfoil surface, what is the Mach number on the airfoil surface? This problem is illustrated in Figure 4. In Figures 1, 2, and 3, the Mach number at x_3 (see Fig. 4) was determined by a linear extrapolation of the Mach number at points 5 and 3. However, this procedure does not take into account the flow field variables at points 2 and 4. Clearly, the Mach number at some point on the surface between x_1 and x_4 should be some sort of suitable average of the Mach numbers at points 1, 2, 3, and 4. Consequently the Mach numbers at x_1, x_2, x_3, x_4, denoted by M_1, M_2, M_3 and M_4, are computed by a linear interpolation between the flow quantities at the points 1, 2, 3, and 4 and their respectively associated flow quantities at the interior point. The resultant Mach numbers are then averaged as are the four abscissas to give a Mach number at a specific point on the airfoil. This procedure for calculating the Mach number on the airfoil surface allows the surface Mach number to depend on a surrounding region rather than on a verticle needle.

IV. Final Results

With these modifications, several calculations were performed for a freestream Mach number of 0.5. The results indicated the need for three more changes in the boundary points describing the airfoil surface. The first two given ordinates for the airfoil nose were not sufficiently close to allow an accurate approximation by a fifth-order polynomial. Consequently, a parabola was fit to the nose section from which additional data were generated. The trailing edge presented another problem as the theoretical trailing edge was a cusp and not a stagnation point. Since it was not known how to simulate a cusp numerically, the trailing edge was treated as a stagnation point. Also, it was noticed that when mesh points in the flow field occurred very close to the airfoil surface, the calculations diverged at those points after about 50 time steps. This implies that $L_1 \to 0$ and consequently very large elements appear in the reflection matrix. In fact, it was found that if L_2/L_1 exceeded about 10, divergence occurred. Apparently, an L_2/L_1 exceeding 10 implies that the effective Δ is reduced so much at the boundary that the Δt is too large for stability. To correct such a situation the verticle mesh lines on the front and rear of the profile must be shifted somewhat to insure that L_2/L_1 is not large.

Having made all the necessary modifications, calculations were once again begun for a freestream Mach number of 0.5. Figure 5 shows the results after 800 time steps and the near-steady state solution has apparently been reached. termining initial conditions as described previously, calculations have also been done for $M_\infty = 0.6$ and 0.704. Figure 6 gives the results for $M_\infty = 0.704$ after 1200 time steps and Table 1 illustrates the changes which occur in the Mach number distributions for increasing time.

The results shown in Figure 6 are quite interesting as a shock wave is apparently predicted. The steady-state solution is more slowly approached than for purely subsonic flow, but Table 1 shows that changes in the Mach number distribution with time-step are quite small after about 1000 time steps. The shock wave is smeared out over about three mesh widths as is characteristic of Lax-Wendroff methods. The shock wave is situated around $x = 4.3$ which is approximately the position of the downstream sonic point predicted by Nieuwland. The discrepancy between Nieuwland's results and the calculated values are apparently due to inaccuracies in the definition of airfoil geometry. It is now known that airfoil ordinates accurate to five decimal places must be furnished to enable the accurate determination of the surrounding potential flow field. In fact, in view of Morawetz's[9] well known analytical work, it would not be too surprising if slight deviations from Nieuwland's isentropic profile did produce a shock wave. It is also interesting to note that the computations show the well known small region of increased flow velocity behind the shock wave in transonic flow over profiles.

V. Conclusions

The Lax-Wendroff difference scheme is apparently capable of predicting both subsonic and transonic flow fields over arbitrary profiles. For subsonic flow, the near-steady-state solution is obtained after several hundred time steps. For transonic flow, the near-steady state solutions require an order of magnitude more time steps. The true steady-state solution, of course, would require many hundreds of time st ps; however, most of the transient effects become negligible after the first several hundred time steps. The method of prescribing the boundary conditions apparently functioned well. A check of the parallel flow requirement at the airfoil surface was performed at intervals of 50 time steps, and it was found that no mass flow was crossing the airfoil surface. The boundary conditions around the outer boundaries of the mesh also caused no difficulties and apparently maintained uniform freestream flow at the entrance boundary without creating large disturbances in the flow field.

The results given in Figure 6 indicate that it would be very interesting to use the Lax-Wendroff method for a profile which is determined accurately to five decimal places, and to see the result when the freestream Mach number increases. Such airfoil data have been given by Boerstoel[10] for a profile which exhibits shock-free transonic flow. This calculation is currently being done using the program described in this paper with one modification. The leading edge is now fit with a circular arc rather than a parabola. These results should be available in a few weeks and will be presented at the AGARD Specialists' Meeting in September.

To be practical, however, consideration must be given to the limits imposed by the computer. The existing program uses a Univac 1108 computer and requires about 50,000 storage locations. The program requires about 5.3 seconds per time step, which emphasizes the need for good initial conditions. Obviously, the program is expensive in terms of computer time and storage requirements. However, optimizing the current program could possibly reduce the running time by a factor of 2, and by the time the present method is developed for arbitrary lifting profiles, bigger and faster machines will be available[11], if past computer development is any clue to the future.

References

1. Godunov, S. K., Zabrodyn, Prokopov, G. P., "A Difference Scheme for Two-Dimensional Unsteady Problems of Gas Dynamics and Computation of Flow with a Detached Shock Wave," Zhurnal Vychyslitelnoi Matematiki i Matematicheskoi Fiziki, Vol. 1, No. 6, p. 1020, November-December 1961. Translated by I. O. Bohachevsky, Cornell Aeronautical Laboratory, Inc.

2. Burstein, S. Z., Finite Difference Calculations for Hydrodynamic Flows Containing Discontinuities, AEC Research and Development Report, NYO-1480-33, September 1965.

3. Bohachevsky, I. O., Rubin, E. L., "A Direct Method for Computation of Nonequilibrium Flows with Detached Shock Waves. I. Two Dimensional Flows," and Bohachevsky, I. O., Mates, Robert E., "II. Axisymmetric Blunt-Body at an Angle of Attack," presented at AIAA 2nd Aerospace Sciences Meeting, New York, Preprint No. 65-24.

4. Thommen, H. U., A Method for the Numerical Solution of the Complete Navier-Stokes Equations for Steady Flows, General Dynamics/Astronautics, San Diego, California, GDC-ERR-AN733, April 1965.

5. Burstein, S. Z., "Numerical Methods in Multidimensional Shocked Flows," AIAA Journal, Vol. 2, No. 12, p. 2111, December 1964.

6. Thommen, H. U., and D'Attorre, L., Calculation of Steady, Three-Dimensional Supersonic Flow-Fields by a Finite Difference Method, General Dynamics/Astronautics, San Diego, California, GDC-ERR-AN718.

7. Yoshihara, H., "Current Status of Transonic Flow Theories," presented at Short Course in "Special Topics in Transonic Aerodynamics," Space Institute, University of Tennessee, March 11-15, 1968.

8. Nieuwland, G. Y., The Computation by Lighthi l's Method of Transonic Potential Flow around a Family of Quasi-Elliptical Aerofoils, NLR-TR T.83, September 1964.

9. Morawetz, C. S., "On the Non-Existence of Continuous Transonic Flows past Profiles I," Comm. Pure and App. Math., Vol. IX, pp. 45-68, 1956.

10. Boerstoel, J. W., A Survey of Symmetrical Transonic Potential Flow around Quasi-Elliptical Aerofoil Sections, National Aerospace Laboratory NLR, NLR-TR T.136, November 1, 1967.

11. Paley, M. D., Scientific Research, p. 17, March 18, 1968.

TABLE I

MACH NUMBER DISTRIBUTION FOR $M_{\infty} = 0.704$

X	K			
	0	1000	1100	1200
3.8017	0.2313	0.2116	0.2091	0.2108
3.8338	0.8005	0.7487	0.7421	0.7443
3.8688	1.0774	1.0378	1.0328	1.0343
3.8846	1.0982	1.0528	1.0508	1.0513
3.9332	1.0389	1.0489	1.0526	1.0550
3.9702	1.0000	1.0391	1.0413	1.0464
4.0003	1.0333	1.1174	1.1167	1.1221
4.0302	1.0206	1.1514	1.1532	1.1614
4.0602	1.0243	1.1650	1.1682	1.1746
4.0902	1.0127	1.1763	1.1846	1.1912
4.1202	1.0122	1.1623	1.1700	1.1756
4.1501	1.0047	1.1723	1.1789	1.1893
4.1800	0.9995	1.1483	1.1507	1.1679
4.2099	0.9896	1.1684	1.1741	1.1833
4.2399	0.9822	1.1316	1.1359	1.1567
4.2698	0.9708	1.1981	1.2095	1.2010
4.3032	0.9636	1.0876	1.0851	1.0689
4.3590	0.9423	1.0463	1.0656	1.0433
4.4190	0.9222	0.9275	0.9160	0.9069
4.4873	0.8805	0.9271	0.9278	0.9406
4.5633	0.8126	0.9086	0.9087	0.8413
4.5937	0.7858	0.8625	0.8587	0.8096
4.6640	0.6985	0.7588	0.7546	0.7009
4.7377	0.5600	0.6081	0.6052	0.5757
4.7817	0.3981	0.4305	0.4283	0.4102

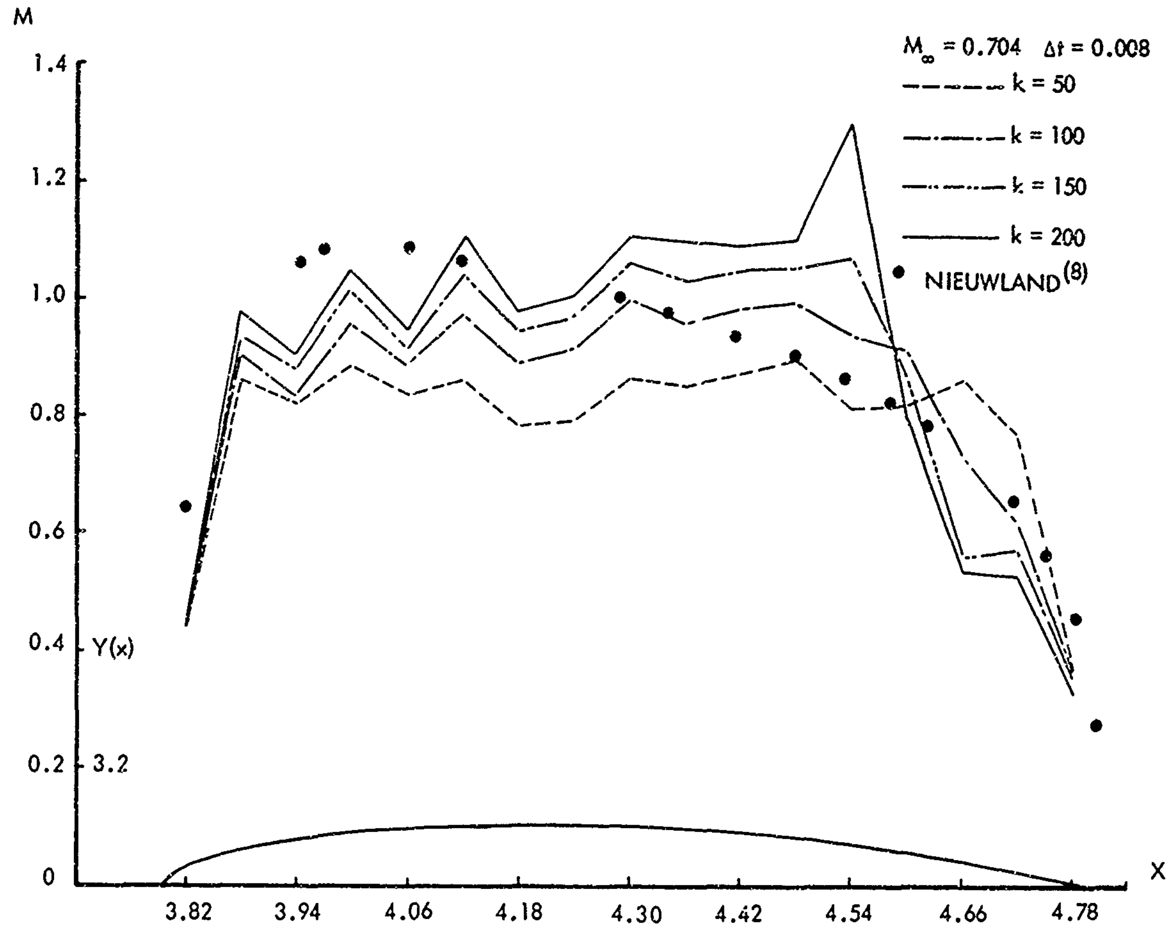

FIGURE 1. THE ONSET OF DIVERGENCE AT $M_\infty = 0.704$

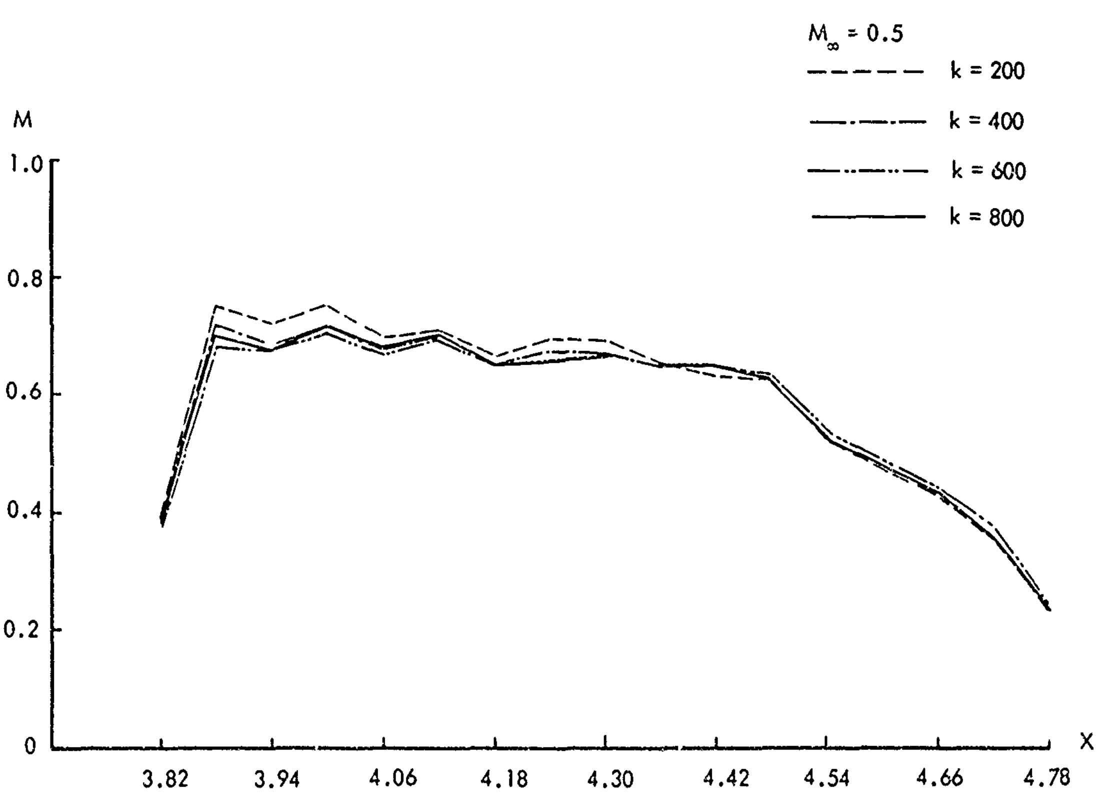

FIGURE 2. THE CONVERGENCE OF CALCULATIONS FOR WHOLLY SUBSONIC FLOW

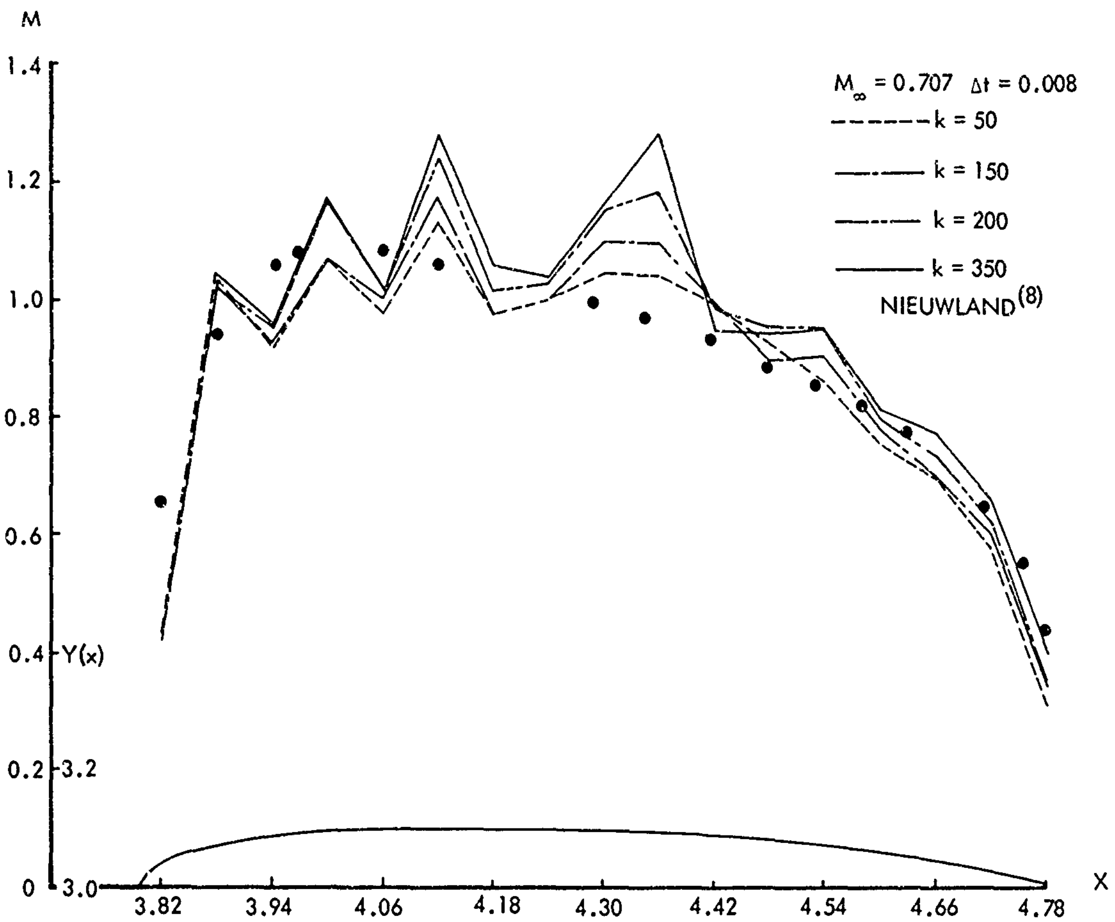

FIGURE 3. THE TRANSONIC FLOW CALCULATION SHOWING HOW OSCILLATIONS INCREASE

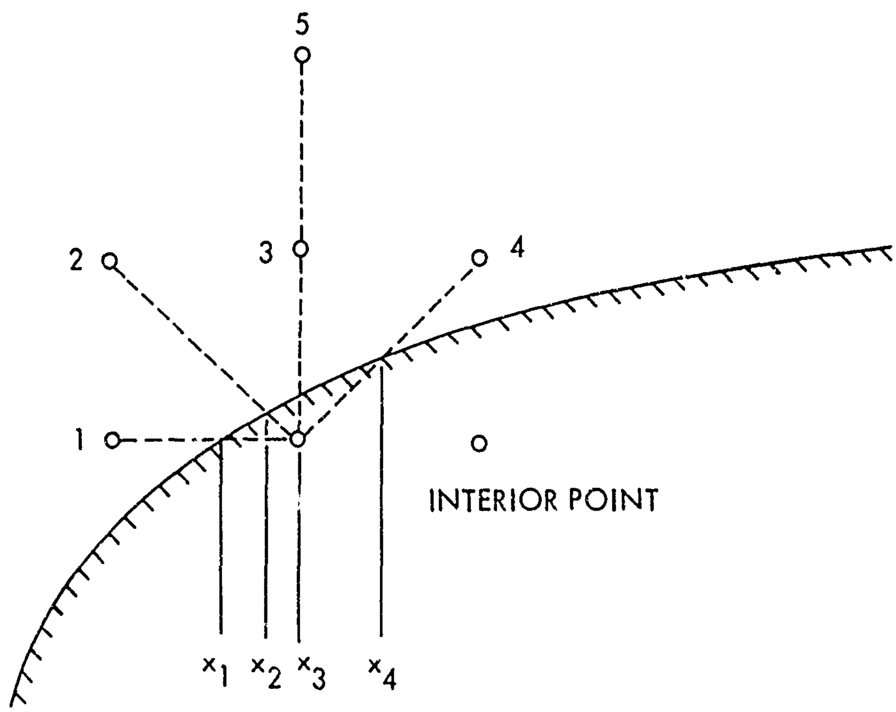

FIGURE 4. EXTRACTION OF MACH NUMBER ON AIRFOIL

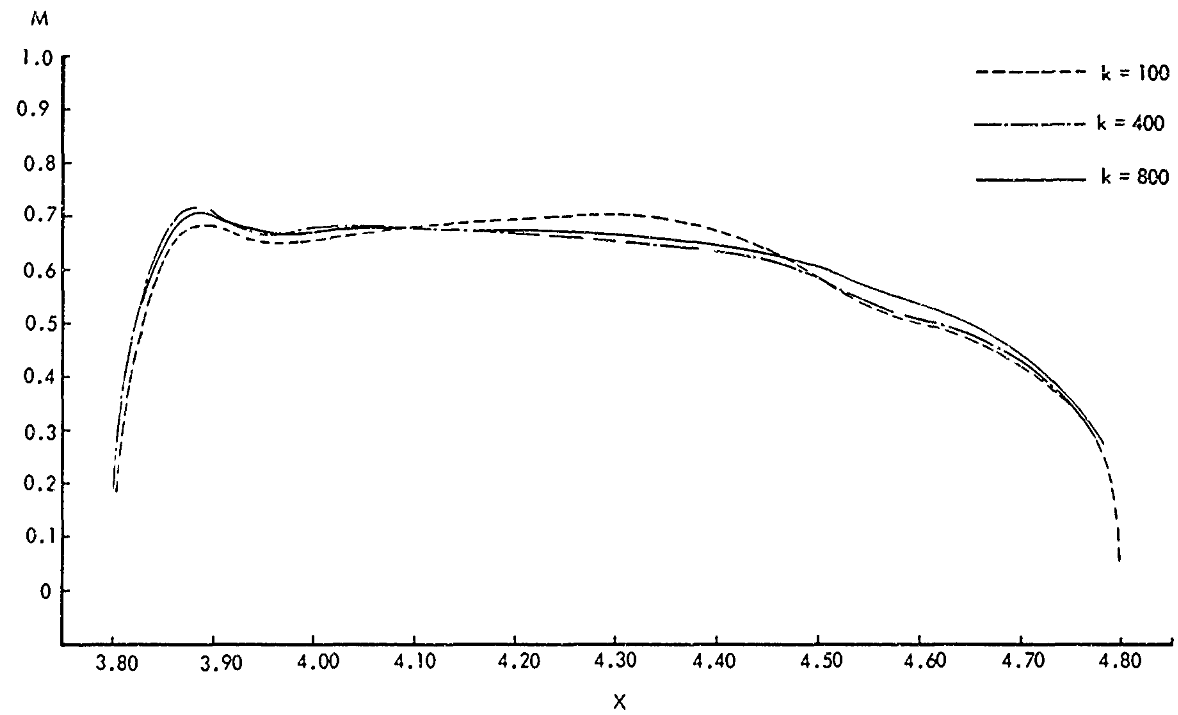

FIGURE 5. MACH NUMBER DISTRIBUTION FOR $M_\infty = 0.500$

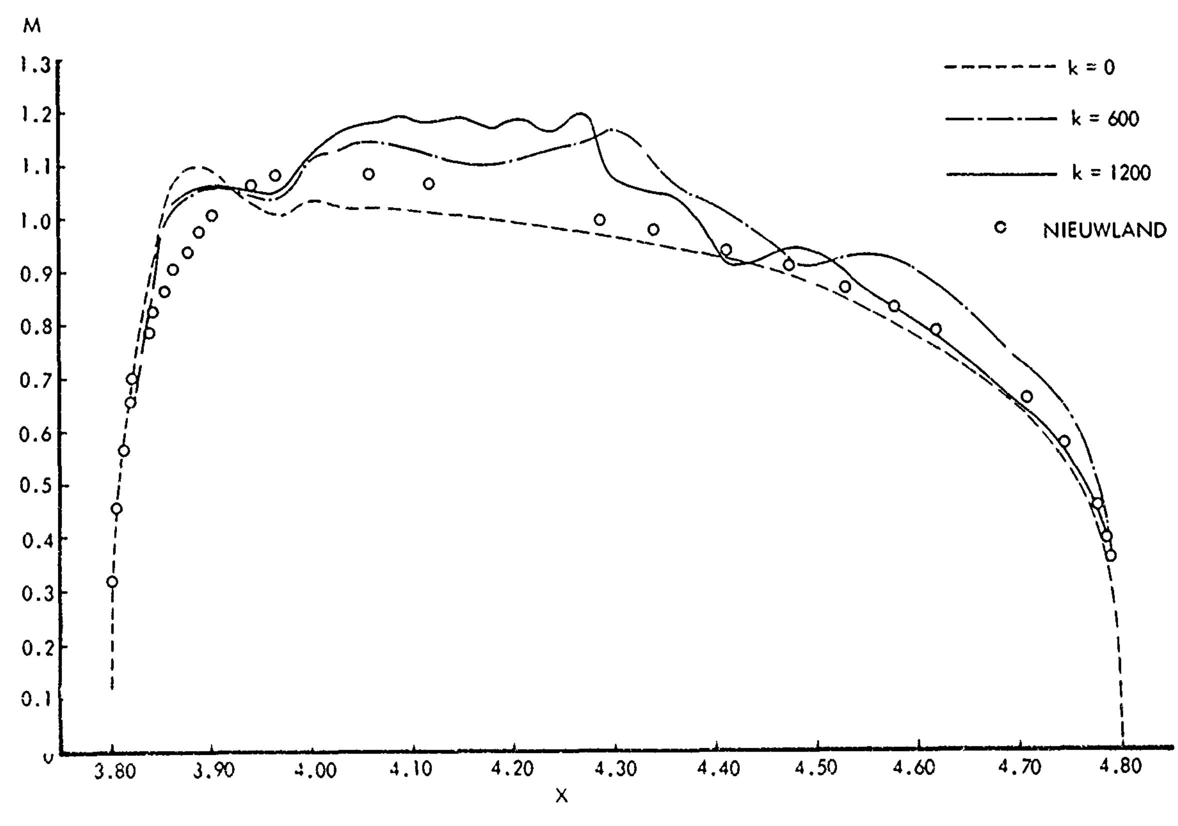

FIGURE 6. MACH NUMBER DISTRIBUTION FOR M 0.704

INVISCID SUPERCRITICAL AIRFOIL THEORY

R. Magnus, W. Gallaher, H. Yoshihara

Convair Division of General Dynamics
San Diego, California

SUMMARY

A procedure is presented to calculate the steady planar flow over a prescribed lifting profile. To obtain a properly-posed problem for the mixed elliptic-hyperbolic flow, an unsteady approach is used, where the desired steady flow is the asymptotic limiting flow for large times arising from a sequence of unsteady flows generated by placing a "leaky" profile in the desired uniform free stream (leakiness initially permitting the free stream to flow through the airfoil unhindered) and then impulsively turning off the leakiness. The resulting motion is calculated by a finite difference analogue of the unsteady Euler equations where a "diffusing" difference scheme is used. With this difference scheme an artificial viscosity is introduced by which shock waves acquire a steep profile appearing at their correct location with the proper jump conditions fulfilled. To obtain the required resolution, fine lattice mesh is embedded in the surrounding coarser mesh at the expected location of the shock wave, as well as about the leading edge. Two examples have been computed. The first is the flow at $M_\infty = 0.85$ over a biconvex airfoil of 8.4% thickness ratio at zero angle of attack, which is intended to demonstrate the ability of the procedure to evolve shock waves. Although the programmed procedures can treat a blunt-nosed profile at angle of attack, we consider instead, for the second example, a blunt-nosed shockless profile at zero angle of attack computed by Nieuwland and Boerstoel using the hodograph method. The intent here is to determine whether this shockless flow is stable, and remains indeed shockless after having been perturbed by the many unsteady disturbances introduced in the process of reaching a steady state.

1. INTRODUCTION

The design of a transonic aircraft frequently involves the consideration of a complex three-dimensional supercritical flow. Nevertheless in the wing design, planar flows play a significant role because of the large extent of such flow, either naturally present as in the case of a high aspect ratio wing, or produced by design as a result of a fuselage contouring to obtain favorable interference effects in the case of smaller aspect ratios. The resulting flow is a viscous one involving a turbulent boundary layer-normal shock interaction. This interaction is a strong interaction, disallowing the usual decoupling of the inviscid and viscid portions, so that an approximate interaction theory as that due to Gadd (Ref. 1) must be used prior to applying the usual iterative scheme. In the latter scheme, an essential ingredient will be the calculation of the overlying inviscid flow. It will be the purpose of the present paper to present an exact procedure to calculate such flows.

There presently does not exist a satisfactory procedure to calculate inviscid supercritical flows. There has been an extensive effort in England on semi-empirical methods characterized by the work of Sinnott and Osborne, but, despite their significant accomplishments, these methods fall short of desired requirements. Similarly the integral equation approach, first considered by Oswatitsch and subsequently expanded by many others, has had surprising success, but it has been unable to handle blunted, lifting profiles. There appears to be no simpler alternative than to start from the full Euler equations using a numerical procedure. The incompatible characteristics of subsonic and supersonic flows, as well as the problem of systematically locating the shock wave, would discourage a steady approach using the relaxation procedure, which inherently is a subsonic method. We shall therefore adopt an unsteady approach where the desired steady flow will be obtained as an asymptotic limit for large times by a marching procedure from a given initial flow. The marching procedure for the initial value problem is properly set for both subsonic and supersonic flows. Initially one will start from a uniform parallel flow corresponding to the free stream conditions. At zero time the boundary conditions representing the body will be impulsively "turned on." The consequent unsteady motion will then be treated using a finite difference analogue of the unsteady Euler equations where a "diffusing" difference scheme (to be described later) is used to approximate the partial derivatives. The use of this difference scheme gives rise to an inherent "artificial viscosity," similar in nature to that of Von Neumann and Richtmyer; and shock waves will acquire a profile, ceasing to be discontinuities, and will appear quite naturally at their proper location. There will thus be no special subroutine required to locate and treat shock waves.

To illustrate the above procedure we shall calculate two examples. The first is a preliminary effort intended to demonstrate the ability of the method to evolve the primary shock wave. For this case we shall consider a sharp-nosed biconvex profile at zero angle of attack. For the second example we shall recalculate one of the shockless flows obtained by Nieuwland and Boerstoel (Refs. 2 and 3) using the exact hodograph equations. Such shockless flows have been questioned by many (see, e.g., Refs. 4 and 5) who have concluded that these flows were unstable leading ultimately to flows with shocks. The purpose of the second example is to attempt to verify this instability (to the extent that one can by a numerical procedure) and to determine whether or not the resulting shock, if it indeed does arise, is weaker than for a comparable "nonoptimum" case. The shockless profile considered is blunt-nosed, symmetric, and nonlifting.

The unsteady procedure used above to calculate these examples is, however, able to handle general lifting profiles, but we shall defer the calculation and the reporting of these cases for a later time.

2. BASIC FLOW EQUATIONS AND AUXILIARY CONDITIONS

The starting point of the numerical approach is the set of Euler equations re-expressed in a conservation form as follows using the usual notations and a cartesian coordinate system

$$\frac{\partial \bar{W}}{\partial t} = \frac{\partial \bar{F}}{\partial x} + \frac{\partial \bar{G}}{\partial y}$$

where the vectors in component form are given by

$$\bar{W} = \begin{Bmatrix} \rho u \\ \rho v \\ \rho \end{Bmatrix} \qquad \bar{F} = -\begin{Bmatrix} \rho u^2+p \\ \rho uv \\ \rho u \end{Bmatrix} \qquad \bar{G} = -\begin{Bmatrix} \rho uv \\ \rho v^2+p \\ \rho v \end{Bmatrix}$$

and the coordinate x being in the free stream direction.

Since, in flows of interest, shock waves are sufficiently weak that one may assume an isentropic flow; thus,

$$p\,\rho^{-\gamma} = \text{Const.}$$

γ taken subsequently as 7/5.

For the boundary conditions, we require the flow to approach at all times a prescribed uniform flow sufficiently far from the airfoil, and at the airfoil we require the impulsive condition

$$(\vec{v} \cdot \vec{n}) \quad H(t) = 0$$

where

$$|\vec{v}| = +\sqrt{u^2 + v^2} \qquad \arg \vec{v} = \arc\tan \frac{v}{u}$$

$\vec{n}$, outward normal to the profile, and

$$H(t) = \begin{matrix} 0 & t < 0 \\ 1 & t \geq 0 \end{matrix}$$

At $t = 0$ we assume a uniform flow at the free stream conditions.

For the lifting case, the Kutta condition is enforced at the pointed trailing edge by requiring the flow in the vicinity of the trailing edge to be locally symmetric about a line bisecting the external angle at the trailing edge.

3. DIFFERENCE SCHEME

In the course of the studies attention has not been confined to a single type of finite difference scheme.

The results presented for the biconvex airfoil at zero angle of attack were obtained with a two step explicit finite difference scheme closely related to the procedure given by Lax and Wendroff, Ref. 6. The results presented for the blunt-nosed airfoil were obtained using a simpler one-step diffusion-stabilized explicit difference scheme for most of the computation field and an iterative implicit scheme to advance the solution in the extra fine mesh region around the airfoil nose.

Since the work being described is exploratory, various methods for satisfying boundary conditions, and applying initial conditions, need to be investigated. Therefore, in order not to be excessively troubled by instability of the computations due to severe starting conditions, or poorly chosen methods for applying boundary conditions, relatively simple difference schemes having easily controllable damping properties have been used. Stability and accuracy in difference schemes are qualities which are more-or-less exchangeable so a more accurate (and less stable) scheme will probably be used in future versions of the program.

4. FIRST EXAMPLE - BICONVEX AIRFOIL

To illustrate the procedure we shall first calculate the flow over a circular arc biconvex airfoil of 8.4% thickness ratio at zero angle of attack at a free stream Mach number of 0.85 in a closed channel. The purpose of this simple example is to examine the ability of the procedure to evolve the essentially normal shock. The simple mesh system was used for this example which is shown in Figure 1. In the dashed region a finer mesh was incorporated at a later time to obtain a better resolution of the shock wave.

It was found that the two-step difference scheme had insufficient damping to prevent a catastrophic instability of the calculation from occurring in the part of he field around the airfoil nose. The characteristic jagged response of the difference scheme to a strong disturbance, see Ref. 6, was sufficiently intense in the nose region that negative absolute pressure would occur at a point somewhat aft of the airfoil nose and the calculation scheme would fail. Extra diffusive damping was added to the difference scheme (which degrades the accuracy) in order to continue the calculation. The resulting pressure distributions on the airfoil are shown in Figure 2 at various times for the coarse mesh and with the addition of the embedded fine mesh. The final Mach number contours in the flow field are next presented in Figure 3 for Mach number increments of 0.02. The contours were obtained by a linear interpolation of the Mach numbers at the mesh points.

5. SECOND EXAMPLE - SHOCKLESS PROFILE

For the calculation of the second example, a procedure has been developed which is capable of handling the flow over a blunt-nosed profile with lift. Here we have incorporated the far field boundary condition, the Kutta condition at the trailing edge, and a variable mesh. For the variable mesh in the vicinity of the blunt nose, an extra fine mesh having a spacing of 0.01 chord is used. The airfoil itself is imbedded in a fine mesh with 0.05 chord spacing and the field external to the airfoil (within a 3.2 chords square) is covered with 0.2 chord coarse mesh. Overlapping the coarse cartesian mesh a polar coordinate grid having 9 non-uniformly spaced rings and 40 rays extends the field to infinity. Here a suitable scale transformation of the radial coordinate is carried out.

For the second example we shall recalculate the flow over a shockless profile calculated by Nieuwland and Boerstoel using the hodograph method, and in particular we shall take the profile denoted by the designation .11-.75-1.375 of Ref. 3. The calculation by the finite difference method is in process and will be presented at the oral presentation.

REFERENCES

1. Gadd, G., "Interactions Between Normal Shock Waves and Turbulent Boundary Layers," British ARC Report No. 22559, 1961.

2. Nieuwland, B. Y., "Transonic Potential Flow Around a Family of Quasi-Elliptical Aerofoil Sections," NLR (Dutch) Report T172, 1967.

3. Boerstoel, J. W., "A Survey of Symmetrical Transonic Potential Flows Around Quasi-Elliptical Aerofoil Sections," NLR Report T-136, 1967.

4. Busemann, A., and Guderley, G., "The Problem of Drag at High Subsonic Speeds," British MAP Volkenrode Report 184, 1847.

5. Morawetz, C., "On the Non-Existence of Continuous Transonic Flow Past Profiles," I, II, and III, Comm. on Pure and Appl. Math., 1956-8.

6. Lax, P. D., and Wendroff, B., "Difference Schemes for Hyperbolic Equations with High Order Accuracy," Comm. Pure and Appl. Math., 1964.

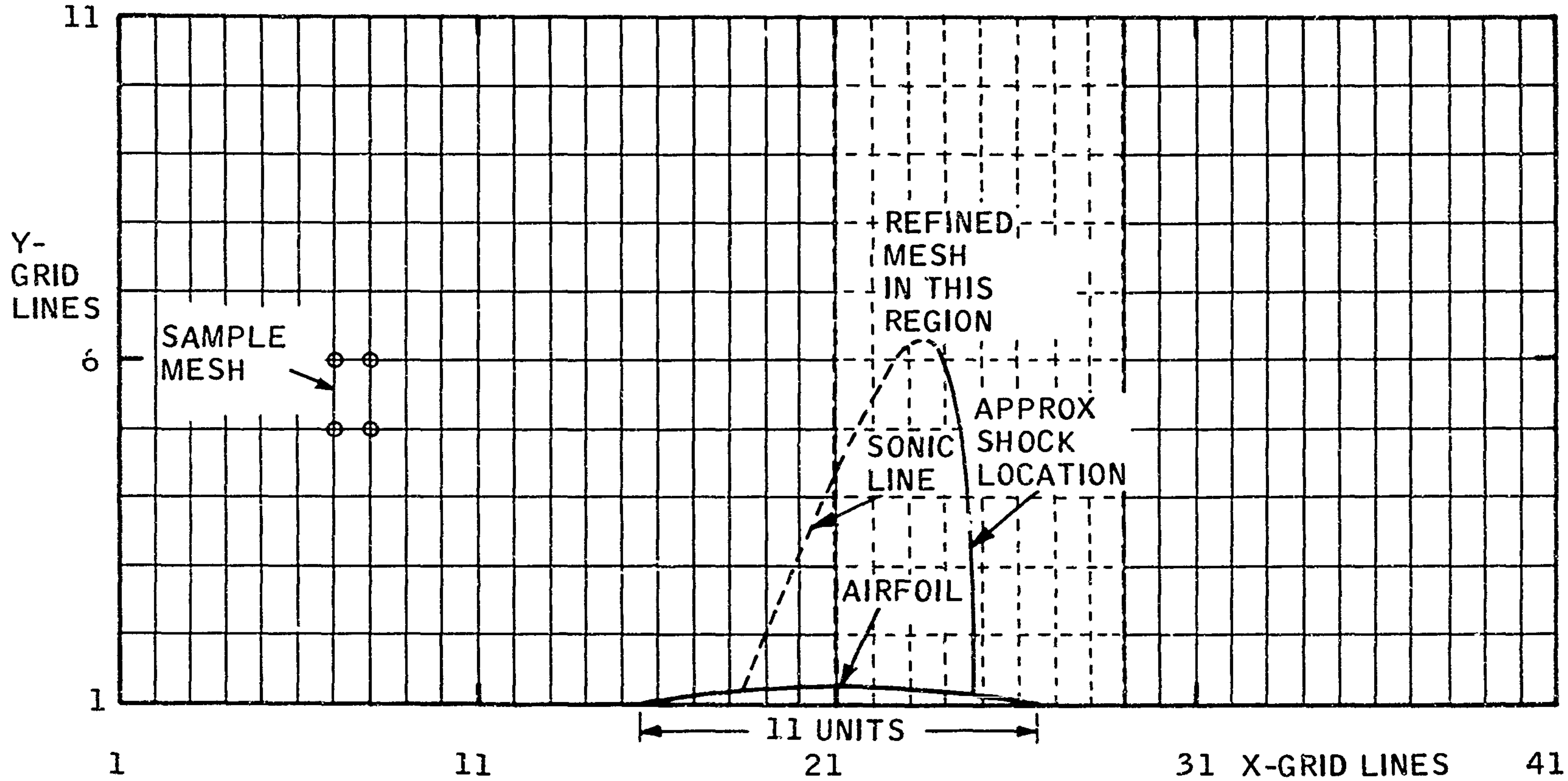

FIGURE 1. MESH CONFIGURATION.

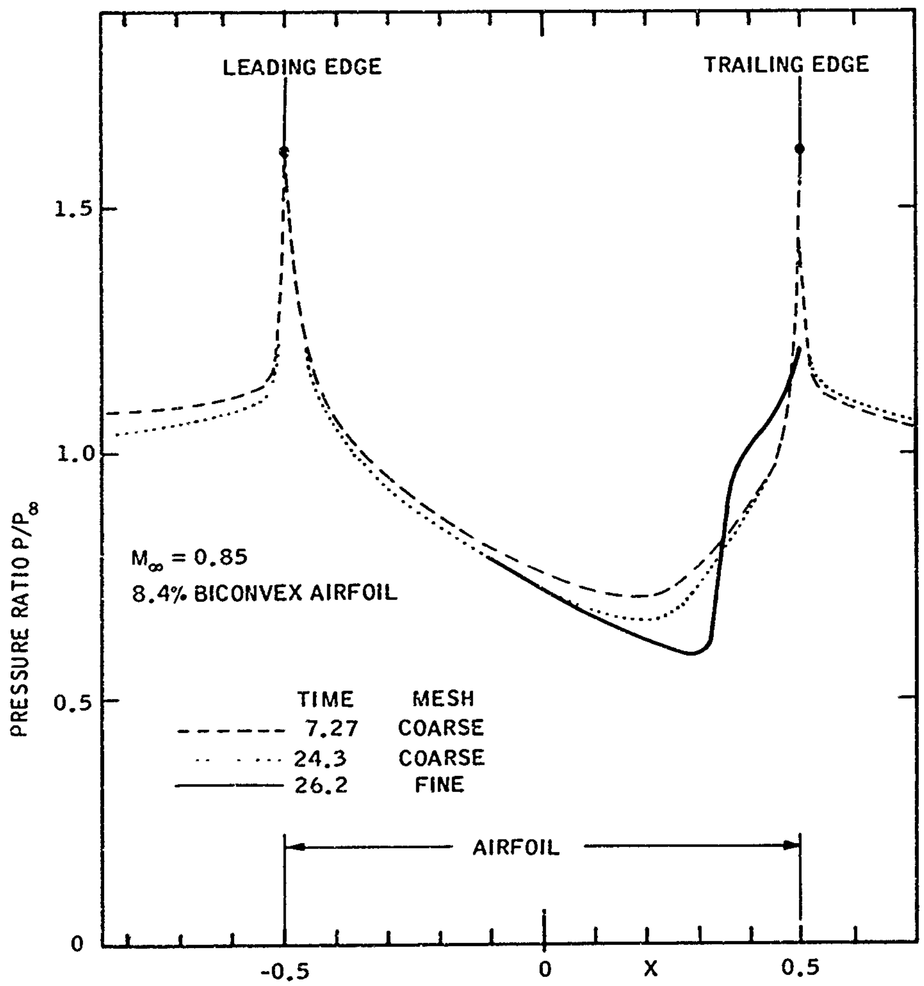

FIGURE 2. PRESSURE DISTRIBUTION ON THE AIRFOIL.

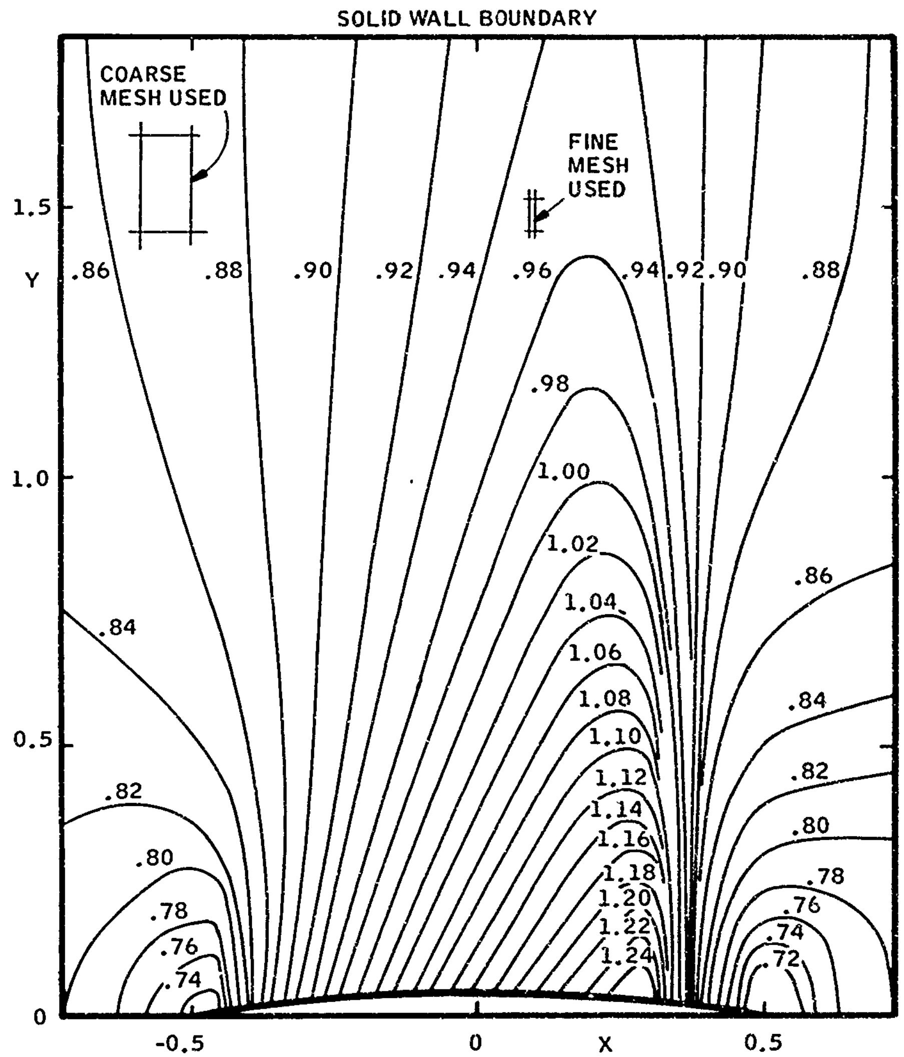

FIGURE 3. MACH NUMBER CONTOURS, 8.4% BICONVEX AIRFOIL IN MACH 0.85 CHANNEL FLOW.

APPLICATION DE LA METHODE DES CARACTERISTIQUES INSTATIONNAIRES AU CALCUL NUMERIQUE D'UN ECOULEMENT PERMANENT COMPRESSIBLE

par

Pierre CARRIERE*

Claude CAPELIER**

O.N.E.R.A. (92 - Châtillon - FRANCE)

* Directeur Scientifique de l'Aérodynamique

** Adjoint Scientifique auprès de la Direction Aérodynamique.

S O M M A I R E

L'écoulement bidimensionnel autour d'un profil est calculé comme limite asymptotique d'un écoulement non permanent. Comme données initiales on peut, par exemple, utiliser une solution connue et modifier continuement en fonction du temps les conditions aux limites, soit encore imposer dès l'instant initial à un écoulement arbitraire les conditions aux limites souhaitées ; l'évolution de l'écoulement per ; être déterminée par la méthode des caractéristiques. Un changement de coordonnées tel que les lignes de courant et leurs trajectoires orthogonales soient représentées par des parallèles aux axes simplifie les relations des caractéristiques ains' que l'organisation des calculs numériques.

L'organisation générale du calcul est décrite ainsi que les solutions adoptées pour lever certaines difficultés : point d'arrêt, condition de JOUKOWSKY, limites du réseau, ondes de choc.

Quelques résultats de calculs programmés en Fortran sont présentés et discutés.

S U M M A R Y

APPLICATION OF THE METHOD OF UNSTATIONARY CHARACTERISTICS

TO THE NUMERICAL COMPUTATION OF A STEADY COMPRESSIBLE FLOW

The two-dimensional flow around an airfoil is computed as an asymptotic limit to an unstationary flow. As initial data it is possible to use, for instance a known solution and modify, as a continuous function of time, the limiting conditions ; or impose, from the initial moment, the desired limiting conditions to an arbitrary flow ; the evolution of the flow can then be determined by the method of characteristics. A change of coordinates such that the current lines and their orthogonal trajectories are represente_ by lines parallel to the axes simplify the relations of the characteristics as well as the organization of the numerical computatic .

The general organization of an computation is described, as will as the solutions chosen to lift certain difficulties : stagnation points, JOUKOWSKY's conditions, network limits, shock wawes.

A few results of computations, programmed in Fortran, are presented and discussed.

L'UTILISATION D'UNE METHODE DE CALCUL en régime instationnaire pour la détermination d'un écoulement stationnaire considéré comme limite asymptotique a été fréquemment proposée pour résoudre des problèmes particulièrement difficiles tels que celui du choc détaché [1-2-3-4].

Quand la solution numérique directe du problème stationnaire impose l'emploi d'une méthode itérative (problème elliptique), il n'est jamais certain a priori que la convergence du procédé plus ou moins arbitraire utilisé assure la convergence ; si, au contraire, on introduit la variable temps, l'existence de caractéristiques réelles dans le nouveau problème permet de déterminer rationnellement un critère de convergence ; celui-ci est d'ailleurs assuré automatiquement si l'on utilise une méthode de calcul basée sur les propriétés mêmes des caractéristiques.

La complication du problème n'est donc qu'apparente : les diverses itérations imposées dans la méthode stationnaire sont alors remplacées par la suite de calculs effectués aux instants successifs

Dans le cas d'écoulements transsoniques, un autre avantage de la méthode instationnaire des caractéristiques est de permettre a priori de prévoir directement l'existence d'ondes de choc dans la solution cherchée et, par conséquent, de choisir la forme du profil pour éviter cet inconvénient.

On peut imaginer un très grand nombre de variantes d'application de la méthode ; citons les suivantes, à titre d'exemple :

- partant d'un écoulement connu autour d'un profil donné (P), on modifie progressivement (P) jusqu'à la nouvelle forme (P'), les conditions (E_∞) à l'infini restant invariantes.

- E_∞ restant fixe, on peut aussi chercher la nouvelle forme (P') satisfaisant à une distribution différente des pressions sur le profil (problème inverse).

- (P) restant fixe, on part d'une solution connue pour (E_∞) et l'on passe progressivement de (E_∞) à (E'_∞).

L'objet de cet exposé est d'indiquer les principes et les premiers résultats obtenus à l'O.N.E.R.A. dans une tentative de mise en oeuvre de ce procédé :

La méthode adoptée se caractérise essentiellement par l'utilisation d'un système de coordonnées (X, Y) constitué à chaque instant par les lignes de courant (Y = cte) et leurs trajectoires orthogonales (X = cte).

Ce choix a entre autres avantages celui de simplifier beaucoup le calcul numérique ; d'une part en effet les conditions aux limites sont écrites toujours sur des lignes X = cte ou Y = cte du réseau; d'autre part, dans ces axes intrinsèques, les équations générales conservent une forme très simple. Ce choix soulève par contre, comme on le verra, quelques difficultés au voisinage des points de vitesse nulle (bord d'attaque par exemple).

EXPOSE DE LA METHODE DE CALCUL

Après avoir défini les formules générales de la méthode, on analysera les problèmes particuliers posés par sa mise en oeuvre.

FORMULATION GENERALE

On étudie un écoulement de gaz parfait uniforme à l'infini (p_∞, V_∞, T_∞), pouvant comporter éventuellement dans certains domaines des variations d'entropie dues à l'apparition d'ondes de choc.

SYSTEME DE COORDONNEES. Les relations des caractéristiques sont rappelées en annexe 1. Ces relations sont particulièrement simples si on les exprime dans des axes locaux x_1, y_1, t, $\bar{x}_1$ étant le vecteur unitaire porté par la vitesse locale à l'instant t et $\bar{y}_1$ le vecteur unitaire directement perpendiculaire, situé dans le plan physique (x, y).

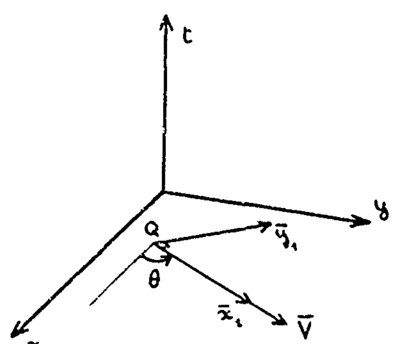

L'angle $\bar{x}$, $\bar{x}_1$ sera appelé θ .

Pour pouvoir utiliser les relations des caractéristiques sous cette forme simple, il est nécessaire de déterminer une transformation biunivoque faisant correspondre à tout point du plan physique (x, y) un point du plan (X, Y) et telle que dans ce dernier plan les lignes de courant et leurs trajectoires orthogonales soient représentées par des parallèles aux axes.

Soit donc (dx_1, dy_1) les composantes d'un élément linéaire en un point Q (x, y, t) suivant les directions $\bar{x}_1$ et $\bar{y}_1$.

Posons

$$(1)\qquad \begin{aligned} dx_1 &= \alpha\,(X, Y, t)\; dX \\ dy_1 &= \beta\,(X, Y, t)\; dY \end{aligned}$$

α et β étant deux fonctions convenablement choisies rendant intégrable à chaque instant t, le système:

$$(2)\qquad \begin{aligned} dx &= \alpha \cos\theta\; dX - \beta \sin\theta\; dY \\ dy &= \alpha \sin\theta\; dX + \beta \cos\theta\; dY \end{aligned}$$

α et β satisfont donc nécessairement à :

$$(3)\qquad \begin{aligned} \frac{\partial \alpha}{\partial Y} &= -\beta\,\frac{\partial \theta}{\partial X} \\ \frac{\partial \beta}{\partial X} &= \alpha\,\frac{\partial \theta}{\partial Y} \end{aligned}$$

D'après les relations (3), α et β s'intègrent sous la forme :

$$(4)\qquad \begin{aligned} \alpha\,(X, Y, t) &= \alpha_0(X, o, t) - \int_0^Y \beta\,\frac{\partial \theta}{\partial X}\, dY \\ \beta\,(X, Y, t) &= \beta_0(-\infty, Y, t) + \int_{-\infty}^X \alpha\,\frac{\partial \theta}{\partial Y}\, dX \end{aligned}$$

Les distributions initiales $\alpha_0(X, o, t)$ et $\beta_0(-\infty, Y, t)$ sont a priori arbitraires.

Il y a intérêt à poser :

$$\alpha = \frac{A\,(X, Y, t)}{V\,(X, Y, t)} \qquad\qquad \beta = \frac{B\,(X, Y, t)}{\rho V\,(X, Y, t)}$$

d'après (3) ; en effet, on a :

$$(5)\qquad \begin{aligned} \frac{\partial A}{\partial Y} &= \alpha.\beta\left(\frac{\partial V}{\partial y_1} - V\,\frac{\partial \theta}{\partial x_1}\right) = \alpha\beta\,\mathrm{rot}\,\bar{V} \\ \frac{\partial B}{\partial X} &= \alpha\;\beta\left(\frac{\partial \rho V}{\partial x_1} + \rho V\frac{\partial \theta}{\partial y_1}\right) = -\alpha\beta\,\frac{\partial \rho}{\partial t} \end{aligned}$$

Ces équations montrent que si l'écoulement est irrotationnel, condition assurée ici en l'absence d'ondes de choc, on a :

$$A = A\,(X, t)$$

fonction arbitraire, qui permettra d'échelonner convenablement dans le plan physique les homologues des lignes X = cte (confondues alors avec des équipotentielles).

On remarquera d'autre part que si rot $\bar{V}$ = o , on a la relation :

$$(6)\qquad B = \frac{\rho}{R}\,\frac{\partial V}{\partial Y}$$

où R représente la courbure locale $\frac{\partial \theta}{\partial x_1}$ de la ligne de courant dans le plan physique.

Cette relation sera utile pour l'étude du voisinage du point d'arrêt.

RELATIONS DES CARACTERISTIQUES. Dans les axes (X, Y, t) précédemment définis, la surface caractéristique d'un point M (X, Y, t + dt) est un cône de sommet M coupant le plan t suivant une ellipse de centre $\Omega\,(X_M - \frac{V}{\alpha}\,dt\,,\,Y_M\,,\,t)$ dont les demi-axes principaux sont parallèles à OX et OY et ont respectivement pour mesures :

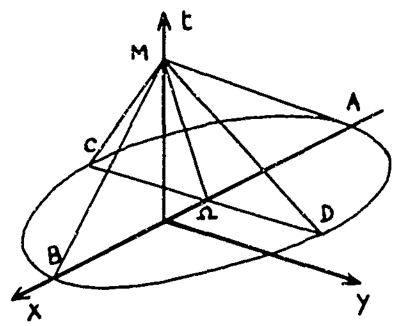

$$\Omega A = \Omega B = \frac{a}{\alpha}\,dt$$

$$\Omega C = \Omega D = \frac{a}{\beta}\,dt$$

a étant la célérité du son.

De cette surface caractéristique, on ne retiendra par exemple que les quatre bicaractéristiques passant par les sommets A, B, C et D de l'ellipse.

Le long de ces bicaractéristiques, les relations suivantes sont vérifiées en général $\left(\gamma = \frac{a^2}{p/\rho}\right)$

$$(7)\qquad \begin{aligned}
\frac{1}{\gamma p}(dp)_{AM} + \frac{1}{a}(dV)_{AM} &= -\frac{V}{\beta}\frac{\partial\theta}{\partial Y}\,dt\\
\frac{1}{\gamma p}(dp)_{BM} - \frac{1}{a}(dV)_{BM} &= -\frac{V}{\beta}\frac{\partial\theta}{\partial Y}\,dt\\
\frac{1}{\gamma p}(dp)_{CM} + \frac{V}{a}(d\theta)_{CM} &= -\frac{1}{\alpha}\frac{\partial V}{\partial X}\,dt\\
\frac{1}{\gamma p}(dp)_{DM} - \frac{V}{a}(d\theta)_{DM} &= -\frac{1}{\alpha}\frac{\partial V}{\partial X}\,dt
\end{aligned}$$

D'autre part, l'entropie satisfait à la relation :

$$(8)\qquad (ds)_{\Omega M} = 0$$

Si on étudie l'écoulement isentropique d'un gaz parfait $\gamma =$ cte, les relations se simplifient en posant $P = \frac{2}{\gamma - 1}\,a$. Du fait de l'isentropie $\frac{a\,dp}{\gamma p} = dP$

Les relations (7) s'écrivent alors :

$$(9)\qquad \begin{aligned}
(dP)_{\substack{AM\\BM}} \pm (dV)_{\substack{AM\\BM}} &= -\frac{(\gamma-1)\,P\,V}{2\beta}\frac{\partial\theta}{\partial Y}\,dt\\
(dP)_{\substack{CM\\DM}} \pm V(d\theta)_{\substack{CM\\DM}} &= -\frac{(\gamma-1)\,P}{2\alpha}\frac{\partial V}{\partial X}\,dt
\end{aligned}$$

Pour simplifier l'exposé, on supposera par la suite que l'écoulement est effectivement isentropique et que l'on peut utiliser ces dernières relations.

ETUDE DE QUELQUES PROBLEMES PARTICULIERS

Le mode de calcul du point courant ne présente aucune difficulté théorique. Par contre, il est nécessaire de discuter quelques problèmes particuliers.

CALCUL DU POINT COURANT. Les trois grandeurs P, V et θ définissant l'écoulement au point courant M (X, Y, t + dt) seront déterminées par l'application des quatre relations caractéristiques (9) nécessairement compatibles que l'on pourra résoudre par la méthode des moindres carrés. On peut éventuellement faire appel à d'autres bicaractéristiques.

POINT SUR LE PROFIL : PROBLEME DIRECT. On convient de représenter le profil sur la coupure $0 \leqslant X \leqslant 1$, $Y = \pm 0$ du plan transformé X, Y, X = 0 correspondant au point d'arrêt 0.

A tout point M (X, $\pm$ 0, t + dt) correspond un point m du profil dont l'abscisse curviligne λ comptée à partir du bord de fuite est donnée par :

$$\lambda = \int_X^1 \alpha(X, \pm 0, t + dt)\, dX$$

La distribution arbitraire α (X, $\pm$ 0, t) ayant été ainsi choisie et le profil étant donné à chaque instant par la répartition $\theta(\lambda, t)$, l'angle $\theta^{\pm}$ est donc connu en chaque point de la coupure $Y = \pm 0$ à condition de connaître le point d'arrêt sur le profil. Les deux autres grandeurs P et V caractérisant l'écoulement au point courant de la coupure ou temps t + dt seront obtenues par les relations (9) le long des trois bicaractéristiques MA, MB et MD pour un point de Y = + 0.

Pour un point de la coupure Y = - 0, il faudra considérer les trois bicaractéristiques MA, MB et MC.

Les deux fonctions $\alpha(X, \pm 0, t)$ peuvent être choisies arbitrairement sous réserve de satisfaire aux conditions de fermeture du profil dans le plan physique.

$$\int_0^1 \alpha^+ \cos\theta^+\, dX = \int_0^1 \alpha^- \cos\theta^-\, dX$$

ou

$$\int_0^1 \alpha^+ \sin\theta^+\, dX = \int_0^1 \alpha^- \sin\theta^-\, dX$$

Nota : Si l'obstacle se déforme, il n'est pas ligne de courant ; l'obstacle défini par affichage de $\theta(\lambda, t)$ sur la coupure est donc distinct de l'obstacle réel pendant la période de déformation $\left(\frac{\partial\theta}{\partial t} \neq 0\right)$; ce point est sans importance pour le problème étudié, car on n'est intéressé par le profil exact que lorsque l'écoulement permanent est atteint.

POINT SUR LE PROFIL : PROBLEME INVERSE. On peut aussi se donner a priori la distribution $P^{\pm}(X, t)$ sur la coupure $0 \leqslant X \leqslant 1$, le profil correspondant étant à déterminer.

Les trois bicaractéristiques utilisées au paragraphe précédent serviront alors au calcul de θ (x, t + dt) et $V^{\pm}$ (X, t + dt) sur cette coupure.

Après intégration, il y aura lieu de vérifier les conditions de fermeture du profil correspondant dans le plan physique :

$$\int_0^1 \alpha^+ \cos\theta^+\, dX = \int_0^1 \alpha^- \cos\theta^-\, dX$$

et

$$\int_0^1 \alpha^+ \sin\theta^+\, dX = \int_0^1 \alpha^- \sin\theta^-\, dX$$

Sinon, on devra poursuivre le calcul en modifiant α^+ par exemple jusqu'à ce qu'il en soit ainsi.

POINT SUR LE SILLAGE. Si le problème est dissymétrique, l'axe Y = 0 (X > 1) doit aussi être considéré comme une coupure (sillage) pendant la phase instationnaire du calcul.

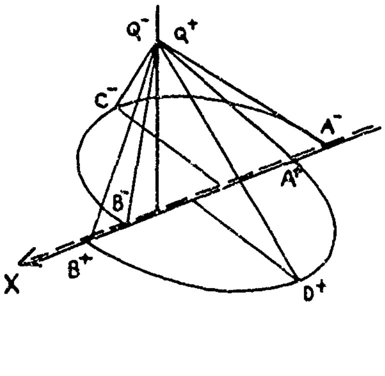

Pour le calcul de deux points $Q^{\pm}$ infiniment voisins de part et d'autre de l'axe Y = 0, on utilisera les six bicaractéristiques QA^+, QB^+, QD^+, QA^-, QB^- et QC^- et on écrira la condition de compatibilité $P^+ = P^-$, $\theta^+ = \theta^-$.

On devra choisir α (X, $\pm$ 0, t) de manière qu'en tout point de la coupure de sillage, on ait :

$$\alpha(X, +0, t) = \alpha(X, -0, t)$$

ce qui assure la coïncidence dans le plan physique des points correspondant aux deux points $Q^{\pm}$, la condition de fermeture ayant été préalablement satisfaite.

POINTS D'ARRET. Au voisinage d'un point d'arrêt, on ne peut calculer l'abscisse curviligne par intégration de :

$$dx_1 = \alpha \, dX$$

car α tend vers l'infini comme $\frac{1}{V}$ au point d'arrêt.

Mais dans son voisinage, on admettra sans démonstration que l'écoulement peut être considéré comme incompressible et irrotationnel.

Son potentiel complexe est alors de la forme $W = K \zeta^n$

avec $\zeta = x + iy$

$$n = \frac{\pi}{\pi - |\theta_0|}$$

θ_0 étant l'angle de déviation au point d'arrêt (pour un impact normal, $\theta_0 = \frac{\pi}{2}$ et $n = 2$).

Ayant posé $\alpha = \frac{A}{V}$, on trouve ainsi qu'au voisinage ΔX d'un point d'arrêt X_0, on a :

$$x_1(X_0 \pm \Delta X) = x_1(X_0) \pm \frac{n . A(X_0)\, \Delta X}{V(X_0 \pm \Delta X)}$$

CALCUL DE P EN UN POINT D'ARRET. On a la relation :

$$0 = \frac{\partial V}{\partial t} + \frac{\partial}{\partial x_1}\left(\frac{p}{\rho} + \frac{V^2}{2}\right) \equiv \frac{\partial V}{\partial t} + \frac{\partial U}{\partial x_1}$$

en posant $U = \frac{(\gamma - 1)^2}{4\gamma} P^2 + \frac{V^2}{2}$

Dans le problème symétrique, $\frac{\partial V}{\partial t} \to 0$ au voisinage d'un point d'arrêt, donc U est stationnaire sur le profil.

On pourra donc écrire :

$$U_0 \equiv \frac{(\gamma-1)^2}{4\gamma} P_0^2 = \frac{1}{2}\left[U(\Delta X) + U(-\Delta X)\right]$$

Dans un problème portant, le point d'arrêt peut varier au cours des itérations, de sorte que $\frac{\partial V}{\partial t} \neq 0$. On admettra néanmoins que le procédé précédent reste applicable, pourvu que cette variation soit très faible, hypothèse généralement vérifiée.

CALCUL DE α et β. Dans tout domaine irrotationnel, α est donné par $\alpha = \frac{A(X, t)}{V(X, Y, t)}$,
A (X, t) étant une fonction arbitraire.

Il est commode de se donner arbitrairement à chaque instant $\alpha(X, \pm 0, t)$ et d'en déduire par itération A (X, t) qui sert ensuite pour le calcul de α dans tout le plan.

Dans les zones rotationnelles de l'écoulement (en aval d'une onde de choc), le procédé précédent n'est pas valable ; on doit alors opérer par calcul pas à pas de α par l'équation $(4)_1$.

Au voisinage d'un point d'arrêt ($X = X_0$), l'intégrale est régulière, mais on peut remarquer que $\overline{\text{rot}\, V}$ étant nul, $\frac{\partial A}{\partial Y} = 0$ ce qui permet d'écrire :

$$A(X_0, \Delta Y, t) = A(X_0, 0, t) = \frac{1}{2}\left[A(X_0 - \Delta X, 0, t) + A(X_0 + \Delta X, 0, t)\right]$$

Quant à β , il sera obtenu par l'intégration $(4)_2$:

$$\beta(X,Y,t) = \beta(X_\infty,Y,t) + \int_{X_\infty}^{X} \alpha \frac{\partial \theta}{\partial Y} dX$$

Dans le problème direct, le calcul de B $(X_0 \pm \Delta X, 0, t)$ singulier en X_0 où $\alpha \rightarrow \infty$ résulte immédiatement de la relation (6), la courbure locale k du profil étant donnée, et la dérivée $\frac{\partial V}{\partial Y}$ pouvant être obtenue par itération.

Dans le problème inverse, k doit aussi être obtenu par itération.

DETECTION DES ONDES DE CHOC. Des ondes de choc peuvent apparaître en cours de calcul soit parce qu'elles existent dans l'écoulement permanent cherché, soit parce que les modifications des conditions aux limites ont été trop rapides et ont provoqué la confluence d'ondes de compression. Il y a donc lieu de détecter leur apparition, soit pour ralentir les modifications des conditions aux limites, soit pour tenir compte de ces ondes de choc par l'application des relations d'HUGONIOT.

Il y a apparition d'une onde de choc entre les instants t et $t + \Delta t$ si le point de contact d'une bicaractéristique quelconque avec son enveloppe est situé dans cet intervalle de temps.

Ce critère doit être appliqué en chaque point du réseau et, en principe, pour toutes les bicaractéristiques.

Nous n'examinerons pas ici la méthode de calcul à appliquer, dans le cas où une onde de choc étant apparue, on veut suivre son évolution au cours du calcul : le principe de la méthode à partir des équations d'HUGONIOT ne présente d'ailleurs aucune difficulté.

PRATIQUE DU CALCUL

RESEAU DE CALCUL

Connaissant l'écoulement dans un plan (X, Y, t) on détermine, par les relations des caractéristiques et compte tenu des conditions aux limites, l'écoulement dans le plan $(X, Y, t + \Delta t)$.

On choisit dans les plans (X, Y, t) un réseau à mailles uniformes ; dans le cas d'un écoulement isentropique, cet écoulement est déterminé par la connaissance des grandeurs P, V et θ en chaque noeud de ce réseau ; il faut également connaître les valeurs de α et β qui déterminent la transformation.

Ce maillage régulier facilite les interpolations et la détermination des dérivées nécessaires aux calculs. Le choix des fonctions arbitraires définissant α et β permet de jouer sur la répartition des points correspondants du plan physique (x, y) ; on peut en particulier reserrer les points au voisinage du profil et surtout au voisinage des points d'arrêt.

Le réseau étant nécessairement borné, il est impossible d'afficher les conditions P_∞, V_∞, et θ_∞ fixées à l'infini : cette difficulté n'a reçu encore aucune solution théorique correcte. On peut, soit utiliser un prolongement analytique de P, V et θ obtenus au stade t pour calculer les points $Q(t + \Delta t)$ à la frontière, soit afficher sur cette frontière la solution de l'écoulement permanent obtenue par une théorie linéarisée.

Afin de minimiser l'influence des erreurs d'affichage sur les frontières du réseau on a, de toutes façons, intérêt à reporter celles-ci le plus loin possible du profil.

EXEMPLES DE MISE EN OEUVRE DU CALCUL

Deux exemples sont donnés pour illustrer la méthode : un problème symétrique et un problème portant.

PREMIER EXEMPLE : PROBLEME DIRECT SYMETRIQUE. On suppose que l'on a déterminé l'écoulement à l'instant t, correspondant à un certain profil défini par la fonction $\varphi(\lambda)$ exprimant, en fonction de l'abscisse curviligne λ comptée à partir du bord de fuite, l'angle φ de la tangente orientée avec la référence fixe $\overline{x}$.

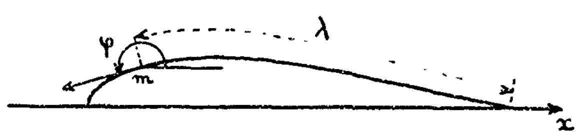

A l'instant $t + \Delta t$, on modifie le profil en écrivant :

$$\varphi(\lambda, t+\Delta t) = \varphi(\lambda, t) + \Delta\varphi(\lambda)$$

Connaissant $\alpha(X, o, t+\Delta t)$, on peut déterminer x_1 et par suite λ en tout point de la coupure $Y = 0$, $0 \leqslant X \leqslant 1$. On connaît donc φ d'où les nouvelles valeurs de θ sur cette coupure.

L'utilisation des relations des caractéristiques entre les plans X, Y, t et X, Y, $t + \Delta t$ permet de déterminer les nouvelles valeurs de P, V et θ en chaque noeud du réseau.

DEUXIEME EXEMPLE : PROBLEME DIRECT PORTANT. La forme du profil est également donnée à l'instant t par la loi $\varphi(\lambda)$

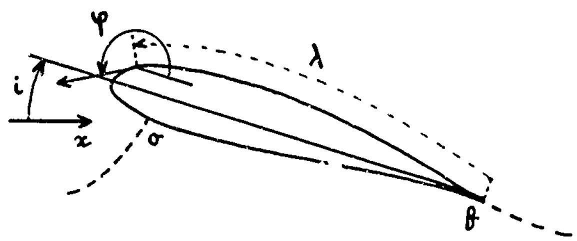

Soit λ_o l'abscisse curviligne du point d'arrêt A et i l'angle d'incidence.

Sur l'intrados et l'extrados, on a respectivement :

$$\theta^- = \varphi(\lambda) - i \qquad x_1^- = \lambda - \lambda_o$$

$$\theta^+ = \varphi(\lambda) - i - \pi \qquad x_1^+ = \lambda_o - \lambda$$

A l'instant $t + \Delta t$, on modifie la position du point d'arrêt et, éventuellement, la forme du profil :

$$\lambda_o(t+\Delta t) = \lambda_o(t) + \Delta\lambda_o$$

$$\varphi(\lambda, t+\Delta t) = \varphi(\lambda, t) + \Delta\varphi(\lambda)$$

On détermine alors, par application des relations des caractéristiques au voisinage du bord de fuite F, la quantité Δi dont il faut faire varier l'incidence pour assurer la condition de JOUKOWSKI au point F (égalité des pressions d'extrados et d'intrados).

Connaissant $\alpha(X, \pm o, t+\Delta t)$, on peut alors, comme précédemment, déterminer la répartition de $\theta(X, \pm o, t+\Delta t)$ sur la coupure.

Puis, on détermine les nouvelles valeurs de P, V et θ en chaque noeud du réseau.

PREMIERS RESULTATS OBTENUS ET DISCUSSION

Un programme a été écrit sur UNIVAC 1108 dans le cas d'un problème symétrique. Il utilise un réseau comprenant au maximum 90 points en X et 30 en Y.

Avant de discuter des premiers résultats obtenus, il est nécessaire d'étudier le comportement de l'écoulement au voisinage des points d'arrêt.

ETUDE DE L'ECOULEMENT AU VOISINAGE D'UN POINT D'ARRET

On a admis qu'au voisinage d'un point d'arrêt, l'écoulement pouvait être considéré comme incompressible et irrotationnel.

S'il s'agit d'un impact normal, le potentiel est celui de l'écoulement autour d'un cercle dont le rayon R est égal au rayon de courbure du profil.

On peut en déduire que sur l'axe Y = 0, la vitesse est donnée par :

$$V^2 = K\,X\,(1 - \frac{X}{4R} + \ldots.) \qquad X > 0$$

(10)

$$V^2 = -K\,X\,(1 - 2\sqrt{\frac{-X}{R}} - \frac{9X}{4R} + \ldots.) \qquad X < 0$$

Quant aux dérivées $\frac{\partial V}{\partial X}$ et $\frac{\partial \theta}{\partial Y}$, elles satisfont aux relations :

$$V^2 \frac{\partial \theta}{\partial Y} = -V \frac{\partial V}{\partial X} = -\frac{K}{2}\,(1 - \frac{X}{2R} + \ldots) \qquad X > 0$$

(11)

$$V^2 \frac{\partial \theta}{\partial Y} = -V \frac{\partial V}{\partial X} = \frac{K}{2}\,(1 - 3\sqrt{\frac{-X}{R}} - \frac{9X}{2R} + \ldots) \qquad X < 0$$

L'angle θ que fait le vecteur vitesse avec l'axe ox dans le cas d'un problème symétrique est donné par :

$$\theta = \operatorname{arctg}\left[\frac{u}{1 + \sqrt{\frac{Y}{2Ru}} + u\sqrt{\frac{uY}{2R}}}\right]$$

(12)

$$u = \frac{X + \sqrt{X^2 + Y^2}}{Y}$$

Si l'impact de la ligne de courant n'est pas normal, la loi d'évolution de la vitesse sur l'axe OX est

$$V = K.|X|^{\frac{n-1}{n}}.\left[1 + b.|X|^{\frac{1}{n}} + \ldots\right]$$

(13)

$$n = \frac{\pi}{\pi - |\theta_o|}$$

θ_o étant l'angle de déviation ou point d'arrêt.

STABILITE DE LA METHODE

Un premier programme ayant été écrit dans le cas d'un problème symétrique, on a cherché à vérifier que, partant d'un écoulement permanent connu, cette solution ne se dégradait pas en cours de calcul.

On a choisi, à cet effet, un écoulement incompressible autour d'un profil de JOUKOWSKI.

Les premiers résultats ont été mauvais comme on peut le voir sur la planche 1 où la courbe représente la loi d'évolution exacte de la vitesse sur ce profil ; les croix représentent la répartition de vitesse obtenue après 9 cycles de calcul.

La dégradation observée provient du fait que les grandeurs en chaque pied des bicaractéristiques étaient obtenues par interpolation linéaire entre les quatre points du réseau qui l'entourent. Les formules (10) montrent que l'interpolation doit porter sur le carré de la vitesse. De même d'après la formule (11), on voit que pour déterminer $\frac{\partial V}{\partial X}$, il faut faire porter la dérivation également sur le carré de la vitesse ; pour $\frac{\partial \theta}{\partial Y}$, on écrit, dans le voisinage immédiat du point d'arrêt :

$$V^2 \frac{\partial \theta}{\partial Y} = -V \frac{\partial V}{\partial X}$$

au cas où la déviation de la ligne de courant au point d'arrêt est différente de $\frac{\pi}{2}$ (cas d'un bord de fuite sans point de rebroussement), l'interpolation et la dérivation doivent porter sur $V^{\frac{n}{n-1}}$

Moyennant ces précautions, la solution ne se dégrade plus comme on peut le voir sur la planche 1 où les points représentent les résultats obtenus avec le nouveau programme après également 9 cycles de calculs.

TEMPS DE CALCUL

La détermination de l'écoulement en chaque point du réseau est relativement rapide. En général, cinq itérations successives sont suffisantes pour obtenir la précision maximale de la machine ; cependant, si les points ne sont pas suffisamment serrés dans les régions à fort gradient de vitesse, le calcul peut ne pas converger ; dans ces cas, l'expérience a montré que le calcul redevenait convergent si, pour chaque nouvelle itération, on prenait comme valeur initiale des inconnues la moyenne entre la valeur initiale et la valeur finale de l'itération précédente.

L'intervalle de temps Δt choisi doit être tel que la trace dans le plan t du cône de Mach du point M $(X, Y, t + \Delta t)$ soit comprise à l'intérieur du maillage entourant le point (X, Y, t). Au voisinage des zones à fort gradient de vitesse où il est nécessaire de resserrer fortement les points, les Δt imposés par la condition précédente deviennent très petits. Si donc, par commodité, on adopte, pour l'ensemble du réseau un Δt unique c'est-à-dire le Δt minimal correspondant à la zone où les points sont les plus serrés, un nombre important de cycles de calculs devient nécessaire pour obtenir un écoulement permanent. Les temps de calculs se révèlent alors prohibitifs : le calcul de l'écoulement autour d'un cercle à M = 0,4, effectué dans ces conditions sur UNIVAC 1108 a dû être interrompu au bout d'une demi-heure de calcul, l'état permanent étant encore loin d'être atteint.

Dans un nouveau programme en cours de mise au point, le réseau de calcul est subdivisé en un certain nombre de sous-réseaux, dont la dimension des mailles est adaptée aux gradients de vitesse locaux ; cette solution permet de resserrer les points dans les régions où cela est nécessaire, sans trop aggraver le temps de calcul total.

CONCLUSION

Les premiers essais d'application de la méthode proposée ont montré qu'elle était viable : le choix du système de coordonnées X, Y facilite grandement la programmation et les difficultés rencontrées ont pu être résolues.

Cependant l'actuel programme utilisant un pas Δt uniforme pour l'ensemble du réseau n'a pu donner de résultats probants, le temps de calcul nécessaire pour atteindre l'état permanent étant alors prohibitif.

Un nouveau programme plus élaboré est en cours de mise au point : il doit ramener le temps de calcul à une valeur acceptable.

REFERENCES

[1] - G. MORETTI et M. ABBETT
"A time dependant computational method for blunt body flows"
A.I.A.A. Journal - Vol. 4 - n° 12, Décembre 1966.

[2] - A. LAPIDUS
"A detached shock calculation by second-order finite differences"
Journal of Computational Physics - vol. 2, n° 2, November 1967.

[3] - H. SAUERWEIN
"Numerical calculations of multidimensional and unsteady flows by the method of characteristics"
Journal of Computational Physics, vol. 1, n° 3, February 1967.

[4] - M. BAUSSET
"Etude du départ d'un obstacle dans un fluide au repos"
Compte Rendu de l'Académie des Sciences de PARIS - 29 Novembre 1965.

ANNEXE

RELATIONS DES CARACTERISTIQUES DANS L'ESPACE x, y, t

On sait que le cône caractéristique, ou "cone de Mach" en un point Q quelconque de l'espace x, y, t est défini de la façon suivante :

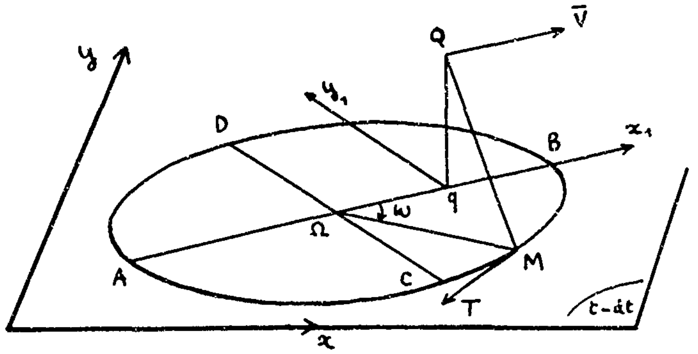

Soit, sur le plan t - dt, q la projection de Q, $\bar{x}_1$ et $\bar{y}_1$ les axes locaux parallèles et perpendiculaires à $\bar{V}$; portons sur x_1 un vecteur $q\Omega = -V\,dt$ et traçons dans le plan (t - dt) un cercle de centre Ω et de rayon adt (a vitesse du son) : ce cercle est la trace du cône de Mach en Q. Soient A, B, C et D les extrémités des diamètres de ce cercle respectivement parallèles à $\bar{x}_1$ et $\bar{y}_1$.

Une génératrice quelconque Q M est bicaractéristique. Soit $\omega = (\widehat{\Omega x_1, \Omega M})$. La dérivation suivant la direction Q M s'écrit :

$$(14) \qquad \left(\frac{D}{Dt}\right)_{QM} = \frac{\partial}{\partial t} + (V - a\cos\omega)\frac{\partial}{\partial x_1} - a\sin\omega\frac{\partial}{\partial y_1}$$

Par une combinaison linéaire des équations de quantité de mouvement et de l'équation de continuité, on peut obtenir la relation des caractéristiques :

$$(15) \qquad \left| \begin{array}{l} \frac{1}{\rho a}\left(\frac{Dp}{Dt}\right)_{QM} - \cos\omega\left(\frac{DV}{Dt}\right)_{QM} - V\sin\omega\left(\frac{D\theta}{Dt}\right)_{QM} = \\[2ex] a\cos\omega\left[\sin\omega\frac{\partial V}{\partial y_1} - \frac{\sin^2\omega}{\cos\omega}\frac{\partial V}{\partial x_1} - V\cos\omega\frac{\partial\theta}{\partial y_1} + V\sin\omega\frac{\partial\theta}{\partial x_1}\right] \equiv \\[2ex] a\sin\omega\left(\frac{DV}{Dt}\right)_{MT} - aV\cos\omega\left(\frac{D\theta}{Dt}\right)_{MT} \end{array} \right.$$

M T étant la tangente en M à la trace du cône de Mach du plan (t - dt).

Cette relation qui ne comporte que des dérivations selon des directions comprises dans le plan tangent au cône de Mach montre bien que celui-ci est surface caractéristique.

Si l'écoulement n'est pas isentropique, il y a lieu de tenir compte de la bicaractéristique particulière Ω Q, le long de laquelle l'entropie est constante.

Si l'on ne s'intéresse qu'aux quatre bicaractéristiques QA, QB, QC et QD, la relation (15) permet d'écrire :

$$(16) \qquad \begin{array}{l} \frac{1}{\rho a}\left(\frac{Dp}{Dt}\right)_{\substack{QA\\QB}} \pm \left(\frac{DV}{Dt}\right)_{\substack{QA\\QB}} = -aV\frac{\partial\theta}{\partial y_1} \\[3ex] \frac{1}{\rho a}\left(\frac{Dp}{Dt}\right)_{\substack{QC\\QD}} \pm V\left(\frac{D\theta}{Dt}\right)_{\substack{QC\\QD}} = -a\frac{\partial V}{\partial x_1} \end{array}$$

TIME DEPENDENT CALCULATION OF THE COMPRESSIBLE FLOW ABOUT AIRFOILS

D. Mac Kenzie* and G. Moretti**

Grumman Aircraft Engineering Corporation

Bethpage, N. Y., U. S. A.

----

* Advanced Development Engineer, GAEC

** Consultant, and Professor, Polytechnic Institute of Brooklyn

SUMMARY

Guidelines for the efficient formulation of time dependent transonic flow calculations are presented. Among the particular points considered are procedures for satisfying boundary conditions at solid boundaries and ensuring well posed problems for flows that are subsonic in the far field. A discussion of the relative merits of the Lax-Wendroff technique and an explicit method of treating imbedded shocks is also included. To illustrate the points made, the results of several calculations are presented and discussed. These include:

1) The subsonic and supersonic flow about a 6% thick biconvex airfoil in a duct;
2) The flow in a converging-diverging nozzle with supersonic exit conditions;
3) The subsonic flow about a circular cylinder in an infinite stream.

The details of the various finite difference techniques used in these calculations are also presented.

TIME DEPENDENT CALCULATION OF THE COMPRESSIBLE FLOW ABOUT AIRFOILS

D. Mac Kenzie* and G. Moretti**

Grumman Aircraft Engineering Corporation

Bethpage, N. Y., U. S. A.

I. INTRODUCTION

The present generation of computers is better-suited to the solution of initial-value problems than to the solution of boundary-value problems. Unsteady flow problems belong to the first category. Steady flows containing subsonic regions can be analyzed, in principle, by solving initial-value problems with the steady state calculated as the unique asymptotic limit of an unsteady flow process starting from an arbitrary distribution of initial values and subject to steady boundary conditions.

A wide variety of transonic flows of practical interest can be generally divided into two categories depending on the nature of the flow at the non-rigid boundaries which enclose the region of interest:

1) Flows which are supersonic in the far field and contain one or more subsonic islands;
2) Flows which are subsonic in the far field and contain one or more supersonic islands.

The most popular example of the first category (and probably the simplest) is the flow past a blunt body in supersonic flight. It has been proven that time-dependent techniques are extremely well-suited to the analysis of the blunt-body problem, and definitively good results from the viewpoint of both accuracy and computational speed have been obtained (ref. 1).

The problems of the second category are much more difficult than those of the first, primarily for the following reasons:

1) The flow field may contain imbedded shocks generated by a coalescence of characteristics in a region of supersonic flow;
2) The flow on at least part of the computational boundaries is subsonic so that the location and the specification of the data on these boundaries may affect the numerical results. Typical problems of this kind are the choked flow in a converging-diverging nozzle and the transonic flow past an airfoil flying at supercritical speeds.

We wish to present some guidelines which we have followed in our research and whose effects are discussed in the present applications.

1. Our aim is to provide computational programs which can be used for practical applications. One of the basic requirements is a high computational speed and this in turn depends primarily on the use of rather coarse meshes. Therefore, it is imperative to use integration techniques for interior points which are accurate to second order. If there are no shocks in the flow, both the Lax-Wendroff conservation technique (ref. 2) and the similar, but simpler, non-conservation technique used by Moretti in the blunt-body problem (ref. 1) work equally well. The advantage of the latter with respect to the former is twofold: namely, it is not necessary to recast the equations of motion in conservation form so that the algebraic manipulations are simpler and more straightforward, and the computational time is shorter by a factor of 2, at least.

2. If shocks are imbedded in the flow, the Lax-Wendroff technique, in principle, leads to a steady pattern where shocks are replaced by abrupt, but continuous, transitions spread over several mesh intervals. The Lax-Wendroff technique has been used in this paper for the calculation of flows containing imbedded shocks. This technique, however, suffers from the following limitations:
   (i) The mesh must be relatively fine in the neighborhood of the shock since the computed shock thickness varies directly with mesh size;
   (ii) The physical parameters near the shock show a wavy pattern reminiscent of truncated Fourier expansions in the vicinity of a discontinuity.

The incorporation of an explicit shock representation into the simpler interior point technique would eliminate these shortcomings and increase both resolution and calculation speed. However, as discussed in section IV, a balance must be struck between these desirable objectives and several additional considerations. Some elementary examples of the explicit shock technique have already been worked out successfully by Moretti (refs. 4 and 5).

3. The boundary conditions at all rigid walls should be imposed using a modified method of characteristics (ref. 3). This is crucial to insure over-all accuracy. Figure 1 shows how well the steady pressure distribution obtained from a two-dimensional time-dependent calculation agrees with the Prandtl-Meyer distribution along a wall with a 15° expansion corner. In this case a second-order non-conservation integration technique has been used at all points except on the wall

---

* Advanced Development Engineer, GAEC
** Consultant, and Professor, Polytechnic Institute of Brooklyn

where a modified method of characteristics has been used.

4. If the computational region does not extend to infinity and the flow on its non-rigid boundaries is subsonic, it is physically impossible to prescribe proper conditions on these boundaries since all signals from the interior region (computed) affect the exterior region (not computed) and vice versa. Consequently, all physical parameters on these boundaries should be allowed to change with time but there is no way of knowing a priori how these changes should occur. While it is true that the flow at some distance from an airfoil or any other obstacle is only slightly perturbed, all artificial limitations on non-rigid boundaries of a computational region will trap out-going waves to some extent. As the computation proceeds in time, these artifically created standing waves may eventually accumulate and cause the calculation to become unstable. In order to provide the computation with a physically well-posed set of boundary conditions, one should extend the computational region to infinity. This goal is achieved by mapping the infinite region surrounding the obstacle onto a finite region where the computation is performed.

The authors are indebted to R. C. Meyer of Grumman whose encouragement and suggestions have significantly aided in the development of the various numerical procedures used in this paper.

II. NOTATION

a	nondimensionalized speed of sound
$\underset{\sim}{A},\underset{\sim}{B}$	matrices $\partial f/\partial w$, $\partial g/\partial w$, respectively
$\bar{a},\bar{b},\bar{c},\bar{d},\bar{e}$	defined in equation (14)
$b(x)$, $h(x)$	functions defining airfoil and duct wall, respectively
C_p	pressure coefficient = $(p-p_\infty)/\frac{1}{2}\rho_\infty V_\infty^2$
E	total energy = $1/(\gamma-1)\,p/\rho + \frac{1}{2}(u^2+v^2)$
F,G	functional representation of coordinate transformations
H	total enthalpy = $E + p/\rho$
i,j	X and Y node point counters in the computation space
$k_1, k_2, \ldots$	constants appearing in coordinate transformations
ℓ,m,n	X_x, Y_x, Y_y respectively
M	Mach number
p	nondimensionalized pressure
P	$\log p$
r,θ,t	polar coordinate system
R	$\log \rho$
u,v	nondimensionalized velocity components in x,y,t coordinate system
$\tilde{u},\tilde{v}$	nondimensionalized velocity components in ξ,η,τ coordinate system
$\vec{V}$	nondimensionalized velocity vector
V_B	nondimensionalized velocity at a surface node point
w,f,g	vectors used in the conservation formulation
x,y,t	coordinates in physical space
X,Y,T	coordinates in computational space
γ	isentropic exponent
$\Delta X, \Delta Y, \Delta T$	mesh spacing in the computational space
$\Delta\tau$	$= \Delta T$
ξ,η,τ	physical coordinates used for characteristics method
$\hat{\xi},\hat{\eta}$	unit vectors in the ξ,η directions
ρ	nondimensionalized density

Subscripts: Subscripting a variable with any of the coordinates indicates partial differentiation while the indices i,j indicates the node point. Thus $w_{TT_{i,j}}$ indicates the second time derivative of w in the computational space at $X = i\Delta X$, $Y = j\Delta Y$

III. ANALYSIS

Several different forms of the equations of motion are used in the calculations described in this paper, depending on the nature of the flow expected, and/or whether or not a solid boundary is involved. In general, solid boundary points are calculated using a modified method of characteristics. Interior (non-boundary) points in shock-free flows are calculated using finite difference analogues of the usual partial differential equations of motion. For flows containing imbedded shocks, finite difference analogues of the equations of motion in conservation form are used for the interior point calculations.

A) Interior Points for Flows with Shocks

The nondimensionalized equations of motion in a cartesian frame can readily be regrouped into what is commonly referred to as conservation form as follows:

$$(\rho)_t + (\rho u)_x + (\rho v)_y = 0$$

$$(\rho u)_t + (\rho u^2 + p)_x + (\rho uv)_y = 0$$
$$(\rho v)_t + (\rho vu)_x + (\rho v^2 + p)_y = 0 \qquad (1)$$
$$(\rho E)_t + (\rho uH)_x + (\rho vH)_y = 0$$

where for a perfect gas,

$$H = E + p/\rho = \gamma/(\gamma-1)\, p/\rho + \tfrac{1}{2}(u^2 + v^2) \qquad (2)$$

For simplicity in subsequent manipulations, the following vector notation is introduced,

$$w = \begin{vmatrix} \rho \\ \rho u \\ \rho v \\ \rho E \end{vmatrix}, \quad f = \begin{vmatrix} \rho u \\ \rho u^2 + p \\ \rho uv \\ \rho uH \end{vmatrix}, \quad g = \begin{vmatrix} \rho v \\ \rho vu \\ \rho v^2 + p \\ \rho vH \end{vmatrix} \qquad (3)$$

so that the equations of motion in conservation form can be rewritten as

$$w_t + f_x + g_y = 0 \qquad (4)$$

An auxiliary computational space is defined by the transformation

$$T = t$$
$$X = F(x) \qquad (5)$$
$$Y = G\,(x,y)$$

The specific forms of the functions F and G depend on the problem to be calculated and are thus deferred until the next section of this paper. In the computational space, the system of equations (4) becomes

$$w_T + \ell f_X + m f_Y + n g_Y = 0 \qquad (6)$$

where

$$\ell = X_x,\ m = Y_x \text{ and } n = Y_y$$

It is noted that the transformation scale factors ℓ,m,n are not incorporated into the X and Y derivatives to yield "conservation equations" in the computational space. It is conjectured that conservation form should be maintained in the physical space rather than in the computational space for calculating shocked flows without explicit shock handling. Following the procedure originated by Lax and Wendroff (ref. 2) the vector w is expanded as a trucated Taylor series in time,

$$w(T+\Delta T) = w(T) + w_T\Delta T + w_{TT}\frac{\Delta T^2}{2} + \ldots\ldots \qquad (7)$$

In equation (7), the vector w_T is immediately available from Equation (6), namely

$$w_T = -\,(\ell f_X + m f_Y + n g_Y) \qquad (8)$$

Assuming the interchangeability of the order of differentiation the second derivative of w with respect to T is given by

$$w_{TT} = -[\ell(Aw_T)_X + m(Aw_T)_Y + n(Bw_T)_Y] \qquad (9)$$

where A and B are the matrices $\partial f/\partial w$ and $\partial g/\partial w$, respectively. Thus both w_T and w_{TT} in the Taylor series are expressible in terms of space derivatives of the vectors f and g.

To obtain the finite difference analogues of these space derivatives, the following conventions are employed:

1) In the evaluation of w_T, the X and Y derivatives are represented by central differences of form

$$\varphi_X = \frac{\varphi_{i+1,j} - \varphi_{i-1,j}}{2\Delta X}, \quad \varphi_Y = \frac{\varphi_{i,j+1} - \varphi_{i,j-1}}{2\Delta Y} \qquad (10)$$

where

$$\varphi_{i,j} = \varphi(i\Delta X,\ j\Delta Y)$$

2) To evaluate the term w_{TT}, considering a typical term, $(Aw_T)_X$, we set

$$(Aw_T)_X + [A_{i+\frac{1}{2},j}\, w_{T_{i+\frac{1}{2},j}} - A_{i-\frac{1}{2},j}\, w_{T_{i-\frac{1}{2},j}}]/\Delta X \qquad (11)$$

where

$$A_{i+\frac{1}{2},j} = (A_{i+1,j} + A_{i,j})$$

$$w_{T_{i+\frac{1}{2},j}} = -(\ell_{i+\frac{1}{2},j}\, f_{X_{i+\frac{1}{2},j}} + m_{i+\frac{1}{2},j}\, f_{Y_{i+\frac{1}{2},j}} + n_{i+\frac{1}{2},j}\, g_{Y_{i+\frac{1}{2},j}})$$

with similar expressions for $A_{i-\frac{1}{2},j}$ and $w_{T_{i-\frac{1}{2},j}}$. Then the derivatives of f and g are represented by

$$f_{X_{i+\frac{1}{2},j}} = (f_{i+1,j} - f_{i,j})/\Delta X$$

$$f_{Y_{i+\frac{1}{2},j}} = (f_{i+1,j+1} - f_{i+1,j-1} + f_{i,j+1} - f_{i,j-1})/4\Delta Y$$

$$g_{Y_{i+\frac{1}{2},j}} = (g_{i+1,j+1} - g_{i+1,j-1} + g_{i,j+1} - g_{i,j-1})/4\Delta Y$$

with similar expressions at the point $i-\frac{1}{2},j$.

This finite difference representation is then used to update the vector w at the interior points of flows in which shocks are expected. This does not of course preclude its use for continuous flows, but more efficient procedures are available for this purpose as discussed below.

B) Interior Points for Continuous Flows

For continuous flows, the conservation form of the equations of motion are not required so that the system to be considered, in the same cartesian frame, is given by

$$\begin{aligned} R_t &= -(u_x + uR_x + v_y + vR_y) \\ u_t &= -(uu_x + uv_y + p/\rho\, P_x) \\ v_t &= -(uv_x + vv_y + p/\rho\, P_y) \end{aligned} \tag{12}$$

where for irrotational flows the energy equation is given by

$$P = \gamma R \text{ and } P = \log p, \quad R = \log \rho \tag{13}$$

This set of differential equations is again transformed into the computational space defined above so that the system becomes

$$\begin{aligned} R_T &= -(\bar{a}R_X + \bar{b}R_Y + \ell u_X + mu_Y + nv_Y) \\ u_T &= -(\bar{a}u_X + \bar{b}u_Y + \bar{c}P_X + \bar{d}P_Y) \\ v_T &= -(\bar{a}v_X + \bar{b}v_Y + \bar{e}P_Y) \end{aligned} \tag{14}$$

where $\bar{a} = \ell u$, $\bar{b} = mu + nv$, $\bar{c} = \ell p/\rho$, $\bar{d} = mp/\rho$, $\bar{e} = np/\rho$ and ℓ, m, n are as previously defined. Again each of the variables R,u,v are expanded as a truncated Taylor Series in time of the form

$$R(T+\Delta T) = R(T) + R_T\Delta T + R_{TT}\frac{\Delta T^2}{2} + \ldots \tag{15}$$

with similar expressions for u and v. The first derivatives, R_T, u_T, v_T are given in terms of space derivatives by the original system of equations. To determine the second derivatives R_{TT}, u_{TT}, v_{TT} we first determine the quantities R_{TX}, u_{TX}, v_{TX} and R_{TY}, u_{TY}, v_{TY} which are expressible in terms of second space derivatives of u, v and P (or R) and first space derivatives of quantities $\bar{a}$, $\bar{b}$, $\bar{c}$, $\bar{d}$ $\bar{e}$, ℓ, m, n. Then, again assuming interchangeability of the order of differentiation, the terms R_{TT}, u_{TT}, v_{TT} are determined. They can ultimately be expressed in terms of first and second space derivatives of u, v and P (or R) and first space derivatives of the quantities ℓ, m, n which are known functions.

At this point, the following central difference formulae are used to represent the first and second space derivatives of the flow variables,

$$\varphi_X = (\varphi_{i+1,j} - \varphi_{i-1,j})/2\Delta X\,, \quad \varphi_Y = (\varphi_{i,j+1} - \varphi_{i,j-1})/2\Delta Y$$

$$\varphi_{XX} = (\varphi_{i+1,j} - 2\varphi_{i,j} + \varphi_{i-1,j})/\Delta X^2\,, \qquad \varphi_{YY} = (\varphi_{i,j+1} - 2\varphi_{i,j} + \varphi_{i,j-1})/\Delta Y^2$$

and

$$\varphi_{XY} = (\varphi_{i+1,j+1} - \varphi_{i-1,j+1} - \varphi_{i+1,j-1} + \varphi_{i-1,j-1})/4\Delta X\Delta Y$$

This finite difference procedure has been found to be faster than the conservation scheme described previously in those flows where both are applicable. The non-conservation formulation will not work in the case of shocked flows unless explicit shock handling is incorporated and the flow rotationality is accounted for.

C. Characteristics Technique for Solid Boundaries

It has been the experience of the authors that the use of reflection techniques and/or non-centered difference techniques to evaluate the flow on arbitrary curved solid boundaries either do not work or are highly inaccurate. Thus in these calculations the solid boundary points are calculated using a technique developed and used with considerable success by Moretti (ref. 3).

This technique determines the flow variables on solid boundaries using a quasi-one-dimensional unsteady characteristic formulation. The basic premise is that wall points are sensitive mainly to signals originating inside the flow and propagating toward the wall at a speed equal to the sum of the sound speed and the flow velocity normal to the wall. Flow distortions due to the two-dimensionality of the flow are treated as forcing functions to the quasi-one-dimensional formulation as discussed below.

At each wall node point, a cartesian frame translating at the local streamwise velocity is defined normal to and parallel with the solid boundary as is indicated in figure 2. In this frame, the equations governing an irrotational flow can be written

$$\begin{aligned} R_\tau + \tilde{u}_\xi + \tilde{u}R_\xi &= -(\tilde{v}_\eta + \tilde{v}R_\eta) \\ \tilde{u}_\tau + \tilde{u}\tilde{u}_\xi + p/\rho\, P_\xi &= -(\tilde{v}\tilde{u}_\eta) \\ \tilde{v}_\tau + \tilde{u}\tilde{v}_\xi + \tilde{v}\tilde{v}_\eta + p/\rho\, P_\eta &= 0 \end{aligned} \tag{17}$$

where

$$\tilde{u} = \vec{V}\cdot\hat{\xi},\ \tilde{v} = \vec{V}\cdot\hat{\eta} - V_B \text{ and } \gamma R = P$$

It is noted that in the continuity and the ξ-momentum equation terms containing η-derivatives are collected on the right hand side and will be considered as constants at each stage of an iterative procedure used to determine the characteristics solution.

The characteristics directions of the first two of equations (17) can readily be shown to be

$$\frac{d_\xi}{d_\tau} = \tilde{u} \pm a \quad , \quad a = \sqrt{\frac{\gamma P}{\rho}} \tag{18}$$

where for the coordinate system defined in figure 2 the + sign represents a characteristic running from within the flow to the wall, and the - sign a characteristic originating within the solid boundary. The compatibility equation along the $(\tilde{u} + a)$ characteristic is given by

$$\frac{dR}{d\tau} + \frac{1}{a}\frac{d\tilde{u}}{d\tau} = -\left(\tilde{v}R_\eta + \tilde{v}_\eta + \frac{\tilde{v}\tilde{u}_\eta}{a}\right) \tag{19}$$

At a particular time step, the $(\tilde{u} + a)$ characteristic passing through the wall node point is projected back in time to the previous time step, intersecting the physical plane at the point (*) indicated in figure 2. The corresponding point in the computational plane is then determined and the flow variables and their X,Y and eventually ξ, η derivatives are determined by interpolation and finite difference procedures. Then, since $\tilde{u}$ at the wall is identically 0, the compatibility relation is sufficient to determine an estimate of R at the wall. The reduced tangentail velocity $\tilde{v}$ is calculated using

$$\tilde{v}(\tau + \Delta\tau) = \tilde{v}(\tau) - [\tilde{v}\tilde{v}_\eta + p/\rho\, P_\eta]d_\tau \tag{20}$$

where we use the fact that $\tilde{u}$ is 0 at the wall. This constitutes the first step in the iterative procedure. A new characteristic is defined by

$$\frac{d\xi}{d\tau} = \tfrac{1}{2}[a_{wall} + (\tilde{u} + a)^*] \tag{21}$$

and the process is repeated until convergence is achieved.

This procedure is used in conjunction with the non-conservation formulation described above for the calculation of shock-free flows. A slightly more complicated version of the characteristics procedure is used with the conservation formulation for flows where imbedded shocks may appear.

IV. CALCULATIONS AND RESULTS

Several different programs have been developed using the finite difference schemes described above to attack the various aspects of the transonic airfoil problem. The specifics of these programs and the results obtained to date are discussed below.

A) Biconvex Airfoil in a Constant Area Duct

Several calculations have been made for the subsonic, and supersonic flow about a 6% biconvex circular arc airfoil aligned with the centerline of a constant area duct. Each of the calculations were made using the conservation formulation for the interior point evaluation and the characteristics procedure on the airfoil surface. The tangency condition on the duct wall was imposed using the reflection technique. For the subsonic calculations, uniform horizontal flow has been specified at $x = \pm\infty$.

The infinitely long duct implied above is reduced to a finite rectangular computing grid using the following stretching and normalization of the streamwise and transverse coordinates.

$$X = k_1 \tanh(k_2 x) \tag{22}$$

$$Y = \frac{y - b(x)}{h(x) - b(x)}$$

where b(x) is the ordinate of the duct centerline and airfoil and h(x) describes the shape of the duct wall, here a constant. For the supersonic calculation the stretching* of the streamwise coordinate is not required so that

$$X = x \tag{23}$$

and uniform supersonic flow and constant streamwise derivatives of the flow variables were specified ½ chord upstream and downstream of the airfoil, respectively.

The centerline and surface pressure distributions for freestream Mach numbers of 0.6, 0.7 and 0.8 are presented in figures 3, 5 and 6. In each case the flow is subcritical so that the aforementioned longitudinal mapping together with the specification of uniform flow at the upstream and downstream boundaries defines a well posed problem. For each of the three freestream Mach numbers an independent theoretical estimate, consisting of a Spreiter Mach correction to the linearized compressible flow prediction for an airfoil in a duct, is superimposed for comparison purposes.

Surface pressure distributions obtained from the time dependent computer program correlate well with these approximate analytic predictions. The influence of surface slope discontinuties at the airfoil leading and trailing edges is seen to cause some local oscillation in the surface pressure, particularly at the lower Mach number. Efforts are being made to minimize this effect. A typical time history of the surface pressure at the mid-chord station is also presented for the M = 0.6 case in figure 4, which indicates the nature of the decay to the asymptotic steady state flow.

The surface pressure distribution obtained at a freestream Mach number of 2.0 is presented in figure 7. A characteristics solution for the same configuration is also shown for comparison. Over the major portion of the airfoil surface the pressure distributions are seen to agree quite well. The chordwise range of good correlation has been observed to improve consistently with mesh refinement. The leading edge precompression and subsequent over-compression effect is inherent in the implicit shock representation employed. A similar comment applies at the trailing edge. A Mach profile at the mid-chord station is included in figure 8, which graphically illustrates the shock representation obtained using the conservation formulation. Greater resolution can be achieved by mesh refinement which implies greater computer times. The decision to switch to an explicit shock representation to obtain further increases in resolution must be carefully weighed against several considerations:

1) Explicit shock representation requires a significant increase in program sophistication;
2) More importantly, it requires a pre-knowledge of the basic shock structure that will develop.

Two approaches have been used in our efforts to obtain supercritical results for the biconvex airfoil. In both cases, successful calculations have not been achieved to date.

The first approach consisted of increasing the Mach number at the upstream and downstream boundaries of the constant area duct. This specification is not rigorous in the supercritical range but is a reasonable approximation in an exploratory investigation of this type. The supercritical calculations showed an initial tendency toward the expected results, but later on in the computation, certain unresolved disturbances developed, which after reinforcement by reflections at the various boundaries, eventually cause the calculation to go unstable. Efforts to resolve this problem are currently in progress.

As noted above, the specification of uniform flow conditions at $x = \pm\infty$ is not precisely correct at supercritical Mach numbers. The flow far upstream may still be specified to be uniform, but, because of losses generated by the airfoil shock system, the correct boundary condition far downstream cannot be specified a priori other than to note that it is a constant pressure subsonic shear flow. This indeterminacy of the exit station flow and its effect on the flow past the airfoil can be removed by introducing a second throat duct configuration as indicated in figure 9. In this way the exit flow is forced to be supersonic and no exit-feedback to the airfoil can occur. The simultaneous introduction of a bell-mouth entry section leading from an infinite reservoir to the constant area test section containing the airfoil constitutes a well posed physical problem. The net result in essence is to create the computational equivalent of a closed throat transonic wind tunnel circuit containing an airfoil model in a parallel walled test section.

Calculations for this airfoil-tunnel configuration at supercritical speeds have been attempted with unsatisfactory results. The problem has been traced to an injudicious choice of inlet geometry which produced disturbances that propagated into the test section and obliterated an otherwise orderly developing supercritical flow. These calculations will be continued in the near future.

B) Nozzle Calculations with a Supersonic Exit

A two-dimensional converging-diverging nozzle affords a natural testing ground for the

---

* The stretching of the streamwise coordinate to permit the specification of boundary conditions at infinity was originally suggested by Dr. R. Melnick of the Grumman Research Department

finite difference techniques that are being considered. The nozzle geometry employed is shown in figure 10. Again, the streamwise and transverse coordinates are stretched and normalized as in the previous set of airfoil calculations, except that here

$$b(x) = 0$$
$$h(x) = -1 + \sqrt{3.34 + .66\,x^2} \tag{24}$$

In the physical plane, the upstream boundary is located at $x = -\infty$ in a reservoir where stagnation conditions are specified. For this purely expansive calculation, the nozzle is truncated somewhat aft of the throat and constancy of the streamwise derivatives constitutes the downstream boundary condition.

The calculations were made using both the non-conservation formulation and the conservation formulation for the interior point evaluations. The centerline and wall pressure distributions obtained using the two techniques are shown in figure 10, with the conservation results shown on the right. The results of the two calculations are practically indistinguishable and straddle the one-dimensional prediction as would be expected.

Results for the same nozzle configuration with a subsonic (shocked) exit condition using the conservation formulation are planned for the near future.

C) Subsonic Flow About a Circular Cylinder

In order to develop the technology required for handling real airfoil shapes, consideration must be given to rounded leading edges. The program and calculations described in this section were made to evaluate schemes for treating simplified shapes with stagnation points in an infinite subsonic domain. A circular cylinder of unit radius has been chosen for simplicity. The non-conservation formulation was used for the interior point evaluations. The system of equations in the physical plane were in polar coordinates but the philosophy of the development of the finite difference equations parallels that indicated for the cartesian frame in section II-B. The transformation used to relate the computational and physical planes is given by

$$X = \pi - \theta$$
$$Y = \tanh k_3\,(r-1) \tag{25}$$

as indicated schematically in figure 11. The computed velocities along the forward and rear stagnation streamlines, along the 90° ray and along the surface are presented in figures 11 and 12. Since the flow Mach number is .1, the results are correlated with incompressible predictions. The agreement between the two is seen to be excellent for the forward stagnation streamline and to diminish somewhat as we procede around the body to the rear stagnation streamline. The excellent correlation in the forward regions of the flow leads us to expect similar results when this technique is applied to rounded leading edge airfoils.

V. FUTURE RESEARCH

Several short term efforts are currently in progress, some of which were indicated in the previous section. These include calculations for:

1) Supercritical biconvex airfoil in both th- onstant area duct and the transonic tunnel;
2) Shocked two-dimensional nozzles;
3) Subsonic Joukowski section in an i ce stream;
4) Supercritical circular cylinder in an infinite stream using the explicit shock formulation.

These short term goals are part of what we consider to be an orderly development of those elements required for the calculation of the supercritical flow about lifting airfoils toward which this research is directed.

As demonstrated in the literature, the time dependent finite difference technique has proven to be a versatile tool for calculating the transonic flow about blunt bodies at supersonic velocities. It was this success which motivated the present application to the equally challenging problem of transonic flow about airfoils. The encouraging results achieved to date tend to justify its use in this application.

VI. REFERENCES

1. Moretti, G., "Inviscid Blunt Body Shock Layers (Two-Dimensional Symmetric and Axisymmetric Flows)," Polytechnic Institute of Brooklyn, PIBAL Rept. No. 68-15 (1968).
2. Lax, P. D. and Wendroff, B., "Difference Schemes for Hyperbolic Equations with High Order of Accuracy", Comm. Pure Appl. Math. 17, 381-398 (1964).
3. Moretti, G., and Abbett, M., "A Time Dependent Computational Method for Blunt Body Flows", AIAA J. 4, 2136-2141 (1966).
4. Moretti, G., "A Critical Comparative Study of Finite-Difference Techniques for Quasi-One-Dimensional Unsteady Flows", Polytechnic Institute of Brooklyn (1968) (in preparation).
5. Moretti, G. and Bastianon, R., "Three-Dimensional Effects in Intakes and Nozzles", AIAA paper No. 67-224 (1967).

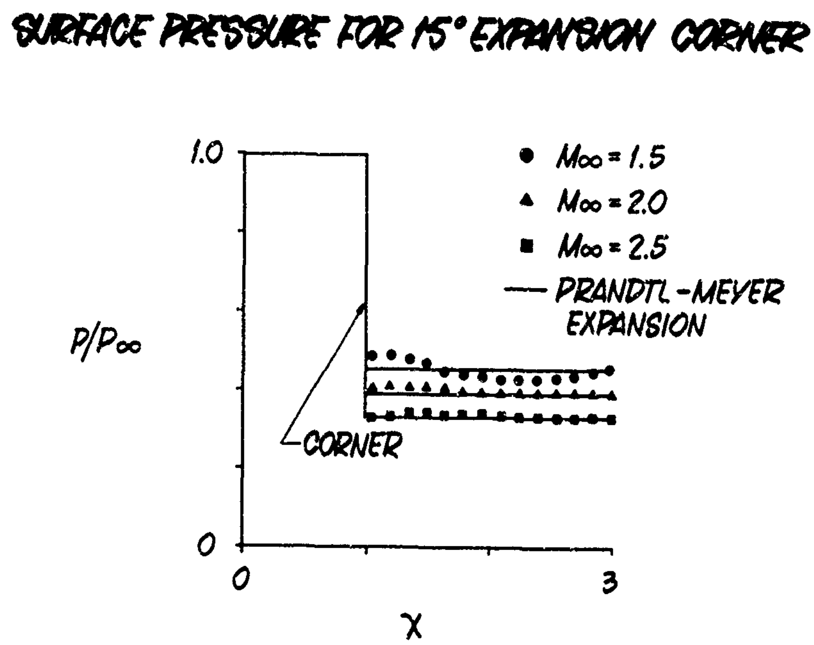

Figure 1 Surface Pressure Distributions for a Two-Dimensional 15° Expansion Corner

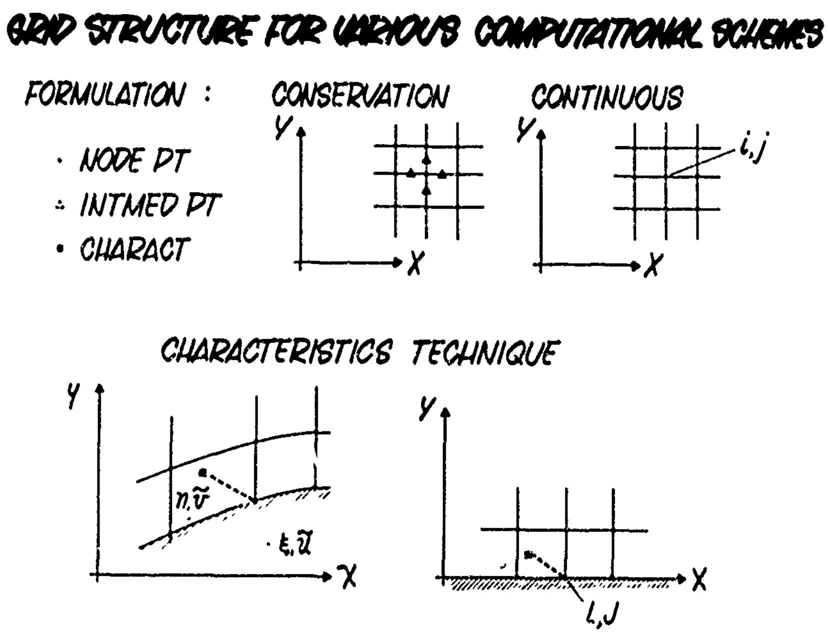

Figure 2 Grid Structures Used for Various Computational Schemes

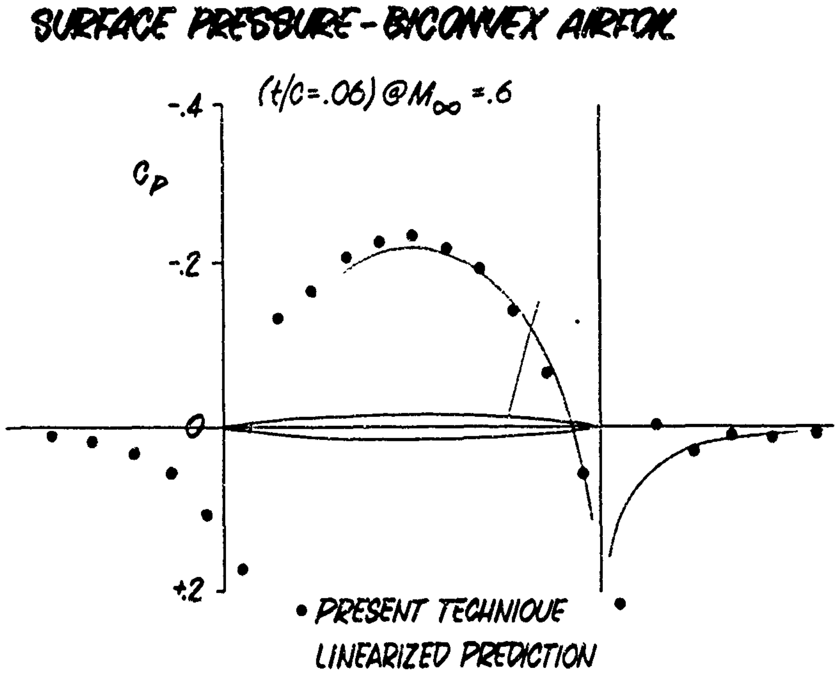

Figure 3 Surface Pressure Distribution on a 6% Thick Biconvex Airfoil at M_∞ = 0.6

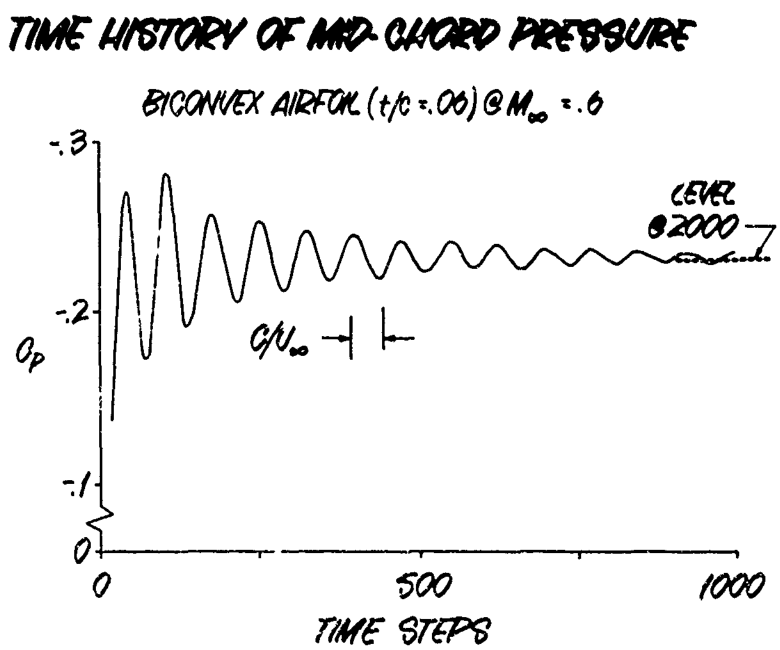

Figure 4 Time History of Mid-Chord Surface Pressure on a 6% Thick Biconvex Airfoil at M_∞ = 0.6

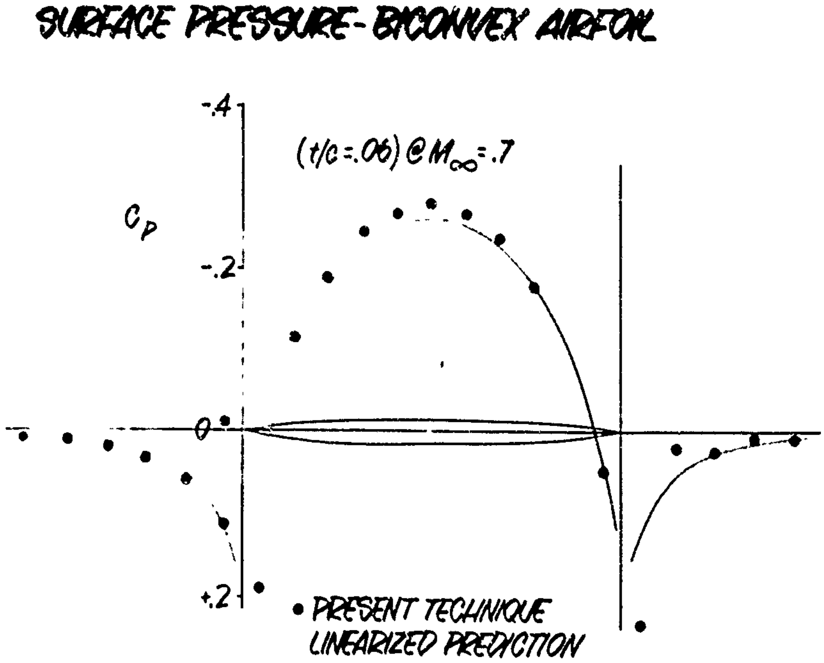

Figure 5 Surface Pressure Distribution on a 6% Thick Biconvex Airfoil at $M_\infty = 0.7$

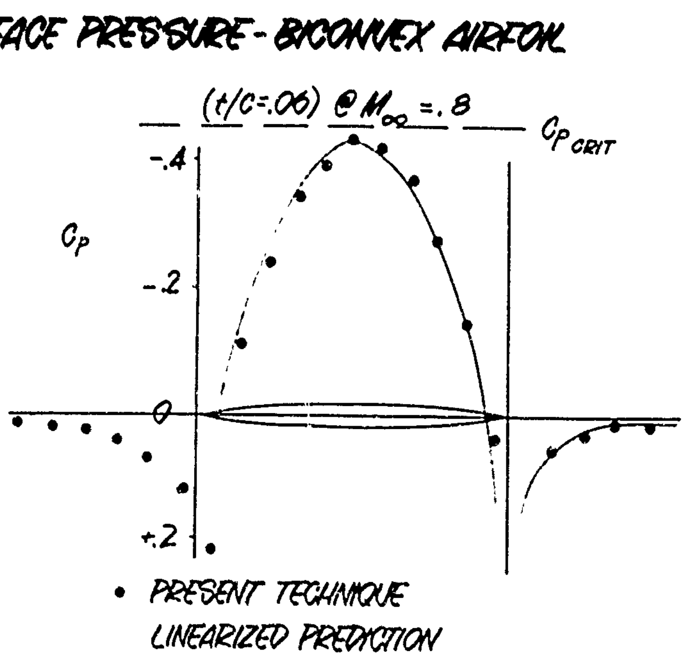

Figure 6 Surface Pressure Distribution on a 6% Thick Biconvex Airfoil at $M_\infty = 0.8$

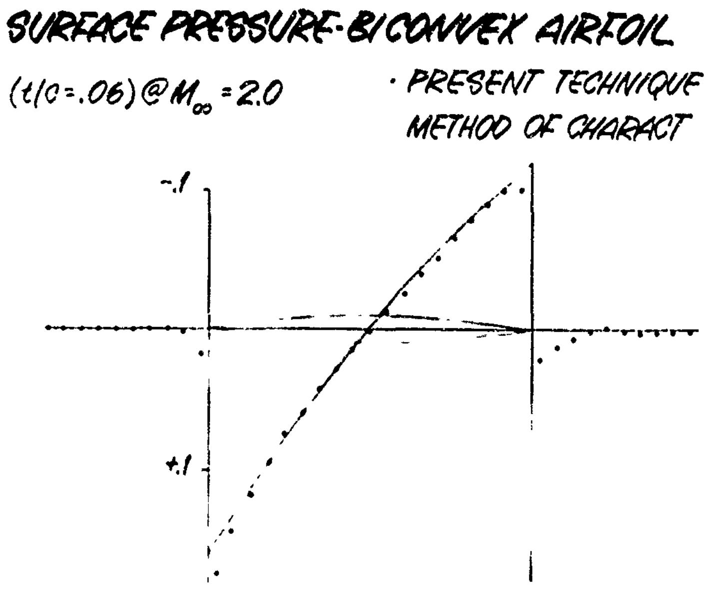

Figure 7 Surface Pressure Distribution on a 6% Thick Biconvex Airfoil at $M_{\infty} = 2.0$

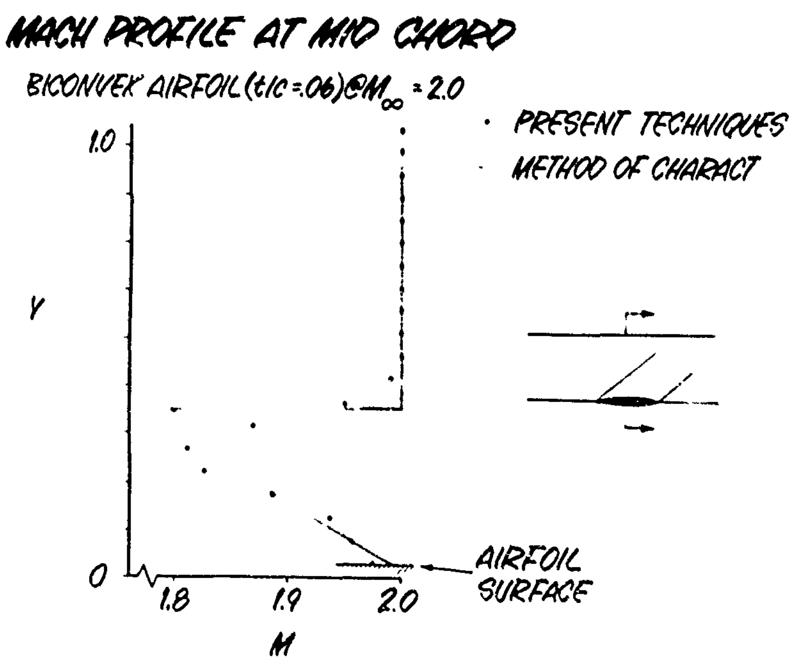

Figure 8 Mach Profile at the Mid-Chord of a 6% Thick Biconvex Airfoil at $M_{\infty} = 2.0$

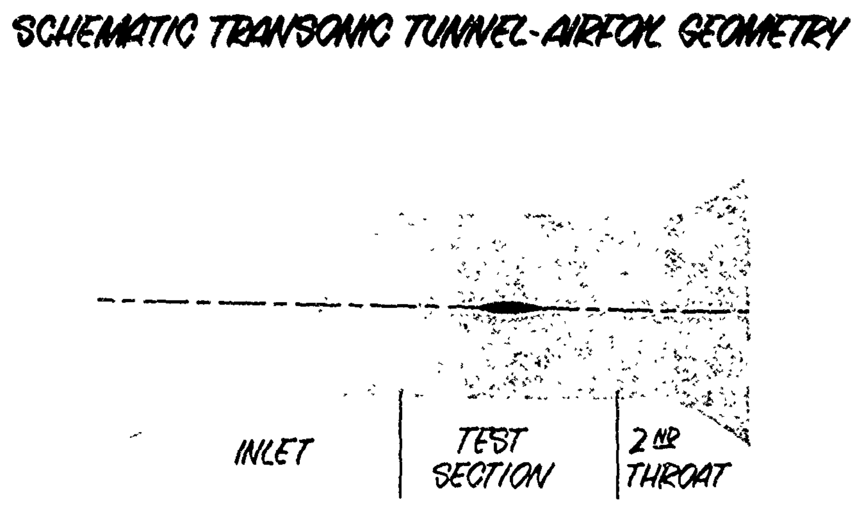

Figure 9 Schematic Transonic Tunnel - Airfoil Geometry for Supercritical Calculations

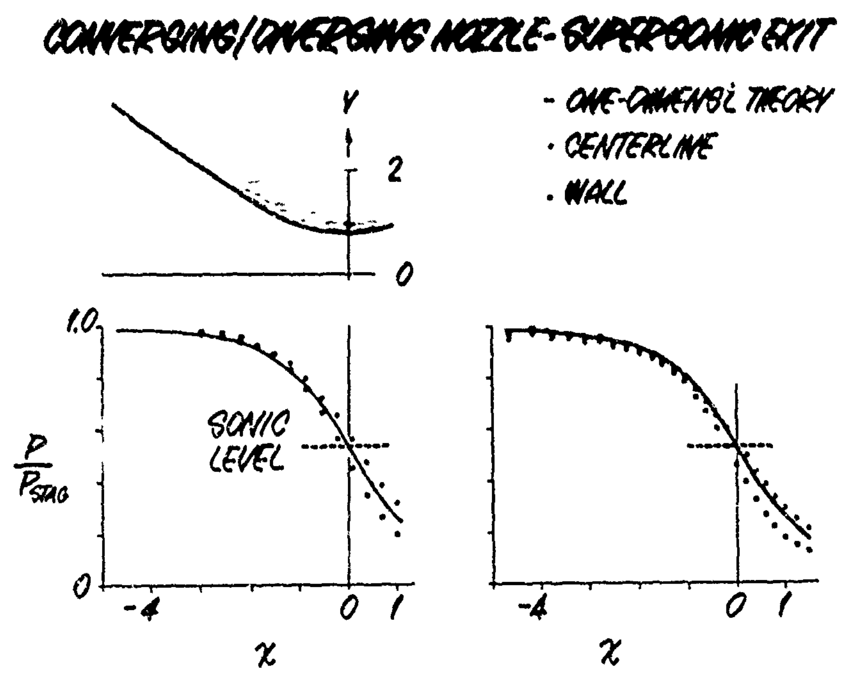

Figure 10 Nozzle Wall and Centerline Pressure Distributions for .. verging-Diverging Nozzle with Supersonic Exit Conditions

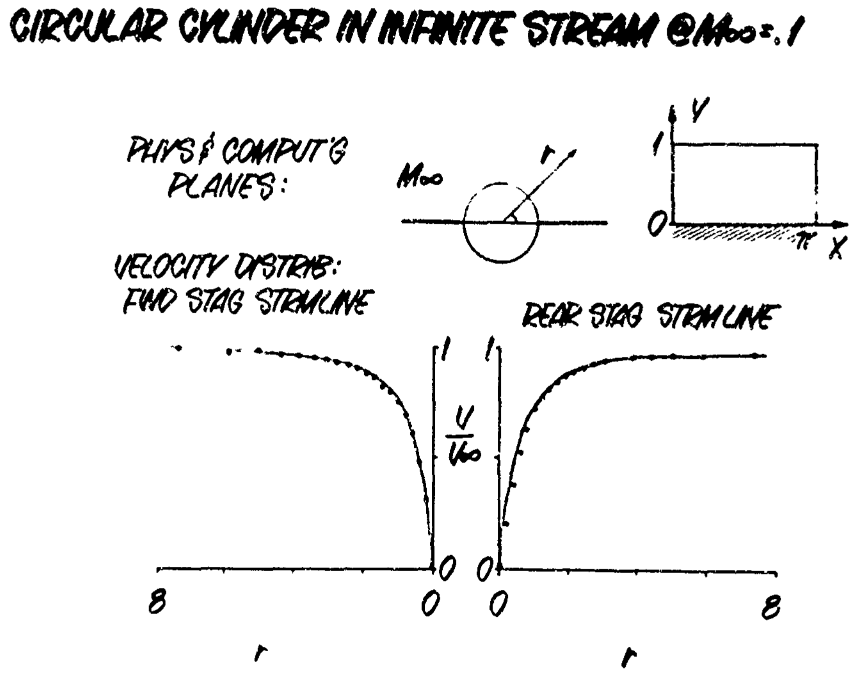

Figure 11 Velocity Distributions on the Forward and Aft Stagnation Streamlines of a Circular Cylinder at $M_\infty = 0.1$

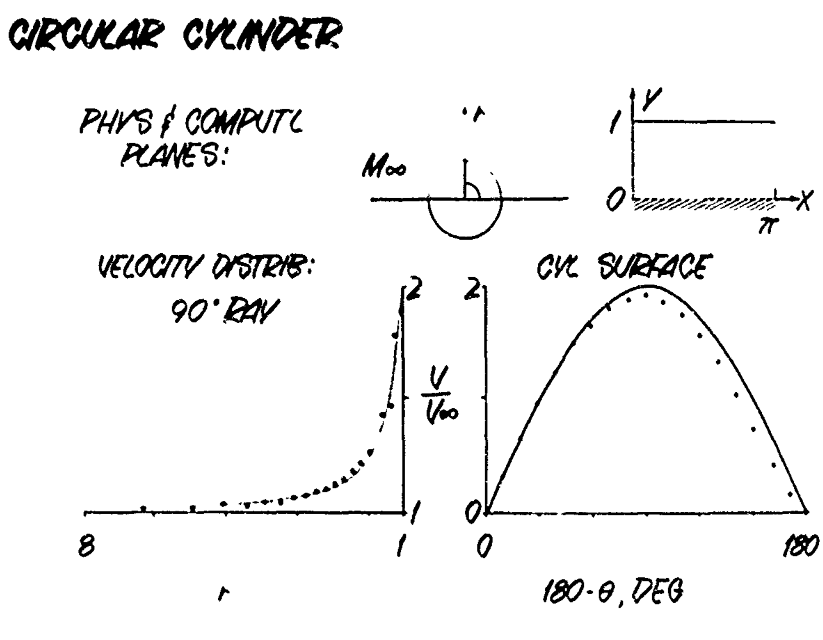

Figure 12 Velocity Distributions on the 90° Ray and the Cylinder Surface at $M_\infty = 0.1$

SUPERCRITICAL TRANSONIC AIRFOIL DESIGN FROM PRESCRIBED VELOCITY DISTRIBUTION

by

M. S. Cahn, H. R. Wasson and J. R. Garcia

Northrop Corporation,
Norair Division

SUMMARY

A method recently developed by Northrop consists of a computer program which will determine an airfoil shape from predetermined supercritical velocity distributions having extensive regions of supersonic flow. The velocity is given versus the distance around the airfoil. This allows a designer to design to a given lift by specifying the required circulation. Also, boundary layer problems can be avoided by restricting adverse velocity gradients.

Starting with a given compressible pressure or velocity distribution with mixed subsonic and supersonic regions an airfoil shape can be determined. This is done by making a transformation that causes the streamline and potential line network to give an equivalent incompressible flow. This incompressible problem is then solved by complex function theory and the solution is transformed back to the compressible plane. A computer program using this method has been applied to several shapes with known solutions. The results indicate that this method is a useful tool for studying supercritical transonic airfoil shapes.

SUPERCRITICAL TRANSONIC AIRFOIL DESIGN FROM PRESCRIBED VELOCITY DISTRIBUTION

by

M.S. Cahn, H.R. Wasson, and J.R. Garcia

NORTHROP CORPORATION, NORAIR DIVISION

INTRODUCTION

Supercritical transonic airfoil design requires the solution of flows with mixed supersonic and subsonic speeds. The solution to the problem has proved to be extremely difficult. The usual approach has been to make approximate corrections to the incompressible flow solutions about a given shape. Because of the sensitivity to small variations in airfoil shape this method has not been wholly satisfactory, especially at supercritical speeds.

Almost complete reliance on wind tunnel testing has been necessary to get good determination of airfoil characteristics. With a combination of wind tunnel testing and subsequent modification of configuration, designers have had some success in obtaining satisfactory design.

It has now been determined that many of the problems of obtaining a satisfactory supercritical wing design can be solved by first starting with a prescribed velocity distribution in the physical plane. This allows the designer to approach more directly the desired airfoil characteristics. Also, and perhaps more important, this leads to a relatively simple solution to the difficult problem of mixed flows with supercritical velocities. This new method will be demonstrated in this paper.

SYMBOLS

V	local velocity	s	distance along streamline
V_∞	free stream velocity	n	distance normal to stream line
ϕ	velocity potential	Z	complex coordinate in compressible plane
ψ	stream function	Z'	complex coordinate in incompressible plane
ρ	density	θ	angle in circle plane
ρ_∞	free stream density	α	local flow angle in airfoil plane
		ξ	complex coordinate in circle plane

OUTLINE OF THEORY

Assume that

$\frac{V}{V_\infty}$ versus S and free stream Mach number are given.

$\phi = \int$ vds can be obtained from a simple integration.

Since $\frac{\partial \phi}{\partial s} = \frac{\rho_\infty}{\rho} \frac{\partial \psi}{\partial n}$, ϕ - lines and ψ - lines form an orthogonal network of rectangles. The length-width ratio of these rectangles are proportional to the local density (ρ)[1]. The equivalent incompressible flow has ϕ and ψ lines orthogonal and the network forms squares. The compressible flow field can then be transformed to an equivalent incompressible flow by substituting s' for s where $ds' = f(\rho)\, ds$. The transformation is discussed in NACA Report No. 789 (1944) by I.E. Garrick and C. Kaplan. Now ϕ versus s' is known for the equivalent incompressible flow.

---

*Mr. Cahn, Mr. Wasson and Mr. Garcia are Research Engineers in the Aerodynamics Group.

[1]Shapiro, Ascher H., The Dynamics and Thermodynamics of Compressible Fluid Flow, Pg 296 (Ronald Press, 1953)

Consider now the transformation of the airfoil into a circle by the equation $Z' = f(\xi)$ where Z' represents the incompressible airfoil plane and ξ represents the circle plane. It can be shown that

$$\ln \frac{dZ'}{d\xi} = \ln \left| \frac{ds'}{d\theta} \right| + i\,(\alpha - \theta - \pi/2)$$

From ϕ versus s' and knowing ϕ versus θ for the flow about a circle, s' versus θ, $\frac{ds'}{d\theta}$, and $\ln \left|\frac{ds'}{d\theta}\right|$ can be determined. Since $\ln \left|\frac{ds'}{d\theta}\right|$ is the real part of an analytic function the imaginary part can be found from its Fourier series representation. The imaginary part allows determination of α, the local surface slope of the airfoil, and from s' and α the incompressible shape can be plotted. The equivalent compressible shape comes from a retransformation by again substituting ds for $\frac{1}{f(\rho)}\,ds'$.

COMPARISONS WITH EXISTING DATA

The method described above for supercritical airfoil design has been programmed for IBM 360/65 system in basic Fortran IV. The program is relatively simple to use and takes only approximately two minutes of computing machine time to run one case.

In order to shed more light on the program's performance, a circular arc profile was computed. The velocity distribution data for this shape comes from NACA report 1217. The results for a circular arc section are shown in Figure 1. The shape of the section for a Mach Number range from 0.6 to 0.87 shows very little change. This indicates that the compressibility effect is well accounted for.

Once the condition for airfoil closure was established the problem consisted of refining the numerical procedure until there was sufficient accuracy at all points of the airfoil.

The accuracy of the program for supercritical flows is shown in Figure 2, where the results of calculations for an NACA 0012 section at 0.75 Mach Number are given. The input data are relaxation computations from NACA TN 1746. The results indicate that the method is feasible and can give good results. A comparison with supercritical experimental data for a NACA 0012 airfoil (Figure 3) shows the computed shape to grow thicker toward the trailing edge. This is believed due to the boundary layer displacement thickness on the actual experimental airfoil. It should be noted that supercritical flow exists on the NACA 0012 airfoil at the Mach Number tested. The local Mach Number is above 1 from 10 to 30 percent chord and reaches a peak of approximately 1.1.

The program has been applied to other supercritical transonic airfoils with more extensive supersonic velocities and the results indicate similar accuracy to that obtained for the NACA 0012. Among these airfoils were asymmetrical and lifting configurations.

APPLICATION TO TRANSONIC AIRFOIL DESIGN

The program described herein is being used by Northrop for the design of transonic airfoils. Three examples are shown in Figures 4 through 9 along with the hodograph plots for these airfoils. The airfoils are designated by a letter and numbers. The letter indicates a specific series. The first two numbers indicate the design Mach Number in 100ths. The next two numbers indicate the design lift coefficient in 100ths and the last three numbers indicate the airfoil thickness in 1000ths of the chord. All of the data shown are at the design conditions.

Airfoil G8027-120 has an extensive region of supersonic flow. The hodograph plot indicates that there is no tangency of the boundary streamline with a characteristic line.

Airfoil G-8022-088 has a smaller region of supersonic flow and the lower surface is made to have free stream velocities over most of its distance.

Airfoil G-8040-076 has a similar upper surface distribution to G-8022-088 but the lower surface velocities were adjusted to give a higher lift.

Further analysis on these and other shapes are planned at Northrop. The analysis will include boundary layer stability calculations.

CONCLUSIONS

Results of calculations of airfoil shapes from supercritical compressible velocity distributions indicate that it is feasible to calculate the shapes with reasonable accuracy using a transformation to an incompressible plane, and that the method can be useful for studying transonic airfoil shapes with supercritical velocities.

The program described herein can be used to assist in the design of improved transonic airfoils. The effect of velocity distribution changes on airfoil shapes can be studied at transonic speeds. Higher drag rise Mach numbers may be obtained by designing to avoid limit lines using the hodograph representation.*

*Cahn, M.S., Journal of Aircraft, May-June 1967 (AIAA).

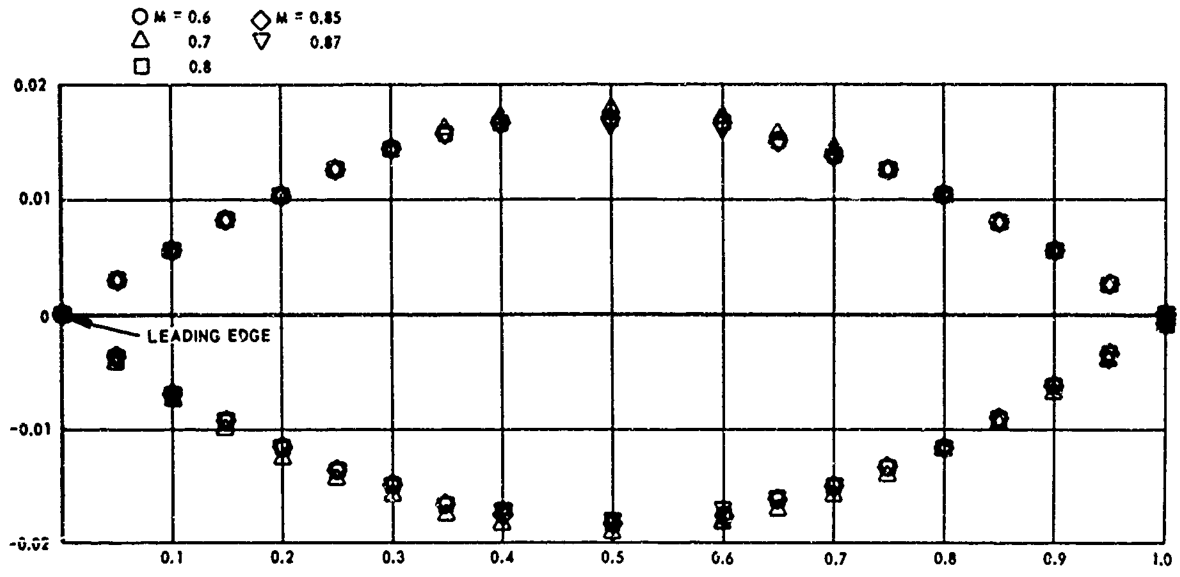

FIGURE 1. CALCULATED CIRCULAR AIRFOIL

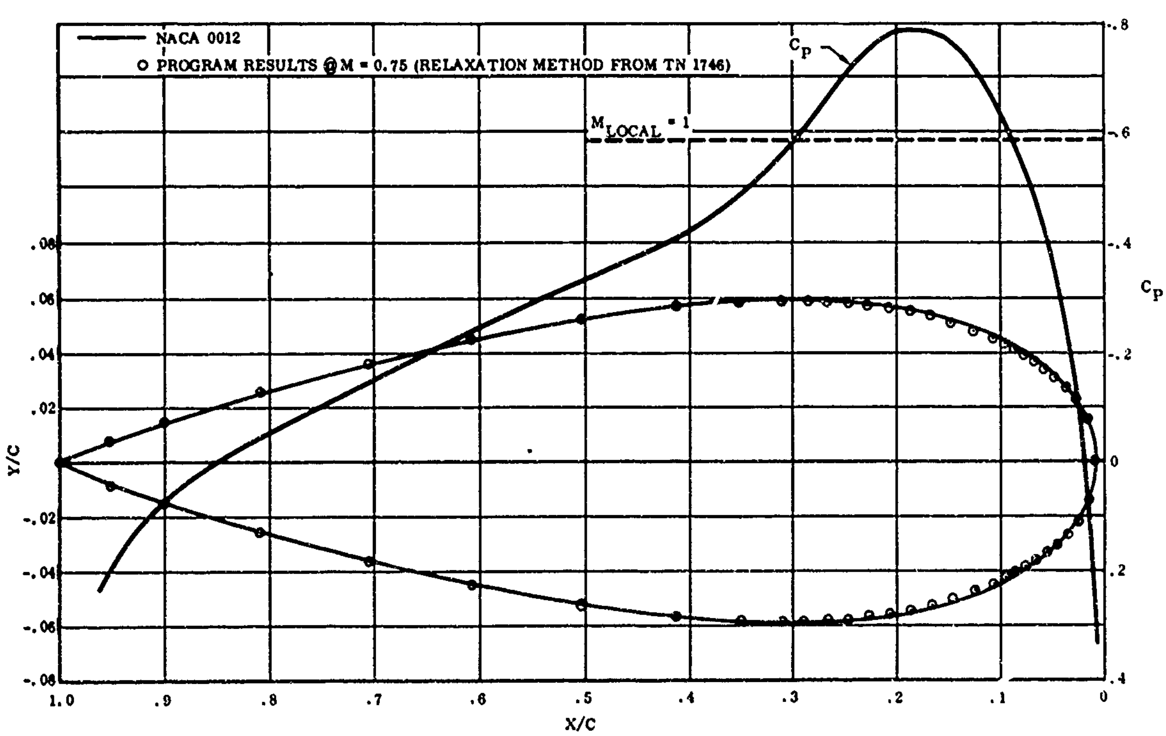

FIGURE 2. AIRFOIL CALCULATION FROM SUPERCRITICAL RELAXATION DATA

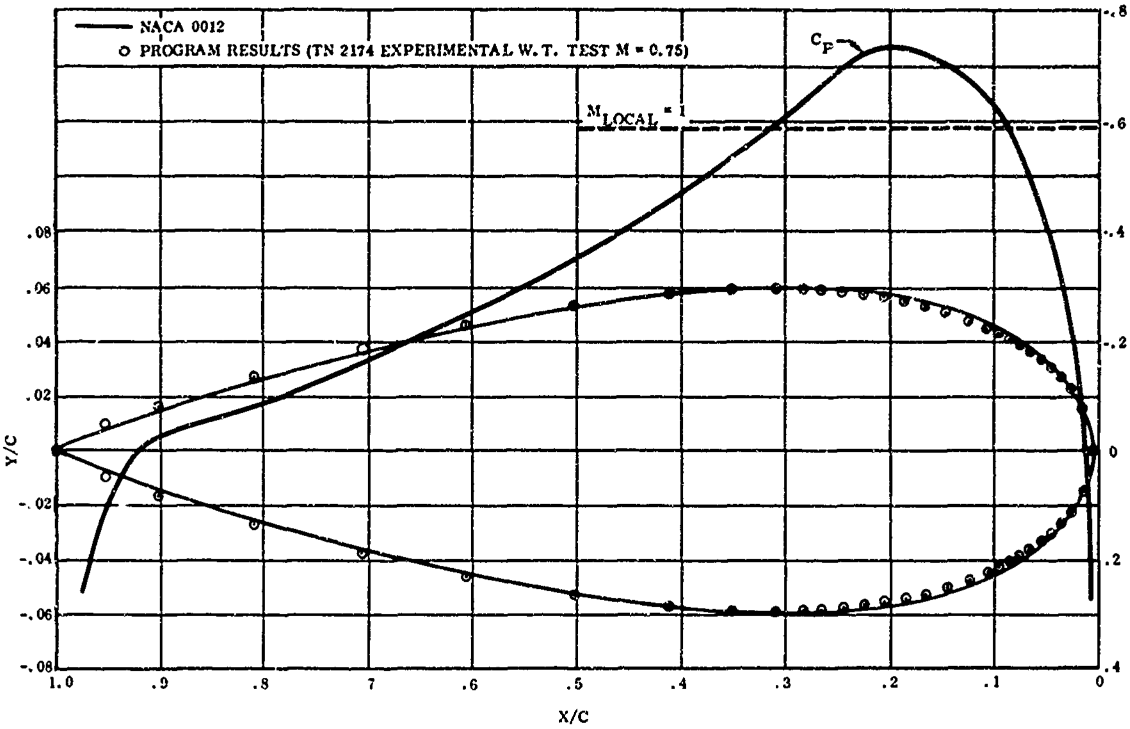

FIGURE 3. AIRFOIL CALCULATION FROM SUPERCRITICAL EXPERIMENTAL DATA

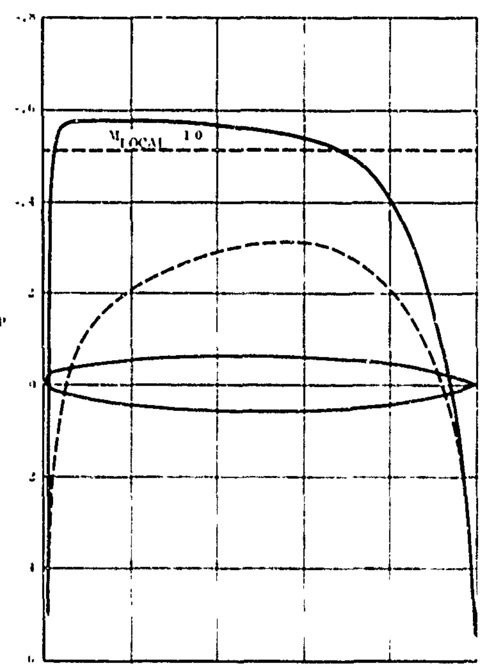

FIGURE 4. AIRFOIL G-8027-120

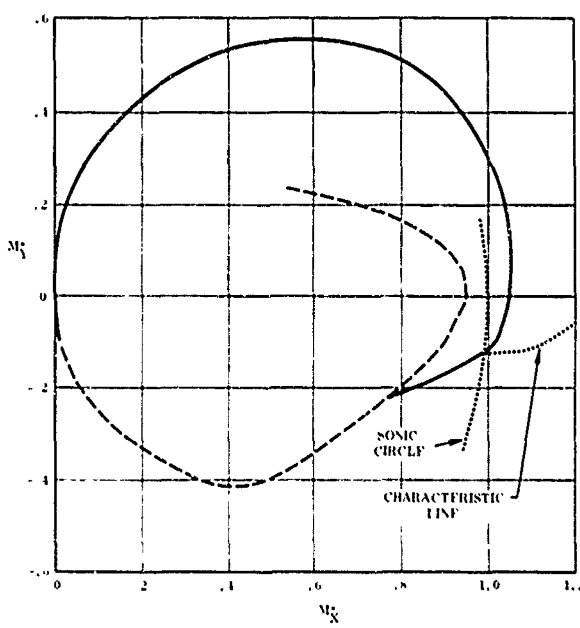

FIGURE 5. HODOGRAPH FOR AIRFOIL G-8027-120

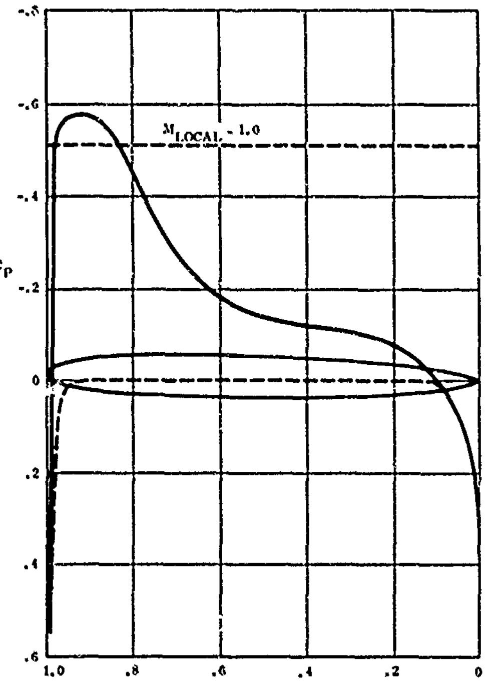

FIGURE 6. AIRFOIL G-8022-088

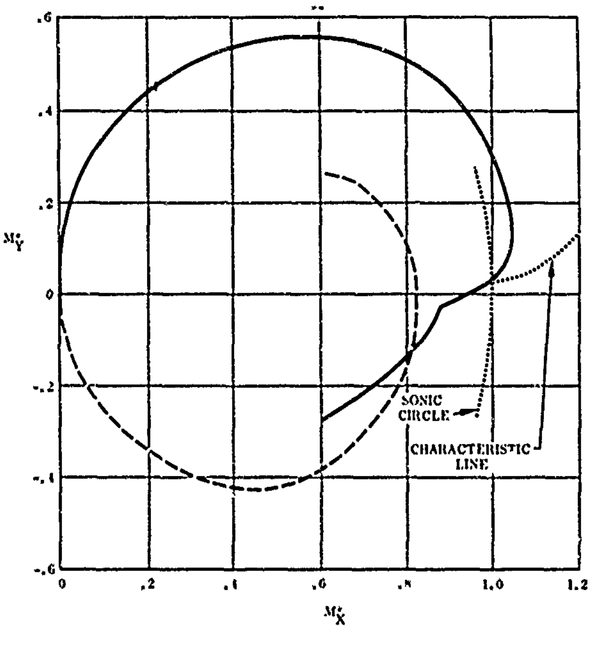

FIGURE 7. HODOGRAPH FOR AIRFOIL G-8022-088

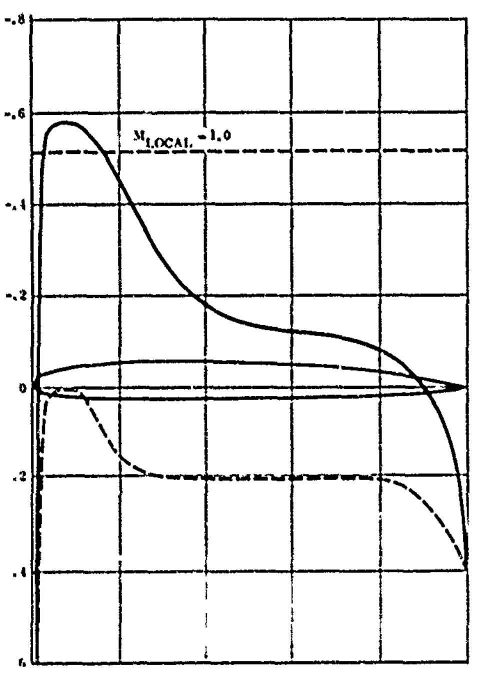

FIGURE 8. AIRFOIL G-8040-076

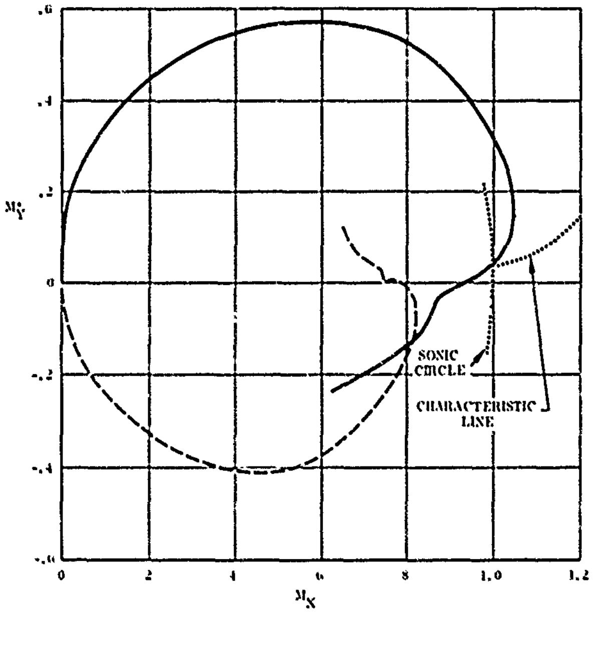

FIGURE 9. HODOGRAPH FOR AIRFOIL G-8040-076

DETERMINATION ANALOGIQUE DE PROFILS D'AILE
EN REGIME TRANSSONIQUE

par

F. RIGAUT

Centre de Calcul Analogique
29, Avenue de la Division Leclerc
Chatillon s/s Bagneux (92)

SOMMAIRE

Une méthode de calcul analogique, basée sur l'emploi des différences finies est appliquée à la détermination d'écoulements transsoniques à partir de leurs hodographes. Après une brève description des méthodes soit analogiques, soit hybrides applicables en ce domaine il est insisté sur l'étude des profils.

Sur ce sujet il est considéré successivement le cas des profils symétriques, le cas des profils à l'incidence de portance nulle et le cas des profils portants. Des exemples et comparaisons sont fournis qui soulignent les possibilités de la méthode. Enfin un algorithme de calcul est proposé pour déterminer, selon une technique hybride, un écoulement comprenant une onde de choc.

Par ailleurs ce procédé est applicable au calcul de grilles d'aubes et différentes possibilités et exemples seront fournis.

EQUATIONS A RESOUDRE.

On considère l'écoulement plan, permanent et irrotationnel d'un fluide compressible. Les grandeurs représentatives : q le module de la vitesse, ρ la masse spécifique, p la pression, φ le potentiel des vitesses, ψ la fonction de courant sont rapportées à leurs valeurs critiques.

En introduisant les variables canoniques θ et σ définies par :

$$\theta : \text{angle de la vitesse} \qquad \sigma = \int_q^1 \frac{\rho}{q}\, dq$$

les fonctions φ et ψ satisfont au système conjugué :

$$\varphi'_\theta = -\psi'_\sigma \qquad \varphi'_\sigma = K(\sigma)\,\psi'_\theta$$

En particulier $\psi(\theta,\sigma)$ est solution de l'équation du second ordre, linéaire et de type mixte :

$$K(\sigma)\,\psi''_{\theta\theta} + \psi''_{\sigma\sigma} = 0 \tag{1}$$

ou $K(\sigma) = (1-M^2)/\rho^2$ est une fonction qui par l'intermédiaire de la relation de S^T Venant reflète la loi de compressibilité du fluide. Cette fonction varie en signe comme σ et selon qu'elle est positive, nulle ou négative, l'équation (1) présentera le type elliptique, parabolique ou hyperbolique ce qui correspond respectivement à un écoulement subsonique, sonique ou supersonique. Précisons qu'un point d'arrêt $q=0$ correspond à $\sigma=\infty$ et que l'axe $\sigma=0$ est l'image de la ligne sonique.

Dans le demi-plan $\sigma<0$ le type hyperbolique (1) implique l'existence de caractéristiques données sous forme différentielle par :

$$d\theta^2 + K(\sigma)\, d\sigma^2 = 0$$

et sur lesquelles la dépendance des coordonnées permet de relier les fonctions φ et ψ par :

$$d\varphi^2 + K(\sigma)\, d\psi^2 = 0 \tag{2}$$

Enfin la correspondance entre les deux plans x, y et θ, σ est donnée par :

$$dx + i\,dy = \frac{e^{i\theta}}{q}\left(d\varphi + i\,\frac{d\psi}{\rho}\right) \tag{3}$$

tandis que les singularités de transformation sont obtenues par les zéro ou infini du Jacobien :

$$J = \frac{D(x,y)}{D(\theta,\sigma)} = -\frac{K(\sigma)\,\psi'^2_\theta + \psi'^2_\sigma}{\rho q^2}$$

METHODE DE RESOLUTION ANALOGIQUE.

Avec les réserves habituelles relatives aux développements limités et en adoptant un maillage irrégulier schématisé figure 1, l'éq (1) peut être écrite sous sa forme aux différences finies. En admettant que les dérivées secondes sont les différences rapportées au pas des dérivées premières on obtient au troisième ordre près (réf. 2)

$$\frac{2\Delta\theta_1}{\Delta\sigma_2+\Delta\sigma_4}\cdot\frac{1}{K_0}(\psi_1-\psi_0) + \frac{2\Delta\theta_3}{\Delta\sigma_2+\Delta\sigma_4}\,\frac{1}{K_0}(\psi_3-\psi_0) + \frac{2\Delta\sigma_2}{\Delta\theta_1+\Delta\theta_3}(\psi_2-\psi_0) + \frac{2\Delta\sigma_4}{\Delta\theta_1+\Delta\theta_3}(\psi_4-\psi_0) + R = 0 \tag{4}$$

avec

$$R = c_1\left(\frac{\partial^3\psi}{\partial\sigma^3}\right)_0 + c_2\left(\frac{\partial^3\psi}{\partial\theta^3}\right)_0$$

L'analogie que l'on se propose consiste à identifier la forme (4) avec la relation exprimant l'état de potentiel électrique en un noeud d'impédance. On considère à cet effet un réseau d'impédances Z_n groupées en croix et siège d'un état de tensions alternatives V_n déphasées de φ_n par rapport aux courants i_n qui y circulent.

A l'aide de la loi de Kirchhoff et de la loi d'Ohm on obtient en un noeud :

$$\frac{e^{j\varphi_1}}{Z_1}(V_1-V_0) + \frac{e^{j\varphi_3}}{Z_3}(V_3-V_0) + \frac{e^{j\varphi_4}}{Z_4}(V_4-V_0) + \frac{e^{j\varphi_2}}{Z_2}(V_2-V_0) = 0 \tag{5}$$

Du rapprochement entre (4) et (5) résultent les relations d'identification :

$$\psi = \lambda V \qquad \varphi = \frac{\lambda}{\mu} I$$

$$Z_1 = \frac{2\,\Delta\theta_1}{\Delta\sigma_2 + \Delta\sigma_4}\cdot\frac{1}{K_0}\cdot e^{j\varphi_1} \qquad Z_2 = \frac{2\,\Delta\sigma_2}{\Delta\theta_1 + \Delta\theta_3}\cdot e^{j\varphi_2} \qquad (6)$$

et des formules analogues pour Z_3 et Z_4 .

Notons que I est la fonction de courant électrique. Elle est accessible à la mesure électrique par l'intermédiaire de sa différentielle qui représente le flux du vecteur intensité ($dI = \vec{n}\cdot\vec{i}\,ds$)

Après avoir choisi un hodographe son domaine utile est quadrillé. Pour la partie elliptique le maillage est pris tel que la frontière ne passe que par des noeuds ; pour la partie hyperbolique le maillage est tel que le réseau de ses diagonales se confonde avec celui des caractéristiques. De plus le maillage est resserré la ou le gradient est fort (voisinage d'une singularité, effet de pointe, ... etc) et est relaché la ou le gradient est faible (point nodal, ... etc).

Ce domaine est ensuite représenté à l'aide d'impédances calculées selon (6) et représentant chacune une maille.

a) si le problème à traiter est elliptique ou elliptique-parabolique la fonction $K(\sigma)$ reste positive. Le réseau représentatif est alors constitué de résistances ($\varphi_n = 0$)

b) si le problème est mixte la fonction $K(\sigma)$ change de signe. On est alors amené à choisir pour les Z_n des impédances imaginaires pures, selfs et capacités telles que le terme en $e^{j\varphi_n}$ affecte les $(V_n - V_0)$ du signe voulu ($\varphi_n = \pm\pi/2$)

L'application aux contours de tels milieux de conditions électriques en accord avec le problème au limite à résoudre conduit à l'établissement des champs $V(\theta,\sigma)$ et $I(\theta,\sigma)$ dont on peut par des mesures électriques relever les valeurs.

Il reste alors à intégrer la relation (3) pour obtenir dans le plan physique toutes lignes désirées de l'écoulement correspondant à l'hodographe choisi.

METHODES DE RESOLUTION ASSOCIEES OU HYBRIDES.

On a vu que suivant les problèmes cherchés il pouvait être utilisé des réseaux soit résistifs, soit composés de selfs et capacités. D'autres procédés sont possibles.

Si l'on remarque que la méthode analogique se prête particulièrement bien à la résolution de problèmes aux limites de type elliptique : Dirichlet ou Neuman et si par ailleurs on constate que le calcul sur ordinateur est très efficace pour la résolution de problèmes aux limites de type hyperbolique : Cauchy ou Goursat on conçoit que dans le cas d'une équation de type mixte les méthodes analogiques ou numériques puissent s'avérer complémentaires.

Les problèmes aux limites rencontrés pour de telles équations permettent en effet un découpage du domaine d'étude en deux sous-domaines de résolution tel que pour l'un il soit préférable d'employer la méthode analogique, pour l'autre la méthode numérique.

D'une façon générale les données d'un problème mixte sont portées par un arc Γ du domaine elliptique et un arc ouvert Δ du domaine hyperbolique fig. (2). Les domaines intérieurs, respectivement Ω_1 et Ω_2 , sont séparés par l'axe parabolique.

Il est souvent possible de remplacer les données sur Δ par des données sur l'axe $\sigma = 0$. On peut alors résoudre un Dirichlet singulier en Ω_1 par analogie ; puis à partir des résultats obtenus déterminer numériquement la solution dans Ω_2 par la résolution d'un problème de Cauchy. C'est le fonctionnement en chaîne ouverte : subsonique d'abord, supersonique ensuite. Tel est le cas dans le calcul de tuyère ou de grille d'aubes.

Dans d'autre cas, les données sur l'axe $\sigma = 0$ ne peuvent être prises arbitrairement et doivent satisfaire à des relations de compatibilité. Dans ce cas il est nécessaire d'opérer des résolutions alternativement en Ω_1 (par analogie) et Ω_2 (par numérique) jusqu'à ce qu'il y ait raccord des solutions le long de l'axe $\sigma = 0$. C'est le fonctionnement en chaîne itérative. Tel est le cas du calcul d'un profil avec choc.

Ces deux modes de résolutions de problème mixte relèvent des possibilités du calculateur Hybride actuellement réalisé au Centre de Calcul Analogique (réf. 3). Le champ subsonique est traité par réseau, le champ supersonique est déterminé par l'ordinateur. L'imposition des conditions aux limites ainsi que la liaison entre Ω_1 et Ω_2 dépendent d'une commutation spéciale.

CALCUL DE PROFILS D'AILE.

Le calcul pratique de profils d'aile à partir de leur hodographe se heurte à trois difficultés. La première provient des singularités introduitent par la transformation de l'hodographe : doublet, point critique, ... etc et qui ont des répercussions sur la précision des calculs. La seconde difficulté apparaît lorsqu'on désire obtenir des profils supportant des répartitions de vitesses partiellement supersoniques: des précautions sont à prendre afin de n'avoir à résoudre que des problèmes bien posés. Enfin la dernière difficulté consiste en la présence éventuelle de choc et sur la manière dont on en conçoit l'hodographe. Bien que dans le problème le plus général ces trois questions sont imbriquées, chacune de ces difficultés sera traitée à part.

1. SINGULARITES ET HODOGRAPHE D'UN PROFIL NON PORTANT.

L'image de l'écoulement autour d'un profil symétrique est représentée figure (3). La courbe $B'C$ D' est l'image du profil, AB et ED sont celles de l'axe de symétrie et le point P correspond à l'écoulement uniforme à l'infini du profil.

Si l'on s'intéresse à la fonction de courant les conditions aux limites sont les suivantes :

- sur $B'CD'$, AB et ED : $\psi = 0$
- BB' et DD' sont des lignes de gradient nul ou :

$$\psi = 0 \quad \text{et} \quad \psi'_\theta = \psi'_\sigma = 0$$

- en $P(\theta_\infty, \sigma_\infty)$ se trouve un point critique d'ordre 2. Il en résulte pour la fonction de courant un développement dont le terme principal est (réf. 7)

$$\psi \simeq \frac{c}{\sqrt{r}} \sin \frac{\omega}{2} \tag{7}$$

$$r^2 = (\theta - \theta_\infty)^2 + K.(\sigma - \sigma_\infty)^2 \qquad \operatorname{tg} \omega = \frac{\theta - \theta_\infty}{\sqrt{K}\,(\sigma - \sigma_\infty)}$$

Sur le réseau correspondant il convient donc :

- Aux frontières $B'CD'$, AB et ED d'imposer un potentiel $V = 0$
- aux infinis BB' et DD' de laisser le potentiel se fixer à la valeur $V = 0$
- En P de tenir compte de l'équation (7). Pour cela il est nécessaire de resserrer le maillage autour de P et de calculer à l'aide de (7) les résistances qui en sont issues. En ce point il est imposé un potentiel $V = 1$.

Si maintenant on considère un profil quelconque et placé à l'axe de portance nulle le développement (7) devient :

$$\psi \simeq \frac{c}{\sqrt{r}} \left(a \sin \frac{\omega}{2} + b \cos \frac{\omega}{2} \right)$$

Dans ce cas on ne peut se limiter à un demi-champ comme précédemment et l'hodographe s'inscrit sur des feuillets de Riemann raccordés en P fig (4).

Pour représenter un tel hodographe il suffit de pratiquer dans le champ une coupure issue nécessairement de P et rejoignant selon un chemin arbitraire un point du profil : le point d'arrêt par exemple. Sur cette coupure la continuité des fonctions φ et ψ donc I et V est assurée par raccord électrique.

Il convient de remarquer que si le profil comporte une bosse ou un creux (fig. 5) la situation se complique par l'apparition d'un point critique distinct de P.

Ce fait se comprend intuitivement si l'on considère que dans le plan de l'écoulement le méandre ainsi créé pour les lignes de courant se résorbe peu à peu au fur et à mesure que l'on s'éloigne du profil jusqu'à s'évanouir en un point de vitesse stationnaire N . Dans le plan θ, σ ce fait se traduit par des boucles des lignes de courant (la vitesse repasse 3 fois par la même inclinaison). Ces boucles sont situées sur des feuillets de Riemann raccordés autour de l'image N' de N Une coupure telle que NT permettra de représenter un tel champ.

2. SINGULARITES ET HODOGRAPHE D'UN PROFIL PORTANT.

Lorsqu'on introduit la circulation, les termes prédominant pour la fonction de courant à l'infini du profil deviennent ceux de l'écoulement uniforme et du tourbillon (réf. 4). Dans le plan θ, σ il en résulte près de P un développement commençant par un terme doublet et un terme tourbillon.

Du fait de cette prédominance les points de vitesse stationnaire restent à distance finie dans le plan x, y et sont distincts de P dans le plan θ, σ.

Il convient maintenant de distinguer deux sortes de points de vitesses stationnaires afin d'aider à la compréhension de l'hodographe d'un profil :

a) tout d'abord le point de vitesse stationnaire "principal" qui résulte de la déformation créée dans l'écoulement uniforme par la présence d'un profil. S'il n'y a pas de portance ce point est à l'infini du plan x, y , s'il y a portance il est à distance finie. Dans le plan θ, σ ceci correspond respectivement à un point critique confondu ou distinct de P , image de l'écoulement uniforme. Sa présence est obligatoire pour des profils biconvexes.

b) Ensuite les points de vitesse stationnaire "secondaires" résultant d'éventuelles bosses ou creux du profil. Dans les cas pratiques leur présence est rare.

c) Enfin il faut noter que pour une certaine classe de profil dont l'intrados et l'extrados présentent la même courbure et dont les bord d'attaque et bord de fuite sont effilés il n'y a pas de points de vitesse stationnaire.

La transformée dans le plan θ, σ de l'écoulement autour d'un profil biconvexe et portant est schématisée figure (6). Sur $ADFDA$ image du profil la fonction ψ prend une vitesse constante. En P image de l'écoulement uniforme la fonction ψ est approchée par la partie imaginaire de :

$$f(\omega) \simeq i\,\frac{\alpha}{\omega} + i\,\beta \log \omega + o(\omega)$$

ou mieux :

$$f(\omega) = i\,\frac{\alpha}{\varepsilon}\,\log\frac{\omega+\varepsilon/2}{\omega-\varepsilon/2} + i\,\beta\log\omega + o\left(\frac{\varepsilon^3}{\omega^3}\right) \tag{8}$$

$$\omega = \sqrt{K}\,(\sigma-\sigma_\infty) + i\,(\theta-\theta_\infty)$$

Enfin en N, ψ prend une valeur finie tandis que ses dérivées ψ sont infinies (réf. 6):

$$\theta_\varphi = \theta_\psi = \sigma_\varphi = \sigma_\psi = 0$$

Par ailleurs, deux conditions supplémentaires sont à assurer pour que l'hodographe corresponde à un écoulement physiquement réel.

La première est celle de fermeture du profil et qui conduit à choisir les constantes α et β de façon à ce que sur un petit cercle entourant P on ait (réf. 5) :

$$\oint_c dz = 0 \qquad \oint_c d\varphi = \Gamma$$

soit

$$\alpha = \frac{\Gamma}{2\pi}\,\rho_\infty \qquad \beta = \frac{\Gamma}{2\pi}\cdot\frac{1}{\sqrt{K}} \tag{9}$$

soit

$$\alpha/\beta = \sqrt{1-M_\infty^2}$$

La seconde est celle de partage, Les conditions de Joukowsky doivent en effet être satisfaites au bord d'attaque et au bord de fuite. Il en résulte que les points A et F images des points d'arrêt sont des points nodaux du champ. En conséquence les deux demi-images de la ligne d'arrêt PA et PF doivent être issues de A et F, milieux des abscisses des segments A_1A_2, F_1F_2 et représentent les discontinuités angulaires de la vitesse.

Sur le réseau correspondant il faut donc :

a) en P représenter d'après (8) le doublet par une source et un puits électrique séparé de ε. Si $\Gamma = 0$ ces sources débitent une intensité électrique reliée à α :

$$I_\alpha = \pm\,\frac{\mu}{\lambda}\,\frac{\alpha}{\varepsilon} \tag{10}$$

b) sur $ABFDA$ imposer un potentiel V_c. L'intensité débitée par cette électrode est reliée à la circulation Γ par :

$$I_\Gamma = \frac{\mu}{\lambda}\,\Gamma \tag{11}$$

c) enfin les points à l'infini A et F ainsi que le point critique N ne sont pas alimentés et prennent d'eux-mêmes leur potentiel V_A, V_F et V_N.

Le réglage des conditions de partage et de fermeture est le suivant :

a) Dans une première expérience ou la circulation est réglée égale à zéro, la constante du doublet est évaluée à l'aide de l'équation (10).

b) le doublet étant maintenu au même niveau de potentiel il est réglé sur $ABFDA$ la circulation assurant d'après (9) et (11) la condition de fermeture. La frontière $ABFDA$ prend alors un potentiel V_c.

c) les potentiels V_A et V_F sont mesurés. S'ils sont égaux à V_c la condition de partage est assurée. Sinon il faut opérer plusieurs essais en jouant sur les positions respectives de P et N puis de rechercher par interpolation la disposition satisfaisant à $V_A = V_F = V_c$.

3. CALCUL DES ZONES DE VITESSES SUPERSONIQUES.

Que le profil soit portant ou non différents types d'hodographes sont à considérer suivant que le Mach amont est inférieur, égal ou supérieur au Mach critique.

Si le Mach amont est inférieur au Mach critique l'écoulement est entièrement subsonique et son hodographe est situé dans le demi-plan $\sigma > 0$ (fig. 7b). Le problème posé est un Dirichlet et sa solution accessible à l'aide d'un réseau résistif.

Si le Mach amont est égal au Mach critique, l'hodographe est tangent à l'axe $\sigma = 0$. Le problème posé est un Dirichlet singulier dont la résolution est toujours possible par la méthode analogique.

En particulier on peut ainsi déterminer des profils dont l'hodographe est limité par un segment LN de l'axe $\sigma = 0$ (fig. 7c). Ces profils supportent une répartition de vitesses du type plateau, le palier étant à $M = 1$. En plaçant judicieusement le segment LN par rapport à P on peut espérer obtenir ainsi des profils qui pour des Machs supérieurs présenteront des distributions Peaky.

Enfin il reste à considérer le cas où le Mach amont est supérieur au Mach critique mais tout en restant inférieur au Mach d'irréversibilité. Dans ce cas l'image du profil déborde dans le demi-plan $\sigma < 0$ et son tracé est continu puisqu'il n'y a pas de choc (fig. 8a).

Un réseau de selfs et capacités permettrait de représenter un tel domaine. Toutefois l'unicité du problème au limite ainsi posé est douteuse la forme de MM' pouvant s'avérer incompatible avec les conditions régnant dans la partie elliptique.

Plusieurs méthodes sont possibles. La première consiste à se donner l'hodographe jusqu'à sa frontière transsonique MSM'(fig. 8b). Il convient alors de résoudre un deuxième problème de Frankl dans le domaine $B'LM'SML$. Ensuite la partie inconnue de la frontière MM' est déterminée par la résolution d'un problème du type I (terminologie de Picard) dans le quadrilatère $SRTR'$.

Une autre possibilité consiste à remplacer la donnée sur les arcs LM et NM' par celle d'une répartition de fonction de courant $\psi(\theta)$ sur l'axe $\sigma = 0$ (fig. 8c). Dans ce cas il faut résoudre un Dirichlet singulier dans le domaine $B'NSLD'$, puis un problème de Cauchy dans le triangle curviligne LNT à partir des distributions $\psi(\theta)$ et $\psi'_{\sigma}(\theta)$ sur LN.

L'inconvénient de ces deux procédés est que l'on ne peut prévoir de façon rigoureuse si les parties supersoniques ainsi calculées sont exemptes de lignes limites, donc de choc.

Toutefois il faut remarquer que de tels écoulements continus ne semblent expérimentalement exister que lorsque la vitesse maximale n'excède pas $M = 1,25$ ou 1,3. Au delà les chocs deviennent nets et il est nécessaire d'en tenir compte dans les schémas de calcul.

Ce fait se comprend si l'on se rappelle que pour que la recompression soit isentropique il est nécessaire qu'aux points du profil où elle ait lieu la courbure soit faible. Si le nombre de Mach maximum est trop fort, cette recompression devra s'étendre sur une portion plus large du profil en sorte que la nécessaire variation de la pente, θ variant au maximum de 90° à 0°, entraînera un choc.

Si maintenant l'on suppose $M_{max} < 1,25$, on comprend à l'aide des schémas de la figure 9 qu'il importe peu pour une telle gamme de vitesse de se poser le problème de l'existence d'un choc. En effet sur la figure 9b on peut voir l'hodographe supposé d'un choc, dont l'image est $L'QL$. Si l'intensité du choc est faible l'hodographe prend l'allure schématisée figure 9c, et devient ainsi très voisin du schéma continu 9a.

Si donc l'on suppose $M_m < 1,25$ on peut supposer qu'un calcul basé sur un schéma continu conduise pratiquement à des résultats voisins de ceux que l'on aurait obtenus en tenant compte d'un choc faible.

Maintenant donc le schéma continu il est possible dans le cadre de ces hypothèses de simplifier l'équation (1). Si en effet dans la zone supersonique σ est petit en valeur absolue, on peut poser

$$K(\sigma) \simeq 0$$

en sorte que (1) devient

$$\psi''_{\sigma\sigma} = 0$$

En se donnant ψ sur le contour $B'MM'D'$ le problème à résoudre est un dirichlet singulier. Pour l'analogie la zone supersonique $NMM'L$ est représentée en reliant l'axe $\sigma = 0$ à la frontière LMN par des résistances.

4. RESULTATS OBTENUS

Plusieurs profils ont ainsi été déterminés. Tout d'abord la méthode a été testée par une comparaison avec des résultats de Nieuwland. L'hodographe obtenu à partir d'une distribution $M = f(\theta)$ (cas e de la référence 7) a été maillé comme l'indique la figure 10. Pour des raisons de commodités le bord de fuite a été pris effilé. Sur la figure 11 on peut voir les résultats obtenus. Les cotes du profil ont été retrouvées avec une erreur au plus égale à 1% de l'épaisseur maximale.

Ce même hodographe a été tronqué à l'axe $\sigma = 0$. Les calculs ont conduit à un profil d'épaisseur moindre et supportant une répartition de vitesses assez voisine (figure 11).

Une autre comparaison a été faite avec des résultats obtenus en soufflerie par Monsieur Vincent de Paul, O.N.E.R.A. Les calculs ont été effectués à partir d'une distribution $M = f(\theta)$ obtenue pour un profil NACA 64A010. Les cotes de ce profil ont été retrouvées avec une erreur de 5% (fig. 12). Toutefois une différence est apparue au bord d'attaque sur l'emplacement de la zone supersonique.

Enfin il a été calculé un cas portant. Pour hodographe il a été pris un contour voisin d'un des résultats de Mr. Vincent de Paul. On peut voir figure 11 les résultats obtenus. Pour ce calcul il est à préciser que la fermeture du profil n'était pas rigoureuse et que des balancements ont été nécessaires. Ces corrections ont entrainé une modification de 1,5% de la portance. Par ailleurs la position du point critique fut délicate à trouver et s'est révélée être très proche de P , image de l'écoulement amont.

5. ALGORITHME DE CALCUL DANS LE CAS D'UN CHOC.

Lorsque le Mach amont approche la valeur du Mach d'irréversibilité, l'hypothèse du schéma continu devient de moins en moins plausible. L'intensité du choc gagne en vigueur et il existe une plage du Mach amont pour laquelle on peut admettre que l'écoulement est irrotationnel en aval du choc. Dans ce cas l'écoulement est toujours à potentiel et la méthode de l'hodographe est applicable.

Sur le plan résolution ce problème comporte plusieurs difficultés. Tout d'abord l'allure de l'hodographe et la correspondance ponctuelle sur les images du choc sont inconnues. Cette difficulté sera en partie levée en s'inspirant de résultats expérimentaux obtenus à la soufflerie de Lille par Messieurs Dyment et Gontier (réf. 9). D'autre part le type de conditions aux limites à satisfaire rend très délicat la recherche de solutions $\psi(\theta,\sigma)$. Un schéma de calcul est ici proposé qui s'inspire de celui de Germain (réf. 8).

En se limitant, pour simplifier, au cas du profil symétrique non portant on peut voir figure 15 le tracé supposé d'un tel hodographe.

Sur cette figure les arcs $B'L_2$ et L_1D' sont les images des parties du profil situées en amont et aval du choc. Sur ces lignes ψ prend une valeur constante.

Les arcs L_2Q et L_1Q sont les images des faces amont et aval du choc. En exprimant la conservation de la composante tangentielle de la vitesse et du flux de masse normal et en tenant compte du fait que les arcs L_2Q et L_1Q ont la même image dans le plan physique on doit satisfaire en des couples de points (θ_1,σ_1) sur L_1Q, (θ_2,σ_2) sur L_2Q les relations :

$$[d\psi]_1 = [d\psi]_2 \qquad [d\varphi]_1 = [d\varphi]_2$$

$$\left[\frac{d\varphi}{d\psi}\right]_1 = \left[\frac{d\varphi}{d\psi}\right]_2 = \pm \frac{m_1 m_2}{q_1 q_2}\sqrt{\frac{q_1^2 - q_2^2}{m_2^2 - m_1^2}}$$

$$\cos(\theta_2-\theta_1) = \frac{m_2 q_2 + m_1 q_1}{m_1 q_2 + m_2 q_1} \qquad (12)$$

$$m_1 = \rho_1 q_1 \qquad m_2 = \rho_2 q_2$$

Ces relations montrent que la correspondance ponctuelle entre L_1Q et L_2Q dépend du champ à calculer. On peut par exemple supposer que le choc est en chaque point droit : $\theta_1 = \theta_2$. Dans ce cas les relations 12 se simplifient considérablement. Malheureusement cette situation, qui conduit à des lignes limites, ne semble pas réelle.

A partir des résultats de Dyment et Gontier un tracé représentant cette correspondance est montré figure 15. Il y apparaît que droite au pied du choc la correspondance évolue de façon imprévisible Notamment au point sonique Q il semble que la correspondance soit la limite d'un choc oblique d'intensité nulle.

Devant la difficulté de prévoir cette correspondance il semble qu'il soit plus simple de ne se fixer qu'une partie de l'hodographe, puis d'en trouver le complément à l'aide de 12. C'est le principe du schéma proposé.

Les parties subsonique et sonique de l'hodographe sont choisies arbitrairement et les solutions $\psi(\theta,\sigma)$ et $\varphi(\theta,\sigma)$ sont calculées par analogie. A partir de ces résultats la partie amont du choc est déterminée numériquement et des relations de compatibilité sont à satisfaire sur la ligne sonique QN

D'une façon plus détaillée on se propose d'opérer de la manière suivante.

L'image $B'N$ et $L_1 D'$ du profil est fixée et supporte la condition $\psi = 0$. Ensuite il est choisi un segment QN pour image de la ligne sonique et un arc QL_1 pour image de la face aval du choc. Sur ces deux lignes il est pris des répartitions de fonction de courant $n(\theta)$ et $f(\theta_1, \tau_1)$ compte tenu éventuellement de la singularité en Q.

Pour l'ensemble du domaine $B'NQL_1D'$ le problème à résoudre est un Dirichlet. Entre autres éléments de solution on obtient les répartitions de dérivées normales $m(\theta)$ et $g(\theta_1, \tau_1)$ sur QN et QL_1

Les répartitions $f(\theta_1, \tau_1)$ et $g(\theta_1, \tau_1)$ permettent alors de trouver le premier membre de (12b) qui joint à (12c) permet pour chaque θ_1, τ_1 de trouver le point θ_2, τ_2 correspondant. L'image de la face amont du choc est alors connue et sur celle-ci les conditions 12a et 12b sont à respecter.

Si cette ligne est comprise entre les deux caractéristiques issues de Q on peut à partir de la double donnée ψ et $d\psi$ qu'elle supporte, résoudre un problème de Cauchy et déterminer l'arc $R L_2$ image d'une partie du profil. De plus on obtient une loi de fonction de courant sur la caractéristique QR.

Il reste enfin à chercher la solution dans le domaine RQN à partir des répartitions de fonction de courant sur QR et QN. En plus de l'arc RN il est trouvé une nouvelle distribution de dérivée normale $m_1(\theta)$ sur QN.

Si $m_1(\theta) \neq m(\theta)$ il faut recommencer tout le calcul mais à partir de $m_1(\theta)$ au lieu de $n(\theta)$ Ce nouveau cycle conduira à une distribution $m_2(\theta)$ et ainsi de suite jusqu'à convergence.

Cette convergence n'est pas certaine et ici il est compté sur plusieurs essais avant de l'obtenir. Par ailleurs ces essais préliminaires montreront comment choisir les données pour que d'une part l'arc QL_2 soit bien compris entre les caractéristiques issues de Q et d'autre part il n'y ait point de ligne limite. Nous espérons pouvoir publier prochainement des résultats.

6. APPLICATION AU CALCUL D'AUBES DE TURBINE.

Le problème de la déter. ation de grille d'aube diffère de celui du profil isolé d'une part par la condition de périodicité du champ de l'écoulement, d'autre part par le fait qu'entre l'amont et l'aval le vecteur vitesse varie.

Trois transitions transsoniques à travers un aubage sont envisageables. Tout d'abord une transition subsonique-supersonique : c'est le régime de Meyer-Laval observé dans les tuyères. Ensuite une transition subsonique-subsonique avec une ou plusieurs zones de vitesse supersonique : c'est le régime de Taylor. Enfin ces zones de vitesses supersoniques peuvent être bordées par un choc.

Dans ce qui suit il ne sera considéré que le régime de Meyer-Laval. Le cas du régime de Taylor avec ou sans choc peut être traité suivant les mêmes techniques que celles décrites plus haut.

On considère donc une grille d'aubes caractérisée par une entrée subsonique (q_1, θ_1), une sortie supersonique (q_2, θ_2), la transition étant du type Meyer Laval (fig. 16). La grille est définie géométriquement par son pas h, sa section au col S, son épaisseur δ. Ses paramètres aérodynamiques sont la déflexion $\delta = \theta_2 - \theta_1$, le coefficient de survitesse $\mu = q_2 / q_1$, le débit Q et la circulation Γ. Les lois de conservations donnent :

$$Q = \Delta\psi = \rho_1 q_1 h \cos\theta_1 = \rho_2 q_2 h \cos\theta_2$$

$$\Gamma = q_2 h \sin\theta_2 - q_1 h \sin\theta_1$$

le caractère périodique de l'écoulement permet de limiter le domaine d'étude à une bande ne comprenant qu'un seul profil et bordée par deux lignes arbitraires $P_1 M P_2$ et $P'_1 M P'_2$, se déduisant l'une de l'autre par une translation $\vec{h}$.

Entre deux points homologues M et M' la fonction de courant augmente d'une quantité constante, tandis que le flux normal est transmis

$$\psi_M = \psi_{M'} + \Delta\psi \qquad \left(\frac{d\psi}{dn}\right)_M = -\left(\frac{d\psi}{dn}\right)_{M'} \tag{13}$$

Aux infinis amont et aval la deuxième de ces relations s'écrit

$$\Delta\psi_1 = q_1 h \sin\theta_1 \qquad \Delta\psi_2 = q_2 h \sin\theta_2$$

Enfin sur le profil la fonction de courant est constante.

Dans le plan de Tricomi (fig. 17) les écoulements amont et aval ont pour images les points p_1 et p_2 et la transformée de l'aube s'applique sur le contour $a\, a_1 d_1\, e\, d_2 b_2 a_2 a$. Le bord d'attaque du profil est arrondi, et son bord de fuite est à rebroussement.

La périodicité du champ se traduira par l'application sur des feuillets de Riemann de chaque bande $p_1 p_2 p'_2 p_1$. Ces feuillets ont en commun les points p_1 et p_2 et sont raccordés par une coupure arbitraire $p_1 m\, p_2$ supportant les conditions 13.

Des singularités de transformation apparaissent aux points a et p_1. Au voisinage de ces points le comportement de ψ s'approche par les développements (réf.11) près de a : $\psi'_\theta = \psi'_\sigma = 0$ près de p_1 :

$$\psi = c \log r \cdot (c_1 \cos\alpha + c_2 \sin\alpha)$$

$$r^2 = k\,(\sigma - \sigma_1)^2 + (\theta - \theta_1)^2 \qquad \mathrm{tg}\,\alpha = \frac{\theta - \theta_1}{\sqrt{k}\,(\sigma - \sigma_1)}$$

Sur la ligne sonique la recherche de solutions se prolongeant analytiquement à travers la frontière transsonique et qui, au-delà, présentent un caractère trivalent (réf. 12) conduit à respecter des distributions de la forme :

$$\psi(\theta) = \tau(\theta) = \sum A_n\, \theta^{2n + \frac{1}{3}} + \sum B_n\, \theta^{2n + 4/3} \tag{14}$$

1° Le caractère mixte de l'écoulement incite à fractionner l'hodographe en sous-domaines de résolution. C'est ainsi qu'on est amené à résoudre successivement un problème de Dirichlet singulier pour le subsonique, un problème de Cauchy pour le transsonique, un problème de Goursat pour le supersonique. Ces calculs nécessitent les données suivantes : un contour $a_1 b_1 b_2 a_2$, une répartition $\tau(\theta)$ une distribution de vitesse sur l'axe de la tuyère de sortie.

2° Le problème de Dirichlet est résolu par la méthode d'analogie électrique. La transposition électrique des conditions aux limites consiste à : sur $a_1 b_1$ et $a_2 b_2$ imposer le potentiel V, sur $b_1 b_2$ imposer selon (14) une répartition $\tau(\theta)$, sur la coupure p_2 satisfaire aux conditions (13) à l'aide de transformateurs. Enfin une intensité I_p est réglée en p_1 de telle sorte que l'image de la ligne d'arrêt aboutisse bien en a. Sa valeur est reliée à l'incidence normale θ_1 par la relation

$$I_p \doteq \cdot\, \mathrm{cotg}\,\theta_1$$

Ce régime électrique établi, l'intégration du champ $V(\theta, \sigma)$ conduit au contour subsonique de l'aube, et la mesure des intensités sur $b_1 b_2$ à la distribution de dérivées normales $\psi'_\sigma(\theta) = \nu(\theta)$

3° Le contour $b_1 c_1 O c_2 b_2 b_1$ de l'hodographe est ensuite déterminé à partir des distributions $\tau(\theta)$ et $\nu(\theta)$. L'équation (1) est écrite en différences finies suivant le maillage schématisé figure 17.

$$\psi_4 = (2\alpha + \beta + 1)\,\psi_0 - \alpha\,(\psi_1 + \psi_3) - \beta\,\psi_2 \qquad \alpha = \frac{\Delta\sigma_4(\Delta\sigma_2 + \Delta\sigma_4)}{2\,\Delta\theta^2} \qquad \beta = \frac{\Delta\sigma_4}{\Delta\sigma_2}$$

Partant de la ligne $b_1 b_2$ le calcul des ψ_4 s'effectue de proche en proche à l'intérieur du domaine $b_1 c_1 O c_2 b_2$. Si le champ obtenu contient une ligne limite il est nécessaire de modifier la distribution (14) en jouant sur les A_n et B_n et de recommencer les deux étapes précédentes. Le retour au plan physique conduit ensuite à la partie transsonique de l'écoulement frontière transsonique incluse.

4° Le calcul de l'aube se termine dans le plan physique par la résolution selon la méthode des caractéristiques d'un problème dont les données initiales sont la frontière transsonique et la ligne de courant issue de O. Sur les caractéristiques descendantes, déterminées de proche en proche, les points du profil sont obtenus en satisfaisant à la condition de débit.

Un calcul a ainsi été effectué à partir d'un hodographe subsonique choisi a priori, d'une distribution $\tau(\theta) = C\,\theta^{1/3}$ et d'une ligne de courant rectiligne issue de O et confondue avec l'extrados du profil. La grille obtenue est présentée par la figure 18.

REFERENCES.

1. P. Germain. Problèmes mathématiques posés par l'application de la méthode de l'hodographe. Symposium transsonicum de l'I.U.T.A.M., 1962.

2. P. Huard de la Marre. Résolution de problèmes d'infiltration au moyen d'analogies électriques. S.D.I.T., n° 340, 1958.

3. L. Malavard, G. Renard. Principe d'un calculateur hybride à réseau d'impédance. C.R.Ac.Sc., t. 265, p. 189, 1967.

   G. Renard, J. Quinio. Réalisation et essai d'un calculateur hybride à réseau résistif. C.R.Ac.Sc., t. 265, p. 263, 1967.

4. S. Bergman. Two dimensional subsonic flows of a compressible fluid and their singularities. Transaction of the American Mathematical Society, vol. 62 n° 3, p. 452-498, 1947.

5. F.N. Frankl. Ecoulement subsonique autour d'un profil comprenant une zone de vitesse supersonique bordée par un choc. Prikladnya matematika i meckanika, t. XX, p. 196, 1956.

6. J.W. Cragg. The Freak down of the hodograph transformation for irrotationnel compressible fluid flow in two dimension. Pac. Cemt. Phil. Soc. 44, p. 360-379, 1948.

7 G.Y. Nieuwland. The computation by Lighthill's method of transonic potential flow around a family of quasi-elliptical aerofoils. NLR - TR T 83, 1964.

   G.Y. Nieuwland. Transonic potential flow around a family of quasi-elliptical aerofoil sections. NLR - TR 172, 1967.

8. P. Germain. Actualité des problèmes transsoniques. Conférence faite au congrès Canadien de Mécanique Appliquée, TP 513, 1967.

9. A. Dyment et G. Gontier. Méthode de détermination des conditions de part et d'autre d'une onde de choc. Note FD 64228 I.M.F., Lille, 1964.

   A. Dyment et P. Gryson. Ecoulements transsoniques plans présentant une zone supersonique sans onde de choc apparente. Note C.B. 67 N 20, I.M.F., Lille

10. F. Rigaut. C.R.Ac.Sc., t. 262, p. 1415 , 1966, t. 264, p. 894, p. 1086, 1967 , t. 265, p. 521, 1967, t. 268, 1968.

11. R. Legendre. Recherche Aéronautique, n° 53, 1956.

12. P. Germain. Ecoulements transsoniques homogènes. Progress in Aeronautical Sciences, 5, Pergamon Press, 1964.

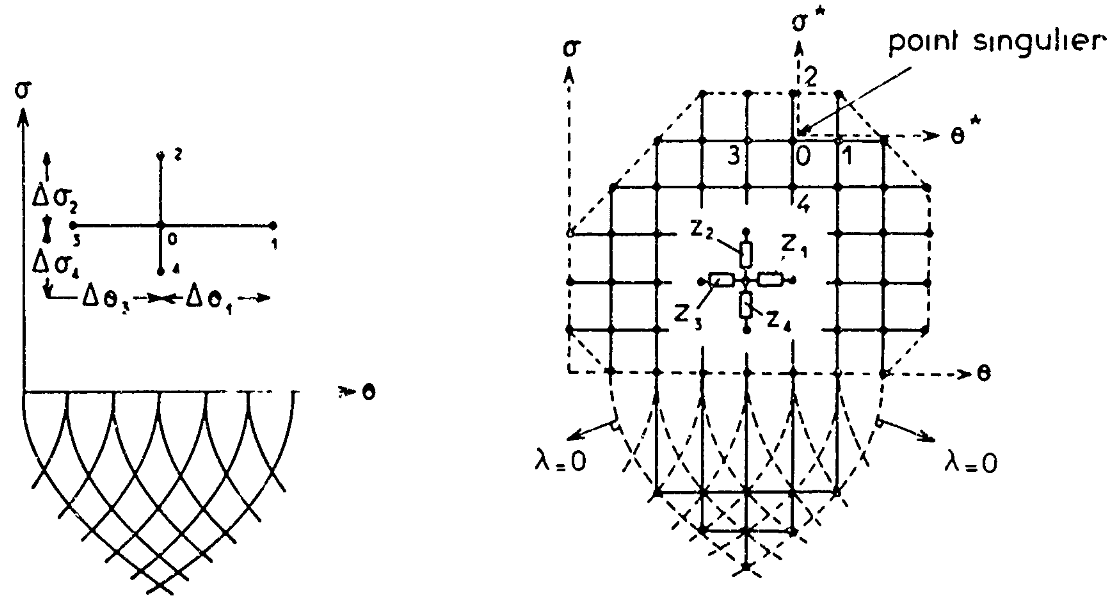

Figure 1

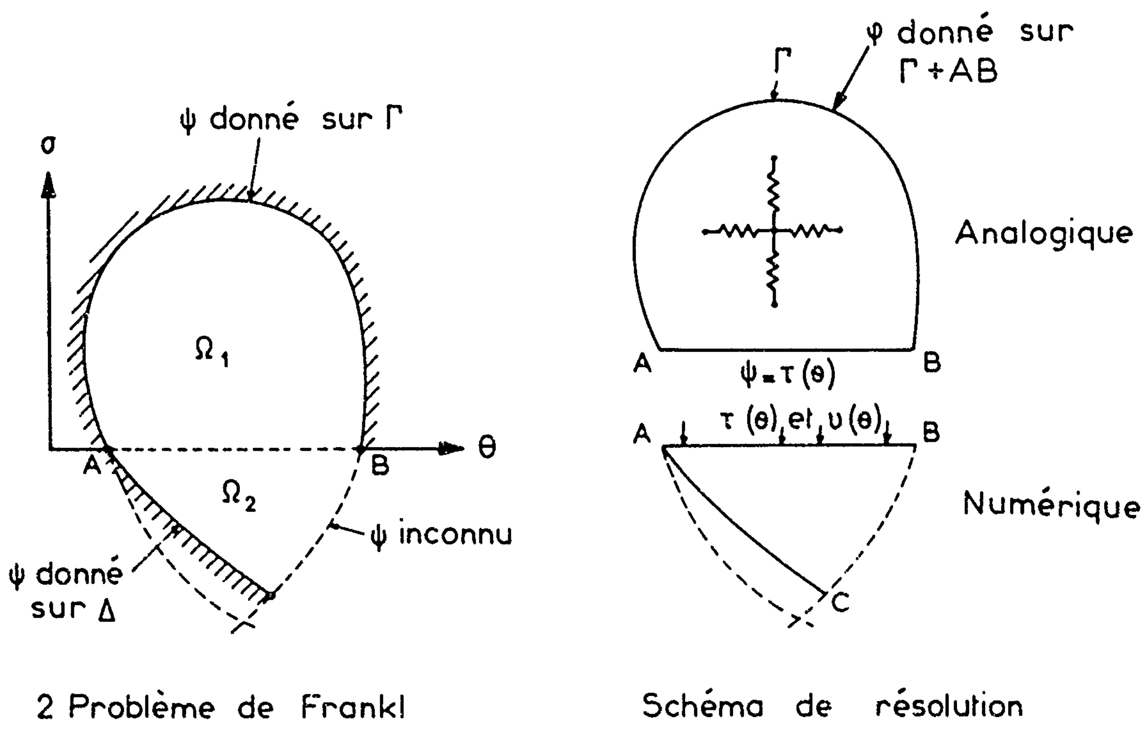

Figure 2

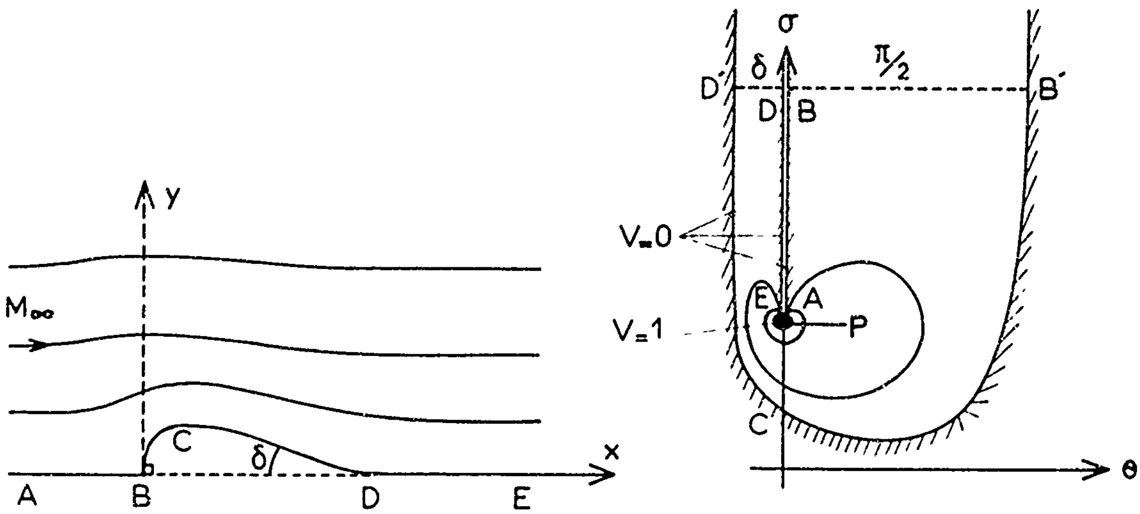

$$\psi_P \simeq \frac{C}{\sqrt{r}} \sin. \frac{\omega}{2}$$

$$r^2 = (\theta - \theta_P)^2 + K(\sigma - \sigma_P)^2$$

$$\mathrm{tg}.\, \omega = \frac{\theta - \theta_P}{\sqrt{K}\,(\sigma - \sigma_P)}$$

Figure 3

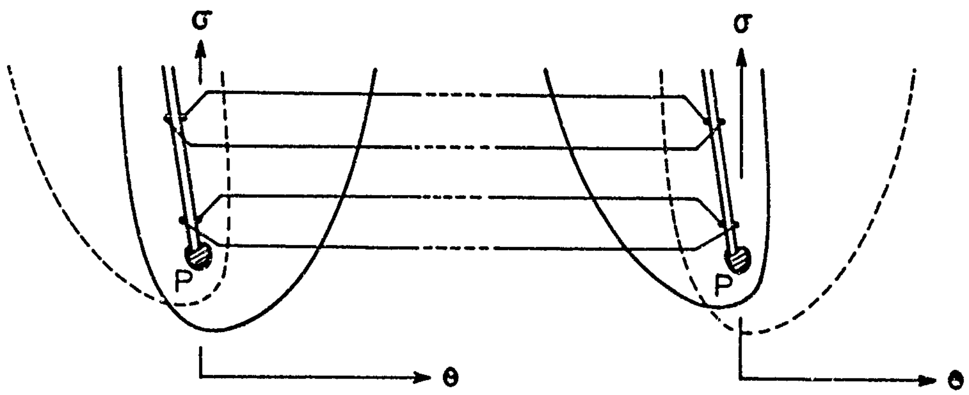

Figure 4

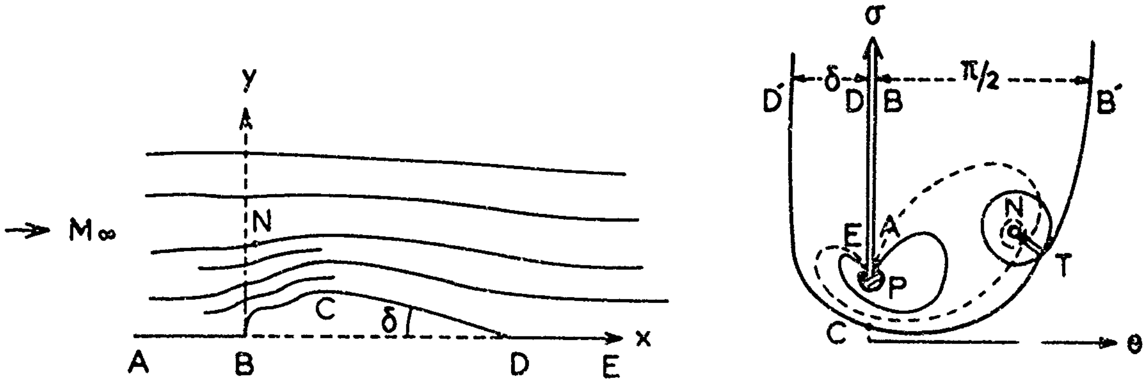

Figure 5

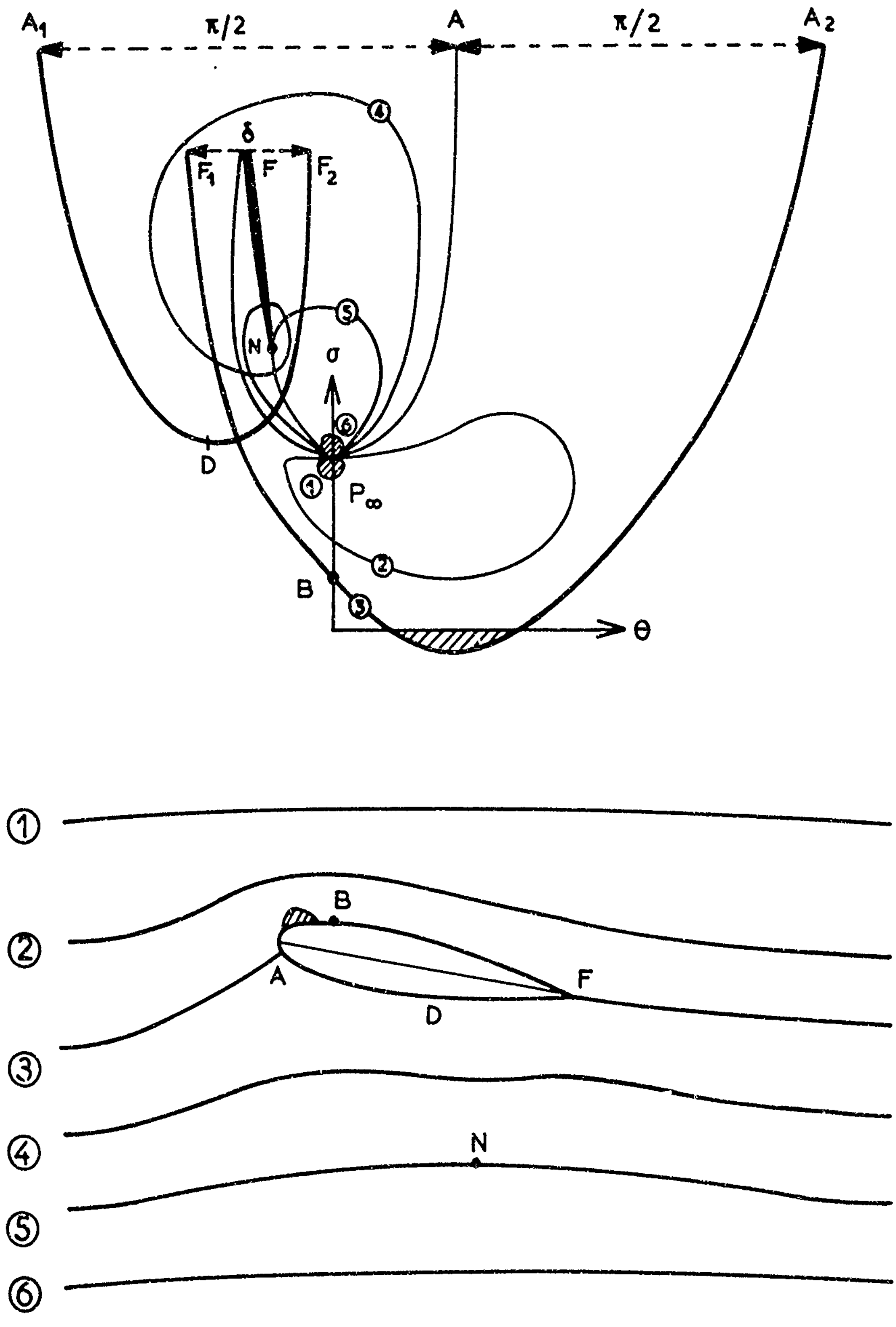

Figure 6

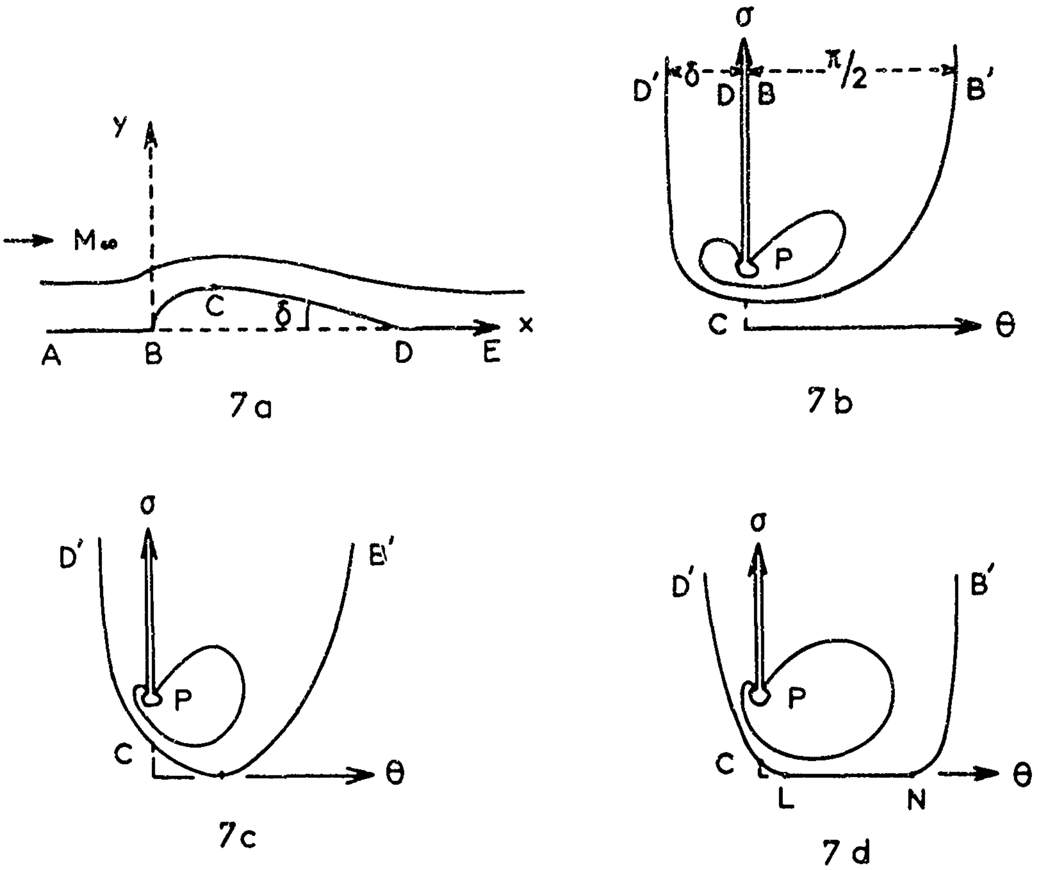

Figure 7

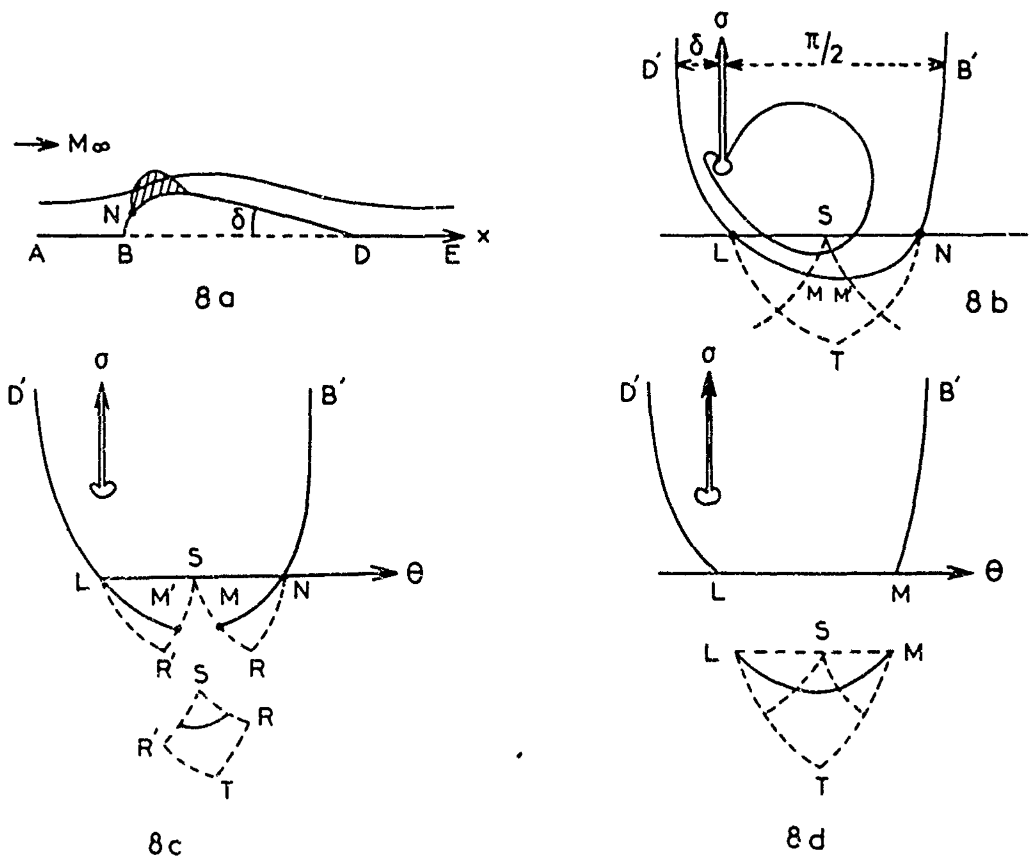

Figure 8

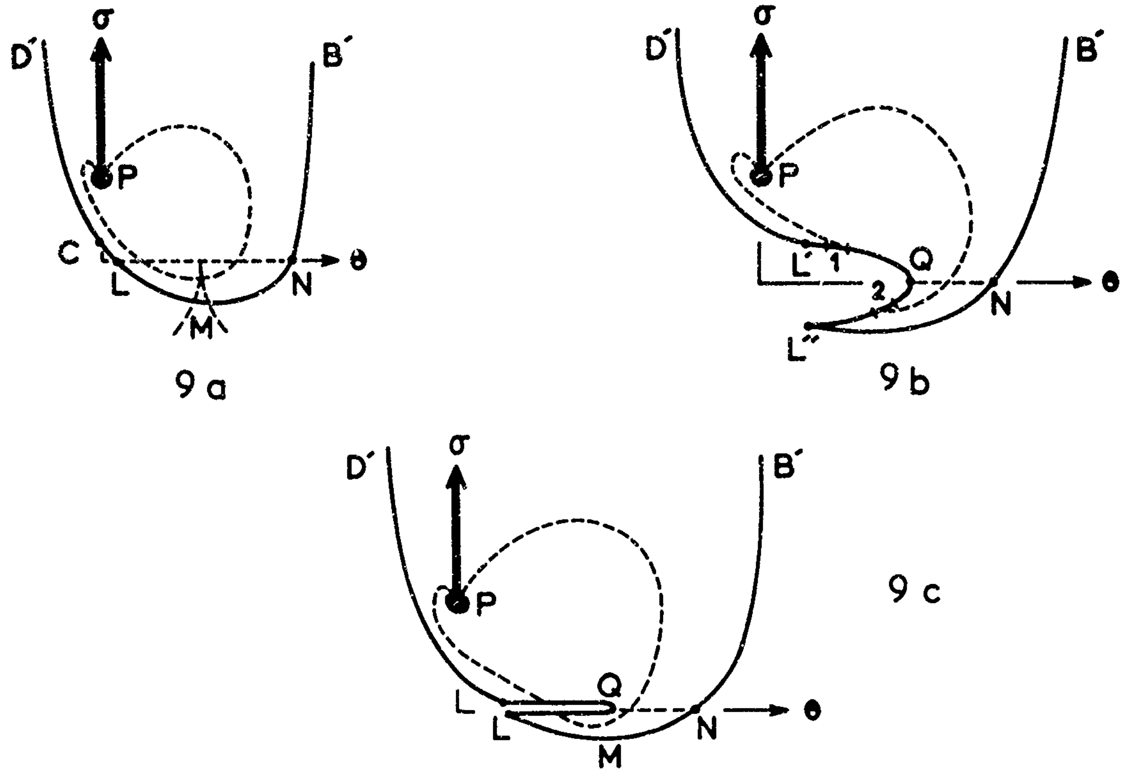

Figure 9

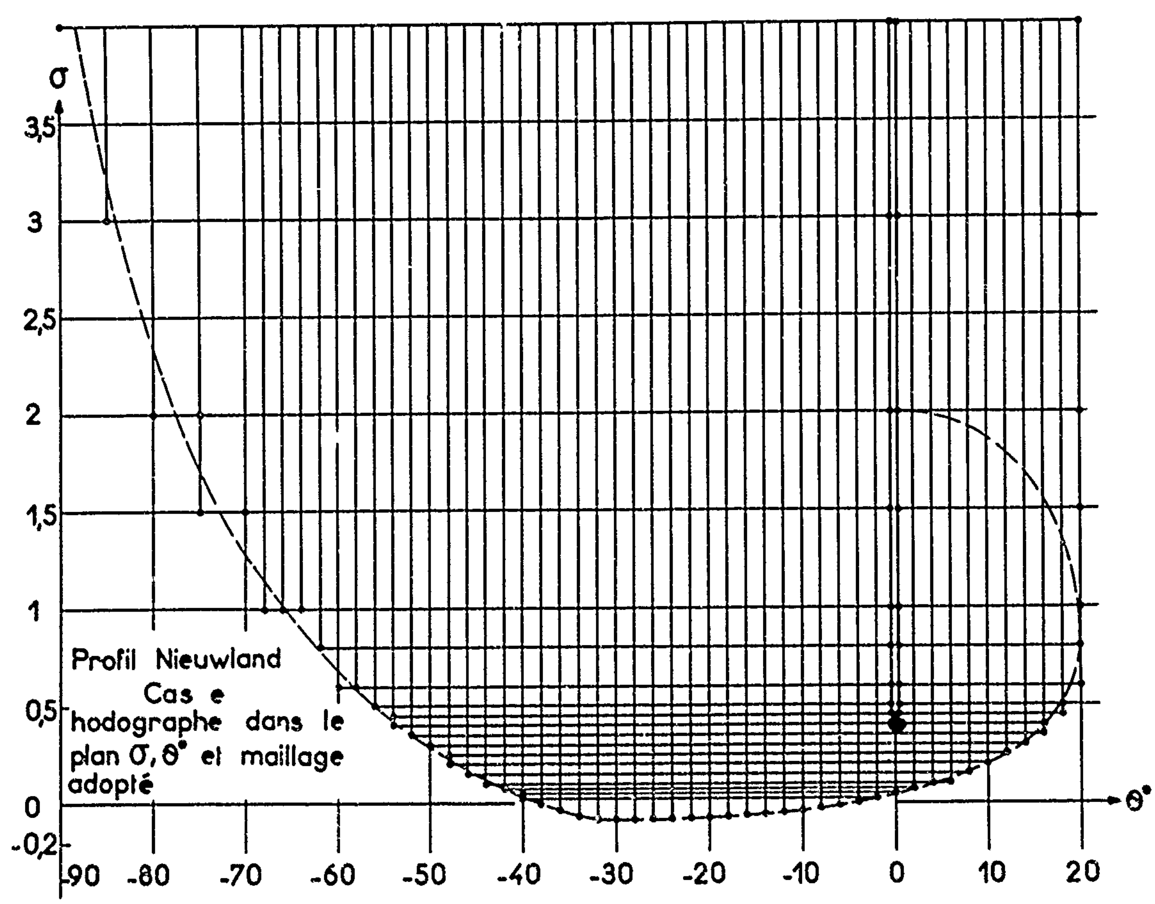

Figure 10

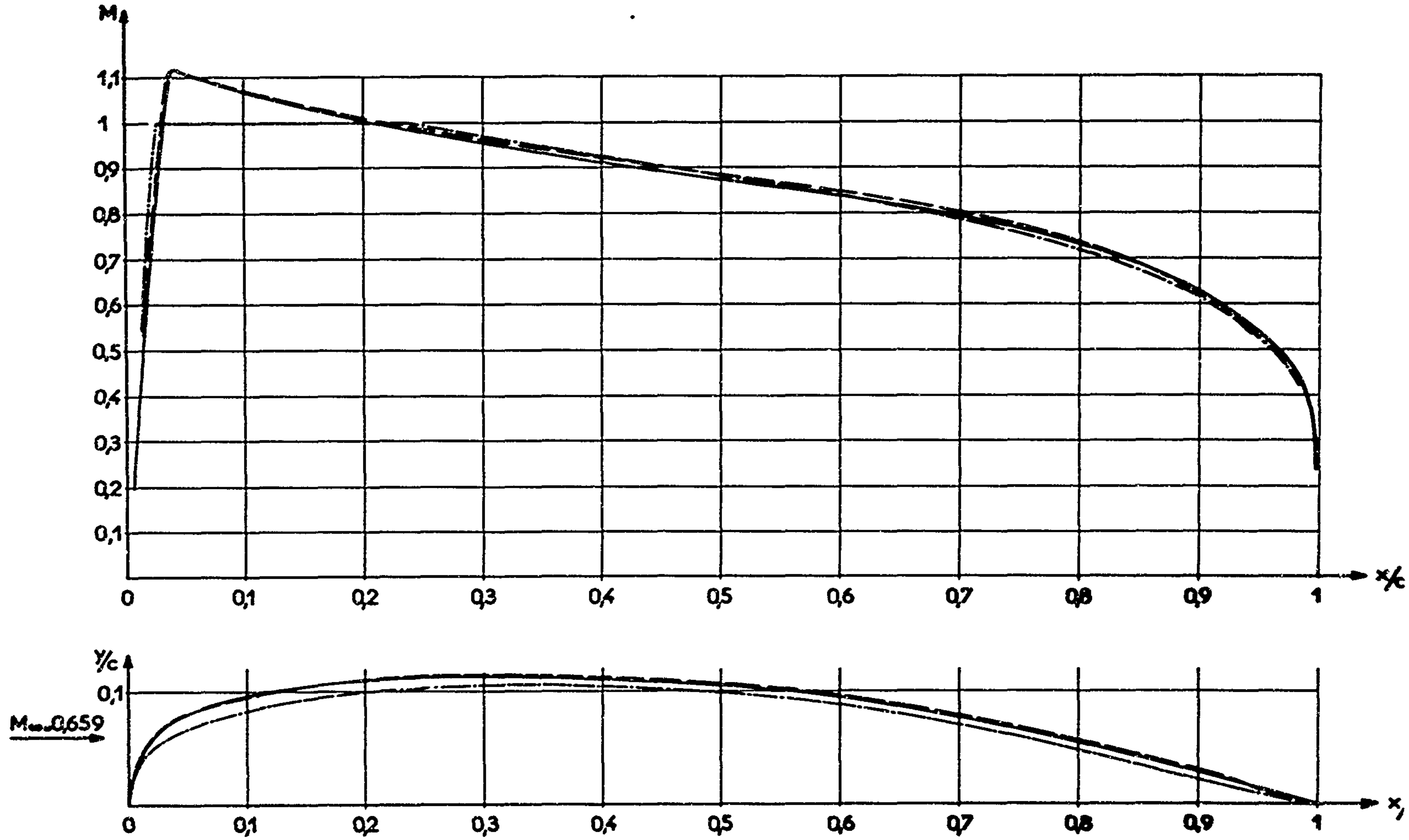

Profil Nieuwland Cas e

Analogique — Calcul Nieuwland — Hodographe tronqué

Figure 11

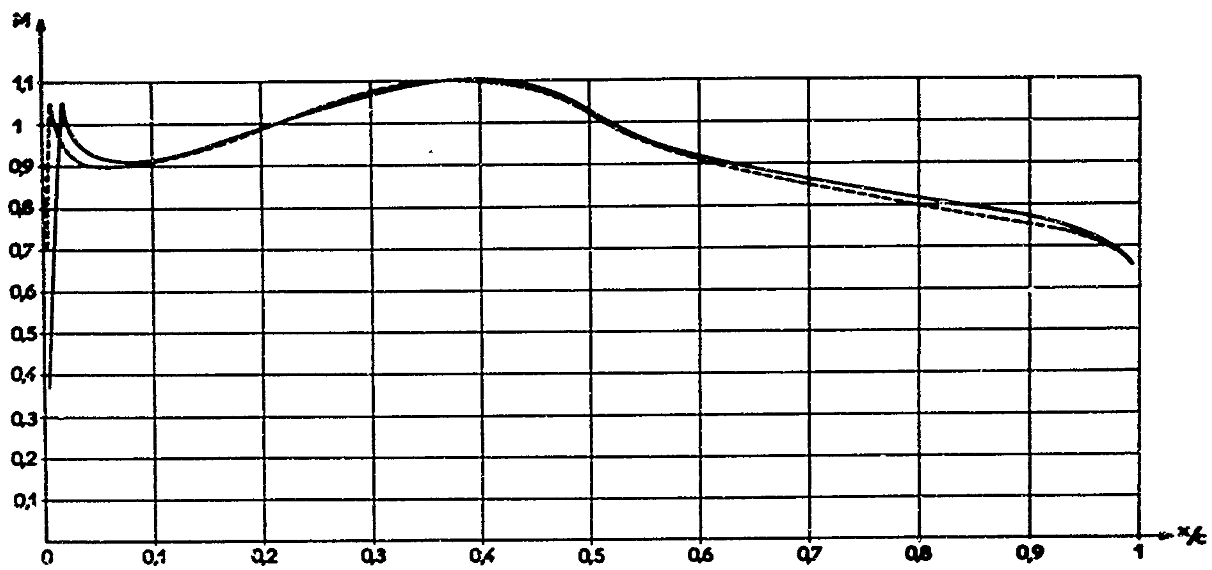

Distributions des nombres de Mach en corde

— mesures O.N.E.R.A

---- calculs analogiques

$\boxed{M_\infty = 0{,}82}$

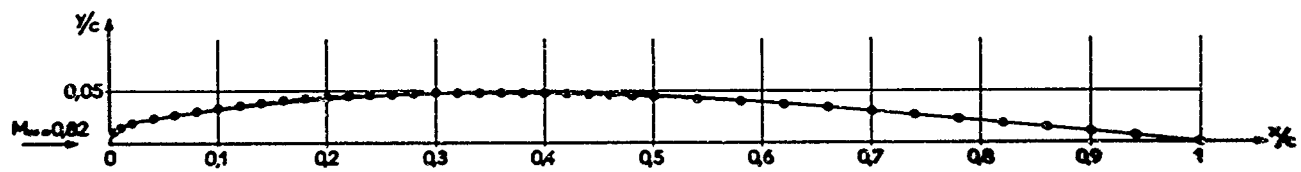

Profil NACA 64A010

— profil expérimenté à l'O.N.E.R.A

-•-•- profil calculé à partir des M = f(s) expérimentaux

$\boxed{M_\infty = 0{,}82}$

Figure 12

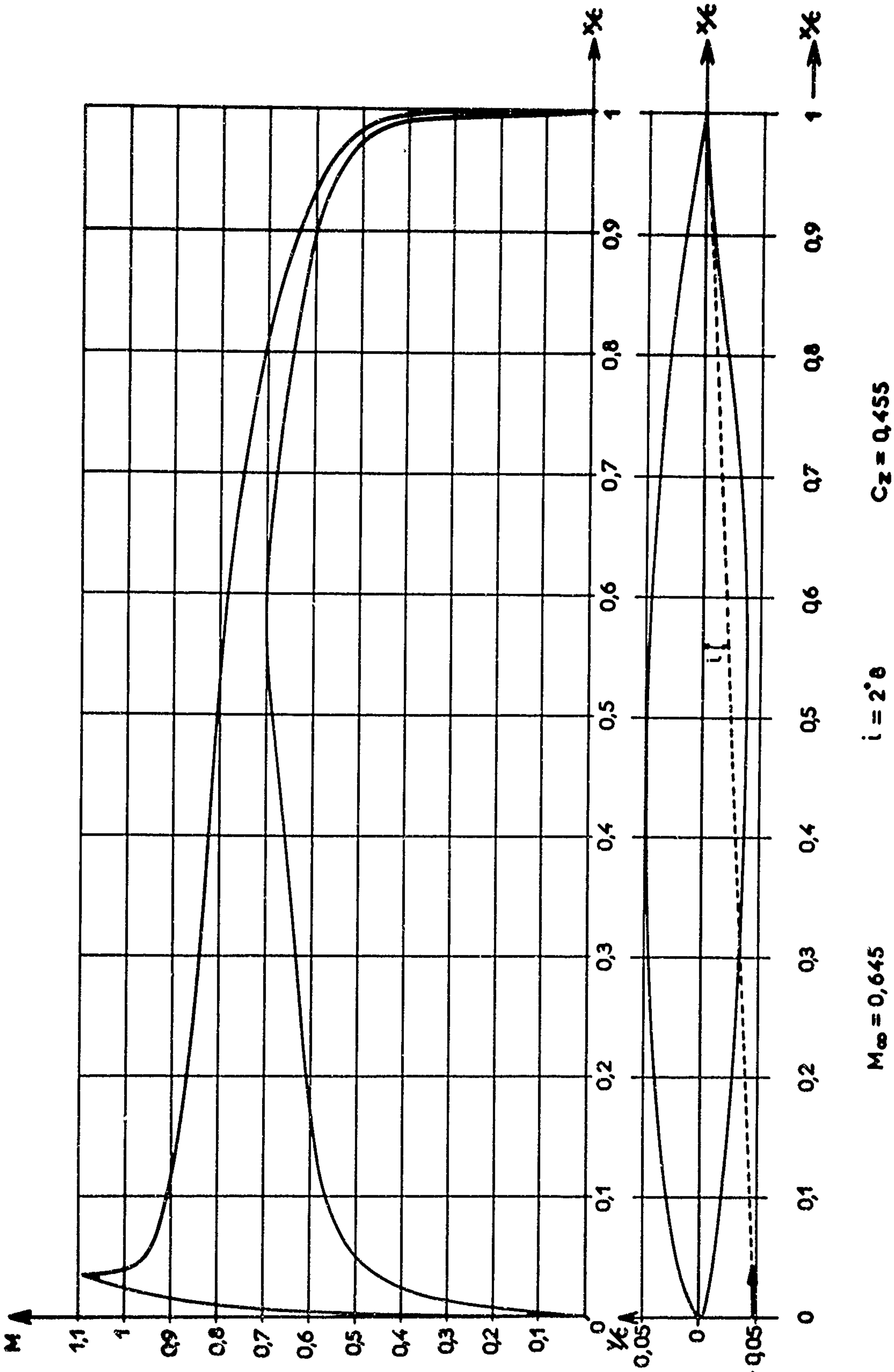
M
1,1
1
0,9
0,8
0,7
0,6
0,5
0,4
0,3
0,2
0,1
0
x/c
0,05
0
-0,05
0,1
0,2
0,3
0,4
0,5
0,6
0,7
0,8
0,9
1
i
$M_\infty = 0,645$
$i = 2°8$
$C_z = 0,455$

Figure 13

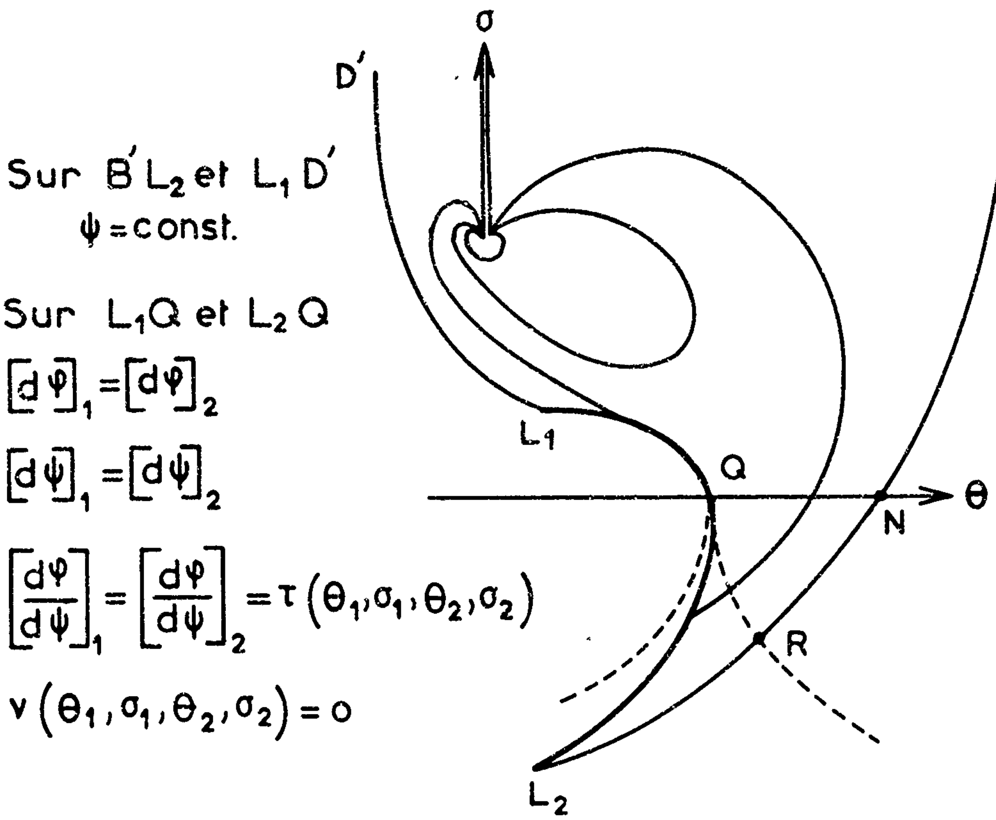

Figure 14

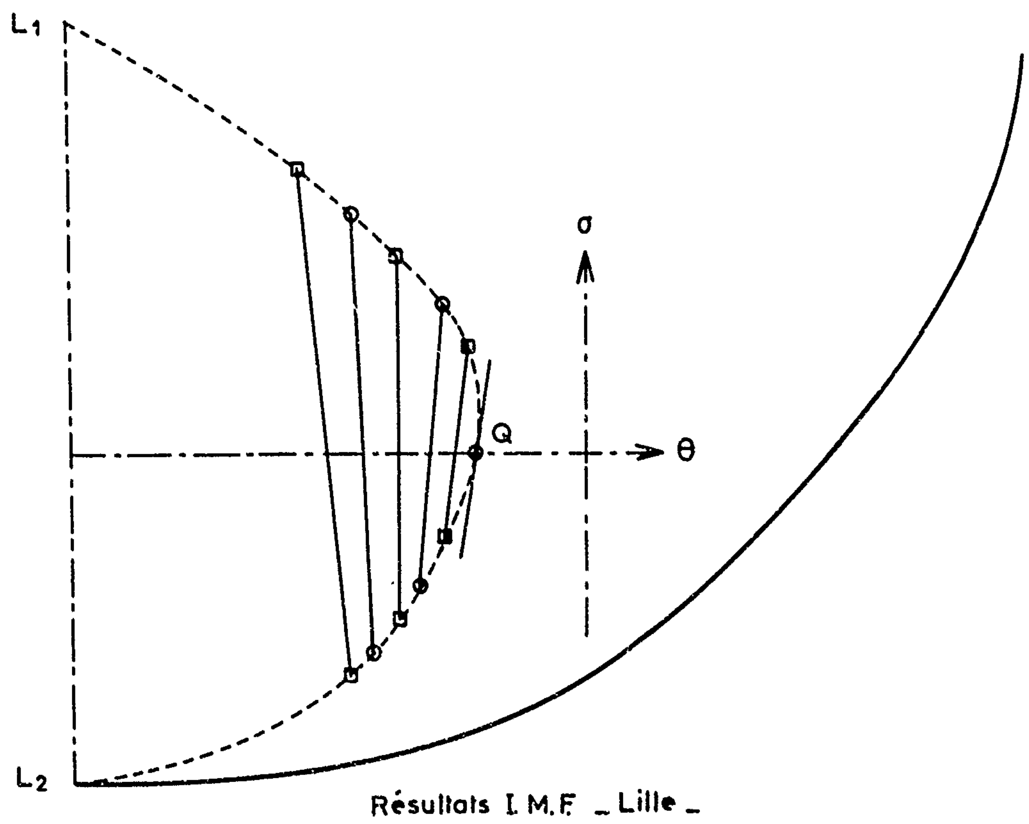

Figure 15

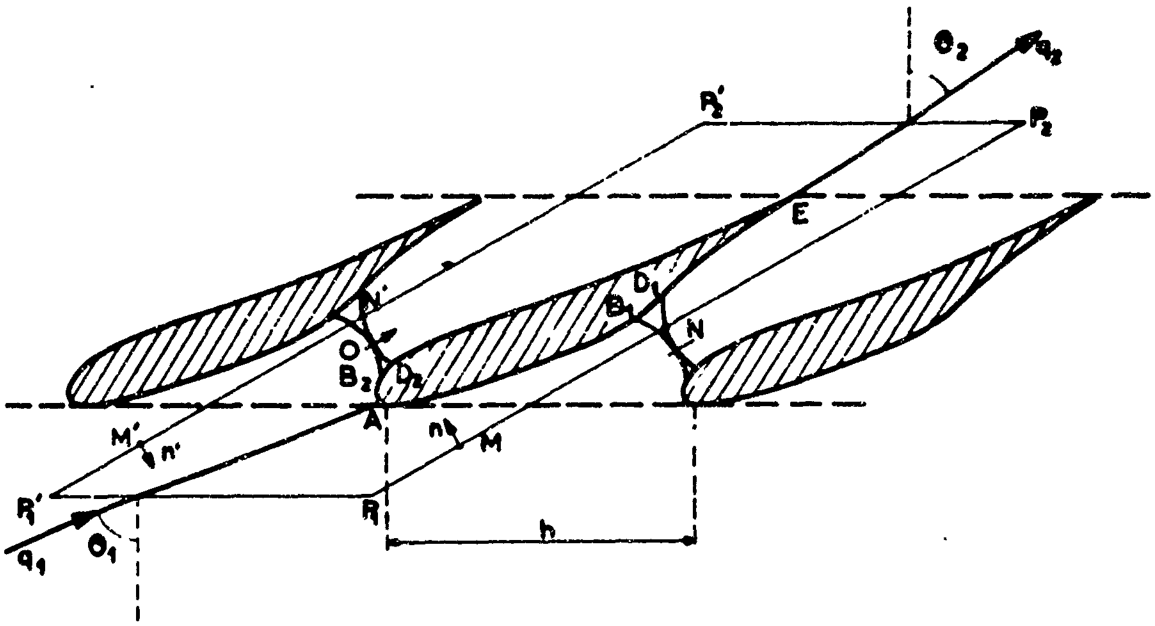

Figure 16

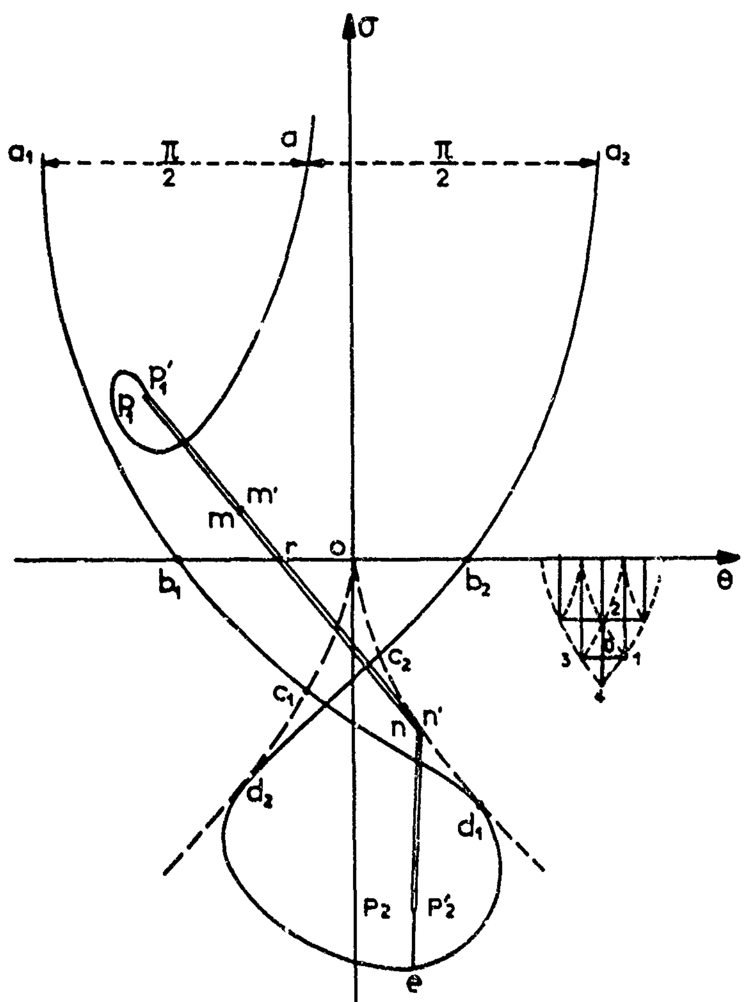

Figure 17

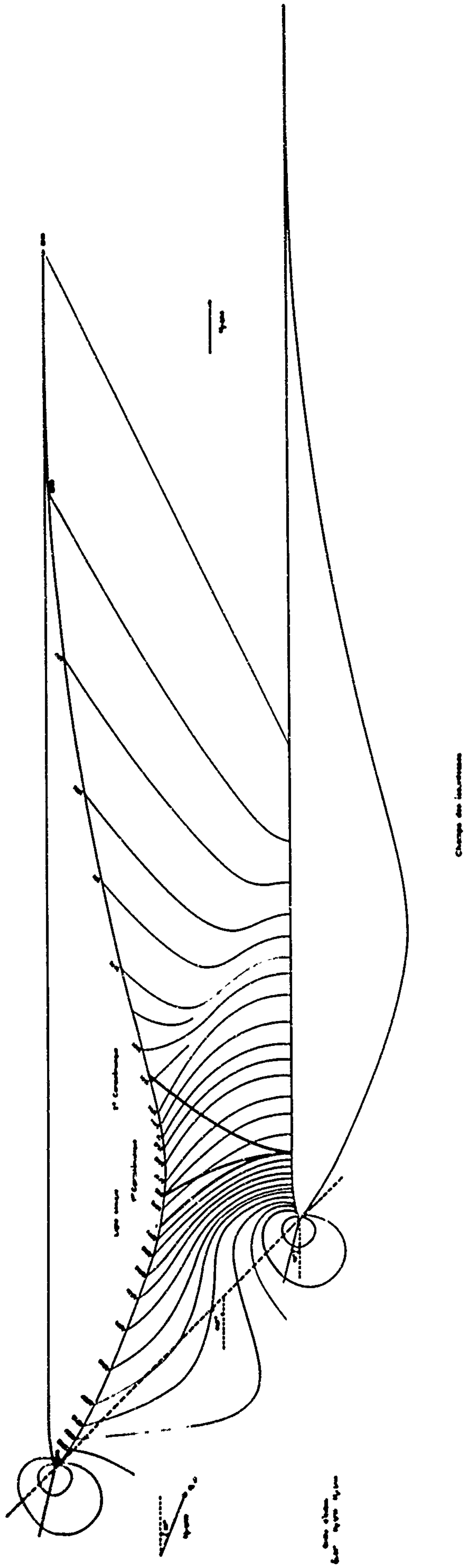

Figure 18

CALCUL NUMERIQUE DE PROFILS D'AILES SUBCRITIQUES

PAR LA METHODE DE L'HODOGRAPHE

par

P. BEVIERRE*

O.N.E.R.A. (92 - Chatillon - FRANCE)

* Chef de Division de Recherches

- SOMMAIRE -

On se donne l'hodographe relatif à l'écoulement sur un profil portant, la vitesse à l'infini étant subsonique. Cet hodographe peut contenir une région légèrement supersonique sans choc.

La première phase du calcul utilise la loi de compressibilité de CHAPLYGIN. Des hodographes du type désiré, dépendant d'un assez grand nombre de paramètres peuvent alors être construits analytiquement, les conditions de fermeture du profil et la position de l'image I du point à l'infini par rapport au contour de l'hodographe étant déterminées avec précision. Partant de ces résultats comme première approximation, on peut par modification de la position de I déterminer des profils répondant à la loi de compressibilité exacte.

Une méthode de calcul, basée sur la détermination d'une fonction permettant de dégager la singularité relative à l'image du point à l'infini, est décrite.

- SUMMARY -

DIGITAL DETERMINATION OF SUB-CRITICAL WING PROFILES BY THE HODOGRAPH METHOD

An hodograph is given for a lifting airfoil with a subsonic velocity at infinity. This hodograph may include a weakly supersonic region without shock.

The first step in the computation involves the CHAPLYGIN compressibility law. Such required hodograph containing a fairly large number of parameters are obtained analytically. The closure conditions of the corresponding airfoils and the location of I (image of the point at infinity) with respect to the hodograph boundary are obtained with accuracy. Starting from these results (first step), the location of I is changed in order to find some airfoils corresponding to an exact compressibility law.

A computational method is then described, involving the determination of a function which exhibits the singular behaviour of the point I.

L'OBJET DE CETTE ETUDE est d'apporter une contribution à la détermination des caractéristiques aérodynamiques de profils portants, soumis à un écoulement uniforme et subsonique à l'infini pouvant comporter un domaine transsonique sans choc.

On utilise une méthode de calcul hodographique basée sur une technique élaborée par R. LEGENDRE, consistant essentiellement à choisir un contour hodographique H ne comportant, dans sa partie utile, aucune autre singularité que le doublet-tourbillon au point I_0, image de l'infini du plan physique.

Une autre originalité de la méthode consiste pour faciliter le calcul numérique à dégager l'effet de la singularité I_0 à l'aide d'un champ auxiliaire induit par une suite régulièrement échelonnée de singularités identiques dont toutes sauf celle située en I_0 sont en dehors du champ utile de l'hodographe H.

Ce champ de singularités une fois connu, le problème est ramené à la détermination de fonctions régulières complémentaires $\delta\varphi$, $\delta\psi$ pour le potentiel et la fonction de courant qui prennent sur le contour de l'hodographe des valeurs bien déterminées. Le calcul de ces fonctions peut alors être effectué à l'aide de réseaux analogiques ou par une méthode de relaxation.

Le choix de l'hodographe H résulte d'un calcul préliminaire, effectué dans le cadre de l'approximation de CHAPLYGIN. Une expression analytique de la solution, contenant un assez grand nombre de coefficients arbitraires, ayant ainsi été établie, le calcul numérique de H a été programmé sur machine de grande capacité.

Cet hodographe, éventuellement, légèrement déformé est ensuite traité à l'aide des équations du fluide réel, la position de la singularité I correspondante étant méthodiquement recherchée au voisinage de I_0. Le retour au plan physique s'effectue ensuite suivant la méthode classique.

Dans ce mémoire, la méthode de calcul basée sur la technique proposée par R. LEGENDRE est décrite. Un exemple numérique de calcul de H dans l'hypothèse du fluide fictif de CHAPLYGIN est présenté. Les tables numériques des principales fonctions nécessaires à l'établissement des valeurs de $\delta\varphi$ et $\delta\psi$, sur un contour d'hodographe pour un écoulement de fluide réel, sont données.

La mise au point du procédé analogique étant encore en cours d'élaboration, aucun résultat concret ne peut actuellement être présenté.

GENERALITES

Après avoir décrit la classe des hodographes envisagés, on indiquera la méthode générale suivie pour le calcul des écoulements entièrement subsoniques, puis des écoulements mixtes.

COORDONNEES ET CLASSE D'HODOGRAPHES CONSIDEREE

q désignant la vitesse locale du fluide et a_i la célérité du son dans les conditions génératrices, on adopte selon les nécessités imposées par le calcul, l'une ou l'autre des variables suivantes :

$$(1) \quad \tau = \frac{\gamma-1}{2}\,\frac{q^2}{a_i^2} \qquad\qquad (2) \quad \sigma = \frac{1}{2}\int_{\tau}^{\frac{\gamma-1}{\gamma+1}} \frac{(1-\tau)^{\frac{1}{\gamma-1}}}{\tau}\,d\tau$$

Le nombre de Mach est :

$$M = \sqrt{\frac{1}{\gamma-1}\,\frac{2\tau}{1-\tau}}$$

Pour la valeur $\gamma = 1{,}4$ du fluide réel, la relation 2) s'intègre en posant $t_c = \sqrt{\frac{2}{\gamma+1}}$ et $t = \sqrt{1-\tau}$ sous la forme :

$$(3) \qquad \sigma = \left| \frac{1}{2}\ln\frac{1+t}{1-t} - t - \frac{t^3}{3} - \frac{t^5}{5} \right|_{t_c}^{t}$$

L'hodographe considéré a la forme représentée fig. 1, dans les axes τ, θ

Le profil correspondant est dissymétrique et portant.

Le point I_∞ est l'image de l'infini du plan physique ; la valeur de τ qui lui correspond est inférieure à la valeur critique : $\tau_i < \frac{\gamma-1}{\gamma+1}$ où γ est le rapport des chaleurs spécifiques. La ligne AMF correspond à l'extrados du profil. La ligne A' M' F' de l'hodographe correspondant à l'intrados du profil présente une boucle destinée à éviter la présence de points critiques dans la partie utile de l'hodographe.

POTENTIEL, FONCTION DE COURANT, EQUATION DU PROFIL

θ désignant la pente locale de la ligne de courant sur la direction de la vitesse à l'infini, on rappelle que le potentiel φ et la fonction de courant ψ satisfont les relations :

$$(4) \qquad \varphi_\tau = \frac{(1-\tau)^{-\frac{\gamma}{\gamma-1}}}{2(\gamma-1)\tau}\left[(\gamma+1)\tau + 1-\gamma\right]\psi_\theta$$

$$(5) \qquad \varphi_\theta = 2\tau(1-\tau)^{-\frac{1}{\gamma-1}}\psi_\tau$$

Avec les variables σ, θ : ψ satisfait la relation :

$$(6) \quad \psi_{\sigma\sigma} + k(\sigma)\psi_{\theta\theta} = 0 \qquad \text{avec} \qquad (7) \quad k(\sigma) = (1-\tau)^{-\frac{\gamma+1}{\gamma-1}}\left[1-\tau\,\frac{\gamma+1}{\gamma-1}\right]$$

ψ étant nul sur le profil. Celui-ci est obtenu par intégration de :

$$(8) \qquad dz = \tau^{-\frac{1}{2}}\, e^{i\theta}\, d\varphi$$

φ étant le potentiel sur le contour.

PRINCIPE DU CALCUL D'UN ECOULEMENT ENTIEREMENT SUBSONIQUE

La forme d'un hodographe du type désiré pour une position de la singularité I_∞, I est d'abord calculé dans l'hypothèse du fluide fictif de CHAPLYGIN. Cette forme est conservée pour l'écoulement compressible en fluide réel et en première approximation la position du point I_∞, image de l'infini du plan physique, n'est pas modifiée. Il est admis, sans souci de rigueur et sans démonstration, que le problème du calcul de la fonction de courant ψ et du potentiel φ est bien posé avec les données ci-dessus.

φ et ψ satisfaisant à des équations linéaires peuvent être décomposées en deux solutions de ces équations (φ', ψ') , $(\delta\varphi, \delta\psi)$:

$$\varphi = \varphi' + \delta\varphi \qquad\qquad \psi = \psi' + \delta\psi$$

La solution (φ', ψ') est une solution ayant en I_∞ la même singularité que la solution (φ, ψ) et n'ayant pas d'autres singularités dans le domaine utile de l'hodographe. Si (φ', ψ') peut être calculée avec précision, il reste à déterminer les fonctions $\delta\varphi$ et $\delta\psi$ régulières dans tout le domaine utile de l'hodographe et telles que $\psi' + \delta\psi$ soit nul sur le contour de celui-ci. On élimine ainsi du calcul par réseau analogique ou par différences finies, les difficultés posées par le voisinage des singularités.

La méthode de R. LEGENDRE consiste à choisir pour (φ', ψ') le champ d'une ligne de doublets-tourbillons en nombre infini, régulièrement espacés sur l'axe parallèle à l'axe des θ passant par I_∞. On peut adopter une suite de doublets-tourbillons identiques espacés de 2π ou mieux, pour réduire l'importance de la solution régulière $(\delta\varphi, \delta\psi)$ une ligne de doublets-tourbillons alternés espacés de π. Dans les deux cas, l'une des singularités est placée en I_∞, les autres se trouvent donc à l'intérieur du champ utile de l'hodographe. φ' et ψ' peuvent alors s'exprimer par des séries de fonctions de CHAPLYGIN qui font intervenir des fonctions hypergéométriques faciles à calculer.

Ces calculs ayant été effectués pour une position donnée de la singularité I_∞, on vérifie si le comportement de la solution au voisinage des points de vitesse nulle est correct. S'il n'en est pas ainsi, on recommence les calculs pour une nouvelle position de I_∞ voisine de la précédente. Ce tâtonnement peut être conduit d'une manière méthodique.

PRINCIPE DU CALCUL D'UN ECOULEMENT TRANSSONIQUE.

Le contour de l'hodographe n'est, dans ce cas, donné que jusqu'à la valeur τ_c de τ égale à la valeur critique fig. 2. Les données sont $\psi = 0$ sur le contour de l'hodographe , $\psi = \psi(\tau_c, \theta)$ et $\psi_\tau = \psi_\tau(\tau_c, \theta)$ sur le segment M_1 , M_2 , ψ étant nul en M_1 et M_2.

La méthode de résolution pour la détermination de ψ' puis de ψ dans le domaine subsonique est identique à celle exposée dans le paragraphe précédent, la valeur de $\delta\psi$ devenant $\psi(\tau_c, \theta) - \psi'$ sur le segment M_1 , M_2. Le contour $\psi = 0$ de la partie supersonique, supposé très voisin de la ligne sonique $\tau = \tau_c$, pourra être obtenu par la linéarisation suivante :

Avec les variables hodographiques classiques σ , θ le potentiel satisfait à la relation $\psi_{\sigma\sigma} + k(\sigma)\psi_{\theta\theta} = 0$ et comme sur le segment sonique M_1 , M_2 , σ et $k(\sigma)$ sont nuls, on a :

$$\psi_\sigma = f(\theta) \qquad\qquad \psi = g(\theta)$$

$f(\theta)$ et $g(\theta)$ étant fixés dans le problème subsonique précédent. La valeur σ_ψ de σ sur le profil est donc donnée au 2ème ordre près en σ sur chaque ligne $\theta = c^{te}$ par la relation :

$$\psi = \sigma_{f} f(\theta) + g(\theta) = 0$$

On en déduit la valeur τ_{f} de τ par la relation (3). La validité de ce procédé a été démontrée pratiquement dans un calcul analogique par la méthode des réseaux.

ANALYSE DETAILLEE DU PROBLEME

Les principes de la méthode de calcul seront exposés ici, sans rappeler les démonstrations rigoureuses établies par R. LEGENDRE ; ils comprennent les différentes phases suivantes :

a) - condition de fermeture du profil,

b) - calcul d'hodographes du type désiré et des profils correspondants dans l'approximation du fluide fictif de CHAPLYGIN,

c) - définition, pour l'étude en fluide réel, des fonctions de CHAPLYGIN intervenant dans le calcul des séries exprimant φ' et ψ',

d) - valeurs des coefficients des termes de ces séries,

e) - positionnement de la singularité dans le champ de l'hodographe de contour donné.

CONDITION DE FERMETURE DU PROFIL.

La singularité au point image de l'infini du plan physique est un doublet-tourbillon. Une étude locale de cette singularité (Annexe I) montre que l'axe du doublet est parallèle à l'axe des θ et que, pour assurer la condition de fermeture, le rapport de l'intensité du doublet B à l'intensité du tourbillon 2C est donné par la relation :

$$B\,(1-\tau_{\infty})^{-\frac{1}{\gamma-1}} + 2C = 0$$

APPROXIMATION DE CHAPLYGIN.

Cette approximation est obtenue en faisant tendre γ vers -1, dans les équations générales, on obtient :

$$\tau = \frac{1}{sh^2\sigma} \qquad\qquad k(\sigma) = 1$$

POTENTIEL DES VITESSES - Le potentiel F est donc une fonction analytique de la variable complexe $\lambda = \sigma + i\theta$ et on peut poser :

$$\text{(9)} \qquad \begin{aligned} F &= t + \frac{1}{t} + 2i \sin\alpha \ln t \\ \lambda &= \sigma_{\infty} - \ln(1-te^{i\alpha}) - \frac{\Theta}{\pi}\ln(1+te^{-i\alpha}) + f(t) \end{aligned}$$

de sorte que la variable auxiliaire t assure la transformation conforme de l'intérieur de l'hodographe en l'intérieur du cercle de rayon 1 dans le plan $t = Re^{i\omega}$

Au bord d'attaque	$\omega = -\alpha$	(point d'arrêt)
Au bord de fuite	$\omega = \pi + \alpha$	(point d'arrêt)
Sur l'extrados	$-\alpha \leq \omega \leq \pi + \alpha$	
Sur l'intrados	$\alpha - \pi \leq \omega \leq -\alpha$	

Θ est l'angle de dièdre du bord de fuite,

$f(t)$ est une fonction régulière à l'intérieur du champ utile de l'hodographe.

L'étude effectuée pour obtenir des hodographes du type désiré a montré que si la fonction $f(t)$ est choisie partout régulière, sa représentation par une série entière devrait retenir un nombre de termes considérables. L'artifice évitant cet inconvénient consiste à introduire, dans l'expression de $f(t)$, des termes singuliers à l'extérieur du cercle d'uniformisation et n'entraînant pas la création de points critiques à l'intérieur du champ utile.

Finalement, l'expression retenue pour $f(t)$ est :

$$\text{(10)} \qquad \begin{aligned} f(t) = {} & (A+iB)\ln\left[1-te^{i\alpha}(1-\varepsilon e^{i\gamma})\right] \\ & + (C+iD)\ln\left[1+te^{-i\alpha}(1-\varepsilon' e^{i\gamma'})\right] + g(t) \end{aligned}$$

$g(t)$ étant une correction régulière dont le développement en série débute par un terme en t^2 pour ne pas affecter la condition de fermeture du profil :

$$g(t) = (a_2 + ib_2)t^2 + \ldots\ldots + (a_n + ib_n)t^n + \cdots$$

CONDITION DE FERMETURE. Au voisinage de la singularité :

$$\lambda = \sigma_\infty + te^{i\alpha} - t\frac{\Theta}{\pi}e^{-i\alpha} + (a_1 + ib_1 t)$$

le dernier terme étant le début du développement de f (t)

d'où $\quad t = \dfrac{\lambda - \sigma_\infty}{A_0 + iB_0} \quad$ avec $\quad A_0 = \cos\alpha - \dfrac{\Theta}{\pi}\cos\alpha + a_1$

La condition de fermeture (Voir Annexe I) impose :

$A_0 = 0 \quad$ et $\quad \dfrac{B_0}{2\sin\alpha} = (1-\tau_\infty)^{\frac{1}{2}} = \operatorname{th}\sigma_\infty$

d'où $\quad a_1 = \cos\alpha\left[\dfrac{\Theta}{\pi} - 1\right] \quad$ et $\quad B_0 = \sin\alpha + \dfrac{\Theta}{\pi}\sin\alpha + b_1 = 2\operatorname{th}\sigma_\infty \sin\alpha$

Le calcul de a_1 et b_1, déduit de l'expression de f (t), conduit aux 2 relations :

$$\begin{aligned}(11)\qquad & \left[1 - \frac{\Theta}{\pi} + C\right]\cos\alpha + D\sin\alpha - \varepsilon' C\cos(\gamma'-\alpha) + \varepsilon' D\sin(\gamma'-\alpha) \\ & - A\left[\cos\alpha - \varepsilon\cos(\alpha+\gamma)\right] + B\left[\sin\alpha - \varepsilon\sin(\gamma+\alpha)\right] = 0\end{aligned}$$

$$\begin{aligned}(12)\qquad & \left[1 + \frac{\Theta}{\pi} - C\right]\sin\alpha + D\cos\alpha - \varepsilon' C\sin(\gamma'-\alpha) - \varepsilon' D\cos(\gamma'-\alpha) \\ & - A\left[\sin\alpha - \varepsilon\sin(\alpha+\gamma)\right] - B\left[\cos\alpha - \varepsilon\cos(\gamma+\alpha)\right] = 2\operatorname{th}\sigma_\infty\sin\alpha\end{aligned}$$

qui assurent la fermeture du profil.

EQUATION DE L'HODOGRAPHE. La séparation des parties réelle et imaginaire de la relation (9) compte tenu de l'expression de (10) de f (t) donne l'équation paramétrique du contour H de l'hodographe cherché :

$$\begin{aligned}\sigma = \;& \sigma_\infty - \ln\left|2\sin\frac{\omega+\alpha}{2}\right| - \frac{\Theta}{\pi}\ln\left|2\cos\frac{\omega-\alpha}{2}\right| \\ & + \frac{A}{2}\ln\left|2 - 2\cos(\omega+\alpha) + \varepsilon^2 + 2\varepsilon\cos(\omega+\alpha+\gamma) - 2\varepsilon\cos\gamma\right| \\ & - B\operatorname{arctg}\left\{\frac{-\sin(\omega+\alpha) + \varepsilon\sin(\omega+\alpha+\gamma)}{1-\cos(\omega+\alpha) + \varepsilon\cos(\omega+\alpha+\gamma)}\right\} \\ & + \frac{C}{2}\ln\left|2 + 2\cos(\omega-\alpha) + \varepsilon'^2 - 2\varepsilon'\cos(\omega-\alpha+\gamma') - 2\varepsilon'\cos\gamma'\right| \\ & - D\operatorname{arctg}\left\{\frac{\sin(\omega-\alpha) - \varepsilon'\sin(\omega-\alpha+\gamma')}{1+\cos(\omega-\alpha) - \varepsilon'\cos(\omega-\alpha+\gamma')}\right\} \\ & + a_2\cos 2\omega - b_2\sin 2\omega + \ldots \quad + a_n\cos n\omega - b_n\sin n\omega\end{aligned}$$

Sur l'extrados $\quad -\alpha \leq \omega \leq \pi + \alpha$

Sur l'intrados $\quad \alpha - \pi \leq \omega \leq -\alpha$

Au bord d'attaque : (point de vitesse nulle) $\quad \omega = -\alpha$

Au bord de fuite : (point de vitesse nulle) $\quad \omega = \alpha - \pi$

La valeur de θ sur l'extrados s'exprime sous la forme :

$$\theta = \frac{\pi - \omega - \alpha}{2} - \frac{\Theta}{\pi}\,\frac{\omega - \alpha}{2} + A \,\mathrm{arctg}\left\{\frac{-\sin(\omega+\alpha) + \varepsilon \sin(\omega+\alpha+\gamma)}{1 - \cos(\omega+\alpha) + \varepsilon\cos(\omega+\alpha+\gamma)}\right\}$$
$$+ \frac{B}{2}\ln\left|2 + \varepsilon^2 - 2\cos(\omega+\alpha) + 2\varepsilon\cos(\omega+\alpha+\gamma) - 2\varepsilon\cos\gamma\right|$$
$$+ C\,\mathrm{arctg}\left\{\frac{\sin(\omega-\alpha) - \varepsilon'\sin(\omega-\alpha+\gamma')}{1+\cos(\omega-\alpha) - \varepsilon'\cos(\omega-\alpha+\gamma')}\right\}$$
$$+ \frac{D}{2}\ln\left|2 + \varepsilon'^2 + 2\cos(\omega-\alpha) - 2\varepsilon'\cos(\omega-\alpha+\gamma') - 2\varepsilon'\cos\gamma'\right|$$
$$+ b_2\cos 2\omega + a_2 \sin 2\omega + \dots \qquad + b_n \cos n\omega + a_n \sin n\omega$$

Sur l'intrados cette quantité est à diminuer de π .

Le point I_∞ image de l'infini du plan physique a pour coordonnées : $\sigma = \sigma_\infty \qquad \theta = 0$

Les paramètres disponibles sont : σ_∞ , α , Θ , A, B, C, D, ε, ε', γ, γ', a_2, b_2, ...

Les 11 premiers doivent satisfaire aux 2 relations (11, 12) qui assurent la condition de fermeture.

On ne discutera pas ici les limitations de choix à imposer aux coefficients arbitraires pour obtenir un hodographe sans points critiques dans la partie utile. Le calcul numérique programmé sur machine de haute capacité, qui est d'ailleurs très rapide, permet d'éliminer, après calcul, les résultats qui ne conduiraient pas à un hodographe de la classe considérée.

Forme du profil dans le plan physique. Un autre critère de bon choix des paramètres arbitraires consiste à vérifier que le profil correspondant dans l'approximation de CHAPLYGIN possède l'allure souhaitée pour les applications (épaisseur relative, rayon de courbure au bord d'attaque, gradient de recompression au bord de fuite, etc...). Ce profil est obtenu, d'après l'équation de l'hodographe, par l'intégration sur l'intrados et l'extrados des relations :

$$\frac{dx}{d\omega} = -8\,\mathrm{sh}\,\sigma\cos\theta\,\sin\frac{\omega+\alpha}{2}\cos\frac{\omega-\alpha}{2} \qquad\qquad \frac{dy}{d\omega} = -8\,\mathrm{sh}\,\sigma\sin\theta\,\sin\frac{\omega+\alpha}{2}\cos\frac{\omega-\alpha}{2}$$

Le rayon de courbure en un point quelconque du profil est : $R = \dfrac{-8\,\mathrm{sh}\,\sigma\sin\frac{\omega+\alpha}{2}\cos\frac{\omega-\alpha}{2}}{\frac{d\theta}{d\omega}}$

Les calculs de x, y et R ont été programmés.

Exemple : valeurs numériques des paramètres :

$\sigma_\infty = 0{,}85 \qquad \alpha = 11° \qquad \frac{\Theta}{\pi} = 0{,}07 \qquad A = 0{,}08843 \qquad B = -0{,}20$

$C = -0{,}054258496 \qquad D = 0{,}0513551$

$\varepsilon = 0{,}05 \qquad \varepsilon' = 0{,}05 \qquad \gamma = -32° \qquad \gamma' = -50°$

a_2 , b_2 $\quad a_n$ .. b_n sont nuls

Avec ces valeurs, les conditions de fermeture (11 , 12) sont satisfaites.

Les résultats des calculs sont indiqués sur les figures (3) , (4) et (5).

La figure (3) donne la forme de l'hodographe. La figure (4) donne la forme du profil. La figure (5) donne la répartition des nombres de Mach sur l'extrados et sur l'intrados dans l'approximation de CHAPLYGIN : $M = \dfrac{1}{\mathrm{ch}\,\sigma}$

L'angle que forme la direction de la ligne de courant aboutissant au bord d'attaque (point d'arrêt), avec la direction de la vitesse à l'infini, est 9°,272. L'angle que forme la bissectrice du dièdre de bord de fuite, avec la direction de la vitesse à l'infini, est 13°,15.

CALCUL DE LA SOLUTION EN FLUIDE REEL.

DEFINITION, POUR L'ETUDE EN FLUIDE REEL, DES FONCTIONS DE CHAPLYGIN INTERVENANT DANS LE CALCUL DU CHAMP DES SINGULARITES. Des deux relations (4) et (5), on déduit en éliminant φ :

$$\tau(1-\tau)\,\psi_{\tau\tau} + \left(1 + \frac{2-\gamma}{\gamma+1}\,\tau\right)\psi_\tau + \frac{1}{4}\left(\frac{1}{\tau} - \frac{\gamma+1}{\gamma-1}\right)\psi_{\theta\theta} = 0$$

Les solutions de CHAPLYGIN sont les solutions périodiques en θ dépendant d'un paramètre n positif

$$\psi = f_n(\tau)\, e^{ni\theta} \qquad \varphi_\theta = 2\tau(1-\tau)^{-\frac{1}{\gamma-1}} f_{n_\tau}(\tau)\, e^{ni\theta} \qquad (13)$$

$$\psi_\tau = f_{n_\tau}(\tau)\, e^{ni\theta} \qquad \varphi = -\frac{2i}{n}\tau(1-\tau)^{-\frac{1}{\gamma-1}} f_{n_\tau}(\tau)\, e^{ni\theta} \qquad (14)$$

$f_n(\tau)$ doit alors satisfaire l'équation :

$$\tau(1-\tau) f_{n_{\tau\tau}} + \left(1 + \frac{2-\gamma}{\gamma-1}\tau\right) f_{n_\tau} - \frac{n^2}{4}\left(\frac{1}{\tau} - \frac{\gamma+1}{\gamma-1}\right) f_n = 0$$

Le calcul de (φ', ψ') fera intervenir deux solutions particulières de la précédente relation.

La première $f_n(\tau)$ est nulle au point d'arrêt ($\tau = 0$).

La deuxième $g_n(\tau)$ est nulle à la vitesse limite ($\tau = 1$).

Solution $f_n(\tau)$. On cherche une solution de la forme : $f_n = \tau^\alpha (1-\tau)^\beta F(\tau)$

avec $\alpha = \pm\frac{n}{2}$ $\qquad \beta = \begin{cases} 0 \\ \gamma/\gamma-1 \end{cases}$

$F(\tau)$ est une fonction hypergéométrique $F(a, b, c, \tau)$.

Seules les solutions correspondant à $c > 0$ sont retenues. La série hypergéométrique représentant F est alors convergente pour $0 < \tau < 1$ avec $\alpha = \frac{n}{2}$. Un calcul facile conduit alors aux résultats suivants : pour $\alpha = \frac{n}{2}$ et $\beta = 0$

$$c = 1 + n \qquad \left.\begin{matrix} a \\ b \end{matrix}\right\} = \frac{n}{2} - \frac{1 \pm\sqrt{n^2(\gamma^2-1)+1}}{2(\gamma-1)}$$

pour $\alpha = \frac{n}{2}$ et $\beta = \frac{\gamma}{\gamma-1}$

$$c = 1 + n \qquad \left.\begin{matrix} a \\ b \end{matrix}\right\} = \frac{n}{2} - \frac{1-2\gamma \pm\sqrt{1+n^2(\gamma^2-1)}}{2(\gamma-1)}$$

Solution $g_n(\tau)$. On pose : $\tau' = 1-\tau \qquad g_n(\tau) = \tau'^\beta (1-\tau')^\alpha F(\tau')$

Avec les mêmes valeurs de α et β que précédemment, F est une fonction hypergéométrique : $F(a', b', c', \tau')$. Ici il convient d'adopter : $\beta = \gamma/\gamma-1$. On trouve alors :

pour $\alpha = \frac{n}{2}$ et $\beta = \frac{\gamma}{\gamma-1}$

$$c = \frac{2\gamma-1}{\gamma-1} \qquad \left.\begin{matrix} a' \\ b' \end{matrix}\right\} = \frac{n}{2} - \frac{1-2\gamma \pm\sqrt{1+n^2(\gamma^2-1)}}{2(\gamma-1)}$$

pour $\alpha = -\frac{n}{2}$ et $\beta = \frac{\gamma}{\gamma-1}$

$$c = \frac{2\gamma-1}{\gamma-1} \qquad \left.\begin{matrix} a' \\ b' \end{matrix}\right\} = -\frac{n}{2} - \frac{1-2\gamma \pm\sqrt{1+n^2(\gamma^2-1)}}{2(\gamma-1)}$$

Valeurs de φ et ψ correspondant à $f_n(\tau)$.

La dérivée de f_n a pour expression :

$$f_{n_\tau} = \tau^{\alpha-1}(1-\tau)^{\beta-1}\left[\alpha(1-\tau) - \beta\tau\right] F + \tau^\alpha (1-\tau)^\beta F_\tau$$

avec $\quad F_\tau = \frac{ab}{c} F(a+1, b+1, c+1, \tau)$

On adoptera pour ψ la partie imaginaire de l'expression (13) : $\psi = f_n(\tau)\sin n\theta$

et pour φ la partie imaginaire de l'expression (14) : $\varphi = -\frac{2}{n}\tau(1-\tau)^{-\frac{1}{\gamma-1}} f_{n_\tau} \cos n\theta$

et on écrira $\quad \varphi = \bar{f}_n(\tau)\cos n\theta$

avec $\quad \bar{f}_n(\tau) = -\frac{2}{n}\tau(1-\tau)^{-\frac{1}{\gamma-1}} f_{n_\tau}$

Pour $\alpha = \frac{n}{2}$ et $\beta = 0$

$$\psi = \tau^{\frac{n}{2}} F(a, b, c, \tau)\sin n\theta$$

$$f_{n_\tau} = \tau^{\frac{n}{2}}\left[\frac{n}{2}\frac{F}{\tau} + F_\tau\right]$$

Valeurs de φ et ψ correspondant à $g_n(\tau)$

$$\psi = g_n(\tau)\sin n\theta$$

D'autre part :

$$g_{n_\tau} = -g_{n_{\tau'}} = -\tau'^{\beta-1}(1-\tau')^{\alpha-1}\left[\beta(1-\tau')-\alpha\tau'\right]F - \tau'^{\beta}(1-\tau')^{\alpha}F_{\tau'}$$

où $\tau' = 1-\tau$

$$\varphi = -\frac{2}{n}\tau(1-\tau)^{-\frac{1}{\gamma-1}}g_{n_\tau}\cos n\theta$$

On écrira : $\varphi = \bar{g}_n(\tau)\cos n\theta$ avec $\bar{g}_n(\tau) = -\frac{2}{n}\tau(1-\tau)^{-\frac{1}{\gamma-1}}g_{n_\tau}$

Pour $\alpha = -\frac{n}{2}$ et $\beta = \frac{\gamma}{\gamma-1}$

$$\bar{g}_n(\tau) = \frac{2}{n}\tau^{-\frac{n}{2}}\left[\frac{\gamma}{\gamma-1}\tau + \frac{n}{2}(1-\tau)\right]F(a',b',c';1-\tau) + (1-\tau)^{\frac{\gamma}{\gamma-1}}\tau^{-\frac{n}{2}}F_\tau$$

Le calcul des fonctions f, g, $\bar{f}$, $\bar{g}$, ne présente pas de difficultés, les fonctions hypergéométriques qui leur correspondent étant convergentes. Un extrait des tables de ces fonctions est donné en annexe.

VALEUR DES COEFFICIENTS DES TERMES DES SERIES EXPRIMANT LE POTENTIEL ET LA FONCTION DE COURANT DES SINGULARITES. Le champ de la file de doublets-tourbillons tous de même intensité, espacés de 2π et dont l'un placé en I_∞ représente la singularité correspondant à l'infini du plan physique, s'obtient par dérivation du champ d'une file de sources par rapport à θ auquel se superpose le champ d'une file de tourbillons.

Champ d'une file de sources distantes de 2π placée aux points I_k $(\tau_\infty, 2k\pi)$. On se propose de déterminer une solution formée par deux séries de fonctions de CHAPLYGIN f_n et g_n définies précédemment, respectivement valables pour $\tau < \tau_\infty$ et $\tau > \tau_\infty$. Les relations entre les coefficients des termes de ces séries sont déterminées de manière à assurer leur raccord sur $\tau = \tau_\infty$ et la représentation convenable du potentiel et de la fonction de courant de ces sources. Pour $\tau < \tau_\infty$, les fonctions f_n, $\bar{f}_n$ étant régulières, le potentiel et la fonction de courant sont donc exprimés par :

$$\varphi_s = \sum_{n=1}^{\infty} a_n\bar{f}_n(\tau)\cos n\theta \qquad \psi_s = \sum_{n=1}^{\infty} a_n f_n(\tau)\sin n\theta$$

Pour $\tau > \tau_\infty$, au contraire, le potentiel et la fonction de courant sont exprimés par les séries de FOURIER :

$$\varphi_s = \sum_{n=1}^{\infty} b_n\bar{g}_n(\tau)\cos n\theta \qquad \psi_s = \pi + \theta + \sum_{n=1}^{\infty} b_n g_n(\tau)\sin n\theta$$

R. LEGENDRE a démontré que φ_s étant uniforme, la condition de raccord entre les deux solutions pour $\tau = \tau_\infty$ s'écrit simplement :

$$a_n\bar{f}_n(\tau_\infty) = b_n\bar{g}_n(\tau_\infty)$$

Pour $\tau = \tau_\infty$, ψ_s est continu si $\theta \neq 2k\pi$ et croît de 2π au passage de chaque singularité I_K $(\theta = 2k\pi)$. La discontinuité correspondante est exprimée par la fonction ESCOLIER :

$$\pi + \theta + \sum_{n=1}^{\infty}\frac{2}{n}\sin n\theta$$

Il en résulte que les coefficients b_n et a_n, assurant cette condition, satisfont les relations :

$$b_n g_n(\tau_\infty) - a_n f_n(\tau_\infty) = \frac{2}{n}$$

Par suite :

$$a_n = \frac{2}{n}\,\frac{\bar{g}_n(\tau_\infty)}{\bar{f}_n(\tau_\infty)g_n(\tau_\infty) - f_n(\tau_\infty)\bar{g}_n(\tau_\infty)} = \frac{2}{n}\,\frac{g_n(\tau_\infty)}{f_n g_{n_{\tau_\infty}} - g_n f_{n_{\tau_\infty}}}$$

$$b_n = \frac{2}{n}\,\frac{\bar{f}_n(\tau_\infty)}{\bar{f}_n(\tau_\infty)g_n(\tau_\infty) - f_n(\tau_\infty)\bar{g}_n(\tau_\infty)} = \frac{2}{n}\,\frac{f_n(\tau_\infty)}{f_n g_{n_{\tau_\infty}} - g_n f_{n_{\tau_\infty}}}$$

Champ d'une file de tourbillons espacés de 2π. On pose comme dans le cas précédent :

pour $\tau < \tau_\infty$

$$\varphi_t = \sum_{n=1}^{\infty} c_n\bar{f}_n(\tau)\sin n\theta \qquad \psi_t = \sum_{n=1}^{\infty} c_n f_n(\tau)\cos n\theta$$

pour $\tau > \tau_\infty$

$$\varphi_t = \pi + \theta + \sum_{n=1}^{\infty} d_n\bar{g}_n(\tau)\sin n\theta \qquad \psi_t = \sum_{n=1}^{\infty} d_n g_n(\tau)\cos n\theta$$

Dans ce problème, la fonction de courant est continue en I_K et le potentiel y subit une discontinuité de 2π.

Un calcul analogue au précédent donne alors les valeurs de c_n et d_n :

$$c_n = \frac{2}{\pi} \frac{g_n(\tau_\infty)}{f_n g_{n\tau_\infty} - g_n f_{n\tau_\infty}} \qquad d_n = \frac{2}{\pi} \frac{f_n(\tau_\infty)}{f_n g_{n\tau_\infty} - g_n f_{n\tau_\infty}}$$

CHAMP D'UN FILE DE DOUBLETS-TOURBILLONS DE MEME INTENSITE SITUES SUR L'AXE $\tau = \tau_\infty$ ET ASSURANT LA CONDITION DE FERMETURE DU PROFIL. Le champ d'une ligne de doublets est obtenu par dérivation par rapport à θ du champ de sources précédent :

$$\varphi_D = B \frac{\partial}{\partial\theta} \varphi_s(\tau_\infty, \tau, \theta) \qquad \psi_D = B \frac{\partial}{\partial\theta} \psi_s(\tau_\infty, \tau, \theta)$$

Le potentiel et la fonction de courant de la ligne de doublets-tourbillons sont alors définis par les relations suivantes :

pour $\tau < \tau_\infty$

$$\varphi' = - B \sum_{n=1}^{\infty} n a_n f_n(\tau) \sin n\theta + 2C \sum_{n=1}^{\infty} c_n f_n(\tau) \sin n\theta$$

$$\psi' = B \sum_{n=1}^{\infty} n a_n f_n(\tau) \cos n\theta + 2C \sum_{n=1}^{\infty} c_n f_n(\tau) \cos n\theta$$

pour $\tau > \tau_\infty$

$$\varphi' = - B \sum_{n=1}^{\infty} n b_n \bar{g}_n(\tau) \sin n\theta + 2C \sum_{n=1}^{\infty} d_n \bar{g}_n(\tau) \sin n\theta + 2\pi C + 2\pi\theta$$

$$\psi' = B + 2B \sum_{n=1}^{\infty} n b_n g_n(\tau) \cos n\theta + 2C \sum_{n=1}^{\infty} d_n g_n(\tau) \cos n\theta$$

Pour réduire l'importance des fonctions complémentaires $\delta\varphi$ et $\delta\psi$ R. LEGENDRE a suggéré divers perfectionnements pouvant être utilisés séparément ou simultanément. Il sera, en particulier, avantageux, ce qui n'introduit pas de complications dans les calculs, de substituer au champ défini précédemment celui de tourbillons et doublets alternés. Les fonctions φ_s , φ_t ,et ψ_s , ψ_t qui viennent d'être définies seront alors remplacées par :

$$\varphi_s(\tau_\infty, \tau, \theta) - \varphi_s(\tau_\infty, \tau, \theta+\pi) \qquad \psi_s(\tau_\infty, \tau, \theta) - \psi_s(\tau_\infty, \tau, \theta+\pi)$$

$$\varphi_t(\tau_\infty, \tau, \theta) - \varphi_t(\tau_\infty, \tau, \theta+\pi) \qquad \psi_t(\tau_\infty, \tau, \theta) - \psi_t(\tau_\infty, \tau, \theta+\pi)$$

POSITION DE LA SINGULARITE DANS LE CHAMP DE L'HODOGRAPHE DE CONTOUR DONNE. Les calculs préliminaires pour la loi de compressibilité de CHAPLYGIN, ont fourni une première approximation de la position relative de I_∞. Cette position doit satisfaire les conditions :

$$\tau^{\frac{1}{3}} \frac{\partial\varphi}{\partial\tau} = 0 \text{ au bord d'attaque,} \qquad \tau^{1-\frac{\pi}{2\Theta}} \frac{\partial\varphi}{\partial\tau} = 0 \text{ au bord de fuite,}$$

Θ étant l'angle du dièdre de bord de fuite. Si ces conditions ne sont pas remplies, les calculs du champ de l'écoulement seront repris pour quelques positions de I, voisins de la position prise en 1ère approximation. Pour chaque position $\tau^{1/3} \partial\varphi/\partial\tau$ au bord d'attaque et $\tau^{1-\pi/2\Theta}$ au bord de fuite sont généralement finis et non nuls. On établira ainsi un moule linéaire permettant d'obtenir deux équations déterminant les coordonnées τ_∞ et θ_∞ du point I.

MISE EN OEUVRE DE CALCULS A EFFECTUER

PARTANT D'UN HODOGRAPHE H fourni par l'approximation de CHAPLYGIN pour une singularité $I_{oCH}(\tau_\infty, \theta_\infty)$ on se propose de déterminer un profil dans le plan physique admettant ce même hodographe dans un écoulement de gaz réel. La position de la singularité I_0 voisine de I_{oCH} est alors déterminée pour satisfaire aux conditions exprimées précédemment. Cette position ayant été déterminée, on calculera les valeurs définitives de $\varphi = \varphi' + \delta\varphi$ surle contour de l'hodographe et on déterminera le profil par intégration. Ces calculs donneront les corrections à apporter au profil du plan physique déterminé dans l'approximation de CHAPLYGIN, pour tenir compte de la loi de compressibilité exacte.

POUR DES VALEURS DE τ_∞ différentes de celles correspondant à l'hodographe H, on devra d'abord faire subir à l'hodographe une légère déformation (allongement ou troncature) localisée au voisinage de $\tau = 0$. La suite des calculs est alors identique à celle qui vient d'être décrite.

CONCLUSION

Un méthode de calcul d'écoulements subsoniques ou transsoniques réversibles autour de profils portants dont les principes ont été établis avec rigueur par R. LEGENDRE, a été mise en oeuvre. Cette méthode applicable à des formes d'hodographe, ne comportant pas, à l'intérieur du champ utile, d'autres singularités que l'image du point à l'infini du plan physique, est guidée par le souci de dégager analytiquement la partie principale de cette singularité et réserver ainsi les méthodes numériques aux différences finies, ou analogiques au calcul de fonctions régulières. Dans cette méthode, le problème transsonique est remplacé par un problème subsonique, dont la solution est prolongeable dans un domaine supersonique modéré.

Les calculs en cours n'ont pu encore aboutir à des résultats concrets dans le cas d'un écoulement de fluide, satisfaisant à la loi de compressibilité exacte.

Les équations des hodographes proposés dans l'hypothèse du fluide fictif de CHAPLYGIN pour servir de base au calcul exact ont été établies et résolues numériquement ; les valeurs numériques des principales fonctions auxiliaires nécessaires à la détermination d'un écoulement quelconque, correspondant à la loi de compressibilité exacte ont été calculées.

- REFERENCES -

M. LIGHTHILL -

On the hodograph transformation for high speed flow.

Quart. Appl. Math. n° 9 - 1951

R. LEGENDRE -

Singularités critiques de l'hodographe.

C.R. Acad. Sc. T. 244 - 1957

R. LEGENDRE -

Calcul de profils pour turbo-machines transsonique.

Progr. in Aer. Sc. - 1960

G. NIEUWLAND -

Transonic potentiel flow around a Family of quasi elliptical aerofoil.

Section N.L.R. T.N. 172 - 1967

R. LEGENDRE -

Singularité de l'hodographe de l'écoulement reversible d'un fluide compressible autour d'un profil portant.

C.R. Acad. Sc. - tome 266 - 1968

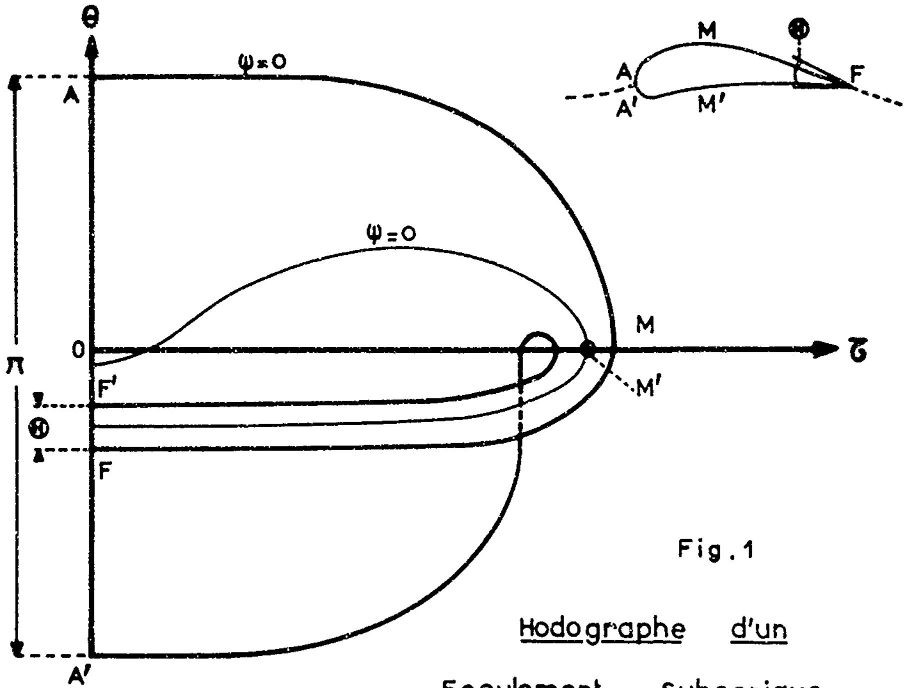

Fig. 1

Hodographe d'un Ecoulement Subsonique

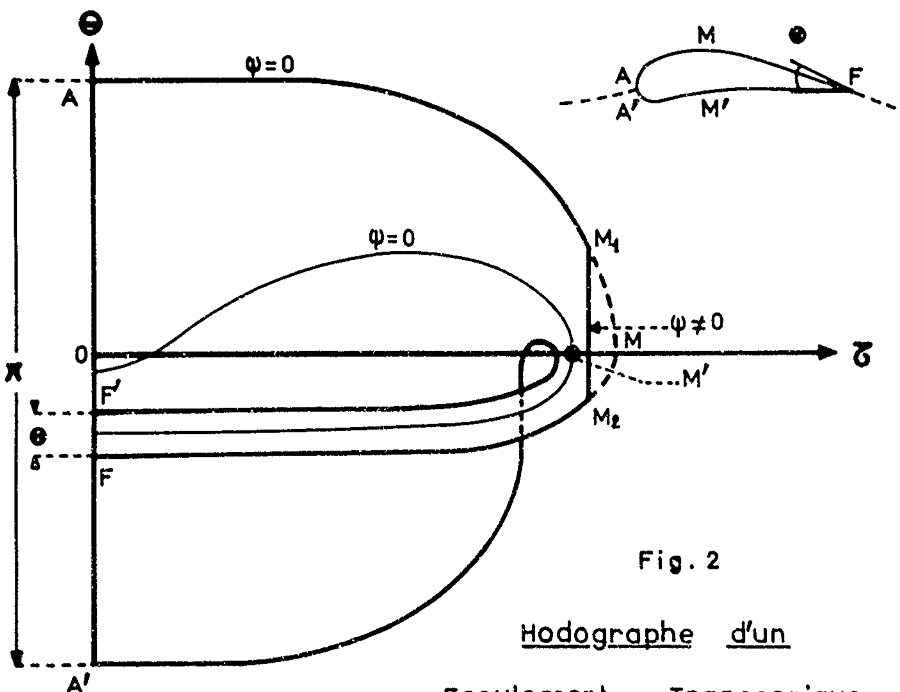

Fig. 2

Hodographe d'un Ecoulement Transsonique

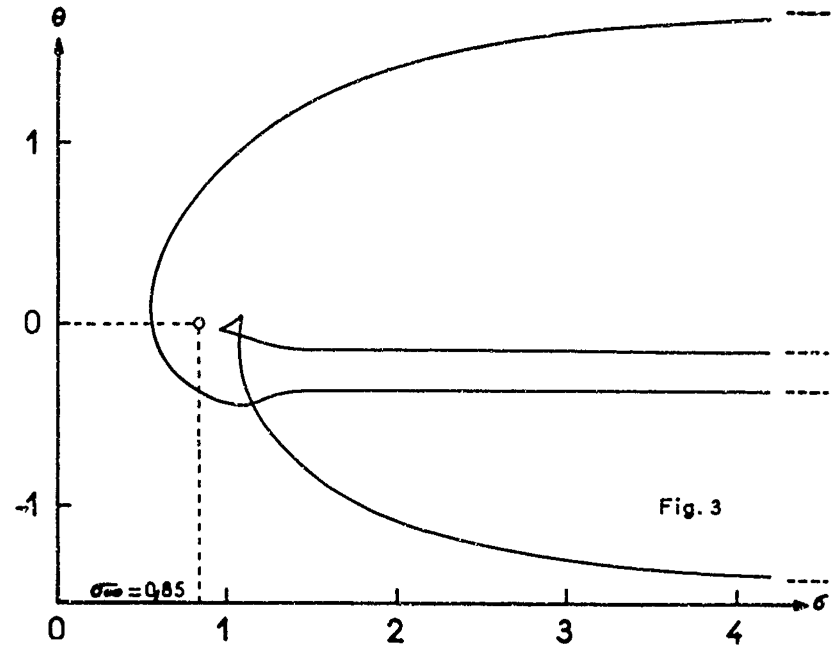

Fig. 3

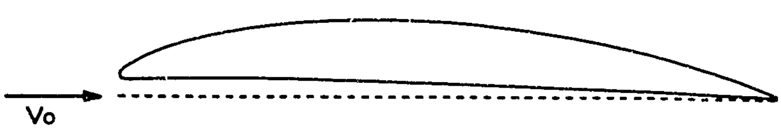

Fig. 4

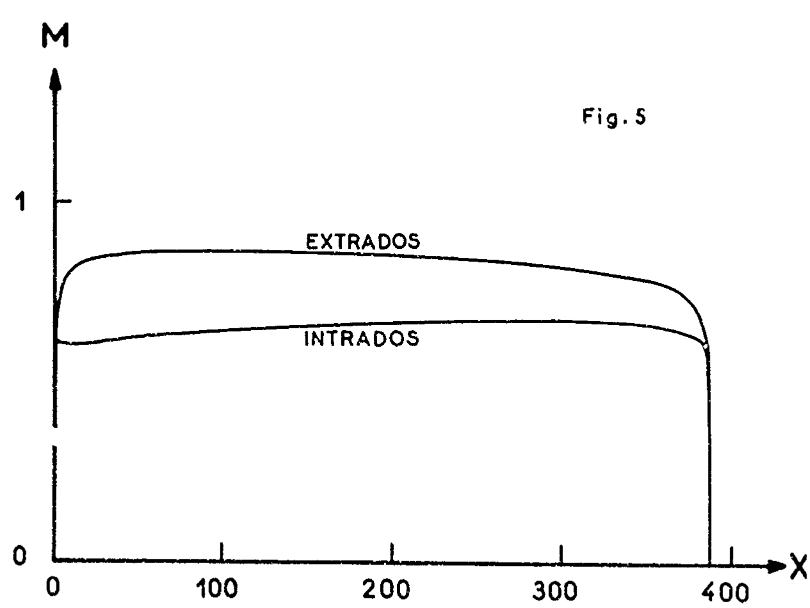

Fig. 5

ANNEXE I

NATURE DE LA SINGULARITE AU POINT IMAGE I DU PLAN PHYSIQUE - CONDITION DE FERMETURE DU PROFIL

Si l'on adopte les variables hodographiques σ et θ , la fonction de courant satisfait la relation :

$$\varphi_{\sigma\sigma} + k(\sigma)\psi_{\theta\theta} = 0 \qquad \text{avec} \qquad k(\sigma) = (1-\tau)^{-\frac{\gamma+1}{\gamma-1}}\left[1-\tau\frac{\gamma+1}{\gamma-1}\right]$$

Au voisinage de I τ et σ tendent vers les valeurs connues τ_∞ et σ_∞ et

$$k(\sigma) \rightarrow k_\infty = (1-\tau_\infty)^{-\frac{\gamma+1}{\gamma-1}}\left[1-\tau_\infty\frac{\gamma+1}{\gamma-1}\right]$$

Après le changement de variables $\sigma^* = \sqrt{k_\infty}\,\sigma$ l'équation de la fonction de courant devient à la limite $\sigma \rightarrow \sigma_\infty$ la relation harmonique

$$\psi_{\sigma^*\sigma^*} + \psi_{\theta\theta} = 0$$

La singularité la plus simple permettant d'obtenir un hodographe sans point critique dans la partie utile est alors un doublet-tourbillon, dont le potentiel complexe est, au voisinage de I, en posant $\lambda^* = \sigma^* + i\theta$

$$F = \frac{A+iB}{\lambda^* - \sigma^*_\infty} - iC\ln\left(\lambda^* - \sigma^*_\infty\right)$$

Le potentiel complexe F_1 du doublet s'écrit en coordonnées polaires locales

$$\sigma^*_0 = \sigma^* - \sigma^*_\infty = r\cos\alpha \qquad \theta = r\sin\alpha$$

$$F_1 = \frac{A\cos\alpha + B\sin\alpha}{r} + i\,\frac{B\cos\alpha - A\sin\alpha}{r}$$

Le potentiel complexe du tourbillon est de même

$$F_2 = -iC\left[\ln r + i\alpha\right]$$

Pour r et θ infiniments petits, la correspondance entre le plan physique et le plan de l'hodographe est fournie par

$$dz = (1+i\theta)\,\tau_\infty^{-\frac{1}{2}}\left[d\varphi + i(1-\tau_\infty)^{-\frac{1}{\gamma-1}}d\psi\right]$$

La variation de z correspondant au doublet sur la circonférence de rayon r ayant le point I_0 comme centre est :

$$dz_1 = \left[1+ir\sin\alpha\right]\tau^{-\frac{1}{2}}\left[\frac{B\cos\alpha - A\sin\alpha}{r} - i\,(1-\tau_\infty)^{-\frac{1}{\gamma-1}}\,\frac{B\sin\alpha + A\cos\alpha}{r}\right]$$

Au parcours de la circonférence de rayon r du plan de l'hodographe, correspond, dans le plan physique, un accroissement z obtenu en intégrant la précédente relation :

$$z_1 = B\tau_\infty^{-\frac{1}{2}}(1-\tau_\infty)^{-\frac{1}{\gamma-1}}\int_0^{2\pi}\sin^2\alpha\,d\alpha - iA\tau_\infty^{-\frac{1}{2}}\int_0^{2\pi}\sin^2\alpha\,d\alpha$$

$$z_1 = \pi\tau_\infty^{-\frac{1}{2}}\left[B(1-\tau_\infty)^{-\frac{1}{\gamma-1}} - iA\right]$$

La contribution du tourbillon à l'accroissement de z est : $z_2 = 2\pi C\tau_\infty^{-\frac{1}{2}}$

La condition de fermeture du profil impose $z_1 + z_2 = 0$, soit :

$$A = 0 \qquad B(1-\tau_\infty)^{-\frac{1}{\gamma-1}} + 2C = 0$$

– Annexe 2 –

TABLE ABRÉGÉE DES FONCTIONS f_n, g_n ET DE LEURS DÉRIVÉES

n = 1

τ	$F(a,b,c;\tau)$	$F'(a',b',c';\tau')$	$f_n(\tau)$	$g_n(\tau)$	$f_{n\tau}$	$g_{n\tau}$	$\tau^{n/2} g_n(\tau)$
0.	0.10000000E+01	0.10000000E+01	0.	∞	∞	$-\infty$	1.
0.50000000E-01	0.93905270E+00	0.10000000E+01	0.20997857E-00	0.37372111E+01	0.18341207E+01	-0.51140784E+02	0,535665
0.10000000E-00	0.88117109E+00	0.10000000E+01	0.27865077E-00	0.21869998E+01	0.10367462E+01	-0.19439998E+02	0,614570
0.15000000E-00	0.82629474E+00	0.10000000E+01	0.32002258E-00	0.14619099E+01	0.65315216E+00	-0.10892662E+02	0,566195
0.20000000E-00	0.77436186E+00	0.10000000E+01	0.34630515E-00	0.10240001E+01	0.41423722E-00	-0.70400006E+01	0,457947
0.25000000E-00	0.72530922E+00	0.10000000E+01	0.36265460E-00	0.73070904E+00	0.24896947E-00	-0.48713936E+01	0,365354

n = 2

τ	$F(a,b,c;\tau)$	$F(a',b',c';\tau')$	$f_n(\tau)$	$g_n(\tau)$	$f_{n\tau}$	$g_{n\tau}$	$\tau^{n/2} g_n(\tau)$
0.	0.10000000E+01	0.52718509E-01	0.	∞	0.10000000E+01	$-\infty$	0,053603
0.50000000E-01	0.88038[illegible]73E+00	0.74319671E-01	0.44019336E-01	0.12421282E+01	0.76607813E+00	-0.21453016E+02	0,062106
0.10000000E-00	0.77121875E+00	0.10017638E-00	0.77121876E-01	0.69280989E+00	0.56300001E+00	-0.57778186E+01	0,069281
0.15000000E-00	0.67200392E+00	0.12975691E-00	0.10080059E-00	0.48978496E-00	0.38879689E-00	-0.29190919E+01	0,073468
0.20000000E-00	0.58225001E+00	0.16265942E-00	0.11645000E-00	0.37244676E-00	0.24150001E-00	-0.19138727E+01	0,074489
0.25000000E-00	0.50146486E+00	0.19857453E 00	0.12536621E-00	0.29020042E-00	0.11914064E-00	-0.14238023E+01	0,072550

n = 3

τ	$F(a,b,c;\tau)$	$F(a',b',c';\tau')$	$f_n(\tau)$	$g_n(\tau)$	$f_{n\tau}$	$g_{n\tau}$	$\tau^{n/2} g_n(\tau)$
0.	0.10000000E+01	-0.12723318E-02	0.	$-\infty$	0.	∞	– 0,001196
0.50000000E-01	0.82480753E+00	-0.16579370E-02	0.92216284E-02	-0.12392121E-00	0.24014933E-00	0.36269275E+01	– 0,001385
0.10000000E-00	0.67285804E+00	-0.17679142E-02	0.21277640E-01	-0.38664280E-01	0.22998680E-00	0.84768742E+00	–0,001223
0.15000000E-00	0.54214555E+00	-0.87040343E-03	0.31495811E-01	-0.84830088E-02	0.17466498E-00	0.44239375E-00	–0,0004928
0.20000000E-00	0.43073460E-00	0.16050526E-02	0.38526075E-01	0.92418699E-02	0.10576939E-00	0.28240299E-00	+0,0008266
0.25000000E-00	0.33576180E-00	0.76609801E-02	0.42095222E-01	0.20638089E-01	0.37930107E-01	0.17856270E-00	+0,0025798

n = 4

τ	$F(a,b,c;\tau)$	$F(a',b',c';\tau')$	$f_n(\tau)$	$g_n(\tau)$	$f_{n\tau}$	$g_{n\tau}$	$\tau^{n/2} g_n(\tau)$
0.	0.10000000E+01	-0.74642099E-04	0.	$-\infty$	0.	∞	– 0,0001344
0.50000000E-01	0.77245104E+00	-0.21806922E-03	0.19311275E-02	-0.72893199E-01	0.66941776E-01	0.20052630E+01	– 0,000182
0.10000000E-00	0.58600114E+00	-0.48132734E-03	0.58600114E-02	-0.33288120E-01	0.83654052E-01	0.27375161E-00	– 0,000333
0.15000000E-00	0.43526405E-00	-0.10190138E-02	0.97934413E-02	-0.25642702E-01	0.70022183E-01	0.87211266E-01	–0,000577
0.20000000E-00	0.31527162E-00	-0.19297158E-02	0.12610865E-01	-0.22092677E-01	0.41170076E-01	0.65176972E-01	–0,000884
0.25000000E-00	0.22146579E-00	-0.31884128E-02	0.13841610E-01	-0.18638418E-01	0.80691474E-02	0.74643104E-01	–0,0011649

n = 5

τ	$F(a,b,c;\tau)$	$F(a',b',c';\tau')$	$f_n(\tau)$	$g_n(\tau)$	$f_{n\tau}$	$g_{n\tau}$	$\tau^{n/2} g_n(\tau)$
0.	0.10000000E+01	0.17360747E-03	0.	∞	0.	$-\infty$	+ 0,00005031
0.50000000E-01	0.72325833E+00	0.11550036E-03	0.40431371E-03	0.17265968E-00	0.17497663E-01	-0.98298925E+01	+ 0,0000965
0.10000000E-00	0.50978842E+00	0.13040181E-03	0.16120926E-02	0.28518872E-01	0.28557065E-01	-0.61880074E+00	+ 0,0000902
0.15000000E-00	0.34832424E-00	0.20394056E-03	0.30353716E-02	0.13250786E-01	0.26387857E-01	-0.15526822E-00	+ 0,00011547
0.20000000E-00	0.2[illegible]99550E-00	0.29341296E-03	0.40963961E-02	0.75113723E-02	0.14991276E-01	-0.90053285E-01	+ 0,0001344
0.25000000E-00	0.14323704E-00	0.30095556E-03	0.44761570E-02	0.35185755E-02	0.61410472E-04	-0.71308274E-01	+ 0,00010996

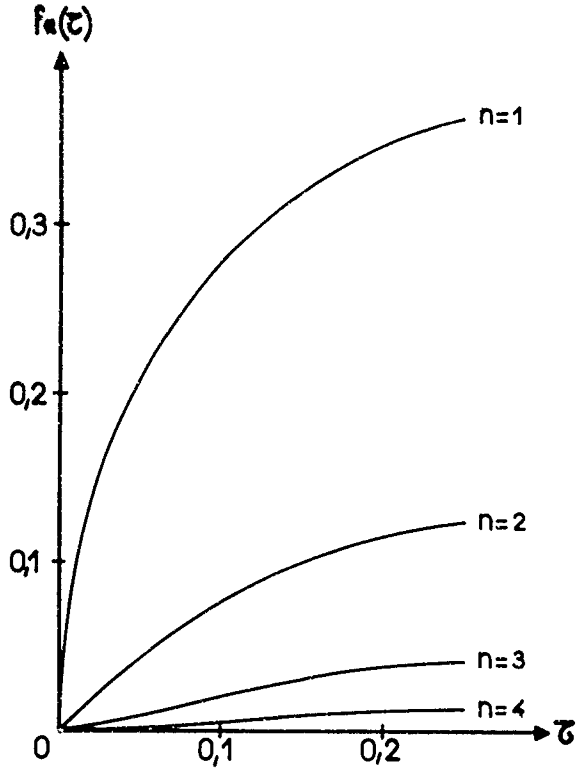
fn(τ)
n=1
0,3
0,2
n=2
0,1
n=3
n=4
0
0,1
0,2
τ

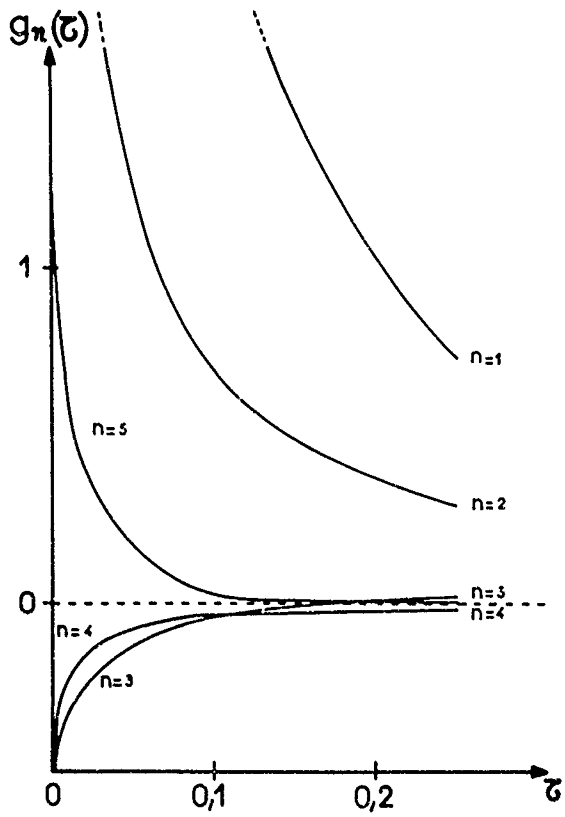
gn(τ)
1
n=1
n=5
n=2
0
n=3
n=4
n=4
n=3
0
0,1
0,2
τ

AN EXPERIMENTAL INVESTIGATION OF UNSTEADY TRANSONIC FLOW BY HIGH-SPEED INTERFEROMETRIC PHOTOGRAPHY

by

G.Meier and W.Hiller

Max-Planck-Institut für Strömungsforschung,
Göttingen, Deutschland

AN EXPERIMENTAL INVESTIGATION OF UNSTEADY TRANSONIC FLOW BY HIGH-SPEED INTERFEROMETRIC PHOTOGRAPHY

G. Meier, W. Hiller
Max-Planck-Institut für Strömungsforschung, Göttingen, Deutschland

Introduction

Some years ago we succeeded in realising a shockfree transonic flow experimentally (Ref.1). This was a plane flow in a curved channel having a supersonic region imbedded into the subsonic flow. The channel boundaries are streamlines of an exact solution of the basic gasdynamic equations. This solution describes the compressible flow around a half plane and has been obtained by a Molenbroek-Tschaplygin transformation (Ref.2).

The experiments showed that the continuous compression of the supersonic flow is relatively stable against pertubations. When the flow speed is decreased continuously the supersonic region will continuously become smaller. In this velocity regime the supersonic flow is also stable against pertubations of the channel boundaries (Ref.1). If on the other hand the design velocity of the channel is exceeded shocks will be generated at the downstream end of the supersonic region. The flow will then in general become unsteady.

Instrumentation

Some of the streamlines of the exact solution are shown in Fig. 1. The chosen boundary streamlines are emphasized. The supersonic region fills one quarter of the smallest channel cross section. The largest velocity is taken on at the vertex of the convex boundary ($M = 1.25$), Fig. 2 shows a schematic drawing of the channel.

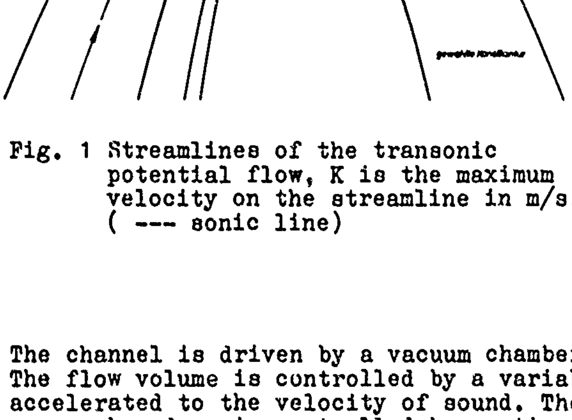

Fig. 1 Streamlines of the transonic potential flow, K is the maximum velocity on the streamline in m/s. (--- sonic line)

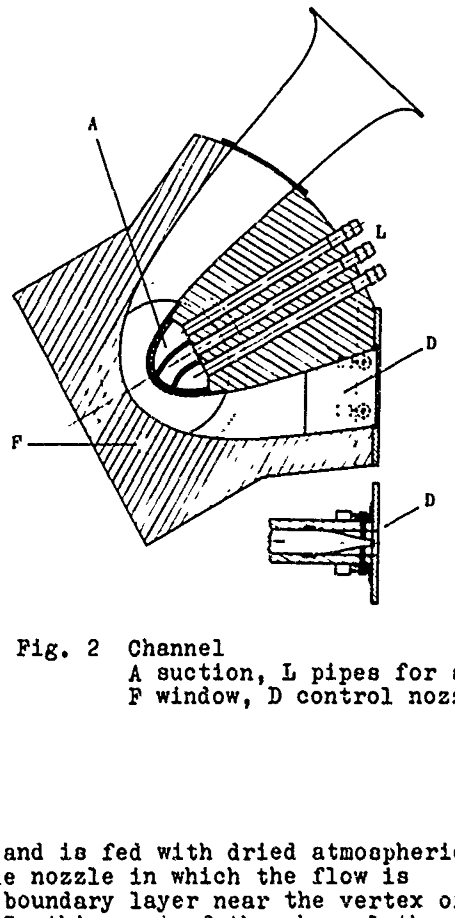

Fig. 2 Channel
A suction, L pipes for suction
F window, D control nozzle.

The channel is driven by a vacuum chamber and is fed with dried atmospheric air. The flow volume is controlled by a variable nozzle in which the flow is accelerated to the velocity of sound. The boundary layer near the vertex of the convex boundary is controlled by suction. In this part of the channel the wall consists of polished sintered sheet metal. The open area ratio is o.o5 approximately. Typical values for the suction velocity are 1-3 m/sec.

The flow field is observed with a Mach-Zehnder interferometer, Fig. 3. The side-walls of the channel in the area of interest are windows of a high optical quality. At the beginning of every experiment the interferometer is adjusted to infinite width of the interference fringes. Thus the interference fringes will be lines of constant density in the photographs to be shown. As long as no entropy changes occur all the variables of state will be constant on the interference fringes. It may be interesting in this connection that the lines of constant variables of state in the case of the exact solution are circles.

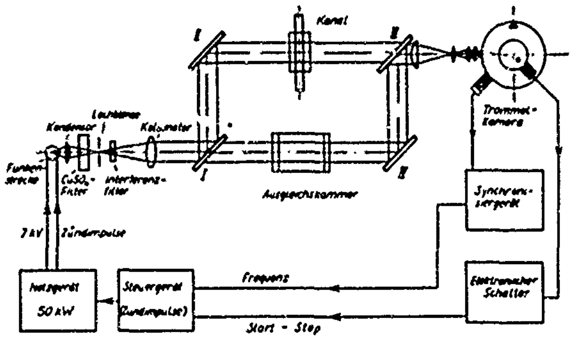

Fig. 3 Equipment for high speed interferometry
I-IV Mirrors of Mach-Zehnder interferometer.
Drum camera
Electronic equipment
Flash light source

The unsteady flow is registered by high frequency cinematography. As a rule the frame frequency will be 1o kHz. Exposure time for a single frame is $1o^{-6}$ sec.

Results

The comparison between an interference mapping obtained from the exact solution and a photograph of the flow field under optimal conditions shows the degree of agreement between the theoretical flow field and its experimental realisation, Fig. 4a, 4b. If starting from this steady shockfree flow the velocity is increased weak shocks will be generated at the end of the supersonic region, Fig. 5. As may be seen from the photographs these shocks are unstable with respect to location and strength.

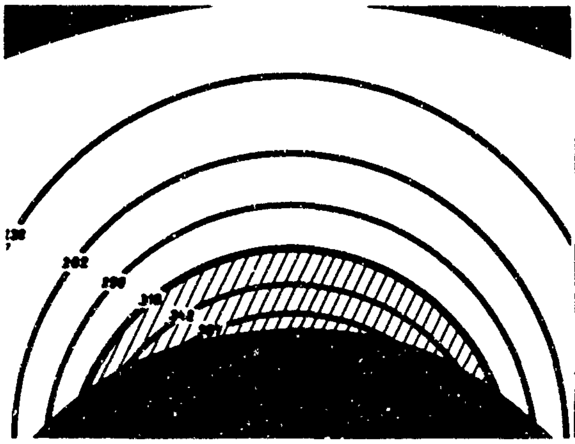

Fig. 4a Calculated interference fringes Numbers indicate velocity in m/s (T = 20°C).

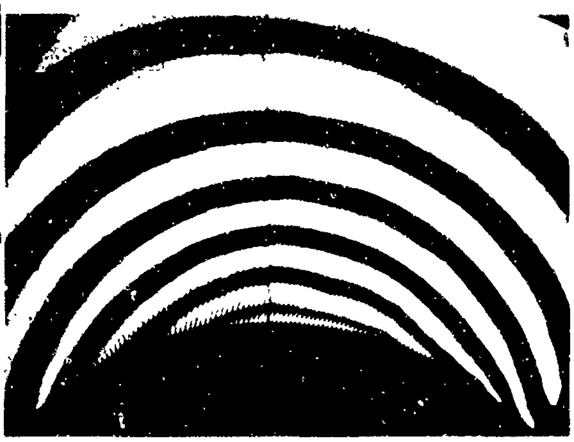

Fig. 4b Shockfree transonic flow. Velocity in the vertex of boundary M = 1.25
Flow direction from left to right

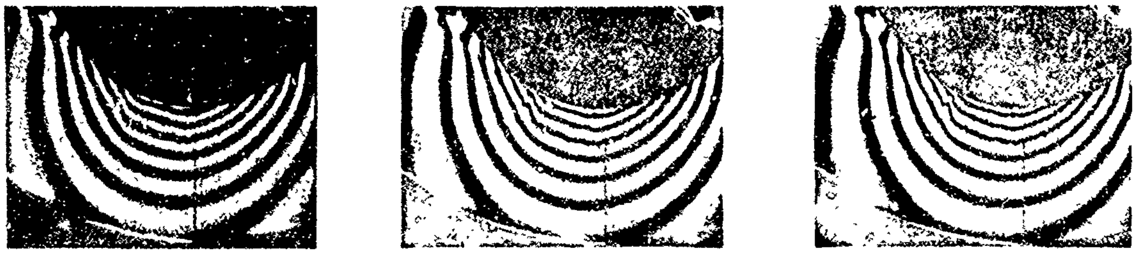

Fig. 5 Weak unsteady shocks at the ond of the supersonic region.
Flow direction from right to left.
Interframetime t = o.4 ms

Further increase of the Mach number leads to stronger shocks, Fig. 6. The pressure jump at the foot of the shock will become so large as to cause the boundary layer to separate. The rapidly growing dead water bubble behind the shock will cause the pressure behind the shock to rise and the shock to move upstream. The point of separation of the boundary layer will move upstream together with the shock. The shock strength will decrease during this phase and the shock will reach areas with small pressure gradients. The flow will therefore become attached to the wall again. The dead water bubble floats downstream. The velocity of the flow field now has a minimum. Thus the shock will be dissolved completely. In the following acceleration phase the supersonic region will grow again. As soon as a certain Mach number at the end of the supersonic region is exceeded a new shock will form.- The whole circle as described will repeat in this example with a frequency of 18o Hz.

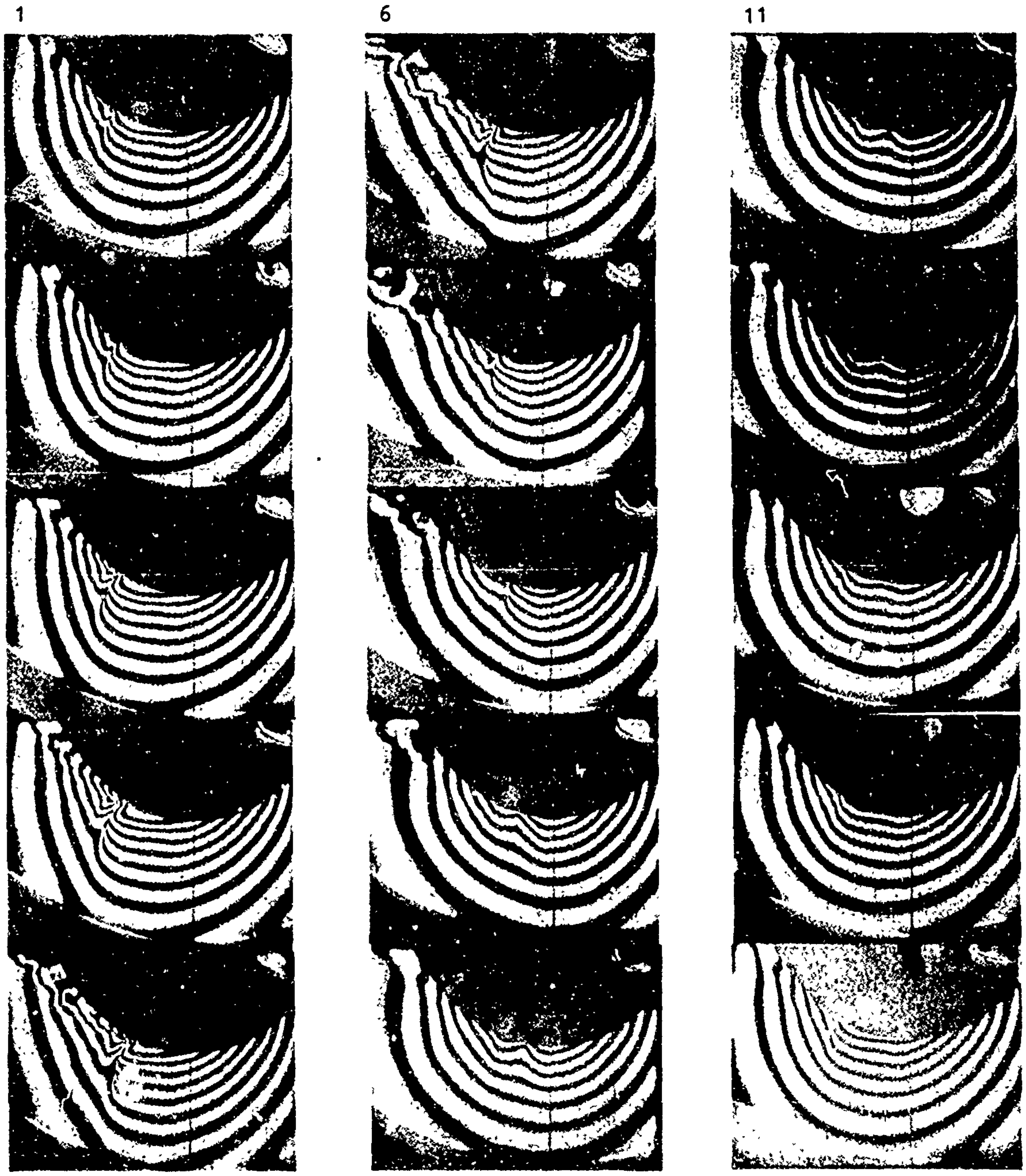

Fig. 6 Full cycle of an oscillation of unsteady transonic flow.
Mach number at the vertex of boundary M_{max} = 1.4 ; M_{min} = 1.2
Flow direction from right to left
Interframetime t = o.4 ms

At greatly reduced suction the boundary layer will be induced to separate even by very weak shocks, Fig. 7. The vibration cycle will be qualitatively the same as in the previous example. However the shock at the end of the supersonic region will be dissolved into a system of compression and rarefaction waves and will move on the separated boundary layer. The frequency is 21o Hz in this case.

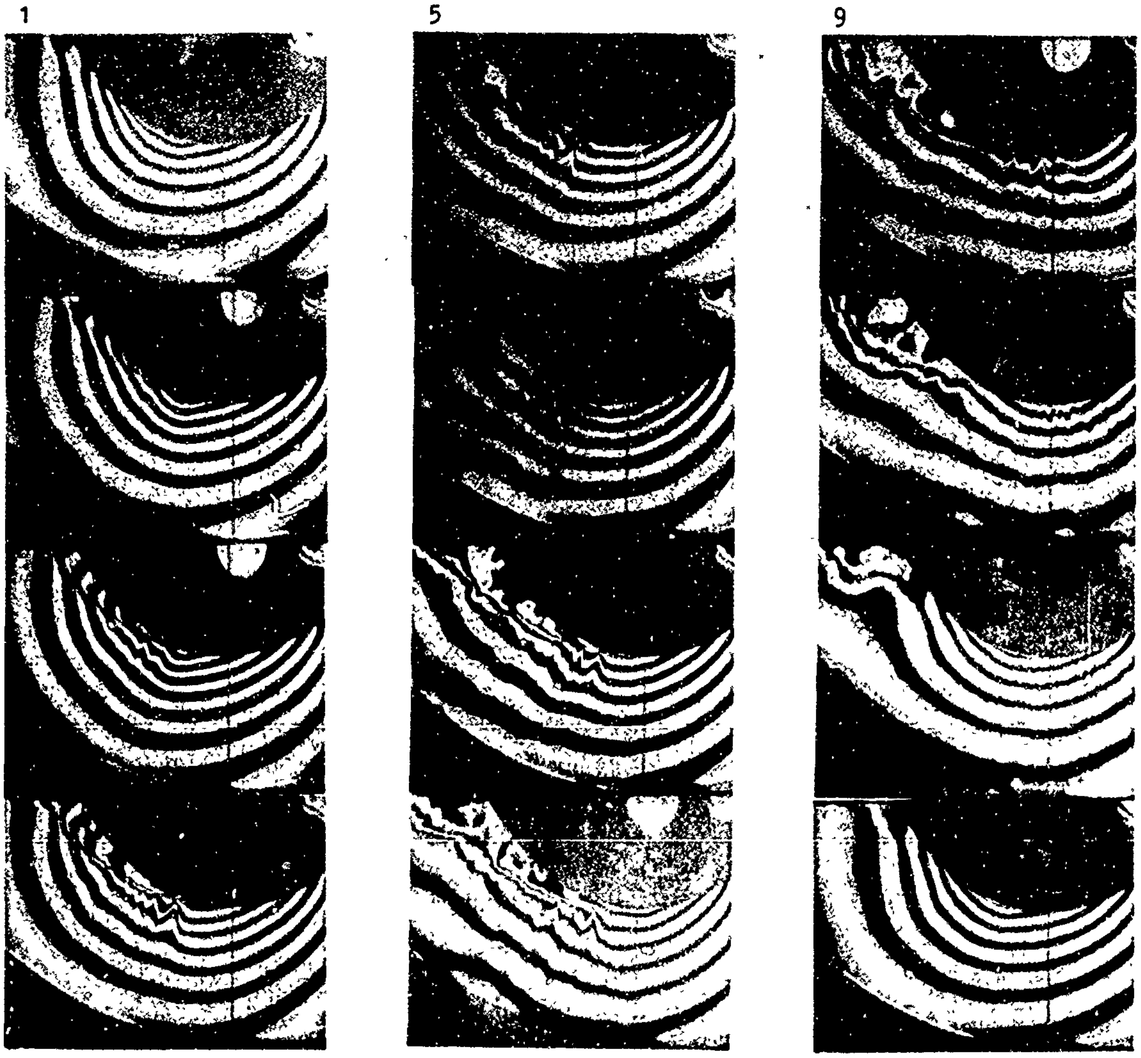

Fig. 7 Full cycle of an oscillation of unsteady flow with reduced suction. Flow direction from right to left. Interframetime t = o.4 ms.

We have studied the influence of the channel geometry, the boundary layer suction and the flow volume on the frequency of the shock vibrations. One result is that a decrease in the distance between supersonic region and flow control nozzle, decrease of suction and increase of flow volume cause the frequency to rise. The measured dependence is shown in Fig. 8. The frequency is plotted versus the

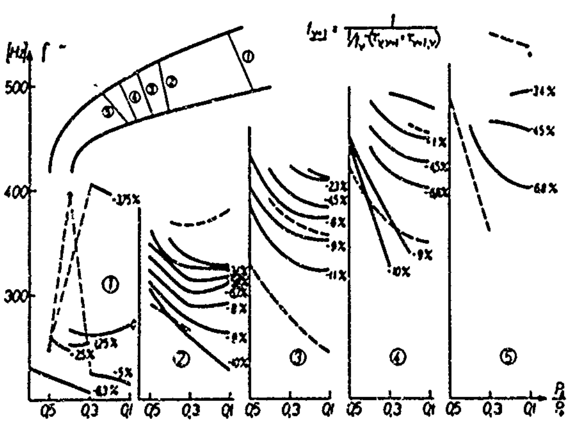

Fig. 8 Frequency of flow oscillations plotted versus suction pressure
Parameters: Length of the duct between vertex of boundary and diffusor ①-⑤, relative change of flow volume in percent.
--- transformed frequency ranges
In 1 excitation of harmonic oscillations

suction pressure p_a/p_o for five different locations of the diffusor, curve parameter is the relative change of flow volume in percent. Vibrations have been observed only for those values of the parameters covered by the curves. The vibration regimes for the five different locations on the flow control nozzle may be brought to coincidence by the transformation given in Fig. 8(dashed curve) This transformation results from the depende..ce of the eigenfrequencies of a resonator carrying flow on the length of the resonator. The part of the channel between the supersonic region and the flow control nozzle obviously acts as such a resonator, determining the vibration regime to a great degree. Even the excitation of higher harmonics has been observed for a very large length of the resonator.

The essential element of instability and vibration generation is however the separation of the boundary layer coupled to the shock. To support this argument the wave propagation in the channel has been investigated. To this end the time dependence of the density has been inferred from the interferogram for approximately fifty scanning points. An example for such a time sequence is given in Fig. 9.

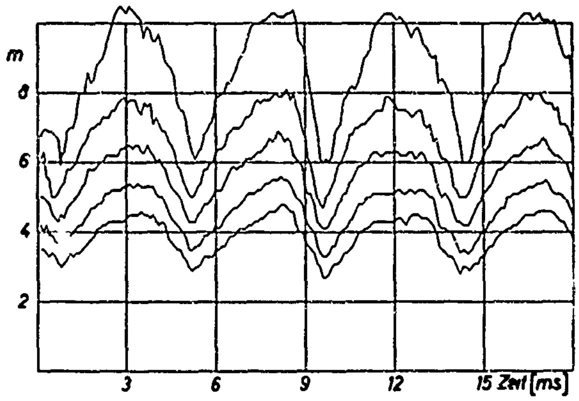

Fig. 9 Density in four scanning points plotted versus time. Density is measured here by the order m of interference fringes

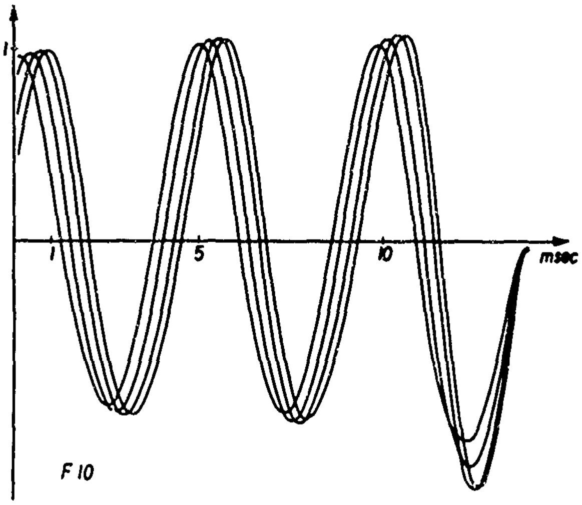

Fig. 1o Example for cross correlations between density time sequencies. Phase shift is indicated by the displacement of the curves

By cross correlating these time sequencies phase relationship for the density waves in the flow may be obtained, Fig. 1o, leading to a so called phase plan. Here the lines of constant vibration phase or wave planes are plotted. Fig. 11 shows the phase plan corresponding to the unsteady flow shown in Fig. 7. This indicates that the wave centre is in that part of the flow, where the boundary layer is induced to separate by the shock.

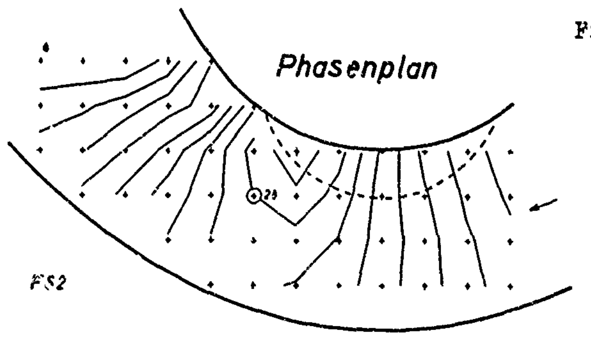

Fig. 11 Phase plan
Wave fronts or lines of constant phase for the flow shown in Fig. 7.
All cross correlations refer to the time sequency of point 28

Special effects
At greatly reduced suction the boundary layer remains separated permanently, Fig. 12. The shocks at the end of the supersonic region then move on the separated boundary layer, which reflects the shocks as rarefaction fans. In this rarefaction fan the flow again expands to supersonic speeds. This supersonic region in turn collapses into another shock. Thus a sequence of shocks is generated, the first of which influences the point of separation of the boundary layer and causes the flow to become unsteady.

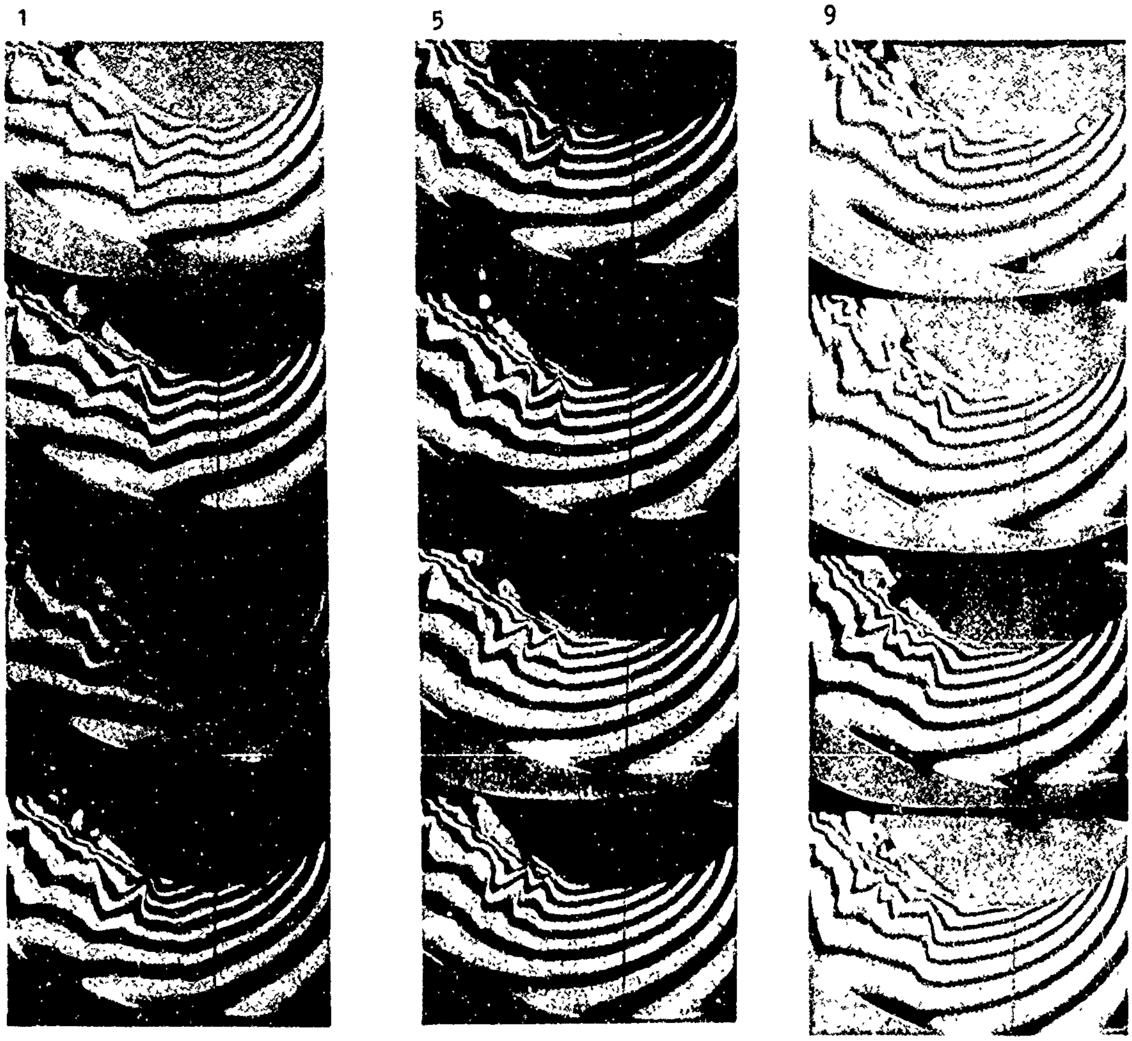

Fig. 12 Unsteady behaviour of the flow when boundary layer is separated permanently.
Suction is reduced considerably. Flow direction from right to left.
Interframetime t = o.1 ms

At very large flow volumes strong λ-shocks may be observed, which penetrate deeply into the subsonic region while moving against the flow. As soon as the foot of the shock comes to rest the shock is split into two. The unsteady part moving further on against the flow leaves behind it a nearly steady normal shock, Fig. 13 This may be explained as a strong reflection becoming especially apparent in the next example.

To investigate the behaviour of the unsteady shock, we generated a shock by a wire explosion in the downstream part of the channel, which moves into a steady transonic flow, Fig. 14. The behaviour of the shock may be described to great extent by geometric acoustic model given down below. In contrast to this model the reflection at the convex boundary is given initially in the form of a normal shock. This strong reflection does not last however. The part of the shock moving forward and becoming weaker is now subject to weak reflection and separates from the strongly reflected part.

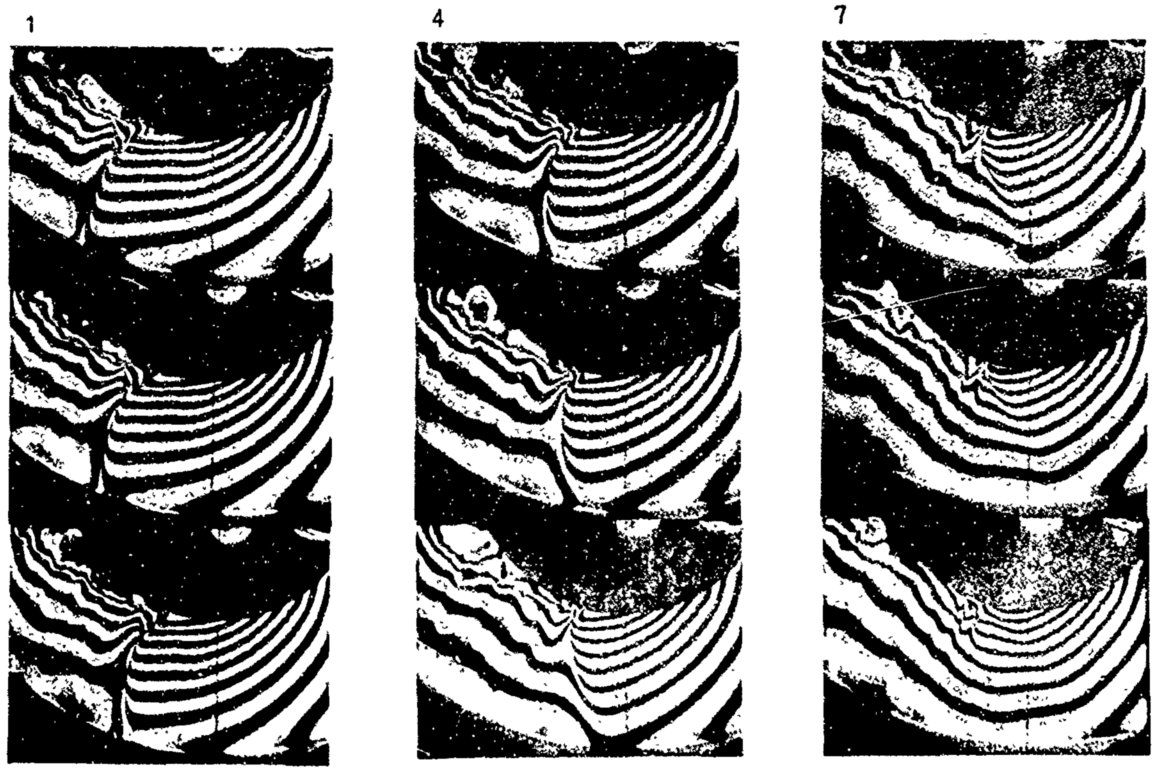

Fig. 13 Splitting of a shock wave
Mach number in the vertex of the boundary M_{max} = 1.5
Flow direction from right to left
Interframetime t = o.1 ms

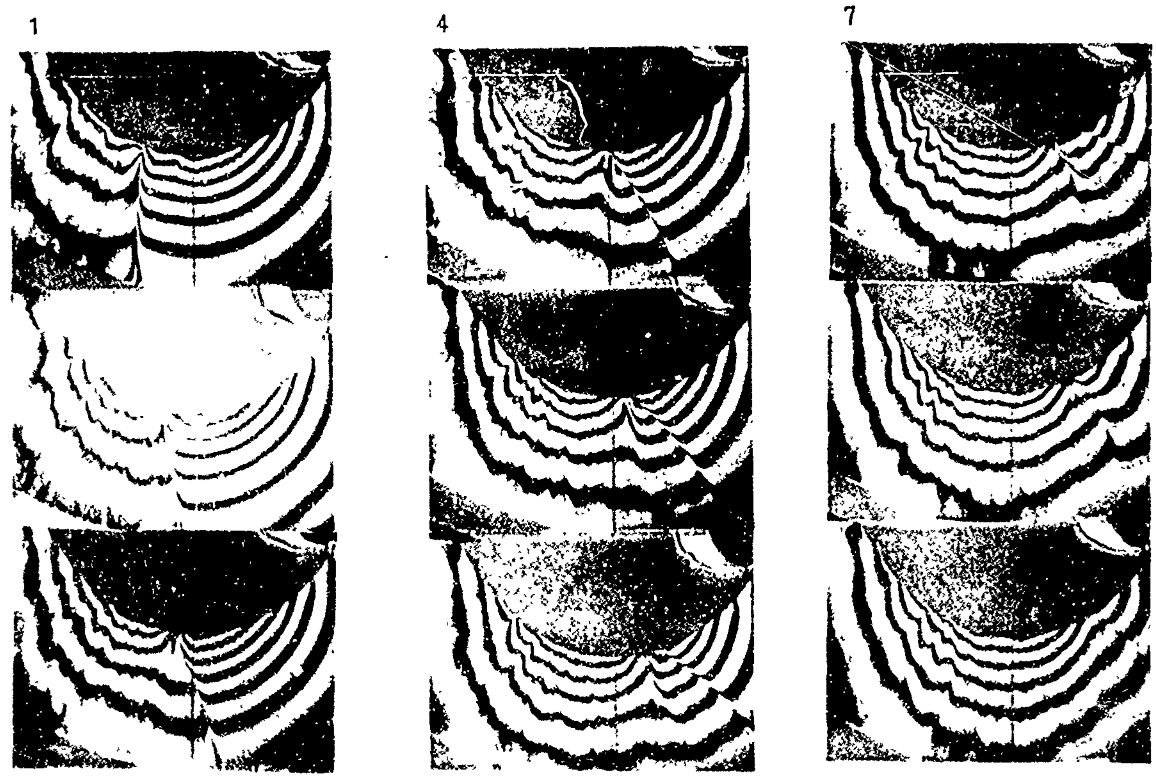

Fig. 14 A shock wave enters a steady transonic flow.
The shock is produced by an exploding wire.
Flow direction from right to left
Interframetime t = o.1 ms

For another sequence of photographs the different locations of the shock have been superimposed into one single figure, Fig. 15.

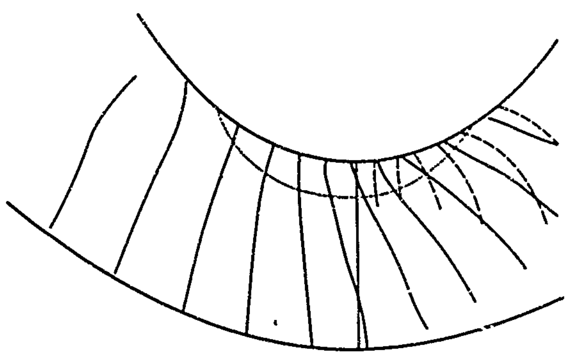

Fig. 15 Positions of a shock wave at different times(t = o.1 ms)
Flow direction from right to left.
Motion of the shock from left to right.
... sonic line
--- reflected shock

It is noted that the reflected part of the shock takes on the same position at a later time as the forerunning part. The fact that two parts of the shock separate may be explained by a difference of their respective components of speed of propagation in the direction of the flow and by the decrease of flow speed along their paths.

Apart from the splitting process however the propagation of the shocks is in accordance with a geometric acoustic model. Fig. 16 shows the calculated propagation of a pertubation situated initially at the vertex of the known flow field.

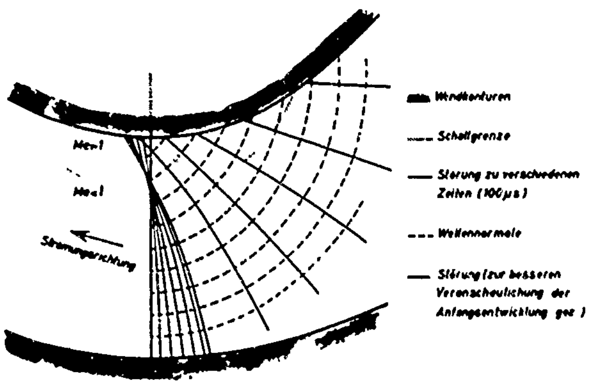

Fig. 16 Calculated motion of a shock.
Geometric acoustic model.
Initial position of the shock is the vertex of the duct.

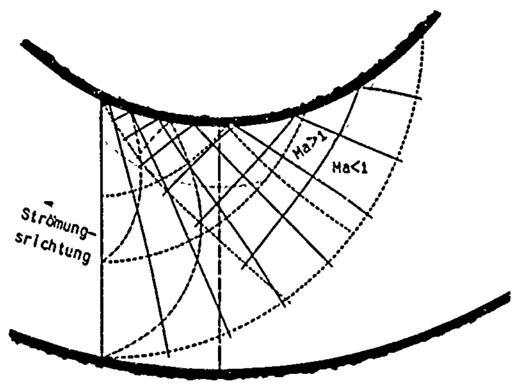

Fig. 17 Calculated motion of a shock
Geometric acoustic model
—— shock and reflected shock
--- direction of phase velocity
-.- direction of group velocity
... sonic line
-..- vertex line

It is seen that the pertubation initially moves downstream in the supersonic region, until it takes on the Mach angle and may propagate into the supersonic region. It must not be concluded however that energy may be transported upstream in the supersonic region. Fig. 17 shows for a different initial position of the pertubation in addition to the orthogonal trajectories giving the direction of propagation of the wave two dot-dash lines, the direction of group velocity. This makes clear that energy propagation has a strong component in the direction of the shock. This at the same time explains the rapid decrease in the strength of the shock during the propagation, Fig. 14, and the initial increase of the strength of the initial shock.

Summary

The formation of unsteady motion in transonic channel flow is studied experimentally. The starting point is a steady shockfree transonic flow corresponding to an exact solution of the gasdynamic equations.

Changes in flow parameters generate shock waves causing a more or less unsteady behaviour of the whole flow field. The essential element of instability is the separation of boundary layer coupled with the shock formation.

The flow is recorded cinematographically by high speed interferometry. The frame rate is 1o kc/s. Characteristic modes of flow oscillation are shown in a motion picture.

The evaluation of the recordings by statistical-numerical methods gives the frequency of oscillation, the propagation of density waves and the origin of the waves. An interesting result of a direct visual evaluation of certain pictures is the splitting of the shock waves under special flow conditions. The propagation of weak unsteady shocks is in accordance with a geometric acoustic model.

References

1. E. Koppe G. Meier	Erfahrungen mit optischen Methoden bei der Untersuchung transsonischer Strömungen. Zeitschrift für Flugwissenschaften, 13(1965) Heft 5, S.149 - 157
2. F. Ringleb	Exakte Lösungen der Differentialgleichungen einer adiabatischen Gasströmung. Zeitschrift für angewandte Mathematik und Mechanik,2o(194o) S.185 - 198

THEORY OF VISCOUS TRANSONIC FLOW - A SURVEY

by

Martin Sichel

The University of Michigan, US

THEORY OF VISCOUS TRANSONIC FLOW—A SURVEY

Martin Sichel*
The University of Michigan

INTRODUCTION

Use of the inviscid transonic equation coupled with the treatment of shock waves as Rankine-Hugoniot discontinuities sometimes leads to paradoxical results or solutions which disagree with experiment. These difficulties usually arise when large velocity gradients, discontinuities in streamline curvature, or highly curved shock waves occur, so that viscous effects cannot be ignored. Such viscous-transonic problems have received increasing attention in recent years, and form the subject of this survey. After briefly discussing some difficulties of the inviscid theory, the development of the viscous transonic equation is given followed by a discussion of applications.

Starting with the early work of G. I. Taylor (1930) studies of the transonic flow near the throat of a converging-diverging nozzle (Görtler 1939, Emmons 1946, Tomotika and Tamada 1950, Ryzhov 1963) indicated that the inviscid theory cannot explain the smooth transition from symmetrical or Taylor type flow with subsonic velocities both upstream and downstream of the throat to the fully developed subsonic-supersonic or Meyer type of flow. Another difficulty of old standing arises when a weak shock wave is adjacent to a curved surface. Then Emmons (1946) has shown that the Rankine-Hugoniot conditions may lead to infinite streamline curvature where the shock touches the surface. Emmons tried to remedy this problem by introducing a sudden inviscid expansion immediately behind the shock, but gradients of velocity and temperature within this expansion are of the same order as in the shock layer itself. Hence, Emmons has suggested that a viscous theory may be required to properly deal with this portion of the flow. Of course this problem is in some sense an academic one for a boundary layer must always be interposed between the shock wave and the wall and would be expected to influence the flow. However experiments (Sinnott 1960, Pearcey 1964, Holder 1964) do indicate that the pressure rise across the shock terminating a pocket of supersonic flow at the surface of a transonic airfoil may be appreciably less than the Rankine-Hugoniot value. It seems reasonable that the difficulties observed by Emmons (1946) and these experimental results are related to each other.

In the analysis of the Mach reflection of weak shock waves use of the Rankine-Hugoniot conditions at the triple point leads to results in serious disagreement with experiment. To deal with this problem Sternberg (1959) introduced a region of non-Hugoniot flow in the neighborhood of the triple point which permits an adjustment of the shock structure from that of the incident and reflected shocks to that of the Mach stem. A global analysis of this viscous region in which the shock structure is no longer one dimensional results in reasonable agreement with experiments.

Limit lines, where the velocity gradient becomes infinite also occur near the sonic circle or sphere when the inviscid equations are solved for the classical problem of compressible source and source-vortex flow (Taylor 1930, Von Mises 1958), and the neglect of viscosity in such regions is clearly inconsistent.

A viscous-transonic theory to deal with such problems has been gradually developed over the past two decades and forms the subject of this survey. The theory is in effect an extension to two dimensions of Taylor's early (1910) analysis of the structure of weak shock waves. In this survey no attempt is made to study viscous phenomena within the boundary layer, rather attention is limited to the theoretical description of viscous effects in the external flow.

THE VISCOUS TRANSONIC EQUATION

In view of the above discussion it is apparent that there are numerous transonic flow problems in which viscous effects must be considered. Szaniawski (1962) has given simple qualitative arguments showing the importance of viscosity in transonic flow. In transonic small disturbance flow it can be shown (Guderley, 1962) that the perturbation potential ϕ' satisfies the approximate equation

$$-(\gamma + 1)\,\phi_x{}'\,\phi_{xx}{}' + \phi_{yy}{}' = \Phi \tag{1}$$

*Professor of Aerospace Engineering.

where Φ represents the dissipative terms. Now $-(\gamma+1)\,\phi_x'\,\phi_{xx}' \approx (1-M^2)\,\phi_{xx}'$ and when the terms $(1-M^2)\,\phi_{xx}'$, ϕ_{yy}', and Φ in Eq. (1) are compared, it is usually found that Φ is negligible compared to the other terms. However, as $M \to 1$, $(1-M^2)\,\phi_{xx}'$ vanishes but Φ need not vanish, so domains $\mathcal{D}$ must exist in which $(1-M^2)\,\phi_{xx}' \sim O(\Phi)$, and where the dissipative terms Φ cannot be neglected. The interior of a shock wave is an important example of such a domain. If the domains $\mathcal{D}$ are small compared to the region of interest, so that they can be regarded as surfaces of discontinuity, then the neglect of Φ may be legitimate. The thickness, η, of weak shock waves (Lighthill 1956) is of order $\bar{\mu}''/\rho^* a^* (M_1^* - 1)$ and so can be quite large as the upstream Mach number $M_1^* \to 1.0$. Hence, the region $\mathcal{D}$ in which convective and dissipative effects are comparable may be very large. Even when $\mathcal{D}$ is very small amplification may cause the viscous phenomena within $\mathcal{D}$ to exert an important influence on the overall flow. Thus, viscous effects in $\mathcal{D}$ may through their influence on jump conditions determine the position of the shock terminating a region of supersonic flow.

A viscous-transonic (V-T) equation was first derived by Liepmann, Ashkenas, and Cole (1948), and was later rederived independently by Ryzhov and Shefter (1964), Sichel (1962, 1963), and Szaniawski (1962, 1963). In the derivation presented here steady flow of a perfect gas with constant specific heats, viscosities, and thermal conductivity will be considered. Variation of the thermodynamic properties is taken into account by Sichel (1963), Szaniawski (1962) and Ryzhov and Shefter (1964), but there is no material change in the results. The critical or sonic values of the flow parameters will be used as reference quantities, and it will be assumed that the undisturbed flow is in the x or axial direction.

From the method of characteristics (Guderley 1962) for inviscid flow or from the transonic Hugoniot conditions across shocks it follows that perturbations in the dimensionless quantities $\bar{p}/\rho^* a^{*2}$, $\bar{a}/a^*$, $\bar{T}/T^*$, and $\bar{\rho}/\rho^*$ will be of the same order as the deviation of the dimensionless x or axial velocity component $\bar{u}/a^*$ from the reference value of unity. If $[(\bar{u}/u^*) - 1] \sim O(\epsilon)$; where $\epsilon \ll 1$, these flow parameters can be expanded as

$$\left.\begin{aligned} u &= (\bar{u}/a^*) = 1 + \epsilon u^{(1)} + \epsilon^2 u^{(2)} + \dots \quad ; \quad \rho = \bar{\rho}/\rho^* = 1 + \epsilon \rho^{(1)} + \dots \\ p &= \bar{p}/\rho^* a^{*2} = (1/\gamma) + \epsilon p^{(1)} + \dots \quad ; \quad T = \bar{T}/T^* = 1 + \epsilon T^{(1)} + \dots \\ a &= \bar{a}/a^* = 1 + \epsilon a^{(1)} + \dots \end{aligned}\right\} \tag{2}$$

Barred quantities are dimensional and reference quantities are indicated by an asterisk. The transverse velocity, $v = \bar{v}/a^*$, is expanded as

$$v = \bar{v}/a^* = \Delta(\epsilon v^{(1)} + \epsilon^2 v^{(2)} + \dots) \tag{3}$$

If the disturbance is caused by a slender body then it follows from the characteristic or oblique shock relations that $\Delta \sim O(\epsilon^{1/2})$. In a normal shock, on the other hand, v and hence Δ are equal to zero. From the method of characteristics or the oblique shock relations it can be shown (Sichel 1963, Guderley 1962) that if L is the characteristic length of the problem, then

$$x = \bar{x}/L \quad ; \quad y = \bar{y}\,\Delta/L \tag{4}$$

are the appropriate dimensionless coordinates.

Introducing these expansions and coordinates in the Navier-Stokes equations and keeping only the largest terms yields the partial differential equations

$$\rho_x^{(1)} + u_x^{(1)} = 0 \qquad \text{continuity} \tag{5}$$

$$u_x^{(1)} + p_x^{(1)} = 0 \qquad \text{x or axial momentum} \tag{6}$$

$$v_x^{(1)} + p_y^{(1)} = 0 \qquad \text{y or transverse momentum} \tag{7}$$

$$T_x^{(1)} - (\gamma - 1)\, p_x^{(1)} = 0 \qquad \text{energy} \tag{8}$$

$$\gamma p^{(1)} = \rho^{(1)} + T^{(1)} \qquad \text{perfect gas} \tag{9}$$

Assuming uniform upstream entropy, Eq. (5), (6) and (8) can be integrated to yield the equations

$$\rho^{(1)} + u^{(1)} = 0 \quad ; \quad u^{(1)} + p^{(1)} = 0 \quad ; \quad T^{(1)} - (\gamma - 1)\, p^{(1)} = 0 \tag{10}$$

which are identical to the relations between $\rho^{(1)}$, $u^{(1)}$, $p^{(1)}$, and $T^{(1)}$ in a leftward propagating acoustic wave. Using Eq. (10) the y momentum Eq. (7) reduces to the irrotationality condition

$$u_x^{(1)} - v_y^{(1)} = 0 \tag{11}$$

Since entropy changes are of higher-order in transonic flows and stagnation enthalpy is assumed constant this result could also have been derived from the Crocco relation.

Equations (5)-(9) are five equations for the five unknowns $\rho^{(1)}$, $u^{(1)}$, $v^{(1)}$, $T^{(1)}$, and $p^{(1)}$; however, since from Eq. (5) and (6) it follows that $\rho^{(1)} = p^{(1)}$ the equations of state and energy are identical so that the set of Eq. (5)-(9) is redundant. The second order equations are redundant in $\rho^{(2)}$, $u^{(2)}$, $v^{(2)}$, and $p^{(2)}$ and upon eliminating the second order expansion coefficients the following equation relating $u^{(1)}$ and $v^{(1)}$ is obtained (Sichel 1963, Ryzhov 1965)

$$\frac{1}{Re\,\epsilon}\left(1 + \frac{\gamma - 1}{Pr''}\right) u_{xx}^{(1)} - (\gamma + 1)\, u^{(1)} u_x^{(1)} + \frac{\Delta^2}{\epsilon}\left(v_y^{(1)} + \frac{k - 1}{y} v^{(1)}\right) = 0 \tag{12}$$

Together with the irrotationality condition (11) this system is sometimes called the viscous-transonic or V-T equation. Re is the Reynolds number $\rho^* a^* L/\bar{\mu}''$, Pr'' is the Prandtl number, $\bar{\mu}'' = (4/3)\,\bar{\mu} + \bar{\mu}'$ is what Hayes (1958) calls the longitudinal viscosity. $\bar{\mu}'$ is the bulk viscosity. The integer k equals two in axisymmetric flow and unity for two dimensional flow. From the method of derivation V-T flow might be considered as an acoustic wave with structure determined by higher order viscous effects.

From the definition of the shock thickness η it follows that $(\epsilon\ Re)^{-1} \sim O(\eta/L)$ so that the viscous term in Eq. (12) will be of O(1) whenever L and η are of the same order. In two dimensional transonic flow it is, as discussed above, appropriate to let $\Delta = \epsilon^{1/2}$, and then all three terms of Eq. (12) will be of equal importance. In one dimensional flow $\Delta = 0$, and then the ordinary differential equation which is left has as one of its solutions

$$u^{(1)} = -\tanh \frac{(\gamma + 1)\,(\epsilon\ Re)}{2\left(1 + \frac{\gamma - 1}{Pr''}\right)}\, x \tag{13}$$

which is identical to Taylor's (1910) solution for the structure of a weak shock.

When (η/L) or $(\epsilon\ Re)^{-1} \ll 1$ a singular perturbation problem arises with respect to Eq. (12). With $\Delta^2 = \epsilon$ the flow should satisfy the inviscid transonic equation

$$-(\gamma + 1)\, u^{(1)} u_x^{(1)} + v_y^{(1)} + [(k - 1)/y]\, v^{(1)} = 0 \tag{14}$$

except for thin viscous regions with a thickness of order η. The singular perturbation nature of the V-T equation may account for some of the difficulties of inviscid transonic theory. A key question which should be posed in all cases is whether solutions of the V-T equation approach the inviscid solution as $(\eta/L) \to 0$.

The coefficient of the viscous term in Eq. (12) can also be written as

$$\delta/a^* L\epsilon = (Re_\delta\ \epsilon)^{-1}$$

where

$$\delta = \frac{\bar{\mu}''}{\rho^*} + \frac{(\gamma - 1)\kappa}{\rho^*\, C_p}$$

is a quantity which Lighthill (1956) calls the "Diffusivity of sound", and is the combination of transport properties governing the attenuation of sound waves. Re_δ is a Reynolds number based on δ, and appears more appropriate than that based on just $\bar{\mu}''$. With $\Delta^2 = \epsilon$ the transformation

$$X = \frac{1}{2}(\gamma + 1)\,\epsilon\, Re_\delta\, x \quad ; \quad u^{(1)} = \frac{1}{2} U$$

$$Y = \left[\frac{1}{2}(\gamma + 1)\right]^{3/2} \epsilon\, Re_\delta\, y \quad ; \quad v^{(1)} = \frac{1}{2}\left(\frac{\gamma + 1}{2}\right)^{1/2} V$$

reduces Eq. (11) and (12) to the normalized form

$$U_{XX} - UU_X + V_Y + [(k-1)/Y]\, V = 0 \tag{15}$$

$$U_Y = V_X$$

in which the properties of the gas do not appear. Equation (15) together with appropriate boundary conditions expresses a viscous-transonic similitude (Sichel 1966) closely related to that of inviscid flow (Guderley 1962). In terms of the potential defined by $U = \phi_X$, $V = \phi_Y$, Eq. (15) can be replaced by the V-T potential equation

$$\phi_{XXX} - \phi_X\phi_{XX} + \phi_{YY} + [(k-1)/Y]\, \phi_Y = 0 \tag{16}$$

Keeping only the largest terms in the energy equation the dimensionless entropy $S = \bar{S}/C_p$, with $\Delta^2 = \varepsilon$, satisfies the equation

$$Pr''\, \epsilon\, S_x = \epsilon^3\, (\eta/L)\, T_{xx}^{(1)} \tag{17}$$

If $(\eta/L) \sim O(1)$, Eq. (17) implies that

$$S = \epsilon^2 S^{(2)} + \epsilon^3 S^{(3)} + \dots$$

is the appropriate expansion for S. Equation (17) is an entropy transport equation which yields the result, $S_1^{(2)} = S_2^{(2)}$, when integrated across a weak shock. Subscripts 1 and 2 refer to upstream and downstream conditions. From the equation for $S^{(3)}$

$$\frac{\partial S^{(3)}}{\partial x} = \frac{1}{Pr''}\frac{\eta}{L}\left(\frac{\partial^2 T^{(2)}}{\partial x^2} + \frac{\partial^2 T^{(1)}}{\partial y^2}\right) + \frac{\eta}{L}(\gamma - 1)\left(1 + \frac{\gamma - 1}{Pr''}\right)\left(\frac{\partial u^{(1)}}{\partial x}\right)^2 \tag{18}$$

it follows that entropy production is of third order since $(\partial u^{(1)}/\partial x)^2$ is always positive. These results regarding entropy are in agreement with weak shock theory, as they should be.

Perturbing with respect to a free stream velocity $\bar{u}_\infty/a^*$ other than sonic the V-T equation becomes

$$(\epsilon\, Re_\delta)^{-1}\, \tilde{u}_{xx}^{(1)} - (\gamma + 1)(B + \tilde{u}^{(1)})\, \tilde{u}_x^{(1)} + \frac{\Delta^2}{\epsilon}\left(v_y^{(1)} + \frac{k-1}{y} v^{(1)}\right) = 0 \tag{19}$$

while the normalized potential equation becomes

$$\tilde{\phi}_{XXX} - 2(B + \tilde{\phi}_X)\, \tilde{\phi}_{XX} + \tilde{\phi}_{YY} + [(k-1)/Y]\, \tilde{\phi}_Y = 0 \tag{20}$$

In these equations $B = \epsilon^{-1}[(\bar{u}_\infty/a^*) - 1]$, and $u^{(1)} = B + \tilde{u}^{(1)} = B + \tilde{\phi}_X$. When $u^{(1)} \ll B$ these equations may be linearized and the linearized potential equation

$$\tilde{\phi}_{XXX} - 2B\, \tilde{\phi}_{XX} + \tilde{\phi}_{YY} + [(k-1)/Y]\, \tilde{\phi}_Y = 0 \tag{21}$$

which may also be derived by direct linearization of the Navier-Stokes equations, has been studied by Rae (1960) in an investigation of viscous acoustics. From Rae's work it is clear the V-T flow is closely related to the longitudinal viscous waves discussed by Lagerstrom (1964).

For both supersonic ($\phi_X > 0$) and subsonic ($\phi_X < 0$) flow the V-T potential equation (16) is parabolic with the three fold characteristic, Y = const. This property is in distinct contrast to the inviscid transonic equation (14) which changes from an elliptic to a hyperbolic equation as the velocity passes from sub to supersonic values. The V-T equation is, thus, in some ways simpler to deal with than the inviscid equation. A limited uniqueness theorem for the two dimensional case gives some indication of properly posed boundary conditions. Given a rectangular domain $\mathscr{R}$ $(X_1 < X < X_2,\ Y_1 < Y < Y_2)$, it can be shown (Sichel 1963) that if ϕ_X is specified on $X = X_1$, and if ϕ is specified on the entire boundary $(X = X_1, X_2;\ Y = Y_1, Y_2)$ of the domain $\mathscr{R}$, then the solution of Eq. (16) is unique provided $\phi_X < 0$ in $\mathscr{R}$. It is significant that only one condition may be specified on the boundaries parallel to the undisturbed flow just as in the inviscid case. Since the mean surface approximation remains valid in V-T flow (Sichel 1962) a tentative conclusion is that the boundary conditions which will represent a slender body will be the same as in the inviscid case. Even though the V-T equation is parabolic it is interesting to note that ϕ must be specified over a closed boundary as for second order elliptic equations. The high order of the V-T equation is responsible for this result.

The mathematical behavior of the V-T potential equation is dominated by the terms ϕ_{XXX} and ϕ_{YY}; therefore, the linear equation

$$\phi_{XXX} + \phi_{YY} = 0 \tag{22}$$

as well as Eq. (21) have been investigated. Partial differential equations of the type of Eq. (22) have been studied in general by Block (1912), and by Dezin (1958, 1959). Detailed solutions have been given by Sichel (1961), Ryzhov (1965) and Sichel, Yin, and David (1968). As mentioned above, Eq. (21) has been studied by Rae (1960) and periodic solutions of Eq. (21) have been investigated by Sichel and Yin (1967).

Higher order equations for $u^{(2)}$, $v^{(2)}$, etc., which are linear and nonhomogeneous, have been formulated by Szaniawski (1963). In the case of one dimensional shock structure higher order corrections to the Taylor weak shock solution (Eq. (13)) have been found in closed analytical form (Sichel 1960, Szaniawski 1966a). Equations for unsteady V-T flow have been formulated by Ryzhov and Shefter (1964). In the one dimensional case V-T flow is governed by Burgers' equation which is discussed in detail by Lighthill (1956); however, unsteady flows are beyond the scope of the present survey.

EXTERNAL FLOW

Determination of the jump conditions across a non-Rankine-Hugoniot shock wave terminating a region of supersonic flow is one of the key problems in the study of external V-T flow (Pearcey 1964). While this problem remains unsolved some progress in the study of V-T flow past bodies has been possible.

Some simple results can be obtained directly from the V-T equation. The structure of an oblique shock which is simply a generalization of the Taylor solution (Eq. (13)) can be shown to be a solution of the V-T equation (Sichel 1963, Szaniawski 1962). The angle between a transonic shock and the y axis is of $O(\epsilon^{1/2})$ and thus can be set equal to $\alpha\epsilon^{1/2}$ where $\alpha \sim O(1)$. In a curved shock α will vary with y, i.e. $\alpha = \alpha(y)$; however, it can be shown that unless $(d\alpha/dy) \sim O(\epsilon)$ or less the oblique shock solution will fail to remain valid. This condition implies that $\eta/\bar{R}_s \sim O(\epsilon^2)$, i.e. the ratio of shock thickness η to shock radius of curvature $\bar{R}_s$ must be second order in ϵ in order that the conventional oblique shock conditions hold (Sichel 1962).

Formal integration of the two dimensional V-T equation (15) with X held constant yields the result

$$U_X - \{1/2\}\, U^2 = -\int V_Y \, dX + K \tag{23}$$

where K is a constant of integration. Thus for constant X the V-T equation behaves like a Riccati equation. This is a highly significant result since many of the solutions of the V-T equation discussed below reduce to the solution of a Riccati equation with different functions of the independent variable on the right-hand side. In the simplest case, of the weak normal shock the right-hand side of Eq. (23) is a constant. In the case of a weak shock with uniform flow upstream and with $\epsilon = (M_1^* - 1)$ Eq. (23) yields the expression

$$U(+\infty,\ Y) = -\left[4 + \int_{-\infty}^{\infty} V_Y \, dX\right]^{1/2} \tag{24}$$

for the value of U downstream of the shock. In a normal shock V = 0 and Eq. (24) yields the usual Rankine-Hugoniot result $U(+\infty) = -2$ or $u^{(1)}(+\infty) = -1$. In an oblique shock with the free stream in the +x direction $V_Y < 0$ within the shock and according to Eq. (24) $U(+\infty, Y) > -2$ as is actually the case. In the shock terminating a supersonic region it appears reasonable that $V > 0$ because of the wall boundary layer. Then if V decays with increasing Y, $V_Y < 0$, and Eq. (24) predicts $U(\infty, Y) > -2$ so that the shock pressure rise is less than the R-H value in agreement with the numerical results of Emmons and with experiment (Sinnott 1960).

Failure of the R-H conditions to hold across shock waves evidently arises whenever the Reynolds number based on shock radius becomes small and the condition $\eta/R_s \sim O(\epsilon^2)$ is an expression of this fact. A general analysis of non R-H shock waves, which may also arise in low density supersonic and hypersonic flows, has been made by Germain and Guiraud (1964). Although not germane to the present survey, the measurements of flow near a hypersonic leading edge by

McCroskey (1967) provide a clear indication that R-H conditions no longer hold when the shock Reynolds number is low.

A desirable objective of any preliminary study of the V-T equation would be to examine the effect of viscosity upon a known inviscid solution. In two dimensional or axisymmetric flow past finite or semi-infinite bodies with sonic velocity at infinity Frankl (1947) and Guderley and Yoshara (1951) have found that the asymptotic behavior of the flow far from the body is described by self similar solutions of the inviscid potential equation of the form

$$\phi = y^{3n-2}\, F(\zeta) \quad ; \quad \zeta = x/(\gamma + 1)^{1/3}\, y^n \tag{25}$$

Investigation of the singularities of the ordinary differential equation for $F(\zeta)$ shows that the solution with $n = 4/5$ represents the asymptotic flow past a finite two dimensional profile while $n = 4/7$ represents flow past finite bodies of revolution.

To examine the effect of viscosity upon these inviscid solutions Ryzhov and Shefter (1964) studied self similar solutions of the normalized V-T potential equation (16) of the same form as Eq. (25), i.e. they assumed $\phi = Y^{3n-2}\Phi(\xi)$ with $\xi = X/Y^n$. For fixed ξ it then follows that the terms of the V-T equation vary as

$$\phi_X\phi_{XX},\ \phi_{YY} \sim O(Y^{3n-4}) \quad ; \quad \phi_{XXX} \sim O(Y^{-2}) \tag{26}$$

Equation (26) leads to the conclusion that for $n > 2/3$ the dissipative term ϕ_{XXX} vanishes faster than the other terms of the V-T equation as $Y \to \infty$, while for $n \leq 2/3$ the dissipative terms will be comparable or greater than the other terms of the V-T equation with increasing Y. Since $4/7 < 2/3 < 4/5$ Ryzhov and Shefter concluded that the two dimensional inviscid solutions with $n = 4/5$ will not be affected by viscosity for large Y, but that viscosity may have important effects on the asymptotic solution for axisymmetric flow with $n = 4/7$. A consideration of the Reynolds and Peclet numbers $Re = \rho^* U\ell/\mu^{*\prime\prime}$, $Pe = \rho^* U\ell/\kappa^*$ provides another explanation for these results Ryzhov (1965). If the characteristic length ℓ is taken as the horizontal distance between two of the generalized parabolas ξ = const, then Re, Pe $\sim O(Y^{3n-2})$ as $Y \to \infty$. Thus for $n < 2/3$, Re and Pe decrease so that viscous effects will be important throughout the flow.

The freedom in the choice of n disappears in the V-T case, a similarity solution of the V-T equation being possible only for $n = 2/3$. In that case, Eq. (25) implies that $U = Y^{-2/3} f(\xi)$, $V = Y^{-1} g(\xi)$ and the function $f(\xi)$ satisfies the ordinary differential equation

$$f'' + (4/9\ \xi^2 - f)\, f' + 4/9\ \xi\, f + 2/3\ (k - 2)\ (c - f\xi) = 0 \tag{27}$$

while

$$g = (2/3)\ (c - f\xi)$$

with c a constant of integration. Numerical solutions of Eq. (27) were compared to the inviscid similarity solution with $n = 2/3$ corresponding to the flow over the semi-infinite body $Y = \sqrt{(8/3)\, cX}$. For slender bodies with $c \ll 1$ the difference between the viscous and inviscid solutions was appreciable.

In the case $c = 0$, $k = 1$, solutions of Eq. (27) such that f remains bounded in $-\infty \leq \xi \leq \infty$ and that $f \to 0$ as $|\xi| \to \infty$ have also been investigated (Sichel 1961). Such solutions satisfy the mass conservation condition $\int_{-\infty}^{\infty} V dX = 0$ for fixed Y, and so may represent the asymptotic behavior of a finite body. Comparison of these solutions with solutions of the linearized two dimensional, $c = 0$, version of Eq. (27)

$$f'' + 4/9\ \xi^2\, f' + 10/9\ \xi\, f = 0 \tag{28}$$

which arises from a similarity solution of the linear V-T equation (22) showed that the non-linear term causes a marked difference between subsonic ($f < 0$) and supersonic ($f > 0$) solutions and completely changes the asymptotic behavior of f as $\xi \to \infty$. It is, thus, clear that linearized V-T solutions must be regarded with considerable caution.

Self similar solutions of the linearized V-T potential equation for axisymmetric flow have been studied by Ryzhov (1965). Then the function $f(\xi)$ satisfies

$$f''' + (4/9)\ \xi^2\, f'' + (4/3)\ (n + 1/3)\ \xi\, f' + n^2\, f = 0 \tag{29}$$

and solutions exist for all values of n. From the asymptotic behavior of this equation as $|\xi| \to \infty$ it is shown that $n = 4/3$ is the first eigenvalue for which f can represent the flow past a finite body. In the case $n = 4/3$ the solutions of Eq. (29) are shown to be confluent hypergeometric functions.

The inviscid similarity solution for a free stream Mach number of unity must have at least one discontinuity at some value of $\xi = \xi_s$ corresponding to a compression shock (Guderley 1962). The key question of whether viscous solutions outside the shock layer approach the inviscid solution as $Re_\delta \to \infty$ was investigated by Szaniawski (1966b) using the method of asymptotic expansions. The flow was divided into outer regions upstream and downstream of the shock wave and an inner or shock layer region, and ordinary differential equations were derived for the first order coefficients of inner and outer asymptotic expansions. It is initially assumed that the terms in these equations with the coefficient Re_δ^{-1} can be neglected everywhere as $Re_\delta \to \infty$ The outer solution then becomes the inviscid Guderley-Frankl solution while the inner solution is closely related to Taylor's weak shock solution. Matching is used to establish a composite expansion and streamline equations are obtained in parametric form. To this point the solution corrects the Guderley-Frankl solution for the finite thickness of the shock layer.

The crux of the analysis lies in the use of the above solution to determine whether the terms with Re_δ^{-1} as coefficient, which were dropped initially, are really negligible. The inviscid outer solution is consistent in the two dimensional case since then the neglected terms do indeed vanish as $Re_\delta \to \infty$. However, in the axisymmetric case the viscous Re_δ^{-1} terms are found to be of the same order as the inviscid terms for sufficiently large $|y|$ in agreement with the results of Ryzhov and Shefter (1964). However, Szaniawski finds that in the axisymmetric case the inviscid outer solutions will remain valid for $|x| \ll \xi_s^7 Re_\delta^2$, $|y| \ll (\xi_s^3 Re_\delta)^{7/2}$, a region which may be very large for large Re_δ. But even when Re_δ is very large the viscous terms may have an important influence on the asymptotic behavior of the solution far from the body.

An approximate viscous transonic solution for the classical problem of flow past a wavy wall has been determined by Sichel and Yin (1967c) following the method used by Hosokawa (1960a, b) in the inviscid case. The normalized potential ϕ is divided into a linear part $\phi^{(\ell)}$ and a correction g such that $\phi = \phi^{(\ell)} + g$. The potential $\phi^{(\ell)}$ then satisfies the linear equation

$$\phi_{XXX}^{(\ell)} - 2B\phi_{XX}^{(\ell)} + \phi_{YY}^{(\ell)} = K\phi_X^{(\ell)} \tag{30}$$

which is readily solved for the periodic wavy wall boundary conditions. K is an appropriately chosen constant and the linear solution enters in the equation for the correction g. Several approximations then lead to the Riccati equation

$$U_o' - U_o^2 = -\frac{B^2}{4} + A \sin(\omega X + \beta) + C \tag{31}$$

for $u^{(1)}(X, 0) = U_o$, the X velocity component at the wall. The constant A and the phase angle β depend on the amplitude and frequency ω of the wavy wall, and upon B while C is an integration constant. Equation (31) can be transformed into the Mathieu equation from which it follows that solutions may be diverging, periodic, or finite but aperiodic depending on the value of the constant C. Physically meaningful solutions should be periodic with the wall frequency, and this periodicity condition was used to determine C.

The inviscid solution of Hosokawa (1960b) and the V-T solution are shown in Fig. 1 for a particular set of flow parameters. Hosokawa must introduce a shock discontinuity in his solution; this is replaced by a smooth transition from supersonic to subsonic flow in the viscous transonic case.

So far attention has been focused on flows in which the fluid decelerates through a shock layer. Viscous transonic effects are also important in establishing the influence of viscosity upon a Prandtl-Meyer expansion from an upstream uniform flow with $M_1 \simeq 1$. Very large velocity gradients occur near the corner in the inviscid Prandtl-Mayer solution and here viscous effects must be significant. This problem was investigated by Adamson (1967) using the method of matched asymptotic expansions for both $M_1 \simeq 1$ and $M_1 > 1$. The flow was divided into an inner region about the first Mach line and an outer downstream region. Since derivatives of the inviscid solution are discontinuous at the first Mach line, the effect of viscosity must be to smooth out these discontinuities.

In the transonic, $M_1 \simeq 1$ case the first order inner flow near the Mach line is irrotational and satisfies the V-T potential equation (16). The similarity solution (Eq. (27)), with $c = 0$, first considered by Ryzhov and Shefter (1964), and Sichel (1961) is found to be the viscous transonic solution which properly matches upstream and downstream boundary conditions. Thus Adamson was also led to an investigation of the equation

$$f'' - ff' + 4/9\ \xi^2 f' + 10/9\ \xi f = 0 \tag{27a}$$

and in the corner problem the appropriate solution of (27a) varies as $(-\xi)^{-5/2}$ as $\xi \to -\infty$, and as ξ^2 as $\xi \to +\infty$. The existence of such solutions is verified numerically.

To this point the boundary layer has not been mentioned although it is clear that consideration of the interaction between the boundary layer and the free stream is essential for a complete understanding of the flow. The trouble is that this interaction problem is very difficult in both the inviscid and viscous transonic cases. However, the role of the boundary layer in viscous Prandtl-Meyer flow has been considered by Adamson (1967) who found that when $M_1 > 1$ the thinning of the boundary layer near the corner will affect the flow more than viscous effects in the expansion region. Although the matter is not entirely clear it appears that this situation reverses when $M_1 \simeq 1$ so that viscous effects in the expansion region will be the most important.

Bertotti (1957) indicated a possible approach to the transonic boundary layer interaction problem by showing that the boundary layer approximation remains valid at the foot of a shock wave provided that the shock wave is sufficiently weak and that the boundary layer thickness is sufficiently small. This idea was applied to a study of the leading edge of the shock tube boundary layer induced by a weak shock wave (Sichel 1962). In that case $V < 0$ and $V_Y > 0$ so that, in agreement with Eq. (23) the pressure rise across the shock was found to be greater than the R-H value.

An analysis of flow near a leading characteristic, considering boundary layer effects has also been made by Bulakh (1966).

Much work has of course been done on the shock-boundary layer interaction problem, generally based upon an inviscid, free stream flow with R-H shock waves. The present survey is not concerned with such problems but rather with the situation in which the boundary layer influences the viscous structure of the free stream, and in this area the literature is sparse.

NOZZLE FLOW

Transonic solutions for the flow near the throat of a converging-diverging nozzle are of practical and theoretical interest. Conditions at the throat are required to start characteristic calculations for the supersonic part of the nozzle. From a theoretical point of view the nature of the transition from wholly subsonic to subsonic-supersonic flow is of particular interest.

Meyer (1908) first computed the potential flow near the throat of a nozzle with asymmetrical subsonic-supersonic flow using a truncated double power series in x and y. Hence such flows are often called Meyer flows. The solution, which is indirect in that the velocity on the nozzle axis is specified rather than the shape of the nozzle, yields a reasonable description of the flow. Much additional work has since been done on the analysis of Meyer flows, particularly on the important direct problem in which the nozzle wall contour is specified, and this work is discussed in the review by Hall and Sutton (1964). It appears that other than for the boundary layer, dissipative effects will not be important in such flows.

The transition from symmetrical flow with subsonic velocity on each side of the throat to asymmetric Meyer flow was first studied by Taylor (1930) also using a power series, and such symmetrical flows are therefore often called Taylor flow. In this case the inviscid theory leads to difficulties. Taylor's calculations showed the development of supersonic pockets near the nozzle surface as the peak velocity on the nozzle axis increased, however, above a certain subsonic value of this peak velocity Taylor found that such symmetrical solutions would no longer exist.

Görtler (1939) showed that the series used by Taylor diverges as the peak velocity on the axis approaches the sonic value, and suggested that this difficulty is caused by neglect of higher order terms in the power series expansion. Görtler attempted to extend Taylor's series solution, however, a number of artificial assumptions regarding the series coefficients makes the convergence of Görtler's solution suspect.

Emmons (1946) applied the method of relaxation to the transition problem and also obtained supersonic pockets near the wall. When the peak centerline Mach number exceeded a value of 0.812 shock waves terminating the supersonic pockets had to be introduced in order to permit the elimination of residuals in the relaxation calculations. Even then there are difficulties for the shock waves appear suddenly and, as mentioned in the Introduction above, a sharp expansion must be introduced immediately behind the shock to avoid a discontinuous streamline curvature. In addition to the experimental results quoted in the Introduction, it is interesting that a rapid pressure rise behind transonic shock waves has also been observed by Ackeret, Feldman and Rott (1946).

Instead of considering approximate solutions of the full equations of compressible inviscid flow as above, another approach is to study exact solutions of the approximate inviscid transonic equation (Eq. (14)). Tomotika and Tamada (1950), and Tomotika and Hasimoto (1950) obtained an exact similarity solution of this equation describing both Taylor and Meyer flow, however their solutions did not provide for a smooth transition between the two types of flow. The similarity solutions describing Taylor flow also contain supersonic pockets but in the solution for which the pockets just meet on the axis the slope of the axial velocity distribution becomes discontinuous at the sonic point. This singularity on the axis, which appears to be a source of much of the difficulty discussed above appears related to the fact that here tangents to the sonic line and the characteristics coincide (Ryzhov 1963).

A large family of two dimensional exact solutions have also been developed starting from the hodograph equations (Falkovich and Chernov 1966, Germain 1964), however, the planar self similar solution of Ryzhov (1963) is of greatest interest here since he considered both the transition from Taylor to Meyer flow and the formation of shock waves. With the sonic point at the origin Ryzhov considers axial velocity distributions of the form

$$U(X,0) = A_1 X \quad , \quad X < 0 \qquad ; \qquad U(X,0) = A_2 X \quad , \quad X > 0 \tag{32}$$

for then the inviscid transonic equation admits self similar solutions of the form

$$U = Y^2 f(\xi) \qquad ; \qquad V = Y^3 g(\xi) \qquad ; \qquad \xi = X/Y^2$$

By an ingenious transformation of variables Ryzhov is able to study the singularities of $f(\xi)$ in detail and thereby determine the properties of the self similar solution. Ryzhov used the criterion that shock waves must appear wherever limit lines along which the acceleration is infinite occur and nozzle flows with shock waves are investigated. These flows all have the feature that the shock is tangent to the sonic line at the center of the nozzle. A weakness of the Ryzhov analysis is the use of the inviscid equations when limit lines with infinite velocity gradients appear.

At this point it appears appropriate to quote from the footnote on page 68 of Guderley's (1962) book:

> "If the nozzle is symmetrical with respect to the throat, then as long as the flow is subsonic along the entire length, there exists a symmetry also in the flow field. This is certainly no longer true when the nozzle is acting as a DeLaval nozzle. One would expect that a study of the transition from one behavior to the other would provide an insight into the phenomena of transonic flow. A direct analysis of nozzles has, however, <u>not in fact led</u> to this hoped for result."

It would appear to be more consistent to begin the investigation of such transitional flows with the V-T equation, and then to determine when viscous solutions approach the inviscid solution as $Re_\delta \to \infty$. This problem has been considered by Szaniawski (1964a, b) and in great detail by Kopystyński and Szaniawski (1965).

Kopystyński and Szaniawski considered flow through a nozzle throat with the contour

$$(\bar{y}_w / \pm L) = 1 + \frac{\gamma + 1}{2} \epsilon^2 f^2(x) \tag{33}$$

where L is the nozzle half height, and f(x) is an increasing function of x with $f(0) = 0$, $f'(0) \neq 0$. Assuming the series development

$$u = 1 + \epsilon\, \hat{U}(x) + \ldots \qquad ; \qquad v = \epsilon^2\, \hat{V}(x)\, y + \ldots \tag{34}$$

the boundary condition (Eq. (33)) then leads to the result that $\hat{V}(x) = \epsilon^2 (\gamma + 1) f(x) f'(x)$ while the V-T equation reduces to the ordinary differential equation

$$\hat{\delta}\hat{U}'' = \hat{U}\hat{U}' - ff' \qquad (35)$$

Here $\hat{\delta}$ is shorthand for $[\epsilon \, Re_\delta (\gamma + 1)]^{-1}$. The flow considered is thus quasi-one dimensional since the variation of u with y is not taken into account. By taking $v \sim O(\epsilon^2)$ instead of $O(\epsilon^{3/2})$ the authors have limited the validity of their analysis to streamlines which are very close to the nozzle axis.

When $\hat{\delta} = 0$ Eq. (35) has the two solutions

$$\hat{U} = \pm f(x) \qquad (36)$$

and the problem is to determine under what conditions solutions of Eq. (35) approach the inviscid solution (Eq. (36)) as $\hat{\delta} \to 0$. Applying the theory of Vasileva (1963a, b) Kopystyński and Szaniawski showed that the viscous solutions will converge to Eq. (36) as $\hat{\delta} \to 0$ everywhere except in the neighborhood of the sonic point $x = 0$.

The stretched variables

$$x = \sqrt{\frac{2}{f'(0)}}\,\hat{\delta}^{1/2}\,\xi \quad , \quad \hat{U} = \sqrt{2\hat{\delta}\, f'(0)}\,[\psi(\xi) + R(\hat{\delta}, \xi)] \quad , \quad \lim_{\delta \to 0} R(\hat{\delta}, \xi) = 0 \qquad (37)$$

are introduced to examine the structure of the flow near the sonic point in greater detail. Then expanding f(x) in a Taylor series about $x = 0$ and keeping only the first term Eq. (35), after one integration reduces to the Riccati equation

$$(d\psi/d\xi) - \psi^2 = -\xi^2 + A \qquad (38)$$

where A is an integration constant. The transformation, $\psi = 2\xi - (v'/v)$, changes Eq. (38) to the second order linear equation

$$v'' - 2\xi v' + (A - 1)v = 0 \qquad (39)$$

The solution of Eq. (39), and hence also of Eq. (38) can be expressed in terms of confluent hypergeometric functions. Depending on the values of A and of the initial value, $\psi_0 = \psi(0)$, solutions may be continuous or discontinuous, and the region of continuous solutions is determined in the ψ_0 - A plane. Typical solutions are shown in Fig. 2 and display a behavior suggesting the initial stages of shock formation near a nozzle throat. The problem of matching these inner solutions to the outer inviscid solutions is also considered.

The solutions shown in Fig. 2 are nonunique for all of them asymptotically approach $\psi = \pm \xi$ as $|\xi| \to \infty$. This is a disturbing result for the solutions should be responsive to the downstream boundary conditions just as in the one dimensional nozzle theory (Shapiro 1953). The difficulty may be related to the quasi-one dimensional nature of the theory which does not take into account the variation of u with y.

A different approach was used by Sichel (1966) who found that a Tomotika and Tamada (1950) type nozzle similarity solution is also possible in the viscous-transonic case. Using the irrotationality conditions to eliminate V the normalized V-T equation expressed in terms of $u^{(1)}$ instead of U becomes

$$u_{XXX}^{(1)} - (u^{(1)^2})_{XX} + u_{YY}^{(1)} = 0 \qquad (40)$$

Substitution of the transformation

$$u^{(1)} = Z(S) + 2\sigma^2 Y^2 \quad ; \quad S = X + \sigma Y^2 \qquad (41)$$

which is the same as that used by Tomotika and Tamada (1950), collapses Eq. (40) to the ordinary differential equation

$$Z''' - 2ZZ'' - 2(Z' - 2\sigma)(Z' + \sigma) = 0 \qquad (42)$$

The function Z is also $u^{(1)}(x, 0)$, the velocity on the axis $Y = 0$. The arbitrary constant σ can be related to the nozzle geometry. Equation (42) is the same as that obtained by Tomotika and Tamada except for viscous term Z'''. The special inviscid solutions $Z = 2\sigma S$, and $Z = -\sigma S$ are also solutions of Eq. (42), and the nozzle velocity distribution obtained from $Z = 2\sigma S$ is identical to that obtained from the first three terms of Meyer's (1908) original series solution. From a study of trajectories in the Z, Z', Z'' space it has been possible to find numerical solutions of Eq. (42) starting from $Z = 2\sigma S$, passing through a maximum value and then asymptotically approaching the inviscid decelerating solution $Z = -\sigma S$, and such solutions are shown in Fig. 3. As the maximum increases beyond the sonic value the deceleration to subsonic velocity ($Z' < 0$) becomes steeper, resembling the transition through a shock wave. These numerical solutions, which are similar to those found by Kopystyński and Szaniawski (1965), also apparently describe the first stages in the transition from Taylor to Meyer flow.

The solution above is indirect in that the shape of the nozzle wall cannot be specified in advance, rather, it is necessary to accept one of the streamlines produced by the similarity solution as the nozzle contour. Each of the solutions shown in Fig. 3 produces a somewhat different nozzle contour and as the centerline velocity maximum increases undulations occur in the nozzle wall streamline. A typical nozzle flow field showing streamlines and constant velocity lines is shown in Fig. 4 for a ratio of throat half height h to throat radius of curvature R_t of 1/4. The beginnings of a shock wave appears just downstream of the nozzle throat. The solutions shown in Fig. 3 are all asymptotic to $Z = -S$ as $S \to \infty$; however, no conclusions regarding uniqueness can be reached since each curve in Fig. 3 represents a different nozzle contour. Axisymmetric similarity solutions have also been determined (Sichel and Yin 1967a) and their asymptotic behavior as they approach the upstream and downstream inviscid solutions has been investigated.

A completely different situation arises in low Reynolds number flow through very slender nozzles. In that case the flow is dominated by the boundary layer, that is the shear stresses rather than the compressive viscous stresses play the key role. This problem has been considered by Williams (1963). In that case the sonic line is concave downstream in a flow accelerating to supersonic velocities rather than being concave upstream as in the Meyer solution. A study of the boundary layer free stream interaction problem will probably require a combination of the V-T solutions described above and the type of analysis considered by Williams.

SOURCE AND SOURCE-VORTEX FLOW

Exact solutions of the equations of two dimensional inviscid compressible flow for source and source-vortex or spiral flow contain limiting circles at or near the sonic velocity where the acceleration becomes infinite (Taylor 1930, von Mises 1958, Oswatitsch 1956). Solutions no longer exist inside these limiting circles, and the inviscid theory clearly fails when velocity gradients become very large. Viscous source flow using the full Navier-Stokes equations was therefore investigated by Wu (1955), Sakurai (1958) and Levey (1954, 1959). Wu and Sakurai were able to find closed form source solutions valid in the region of transonic flow and it has been possible to show that these solutions are also a similarity solution of the V-T equation (Sichel and Yin, 1967b). With the transformation

$$u^{(1)} = f(S) \qquad , \qquad S = X + \lambda Y \tag{43}$$

which was first introduced by Tomotika and Tamada (1950), the V-T equation, in the form of Eq. (40) can be reduced to the Riccati equation (Sichel and Yin 1967)

$$f' - f^2 + \lambda^2 f = -C_1 S + C_2 \tag{44}$$

The solution (Eq. (43)) may be interpreted as a source-vortex flow with S corresponding to the radial distance from the sonic circle while the arbitrary parameter λ determines the circulation and is zero for source flow. The magnitude of the integration constant C_1 depends on the source strength.

Without the viscous f' term the solution of Eq. (44) becomes

$$S + (\lambda^4/4C_1) = (1/C_1)[f - (\lambda^2/2)]^2 \tag{45}$$

with a limit circle at $S = -(\lambda^4/4C_1)$ where $df/dS \to \infty$. In the transonic regime the solution (Eq. (45)) is identical to that of Taylor (1930), and has an accelerating or supersonic branch and a decelerating or subsonic branch. The inviscid solution provides no mechanism for transition from one branch to the other. The viscous solution of Eq. (44) can be found in closed form in terms of Airy functions, and is identical to that found by Wu (1955) and Sakurai (1958). Inclusion of the viscous term eliminates the singular behavior at the sonic point. where the acceleration now remains finite. Viscous solutions exist which first approach the supersonic branch of the inviscid solution, pass through a shock like compression, and then approach the subsonic branch of the inviscid solution. All the solutions asymptotically approach the subsonic branch of the inviscid solution as $S \to \infty$. While the inclusion of the viscous term has eliminated the singular behavior near the sonic point, the solution still diverges at some point inside the sonic circle, where the V-T equation apparently fails. The V-T radial solution discussed above remains valid only if the sonic radius $\bar{r}^*$ is of order η/ϵ^2 where, as before, η is of the order of the shock thickness. It is interesting that $\bar{r}^*$ is thus of the same order as the shock radius of curvature $\bar{R}_S$ for which the V-T oblique shock solution remains valid.

Compressible radial flow in the presence of a gravitational field behaves like the flow in a converging diverging nozzle in that the flow can accelerate from subsonic to supersonic values, and such flows have been used as a model for the solar and stellar wind (Axford and Newman 1967). As in the case of nozzle flows the inviscid theory fails to provide a smooth transition from flows subsonic throughout to accelerating subsonic-supersonic flows. Consequently Axford and Newman (1967) studied viscous transonic solutions for such radial flows with a gravitational field. Axford and Newman used a series expansion similar to that used above to develop a viscous-transonic equation which now includes a body force term. Since the problem is one dimensional, integration and suitable transformation of variables reduces the V-T equation to a Riccati equation for which solutions can be found in terms of parabolic cylinder functions. While some of these solutions diverge, there is also a family of solutions which provide a smooth shock like transition from the accelerating to the decelerating branch of the inviscid solution just as in the nozzle problem.

CONCLUSIONS

Use of the viscous-transonic instead of the inviscid equation seems to resolve some of the difficulties of the inviscid theory discussed in the Introduction. The viscous transonic solutions provide for a smooth transition from the Taylor to the Meyer type of nozzle flow; however, the problem of obtaining a truly two dimensional V-T solution for flow near the throat of a nozzle of specified shape remains to be solved. The key problem of determining the jump conditions across a weak shock adjacent to a curved wall has not been solved; however, some progress has been made in evaluating the effect of viscosity on the asymptotic behavior of the flow about bodies. The precise role of viscosity in axisymmetric flows remains to be clarified. The V-T equation appears to resolve the limit line behavior near the sonic velocity in source vortex flows, and actually the V-T solution is a part of the more general solution of the viscous source-sink problem by Wu (1955), and Sakurai (1958). It appears necessary to include viscous effects whenever limit lines occur in the inviscid transonic flow theory. At the very least, in these cases, the question of whether in the limit $Re_\delta \to \infty$ the flow can be represented by inviscid regions separated by Rankine-Hugoniot discontinuities needs to be investigated.

The theory of viscous transonic flow is an extension of the Taylor (1910) theory for the structure of weak shock waves. The Riccati equation appears to play a central role in the study of V-T flows. Thus for fixed X the V-T equation can be formally reduced to a Riccati equation, and many of the V-T problems discussed in this survey, in the end, involved the solution of a Riccati equation. The fact that the Riccati equation can be transformed to a second order linear equation, made it possible in many cases to obtain solutions in closed form. Almost invariably there were then divergent solutions and solutions which contained shock like transitions from supersonic to subsonic flow. Even such a simple equation as

$$z' - z^2 = - b^2$$

has the solutions $z = - b \coth bx$, $- b \tanh bx$. Of these the solution $- b \coth bx$ diverges at $x = 0$ while $- b \tanh bx$ is the same as the Taylor weak shock solution. It is to be expected that this Riccati type behavior will also arise in more complicated V-T flows. In any case a key advantage of the V-T approximation is that the interaction between convection and dissipation is reduced to a mathematically simple form.

It is felt that the V-T equation may be able to shed some light on the well known "transonic controversy" regarding the existence of smooth pockets of supersonic flow imbedded in an outer subsonic flow. This controversy has been reopened by the inviscid calculation of transonic profiles by Nieuwland (1967) and by the shock free supersonic pockets produced experimentally by Pearcy (1962). It would be interesting to see how viscosity influences the mathematical question of existence or nonexistence of smooth pockets of supersonic flow. In the case of the nozzle problem the V-T theory quite naturally describes the gradual formation of shock waves terminating th supersonic pockets at the wall.

The question of the stability of various viscous-transonic flows appears not to have been investigated. There are also a number of magnetohydrodynamic and relaxing transonic flows where viscosity may play an important role.

No comparison between theory and experiment are presented in this review, and this fact reflects a serious gap in the theory of V-T flow. There is a decided need for a checkpoint between theory and experiment if the theory of V-T flow is to do more than provide qualitative explanations.

ACKNOWLEDGMENT

The author would like to express his appreciation to the Army Research Office, Durham, North Carolina which supported this work under contract DAHC 04-68-C-0008.

REFERENCES

Ackeret, J., Feldman, F., and Rott, N., 1946, NACA TM No. 1113.
Adamson, T.C., 1967, Phys. Fluids, 10, 953.
Axford, W.L. and Newman, R.C., 1967, Astrophys. J., 147, 230.
Bertotti, B., 1957, Instituto Lombardo, Rend. Sc., A92, 132.
Block, H., 1912, Arkiv For Matematik, Astronomi Och Fysik., 7, Part I, No. 13, 7, Part II, No. 21, 8, Part III, No. 23.
Bulakh, B.M., 1966, Prikl. Mat. i Mekh., 30, 607.
Dezin, A.A., 1958, Dokl. Akad. Nauk. SSSR, 123, No. 4.
Dezin, A.A., 1959, Usp. mat. Nauk, 14, No. 3.
Emmons, H., 1946, NACA TN 1003.
Emmons, H., 1948, NACA TN 1746.
Fal'kovitch, S.V. and Chernov, I.A., 1966, Prikl. Mat. i Mekh., 30, 848.
Frankl', F.I., 1947, Dokl. Akad. Nauk. SSSR, 57, No. 7.
Germain, P., 1964, Symposium Transsonicum (ed. K. Oswatisch), Berlin: Springer.
Germain, P. and Guiraud, J.P., 1964, J. Math. pures et appl., 45, 311.
Görtler, H., 1939, Z. angew. Math. Mech., 19, 325.
Guderley, K.G., 1962, The Theory of Transonic Flow. Reading: Addison Wesley.
Guderley, K.G. and Yoshihara, H., 1951, Quart. Appl. Math., 8, No. 4.
Hall, I.M. and Sutton, E.P., 1964, Symposium Transsonicum (ed. K. Oswatisch), Berlin: Springer.
Hayes, W.D., 1958, Fundamentals of Gas Dynamics, Sec. D., Princeton University Press.
Holder, D.W., 1964, J. Royal Aeronaut. Soc., 68, 501.
Hosokawa, I., 1960a, J. Phys. Soc. Japan, 15, 149.
Hosokawa, I., 1960b, J. Phys. Soc. Japan, 15, 2080.
Kopystyński, J. and Szaniawski, A., 1965, Archiwum Mechaniki stosowanej, 17, 453.
Lagerstrom, P.A., 1964, Theory of Laminar Flows, Sec. B., Princeton University Press.
Levey, H.C., 1954, Quart. of Applied Math., 12, 25.
Levey, H.C., 1959, Quart. of Applied Math., 17, 77.
Liepmann, H.W., Ashkenas, H., and Cole, J.D., 1948, U.S. Air Force Tech. Rept. 5667 [See also Hilton, W.J., 1952, High Speed Aerodynamics, London, New York Toronto: Longmans Green].
Lighthill, M.J., 1956, Surveys in Mechanics (ed. G.K. Batchelor and R.M. Davies), Cambridge University Press.
McCroskey, W.J., Bogdonoff, S.M., and Genchi, A.P., 1967, Rarefied Gas Dynamics (ed. C.L. Brundin), Suppl. 4, Vol. II, 1947, New York: Academic Press.
Meyer, T., 1908, "Über zweidimensionale Bewegungsvorgänge in einem Gas, das mit Überschallgeschwindigkeit strömt," Ph.D. Dissertation, Gottingen (See also Carrier, G., 1951 Foundations of High Speed Aerodynamics, New York: Dover).
Nieuwland, G.Y., 1967, National Aerospace Lab., Netherlands, Rept. NLR-TR-T172.
Oswatitsch, K., 1956, Gas Dynamics, New York: Academic Press.
Pearcey, H.H., 1962, Advances in Aeronautical Sciences, Vol. 3, New York: The MacMillan Co.
Pearcey, H.H., 1964, Symposium Transsonicum (ed. K. Oswatisch) Berlin: Springer.
Rae, W.J., 1960, Cornell Univ., Rept. TN 60-409.
Ryzhov, O.S., 1963, Prikl. Mat. i Mekh., 27, 309.
Ryzhov, O.S., 1965, Prikl. Mat. i Mekh., 29, 1004.

Ryzhov, O. S. and Shefter, G. M., 1964, Prikl. Mat. i Mekh., 28, 996.
Sakurai, A., 1958, Quart. Journ. Mech. and Applied Math., 11, 274.
Shapiro, A. H., 1953, The Dynamics and Thermodynamics of Compressible Fluid Flow, Vol. I, New York: The Ronald Press.
Sichel, M., 1960, J. Aerospace Sci., 27, 635.
Sichel, M., 1961, Princeton Univ. Dept. of Aero. Engrg., Rept. 541. (See also Ph.D. thesis.)
Sichel, M., 1962, Phys. Fluids, 5, 1168.
Sichel, M., 1963, Phys. Fluids, 6, 653.
Sichel, M., 1966, J. Fluid Mech., 25, 769.
Sichel, M. and Yin, Y. K., 1967a, J. Fluid Mech., 28, 513.
Sichel, M. and Yin, Y. K., 1967b, Univ. of Michigan ORA Rept. 07146-2-T.
Sichel, M. and Yin, Y. K., 1967c, "Viscous Transonic Flow Past a Wavy Wall," VIII Symposium on Advanced Problems and Methods in Fluid Mechanics, Tarda, Poland, Sept. 18-23.
Sichel, M., Yin, Y. K., and David, T. S., 1968, Univ. of Michigan ORA Rept. 07146-3-F.
Sinnott, C. S., 1960, J. Aerospace Sci., 27, 767.
Sternberg, J., 1959, Phys. Fluids, 2, 179.
Szaniawski, A., 1962, Archiwum Mechaniki stosowanej, 14, 905.
Szaniawski, A., 1963, Archiwum Mechaniki stosowanej, 15, 904.
Szaniawski, A., 1964a, Archiwum Mechaniki stosowanej, 16, 643.
Szaniawski, A., 1964b, "Importance des effects de dissipation en ecoulement transsonique," Internat. Council of Aeronaut. Sci. Congress, Paris, Paper No. 64-587.
Szaniawski, A., 1966a, Archiwum Mechaniki stosowanej, 18, 127.
Szaniawski, A., 1966b, "The Asymptotic Structure of Weak Shock Waves in Flows over Symmetrical Bodies at Mach Number Unity," Royal Inst. of Tech., Stockholm, Sweden, Rept. KTH No. 70, Gasdynamics.
Taylor, G. I., 1910, Proc. Roy. Soc., A, 84, 371.
Taylor, G. I., 1930, ARCR and M Nos. 1381 and 1382. See also The Scientific Papers of G. I. Taylor, (ed. G. K. Batchelor), Vol. 3, p. 128, 142, Cambridge University Press.
Tomotika, S. and Tamada, K., 1950, Quart. Appl. Math., 7, 381.
Tomotika, S. and Hasimoto, Z., 1950, J. Math. Phys., 29, 105.
Vasileva, A. B., 1963a, Uspekhi Matematicheskikh Nauk, 18, 15.
Vasileva, A. B., 1963b, Vychislitel'noi Matematiki i Matematicheskoi Fiziki, 3, 611.
Von Mises, R., 1958, Mathematical Theory of Compressible Fluid Flow, New York: Academic Press, p. 73.
Williams, J. C. III, 1963, Amer. Inst. Aeronaut. and Astronaut. J., 1, 186.
Wu, T. Y., 1955, Quart. Appl. Math., 13, 393.

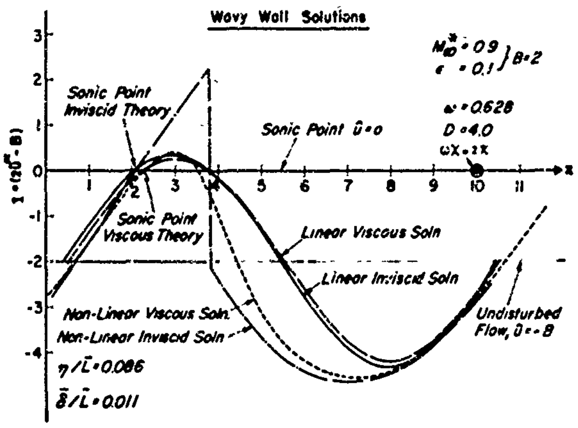

Fig. 1. Comparison of the Inviscid and Viscous Transonic Wavy Wall Solutions (Sichel and Yin 1967c).

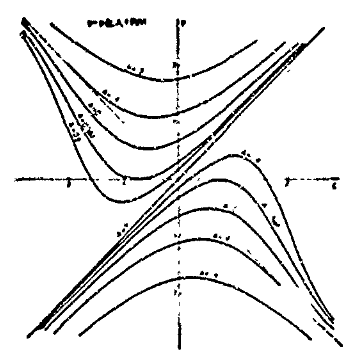

Fig. 2. Viscous Transonic Nozzle Solutions of Kopystynski and Szaniawski (1965).

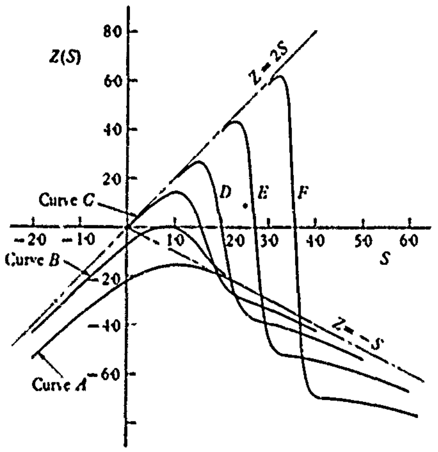

Fig. 3. Numerical Solutions of Eq. (42) for the Axial Velocity Z (Sichel 1966).

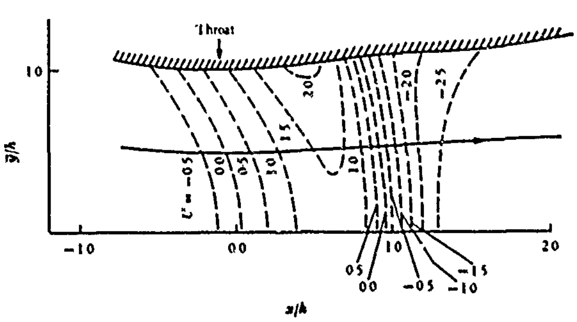

Fig. 4. Nozzle Isotachs and Streamlines Corresponding to Curve C of Fig. 3 and for $h/R_t = 0.25$ (Sichel 1966).

The interaction between local effects at the shock and rear separation - a source of significant scale effects in wind-tunnel tests on aerofoils and wings

H.H. PEARCEY , J. OSBORNE

Aerodynamics Division, National Physical Laboratory,
Teddington, England

and

A.B. HAINES

Aircraft Research Association Limited,
Bedford, England.

SUMMARY

Attention is drawn to important restrictions to the range of applicability of the flow model developed in earlier work on shock-induced separation of turbulent boundary layers on aerofoils and wings, and also corresponding restrictions to the conclusion then drawn that full-scale behaviour could readily be reproduced at low Reynolds numbers. These restrictions arise because the model of a bubble growing progressively from the foot of the shock towards the trailing edge does not include the interaction that sometimes occurs between the disturbance at the foot of the shock and a subsonic-type rear separation if one exists, or is incipient, in the continuous adverse gradient further downstream.

Such interactions are shown to be of increasing importance at wind-tunnel scale (as the possibilities of using thicker and more highly loaded wing sections develop) and to introduce real difficulties in reproducing full-scale behaviour at low or moderate Reynolds numbers.

NOTATION

M	- Mach number	
p	- static pressure	
H	- stagnation pressure	
C_p	- pressure coefficient	$[= (p - p_o)/\frac{1}{2}\gamma p_o M_o^2]$
C_L	- lift coefficient	
R	- Reynolds number (based on wing chord)	
b	- wing span	
c	- wing chord	
x	- chordwise co-ordinate	
α	- angle of incidence	
γ	- ratio of specific heats	

Suffices

o	- value in the undisturbed stream
L	- value locally on the wing surface.

1. Introduction

In considering shock-induced boundary-layer separation on aerofoils and wings, and the effects that it has on loads and moments, certain broad features have to be taken into account in addition to the local interaction between the foot of the shock and the boundary layer (Fig. 1). Three such features in particular are often more important than the details of the local interaction:

(a) the presence of mixed supersonic/subsonic flow, and the compression from one to the other, in the flow external but immediately adjacent to the separated flow;

(b) the presence of a continuous adverse pressure gradient in the subsonic flow over the rear of the aerofoil downstream of the shock and following the near-discontinuous gradient through the shock itself; and

(c) the special importance of the trailing edge, and of the variation of trailing-edge pressure in determining the overall circulation and lift on the aerofoil - the significant effects on the overall flow do not develop until the separation has disturbed the pressure at the trailing edge.

The pattern of development of the separation and of its effects - and the influence of such variables and parameters as free-stream Mach number, incidence, shock strength, Reynolds number, transition position - can best be understood by postulating a flow model that incorporates these broad features.

The flow model that has often been used satisfactorily for this purpose in the past[1,2,3,4] is one in which the influence of features (a) and (c) tend to be dominant. The bubble that forms at the foot of the shock remains localised so long as the steep pressure rise through such a localised interaction is able to decelerate the upstream supersonic flow to a subsonic one. As soon as the upstream Mach number has increased to a value for which this is no longer possible, the bubble spreads rapidly towards the trailing edge, and in doing so triggers a rapid fall in trailing-edge pressure through its effect on the boundary layer there. It is this fall in trailing-edge pressure that leads to the first significant effects on the overall circulation and loads on the aerofoil and wing.

The success of this model stemmed from the fact that the effects on the boundary layer at the trailing-edge position were dominated by the rapid bubble growth that is triggered by the spread of supersonic velocities along the edge of the bubble. The influence of the adverse gradient in the downstream subsonic flow (feature (b)) was not sufficient to modulate this pattern.

In particular, scale effects that could stem from differences in boundary-layer thickness over the rear of the aerofoil were noticeably absent. It was shown[4] that, provided the boundary layer was turbulent at the initial separation point, full-scale behaviour could be well reproduced at quite moderate values of Reynolds number ($\sim 1.5 \times 10^6$). This was because the form of the recompression from supersonic to subsonic flow was well represented, and hence the rapid growth of the bubble.

The major scale effects were then confined to cases for which the boundary layer remained laminar up to the separation point. For these, the precise position of transition in the separated shear layer could influence the nature and magnitude of the steep pressure rise and so determine whether or not subsonic flow was re-established for a given shock strength. Even these scale effects could be eliminated by fixing transition artificially at wind-tunnel scale because the boundary layer was likely to be turbulent at the foot of the shock for all relevant full-scale applications.

This remained valid for as long as the wings that were used for excursions into the transonic flow régime remained relatively thin and lightly loaded; for such wings the adverse gradients in the subsonic flow downstream of the shock were not strong enough to influence the overall pattern.

However, progress in the design of swept-wing aircraft in recent years has called for the use of progressively thicker and more highly loaded sections. Inevitably, this has led to steeper adverse pressure gradients in the rear subsonic flow, gradients that now modulate the gross effect represented in the flow model originally postulated. Clearly, therefore, a new, more comprehensive model is needed which will incorporate this modulation. In particular, and especially at wind-tunnel scale, a second separation tends to occur in the downstream subsonic flow and to spread forward from the trailing edge.

This second separation (Fig. 1b) is the rear, subsonic type which is known to depend critically on the thickness and the velocity profile of the boundary layer approaching the trailing edge as well as on the local pressure gradients. Even in the absence of a shock wave, the occurrence and development of such separations are known, for example, to be sensitive to the effects of Reynolds number and to the manner in which transition is fixed at tunnel Reynolds number in attempting to simulate full-scale conditions. It is not surprising, therefore, to find these sensitivities carried over into the flows in which the rear separation and the local effects of the shock interact with one another, nor indeed, to find them amplified by the interaction.

With the progress in swept-wing design, the tendency has developed for rear separations to occur in wind-tunnel experiments and to bring with them the scale effects inherent in the alternative flow model now to be described, and inherent in the change from one flow model to the other as full-scale conditions are approached. The correct full-scale behaviour, for cruise and moderate lift coefficients at least, is probably still represented by the original flow model, but this has become much more difficult to reproduce at wind-tunnel scale.

The paper will draw on detailed flow observations - for the idealised situation provided by two-dimensional aerofoils - to describe the differences between the two flow models and to contrast the sensitivity to scale for the alternative one with the insensitivity for the original. Some examples will be shown to support the details postulated for the alternative model, and to illustrate the order of the scale effects that can be introduced by differences in chord Reynolds number and in the type and location of the agency used to fix transition artificially.

The relevance of this to swept wings will be briefly illustrated by reference to similar observations on a representative model.

Finally, some tentative remarks will be made to indicate the increased difficulties of achieving correct simulation in wind-tunnel tests.

2. The original flow model, A

The development of the flow according to this model is indicated diagrammatically by the sequence of sketches in the extreme left-hand column of Fig. 2. The sequence I to VI can be taken as successive stages in a progressive increase of free-stream Mach number or of incidence - in either case the parameter that first caused the separation and then increased its severity would be the increasing shock strength. This is illustrated, for example, by the family of upper surface pressure distributions shown in Fig. 3 for an increase in free-stream Mach number with incidence held fixed. The shock wave is, of course, the steep pressure rise in the middle part of the chord. It first appears at about $M_0 = 0.7$, corresponding to stage I, say, of the sketches in Fig. 2. From there on, the increasing shock strength is at first revealed in the increasing magnitude of the pressure rise associated with an increasing local Mach number immediately upstream of the shock; later, after separation has occurred, the steep pressure rise at the surface is limited by the separation itself, but the strength of the shock away from the surface is, nevertheless, progressively increasing.

The influence of the local bubble at the foot of the shock is first evident for $M_0 = 0.76$ (the first curve after that labelled 0.74), corresponding to stage III in the sketches. The progressive spread of the bubble towards the trailing edge is revealed by the distributions for subsequent free-stream Mach numbers. The rate at which the pressure at the trailing edge varies with Mach number is first influenced(first divergence of trailing-edge pressure[2]) for the free-stream Mach number just below $M_0 = 0.8$, corresponding to stage V of the sketches, and the bubble itself spreads to the trailing edge immediately after $M_0 = 0.8$, corresponding to stage VI.

The progressive growth of the bubble is thus a prominent feature, with the separation point fixed to the toe of the shock and the reattachment point moving downstream towards the trailing edge as the overall strength of the shock increases. For a range of shock strengths beyond that for which separation first occurs, the boundary layer remains attached to the surface between the bubble and the trailing edge; for the first part of this range, the boundary layer at the trailing edge is not sufficiently disturbed to influence the trailing-edge pressure or, through it, the overall circulation and loads.

It is a further feature of this flow model that the influence on trailing-edge pressure and circulation develops rapidly from a particular, fairly clearly defined stage. If one considers the flow with a well developed bubble (Fig. 1a), one finds[5] that a "tongue" of local supersonic flow extends along the edge of the bubble downstream of the toe of the shock. This tongue is existing in a region in which pressure is rising in the downstream direction and so the stream tubes are contracting. The contraction offsets the tendency for the shear layer to reattach and delays the closure of the bubble. In contrast, a local subsonic flow with expanding stream tubes would help to promote reattachment, and for as long as the pressure rise near the forward part of the bubble re-established subsonic flow, the bubble size would tend to be self-limiting. The self-limiting influence is removed immediately the supersonic tongue appears, and this in turn leads to a snowballing effect[1] and a rapid bubble expansion.

We thus have the situation in which the rapid divergence of trailing-edge pressure - "significant effects of separation" - occurs in response to a rapid bubble growth triggered from the toe of the shock. This is a situation which is not particularly sensitive to the thickness or profile of the boundary layer (provided it is turbulent at sep[illegible]) and one in which the growth of bubble from the shock rearwards is too rapid to be strongly [illegible]ced by smaller changes spreading forward from the trailing edge.

This is why it was possible to reproduce in wind-tunnel tests at relatively low Reynolds number the same flow developments as were obtained in flight[6]. For example, the comparison in Fig. 5 shows clearly a very similar bubble development between tunnel and full scale from shock strengths that correspond quite closely (although the section shapes differed slightly - giving slightly further aft shock positions in flight).

Of course, some scale effects can occur even with this type of flow, due to changes in the detailed interaction at the foot of the shock reflecting in changes in the magnitude of the steep pressure rise and hence in the range of local upstream Mach numbers for which subsonic flow is re-established in the steep pressure rise[7]. The repercussions of such changes are usually small so long as the overall flow conforms to this model; the real impact of such changes can occur in the alternative flow model because, as we shall see, there is likely then to be an amplifying process involved.

Some further analysis at this stage, of the manner in which surface pressures are affected by separation developing according to the original model, A - and of how the surface pressures can be used to detect the essential features of the flow - will help later in drawing the contrast between the two flow models.

The product $C_p(1 - M_0^2)^{\frac{1}{2}}$ for a fixed chordwise station (Figs. 7 and 8) varies little with free-stream Mach number until the pressure at the station in question is subjected to the local influence of the shock wave (as at point X of the upper left diagram of Fig. 7) or of the separation bubble (as at point X of the upper right diagram of Fig. 7). The curves for fixed stations at the rear of the chord will take the form shown in the lower diagram of Fig. 8, with the first influence of separation indicated by the divergent fall in pressure.

The development represented in Fig. 3, then, produces the series of curves shown in Fig. 8 for fixed stations X1 to X6 (indicated on Fig. 3). These again demonstrate clearly that the influence of the shock-induced separation spreads rearwards from X1 to X6 as the flow develops, reaching the trailing edge, X6, last. This is indicated both by the locus of crosses, marking the first influence of the separation, and by the points A, B, C, D, marking a certain approximate level of static pressure in the disturbed flow.

3. The alternative flow model, B

The essential difference between this model and model A is the inclusion of a second separation in the subsonic flow approaching the trailing edge (Fig. 2).

This second separation is the classical subsonic, rear, turbulent separation occurring in the adverse gradient over the rear of the aerofoil. The occurrence and development of this type of separation is known to depend on the magnitude of the pressure gradient approaching the trailing edge and on the boundary-layer thickness and profile, i.e. on the local pressure gradient and on the upstream history of the boundary layer. It is the upstream history that is of the greater importance in considering the occurrence and/or the progressively increasing severity of the rear separation in the flow developments that are now in question and that occur as either free-stream Mach number or incidence is increased (down the page in the schematic representation of Fig. 2). The downstream pressure gradients themselves are changing only slowly through any particular one of the sequences shown, but the disturbances to the boundary-layer thickness and profile at the foot of the shock are increasing progressively as the shock strength increases.

This local shock interaction catalyses the development of a rear separation that was already either incipient or actually present in the subsonic rear gradients before shock waves appeared. When the rear separation occurs, there is a strong, more extensive interaction between the disturbances at the foot of the shock and the rear separation, and this larger interaction accelerates and intensifies the influence of the shock-induced phenomena on the overall flow including the circulation. The larger interaction is now sufficiently strong to produce a modulation to the pattern of development previously described for the model-A type of flow. This applies particularly to the well-defined interval between the first appearance of a local bubble at the foot of the shock and the first significant effects on the circulation that stem from changes in the pressure at the trailing edge, and to the connection between this interval and the spread of local supersonic flow downstream from the immediate vicinity of the steep pressure rise at the toe of the shock.

The rear separation is the common feature that distinguishes this flow model from model A, but it can appear and influence the flow development in a variety of ways that differ from one another in detail. It is useful to take note of these differences at this stage, although in certain overall respects they are differences only of degree, especially, for example, in contrasting the sensitivity of this flow model to scale effects with that of model A.

The differences between the various sequences sketched in Fig. 2, as distinct from developments in each sequence, are strongly dependent on the severity of the local pressure gradients in the downstream subsonic flow, as well as on the thickness and profile of the boundary layer.*

---

* This applies also to the differences between the model A sequence and the others.

Thus, the combination of downstream gradient and of boundary-layer thickness and profile might be such that the rear separation does not appear until there is a bubble at the foot of the shock (variant B1), that is, until the local interaction with the shock causes a substantial disturbance to the boundary layer approaching the trailing edge.*

With a somewhat steeper downstream gradient or with a turbulent boundary layer that is thicker as it approaches the shock (e.g. at lower unit Reynolds number or for a more forward transition position), the interaction with the foot of the shock would be sufficient to develop the incipient rear separation before it produced an actual shock separation bubble (variant B2).

For more severe downstream gradients still (e.g. for a thicker or a more highly loaded aerofoil) or for thicker boundary layers still, the rear separation could be present even before the appearance of shock waves (variant B3).

An important feature of all three variants is that the interaction between the local disturbance at the foot of the shock and the rear separation accelerates the development of the whole shock-induced phenomenon as compared with model A. In turn, the forward spread of the rear separation to link up with the bubble at the foot of the shock, or with the foot of the shock itself, is an important agent in this acceleration; in this connection it is convenient, for variants B2 and B3, to distinguish between the cases where the link up is with a local separation that is already present at the foot of the shock, B2a and B3a, and those for which the rear separation spreads to the foot of the shock before separation would otherwise have occurred there, B2b and B3b.

Some divergence of trailing-edge pressure, and hence influence on circulation and loads, starts as soon as the rear separation is present; it builds up as the rear separation spreads forward under the influence of the growing disturbance at the foot of the shock. The link up between the two separations, or between the rear separation and foot of the shock, leads to a greatly accelerated divergence. The rate of development of the rapid divergence of trailing-edge pressure thus differs from one variant to another and in particular between variants B2a and B2b on the one hand and between B3a and B3b on the other.

We are now in a position to compare the surface-pressure distributions observed for a flow of this type with those described for model-A flow in the preceding section; this will also provide a better background for subsequent discussions of the part now played by the spread of local supersonic flow downstream from the toe of the shock, of the work of others with flow models falling in this general category[7,8] and of the nature of the important scale effects to which this flow model is prone.

The family of upper surface distributions reproduced in Fig. 4 illustrates the developing effects of separation for a model-B type flow† as free-stream Mach number is increased for a fixed angle of incidence. In the same way as for the corresponding family for model-A flow (Fig. 3), the increasing shock strength is the parameter that produces the occurrence and progressive development of shock-induced separation. Although the aerofoil (NPL 9240) is different from that used for the earlier illustration (NPL 9230), the angle of incidence is chosen so that the increasing shock strength covers approximately the same range of values and takes place in approximately the same range of free-stream Mach numbers. In particular, the shock first appears at about $M_0 = 0.7$ and the separation develops strongly between $M_0 = 0.74$ and 0.85 as before.

The Reynolds numbers were the same for the two cases, and transition was fixed in the same manner in the same chordwise position, so that the thickness of the turbulent boundary layer approaching the shock should have been closely similar (there may have been small differences due to the small differences in the pressure gradients upstream of the shock and in the shock positions). The most relevant difference between the two aerofoils in the present context is in the severity of the pressure gradient in the subsonic flow over the rear of the aerofoil. This feature is better demonstrated by the low-speed ($M_0 = 0.6$) pressure distributions reproduced in Fig.14.

The result of the significantly more severe gradient for the NPL 9240 aerofoil is a major difference in the development of the separated flow, and this is shown clearly by the pressure distribution over the rear of the aerofoil for Mach numbers between 0.74 and 0.85 (Fig. 4). In contrast to the progressively rearward bulging of the curves for the model-A flow (Fig. 3), reflecting the progressive rearward growth of the bubble, the curves for the model-B flow (Fig. 4) illustrate a fan-like development centred on the foot of the shock. This reflects the fact that, at a certain stage, the rear separation links immediately to the foot of the shock to give a flow that is completely separated from shock to trailing edge. The pressures at all points over the rear of the aerofoil, including the trailing edge, are influenced right from the start of this process, and the pressure at the trailing edge most strongly of all. It can readily be inferred that this will have a strong bearing on the nature of the trailing-edge pressure divergence and, through it, on the effects on the overall circulation and forces.

---

* In postulating the model-A flow, it was, of course, assumed that the combination of downstream gradient and boundary-layer thickness were such (i.e. less severe than for B1) that a rear separation would not appear before the rapid rearwards growth of the shock bubble, triggered by events near the toe of the shock, had dominated the overall development.

† It will be evident later that this is an example of the B3a variant.

This is further illustrated in Figs. 9 and 10 by the analysis of the variation of pressure at fixed chordwise positions. The sketches in the upper part of Fig. 9 indicate the manner in which the chordwise pressure distribution is disturbed by the occurrence of rear separation: at the rear, under the separated flow itself, the pressures are lower than they otherwise would be, but further forwards, just upstream of the separated flow, they are higher. As the separation point moves forward, e.g. with increase of free-stream Mach number from (a) to (b), so the disturbance at points like X_{n-1} changes from an increase in pressure to a decrease. Thus, when the pressures at fixed points, X_n, X_{n-1}, say, are plotted against M_0 in the form shown in the lower diagram, the first influence of rear separation is seen as a fall in pressure at the extreme rear of the chord and an increase further forwards. As the separation spreads and becomes more severe with increasing M_0, the pressures at the rear, e.g. at point X_n, fall progressively; those at points further forward, e.g. at point X_{n-1}, start to fall as the separation point moves forward over the points in question.

The curves in Fig. 10 have been cross-plotted from the family of chordwise distributions of Fig. 4. The upwards divergence (fall in pressure) in the curve for the trailing edge, X_6, indicates that some rear separation was present from about $M_0 = 0.5$ onwards, i.e. before the appearance of shock waves. We thus have a model-B3 flow.

As M_0 was increased to 0.74, the mild upwards-divergence spreads forwards in turn to positions X_5 and X_4, indicating a gradual forward spread of the separated flow.

Increase in M_0 beyond 0.74 produced an abrupt change in which the separation point spread forwards suddenly; the pressure started to fall at several positions simultaneously, and the rate of fall at the trailing edge increased substantially.

The abrupt change in the pressure variations was obviously associated with a correspondingly abrupt change in the development of the rear separation that was in turn caused by a change in the disturbance at the foot of the shock. The fact that shock waves were already present for $M_0 = 0.72$ and 0.74 (Fig. 4), and not then noticeably disturbing the previously established pattern of slow development in the rear separation, suggests that it was the occurrence of a local bubble at the foot of the shock that triggered the subsequent abrupt change, and, further, that in this change the rear separation point jumped forwards to link with the shock bubble as postulated for the model-B3a flow.

These curves illustrate clearly how the interaction between the two separations serves to transmit the effect of the shock-induced separation immediately, and in a magnified form, to the trailing edge - in contrast to the situation for model-A flow. In the process of transmitting the effect of the disturbance at the foot of the shock to the overall circulation about the aerofoil, the rear separation thus acts both as a relay and as an amplifier.

The amplification would be expected to apply to the effect of small differences in the shock interaction region, and this was well illustrated by the work of Little[7]. He studied in detail the steep pressure rise at the toe of the shock and the ability of this to re-establish subsonic flow downstream. He showed that a three-fold increase in the thickness of the turbulent boundary layer approaching the shock toe (equivalent to a proportional decrease in unit Reynolds number of over 200) led to a reduction of the upstream Mach number for which subsonic flow could be re-established from 1.26 to 1.21. By itself, (i.e. with model-A flow), such a change would be expected to produce only a slowly developing effect of decreasing Reynolds number. But in his experiment in which a rear separation was also present (model-B3a flow), the effect was considerably magnified because the rear separation spread immediately forward to the shock bubble as soon as the supersonic tongue began to appear downstream of the shock toe. Here then is one particular mode by which the relaying and amplifying processes can lead to substantial scale effects.

Thomas[8] has also examined theoretically the nature of scale effects that can exist with model-B flows. He postulated the B2b variant in which the shock modifies the profile of the turbulent boundary layer at its foot without causing it to separate locally, but in which even this modification leads to the occurrence and development of a rear separation: the rear separation point moves rapidly forward to the foot of the shock as the shock strength increases. He derived the disturbance to the boundary-layer profile at the foot of the shock by assuming that the pressure rise was the Sinnott "equivalent shock pressure rise"[9] and that this rise was spread sufficiently (over about five boundary-layer thicknesses) to be treated by conventional boundary-layer theory.

Gadd[10] has also studied experimentally the process by which shock separation links with that at the trailing edge.

4. Experimentally observed scale effects with model-B flows

Some of the clearest evidence of the really serious discrepancies that can occur between wind tunnel and flight was presented by Loving[11] and the pressure distributions shown in Fig. 6 are reproduced from his paper. Although the results of these measurements are not available in sufficient detail to analyse in the manner described above, it is a reasonable inference from the contrast with the earlier results presented in Fig. 5 that the flow was of model-B type for these later wind-tunnel experiments. For example, the strong differences that Loving observed between tunnel and flight undoubtedly stem from the poor pressure recovery downstream of the shock in the wind-tunnel tests; the more forward shock position, and the differences in circulation that would result from the different trailing-edge pressure, are direct consequences of this poor pressure recovery[1]. Furthermore, there is no evidence of the inflection point between shock and trailing edge that is characteristic of the closed bubble, as in Fig. 3, for example.

This inference will be supported by the ensuing discussion of a wider selection of wind-tunnel results, (a) for aerofoils in a given range of unit Reynolds number but with differences in boundary-layer thickness at the shock and downstream introduced by differences in fixing transition upstream; (b) for aerofoils at different Reynolds numbers; and (c) for a swept wing at different Reynolds numbers. These examples have been chosen in such a way that they illustrate a variety of the problems introduced by model-B flows.

(a) Aerofoils with differences in fixing transition

The two widely different curves of variation of lift coefficient with increasing Mach number shown in Fig. 11 were obtained on the same aerofoil with different transition bands. The chord Reynolds number increased with Mach number (atmospheric stagnation pressure) from 1.3 to 2.0×10^6. The lower, chain-dotted curve was obtained with a relatively coarse transition band, near the leading edge, that provoked transition at or very near the end of the band (i.e. in the region of 5% chord). The upper, full curve corresponds to a finer band, further back, for which transition occurred significantly further downstream, well beyond the end of the band even; although transition was complete upstream of the shock (at about mid-chord), the thickness of the turbulent layer approaching the shock would have been significantly smaller.

The main feature of interest in the curves is the break from a rising coefficient to a falling one, at about $M_0 = 0.7$, that was caused by the shock-induced separation. The main difference between the curves is that the break is earlier and more severe for the thicker boundary layer. This difference is a direct result of the rear separation - and, more specifically, of its interaction with the disturbance at the shock - that developed in the model-B type flow for the thicker boundary layer. The curves begin to diverge slowly from one another before the break because a mild rear separation began to form even before shocks were present, but the really large differences developed later as the local separation at the shock increased the severity of the rear separation and produced an interaction between the two separations.

The pressure distributions corresponding to points A and B of Fig. 11 are reproduced in Fig. 12. The pressure recovery downstream of the shock is noticeably stronger for A than for B, and indeed, there is an indication of the inflection point expected in the presence of a bubble tending to close. This comparison is closely similar to that shown between flight and tunnel in Fig. 6. In addition, it illustrates how the difference in trailing-edge pressure influences the pressures on the lower surface; the lower pressures for curve B are associated with the reduced circulation that results from the more severe separation. Reference back to Fig. 5, for which no such differences appeared, serves to emphasise that such scale effects as this were absent so long as model A was appropriate for both wind tunnel and full scale.

An illustration of the importance of the rear pressure gradient in the development of model-B type flows is provided by the comparisons in Fig. 13. The two lift curves of Fig. 11 (for the NPL 9240 aerofoil) are compared with a corresponding pair for a slightly modified aerofoil (NPL 9241). The modification and the nature of its influence on the rear pressure gradient (in the absence of shock waves) are illustrated in Fig. 14.

For both aerofoils, the effects of shock-induced separation were amplified by the strong model-B interactions that occurred when the thickness of the turbulent boundary layer at the foot of the shock was increased (by the change in transition band). The difference in lift coefficient produced by the amplification is in each case indicated by a vertical arrow from the curve for thin boundary layer to that for the thick. The difference in the length of the two arrows shows that the amplification was much smaller for the modified aerofoil (NPL 9241) than for the original one (NPL 9240).

The influence of the strong model-B interactions (with the thicker boundary layer) was here clearly affected by some small change in the flow, probably a small change from one aerofoil to the other in the degree to which the rear separation had developed before the shock appeared. This is an indication of how critically this type of scale effect, as between wind tunnel and flight, might depend on the precise conditions reproduced in the wind-tunnel experiments.

Of at least equal importance is the demonstration that the comparison between the two aerofoils was completely distorted by the strong model-B interactions. The small differences in aerofoil profile had practically no effect on the results when the turbulent boundary layer approaching the shock was reasonably thin (upper two curves), but a very significant effect when the boundary layer was thick (lower two curves). The inference of this is that completely misleading results can be obtained with model-B type flows even when the object of the wind-tunnel tests is restricted to producing a qualitative comparison between different designs.

The results in Fig. 15 show that similar differences occur for a shock-induced separation developing with increasing incidence at fixed Mach number. The three different curves represent different transition bands. The chord Reynolds number was the same for the three cases, but the thickness of the boundary layer approaching any given chordwise position decreased as the band was moved further aft towards that position. The three curves are different even for the low values of incidence for which the flow was attached because the viscous effects on circulation were already greater for the larger boundary-layer thicknesses. These relatively small differences were, however, magnified by interactions that occurred as the separated flow developed near the incidence for maximum C_L and beyond.

The pressure distributions for the three points a, b, c, near the position of maximum C_L on the respective curves, are shown in Fig. 16a. These reveal that the shock that produced the stall was situated at about 30% chord.

For points b and c, corresponding to the intermediate and furthest forward transition positions respectively, the steep pressure rise is that characteristically associated with a turbulent separation at the toe of the shock (confirmed by flow photographs not here reproduced) and is just re-establishing subsonic flow. In other words, a further increase in shock strength (i.e of incidence) would be expected to produce a rapidly expanding bubble and hence rapidly developing separation effects, as indeed is confirmed by the subsequent fall in C_L. The most significant difference between these two curves is probably the small difference in trailing-edge pressure which is indicative of a slightly more severe rear separation for point c than for point b. (The difference near the shock for point 'a' is also of considerable significance, but for different reasons - see below.)

For an increase of incidence to that corresponding to points B and C (Fig. 15), the pressure distributions, Fig. 16b, show how the more severe rear separation interacts with the expanded bubble at the foot of the shock to magnify the difference between the two cases. The differences in pressure at the trailing edge indicate that the rear separation for C is increased more in severity than is the one for B, and that, as a result of the greater reduction in circulation associated with this, the forward displacement of the shock[1] is greater; the supersonic flow at the leading edge is in fact about to collapse[12]. The sequence here, then, was almost certainly that (i) the difference in the thickness of the boundary layer approaching the shock led to a small difference in the strength of the disturbance at the foot of the shock; (ii) this difference, in turn, led to an amplified difference in the severity of the rear separation; (iii) although, even in its amplified form, the difference in rear separation was relatively small, it produced a significant difference in the overall flow development at a critical stage.

For this example there is an indication, in the pressures near the immediate trailing edge, that some small degree of rear separation remained even for the curve B, corresponding to the intermediate transition band. Even this, therefore, might be subject to some of the effects expected for model-B type flow.

However, other and different difficulties were encountered on moving the transition band still further aft in an attempt to eliminate these effects at the Reynolds number of these tests (1.6×10^6). Transition no longer occurred upstream of the separation point at the toe of the shock, but immediately downstream in the separated layer. As a result, the steep pressure rise was greater in magnitude (see Fig. 16a, point 'a' and Fig. 16b, point A) and sufficient to re-establish subsonic flow. Reduced effects of separation would then be expected on this score alone, and it is impossible to resolve how much of the difference that resulted from the second shift of the transition band was due to this, and how much to the elimination of the model-B interactions.

It is indeed frequently and characteristically more difficult to eliminate the spurious influence of model-B flows in wind-tunnel tests as incidence is increased and the shock moves forward towards the leading edge. With the rearward shocks that occur at low incidences one is able to offset some of the effect that reduced unit Reynolds number has - in increasing boundary-layer thickness - by allowing the boundary layer to remain laminar over more of the chord; transition can be considerably further aft in the wind tunnel than at full scale but still be complete upstream of the shock. This is no longer possible with the forward shock positions, and one is driven to the need for higher Reynolds numbers in the wind-tunnel tests so that transition can be fixed upstream of the shock without provoking a spurious rear separation.

(b) <u>Aerofoils at different Reynolds numbers</u>

Fig. 17 illustrates the effect of increasing Reynolds number, again for a case in which the shock-induced separation develops with increasing incidence at fixed Mach number.

The curve for Reynolds number = 1.6×10^6 was obtained, from a similar set of measurements to those of Fig. 15, in the NPL 20 in x 8 in tunnel (0.51 m x 0.20 m) with a transition band for which transition was not complete upstream of the shock. The curves for higher Reynolds numbers were obtained in a BAC 4 ft x 4 ft tunnel (1.22 m x 1.22 m); transition was provoked early on the chord by disturbances from pressure holes near the leading edge.

These results help to confirm that low Reynolds-number tests with transition incompletely fixed give spuriously favourable lift curves by comparison with high Reynolds-number results. On the other hand, by comparison with Fig. 15, it can be deduced that the effects of shock-induced separation are less severe for the high Reynolds-number tests than they would spuriously have been at low Reynolds number with transition fixed near the leading edge.

The difficulties in simulating full-scale flows vary in severity from one part of the range of Mach number and incidence to another. This is illustrated by the results presented in Fig. 18. The curves without hatching are the loci of conditions, or boundaries, for which significant effects of separation - defined by the rapid divergence of trailing-edge pressure - were first encountered in tests on an aerofoil for three different Reynolds numbers. The wind tunnels and transition conditions were the same as those described above for the results in Fig. 17.

The Mach number range has been divided into four parts, starting from the highest, I, which stretches from just over 0.7 upwards, and progressing to IV, which stretches from about 0.56 downwards.

In range I, the separation was induced by a shock well back on the chord at relatively low lift coefficients. Even for the lowest Reynolds number, transition could be fixed well back and still be upstream of the shock, and, moreover, the pressure gradients at the rear were at their weakest for the given design. Model-A flows thus applied for all cases and the effects of Reynolds number on the initial developments of separation were minimal.

In range II, with the shock having moved further forwards, transition was incomplete at the shock for the lowest Reynolds number. The initial developments of separation were thus postponed in relation to the high Reynolds-number results. A more forward transition band may have been beneficial for the upper part of this range but not for the lower part because it would almost certainly have led to rear separations and the spurious results associated with model-B flows.

These spurious results are evident in range III. The presence of rear separation for lift coefficients above about 0.6 is indicated by the appropriate hatched line*.

Rear separation was present even for the highest Reynolds numbers in range IV, and it is difficult to know just how closely the results for these would be representative of full scale. As one moves downwards in Mach number in this range, one approaches the régime of low-speed stall which could involve some rear separation even at full scale. The correct simulation might therefore involve the simulation of the rear separation itself and its interaction with any development of local supersonic flow[13] and shock waves that may be present near the leading edge. As far as the authors know, there have been even fewer systematic studies of scale effects in this range of Mach numbers than in the others.

(c) Swept wings at different Reynolds numbers

Relevant results are available for a wing with 55° of sweep for which the shock-induced separation occurred at low supersonic speeds. The flow was then similar in principle to that for an unswept wing or aerofoil at Mach numbers corresponding to the values of the component normal to the leading-edge of the swept wing. More specifically, tests on the two-dimensional aerofoil corresponding to the section shape normal to the leading edge of the swept wing have confirmed the broad similarity between the two for the pattern of occurrence of the shock-induced and rear separations that were present in the model-B type flows≠. Furthermore, none of the tests on less highly swept, subsonic wings to which the authors have had access has revealed any features that would run counter in a broad qualitative sense to those here described for aerofoils at one extreme and for the 55° swept wing at the other.

The results shown in Fig. 19 were obtained in the NPL 25 in x 20 in tunnel (0.63 m x 0.51 m) - the lowest Reynolds number - and in the ARA 9 ft x 8 ft tunnel (2.74 m x 2.44 m) - the two higher Reynolds numbers. Transition was fixed upstream of the shock in all cases.

The basic section was such that the adverse gradients in the downstream flow produced a tendency to model-B flows. Thus, for the lowest Reynolds number (2×10^6), rear separation was already present at the lowest Mach number (0.9), that is, before the appearance of a shock wave. For this Reynolds number, therefore, one would expect the effects of shock-induced separation to be amplified in a model-B3 type of flow. The differences observed between the results for this Reynolds number and those for the higher ones confirm this, and are strikingly similar to the differences between tunnel and full scale shown for a subsonic swept wing in Fig. 6, and between two different transition positions shown for a two-dimensional aerofoil in Fig. 12.

In all these cases, the differences can be attributed to the effect of differences in the thickness of the turbulent boundary layer approaching the shock.

In the present case, the detailed form of the curve for the lowest Reynolds number at $M_o = 1.145$ suggests that the rear separation spread right forward to the shock at an early stage, linking either with a small bubble (model B3a) or with the shock itself (model B3b). Results are not available at close enough intervals of Mach number to resolve this difference.

The increase in M_o from 0.90 to 1.145 produces an interesting change also in the differences between the curves for the two higher Reynolds numbers (8 and 12×10^6). At $M_o = 0.90$, a small difference in the rear separation is just discernible in the pressures near the trailing edge, but this difference is significantly magnified at $M_o = 1.145$, indicating the great extent to which the rear separation amplifies the differences in the degree of disturbance at the foot of the shock.

---

* The rear separation disappeared as Mach number increased above a certain value because of favourable changes in pressure gradient - and hence boundary-layer growth - upstream of the shock.

≠ Of course, for this highly swept wing, the spanwise drift in the separated flow itself tended to aggravate the severity of the separation, and the shock and separation positions at any given spanwise station were subject to some influence from other parts of the span.

The resulting difference in trailing-edge pressure at $M_0 = 1.145$ could be sufficient to produce a significant difference in circulation. In this case, however, the position of the shock itself was not affected. By the time the free-stream Mach number had increased to 1.35, the separation was fully developed from the shock to the trailing edge with little difference remaining between the two Reynolds numbers.

5. Concluding remarks

For flows that conform to the original model A, the pattern of development depends primarily on changes in the immediate vicinity of the shock, and more on those in the external flow adjacent to the separating boundary layer than on those in the boundary layer itself. This applies particularly to the rapid rearwards growth of the shock bubble and to the manner in which the rapid growth starts at a particular stage. It follows, therefore, that for a given shock strength, at a given condition of free-stream Mach number or incidence, the whole shock-induced phenomenon is relatively insensitive to scale effects, and to differences in boundary-layer thickness or profile, provided the boundary layer is turbulent at the separation point. The full-scale pattern of development can thus be fairly readily simulated in wind-tunnel tests.

For model-B flows, on the other hand, the rear separation - already present or incipient when the shock and the separation at the foot of the shock appear - modulates the rate and magnitude of the development, and in many cases dominates it.

The rear separation at first increases rapidly in severity as the disturbance at the foot of the shock increases, and then links up with this disturbance to modify it directly. This interaction between the two separations produces a significant amplification of the effects of the disturbance at the foot of the shock. The amplification applies in a broad sense to the pattern of development with increasing Mach number or incidence for a given upstream boundary layer, and in a more specific sense to the differences that are introduced by differences in the upstream layer for a given Mach number or incidence. In the broad sense, the repercussions on the circulation about the aerofoil or wing appear earlier than they otherwise would, and in a magnified form. In the specific sense, small changes in the disturbance at the foot of the shock, resulting from differences in the thickness or profile of the boundary layer approaching the shock, assume much greater significance than they otherwise would. It is the amplification of the effects of such changes that, it is postulated, leads to the greatly increased sensitivity to scale effects and to the increased difficulty in achieving correct simulation in wind-tunnel tests.

Recent evidence confirms that a boundary layer that is laminar as it approaches the shock leads to an interaction that cannot be relied upon to reproduce full-scale conditions[4]. The example shown in Fig. 20, from some current tests, is typical of the spuriously favourable effects that are produced when the boundary layer is on the point of transition at the separation point.

The prime requirement for correct simulation thus remains a boundary layer that is turbulent at the point of interaction with the shock. It is now also clear, however, that there is a further requirement of almost equal importance and generality: this turbulent layer must be of a thickness that is <u>not</u> so magnified in relation to full scale (and must have a profile that is <u>not</u> so distorted) that after interaction with the shock it will provoke a rear separation that would <u>not</u> be present at full scale, or will increase significantly the severity of such rear separation as might be present at full scale.

To achieve this second requirement for the cases in which rear separation would not be present at full scale, i.e. model-A would apply at full scale, tunnel Reynolds number should be high enough for transition to occur naturally at an appropriate point or at least high enough for transition to be provoked artificially with a minimal disturbance. Transition has to be complete upstream of the shock but it need not be as far forward as it would be in full scale. The difference in transition position can thus be used to offset the effect of the reduced Reynolds number of the wind-tunnel tests. Moreover, for many cases, the relative thickness of the turbulent layer approaching the shock could be greater than for full scale without provoking the offending rear separation.

The difficulties of achieving either of these alternatives will tend to increase with a number of factors.

First, as attention moves from cruise lift coefficients with shock waves that are well aft on the chord to higher lift coefficients and lower Mach numbers for which the shocks approach the leading edge, so the range of difference in transition position that is available for compensating the effects of reduced Reynolds number becomes smaller and smaller.

Secondly, the same increase in lift coefficient will increase the pressure gradients in the downstream flow and hence reduce the margin of boundary-layer thickness for which rear separation can be avoided.

Finally, the current trends in design towards ultimate limits of acceptable adverse pressure gradient are reducing the margin of boundary-layer thickness for which the spurious rear separations can be avoided even at cruise lift coefficients.

If one turns now to the cases for which some rear separation is present even at full scale (i.e. model-B flow applies at full scale), the simulation of the full-scale pattern for the development of shock-induced separation would appear to present formidable problems. There might, for example, be no real alternative to reproducing the actual boundary-layer thickness at the foot of the shock and hence to a close approach to full-scale Reynolds numbers. This is tantamount to suggesting that higher Reynolds numbers will be necessary than those that are used to give realistic values of C_L max in the low-speed stall for which rear separations, in the form of rear stall, are very frequently inherent. The underlying justification for such a suggestion is that the shock-induced separation upstream of the rear separation introduces a critical factor that is not always present in the low-speed stall. The scale effects are larger as a result and may not decrease to negligible proportions until the higher Reynolds number is reached.

For such cases, and also for the cases where it was suggested that there would be no margin of boundary-layer thickness (relative to wing chord) above the full-scale value for which rear separation could be avoided, some further systematic theoretical investigations of the type made by Thomas[8] would be a valuable complement to the additional experimental work that is clearly desirable. Such investigations could, for example, be based on a flow model in which the turbulent boundary-layer growth up to rear separation could be studied in the presence of representative pressure gradients, with a rapid gradient representing the shock superimposed on the more gradual adverse gradient. Boundary-layer thickness, Reynolds number and pressure gradient could be varied parametrically. It is difficult to envisage that the precise nature of the disturbance at the foot of the shock could be introduced theoretically, especially since this usually involves a separation bubble that is critically influenced by the form of the compression from supersonic to subsonic flow, but the effect of the disturbance could probably be simulated by a variable disturbance to boundary-layer thickness and profile.

In the meantime, the evidence available to the authors is inconclusive as to what value of chord Reynolds number may ultimately have to be used to eliminate the scale effects of the type now being encountered. But this could well be at least of an order of magnitude greater than the value of about 1.5 to 2×10^6 that was acceptable when the original flow model was applicable for all conditions.

LIST OF REFERENCES

1. H.H. PEARCEY — Some effects of shock-induced separation of turbulent boundary layers in transonic flow past aerofoils. ARC R & M No. 3108. (1955)

2. H.H. PEARCEY — A method for the prediction of the onset of buffeting and other separation effects from wind-tunnel tests on rigid models. ARC 20 631 ; AGARD Report 223. (1958)

3. H.H. PEARCEY and D.W. HOLDER — Simple methods for the prediction of wing buffeting resulting from bubble-type separation. ARC 23 884 ; NPL Aero Report 1024. (1962)

4. A.B. HAINES, D.W. HOLDER and H.H. PEARCEY — Scale effects at high subsonic and transonic speeds, and methods for fixing boundary-layer transition in model experiments. ARC R & M No. 3012 (1954)

5. J. SEDDON — The flow produced by interaction of a turbulent boundary layer with a normal shock wave of sufficient strength to cause separation. ARC R & M No. 3502 (1960)

6. H.H. PEARCEY and D.W. HOLDER — Examples of the effects of shock-induced boundary layer separation in transonic flight. ARC R & M No. 3510 (1954)

7. B.H. LITTLE Jr. — Effects of initial turbulent boundary layer on shock-induced separation in transonic flow. V.K.I. Technical Note No. 39 (1967)

8. F. THOMAS — The determination of buffet boundaries for wings in the transonic speed régime. W.G.L.R. Jahrbuch, 1966, pp 126.

9. C.S. SINNOTT and J. OSBORNE — Review and extension of transonic aerofoil theory. ARC R & M No. 3156 (1958)

10. G.E. GADD — Interactions between normal shock waves and turbulent boundary layers. ARC R & M No. 3262 (1961)

11. D.L. LOVING — Wind tunnel - flight correlation of shock-induced separated flow. NASA TN D-3580 (1966)

12. H.H. PEARCEY — Shock-induced separation and its prevention by design and boundary layer control. Part IV Boundary layer and flow control; edited by G.V. Lachmann; Vol. 2, Pergamon Press (1961)

13. L.R. WOOTTON — The effect of compressibility on the maximum lift coefficient of aerofoils at subsonic speeds. J.Roy.Aero.Soc. Vol.71, No.679, July 1967.

14. H.A. CARVER and M.M. PAYNE — Tabulated pressure coefficients and aerodynamic characteristics measured on the wing of the Bell X-1 Airplane in level flight at Mach numbers from 0.79 to 1.00 and in a pull up at a Mach number of 0.96. NACA RM L50 H 25 (1950).

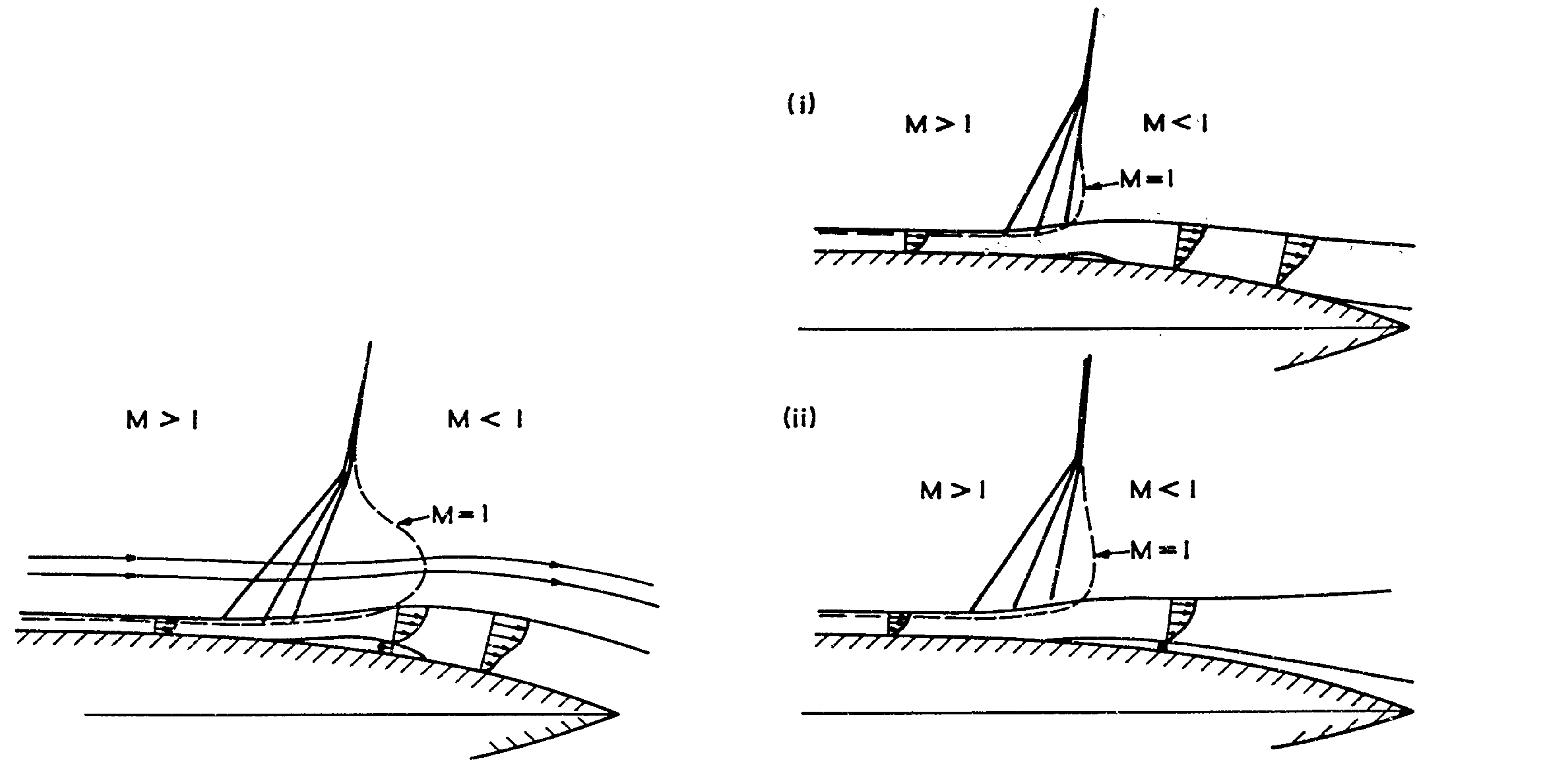

(a) Model A at expanding bubble stage

(b) Model B (i) at early stage with localised shock bubble <u>and</u> rear separation
(ii) at later stage with one separation extending from shock to trailing edge

FIG. 1 SOME DETAILS (SCHEMATIC) OF THE REGION OF INTERACTION BETWEEN TURBULENT BOUNDARY LAYER AND SHOCK WAVE

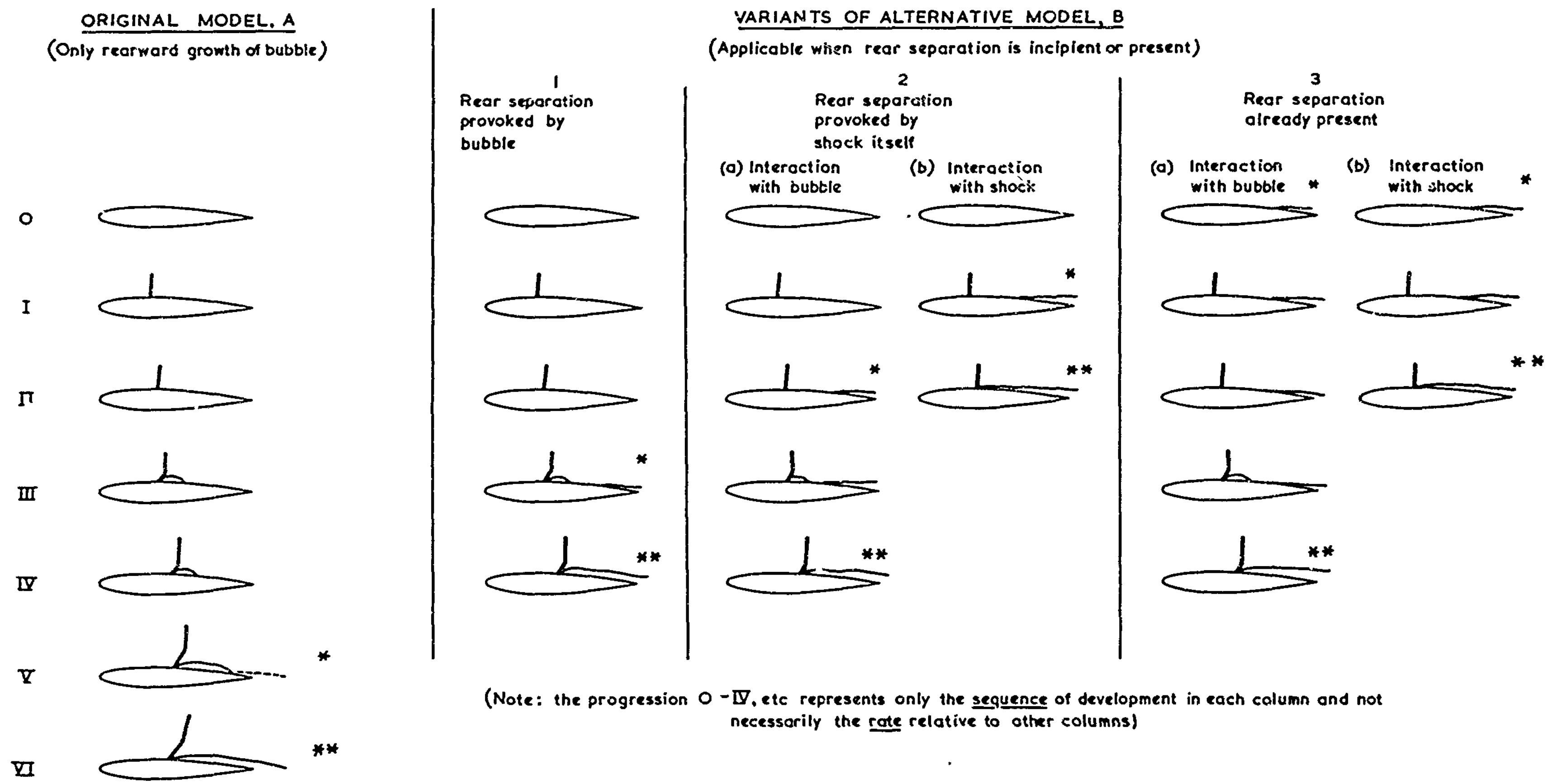

FIG. 2 ; FLOW MODELS FOR THE INITIAL DEVELOPMENT OF SHOCK INDUCED SEPARATION (SCHEMATIC); TURBULENT BOUNDARY LAYERS

(Successive stages in a Mach number or incidence increase)

Shock
Bubble at foot of shock
Rear separation in downstream pressure gradient
Separation from shock to trailing edge
* First divergence in trailing-edge pressure (first effect on circulation)
** Rapid divergence in trailing-edge pressure (major effects on circulation)

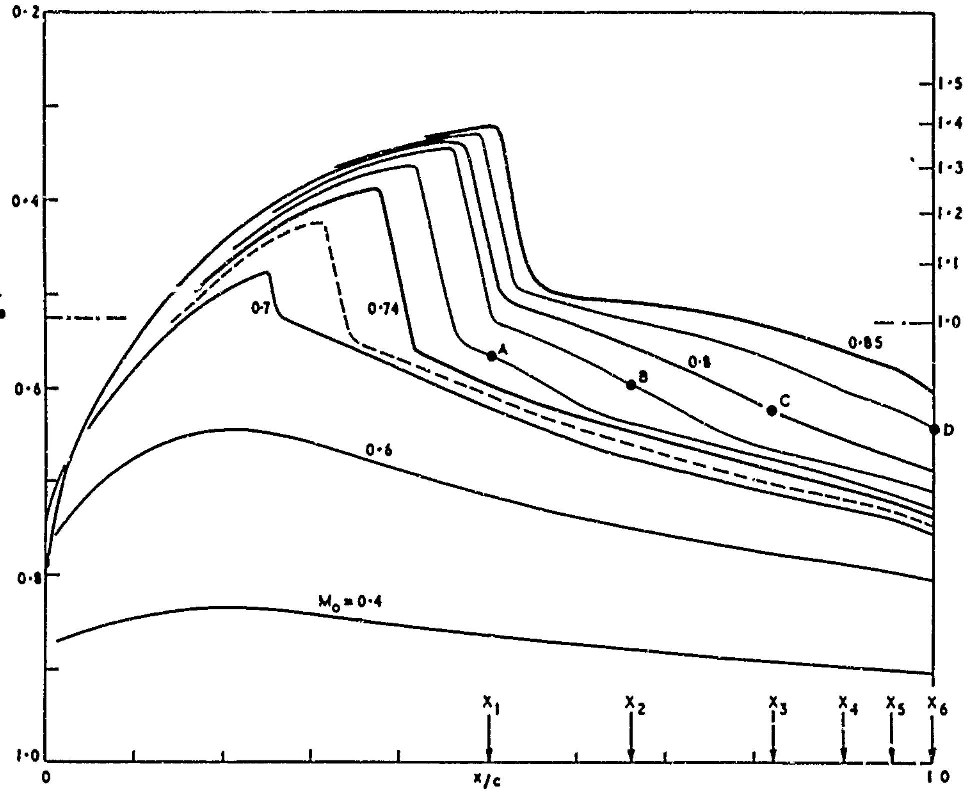

FIG.3 BUBBLE DEVELOPING REARWARD FROM FOOT OF SHOCK (FLOW MODEL B) $M_0 = 0·74$ to 0·85

(Upper-surface pressure distributions for NPL 9230 aerofoil at 2° incidence; transition fixed at 0·05c; $R = 1·1$ to $1·9 \times 10^6$)

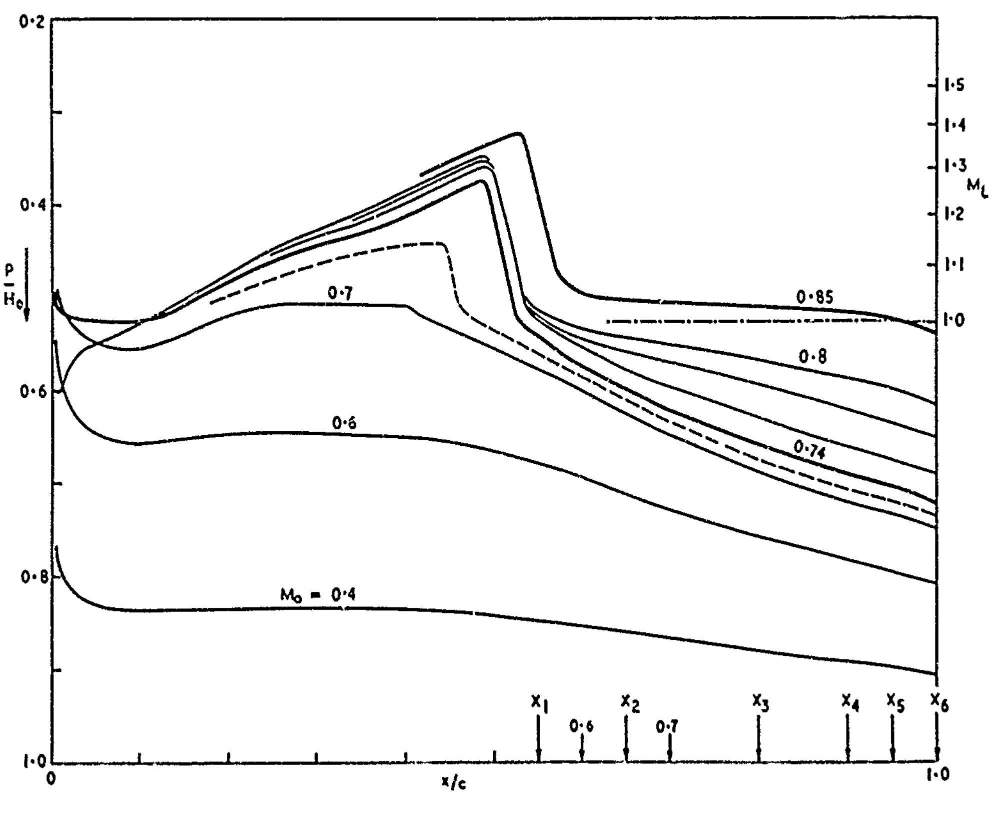

FIG.4 SHOCK SEPARATION LINKING IMMEDIATELY WITH REAR SEPARATION (FLOW MODEL B), $M_0 = 0·74$ TO 0·85

(Upper surface pressure distributions for NPL 9240 at 3·5° incidence; transition fixed at 0·05 chord; $R = 1·1$ to $1·9 \times 10^6$)

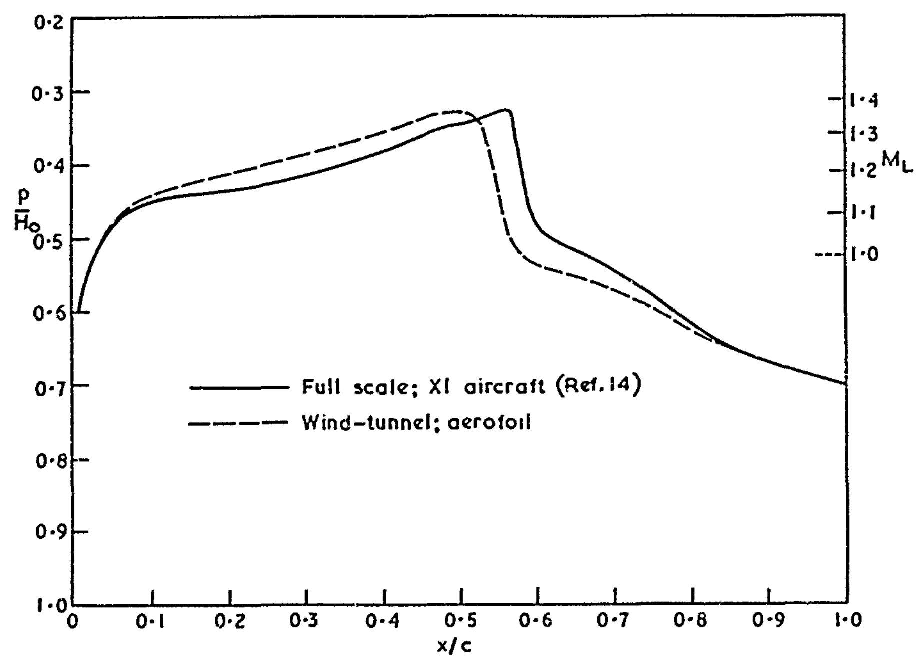

FIG. 5 CLOSELY SIMILAR UPPER-SURFACE PRESSURE DISTRIBUTION IN TUNNEL AND FLIGHT — FLOW MODEL A

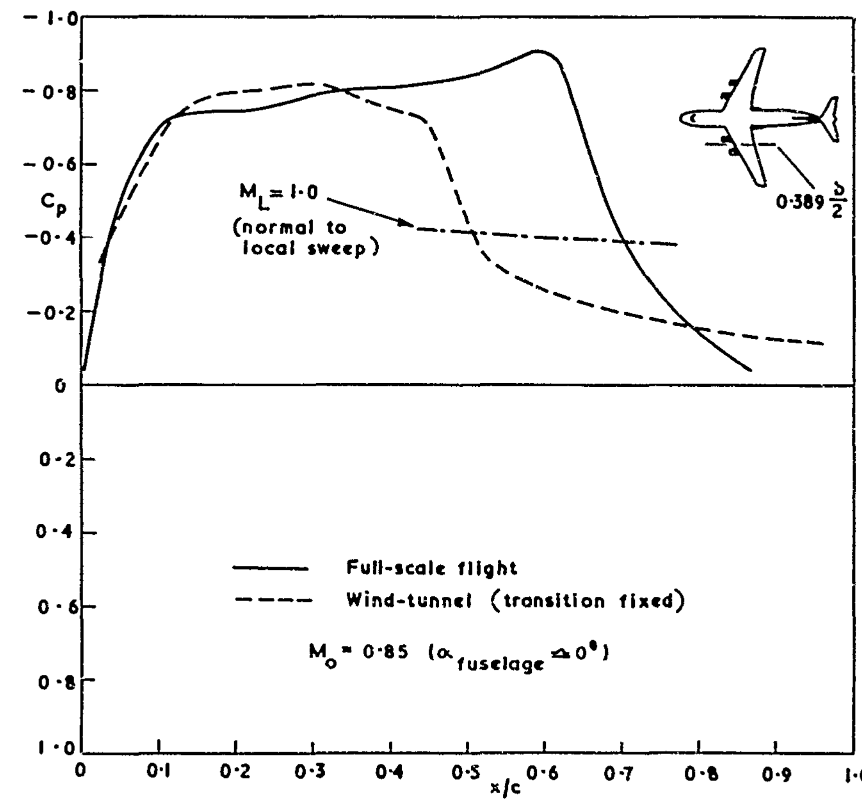

FIG.6 WIDELY DISSIMILAR UPPER-SURFACE PRESSURE DISTRIBUTIONS — MODEL B TYPE FLOW (From Ref.11)

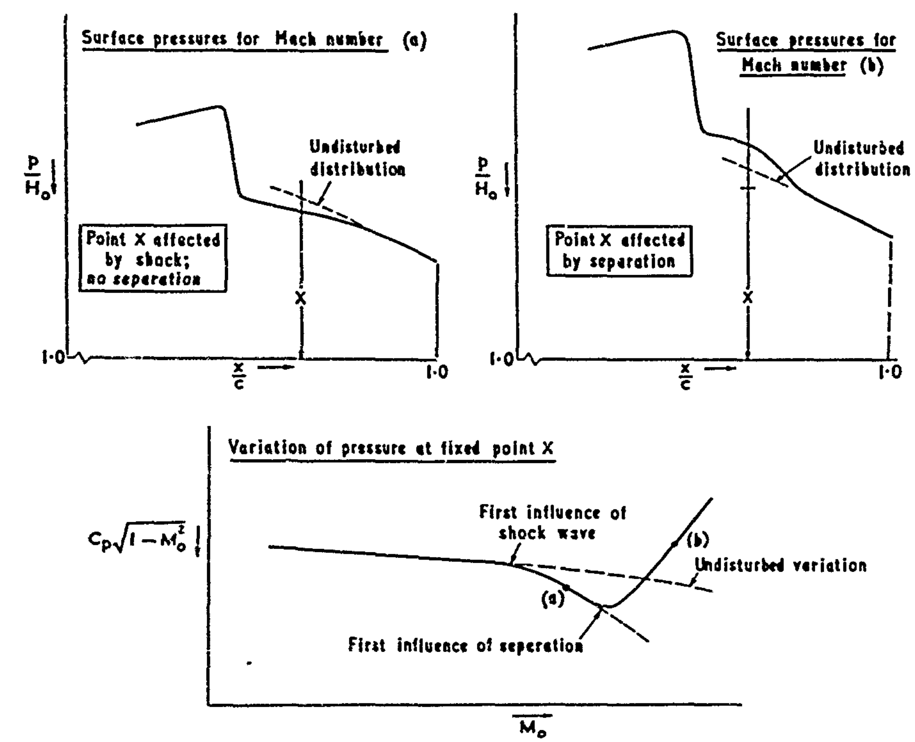

FIG.7 PRESSURE TOWARDS REAR OF AEROFOIL, SHOWING FIRST THE INFLUENCE OF THE SHOCK WAVE AND THEN OF THE SHOCK-INDUCED BUBBLE SEPARATION
(MODEL A FLOW)
(KEY TO FIG.8)

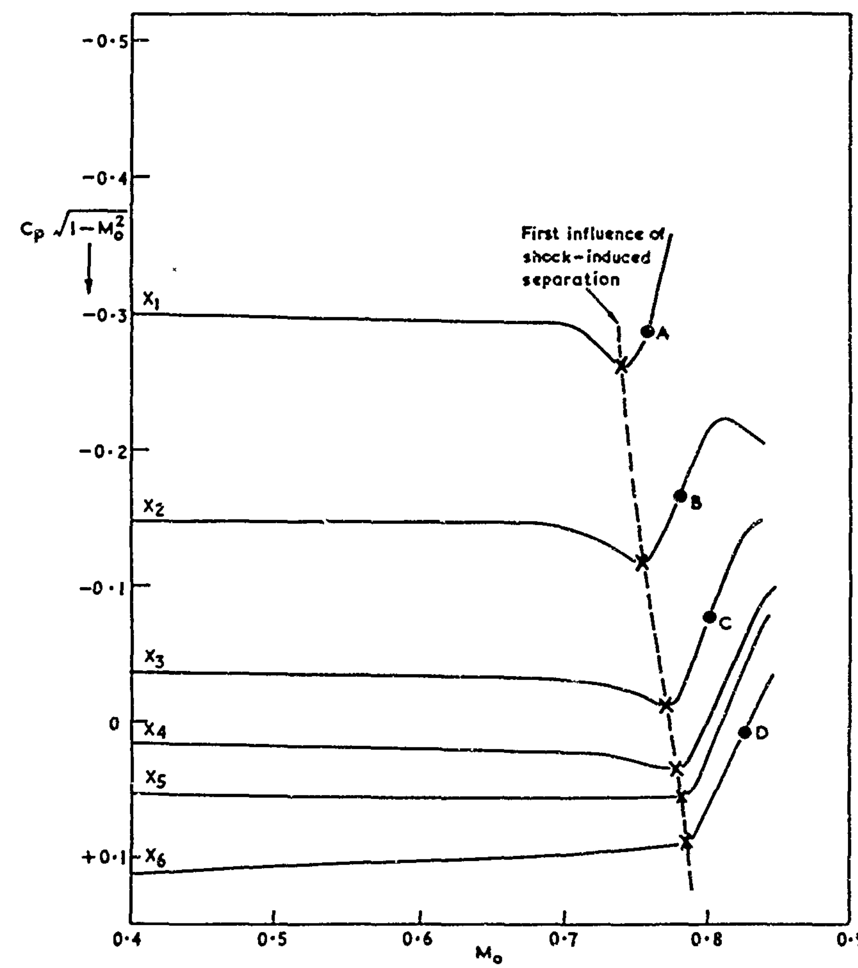

FIG. 8 PRESSURES AT FIXED CHORDWISE POSITIONS FOR STRAIGHTFORWARD BUBBLE DEVELOPMENT (MODEL A); (Cross-plotted from Fig. 3)

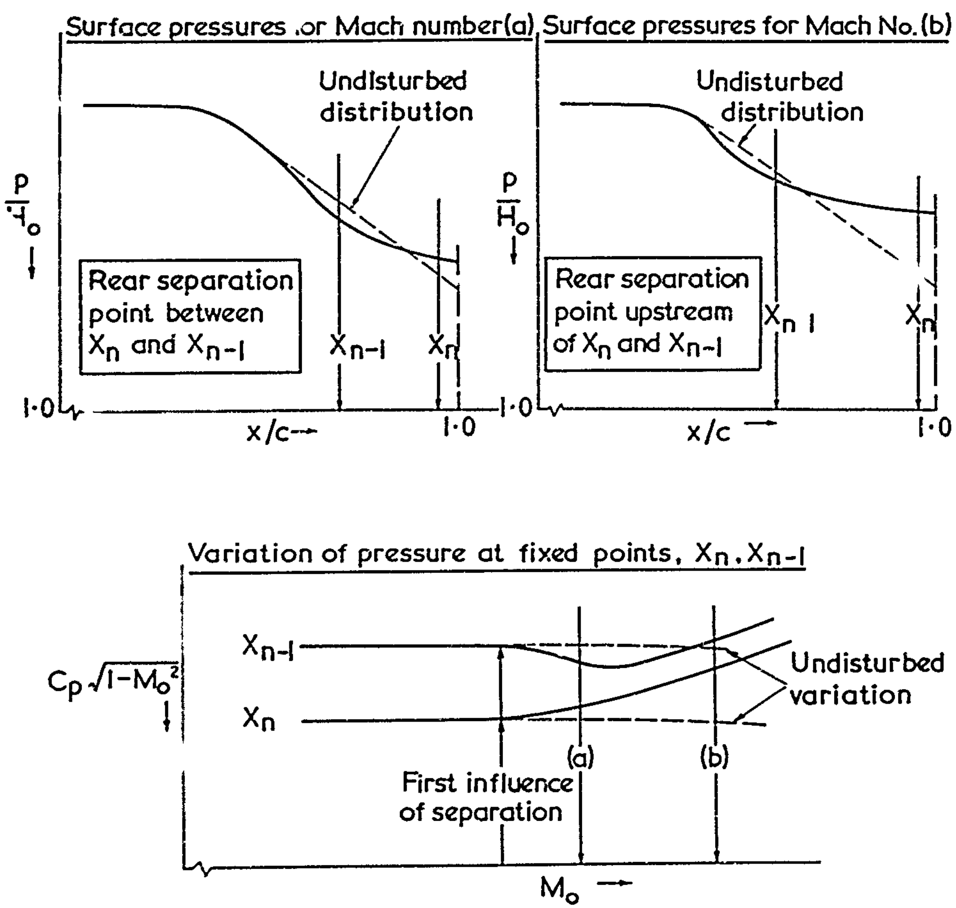

FIG. 9: PRESSURES TOWARDS REAR OF AEROFOIL SHOWING INFLUENCE OF REAR SEPARATION ONLY (KEY TO FIG. 10)

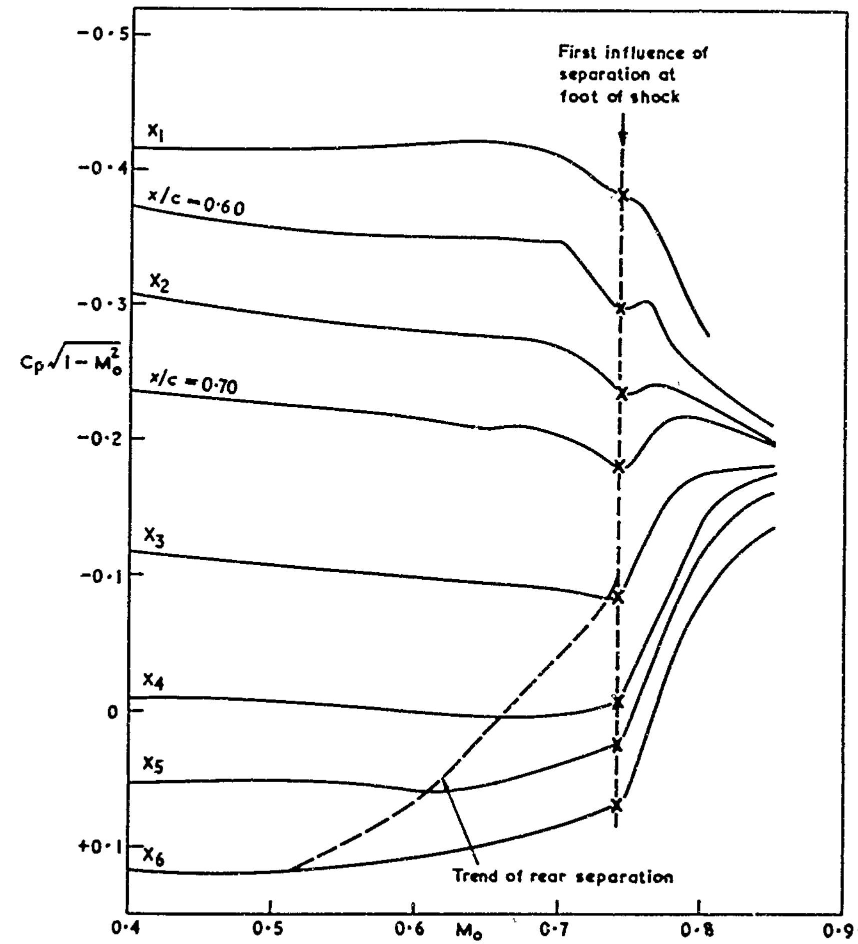

FIG. 10 PRESSURES AT FIXED CHORDWISE POSITIONS FOR REAR SEPARATION INTERACTING WITH SHOCK SEPARATION (MODEL B);

(Cross-plotted from Fig. 4)

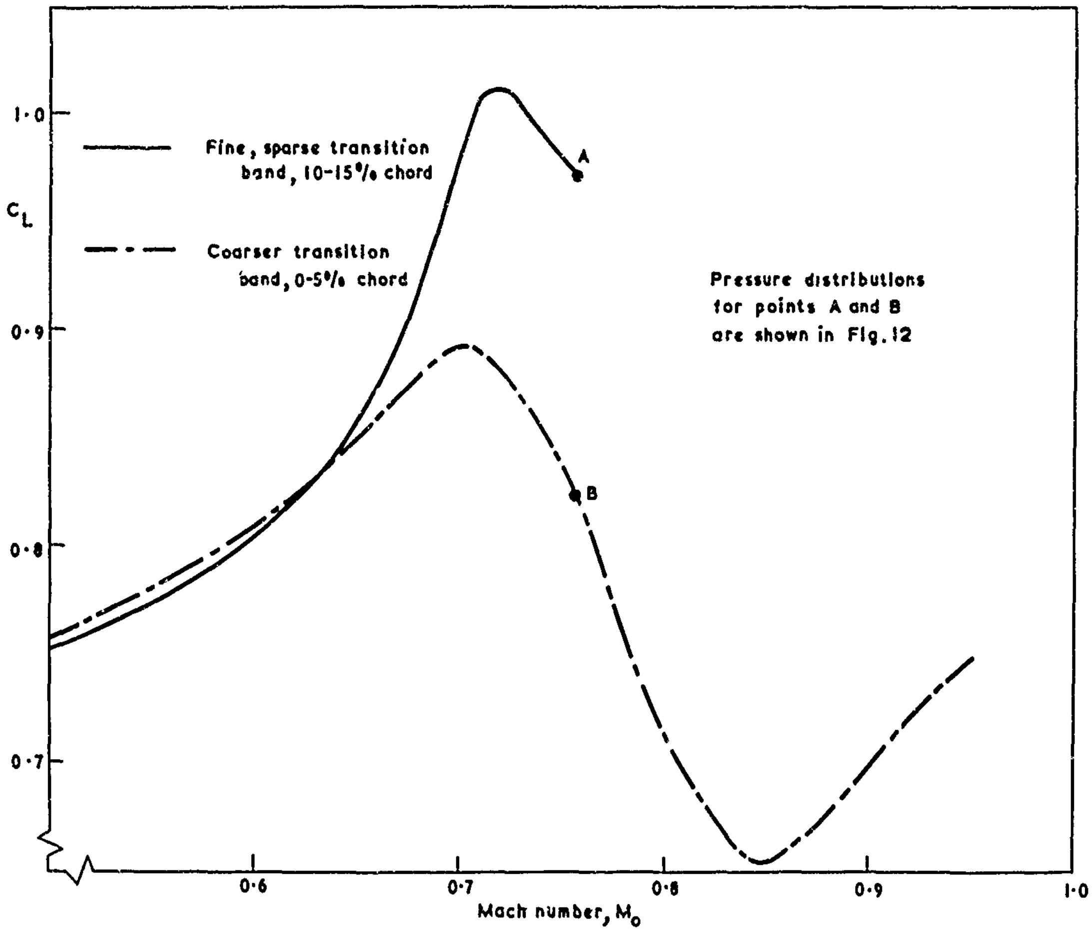

FIG 11 INFLUENCE OF BOUNDARY-LAYER THICKNESS ON EFFECT OF SHOCK-INDUCED SEPARATION OF TURBULENT BOUNDARY LAYERS FOR MODEL B-TYPE DEVELOPMENT (NPL 9240 AT 5·5° INCIDENCE, $R = 1·3$ to $2·0 \times 10^6$)

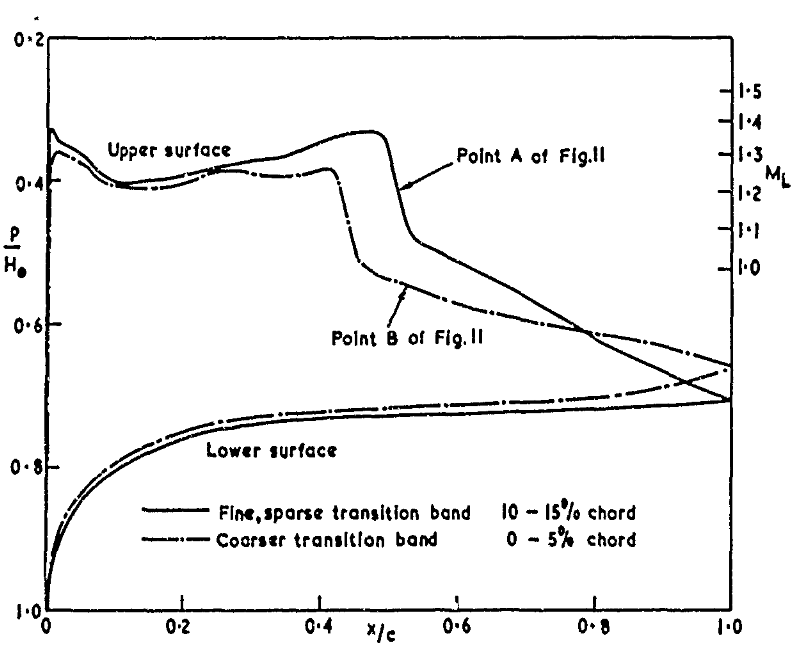

FIG.12 PRESSURE DISTRIBUTIONS FOR POINTS A and B OF FIG.11 ; $M_0 = 0·76$, $R \sim 1·8 \times 10^6$

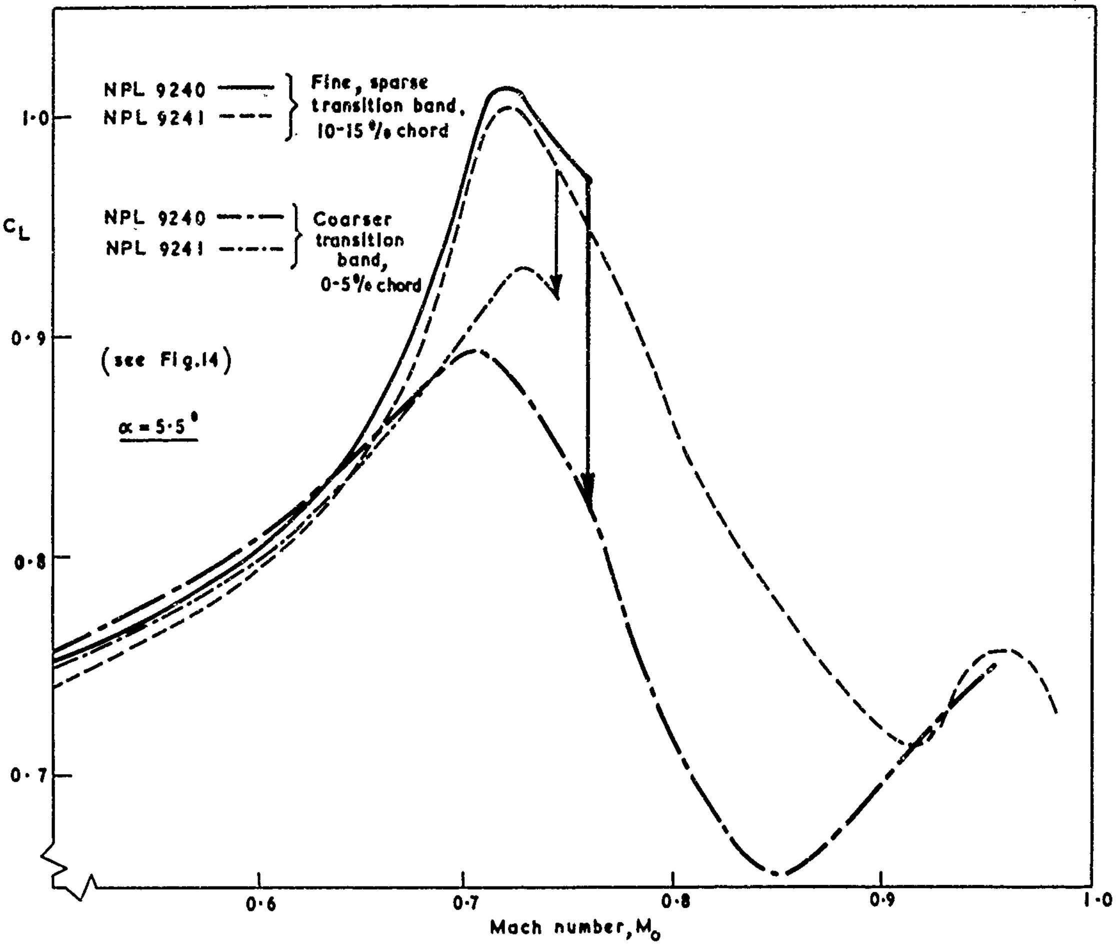

FIG.13 "SCALE EFFECTS" (INFLUENCE OF THICK BOUNDARY LAYERS) MAGNIFIED BY SMALL CHANGES IN AEROFOIL SHAPE, OR, CONVERSELY, EFFECTS OF AEROFOIL SHAPE MAGNIFIED BY SCALE EFFECTS (MODEL B – TYPE FLOW)

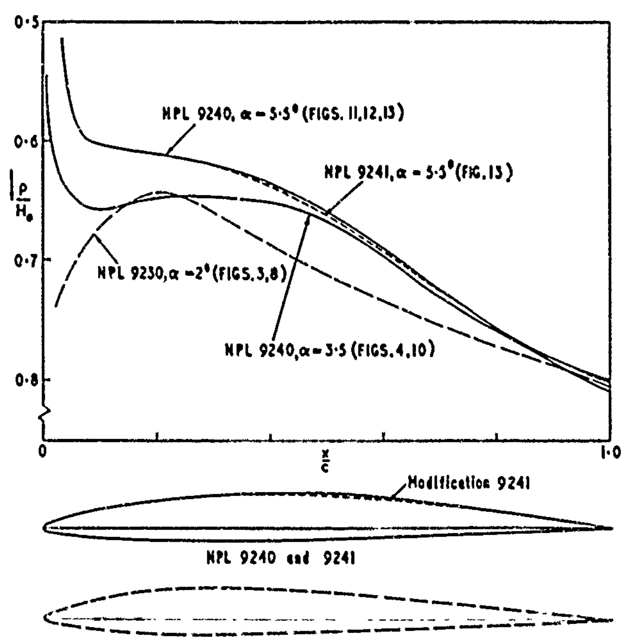

FIG.14 AEROFOIL SHAPES AND LOW-SPEED (H_o = 0·6) PRESSURE DISTRIBUTIONS (Upper surface only)

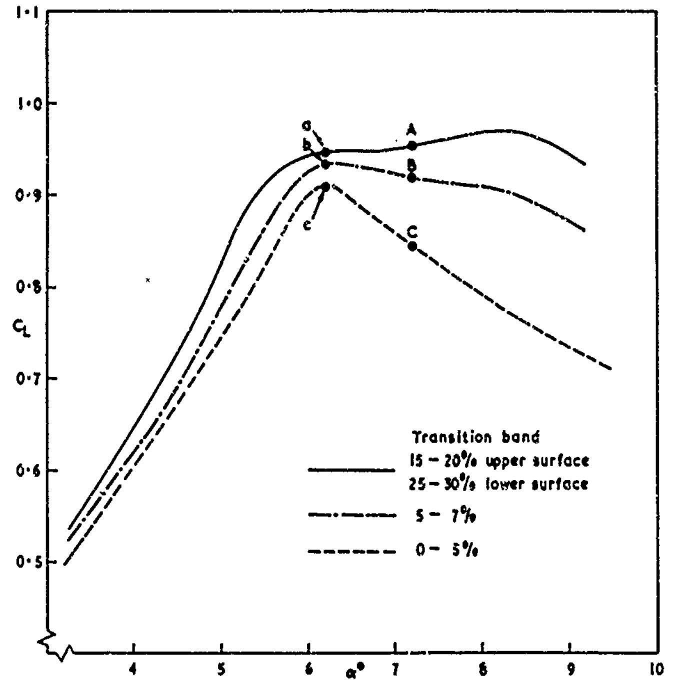

FIG. 15 MAGNIFICATION OF EFFECTS OF BOUNDARY-LAYER THICKNESS NEAR $C_{L_{max}}$ (NPL 3121 at M_0 = 0·66, R = 1·6 x 10^6)

(See also Fig.16)

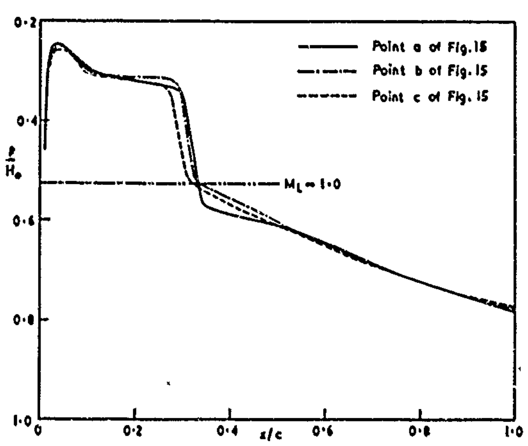

FIG.16a UPPER SURFACE PRESSURE DISTRIBUTIONS FOR POINTS a, b and c OF FIG.15 (NPL 3121 AT M_0=0·66, α = 6·2°, R = 1·6 x 10^6)

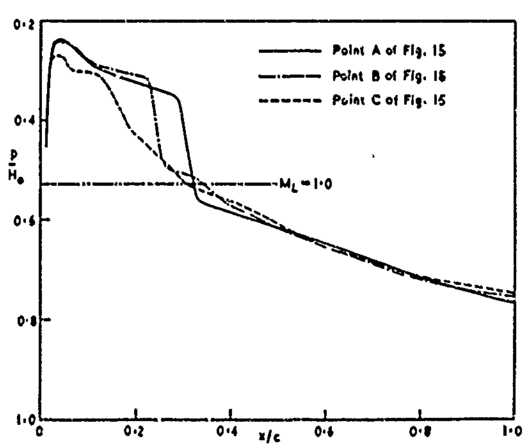

FIG 16b UPPER SURFACE PRESSURE DISTRIBUTIONS FOR POINTS A, B AND C OF FIG. 15 (NPL 3121 at M_0=0·66, α = 7·2°, R=1·6 x 10^6)

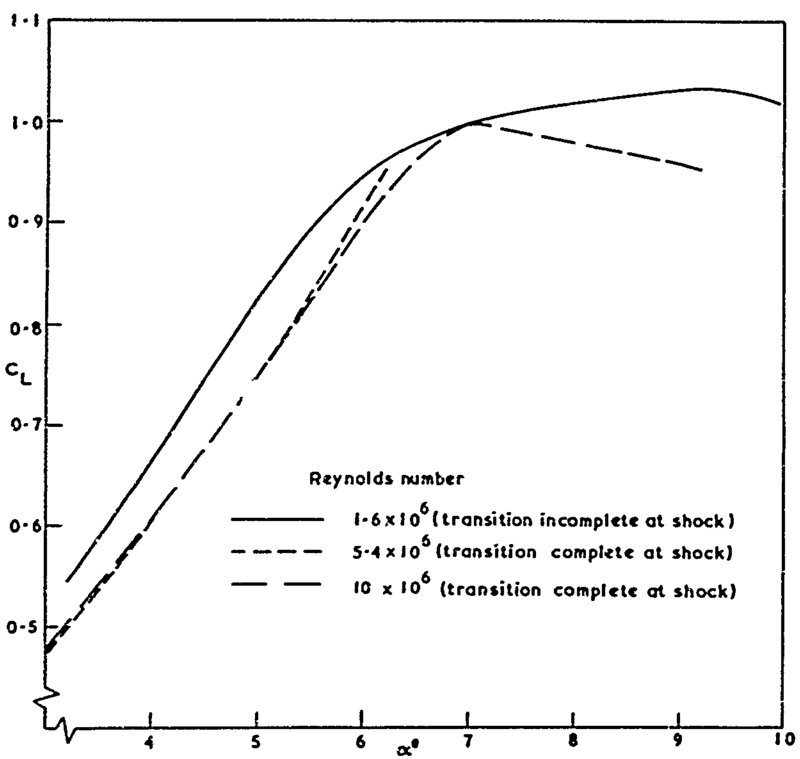

FIG. 17 EFFECTS OF REYNOLDS NUMBER ON A SHOCK-INDUCED STALL (NPL 3111 AEROFOIL AT M_o=0·66)

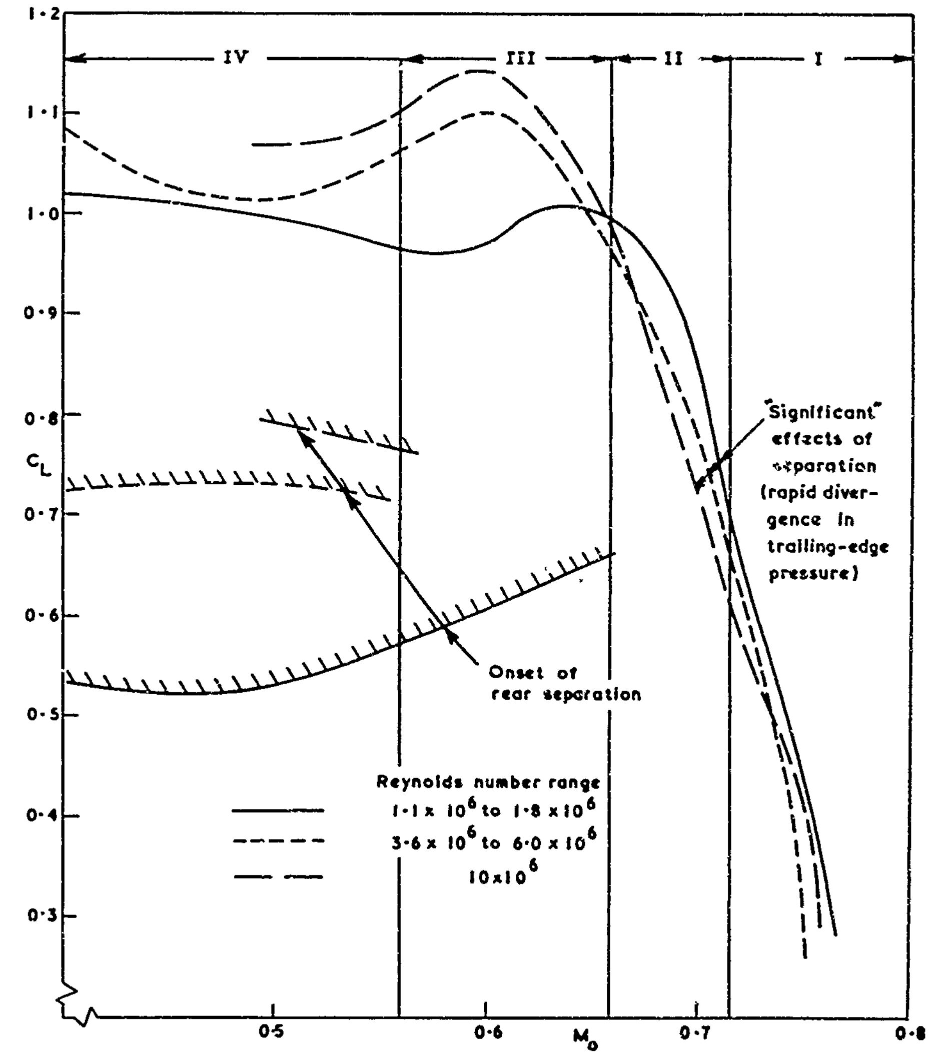

FIG. 18 BOUNDARIES FOR SIGNIFICANT EFFECTS OF SEPARATION, SHOWING HOW THE INFLUENCE OF REYNOLDS NUMBER VARIES THROUGHOUT THE $C_L - M_o$ PLANE (NPL 3111 AEROFOIL)

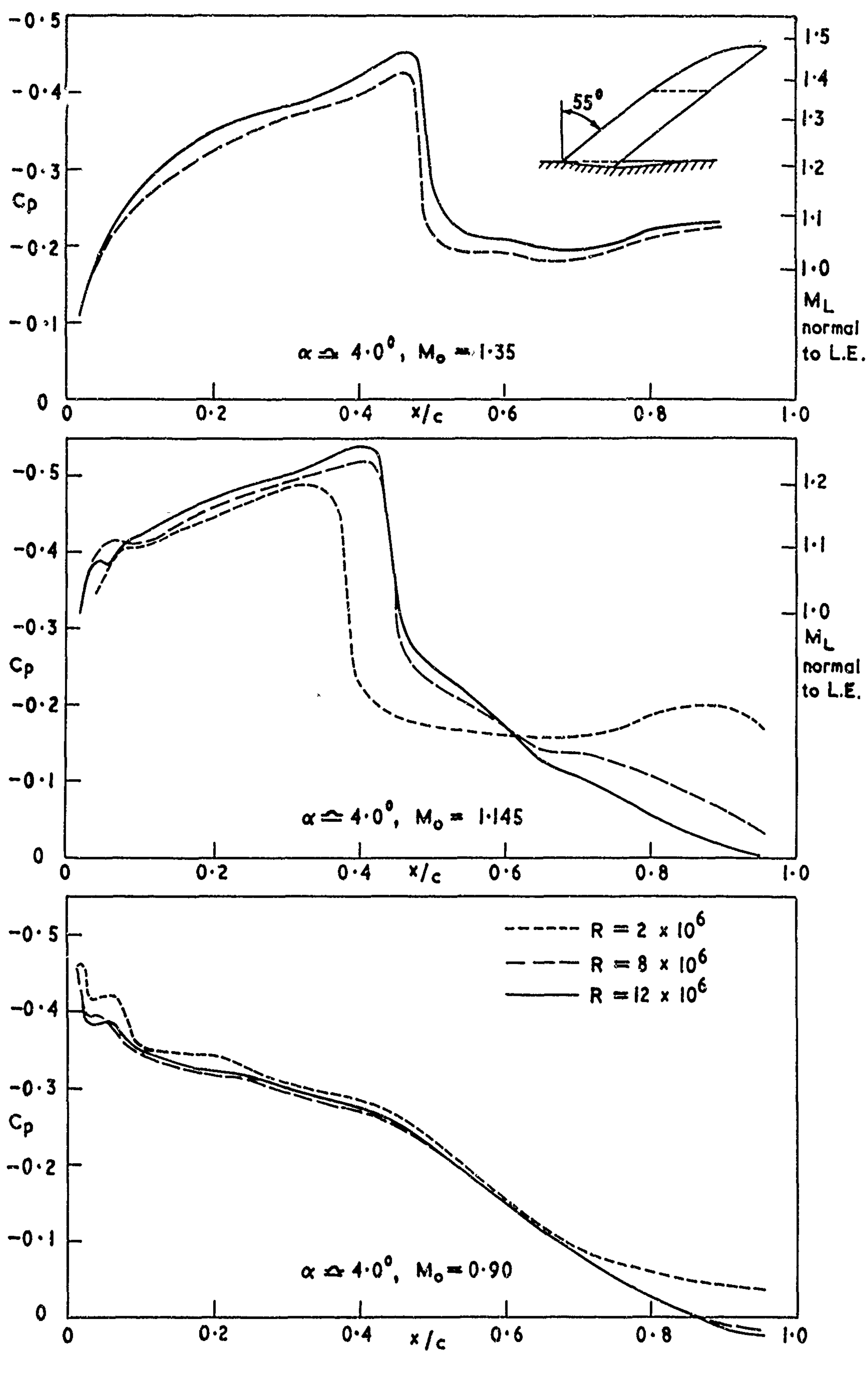

FIG. 19 EFFECT OF REYNOLDS NUMBER FOR A HIGHLY SWEPT WING WITH TENDENCY TO MODEL B FLOW

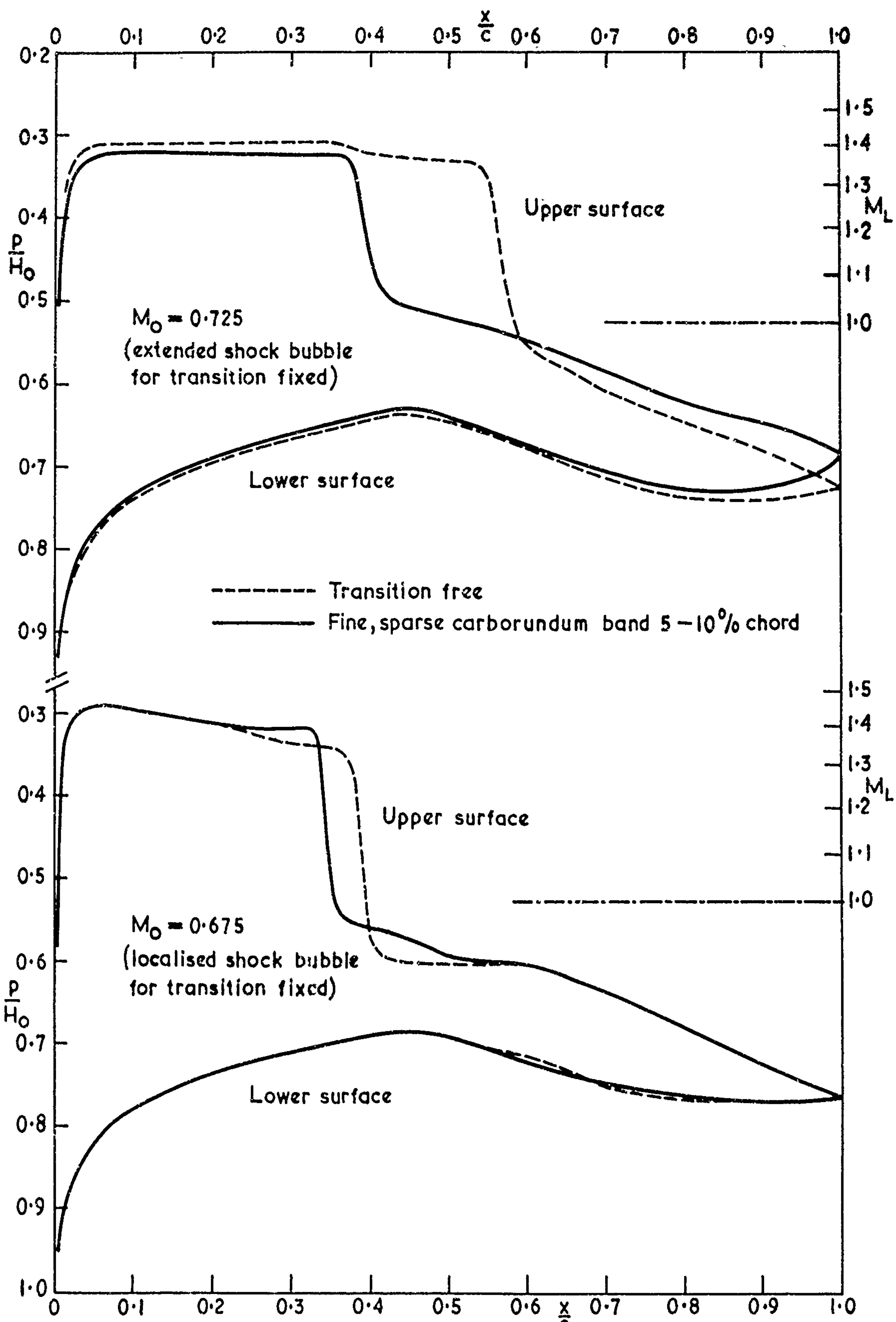

FIG. 20; A RECENT EXAMPLE OF SPURIOUSLY FAVOURABLE RESULTS
(More rearward shock position and greater circulation at $M_o = 0{\cdot}725$)
Obtained when transition is incomplete at the shock;
NPL 5201 aerofoil; $\alpha = 5^\circ$; $R \approx 1{\cdot}7 \times 10^6$; pressure distributions

The Prediction of Aerofoil Pressure Distributions for Sub-Critical Viscous Flows

by

R.C. Lock, Aerodynamics Division, National Physical Laboratory
B.J. Powell, Kingston College of Technology
C.C.L. Sells, Aerodynamics Department, Royal Aircraft Establishment
and P.G. Wilby, Aerodynamics Division, National Physical Laboratory.

Summary

The paper summarises recent advances in practical methods for predicting pressure distributions on aerofoils in two-dimensional sub-critical flows. First, a finite difference method is described for solving numerically the full equations of motion for compressible flow, starting with a conformal mapping of the region exterior to the aerofoil onto the inside of a circle. Next, it is shown how standard second order theory can be modified and extended to provide a rapid approximate method which gives adequate accuracy for most aerofoils up to the critical Mach number; several comparisons with exact theory are given. Finally, an iterative method is described for estimating the effect of viscosity, calculating successively the displacement effect of the boundary layer and wake on the aerofoil pressure distribution, and the development of the boundary layer under a given external pressure distribution; several comparisons are given with recent experimental results.

1. Introduction

An essential item in the equipment of an aircraft designer or project engineer is the capability of predicting accurately the pressure distribution on an aerofoil in a real compressible viscous flow; the information is needed for example in the estimation of drag-rise Mach number or the calculation of profile drag - in either case at a given value of the lift coefficient or incidence. Now it is clear that in practice the development of the flow field about an aerofoil is crucially dependent on two effects, compressibility and viscosity; and this fact has made the problem a difficult one to solve satisfactorily, even for sub-critical flow. In the past it has been necessary to rely on a variety of approximate or empirical methods for the inviscid part of the problem, all of doubtful validity and although the general principles whereby the influence of viscosity can be obtained, through the displacement effect of the boundary layer and wake, have been known for some time (see e.g. Ref. 11), it has not previously proved feasible to incorporate these efficiently into a practical calculation method.

In the past few years important developments in inviscid theory have been made by Sells[1] and Nieuwland[2], using advanced numerical methods in conjunction with the full equations of motion for a perfect gas; and these have at last enabled us to break the vicious circle that has previously bedevilled the problem, by removing the empiricism from one half of it. It has thus become possible to effect a major improvement in accuracy in a rapid approximate theory for inviscid flow, using the 'exact' numerical methods as a check; and then to incorporate this method into an iterative procedure for calculating the effect of the boundary layer on the pressure distribution, by applying the principle mentioned above in conjunction with an appropriate calculation method for laminar and turbulent boundary layers.

The purpose of the present paper is to give a survey of the developments mentioned in the previous paragraph. First, a brief account is given of the principles used in the 'exact' method of Ref. 1 for the inviscid problem. In the next section it is shown how standard second order theory can be modified and extended to give acceptable accuracy for most aerofoil shapes up to the critical Mach number, and a number of comparisons with exact results are given. In the final section we describe a method for estimating the major effects of the boundary layer, and conclude with comparisons with experimental results for two aerofoils over a range of Mach number and incidence.

2. Numerical method for the solution of the full equations of motion for inviscid compressible flow

The method, which is described in detail in Ref. 1, depends on the existence of a conformal mapping of the aerofoil and its exterior in the z plane onto the unit circle and its interior in the σ plane; we will assume that such a mapping has been done, numerically or analytically. Then plane polar coordinates (r, θ) are set up in the circle (σ) plane and a uniform grid in these variables is used as a computing grid (see sketch (a)); this has the advantage that in the physical (z) plane the grid is refined near the nose and tail, where flow variations are greatest (see sketch (b)).

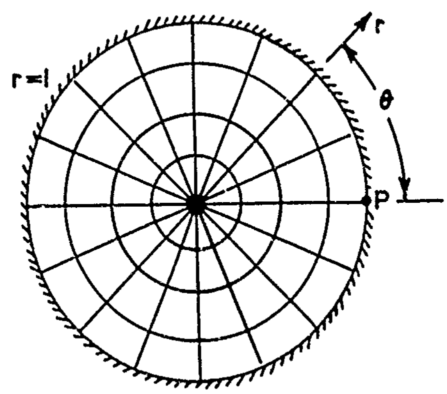

$\boxed{\sigma = re^{i\theta}}$

Sketch (a): Regular grid in the working (σ) plane

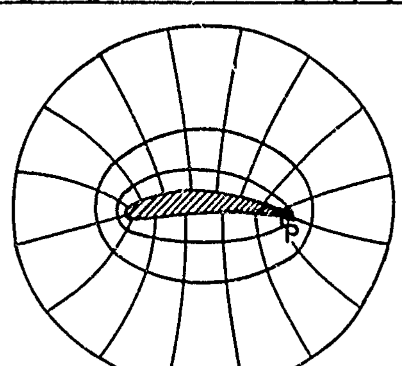

$\boxed{z = x + iy}$

Sketch (b): Grid in the physical (z) plane

The equations to be solved are:

the equation of continuity $\quad \operatorname{div}(\rho \underline{q}) = 0$, $\quad$ ... (2.1)

the equation of irrotational flow $\quad \operatorname{curl} \underline{q} = 0$, $\quad$ ... (2.2)

and Bernouilli's equation for isentropic flow, written in the form

$$\frac{\rho^{\gamma-1}}{(\gamma-1)M_\infty^2} + \tfrac{1}{2} q^2 = \frac{1}{(\gamma-1)M_\infty^2} + \tfrac{1}{2}, \qquad \text{... (2.3)}$$

where ρ is the density (scaled with respect to free stream density)
M_∞ is the free stream Mach number
$\underline{q}$ is the local velocity (scaled with respect to free stream velocity)
and γ is the ratio of specific heats.

Taking $\rho q = f$ (the local mass flow)
and $\tau = \rho/\rho_0$ (suffix o indicates stagnation conditions),
Bernouilli's equation (2.3) can be re-written in the universal form (independent of Mach number)

$$F = \tau^2(1-\tau^{\gamma-1}) \,. \qquad \text{... (2.4)}$$

where

$$F = \tfrac{1}{2}(\gamma-1)\, f^2/(\rho_0{}^2 a_0{}^2) \,.$$

The continuity equation (2.1) admits the introduction of a stream function ψ, such that

$$u_r = \frac{1}{\rho h_2}\frac{\partial\psi}{\partial\theta}, \quad u_\theta = -\frac{1}{\rho h_1}\frac{\partial\psi}{\partial r}$$

where u_r, u_θ are the velocity components in the physical plane normal to the curves corresponding to r = constant, θ = constant respectively in the σ plane (see sketches (a) and (b)), and h_1, h_2 are the curvilinear metrics, given by $h_1 = B$
$h_2 = rB$

$$\text{and } B = \left|\frac{dz}{d\sigma}\right|$$

The equation of irrotational flow (2.2) can then be written in the form

$$\frac{\partial}{\partial r}\left(\frac{r}{\rho}\frac{\partial\psi}{\partial r}\right) + \frac{\partial}{\partial\theta}\left(\frac{1}{r\rho}\frac{\partial\psi}{\partial\theta}\right) = 0 \,. \qquad \text{... (2.5)}$$

Finally, the mass flow f is related to the stream function by

$$f = \frac{1}{B}\left\{\frac{1}{r^2}\left(\frac{\partial\psi}{\partial\theta}\right)^2 + \left(\frac{\partial\psi}{\partial r}\right)^2\right\}^{\frac{1}{2}} \qquad \text{... (2.6)}$$

Before the fundamental system of equations (2.4), (2.5) and (2.6) can be solved numerically, it is necessary to consider the singular behaviour of the stream function at the centre of the basic circle in the σ plane, corresponding to the 'point at infinity' in the physical (z) plane.

It can be shown (see Ref. 1) that near $r = 0$

$$\psi \sim -\frac{1}{r}\sin(\theta+\alpha) + E\ln r - \tfrac{1}{2}E\ln\left[1-M_\infty^2\sin^2(\theta+\alpha)\right] + \beta + O(r) \qquad \text{... (2.7)}$$

and that

$$\rho \sim 1 - \frac{M_\infty^2 E\sin(\theta+\alpha)}{1-M_\infty^2\sin^2(\theta+\alpha)}\, r + O(r^2) \,; \qquad \text{... (2.8)}$$

here α is the angle of incidence of the aerofoil and E and β are constants, to be determined as part of the solution. It is seen that the stream function has two singularities at the centre of the circle; the first, of dipole type, corresponding to the undisturbed stream in the physical plane, and the second, of vortex type, due to the circulation round the aerofoil. The constant E is in fact directly related to the circulation Γ, by the equation

$$\Gamma = -\frac{2\pi E}{\sqrt{(1-M_\infty^2)}} \qquad \text{... (2.9)}$$

and is determined by satisfying the Kutta condition of zero velocity at the trailing edge of the aerofoil.

In order to arrive at a numerically regular problem, the two singular terms have to be subtracted from ψ, giving a modified stream function

$$\chi(r,\theta) = \psi + \frac{1}{r}\sin(\theta+\alpha) - E\ln r \qquad \ldots (2.10)$$

which is finite everywhere but whose value at $r = 0$ depends on the angle θ:

$$\chi(0,\theta) = -\tfrac{1}{2}E\ln\left[1-M_\infty^2\sin^2(\theta+\alpha)\right] + \beta \qquad \ldots (2.11)$$

The corresponding boundary condition on $r = 1$, derived from the condition $\psi = 0$, is

$$\chi(1,\theta) = \sin(\theta+\alpha) \qquad \ldots (2.12)$$

The two equations (2.5) and (2.6) involving ψ are written in terms of χ, and all partial derivatives occurring in these equations are replaced by central differences on the uniform (r,θ) mesh in the σ plane (see sketch (a)); the truncation errors are thus of second order in mesh size. There are four basic unknowns to be determined: the stream function $\psi(r,\theta)$ (or the modified χ), the density ratio $\rho(r,\theta)$; the circulation parameter E; and the parameter β.

The solution proceeds iteratively, starting with the basic elliptic partial differential equation (2.5) (written in terms of χ), together with the boundary conditions (2.11) and (2.12). The resulting difference equations are soved by block Gauss-Seidel iteration (see Ref. 1 for details). Next, the Kutta condition is used to calculate the parameter E; and the second parameter β is determined by means of Kelvin's circulation theorem, thus ensuring that the circulation round any basic circuit, corresponding to r = constant in the σ plane, really is Γ. Finally, the density ρ is found from equations (2.6) and (2.4); and the whole process is repeated until convergence is obtained.

The criterion used for convergence is the density ratio ρ; since it changes rapidly when the local Mach number M approaches unity, but only slowly when M is small, this test is coarse for near-incompressible flows but is delicate for near-critical flows. When M exceeds about 0.8 it is necessary to employ under-relaxation in the iterative matrix solution for the modified stream function χ. If a supercritical case is attempted, the under-relaxation factor (which is automatically modified in the program) decreases rapidly, and when it is less than 1/16 the computation stops. With under-relaxation factor of 1/16 solutions with local Mach numbers of 0.98 to 0.99 are attainable.

In a problem of this nature, with no exact solutions available for comparison, it is difficult to arrive at a precise estimate of the accuracy to be expected. From various internal checks that have been applied it appears that with the mesh size commonly used (10 elements in the r direction, 60 in the θ direction) the error should not exceed 1% in perturbation velocity, and in most cases should be considerably less; though it must be stressed that the accuracy of the compressible calculation is vitally dependent on extreme accuracy in the initial conformal transformation.

A useful independent check is also provided by a comparison with the third order solution for an ellipse at zero incidence, obtained by Hantzsche[3]; this is given in the table below (see also Fig. 1)

Table I

Maximum velocity on ellipses at zero incidence

a) t/c = 0.10

M_∞	Numerical method (Sells)	3rd order (Hantzsche)	Approximate method (Wilby : equation 3.2)
0.4	1.1111	1.1104	1.1100
0.5	1.1178	1.1178	1.1176
0.6	1.1292	1.1295	1.1297
0.7	1.1494	1.1500	1.1511
0.8	1.2006	1.1956	1.1990

b) t/c = 0.20

M_∞	Numerical method	3rd order	Approximate method
0.4	1.2239	1.2235	1.2220
0.5	1.2405	1.2410	1.2398
0.6	1.2691	1.2706	1.2710
0.7	1.3324	1.3280	1.3338

It is clear that the agreement between the present numerical method and third order theory is excellent except at the highest Mach number in each case, when (since the maximum local Mach number is about 0.98) even the third order expansion would not be expected to be sufficiently accurate.

Further examples obtained by the numerical method will be given later in connection with the approximate method to be described in the next section.

3. Development of a new approximate method for inviscid flow

The basic two-dimensional inviscid problem can be solved numerically (for subcritical flow) to a high degree of accuracy by the method described in the preceding section. For practical application, however, particularly to aerofoils in a real viscous flow or with a view to possible extensions to three-dimensional wings, it is still essential that an adequate rapid approximate method should be available; and the advent of 'exact' numerical solutions has revealed that no existing method is of sufficient accuracy for this purpose. It is therefore necessary to adapt and extend the existing second-order 'small disturbance' theory, using the exact solutions as a guide.

We start from the standard second order solution for the velocity on an aerofoil in compressible flow, due to Van Dyke[4] or Gretler[5], which may be written in the form (valid away from the leading edge)

$$q = 1 + u_1/\beta + \tfrac{1}{2}(K-1)\,u_1^2 + K\left(u_2 + YY'' + \tfrac{1}{2}Y'^2\right) \qquad \dots (3.1)$$

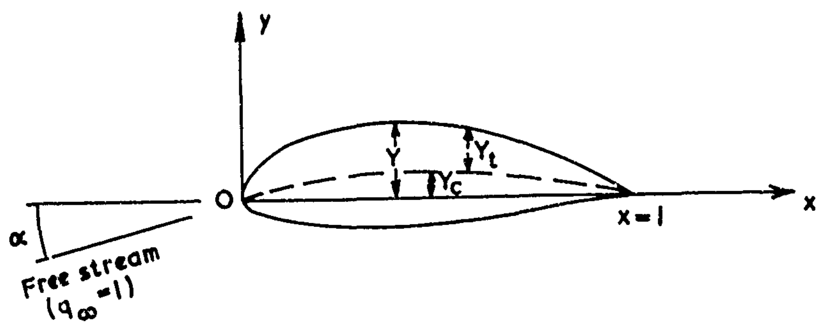

Sketch (c)

Here

M_∞ is the free stream Mach number,

$\beta = \sqrt{1-M_\infty^2}$

$K = \dfrac{(\gamma+1)M_\infty^4 + 4\beta^2}{4\beta^4}$,

Y is the local aerofoil ordinate (see sketch (c))

Y', Y'' are its first and second derivatives with respect to x

and u_1, u_2 are respectively the first and second order velocity perturbations in the x direction on y = 0 for <u>incompressible</u> flow. These can be expressed in terms of the basic integrals*

$$S^{(1)} \langle f(x) \rangle = \frac{1}{\pi}\int_0^1 \frac{f'(\xi)}{x-\xi}\,d\xi$$

*Using the notation of Weber (see e.g. Ref. 7, pp 46-47) and $$S^{(4)} < f(x) > \; = \; \frac{1}{\pi}\sqrt{\frac{1-x}{x}}\int_0^1 \sqrt{\frac{\xi}{1-\xi}}\,\frac{f'(\xi)}{x-\xi}\,d\xi ,$$

as follows (alternative signs denote values on the upper and lower surfaces respectively):-

$$u_1 = u_{1_t} \pm u_{1_l}$$

where $$u_{1_t} = S^{(1)} < Y_t >$$

and $$u_{1_l} = \alpha\sqrt{\frac{1-x}{x}} + S^{(4)} < Y_c > ;$$

and $$u_2 = u_{2_t} \pm u_{2_l}$$

where $$u_{2_t} = -\tfrac{1}{2}\alpha^2 + S^{(1)} < u_{1_t} Y_t + u_{1_l} Y_c >$$

and $$u_{2_l} = S^{(4)} < u_{1_t} Y_c + u_{1_l} Y_t > ;$$

here Y_t and Y_c are respectively the half-thickness and camber ordinates of the aerofoil (see sketch (c)).

The values for the maximum velocity on ellipses at zero incidence, predicted by equation (3.1), are shown in Fig. 1 where they are compared with the exact results of Sells[1] and with the third order theory of Hantzsche[3]; it is clear that second order theory is inadequate for near-critical conditions and that some allowance must be made for higher order effects. It was pointed out by Wilby[5] that a good approximation to these effects could be obtained empirically by replacing the terms

$$u_1/\beta + \tfrac{1}{2}(K-1)\,u_1^2$$

by the expression

$$u_1/B \qquad \ldots (3.2)$$

where $$B = \{1 - M_\infty^2 (1 - M_\infty C_{pi})\}^{\frac{1}{2}}$$

and C_{pi} is the local incompressible pressure coefficient. Corresponding values of the velocity ratio q are given in Table I (p.3) and shown in Fig. 1, and are seen to agree closely (to better than 1% on perturbation velocity) with the nominally exact values obtained by Sells' method.

For the ellipse at zero incidence at the maximum thickness position, the remaining second order terms in equation (3.1) are identically zero. In other cases, particulary when lifting effects are to be included, these terms must be retained. For the present the factor K which multiplies them is left unaltered, giving

$$q = 1 + u_1/B + K\,(u_2 + YY'' + \tfrac{1}{2}Y'^2) \qquad \ldots (3.3)$$

where B is now defined using the local value of C_{pi} derived at the same incidence.

In order to make this expression uniformly valid at the leading edge, we write it in the form

$$q = 1 + u_1/B + K\,(u_2^* - \tfrac{1}{2}Y'^2) \qquad \ldots (3.4)$$

where $$u_2^* = u_2 + \frac{d}{dx}(YY') .$$

Here u_2^* behaves like u_1 at the leading edge; it is finite for symmetrical cases and $O(x^{-\frac{1}{2}})$ in lifting cases. Equation (3.4) at once suggests the equivalent uniformly valid approximation

$$q = \frac{1 + u_1/B + K\,u_2^*}{(1 + K\,Y'^2)^{\frac{1}{2}}} \qquad \ldots (3.5a)$$

In this expression the denominator is similar to the Riegels factor used in incompressible flow; the multiplier K which now appears is an essential feature of the present method, since it provides the necessary distortion of the shape of the pressure distribution near the leading edge as the Mach number increases. It has been found from experience that in lifting cases slightly greater accuracy near the leading edge on the upper surface can be obtained by replacing K in the denominator by B^{-2} (which is of the same order of magnitude; see Ref. 6), leading to

$$q = \frac{1 + u_1/B + Ku_2^*}{\{1 + (Y'/B)^2\}^{\frac{1}{2}}} \quad \ldots (3.5b)$$

a similar replacement has also been tried in the numerator, but the differences produced are trivial in most cases.

The incompressible second-order velocity perturbation u_2^* contains a number of terms; but in cases where

a) the thickness form (particulary near the leading edge) does not differ too much from an elliptical shape - and this is true of most 'standard' thickness distributions

and b) the curvature of the camber line is everywhere very small (or zero), then all but one of these terms (the one due to the interaction between thickness and incidence) may be safely neglected, leading to a simplified version of the basic formulae which may be written

$$q = \frac{1 + \frac{1}{B}\left[S^{(1)} \pm S^{(4)}\right] \pm \frac{\alpha}{B}\sqrt{\frac{1-x}{x}}\left[1 + \frac{S^{(3)}}{B}\right] - \frac{1}{2}\alpha^2/B^2}{(1 + Y'^2/B^2)^{\frac{1}{2}}} \quad \ldots (3.5c)$$

the functions $S^{(1)}$, $S^{(3)}$ and $S^{(4)}$ are as defined in Ref. 7 (p.47), and the alternative signs refer as usual to the upper and lower surfaces respectively. This simplified formula has been used in the theory for viscous flows which follows in section 4.

In all cases the pressure coefficient C_p is finally calculated from the velocity q by means of the standard isentropic flow relation

$$C_p = \frac{2}{\gamma M_\infty^2}\left\{ \left[1 + \tfrac{1}{2}(\gamma-1) M_\infty^2 (1-q^2)\right]^{\frac{\gamma}{\gamma-1}} - 1 \right\} \quad \ldots (3.6)$$

In Figs. 2 to 7 some comparisons are made between the approximate theory described above and the exact numerical results of Sells (Ref. 1, see section 2 of the present paper) and Nieuwland[2]; some other approximate theoretical results are also included.

First, some further examples are given for ellipses. Fig. 2 shows the overall pressure distribution for $t/c = 0.2$, $\alpha = 0$, $M_\infty = 0.7$ (near the critical value). The superiority of the present method near the maximum thickness position is confirmed; further forward the distortion of the shape of the pressure curve due to compressibility is still slightly underestimated (so that the local velocities are overestimated), but the errors remain small. The next two figures (3 and 4) refer to an ellipse with $t/c = 0.15$, $M_\infty = 0.68$ at incidence $\alpha = 2°$, with the rear stagnation point fixed artificially at the trailing edge. In this case the load distribution (Fig. 3) is well predicted by the present method, as is the overall pressure distribution (Fig. 4); but the velocities on the upper surface just aft of the leading edge (near the peak suction position) are again slightly overestimated just as at zero incidence (cf. Fig. 2).

The remaining examples refer to practical aerofoil shapes, as follows:

		t/c	α	M_∞
<u>Fig. 5</u>	RAE 101 (uncambered)	.10	2°	.655
<u>Fig. 6</u>	NPL 3111 (cambered)	.14	1.2°	.667
<u>Fig. 7</u>	Quasi-elliptic (Ref. 2 - negligible camber)	.16	3.5°	.614

In the first two cases the Mach number is just sub-critical, and in the third just supercritical. In all cases the agreement between the present method (equation (3.5b)) and the exact solutions is reasonably good; the chief discrepancies are usually near the leading edge on the upper-surface where the velocities tend to be overestimated when the pressure curve is of 'roof top' type (Fig. 6) but underestimated when there is a high forward suction peak (Figs. 5 and 7). In Fig. 6 are also included the results from the simplified formula (3.5c), which in this case happens to be better on the upper-surface near the leading edge, but worse near the position of maximum velocity; and in Figs. 6 and 7 the results from a former widely-used method (Ref. 7, section 6.1, equation (4.4)) are given to demonstrate the order of improvement now obtained.

The results given here are typical of the order of agreement between the approximate and exact theories that have been obtained for a wide selection of aerofoils. It should however be mentioned that there are cases, notably when the leading edge shape is particularly blunt, when the approach suggested above - essentially an extension of second-order theory - fails near the leading edge, even in incompressible flow. In such cases the device suggested by Labrujere, Loeve and Slooff[8], who base their method on an <u>exact</u> (rather than second-order) solution for incompressible flow, should prove advantageous in conjunction with the present method.

4. Viscous flows

The general principles of the way in which the lift and pressure distribution of an aerofoil are altered by the presence of an attached boundary layer are well known (see for example Ref. 11, Ch. IV). The principal influence is the displacement effect of the boundary layer and wake; and this can be estimated to a first approximation by calculating the inviscid flow about the net displacement surface, as shown in sketch (d), the circulation being fixed by the condition that the velocities at the upper and lower edges of the boundary layer at the trailing edge shall be equal.

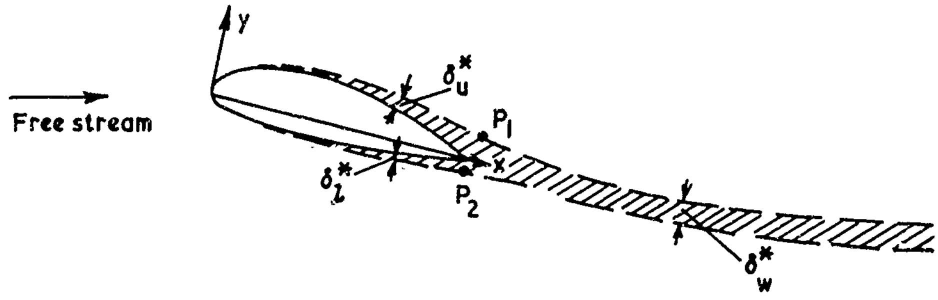

Sketch (d)

It is desirable for computational purposes to modify the criterion that is used to fix the circulation, replacing it instead by the condition that the velocities should be equal at the edges P_1, P_2 of the displacement surface, rather than at the actual edges of the boundary layer; this is equivalent to first order to applying the Kutta condition at the trailing edge of a fictitious equivalent camber line (see sketch (f) below).

It is then possible to treat the inviscid flow about the displacement surface by small perturbation theory, and to split it into two parts:

(a) Symmetrical flow (at zero incidence) about the thickness part of the displacement surface given by $y = \pm\ Y_t^*$, where

$$\begin{aligned} Y_t^* &= Y_t + \tfrac{1}{2}(\delta_u^* + \delta_l^*) \qquad (0 < x < 1) \\ &= \tfrac{1}{2}\,\delta_w^* \qquad (x > 1) \end{aligned} \qquad \ldots (4.1)$$

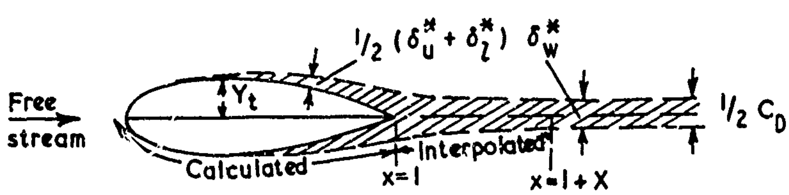

Sketch (e)

where δ_u^*, δ_l^* and δ_w^* are the displacement thicknesses of the upper and lower surface boundary layers and of the wake.

The first order perturbation velocity is given, just as in the inviscid case for an aerofoil, by

$$u_{1t}^* = \frac{1}{\pi}\int_0^\infty \frac{d\,Y_t^*(\xi)}{x-\xi} \qquad \ldots (4.2)$$

the only difference being the extension of the range of integration to infinity to take into account the thickness effect of the wake.

The boundary layer displacement thickness over the aerofoil can be calculated (when the external pressure distribution is known) by any sufficiently accurate method. The calculation of the displacement thickness of the wake is a more difficult problem, which has not yet been solved. To overcome this difficulty it has been suggested by Powell[9] that δ_w^* should be estimated by interpolation between the calculated shape of the displacement surface (aerofoil + bounday layer) ahead of the trailing edge, and the known value $\delta_w^* \propto \frac{1}{2} C_D$⁺ at infinity downstream assuming continuity of slope of the displacement surface at the trailing edge.

⁺This relationship is precisely true only for incompressible flow[12], but for the subcritical Mach numbers considered in this paper no appreciable errors will be introduced by this assumption.

It has been found from experience that the predicted distributions are not particularly sensitive to the assumed shape of the wake, and the further simplification has been made of assuming that the wake thickness attains its asymptotic value ($\approx \frac{1}{2}\ C_D$) at a finite distance X downstream of the trailing edge. The computation is then simplified as the interpolation can be done by means of a simple cubic polynomial (see Ref. 9 for details).

Equation (4.2) is thus modified to

$$u_{1_t}{}^* = \frac{1}{\pi}\int_0^{1+X} \frac{dY_t{}^*(\xi)}{x-\xi} \qquad \dots (4.2a)$$

(b) <u>Anti-symmetrical</u> flow about the distorted camber line, given by

$$Y_c{}^* = Y_c + \tfrac{1}{2}(\delta_u{}^* - \delta_l{}^*)$$

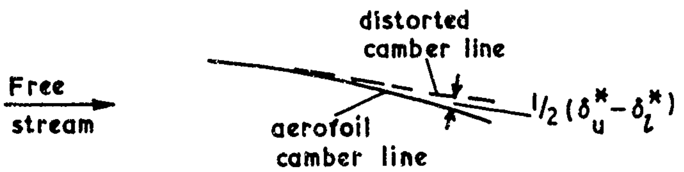

Sketch (e)

This is equivalent to an effective change of incidence to $\alpha^* = \alpha + \Delta\alpha$, where

$$\Delta\alpha = -Y_c{}^*(1) = -\tfrac{1}{2}(\delta_u{}^* - \delta_l{}^*)_{T.E.},$$

and an effective camber $\qquad Y_s{}^* = Y_c{}^* - x\,Y_c{}^*(1)\,.$

The corresponding first order velocity perturbation is thus

$$u_{1_1}{}^* = \alpha^*\sqrt{\frac{1-x}{x}} + S^{(4)} < Y_s{}^* > \qquad \dots (4.3)$$

the Kutta condition at the fictitious trailing edge having been used to fix the circulation.

Finally, the first order velocity perturbations derived from equations (4.2) and (4.3) are combined, together with the principal second order (thickness/incidence) term and compressibility corrections as described in section 3, to give the velocity ratio

$$q = \frac{1 + \frac{1}{B}\left[u_{1_t}{}^* \pm S^{(4)} < Y_s{}^* >\right] \pm \frac{\alpha^*}{B}\sqrt{\frac{1-x}{x}}\left[1 + \frac{S^{(3)} < Y_t{}^* >}{B}\right] - \frac{1}{2}\,\alpha^{*2}/B^2}{(1 + Y'^2/B^2)^{\frac{1}{2}}} \qquad \dots (4.4)$$

an expression precisely analagous to the 'simplified' formula (3.5c) above.

To develop a procedure for performing the calculations ab initio, it is necessary to iterate between successive calculations of a) the inviscid pressure distribution over the displacement surface (using equation (4.4)) and b) the boundary layer development for a give pressure distribution (the 'local equilibrium' method of Nash and Macdonald[10] has been used for the calculations presented in this paper), starting with a modified inviscid pressure distribution for the basic aerofoil as a first approximation.

A computer program has been written which requires as input

(i) aerofoil ordinates
(ii) Angle of incidence, Reynolds number and Mach number
(iii) Transition positions on the two surfaces.

Some under-relaxation is necessary to obtain adequate convergence, the calculation requiring about 10 iterations. The output from the program includes overall lift coefficient and pressure distribution, boundary layer characteristics and drag coefficient.

As no reliable method exists for predicting the transition positions, these must be specified in advance. Experience has shown that in general the predicted pressure distributions are comparatively insensitive to the transition positions. The calculated boundary layer, assuming continuity of momentum thickness, has a discontinuity of δ^* at the specified transition position. In the iterative process thus discontinuity is smoothed out in a simple way.

The method described above has been found to give good general agreement with measured pressure distributions, particularly if the comparison is made at the same value of the lift coefficient. The situation with regard to prediction of the lift coefficient (and the detailed pressure distribution) at a given incidence appears to be confused. It has been a matter of general experience that in the case of experiments made in solid walled tunnels, with standard lift-interference corrections applied to the measured incidence and lift coefficient, the simple 'boundary layer camber' model used in the present method usually overestimates the lift coefficient at a given incidence (i.e. underestimates the reduction in lift produced by the boundary layer) by up to about 5% of total C_L at incompressible speeds (see e.g. Ref. 11, p.196 Table V.2), rising to perhaps 10% near the critical Mach number; a similar conclusion has also been reached in the majority of slotted wall tunnels. On the other hand the careful experiments made recently by Firmin and Cook[12] in the 8 ft × 6 ft (2.4 m × 1.8 m) tunnel at RAE Farnborough, using models of different size with both slotted and solid wall configurations, led to corrected experimental values of C_L which were actually slightly higher than the corresponding theoretical values (see Ref. 12, Fig. 10). There is thus a need for further research on wind tunnel interference on lifting aerofoils.

In view of the situation described in the previous paragraph, all comparisons with experiment in the present paper will be made with the incidence used in the calculations adjusted until the lift coefficient agrees with the experimental value. We have chosen as examples two aerofoils considered in section 3 above, for both of which extensive pressure measurements have been made recently at the Royal Aircraft Establishment by Firmin and Cook*; these are the 10% thick RAE 101 (uncambered) and the 14% thick NPL 3111 (cambered). Results for the RAE 101 aerofoil at $\alpha = 2°$ nominal (about 1.8° corrected), at Mach numbers 0.4 and 0.675, are shown in Figs. 8 and 9; and for the NPL 3111 aerofoil at Mach numbers 0.4 and 0.67, over a range of incidence, in Figs. 10 to 12. It is clear that the general level of agreement between theory and experiment is very good, and can only be faulted very close to the trailing edge and over small regions of the upper surface. The discrepancies near the trailing edge (see in particular Figs. 8 and 9) may be due to deficiencies in the simplified model assumed for the displacement surface, both in the boundary layer just upstream and in the wake downstream of the trailing edge; they could probably be removed by modifying this model in the light of recent experimental measurements of the boundary layer and wake such as those reported in Ref. 12. On the other hand the discrepancies further forward on the upper surface, near the suction peak induced by incidence (Figs. 8, 9 and 10) or further aft near the maximum thickness position as the critical Mach number is reached (Fig. 11) are mainly due to errors in the approximate inviscid theory used in the calculation method (cf. Section 3 and Figs. 5 to 7). In the final figure (Fig. 12) it is shown how, at least in one particular case, a further small but significant improvement in the agreement between theory and experiment can be achieved by adjusting the theoretical result to allow for the difference between the approximate (equation 3.5c) and exact (section2) theories for inviscid flow about the same arofoil at the same lift coefficient (see Fig. 6).

Acknowledgements

The authors are indebted to Dr. J. Weber (R.A.E.) for contributions to the assessment of the approximate method described in section 3, and to M.C.P. Firmin and T.A. Cook (R.A.E.) for providing the unpublished experimental results quoted in section 4.

*These experiments are described in Ref. 12, although the measured pressure distributions are not quoted there.

References

1. C.C.L. Sells — Plane sub-critical flow past a lifting aerofoil. R.A.E. Tech. Rep. 67146 (1967)

2. G.Y. Nieuwland — Transonic potential flow around a family of quasi-elliptical aerofoil sections. N.L.R. Tech. Rep. 172 (1967)

3. W. Hantzsche — Die Prandtl-Glauertsche Nauherung als Grundlage fur ein Iterationsverfahren zur Berechnung kompressibler Unterschallstromungen. Z. angew. Math. u. Mech., 23 (4), 185-199 (1943)

4. M.D. Van Dyke — Second order subsonic aerofoil theory including edge effects. N.A.C.A. Rep 1274 (1956)

5. W. Gretler — Neuere Methode zur Berechnung der ebenen Unterschallstromung an dunnen Profilen bei kleinen Anstellwinkeln. Acta Mechanica. 1, No. 2 (1965)

6. P.G. Wilby — The calculation of sub-critical pressure distributions on symmetric aerofoils at zero incidence. N.P.L. Aero Rep. 1208 (1967)

7. J.A. Bagley — Aerodynamic principles for the design of swept wings (section 6.1). Progress in Aeronautical Sciences, 3, 1-81. Pergamon Press, 1962

8. T.E. Labrujere, W. Loeve, J.W. Slooff — An approximate method for the determination of the pressure distribution on wings in the lower-critical speed range. Paper to be presented at A.G.A.R.D. Specialist's Meeting on Transonic Aerodynamics, Paris, September 1968

9. B.J. Powell — The calculation of the pressure distribution of a thick cambered aerofoil at subsonic speeds including the effect of the boundary layer. N.P.L. Aero Rep 1238 (1967)

10. J.F. Nash, A.G.J. Macdonald — The calculation of momentum thickness in a turbulent bounday layer at Mach numbers up to unity. N.P.L. Aero. Rep. 1207 (1966)

11. ed Thwaites — Incompressible Aerodynamics. O.U.P. 1960

12. M.C.P. Firmin, T.A. Cook — Detailed exploration of the compressible viscous flow over two-dimensional aerofoils at high Reynolds numbers. Paper to be presented at 6th I.C.A.S. Conference, Munich, September 1968.

3th July 1968
3M

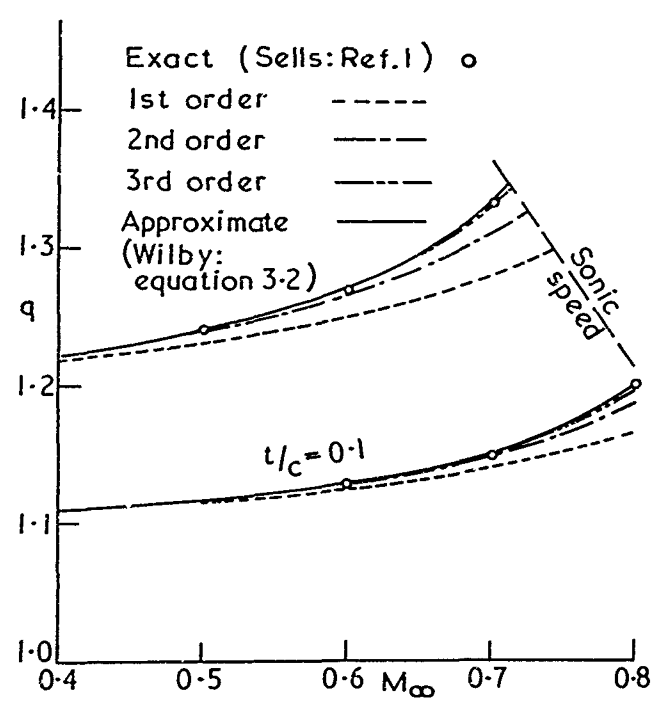

FIG.1 Velocity at maximum thickness of ellipses

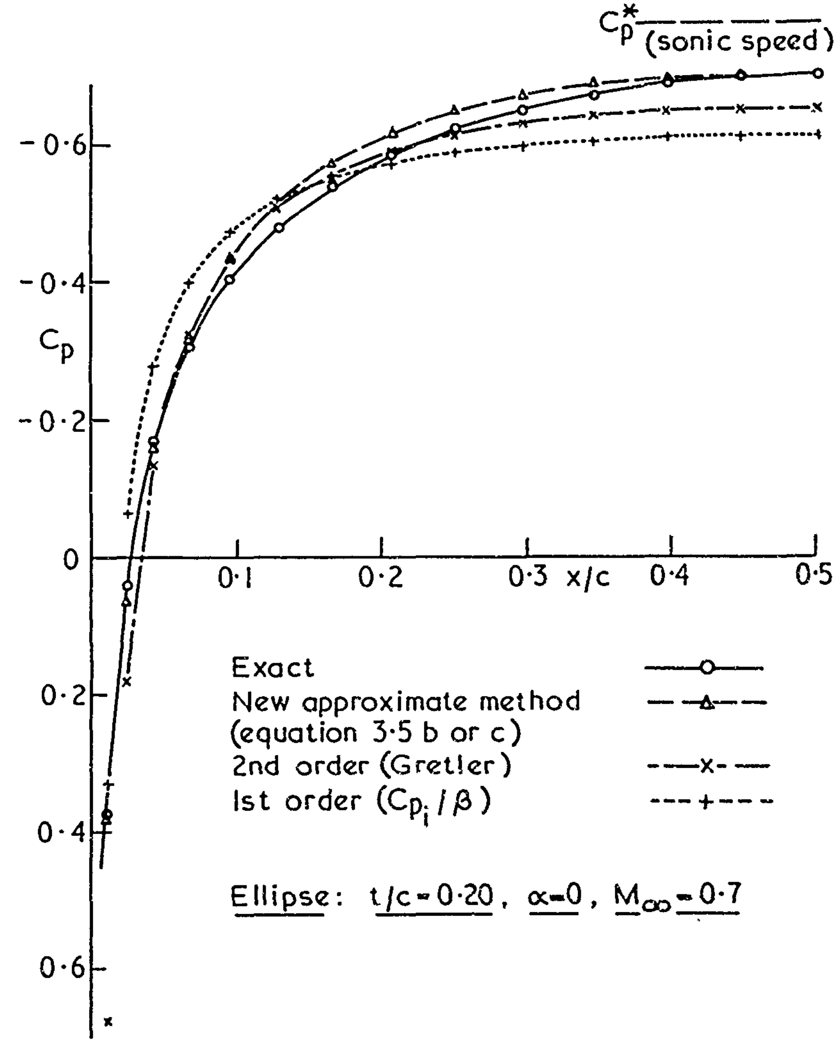

FIG. 2 Pressure distribution on an ellipse at zero incidence

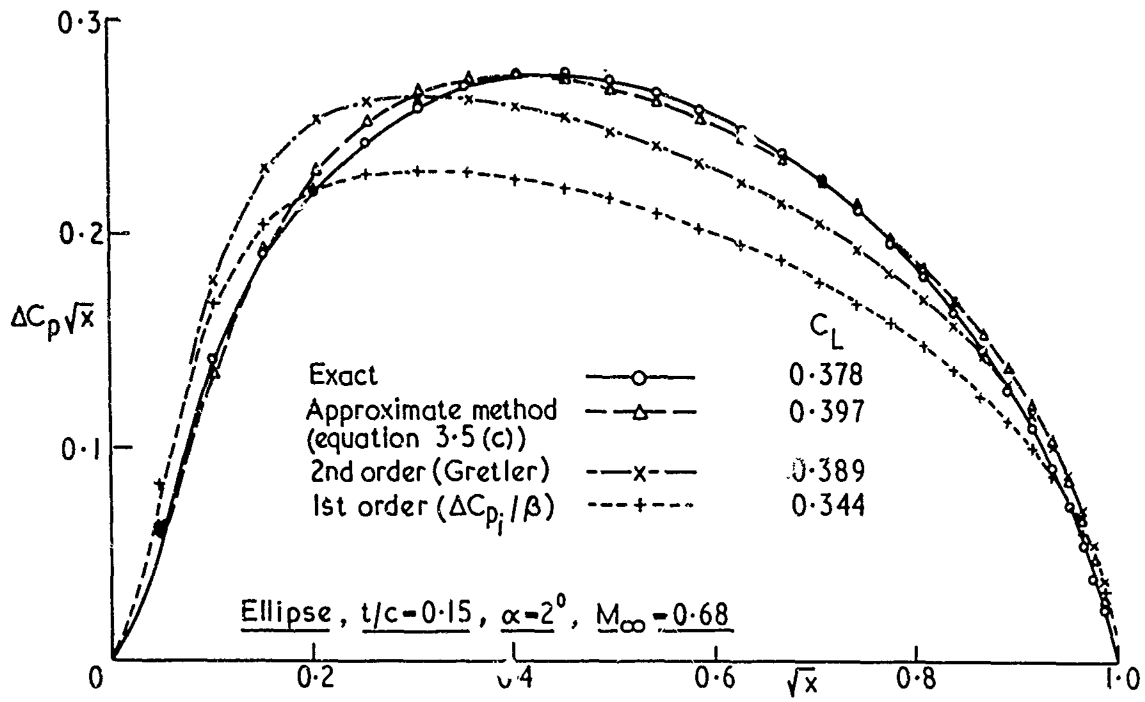

FIG.3 Load distribution on an ellipse at incidence

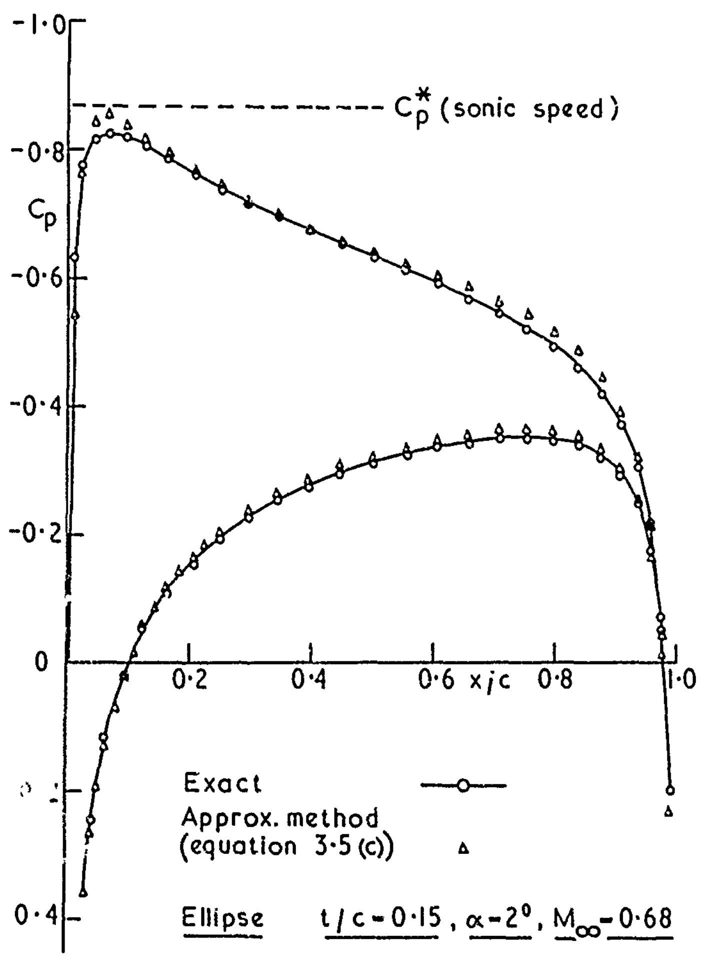

FIG.4 Pressure distribution on an ellipse at incidence

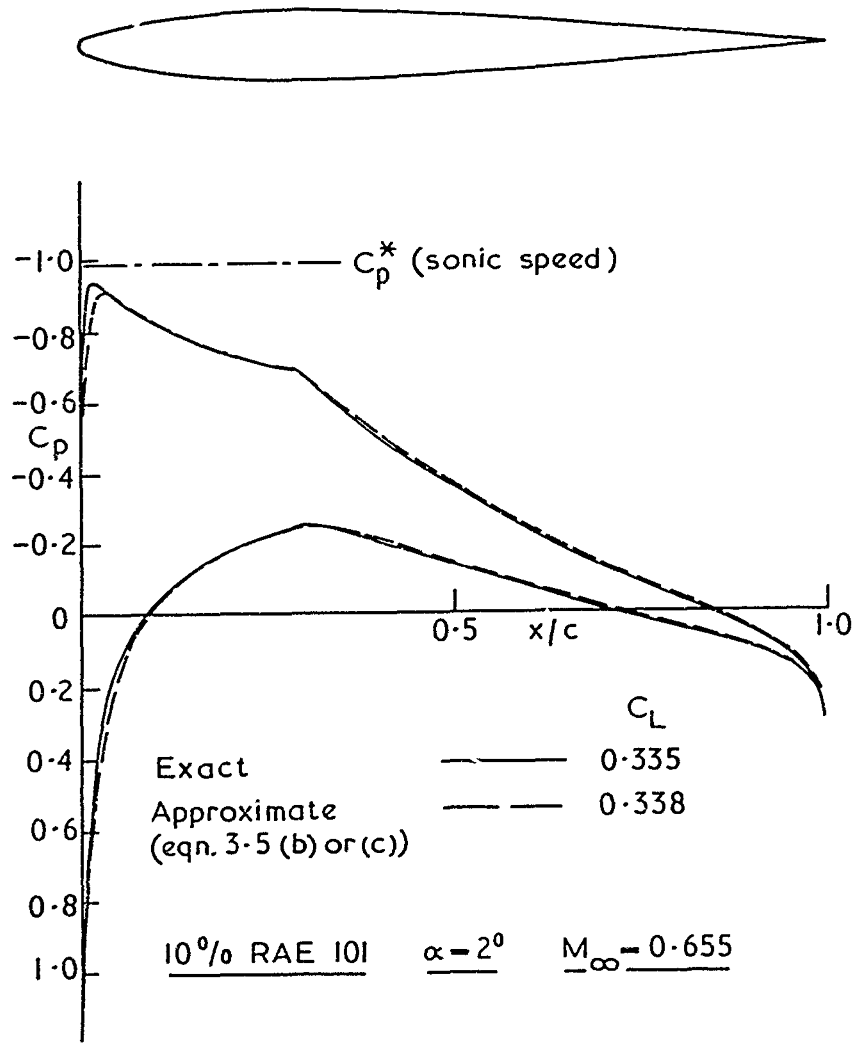

FIG. 5 Inviscid pressure distributions

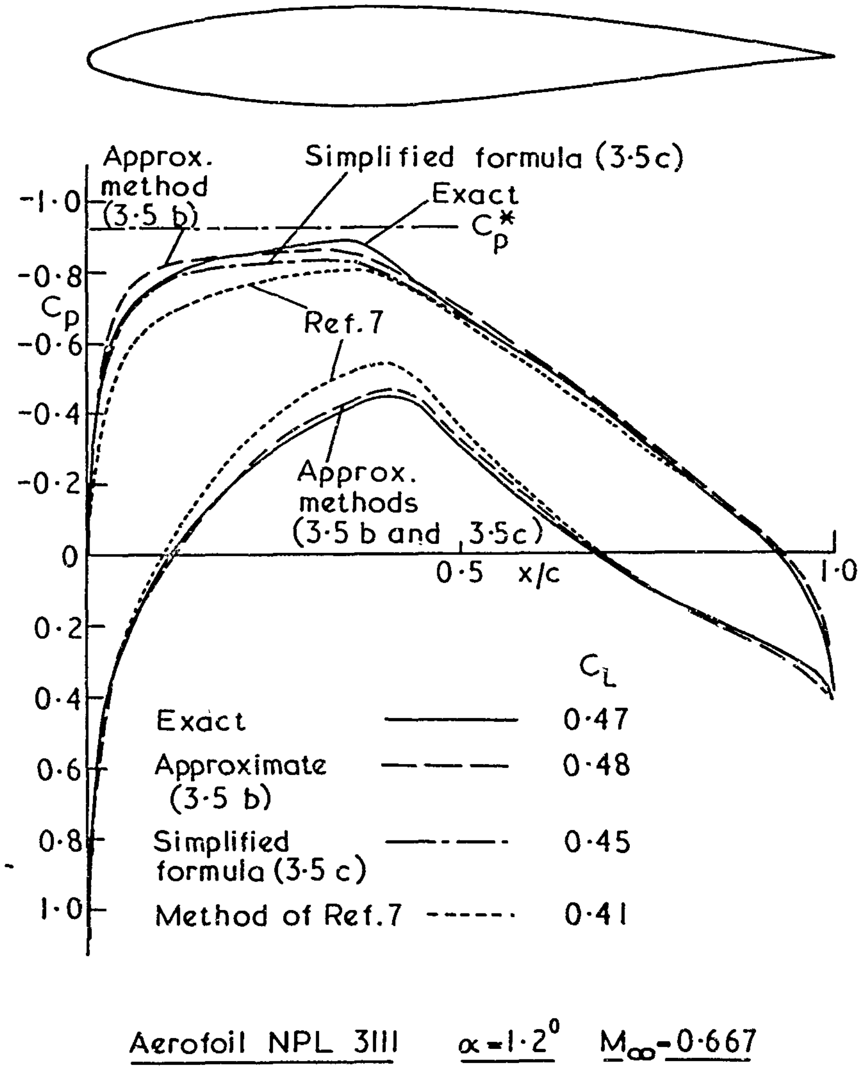

FIG. 6 Inviscid pressure distributions

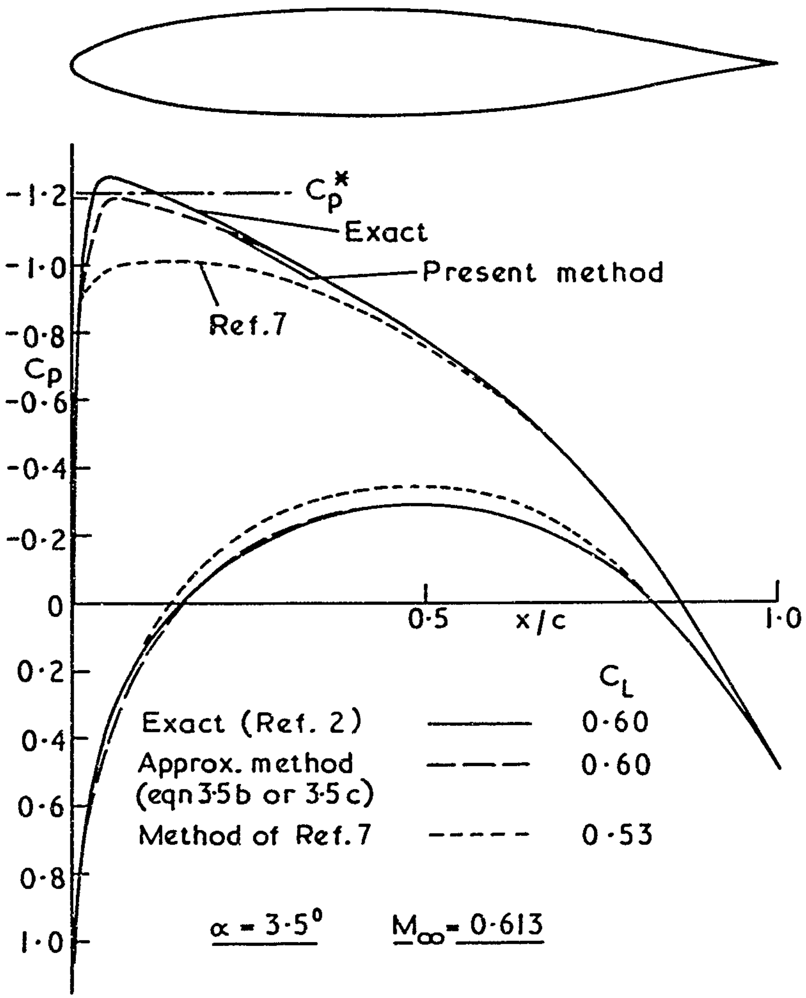

Quasi-elliptic aerofoil ($\tau_1 = 0{\cdot}7, \epsilon_0 = 0{\cdot}65, \alpha_0 = 0{\cdot}07, \Gamma = 0{\cdot}945$)

FIG.7 Inviscid pressure distributions

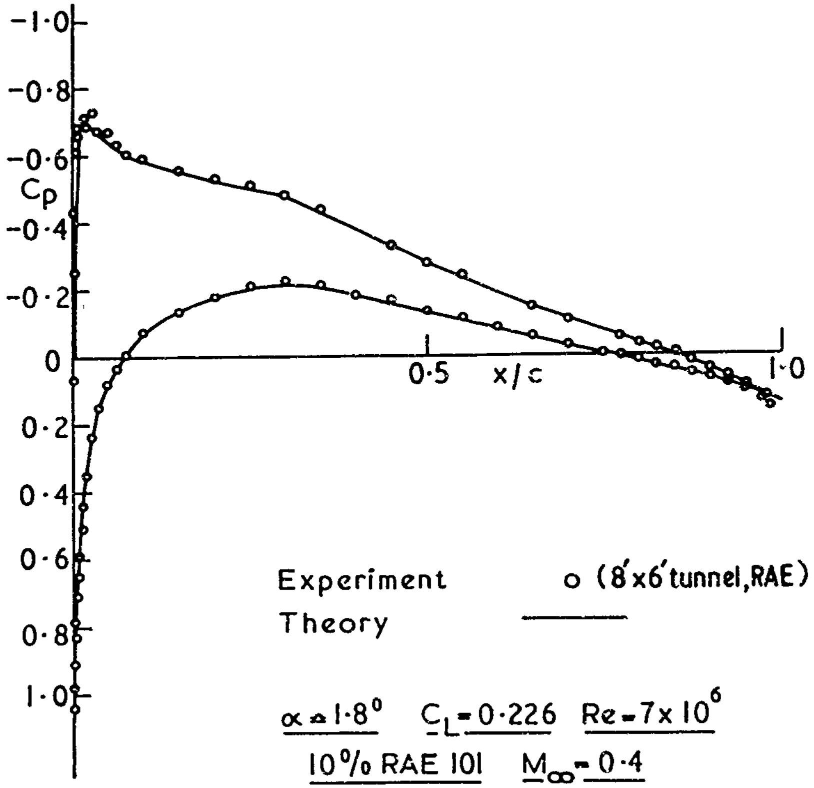

FIG.8 Pressure distributions in viscous flow

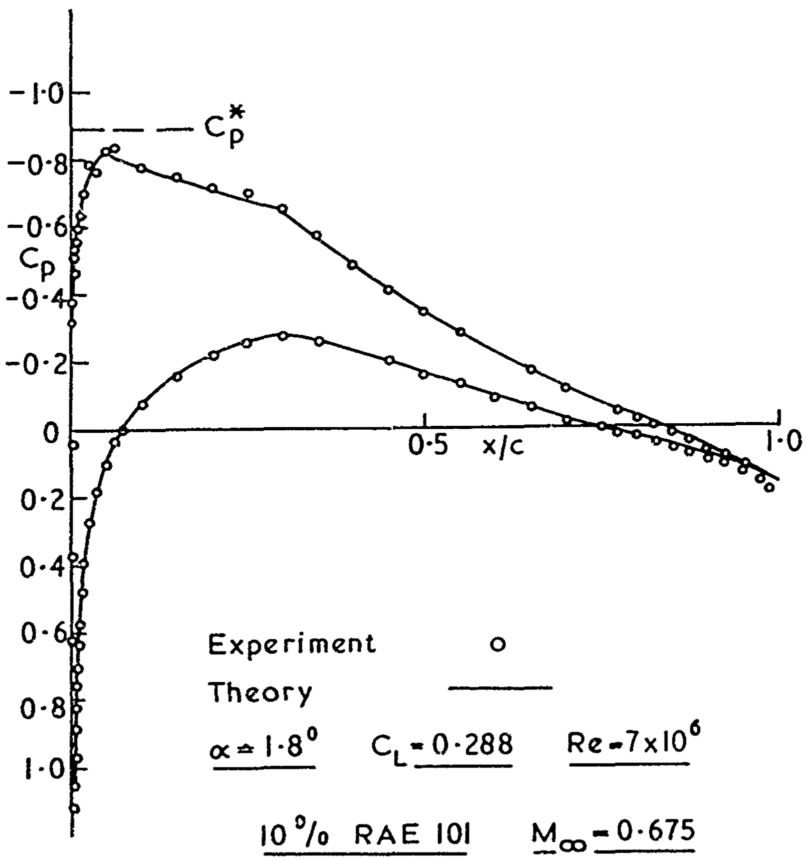

FIG.9 Pressure distributions in viscous flow

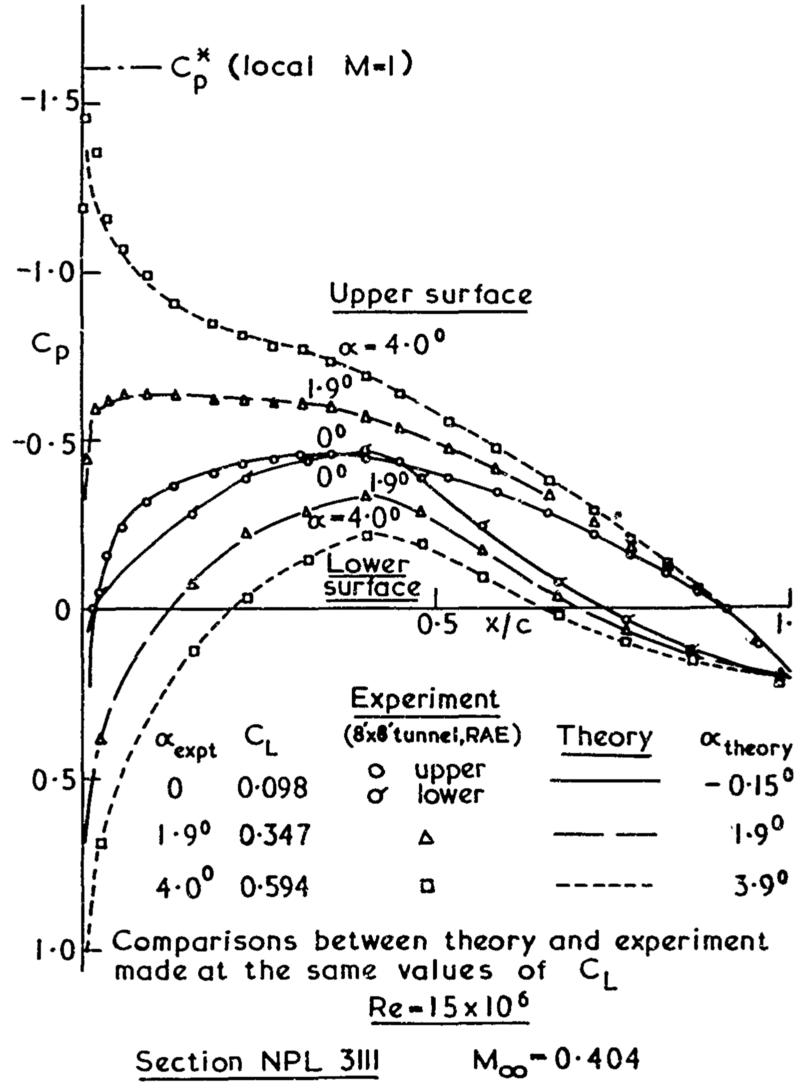

FIG.10 Pressure distributions in viscous flow

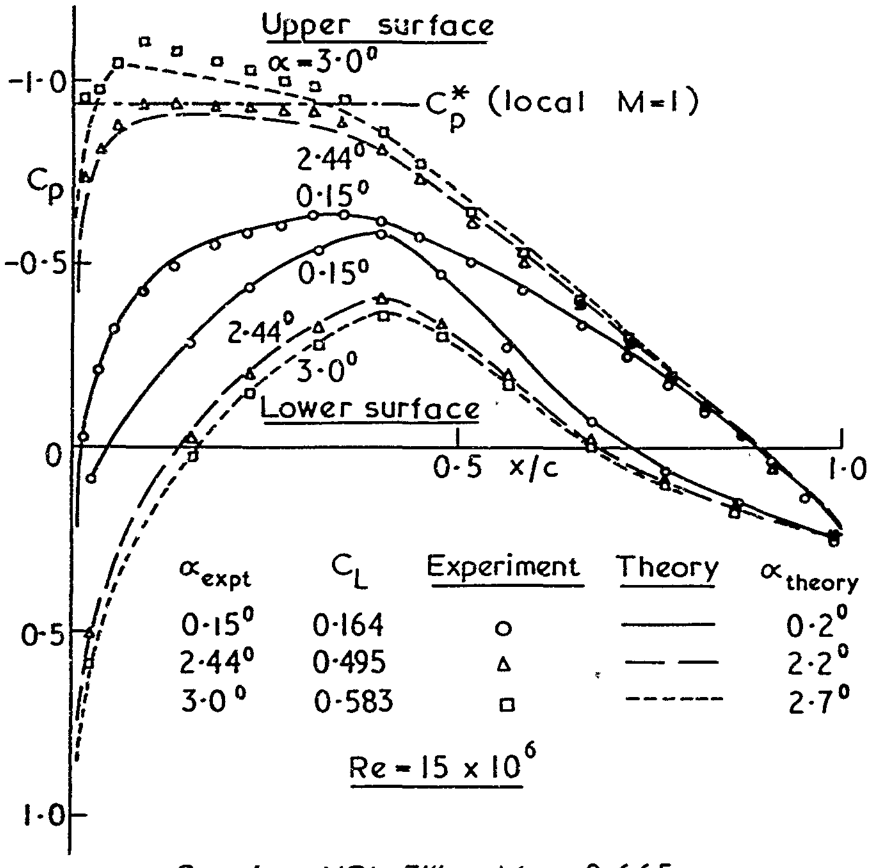

Section NPL 3111 $M_\infty = 0{\cdot}665$

FIG. 11 Pressure distributions in viscous flow

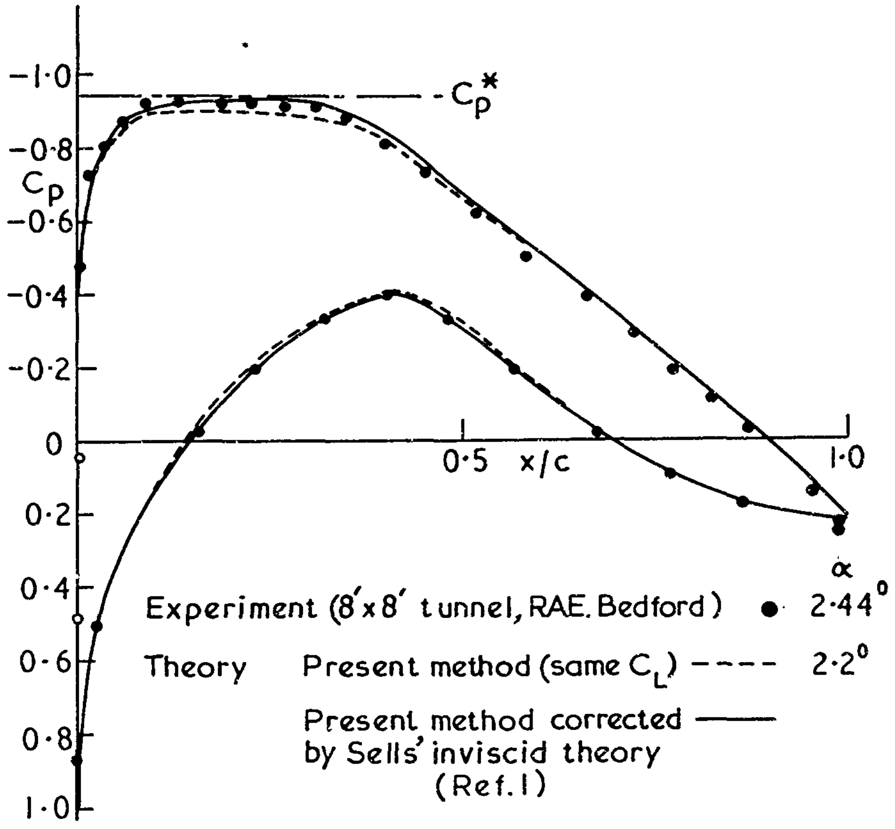

NPL 3111 $M_\infty = 0{\cdot}665$, $Re = 15 \times 10^6$, $C_L = 0{\cdot}50$

FIG. 12 Corrected pressure distribution

RECHERCHES EXPERIMENTALES SUR DES PROFILS D'AILES SUPERCRITIQUES

par

M. VINCENT DE PAUL*

O.N.E.R.A. (92 - Chatillon - FRANCE)

* Ingénieur de Recherches

- SOMMAIRE -

Cette communication a pour objet l'étude des répartitions de vitesse d'extrados présentant un pic au voisinage du bord d'attaque. Il est bien connu que ce type de répartitions apparaît toujours lors de la mise en incidence des profils, mais on peut également l'imposer à l'incidence d'adaptation. Dans le premier cas, l'importance du pic régit les décollements de bord d'attaque, aux basses vitesses et aux portances élevées ; dans le second cas, aux portances modérées du vol à grande vitesse, ce pic détermine le mécanisme de la formation des chocs.

Pour préciser ces problèmes, une famille de profils symétriques a été définie, à partir de lois de répartitions de vitesse imposées en incompressible, à incidence nulle, en fonction de la position et de l'intensité du pic ainsi que du gradient de recompression qui lui fait suite.

L'étude de l'évolution de la courbure dans la région du bord d'attaque des profils calculés a permis de les classer en 4 grandes catégories. L'analyse expérimentale doit permettre une critique des qualités aérodynamiques de tels profils aussi bien aux basses vitesses (portance maximale) qu'en transsonique (Mach de divergence en traînée et en portance).

Les premiers résultats expérimentaux présentés sont relatifs aux essais dans le domaine transsonique.

EXPERIMENTAL RESEARCH ON SUPERCRITICAL WING PROFILES

- SUMMARY -

The purpose of this paper is to study some upper-surface velocity distributions having a peak near the profile leading-edge.

It is well known that this type of distribution always appears when profiles are at incidence but it can also be imposed at the design incidence. In the first case the peak governs the separation at the leading-edge, at low speed and high lift ; in the second case, at the moderate lift encountered at high speed, this peak determines the mechanism of the shock formation.

To examine these problems, a family of symetrical profiles has been defined, starting from velocity distribution laws in incompressible flow, at zero angle of attack, as a function of the peak position and intensity and also of the following recompression gradient.

The study of the evolution of the curvature in the leading-edge region of the calculated profiles, led to classify them into four main categories. The experimental analysis aims at criticizing the aerodynamic qualities of such profiles at low speed (maximum lift) as well as in the transonic range (drag and lift divergence Mach number).

The first experimental results presented concern tests in transonic flow.

IL EXISTE EN PRATIQUE deux domaines où les phénomènes transsoniques limitent les performances d'une voilure (Planche 1).:

- aux portances élevées et aux nombres de Mach faibles,

- aux portances modérées ou nulles et aux grandes vitesses.

AUX GRANDES INCIDENCES un pic de survitesse se développe dans la région du bord d'attaque ; à partir d'un nombre de Mach M_0 de 0,3 environ et d'une portance de l'ordre de 1, une zone supersonique apparaît dans cette région ; un décollement de la couche limite s'ensuit en général, dû probablement à la formation d'un choc, qui provoque une chute précoce de la portance.

Ce phénomène se rencontre notamment à l'extrémité de la pale reculante d'un rotor et limite sa capacité sustentatrice. Pour le comprendre et essayer de le retarder une étude très complète de la région du bord d'attaque doit être faite.

AUX PORTANCES MODEREES ou faibles et aux grandes vitesses, une zone supersonique étendue se développe à l'extrados de l'aile (et aussi à l'intrados pour les portances faibles). L'apparition des chocs entraîne un accroissement de traînée et provoque le décollement de la couche limite et par suite une chute de la portance, et des variations du moment de tangage;aux faibles portances les déplacements différents des chocs à l'intrados et à l'extrados peuvent être aussi à l'origine de fortes perturbations de ce moment de tangage.

Ce domaine intéresse les avions de transport subsonique , ainsi que l'extrémité de la pale avançante des rotors.

Pour retarder ces troubles transsoniques on a cherché à obtenir des profils pouvant admettre une zone supersonique importante sans chocs suffisamment intenses pour détériorer les performances.

Des travaux effectués au N.P.L. [1] ont montré qu'il existait de tels profils (profils de type "peaky").

En particulier, supposons que la géométrie d'un profil soit telle qu'un faisceau d'ondes de détente assez intense prenne naissance au début de la zone supersonique (Planche 2) ; ces ondes vont se réfléchir sur la ligne sonique en ondes de compressions de même intensité qui, si elles ne focalisent pas avant d'atteindre la surface, s'y réfléchiront en ondes dont la nature et l'intensité dépendent de la courbure du profil dans la région d'impact ; pour une certaine loi de courbure, qui dépend de l'intensité de la détente initiale, on pourra notamment obtenir une recompression par ondes simples.

Lorsqu'on possède un profil fournissant un faisceau de détente d'intensité convenable, il est possible de corriger la courbure de l'extrados de manière à tendre vers une recompression quasi isentropique ; c'est ainsi que le N.P.L. a mis au point une méthode approximative simple, basée sur le calcul des caractéristiques, qui permet, si l'on connaît les répartitions de pression expérimentales sur le profil de faire cette correction. Le problème consiste donc à obtenir un faisceau initial de détente adéquate. Il faut à cet effet, que la région de forte courbure du bord d'attaque coïncide avec l'origine du domaine supersonique. Les répartitions de vitesse de tels profils présenteront alors un pic près du bord d'attaque.

On constate donc que, tant en transsonique qu'aux basses vitesses la région du bord d'attaque joue un rôle prépondérant. Aussi le but de l'étude dont on présente ici les premiers résultats est-il d'analyser les divers aspects de la formation de ces pics de survitesse de leur évolution et de leur répercussion.

DEFINITION D'UNE FAMILLE DE PROFILS PRESENTANT UN PIC DE SURVITESSE PRES DU BORD D'ATTAQUE

UNE FAMILLE DE PROFILS SYMETRIQUES a été calculée en incompressible, à partir de répartitions de vitesse à l'incidence nulle, dont le pic près du bord d'attaque diffère par sa position x_p , son intensité V_p et enfin par la valeur des paramètres liés à la décroissance plus ou moins rapide de la vitesse après ce pic (Planche 3):

- pour $0 \quad x < x_p$ la vitesse a été prise sous la forme $\frac{V}{V_0} = \frac{1}{2}\sqrt{\frac{x}{x_p}}\left(3 - \frac{x}{x_p}\right)$,
- pour $x_p < x < x_R = 0{,}4\ c$ la vitesse est donnée par une équation dépendant de deux paramètres liés à la position du point d'inflexion I et à la pente en ce point,
- pour $x > x_R$ la distribution des vitesses est la même pour tous les profils ; elle est linéaire de $x = 0{,}45\ c$ à $x = 0{,}8\ c$.

LE CALCUL DE CES PROFILS $z = z(x)$ est effectué d'après [2] en considérant la vitesse sous la forme :

$$\frac{V}{V_0} = \left(1+\bar{u}\right)\cos\varphi$$

avec comme valeur approximative de $\bar{u}$: $\bar{u} = \frac{1}{\pi}\int_0^1 \frac{dz}{dx}(\xi)\frac{d\xi}{x-\xi}$

avec $\frac{dz}{dx} = tg\,\varphi$

L'inversion de l'intégrale permet d'exprimer la pente du profil sous la forme

$$\frac{dz}{dx} = \frac{1}{\pi\sqrt{x(1-x)}}\left[\frac{z_{BF}}{2} - \int_0^1 \frac{\bar{u}(\xi)\sqrt{\xi(1-\xi)}}{x-\xi}\,d\xi\right]$$

où z_{BF} est la demi épaisseur du bord de fuite. La vitesse étant donnée, cette pente est alors calculée par itérations.

L'erreur commise par cette méthode est faible et localisée dans une région très proche du bord d'attaque. Une comparaison entre la répartition de vitesse imposée pour le calcul d'un profil par la méthode précédente, et la répartition déterminée à partir d'une distribution de singularités disposée sur le contour de ce profil, montre notamment que l'intensité du pic est un peu plus faible que prévu (Planche 4).

ETUDE DE LA REGION DU BORD D'ATTAQUE

La planche 5 montre les différentes lois de courbure obtenues pour des profils de la famille ayant un pic de même intensité mais une position (x_p) différente. La courbure est représentée en fonction de φ angle de la vitesse avec la direction Ox, ce qui permet de dilater sur la figure la région correspondant au bord d'attaque. On voit que lorsque le pic se rapproche du bord d'attaque, la courbure en ce point diminue et son évolution est totalement différente. On obtient des courbes analogues quand pour une position fixée du pic on fait varier son intensité.

On a pu ainsi mettre en évidence quatre types principaux d'évolution de la courbure dans la région du bord d'attaque. Ils sont représentés sur la Planche 6, où l'on a schématisé des lois de courbures symétriques ; mais il est bien sûr possible d'obtenir de part et d'autre du bord d'attaque deux types de courbures différents.

Le type n° 1 est classique - La courbure est maximale au bord d'attaque (A) et décroît ensuite régulièrement. Une augmentation du rayon au bord d'attaque, diminue les variations de courbure ; d'autre part, le point d'arrêt évolue moins rapidement en fonction de l'incidence ; aussi les pics de survitesses aux fortes incidences sont-ils en général plus faibles. Il en résulte qu'en incompressible où le gradient de recompression est plus faible, ainsi que dans le domaine $0,3 < M_0 < 0,5$ où la zone supersonique apparaît plus tard, les décollements de bord d'attaque sont retardés ce qui entraîne un gain dans les performances.

La courbure, dans le type n° 2 - est aussi maximale en A mais son évolution présente une variation plus rapide à partir d'un certain point P. Cette variation qui peut être assez brutale est intéressante en transsonique car elle peut permettre d'obtenir la détente nécessaire pour des profils du type "peaky". Aux basses vitesses et aux incidences croissantes, suivant la position de P et la loi de courbure en amont de ce point, le pic pourra être dû soit uniquement à l'effet d'incidence (comme dans le type 1), la variation de courbure en P n'intervenant que dans la recompression, soit à l'effet simultané de l'incidence et de la variation de courbure en aval de P. Le premier cas pourrait être avantageux car il permettrait d'avoir un pic de survitesse autour de l'adaptation, qui ne viendrait pas ultérieurement renforcer l'intensité du pic dû à l'incidence croissante ; la zone supersonique n'apparaîtrait donc pas prématurément aux grandes incidences. Par contre l'influence de la variation de courbure en P sur la recompression pourrait être défavorable.

La région du bord d'attaque du type 3 est ~~circulaire~~. En transsonique elle peut permettre aussi d'obtenir des profils de type "peaky". Aux basses vitesses et en incidence la variation de courbure en P régira toujours le pic de survitesse.

Enfin, dans le 4ème type, la courbure maximale ne se trouve plus au bord d'attaque mais en P. Dès l'adaptation on simule ainsi un effet d'incidence qui pourrait réduire l'incidence de décrochage aux basses vitesses.

---

* - adaptation = incidence d'attaque idéale pour l'aile supposée réduite à son squelette.

ETUDE EXPERIMENTALE AUX GRANDES VITESSES

CONDITIONS D'ESSAIS -

Les résultats présentés ont été obtenus dans la soufflerie transsonique de l'Institut de Mécanique des Fluides de LILLE, dont les principales caractéristiques sont mentionnées dans la Planche 7. Les faibles nombres de Reynolds atteints dans cette soufflerie avec des profils de 80 mm de corde, obligent à déclencher la transition artificiellement. On utilise pour cela la diffusion transversale de la turbulence créée par des fils longitudinaux régulièrement espacés en envergure ; cette méthode a pour avantage de ne pas trop perturber l'écoulement non visqueux (en particulier elle ne modifie pas le pic de survitesse) ; en outre les perturbations produites dans la couche limite permettent de visualiser les ondes de Mach dans les zones supersoniques.

Avec des maquettes aussi petites (80 mm de corde) la réalisation doit être très soignée

L'écart trouvé sur la cote z est inférieur à $\pm$ 0,02 mm (sauf pour le profil B première maquette fabriquée où il était de $\pm$ 0,04 mm et pour le profil C dans la région du bord d'attaque ($x < 0,6$ mm)). L'influence de cette erreur sur les lois de courbure, notamment près du bord d'attaque apparaît sur la Planche 8.

PROFILS ESSAYES EN SOUFFLERIE -

Quatre profils ont jusqu'à présent été étudiés en soufflerie : un profil de référence (désigné en abrégé par la lettre A) dont la répartition de vitesse est constituée d'un plateau ($V_R/V_0 = 1,125$) de 2 à 40 % du profil, et 3 autres profils dont la répartition présente un pic de survitesse situé à la même abscisse $x_p = 0,02$ c. Les profils B et C ne diffèrent que par la loi de recompression immédiatement après le pic ; le profil D a un pic beaucoup plus intense. Ces profils ont, dans la région du bord d'attaque, une loi de courbure du type 2. Les planches 9 & 10 montrent leurs principales caractéristiques géométriques et leurs répartitions de vitesse en incompressible à incidence nulle.

ETUDE DU PROFIL DE REFERENCE (A) -

Ce profil est d'abord comparé (Planche 11) à un profil bien connu, le NACA 64 A 010, symétrique lui-aussi, d'épaisseur relative très voisine (10 % au lieu de 10,17 %) et dont le maître couple se situe aussi un peu avant 40 % de la corde. Ce profil a été essayé dans la soufflerie $S4_L$ de CHALAIS, dans des conditions tout à fait analogues de celles de l'I.M.F.L. On constate qu'un gain important a été réalisé sur le nombre de Mach de divergence de traînée.

Ce profil de référence (A) a des propriétés extrêmement intéressantes en incidence, en particulier à l'incidence de 2,5°. A $M_0 = 0,79$ (Planche 12) ni les pressions à la paroi du profil, ni la strioscopie ne mettent en évidence un choc à la fin de la zone supersonique ; la strioscopie permet de voir la structure de cette zone supersonique : ondes de détente et ondes de compression. Le calcul de cette zone a été effectué par la méthode des caractéristiques à partir de la répartition de pression expérimentale trouvée sur le profil (sans tenir compte de la couche limite). La ligne sonique a pu ainsi être extrapolée.

On a reporté sur la photographie des lignes caractéristiques ainsi calculées (une onde de détente et ses réflexions successives sur la ligne sonique et le profil) ; la comparaison avec les ondes visualisées sur la strioscopie est très bonne. Cela prouve notamment que le caractère bidimensionnel de l'écoulement est fort peu perturbé et confirme la valeur et l'intérêt des renseignements donnés par cette visualisation. L'augmentation localisée de vitesse, observée sur la répartition des nombres de Mach locaux à la fin de la recompression est due à l'accroissement de courbure imposé au profil dans cette région (voir la Planche 16).

Sur la Planche 13 on a reporté des caractéristiques calculées et les courbes $\varphi \pm \omega$, ω , étant l'angle de PRANDTL MEYER sur la paroi du profil. Ces courbes montrent que la recompression ne s'effectue pas rigoureusement par ondes simples (dans ce cas la courbe $\varphi - \omega$ serait une horizontale : $\varphi - \omega = c^{te}$). Cependant après $x/c = 0,15$ la pente de cette courbe est très faible : les ondes réfléchies par la paroi du profil sont toujours des ondes de détente dont l'intensité décroît au cours des réflexions successives pour devenir négligeable. Cet exemple est intéressant car il prouve que l'on peut obtenir des profils présentant une zone supersonique terminée par une recompression quasi isentropique avec des profils qui ne sont pas vraiment de type "peaky" dans le sens qui ressort des travaux du N.P.L.

La Planche 14 montre le champ aérodynamique autour du profil dans les mêmes conditions que précédemment ($i = 2,5°$ et $M_0 = 0,79$) ; ce champ est déduit des pressions relevées à la paroi de la soufflerie ; là encore aucun choc n'est mis en évidence. Ce relevé permet de préciser encore la structure de la dernière partie de la zone supersonique.

La comparaison (Planche 15) des zones supersoniques déduites de ces pressions à la paroi, et du calcul déjà mentionné, basé sur les pressions relevées sur le profil, montre un écart assez important surtout au début de la zone supersonique. Ceci est dû à la couche limite assez épaisse qui se développe sur la paroi de la soufflerie, et aussi à l'imprécision du calcul dans cette région.

EFFET D'UN PIC DE SURVITESSE

La planche 16 montre une comparaison à l'incidence nulle de l'évolution des vitesses sur le profil A de référence et sur le profil D qui présente un pic de survitesse près du bord d'attaque. Ce pic n'est pas assez intense pour donner lieu vers l'aval à une zone supersonique étendue à l'extrados. En effet après $x = 0,1$ C les vitesses évoluent de la même manière sur A et sur D. On remarque cependant une légère différence en aval du maître couple. Sur le profil A il se produit une recompression avant le choc; ceci n'est pas dû, comme on pourrait le penser, à un choc en λ caractéristique d'une couche limite laminaire mais comme la strioscopie le confirme à un effet de la géométrie du profil qui comporte à cet endroit un accroissement de courbure traduisant la répartition de vitesse choisie en incompressible ; le profil D ne présente pas cette anomalie à cause d'une légère imprécision de réalisation de la maquette dans cette région (voir Planche 8).

Sur la planche 17 on remarque que la traînée est plus forte sur le profil D malgré le gain de succion représenté par le pic. Pour en mettre en évidence l'origine on a tracé à un nombre de Mach nettement subsonique la répartition des pressions suivant l'axe o z perpendiculaire à la vitesse à l'infini. La courbe ainsi obtenue, qui donne la traînée par intégration, est décomposée en deux boucles, une boucle de succion qui représente une poussée et une boucle de traînée. Pour le profil D cette dernière boucle est plus importante que pour A ; on a vérifié que des modifications de la loi de vitesse que l'on s'était imposé a priori en amont du pic lors du calcul de ce profil, permettaient de réduire cette boucle de traînée. Mais les lois de courbure correspondantes dans la région du bord d'attaque tendent alors à passer du type 2 au type 3 ou même 4 ce qui risque d'être moins favorable aux basses vitesses.

La planche 18 montre la comparaison des nombres de Mach locaux à l'extrados des profils A et D à l'incidence 2,5° et à $M_0 = 0,8$, suivant les axes ox et oz (boucle de succion). Pour (D) le choc se produit très légèrement en amont de la crête (point du profil où la tangente est parallèle à la vitesse à l'infini). Pour (A) au contraire le choc se forme en aval de la crête ce qui a pour effet de diminuer la boucle de succion. Sur la Planche 19 on a effectué l'intégration séparée des boucles de traînée et de succion ; cela met en évidence le fait bien connu [1] que l'accroissement initial de la traînée est lié à la seule perte de succion (la boucle de traînée reste en effet sensiblement constante).

La diminution de la succion s'effectue à un nombre de Mach plus élevé pour le profil D ce qui se traduit par un nombre de Mach de divergence de traînée (où par convention $dC_x/dM = 0,1$) plus grand. On constate aussi qu'à cette incidence la portance est maximale à un nombre de Mach (Mach de divergence de portance) plus élevé aussi.

La Planche 20 permet de comparer les profils B et C. Leurs répartitions de vitesse présentent un pic de même intensité mais la loi de recompression est différente. Le profil B pour lequel le gradient de recompression est plus important, donne un gain non négligeable sur le nombre de Mach M_{Dx}.

La Planche 21 montre les strioscopies de l'écoulement.

CONCLUSION

Il est difficile de conclure d'après ces quelques exemples, sur les améliorations à espérer avec un profil présentant, à l'incidence d'adaptation, un pic de survitesse près du bord d'attaque par rapport à un profil à répartition du type "plateau". On a cependant montré que ce pic devait, être défini avec soin pour pouvoir espérer un gain appréciable, sur la traînée notamment.

Des éléments nous manquent encore pour faire une critique assez complète des types de répartition de vitesse et des lois de courbure près du bord d'attaque, qui permettraient d'obtenir de la façon la plus satisfaisante possible, les performances recherchées tant en transsonique qu'aux basses vitesses ; c'est pourquoi ces études vont être poursuivies aussi bien aux vitesses élevées qu'aux basses vitesses notamment dans des souffleries à densité variable, ceci afin d'analyser également l'influence du nombre de Reynolds et d'essayer d'éviter le problème très difficile du déclenchement artificiel de la transition sur ce type de profil.

REFERENCES

[1] H.H. PEARCEY -

The aerodynamic design of section shapes for swept wings.

Advances in aeronautical sciences (Vol. 3) - Pergamon Press Ltd - LONDRES (1962)

[2] J. WEBER -

The calculation of the pressure distribution over the surface of two-dimensional and swept wings with symmetrical aerofoil sections.

ARC - R et M 2918 (1956).

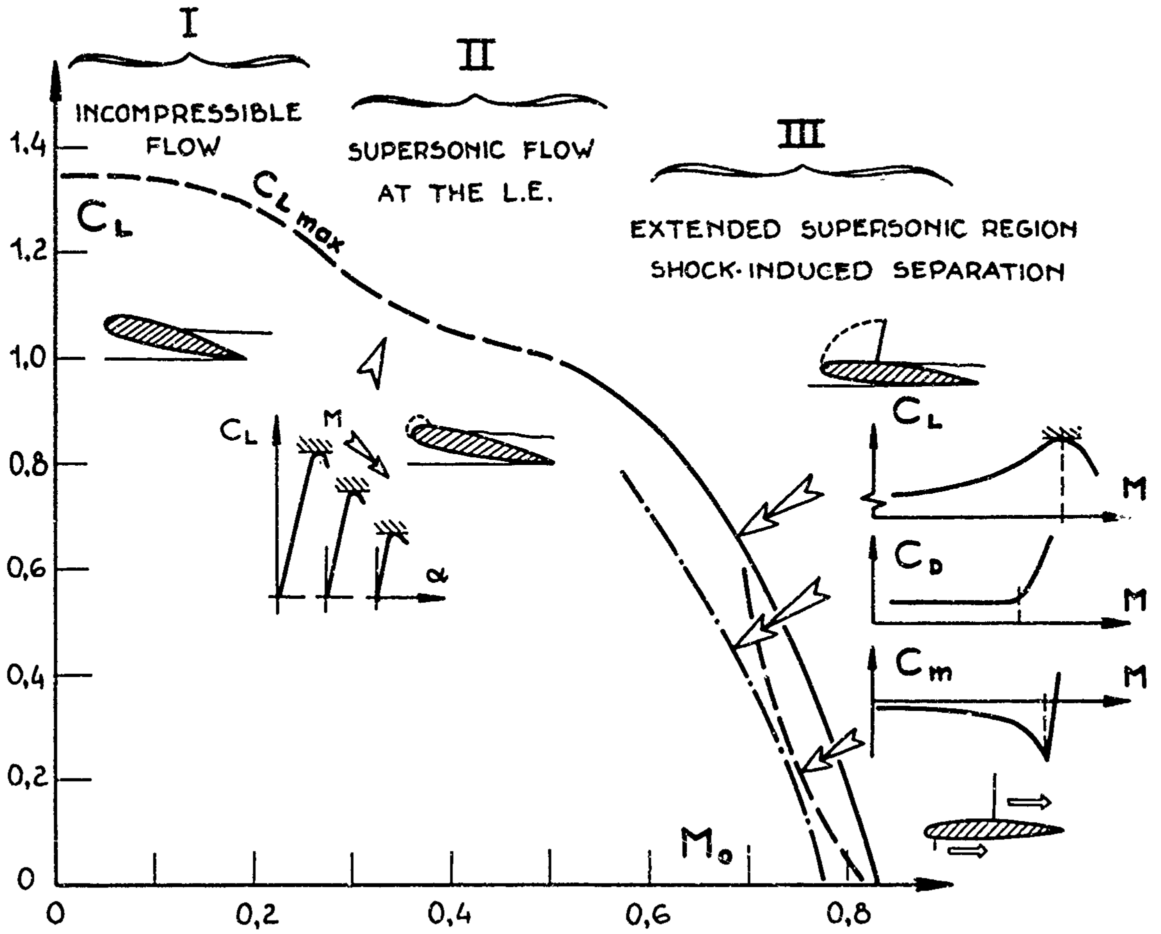

Fig. 1   Les différents types d'écoulement autour d'une aile.

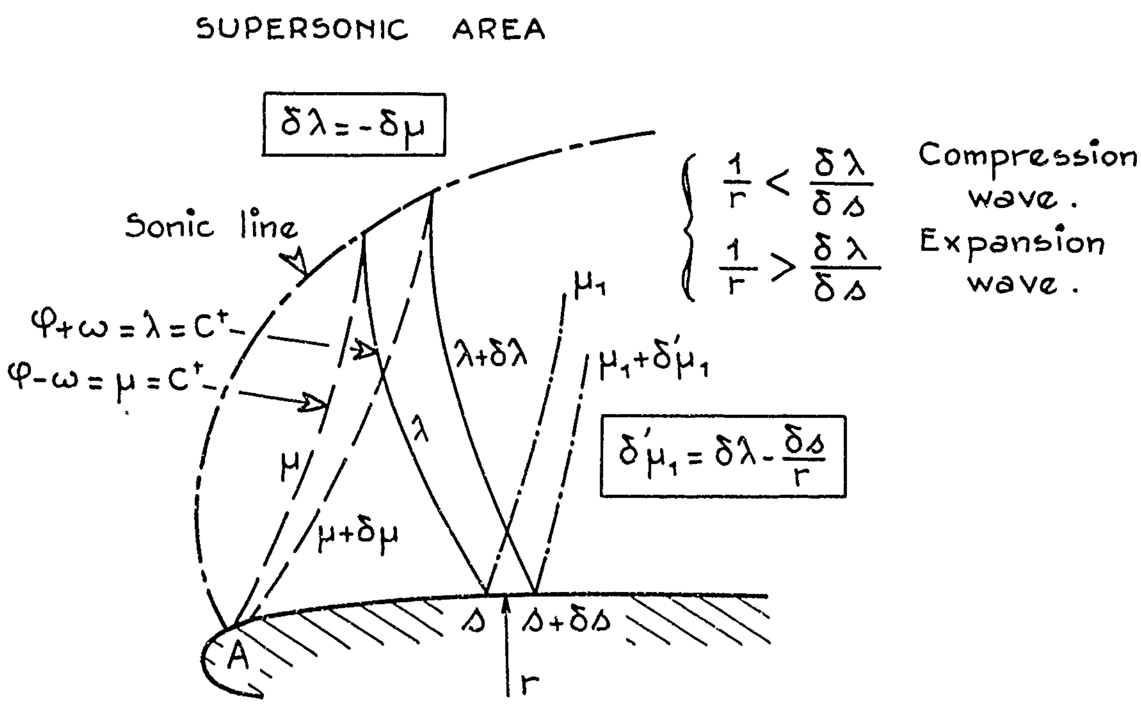

Fig. 2   Structure de la zone supersonique.

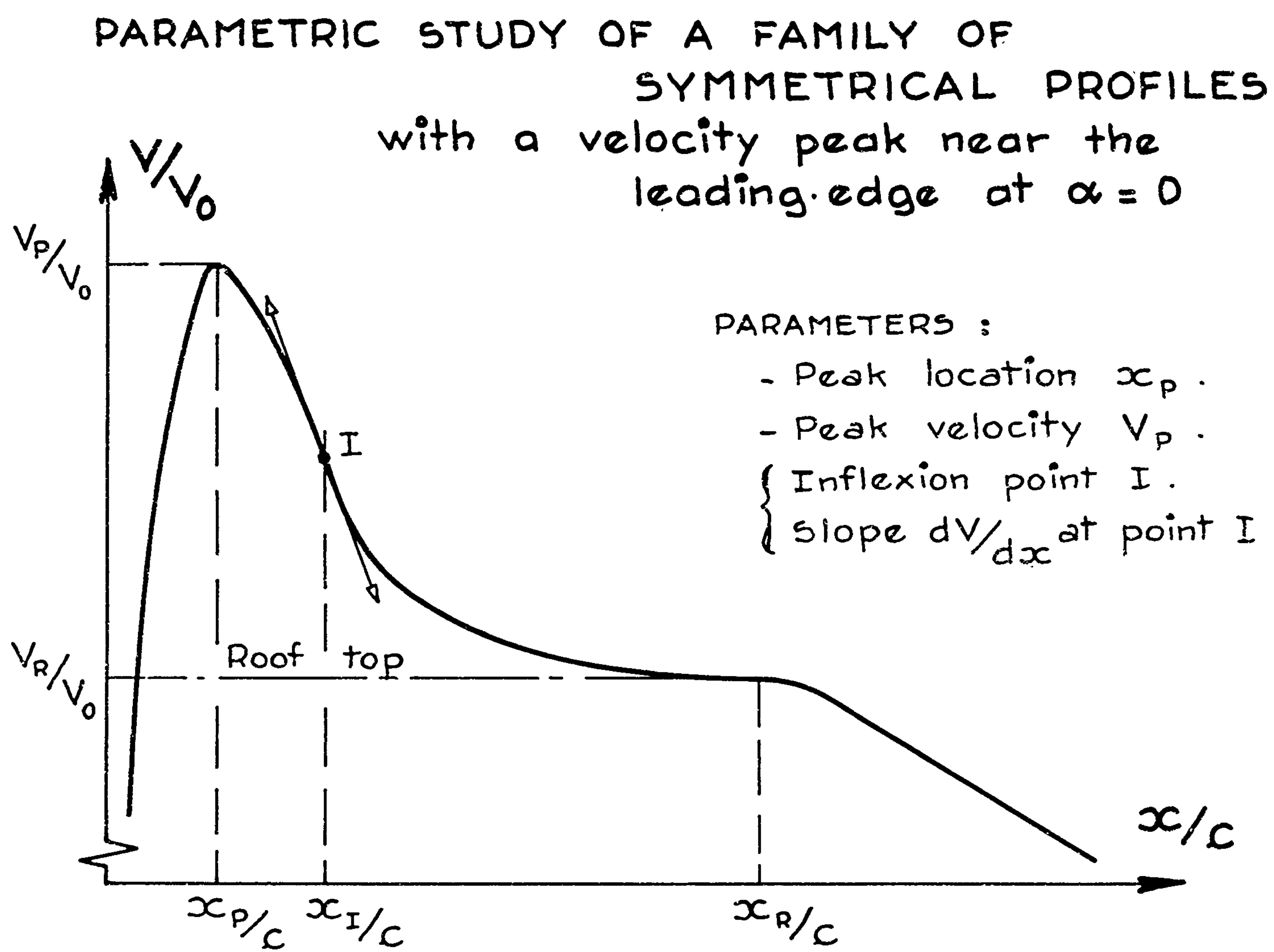

Fig. 3 Définition des différents paramètres retenus pour la famille de profils étudiés.

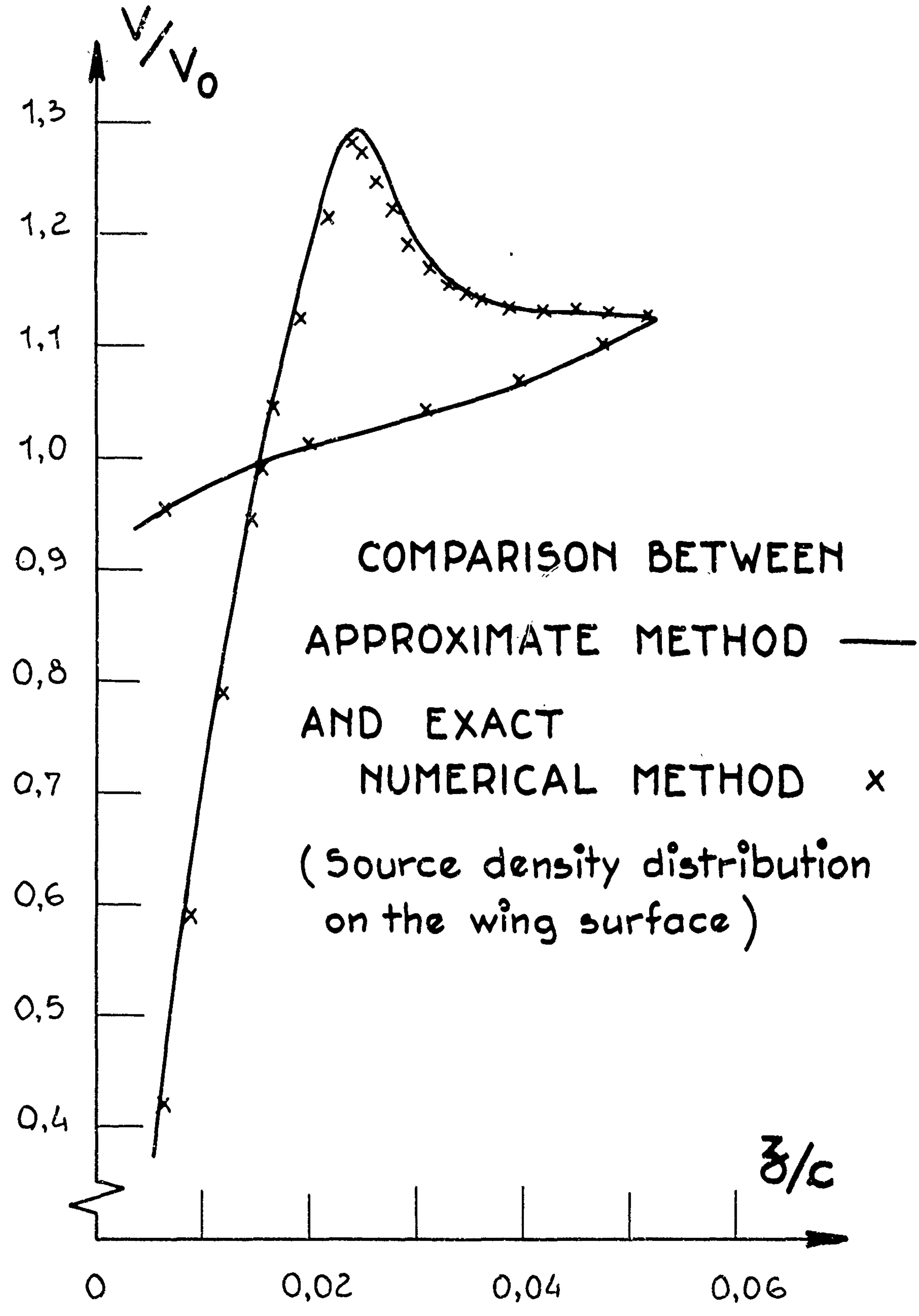

Fig. 4 Comparaison entre la méthode de calcul approchée et une méthode numérique exacte.

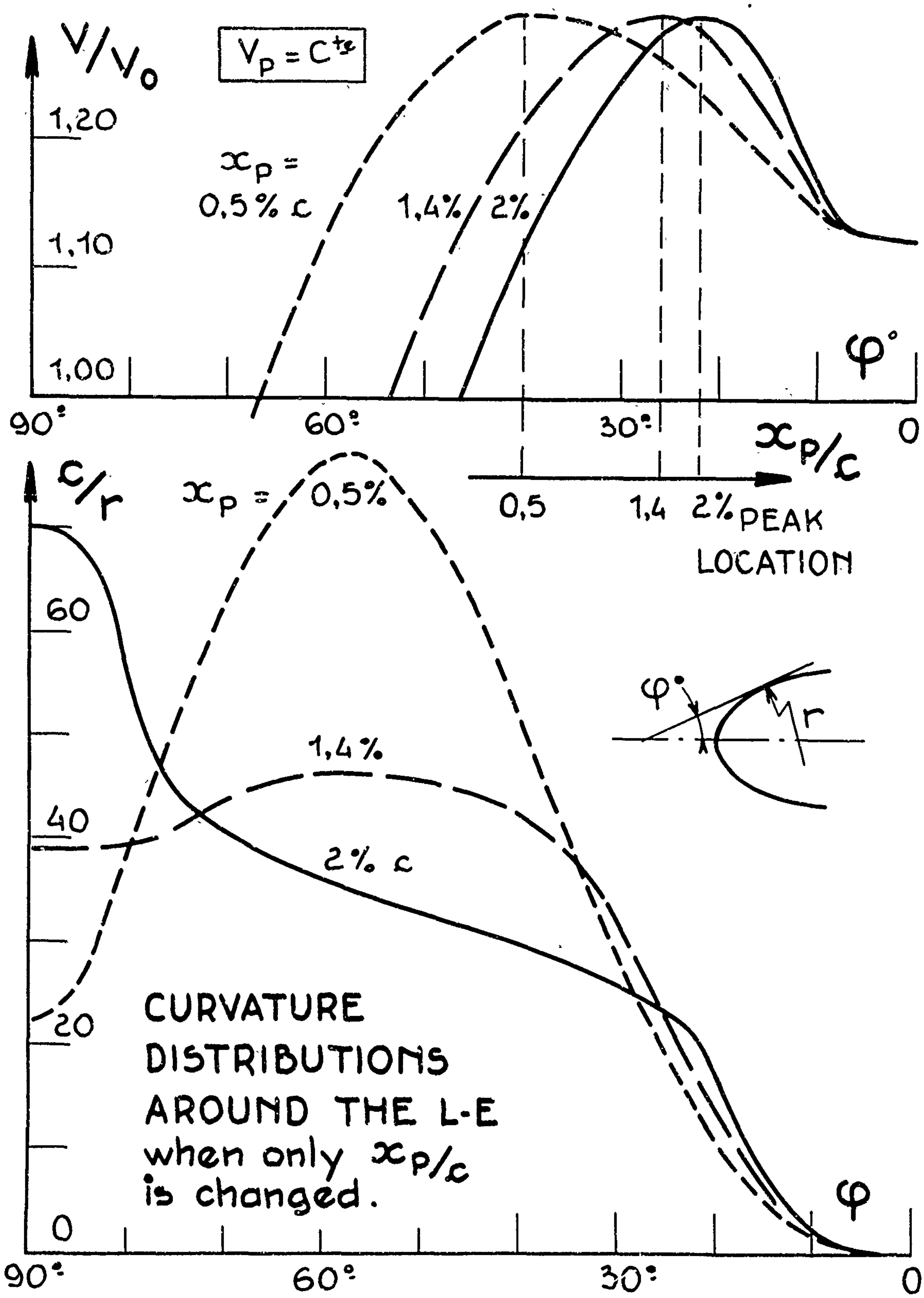

Fig. 5 Evolution des lois de courbure près du bord d'attaque en fonction de la position du pic de survitesse.

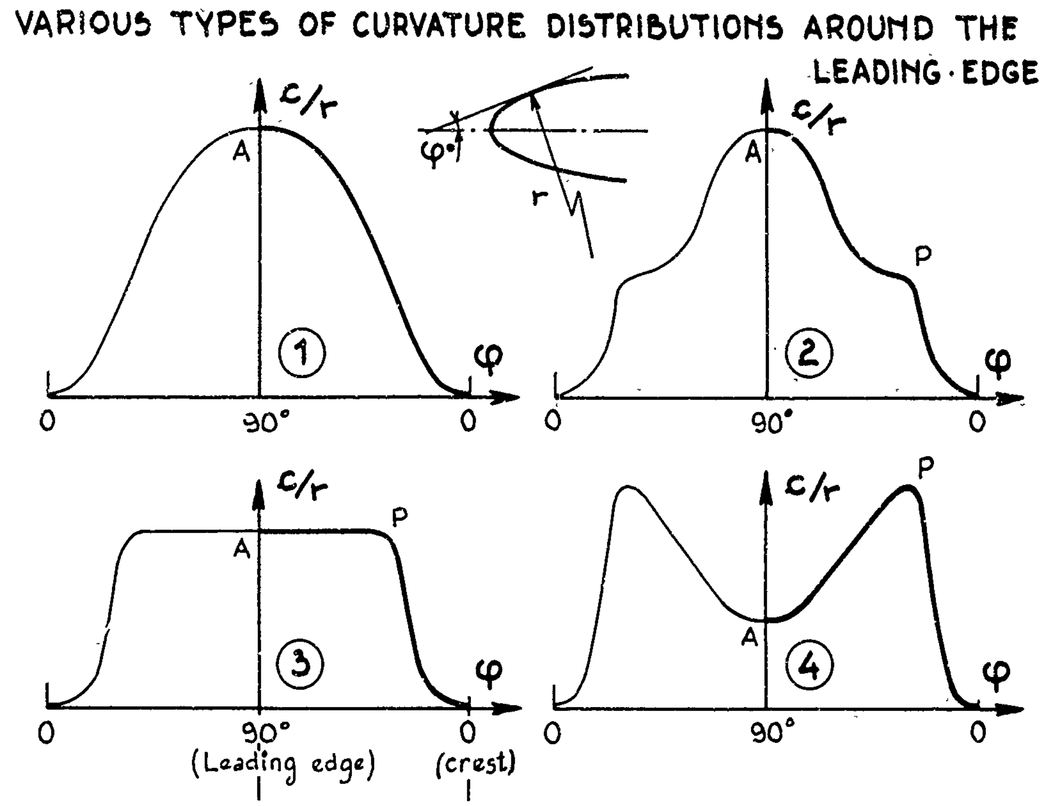

Fig. 6 Différents types de distribution de courbure autour du bord d'attaque.

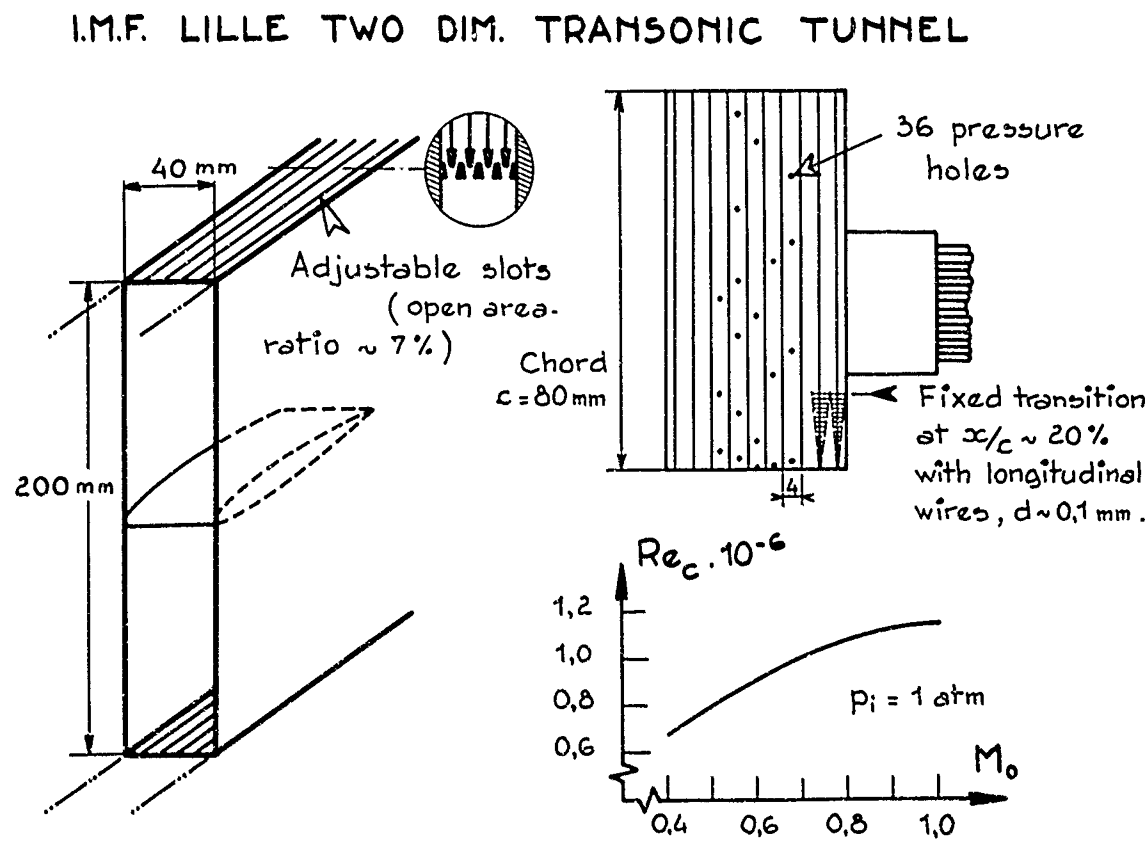

Fig. 7 Soufflerie transsonique de l'I.M.F. LILLE.

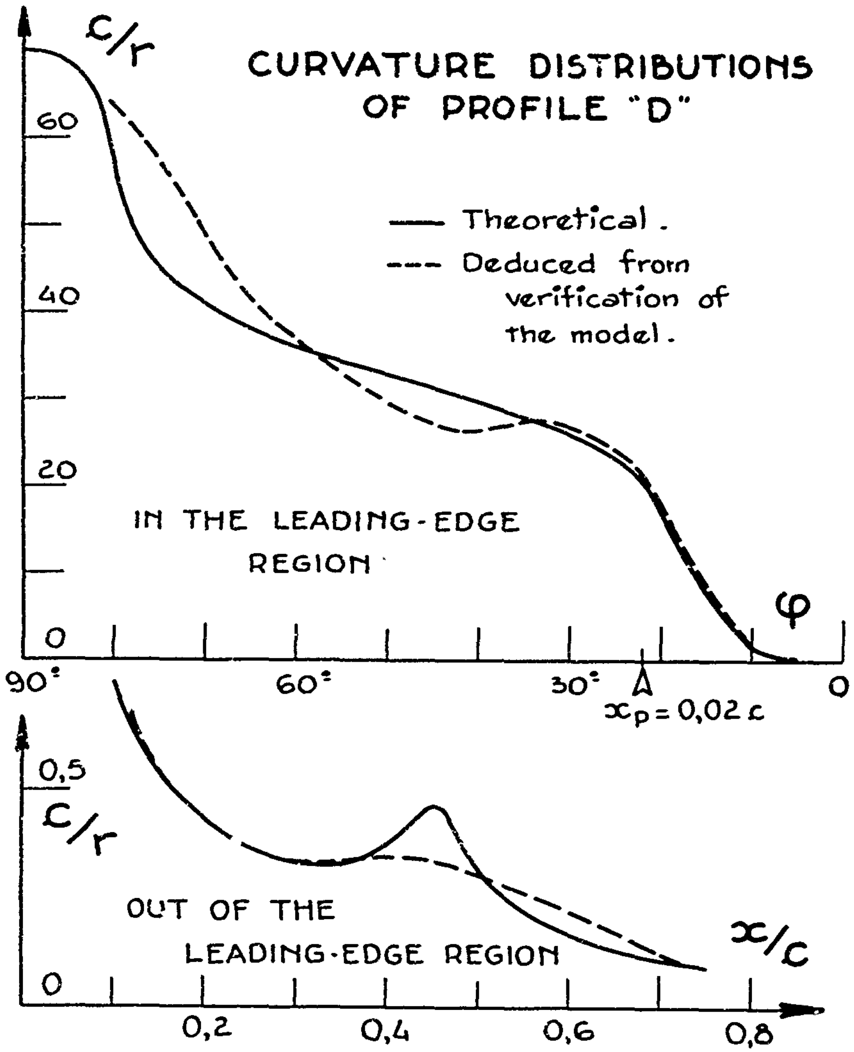

Fig. 8 Comparaison des courbures théoriques et effectivement réalisées sur maquette du profil D.

ONERA PROFILES TESTED IN 2 DIM. TRANSONIC FLOW

			$(t/c)_{max}$	x_{mt}/c	r_0/c
NACA 64_A010			10	37,7	0,69
			%	%	%
ONERA	1 02 00	A	10,17	37,9	0,57
	1 02 05 03 13	B	10,28	37,6	0,87
	1 02 05 10 04	C	10,49	36,6	1,20
	1 02 15 03 13	D	10,47	36,9	1,43

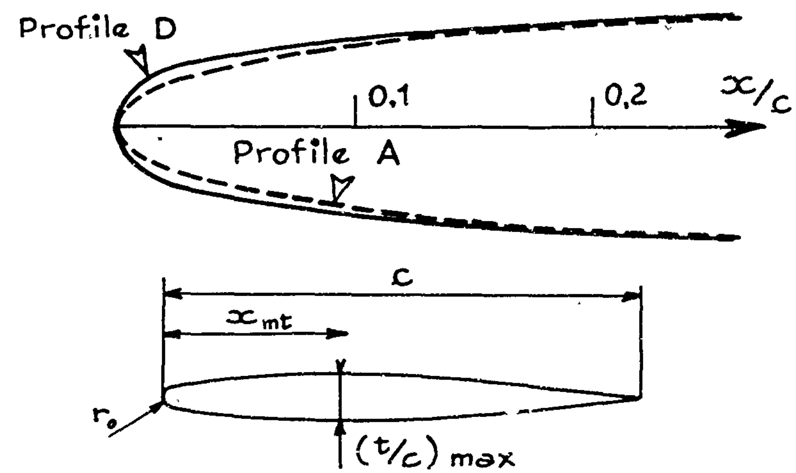

Fig. 9 Principales caractéristiques géométriques des profils étudiés.

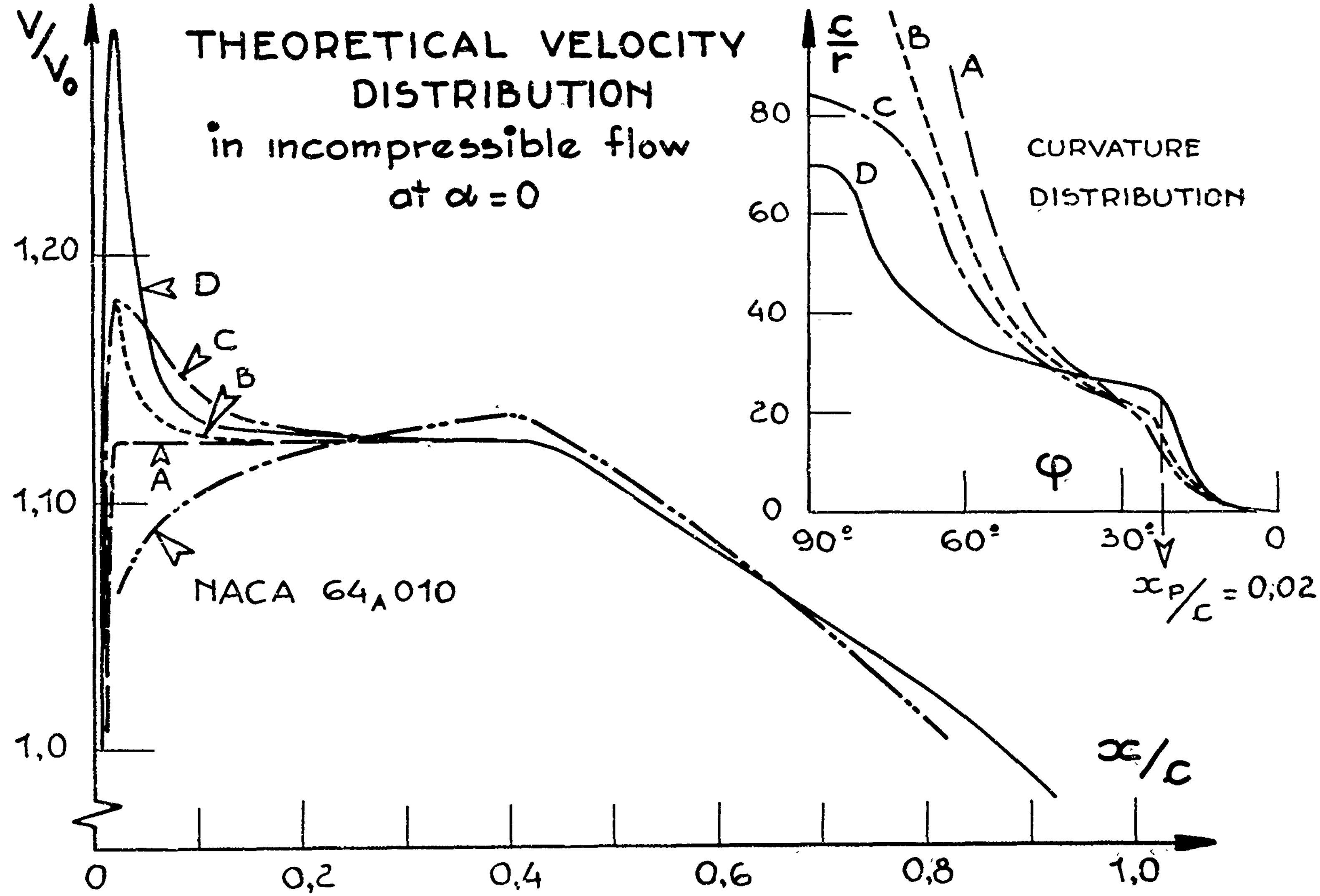

Fig. 10 Distribution de vitesse théorique des profils étudiés.

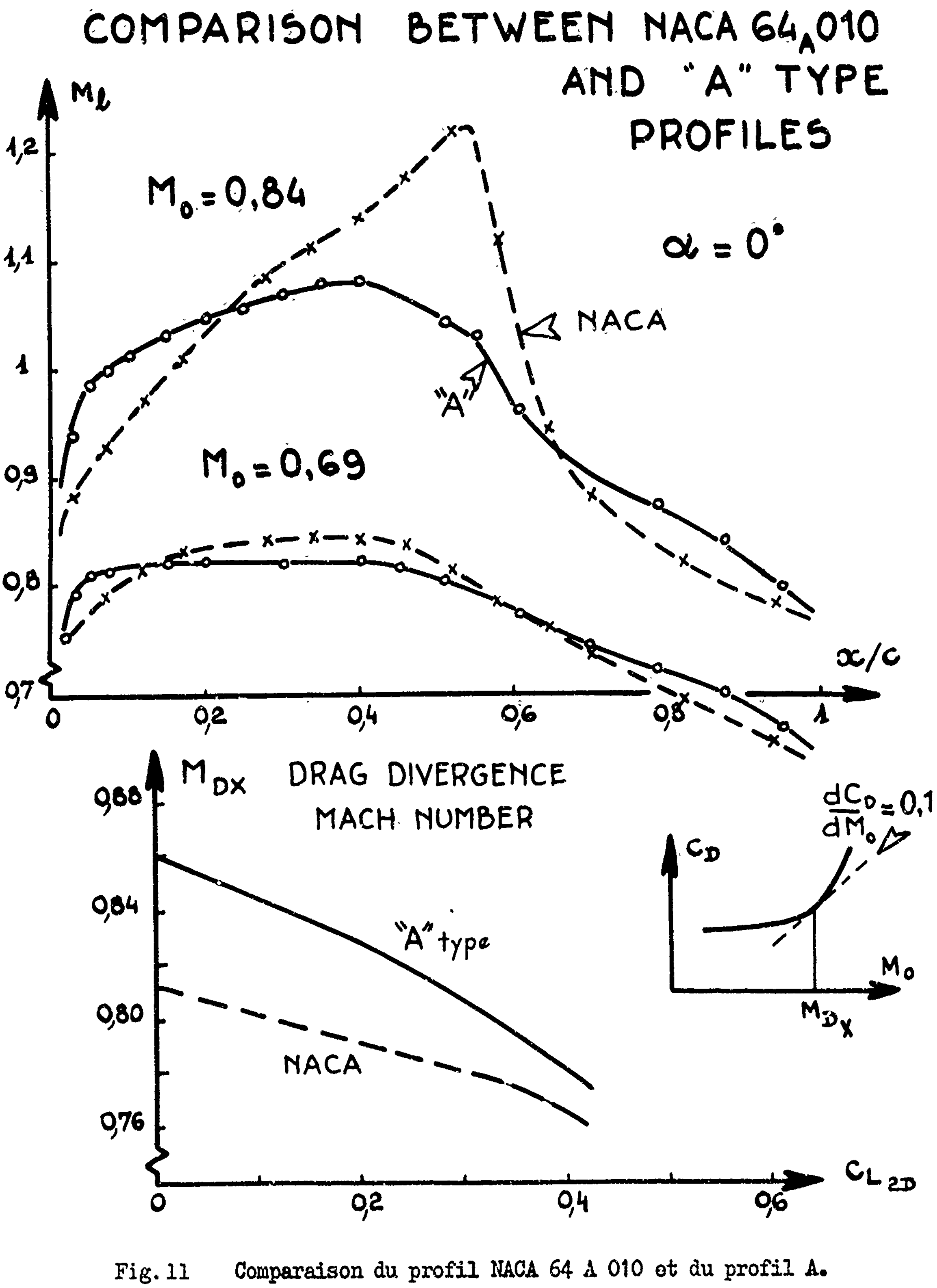

Fig. 11 Comparaison du profil NACA 64 A 010 et du profil A.

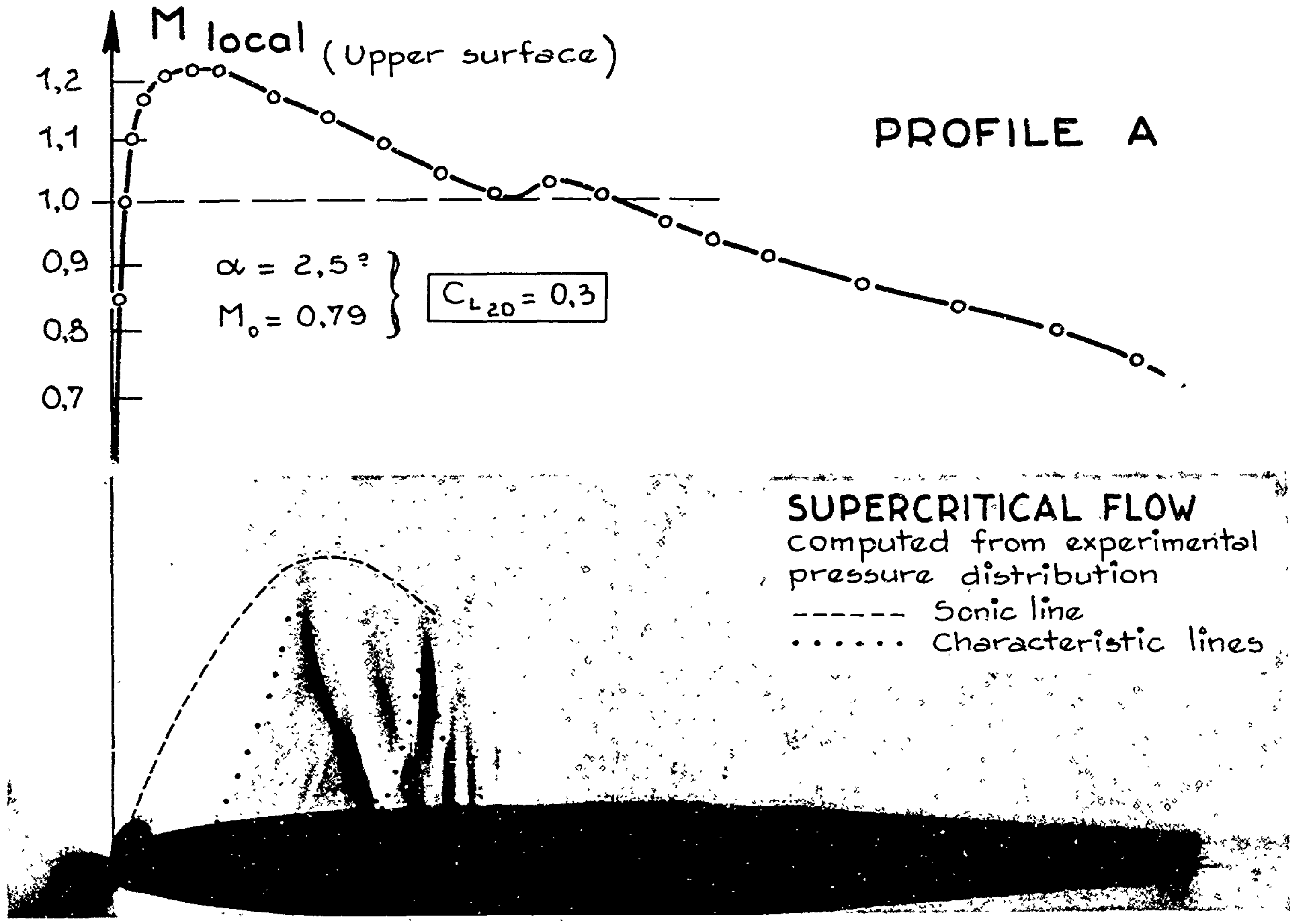

Fig. 12 Ecoulement à l'extrados du profil A pour $\alpha = 2{,}5°$ et $M_0 = 0{,}79$.

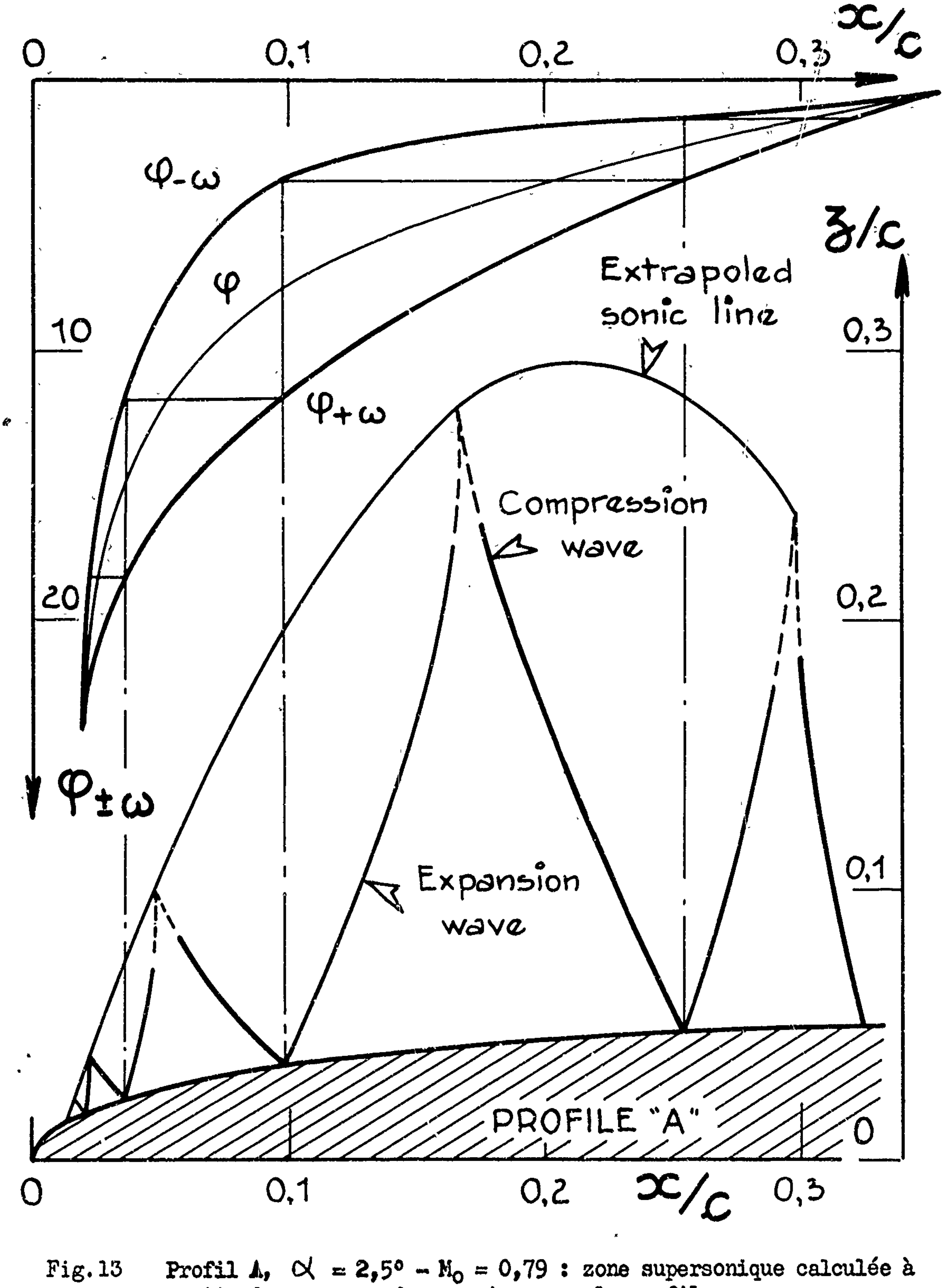

Fig. 13 Profil A, $\alpha = 2{,}5°$ – $M_0 = 0{,}79$: zone supersonique calculée à partir des mesures de pressions sur le profil.

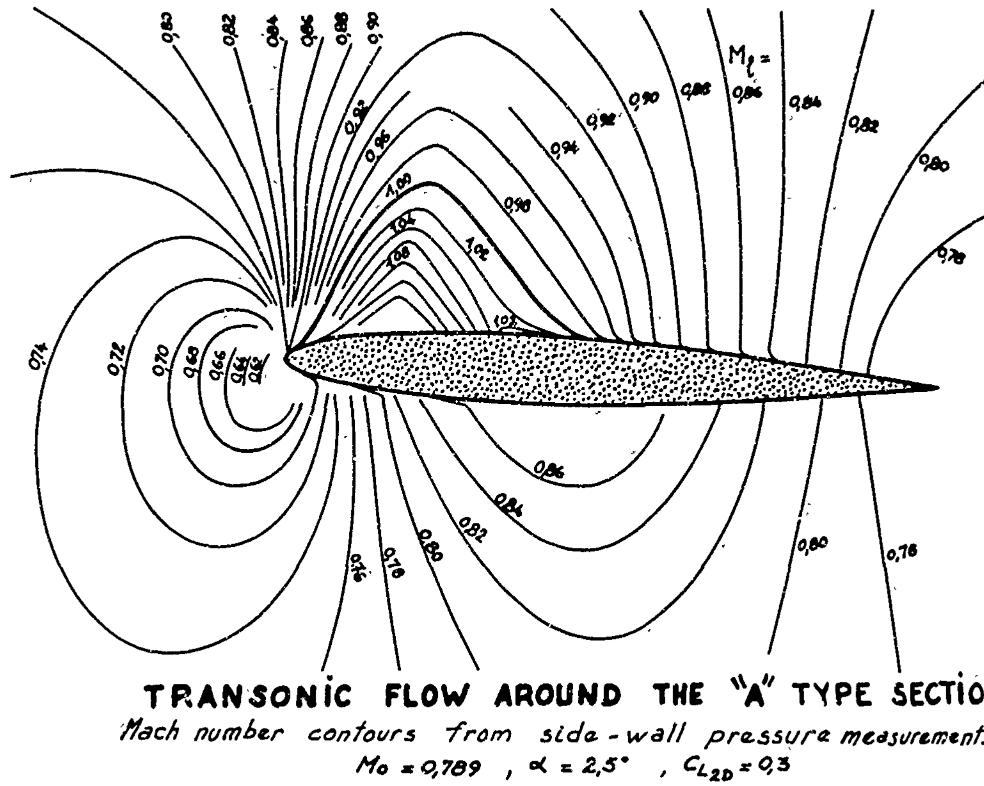

Fig. 14 **Profil A, $\alpha = 2{,}5° - M_0 = 0{,}79$: lignes isobares autour du profil, déterminées à partir de mesures de pression sur la paroi latérale de la soufflerie.**

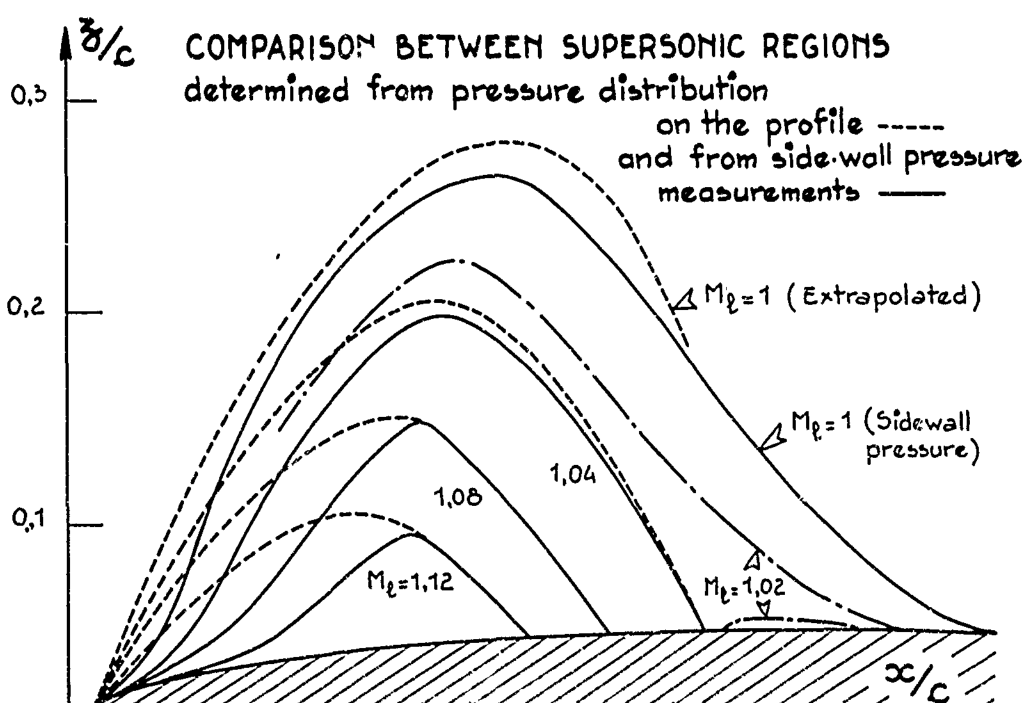

Fig. 15 Comparaison de la zone supersonique calculée à partir des mesures de pression sur le profil et de celle déduite de mesures de pression à la paroi de la soufflerie.

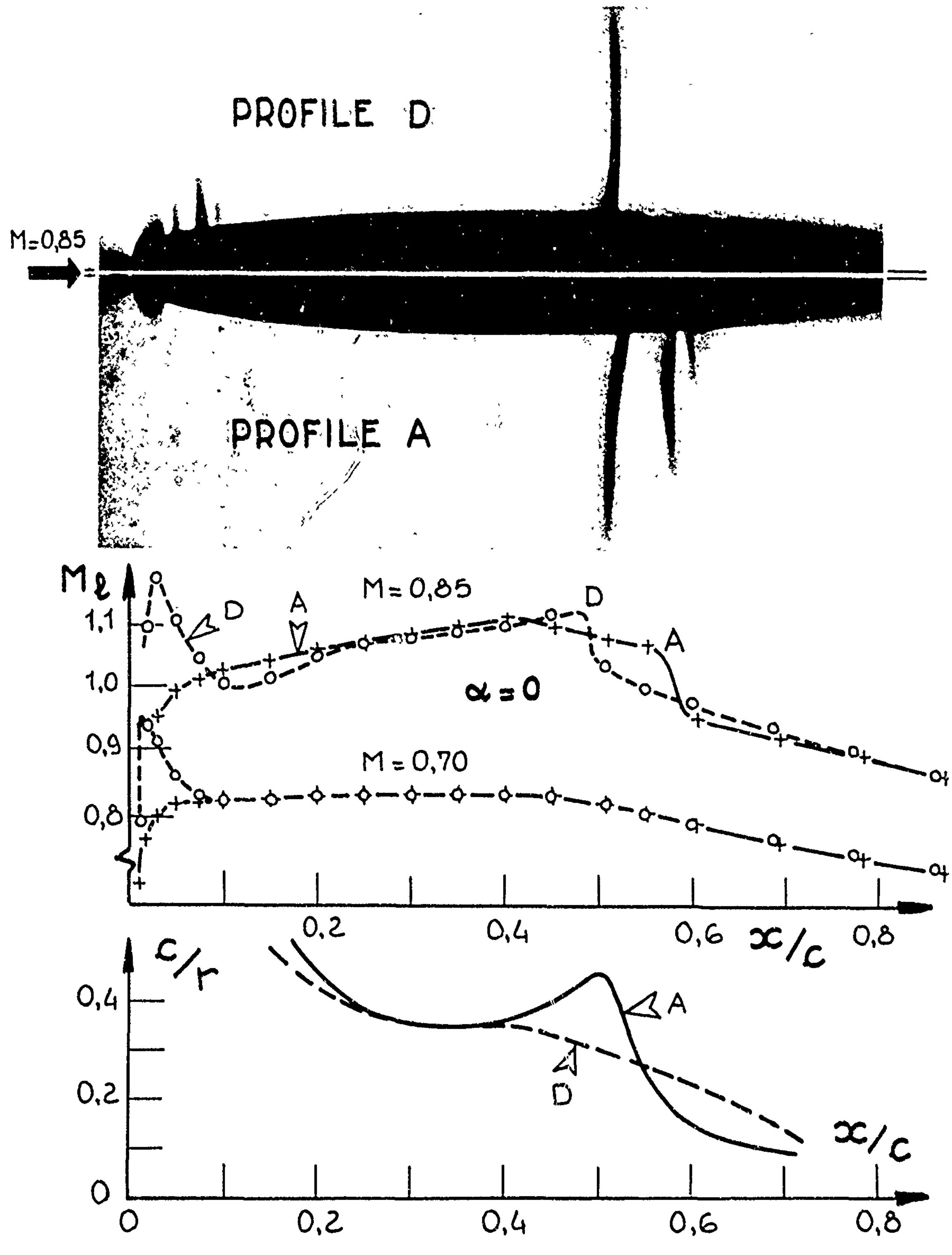

Fig. 16 Comparaison des profils A et D à incidence nulle.

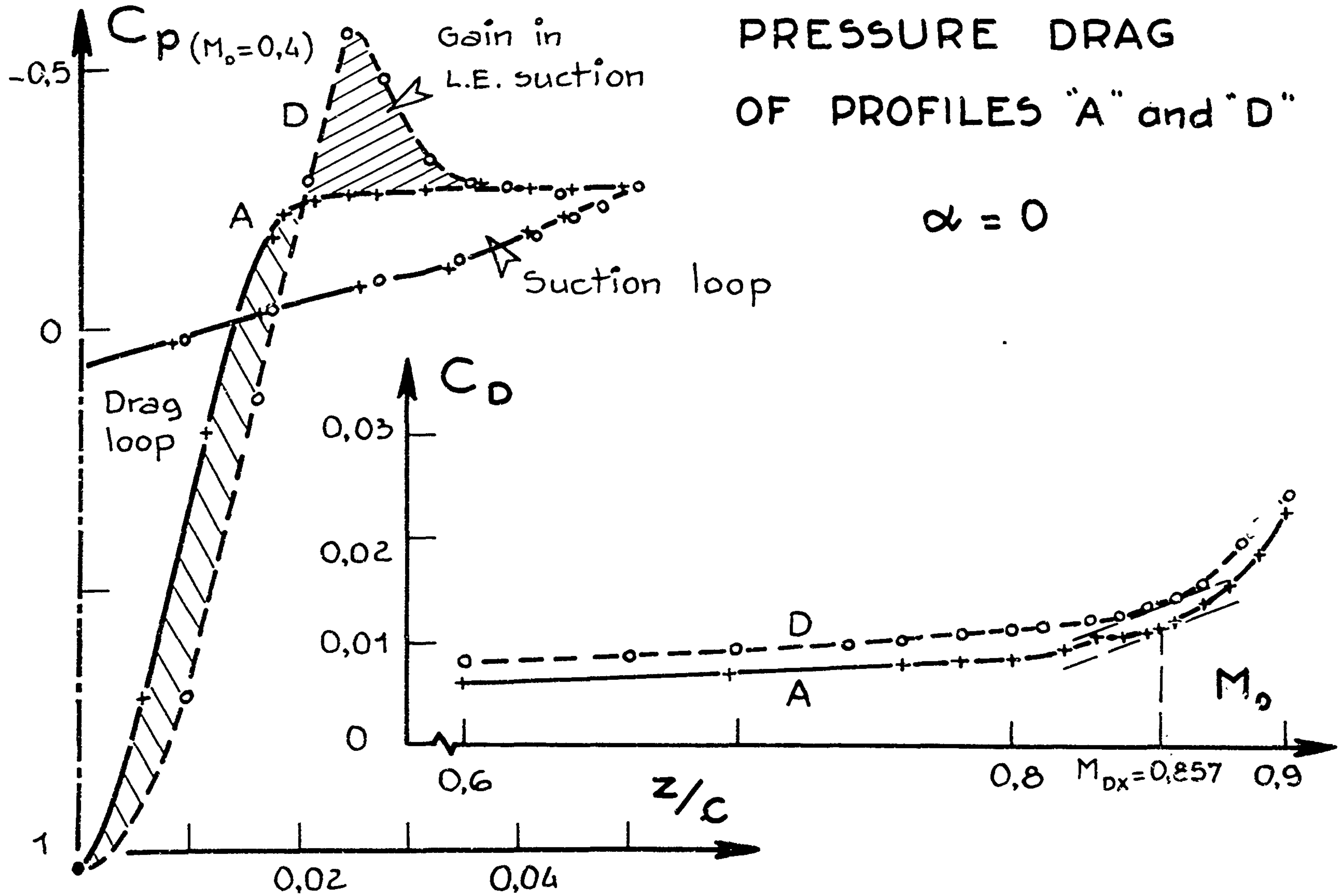

Fig 17 Traînée des profils A et D à incidence nulle.

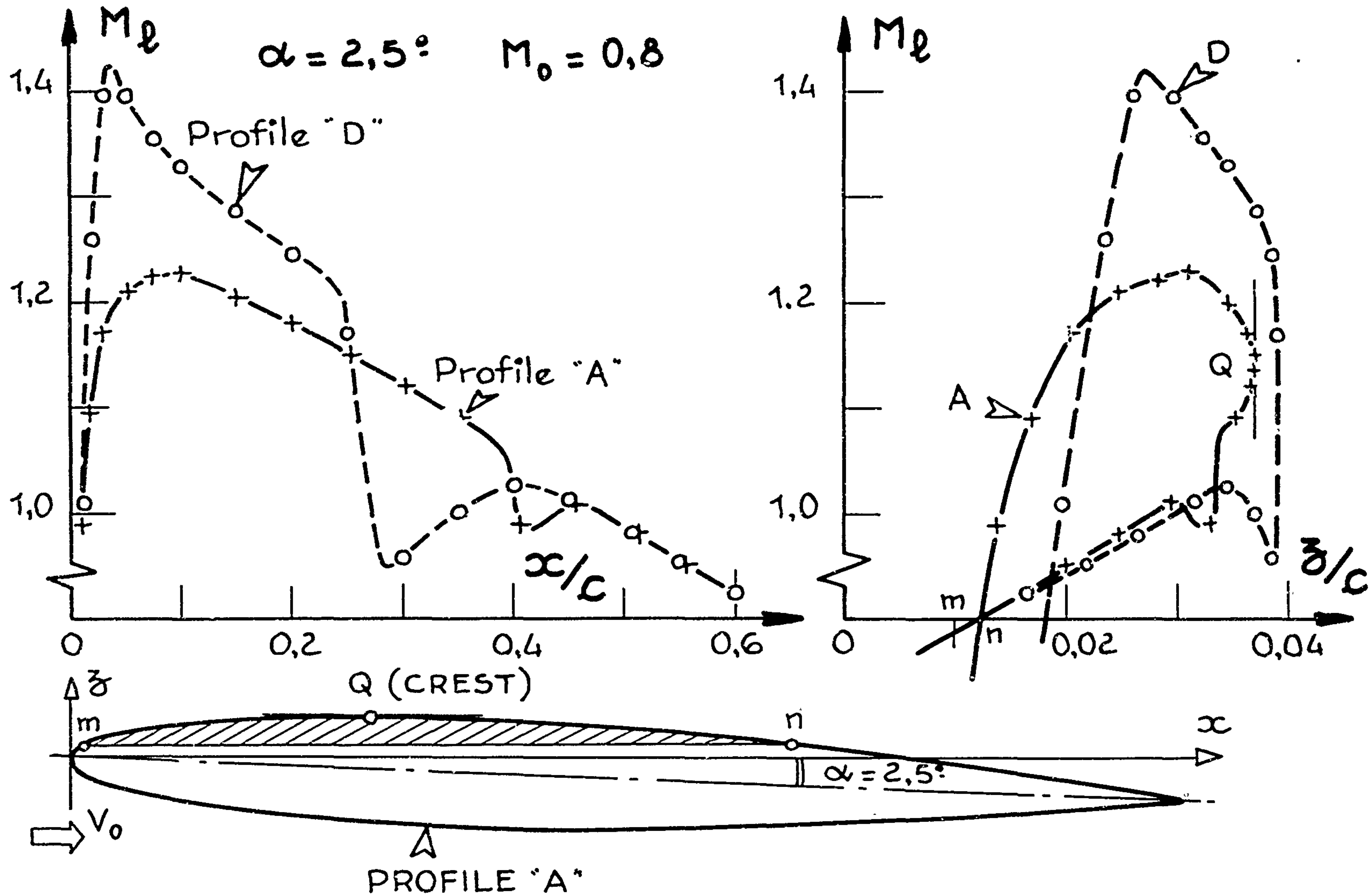

Fig. 18 Comparaison des répartitions de Mach locaux à l'extrados des profils A et D à $\alpha = 2,5°$.

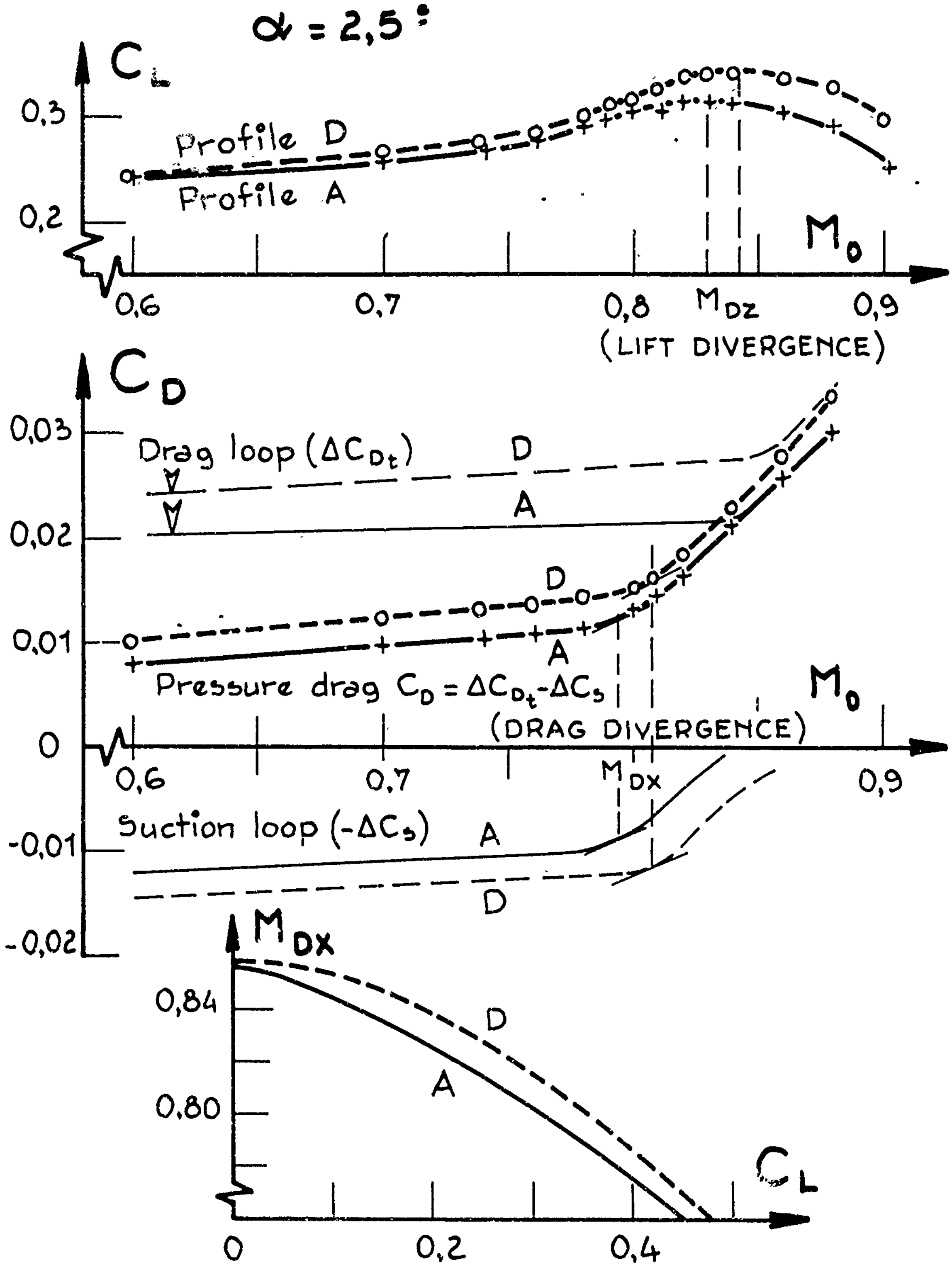

Fig. 19 Portance et traînée des profils A et D à $\alpha = 2{,}5°$

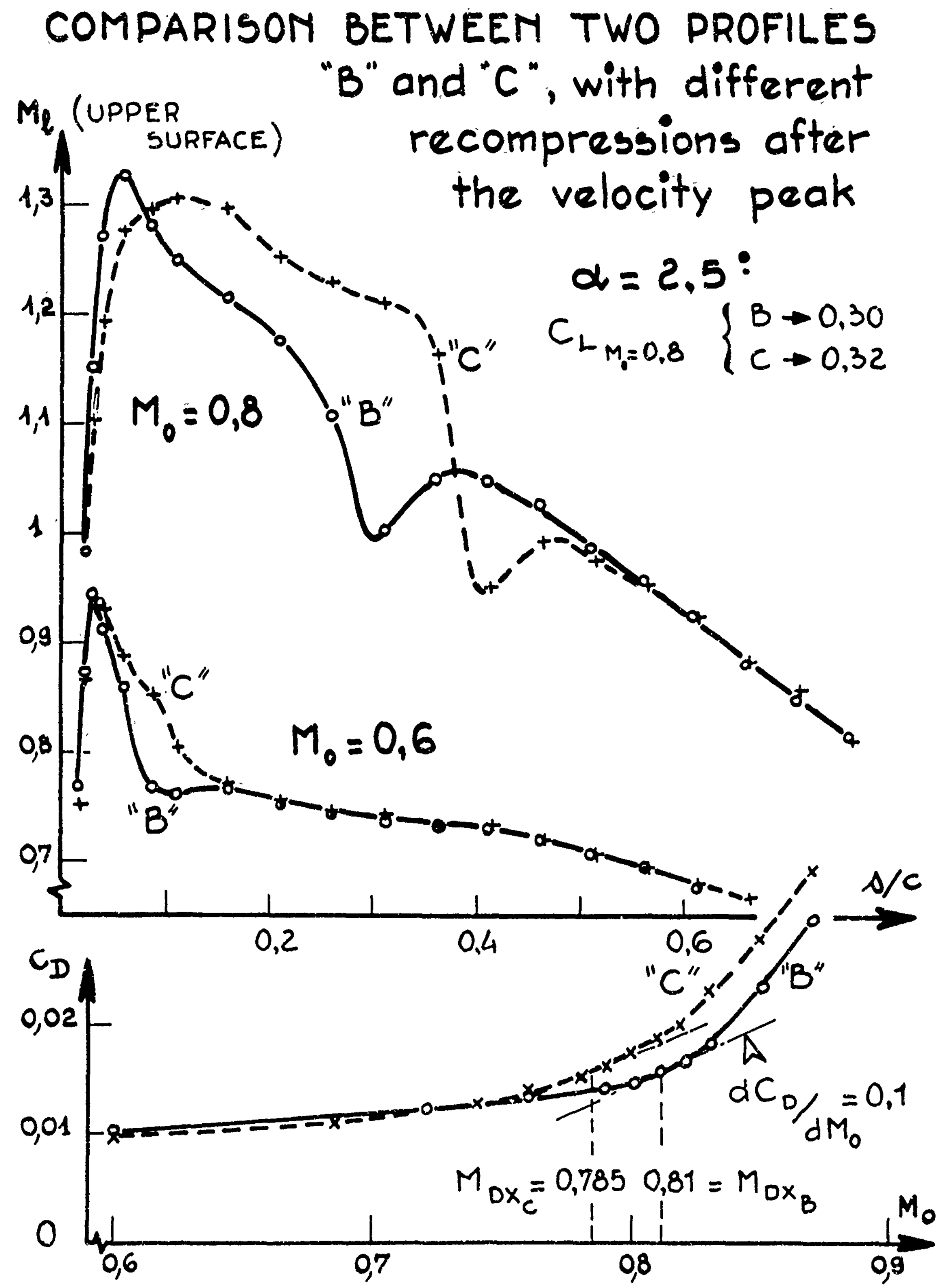

Fig. 20 Comparaison des profils B et C à $\alpha = 2,5°$.

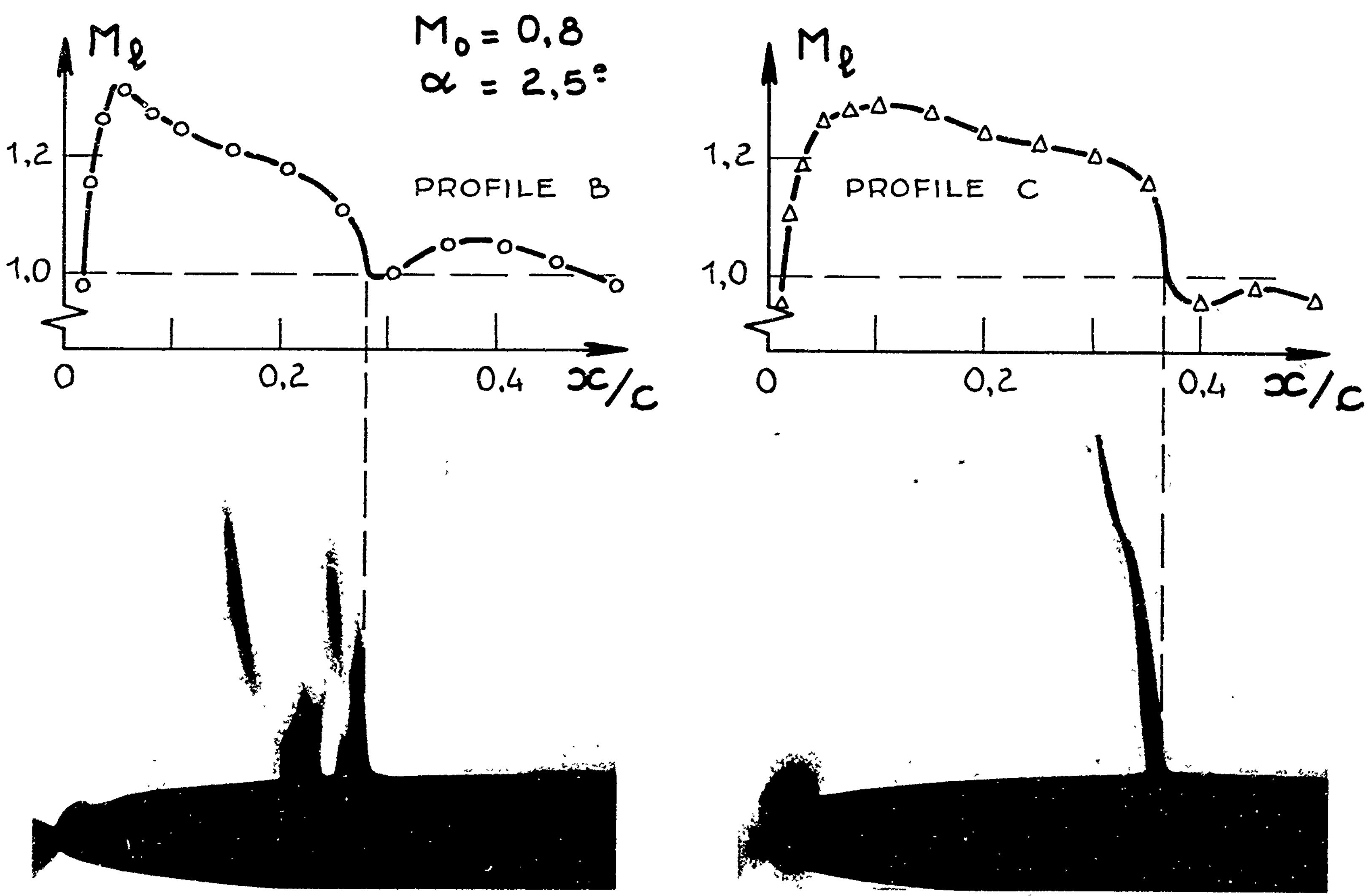

Fig. 21 Visualisations de l'écoulement autour des profils B et C à α = 2,5° et M_0 = 0,8.

LEADING-EDGE SUPERSONIC VELOCITY PEAKS AND THE DETERMINATION OF THE VELOCITY DISTRIBUTION ON AN AEROFOIL IN A SONIC STREAM

N. Thompson*

(Engineering Sciences Data Unit)

P.G. Wilby **

(National Physical Laboratory)

* Senior Engineer

** Senior Scientific Officer

SUMMARY

The geometric features of an aerofoil that are required to produce a supersonic velocity peak at the leading-edge are examined, and a rule is presented for relating the compressible velocity on a round leading-edge to the incompressible velocity. For a supersonic peak, the sonic point must lie on a region of sustained high curvature, and the dependence of the recompression on the way in which the curvature is reduced is indicated.

An empirical method for determing the complete velocity distribution downstream of the sonic point is given for an aerofoil in a sonic stream. The velocity distribution for a given aerofoil is shown to be given by a universal function which is modified by a parameter based on geometry and one involving the position of the sonic point. Several comparisons of predicted and measured velocity distributions are presented.

NOTATION

c	aerofoil chord
C_p	pressure coefficient
f	thickness parameter $f = 0.1/\left[2(z/c)_{max}\right]$
$F(\ )$, $F_o(\ )$	general function
H	stagnation pressure in undisturbed stream
K	influence factor pertaining to large disturbance flow near leading-edge
M	local Mach number
p	local static pressure
r	local surface radius of curvature
s	distance along surface
t	aerofoil maximum thickness
U	local velocity
x	chordwise distance measured from leading-edge
z	aerofoil ordinate measured from chord line
α	angle of incidence
θ	aerofoil surface slope relative to chord line
Θ	aerofoil surface slope relative to free-stream direction
λ	influence factor pertaining to supersonic region of flow
ρ	local surface curvature
ϕ	angle between local tangent at surface and tangent at stagnation point
ω	Prandtl-Meyer angle

Suffixes

A	pertaining to value at sonic point or point corresponding to $r/c = 0.2$ whichever is larger
e	pertaining to experimental value
i	pertaining to incompressible flow value
s	pertaining to value at sonic point
∞	pertaining to free-stream conditions

PART I

LEADING-EDGE SUPERSONIC VELOCITY PEAKS

P.G. Wilby

1. INTRODUCTION

As incidence or free-stream Mach number increases, the velocity on the surface of an aerofoil increases and eventually reaches sonic value at some point. With further increases of incidence or Mach number a region of supersonic flow appears on the aerofoil and is usually terminated by a shock wave which eventually becomes strong enough to cause the boundary-layer to separate. Now the strength of the shock wave has been found to depend upon the way in which the supersonic flow develops, and it can be considerably reduced if the pressure distribution is of the peaky type. The latter involves a rapid expansion to a peak velocity at the leading-edge, followed by a compression which is mainly isentropic but usually finishes with a weak shock. This type of pressure distribution is essential if one is to achieve a large margin in incidence or Mach number between the first appearance of supersonic flow and shock induced separation.

However, not all pressure distributions with leading-edge suction peaks are necessarily desirable ones. On the one hand, the peak may grow very quickly with incidence, resulting in a high peak followed closely by a strong shock wave, and on the other hand the peak growth may be too small in which case the peak is followed by a weak compression and then a further slow expansion that terminates in a strong shock. The way in which the peak develops with incidence or Mach number depends to a large extent upon the geometry of the leading-edge and it is necessary to find out what the controlling influences are before it is possible to design an aerofoil that will have the most beneficial development of supersonic flow.

2. THE FORMATION OF A LEADING-EDGE VELOCITY PEAK

As a first step in the study of leading-edge supersonic suction peaks, it is essential to understand the geometric features of an aerofoil that are responsible for the formation of such a peak. The region of immediate interest is that in which the velocity of the air is supersonic and thus the sonic point is a useful reference point. If the sonic point is very close to the leading-edge then it lies in a region of fairly high surface curvature and the flow continues to expand beyond the sonic point as it turns to follow the aerofoil profile. This expansion of the flow can be considered to take the form of a succession of descrete expansion waves generated at the surface, which are transmitted to the rest of the flow field along characteristic lines (Fig. 1). Along each of these lines the value of $\theta - \omega$, where ω is the Prandtl-Meyer function, is constant. If the entire flow field were supersonic then these characteristics or expansion waves would continue to infinity and the change in Prandtl-Meyer function (which is a measure of the velocity) as the flow followed the profile would simply be the change in surface slope. However, the flow field under consideration is a mixed one, being mainly subsonic but containing a small supersonic region. The two regions are separated by the sonic line at which the expansion waves can be considered to be reflected as compression waves. These compression waves are of course members of the second family of characteristics, along each of which $\theta + \omega$ is constant, and result in a weakening of the generated expansion at the surface of the aerofoil. If there is to be a net expansion then the compression waves must be more widely spaced than the expansion waves, and furthermore, if the expansion is to be very rapid then the expansion waves that are produced at the beginning of the supersonic region must be generated in quick succession. Now the value of the Prandtl-Meyer function ν on the generated expansion waves is directly proportional to the expansion angle or the change in slope. Thus if s is the distance along the surface

$$\frac{\partial \nu}{\partial s} = -\frac{\partial \theta}{\partial s}$$

$$= \rho \text{ (the surface curvature)}, \tag{1}$$

and for a rapid initial rate of expansion a high value of curvature is required. The magnitude of the net expansion will depend upon how long the high curvature is maintained, and the strength of the reflected system of compression waves. Now if surface curvature is maintained at a high value for a considerable range of surface slope then there must, for geometric reasons, follow a rapid reduction of curvature to a very low level in order that the resulting profile should be of the aerofoil type. The simplest form of such a profile is shown in Fig. 2 and is an aerofoil formed mainly by an arc of a circle of large radius but having a circle of small radius for a leading-edge, a small circle being the best way of producing a sustained rapid expansion. Suppose that the sonic point lies on the leading-edge circle where the surface slope is θ_s; then at some point on the leading-edge circle, downstream of the sonic point, the net rate of expansion will be given by the combined effects of the generated rate of expansion ρ_0 $(= 1/r)$ and the rate of compression from the reflected system of waves. If the latter is expressed as ρ_0 , then the net expansion is

$$\frac{\delta\omega}{\delta s} = \rho_0 - \eta\rho_0$$

i.e.

$$\frac{\delta\omega}{\delta s} = (1 - \eta)\ \rho_0 . \tag{2}$$

If is constant then equation 2 can be integrated to give

$$\omega = (1 - \eta)\ (\theta_s - \theta). \tag{3}$$

In Fig. 3, values of ω measured on a circular leading-edge are plotted against ( ) and apart from the initial curve, the relationship is seen to be effectively linear, indicating that η is in fact constant ($\eta \simeq 0.5$) and that equation 3 is valid. This initial curved portion of the graph is expected as it can be shown theoretically that $\delta\omega/\delta\theta = 0$ at $M = 1$. Experimental evidence so far collected indicates that for well established supersonic flow the value of η is effectively independent of free stream Mach number, incidence and leading-edge radius.

Consider now what happens when the curvature discontinuity is reached. Here, the rate at which expansion waves are generated is dramatically reduced from ρ_0 to ρ_1 ($= 1/R$ where R is the radius of the arc of the large circle). On the other hand it can be expected that the rate at which compression waves arrive at the surface does not immediately change as it depends upon the upstream conditions. Thus the net rate of expansion can probably be given by

$$\frac{\delta\omega}{\delta s} = \rho_1 - \eta\rho_0 \tag{4}$$

which is a negative quantity as $\rho_1 \ll \eta\rho_0$, and the net effect is a strong compression. The curvature discontinuity is seen to be the point at which a net expansion is replaced by a net compression and must therefore be the point at which maximum velocity is reached, that is the position of the velocity peak. A typical case for this type of aerofoil is shown in Fig. 4 where an experimental pressure distribution is superimposed on the curvature distribution. In the lower part of the figure the pressure is plotted against distance from the leading-edge and it is seen that the compression that follows the suction peak is so strong that a shock wave is formed. However, with such a curvature distribution it is possible to locate the position of the suction peak precisely, and give a close estimate of its magnitude. It thus forms a useful basis on which to study the effects on the suction peak of such parameters as leading-edge radius, Mach number and incidence. Before moving on to these topics it is necessary to examine the way in which velocity increases from the stagnation point up to the supersonic region.

3. VELOCITY DISTRIBUTIONS ON ROUND LEADING-EDGES

An experimental investigation of velocity distributions on round leading-edges has shown that for any free-stream Mach number in the range $0 < M \leqslant 1$ the velocity U can be related to the incompressible velocity in the form

$$U/U_\infty\ (M_\infty,\phi) = U_i/U_\infty\ (b\phi), \tag{5}$$

where θ is the angular displacement from the stagnation point, and

$$b = 1 - \mu M_\infty^2 . \tag{6}$$

However, μ was found to vary according to the effective profile. That is, it varies from profile to profile and it also varies as the stagnation point moves on a given aerofoil. An empirical relation between μ and the corresponding incompressible velocity distribution was found to be

$$\mu = \sqrt{\frac{1 + \tau}{2}}\ 0.42 \tag{7}$$

where $1 + \tau$ is the initial value of the slope of the curve U_i/U_∞ against $\sin\phi$. When $\tau = 1$ Eqn. 6 reduces to the result suggested in Ref. 1 for circular cylinders and aerofoils with sustained circular leading-edges. The validity of the above relationships is demonstrated in Figs. 5 to 7 where measured values of U/U_∞ are plotted against $b\phi$ for a variety of leading-edge shapes (the appropriate curvature distribution is shown in each figure), and for each case the experimental points are found to collapse fairly well on to a single curve which is very close to the theoretical inviscid incompressible solution. It will be noted that Eqn. 5 indicates that local velocity ratio decreases as free-stream Mach number increases, but it is well known that over most of the aerofoil profile, where the surface slope is small, the reverse is true. Thus Eqn. 5 cannot be expected to hold for large values of ϕ . However, it does hold for aerofoils at incidence (see Fig. 8) and if conditions are such that a well established region of supersonic flow exists close to the leading-edge then it is sufficient to give the velocity up to and including the sonic point. In all cases the compressible velocity distribution can be related only to the incompressible velocity distribution that has the identical stagnation point.

4. THE EFFECTS OF LEADING-EDGE GEOMETRY AND MACH NUMBER ON THE ZERO INCIDENCE VELOCITY PEAK

With the aid of the above velocity rule it is possible to examine further the geometric features that are required to generate a supersonic velocity peak at zero incidence. It is seen in Figs. 5 to 7 that the longer the leading-edge circle is sustained, the steeper the velocity gradient becomes and the greater the maximum velocity is, hence the greater the likelihood of sonic velocity being attained at a moderately high value of surface slope. Fig. 9 shows the experimental pressure distribution at $M_\infty = 0.8$ for the aerofoil referred to in Fig. 5, and the supersonic velocity peak will be noted. In contrast, the theoretical velocity distribution (calculated by the approximate method of Ref. 2) at the same Mach number for an elliptic aerofoil of the same thickness is seen to be everywhere subsonic. This once more demonstrates the importance of a considerable extent of high surface curvature.

Returning to the geometrically simple profile defined by two circular arcs (Fig. 2) joined at a large curvature discontinuity at a fairly low value of surface slope, the velocity distribution on the leading-edge of such a profile will be close to that for a circular cylinder. The way in which the leading-edge velocity rule predicts that the sonic point will vary with Mach number for this case is shown in Fig. 10. A supersonic peak will begin to form as soon as the sonic point first appears on the leading-edge circle and will grow as Mach number increases and the sonic point moves further forward of the curvature discontinuity. Maximum peak will first be reached when the sonic point reaches its most forward position at $M_\infty = 0.9$. Consider now a family of this type of aerofoil where each member has the same maximum thickness and the same chordwise position of maximum thickness. The profile of each member is then determined by the value of the leading-edge radius and in Fig. 11 it is seen that as leading-edge radius increases, the curvature discontinuity moves to a lower value of surface slope. Thus for a fixed Mach number and sonic point position (assuming that the sonic point lies on the leading-edge circle), the supersonic velocity peak will grow as leading-edge radius is increased. This is a tendency in the case of more general profiles. It will of course be realised that the sonic point will not in fact remain stationary as the geometry changes but will move in a way that accentuates the effect described.

5. THE VELOCITY PEAK ON AN AEROFOIL AT INCIDENCE

A lifting aerofoil is naturally of greater interest but presents a further problem due to the movement of the stagnation point with incidence and Mach number. As the stagnation point moves round to the lower surface with increase of incidence, the sonic point moves further forward and the velocity peak grows. Thus as the design incidence increases then, in order to prevent the velocity peak becoming too high, the leading-edge geometry must be changed so that the rapid drop in curvature occurs at a higher value of surface slope. There is now an added effect of Mach number on peak height as for a fixed incidence the stagnation point moves forward as Mach number increases, and the movement of the sonic point is now a combination of its movement relative to the stagnation point and the movement of the stagnation point itself. Fig. 12 illustrates the situation for a particular aerofoil at 3° incidence and shows the measured variation of surface slope at the stagnation point and the calculated variation of ϕ (the angular separation of the sonic and stagnation points), which combine to give the surface slope at the sonic point. The most forward position of the sonic point is seen to be at $M_\infty = 0.7$ and this is thus the Mach number for maximum peak height at this particular incidence. This result, together with the zero incidence result, indicates that the Mach number for maximum velocity peak varies with incidence.

The idealised situation, of an aerofoil at incidence which generates a supersonic velocity peak followed by an isentropic compression, is depicted in Fig. 13 and helps to illustrate the various design problems involved. The acceleration from the stagnation point, located on the lower surface, is shown with sonic velocity reached on the leading-edge circle. Then follows the supersonic acceleration which is modulated by the reflected compression waves. The latter become dominant after the rapid fall of curvature and it is the delicate balance between the generated expansion and the reflected compression that maintains the isentropic compression. How to design for this ideal case is not in general known although Nieuwland has produced some particular solutions.

Although the ideas expressed here are far from providing a complete solution, they do assist the appreciation of the various factors involved in the generation of a supersonic velocity peak at the leading-edge of an aerofoil.

REFERENCES

1. WILBY, P.G. Velocity distributions on round leading-edges for free-stream Mach numbers between zero and unity. Part 1. NPL Aero Report 1225, March 1967.

2. WILBY, P.G. The calculation of sub-critical pressure distribution on symmetric aerofoils at zero incidence. NPL Aero Report 1028, March 1967, ARC C.P. No. 993, 1968.

PART II

THE DETERMINATION OF THE VELOCITY DISTRIBUTION ON AN AEROFOIL IN A SONIC STREAM

N. Thompson

1. INTRODUCTION TO PART II

The need to be able to predict the velocity distribution on aerofoils with regions of supercritical flow is an important step in the design of the modern generation of high-subsonic cruise aircraft. The practical significance of this need lies, for example, in the prospect of relating the shock strength to that required to provoke shock-induced separation.

Part I has shown in particular how, for round-nosed aerofoils, a velocity rule may be used to determine local velocities in the initial rapid flow expansion from the stagnation point in the Mach number range $0 < M_\infty < 1.0$. The rule is only valid upstream of the small-disturbance flow region but, in most cases of practical interest, can be used to determine where the sonic point occurs in the initial flow expansion for free-stream Mach numbers within the transonic speed range. Part II of this paper deals specifically with conditions at $M_\infty = 1.0$ and considers, in particular, the problem of predicting local supersonic regions of flow between the sonic point and the shock wave terminating the supersonic region of flow. The derivation of a rapid, but accurate, method is described for obtaining surface pressures in the supersonic region of flow at $M_\infty = 1.0$ which may be applied to any arbitrary round- or sharp-nosed, lifting or non-lifting aerofoil once the sonic point (or the flow condition at some point downstream of the sonic point) has been determined from priori considerations.

2. THE REGION OF LOCAL SUPERSONIC FLOW

The purpose of this section is to show how the local supersonic velocity distribution at $M_\infty = 1.0$ on any arbitrarily-defined section may be expressed in the form of a simple correlation with chordwise distance of a parameter, involving only the local Prandtl-Meyer angle, the aerofoil geometry and a factor dependent on the sonic point location. It follows that for any aerofoil for which the sonic point location and the geometry are known, a method of predicting the local supersonic region of flow is embodied in this simple correlation curve.

The method, derived here, is based on a consideration of the characteristics network between the aerofoil surface and the sonic line and certain transonic similarity laws. The characteristics network, as noted in Part I, can be considered to consist of a family of expansive simple waves (of the $\theta - \omega$ type), generated by a change in slope at the surface, onto which is superimposed a family of compressive waves (of the $\theta + \omega$ type) that account for the non-uniformity of the flow approaching the sonic line. Thus, the total compressive effect that returns to the surface up to any particular chordwise point is given by $(\theta_s - \theta) - \omega$. The chordwise variation of $\theta + \omega$ therefore gives a measure of this total compressive effect that reaches the surface from the sonic line and, in particular, the value of $\partial(\theta + \omega)/\partial(x/c)$ is the strength of the compressive disturbance at any particular point.

A consideration of the transonic similarity laws (Ref. 1) shows that for families of symmetrical aerofoil sections given by

$$z/c = \pm (t/c)\, F_o\, (x/c) \tag{1}$$

the transonic flow fields about the aerofoils at zero incidence are similar if the parameter

$$\xi_\infty = \frac{1 - M_\infty^2}{\left[M_\infty^2(\gamma + 1)(t/c)\right]^{2/3}} = \text{constant.} \tag{2}$$

This implies that for $M_\infty < 1.0$ the flow fields about a family of symmetrical aerofoils, varying only in t/c, will not be similar at the same value of M_∞. However, at $M_\infty = 1.0$ the flow fields will be similar since the parameter ξ_∞ = constant = 0.

Consider now the similar flow fields, for $M_\infty = 1.0$, about two related aerofoils as illustrated in Fig. 14. In the flow field at, and away from, the surface it may be deduced from Ref. 1, within the framework of small-disturbance assumptions, that related points in the two similar flows, at corresponding values of x/c, will obey the relationships

$$C_p/(t/c)^{2/3} = C_p'\,(t'/c)^{2/3} \tag{3}$$

$$Z\,(t/c)^{1/3} = Z'(t'/c)^{1/3} \tag{4}$$

and $$\theta/(t/c) = \theta'/(t'/c) \tag{5}$$

(where Z and Z' denote ordinates of related points in the flow fields measured from the aerofoil surface and θ and θ' are the corresponding local flow directions referred to the free-stream direction). Thus, at the surface, points at a given value of x/c in the two similar flow fields are related points. Furthermore, since at the sonic line

$$C_p/(t/c)^{2/3} = C_p'/(t'/c)^{2/3} = 0$$

points P and P' (which correspond to the same value of x/c) on the sonic line in the two similar flow fields are also related points. It therefore follows that, as in Fig.14, the two pairs of characteristic lines $(\theta_1 - \omega_1)$, $(\theta_2 + \omega_2)$ and $(\theta_1' - \omega_1')$, $(\theta_2' + \omega_2')$, which meet the sonic line at the related points P and P', will also originate from, and return to, the surface at the same (related) chordwise points, A and A', B and B'. (The values of $\theta_1, \omega_1, \theta_2, \omega_2$ etc. here relate to local values away from the surface.)

Along a given characteristic of either the $(\theta_1 - \omega_1)$ or $(\theta_2 + \omega_2)$ family

$$\theta_1 - \omega_1 = \theta_2 + \omega_2 = \theta_L \text{ (at the sonic line).} \tag{6}$$

Similarly $$\theta_1' - \omega_1' = \theta_2' + \omega_2' = \theta_L'\,. \tag{7}$$

Thus, in particular, from equations 5, 6 and 7

$$(\theta_2 + \omega_2)/(t/c) = (\theta_2' + \omega_2')/(t'/c) \tag{8}$$

Therefore, for families of symmetrical aerofoils at zero incidence, the value of $(\theta + \omega)$ at any specific chordwise point on the surface is proportional to t/c. (This relationship is, of course, also applicable to related points away from the surface.) Defining a transonic similarity parameter $f = 0.1/(t/c)$ (the factor 0.1 being included so that values of f are close to unity) a general relationship for affinely related symmetrical aerofoils at zero incidence therefore exists, of the form

$$(\omega + \theta) f = F(x/c) \tag{9}$$

and is applicable to points at the surface.

For affinely related cambered aerofoils at zero incidence a similar relationship may be established by defining f in an appropriate manner, because disturbances on the lower surface do not significantly affect the upper surface supersonic region of flow (and vice-versa). The similarity parameter, f, for cambered aerofoils at zero incidence, is, therefore, based on the maximum upper (or lower) surface ordinate instead of the overall value of t/c,

$$\text{i.e.} \quad f = \frac{0.1}{2(z/c)_{max}}\,. \tag{10}$$

The relationship may also be extended to aerofoils at incidence by including an allowance for the effective change in surface slope relative to the free-stream direction attributable to the incidence setting. Effectively, at the surface, the slope, relative to the free-stream direction, changes from θ to $\Theta = \theta - \alpha$. A general relationship of the form

$$(\omega+\Theta)f = F(x/c) \tag{11}$$

may therefore be established for a family of aerofoils, which is exact for affinely related symmetrical aerofoils at zero incidence (within the framework of small disturbance assumptions) and is approximately true for other cases.

For a family of aerofoils the function F (x/c) is, therefore, unique. However, this is not so for aerofoils which are unrelated, as demonstrated in Fig. 16* where values of $(\omega+\Theta)f$, obtained from an analysis of experimental data for a wide range of round-nosed section shapes tested in a sonic stream, are presented as a function of $(x/c)^{1/3}$. (The abscissa scale of $(x/c)^{1/3}$ is chosen simply to expand the scale of x/c near the leading edge where the variation of $(\omega+\Theta)$ with x/c is very rapid.) The analysis demonstrates that the compressive effect (given by the chordwise variation of $(\omega+\Theta)$ varies monotonically with x/c from the sonic point, as illustrated also in the sketches of Fig. 27. This is true even during a very rapid flow expansion from the sonic point and during the flow recompression, brought about by particular local chordwise variations in θ or r/c, that often follows such a rapid flow expansion, as discussed in Part I. In addition the chordwise variations of $(\omega+\Theta)f$, although not identical in each case, are very similar for a wide range of section shapes.

The similarity between the chordwise variations of $(\omega+\Theta)f$ with x/c in Fig. 16 for aerofoils which are not related suggests that the approximate collapse of data points about the mean curve of Fig. 16 can be made even more complete by formulating a general affine relationship. The simplest form that such a relationship could take is

$$(\omega+\Theta)f\lambda = F(x/c) \tag{12}$$

where λ is a simple numerical constant for any one aerofoil at a particular incidence. The adequacy of this simple form can be evaluated from experimental data by calculating λ at one particular chordwise station from the relationship

$$\lambda = (\omega_{\bullet}+\Theta)f/\overline{(\omega+\Theta)f} \tag{13}$$

(where the whole denominator is given by the mean curve of Fig. 16) and then examining the completeness of the collapse of experimental data for other chordwise stations when presented in the form of Equation 12. This has been done by defining λ at the sonic point and the resulting data collapse is shown in Fig. 17.

Assuming that F(x/c) is a unique function for any aerofoil shape (and this is confirmed, to a close approximation, by the collapse of data in Fig. 17), it is interesting to note that, at the sonic point

$$\frac{(\omega+\Theta)f\lambda}{\partial(x/c)} = f\lambda \frac{\partial\theta_s}{\partial(x/c)} = F'(x/c)_s \tag{14}$$

(since, when $\omega = 0, \partial\omega/\partial(x/c) = 0$) and that

$$\lambda = \frac{F'(x/c)_s}{f \dfrac{d\theta_s}{d(x/c)}} . \tag{15}$$

Thus the factor λ (and hence also the local rate of compression at any chordwise point) is, therefore, dependent on the sonic point location and in particular on the rate of change of surface slope at this point, i.e., to a close approximation, the curvature at the sonic point. The factor λ may, therefore, be considered to represent the influence of conditions at the sonic point (and, in turn, the influence of the subsonic region of flow) on the downstream supersonic region of flow. Since values of $(\omega+\Theta)f$ decrease to a value of about unity at the trailing edge the significance of λ in determining the downstream rate of compression becomes less as $x/c \rightarrow 1.0$.

Evaluation of λ thus requires a knowledge of the sonic point and this is obtained from a prediction of the subsonic flow. The correlation presented in Fig. 17 is based on experimental data obtained at the National Physical Laboratory. In Section 3 it is shown how mathematical solutions for certain section shapes are also embraced by the empirical correlation of Fig. 17 and hence add to the generality of the method. However, before proceeding to these considerations, it is necessary to consider the behaviour of thin, round-nosed aerofoils which have shown certain exceptions to the general affine relationships established up to now.

---

* although the scatter about the mean curve is not particularly great.

2.1 The variation of the parameter f for thin aerofoils

In certain cases the analysis of experimental data indicates that the strength of the compressive effect at the surface (represented by $\partial(\omega+\Theta)/\partial(x/c)$) is not as large as might be expected from the correlation presented in Fig. 17. These particular cases occur on the upper surface of thin aerofoils at positive incidence for which the initial expansion is rapid. An explanation for this phenomenon is suggested below from a consideration of the characteristics pattern on a thin aerofoil.

The relationship given by equation 3 indicates that for affinely-related aerofoils at zero incidence the thinner the aerofoil the smaller are local surface velocities. However, this trend of thickness effect breaks down if, as for thin round-nosed aerofoils at incidence, the sonic point moves onto the more highly curved region near the leading edge, as illustrated in Fig. 15. In this case the high curvature region just downstream of the sonic point produces strong expansions giving high local Mach numbers. The chordwise variation of the compressive disturbance that can be considered to originate at the sonic line is then reduced for two reasons. Firstly, expansion waves of the $\theta-\omega$ family, originating at the surface near the sonic point, meet the sonic line higher above the surface than on an affinely-related thicker aerofoil at an equivalent incidence, as illustrated in Fig. 15. The reflected compressive waves from the sonic line (of the $\theta+\omega$ family) therefore return to the surface proportionately further along the chord than in the case of the thicker aerofoil. Secondly, the high local Mach number region, produced by the high surface curvature, causes the incoming family of compressive waves to be deflected even further along the surface than would occur if the initial expansions were weaker. Both these effects therefore cause the strength of the chordwise distribution of the compressive disturbance to be weakened, particularly in a region near to the sonic point. Thus, as incidence increases, and the initial expansion grows stronger, the chordwise distribution of the compressive effect that actually occurs on a thin aerofoil is less than that indicated by the correlation of Figure 17* which is not based, primarily, on data for thin aerofoils.

This effect can be represented by a variation of the factor f with chordwise distance. A study of experimental data indicates that when $f > 1.3$ (i.e. $(z/c)_{max} \leq 0.0385$) and $\alpha > 0$ then the variation of f ($= f_L$) with x/c, downstream of the high curvature region (the limit of which may be taken as the point corresponding to $r/c = 0.2$), is given by the relationship

$$f_L = f - k \frac{\alpha}{57.3} \frac{1}{2(z/c)_{max}} \tag{16}$$

where the variation of k with x/c is given by Fig. 18. The variation of f_L and $(\omega+\Theta)f\lambda$ with x/c, given by equation 16 and Figure 17, is such that the increased expansive effect will be greatest in a region downstream of, but near to, the sonic point and almost negligible in a region near the trailing edge.

3. THEORETICAL SOLUTIONS FOR SOME SPECIAL AEROFOIL SHAPES

The purpose here is to examine some theoretical solutions that are available at $M_\infty = 1.0$ for some special shapes and, in particular, to see how these solutions compare with the results obtained using the empirical relationships obtained in Section 2 for the region downstream of the sonic point.

3.1 Results for a family of sharp-nosed aerofoils

Spreiter and Alksne in Ref. 2, and Rubbert and Landahl in Ref. 3, present theoretical results for a family of sharp-nosed aerofoils at zero incidence defined by the equations

$$\frac{z}{c} = A\left[\frac{x}{c} - \left(\frac{x}{c}\right)^n\right] \tag{17}$$

and

$$\frac{z}{c} = A\left[\left(1 - \frac{x}{c}\right) - \left(1 - \frac{x}{c}\right)^n\right] . \tag{18}$$

Equations (17) and (18) give a family of aerofoils having the position of maximum thickness aft of the mid-chord point and forward of the mid-chord point respectively. The maximum thickness position is determined by n while t/c is determined by A.

---

* i.e., the actual value of $(\omega_e+\Theta)f\lambda$ at any chordwise point is larger than the corresponding value given by Figure 17.

In Refs. 2 and 3, theoretical results are presented for the five aerofoils with the position of maximum thickness at, or near, $x/c = 0.3$, 0.4, 0.5, 0.6 and 0.7 and these results are compared with experimental data from Ref. 5. These experimental data were obtained from wind tunnel wall bump tests and using a ventilated working section that may not have been adjusted precisely for interference-free conditions. As a result the experimental data are influenced by the initial wall boundary layer and tunnel-interference effects. However, Spreiter and Alksne's theoretical result for the parabolic-arc section (maximum thickness at $x/c = 0.5$) is considered to be almost exact over most of the chord (as demonstrated in Ref. 6). The differences between the theory and the experimental data of Ref. 5 for this aerofoil can therefore be considered to be that due to the effects noted above, except near the trailing edge where viscous effects, associated with shock-wave/boundary-layer interaction, are predominant. If an assumption is then made that these same differences are applicable to the experimental data for the other models, at the same values of t/c and at corresponding chordwise stations, then the modified pressure distributi s should be more nearly correct than the original data.

In Figs. 19-23, the theoretical results of Refs. 2 and 3 for the five aerofoils, and the experimental data of Ref. 8 corrected in the way outlined above, are compared with predicted pressure distributions downstream of the sonic point estimated using the correlations derived in Section 2. Since the velocity rule derived in Part I breaks down when the surface slope is small and the flow is governed by the laws of small-disturbance theory, an alternative method is required to determine the subsonic region of flow up to, and including, the sonic point for these five aerofoils. The alternative method used here is given in Ref. 4 and may be used to predict the occurrence and nature of the small-disturbance subsonic region of flow on both sharp and round-nosed aerofoils in a sonic stream. A value of $t/c = 0.08$ was chosen for all the comparisons since this is the only common value for which experimental data from Ref. 5 were available for all five aerofoil shapes.

The comparisons in Figs. 19 and 20 show that when the point of maximum thickness is forward of the mid-chord point then Rubbert and Landahl's method and the present method are in substantial agreement over the rear 50% of the chord. The method of Spreiter and Alksne, predicts pressures which are considerably lower in this region. For the aerofoil with maximum thickness at $x/c = 0.3$, Figure 19 shows that Rubbert and Landahl's method, the present method and the experimental data indicate a region of decelerating flow over the rear part of the chord. The method of Spreiter and Alksne, on the other hand, cannot predict this since the method fails when $dU/dx \leqslant 0$. For the aerofoil shapes with maximum thickness at or beyond the mid-chord point Figs. 21-23 show that all three prediction methods are in substantial agreement, in the supersonic region of flow at least.

3.2 Results for a particular round-nosed aerofoil

The theoretical methods for evaluating the complete flow about sharp-nosed aerofoils in a sonic stream, such as Refs. 4 and 6, are based on a solution of the approximate small-disturbance form of the transonic flow equation and are therefore not strictly applicable to round-nosed aerofoils. However, Graham, in Ref. 7, outlines a method for designing a round-nosed aerofoil having a simple-wave compression over most of the forward half of the chord at $M_\infty = 1.0$. Starting with a circular leading edge, which is maintained until the surface slope falls to a value of 12.5°, Graham uses Chuskin's theoretical solution for a circular cylinder at $M_\infty = 1.0$ (Ref. 8) to determine the initial rapid flow expansion on the circular region. He then uses the method of characteristics in an inverse manner to derive an after-body-shape that, theoretically, gives a simple wave compression up to the point where the surface slope is about 0.6°. From this point to the trailing edge Graham uses part of a circular-arc in order to obtain a closed symmetrical aerofoil shape and assumes that the flow is given by simple wave expansion theory in this region.

Graham's theoretical results for this aerofoil, designated NPL 9431, are plotted in Fig. 24 for $\alpha = 0$ together with experimental data obtained at N.P.L. The predicted pressure distribution obtained using the method outlined in Section 2 downstream of the sonic point (the sonic point occuring in the rapid flow expansion from the stagnation point given by Chuskin's solution for the circular cylinder) is given in the same figure. Clearly, there are fairly considerable differences between Graham's theoretical and experimental results between 0.1c and 0.5c. The prediction obtained using the present method follows the experimental results more closely over this part of the chord. Graham only calculates theoretical results for the NPL 9431 aerofoil at zero incidence. However, in Fig. 25 a prediction of the upper-surface pressure distribution at $\alpha = 2^\circ$, obtained using the present method, is compared with experimental data for $M_\infty = 1.0$. Apart from a certain amount of "waviness" in the experimental pressure distribution, and some discrepancies in the region near $x/c = 0.4$, the comparison between present prediction and experiment remains satisfactory.

4. THE LEADING-EDGE FLOW RECOMPRESSION

An examination of the continuity between the subsonic flow on a round leading-edge and the supersonic flow further downstream has also revealed some interesting flow phenomena which are now worth considering.

The rapid flow expansion from the stagnation point exhibited by many sections is invariably followed by a flow recompression (as illustrated, for example, in Figs. 26a to 26d) as the local surface radius of curvature increases rapidly from the leading-edge value.

The means whereby this recompression may occur downstream of the initial peak velocity may be of one, or a combination, of several forms. If, for example, in the initial rapid flow expansion, supersonic velocity is attained before the peak value of velocity occurs then some isentropic recompression may occur (Figs. 26a, 26b) and may (Figs. 26b, 26c), or may not (Fig. 26a), be terminated by a local shock compression, downstream of which the flow will be subsonic if a strong shock wave occurs. In addition a local compression in the subsonic flow upstream of the sonic point may occur as illustrated, for example, in Fig.26d. The various forms the recompression may take, and the conditions under which each form is to be expected, are discussed in the following Sections. Examples of some of the forms of leading-edge flow compressions referred to are presented in Section 5 and are there compared with predicted results obtained using the methods outlined below.

4.1 Recompression occurring in the supersonic region of flow

The flow mechanism generating isentropic recompression in the supersonic region of flow and, in some cases, causing the formation of weak (oblique) shock waves* is discussed in Part I and Refs. 9 and 10 from a consideration of the characteristics network in the leading-edge region.

The presence of isentropic recompression in the supersonic region of flow and/or a weak (oblique) shock wave (downstream of which the flow is supersonic) will be given, automatically, by the prediction method implicit in Section 2. Since a chordwise variation of $\theta-\omega=$ constant represents a simple-wave compression, a chordwise variation of $\theta - \omega$ which increases with increasing x/c indicates a compression greater than a simple wave, i.e., a shock wave. Applying this criterion, therefore, will indicate whether an oblique shock occurs in the flow as illustrated in Fig. 27b. That the applicability of the method given by Section 2 is still valid when a weak oblique shock occurs in the flow presumably arises from the fact that the shock, in this particular case, is merely a weak convergence of compression waves. The usual losses associated with the flow through a shock wave are therefore a minimum and the flow compression is nearly isentropic.

4.2 Other forms of leading-edge flow compressions determined by the requirements for flow continuity

A strong shock wave may occur in the leading-edge flow if the surface radius of curvature increases sufficiently rapidly, downstream of the leading-edge on which supersonic flow has initially developed, such that the surface geometry is not compatible with the presence of supersonic flow. The over-expanded leading-edge flow then breaks down and is recompressed to a subsonic level, compatible with the downstream section shape, through a normal, or near normal, shock wave. Downstream of the shock the flow expands, reaching sonic velocity again at some point further along the surface. The expansion to sonic velocity downstream of the shock obeys the laws of small-disturbance theory and the occurrence and magnitude of local subsonic velocities in this region may be obtained from the method noted earlier, in Ref. 4. The existence and location of such a shock may be determined to a close approximation, as illustrated in Fig. 26b, by the assumption that the shock upstream velocity (within the supersonic region of flow), predicted by Section 2, and the shock downstream velocity (in the downstream region of subsonic flow) are compatible with the normal shock relationship. An example of this form of leading-edge compression is given in Fig. 29.

Thus an over-expanded leading-edge flow, in which local velocities have reached a supersonic level, may establish continuity with the presence of a downstream region of subsonic flow, dictated by the section geometry, by the occurrence of a normal shock wave. However, in some cases the shock compression that would be required to compress the flow from a supersonic level (achieved in the absence of any downstream influence arising from a requirement for flow continuity with a downstream region of local subsonic flow) to the subsonic level (dictated by the downstream section shape) may be greater than that which can be achieved through the occurrence of a normal shock. In this case experiment suggests that the downstream surface shape exerts an influence on the upstream flow reducing the rate of flow expansion from the stagnation point sufficiently either for the remaining compression to subsonic velocity to be achievable through a normal shock or that sonic velocity is not achieved in the initial expansion. In the latter case the recompression of the flow to velocities compatible with the downstream surface shape takes place at an entirely subsonic level.

An analysis of experimental data, particularly for such cases referred to above, has suggested that when a region of small disturbance subsonic flow exists, its influence on the upstream flow, arising from the requirement for flow continuity, may be represented by an influence factor K. The factor K is a variable and is so defined that the value of KU/U_∞ in the upstream large disturbance flow, may be considered to be the local velocity that would occur in the absence of this downstream influence. Thus the large-disturbance velocity distribution, as predicted, for example, by the methods outlined in Part I and Section 2 of Part II, should, more correctly, be interpreted as KU/U_∞ even if a leading-edge recompression does not occur. It is then necessary to establish whether any leading-edge flow readjustment is required (i.e., $K \neq 1.0$) in order to maintain flow continuity and exclude any incompatibility between the upstream large-disturbance flow and any downstream small-disturbance

---

* formed when "reflected" compressive waves from the surface coalesce as illustrated in Figure 27b.

subsonic flow that might exist. A method for determining local values of K, for the case of an aerofoil in a sonic stream, is given in Ref. 4. The method suggests that near the stagnation point K is approximately unity but that at, and near, the transition from the large- to the small-disturbance regions of flow K may be significantly greater than unity.

The case when the initial flow expansion rate is reduced so that a normal shock occurs is illustrated in Fig. 26c. Here the locus of possible values of shock-upstream velocity (obtained by applying the normal shock velocity relationship to the downstream small-disturbance subsonic flow) is always lower than the predicted upstream variation of KU/U_∞. The case occurring when a larger downstream influence causes the leading-edge flow compression to take place at an entirely subsonic level is illustrated in Fig. 26d and an example is given in Fig.31. This case will occur whenever the locus of possible values of shock-upstream velocity is always greater than the predicted upstream variation of KU/U_∞.

Instances when K is significantly greater than unity are only likely to occur for aerofoils with a radius of curvature (r/c) distribution such that a sustained region of small r/c is followed by a very rapid increase immediately downstream. This type of aerofoil geometry, associated with a low or negative incidence, and particularly at free-stream Mach numbers approaching unity, often leads to the form of velocity distribution featuring a compression in the subsonic region of flow close to the leading edge.

5. FURTHER COMPARISONS OF PREDICTED AND EXPERIMENTAL PRESSURE DISTRIBUTIONS AT $M_\infty = 1.0$

The comparisons of predicted and experimental pressure distributions for $M_\infty = 1.0$ made so far have been for some special aerofil shapes. In this section some further comparisons are made for two arbitrarily-defined aerofoil shapes, the latter example being chosen to illustrate the applicability of the present methods in predicting several forms of the particular types of pressure distributions discussed in Section 4.

5.1 NPL 3161 aerofoil, $\alpha = 5.2^\circ$

The NPL 3161 aerofoil is a thick (t/c = 0.14), cambered aerofoil with a variation in local surface radius of curvature which increases monotonically with increasing x/c. The variation of local curvature near the leading edge does not produce a pressure peak in this region, but the surface near the trailing edge on the lower surface is concave which, at $M_\infty = 1.0$, produces a substantial region of decelerating flow over the rear part of the chord. The comparison of predicted and experimental pressure distributions is shown in Fig. 28.

5.2 NPL 9422 aerofoil, $\alpha = 0^\circ, 4^\circ$

The NPL 9422 aerofoil has a circular leading-edge region maintained until the surface slope falls to a value of 10°. This feature produces the rapid flow expansion from the stagnation point and subsequent flow compression, referred to earlier. The rapid increase in the local radius of curvature downstream of the circular region is such that, at $\alpha = 0$, the conditions for flow continuity, referred to in Section 4.2 and illustrated in Fig. 26b, between the upstream large-disturbance supersonic flow and the downstream small-disturbance subsonic flow, indicates that a normal shock wave occurs in the leading-edge flow compression at about 0.036c. A comparison between predicted and experimental data is shown in Fig. 29.

At $\alpha = 4^\circ$ the upper-surface pressure distribution takes the form indicated in Fig. 30. Between about 0.01c and 0.03c both the predicted and experimental variations of $(\theta-\omega)$ indicate that a compression occurs through an oblique shock.

On the lower surface of this aerofoil at $\alpha = 4^\circ$ the condition for flow continuity, given in Section 4.2 and illustrated in Fig. 26d, indicates that a subsonic compression occurs in the leading-edge region. The predicted variation of local pressure in the leading-edge region, calculated using the methods referred to in Section 4.2, is presented in Fig. 31 as a function of surface slope. Fig. 30 presents the complete predicted and experimental chordwise variations of local pressure over the whole chord.

6. CONCLUDING REMARKS

The method presented in Part II of this paper, for predicting the supersonic region of flow on any arbitrary aerofoil shape, has proved to be both simple in application and reliable for a wide range of round and sharp-nosed, lifting and non-lifting section shapes. Because the method is founded on experimental data viscous effects, other than boundary-layer/shock-wave interaction near the trailing edge, are included. Also, since the results of applying this method agree well with other inviscid theories where comparison is possible, it follows that the method may be applied over a wide range of Reynolds number.

7. ACKNOWLEDGEMENT

The author wishes to thank the Transonic Aerodynamics Committee of the Royal Aeronautical Society for their discussion and suggestions made during this work and the Aerodynamics Division of the NPL for making available most of the experimental data used in the correlations.

8. REFERENCES

1. SPREITER, J.R. — On the application of transonic similarity rules to wings of finite span. NACA Report 1153, 1953.

2. SPREITER, J.R., ALKSNE, A.Y. — Thin aerofoil theory based on approximate solution of the transonic flow equation. NACA Report 1359, 1958.

3. RUBBERT, P.E., LANDAHL, M.T. — Solution of the transonic airfoil problem through parametric differentiation. AIAA Journal Vol. 5, No. 3, March 1967.

4. - — A method for estimating the pressure distribution on the surface of an aerofoil in a sonic stream. R.Ae.S. Transonic Data Memorandum (to be issued early 1969).

5. MICHEL, R., MARCHAUD, F., Le GALLOW, J. — Influence de la position du maitre-couple sur les ecoulements transsoniques autour de profils a pointes. ONERA Pub. No. 72, March 1954.

6. GRAHAM, W.J., MacDONALD, A.G.J. — Interference effects at sonic speeds for a biconvex aerofoil in a wind tunnel with slotted liners. Jl. R. Aeronaut. Soc. Vol. 70, March 1966.

7. GRAHAM, W.J. — A method for the calculation of the flow about blunt leading-edge aerofoils at sonic speed. NPL Aero Report 1179, January 1966.

8. CHUSKIN, P.I. — Calculations of certain sonic flows of a gas. RAE Trans. 816, April 1959.

9. PEARCEY, H.H. — The aerodynamic design of section shapes for swept wings.
Advances in Aeronautical Sciences (Vols. 3-4), Pergamon Press Ltd, 1962.

10. GRAHAM, W.J. — The flow about a family of simple, blunt and sharp leading-edged, two dimensional aerofoils at transonic and low supersonic speeds. NPL Aero Report 1189, February 1966.

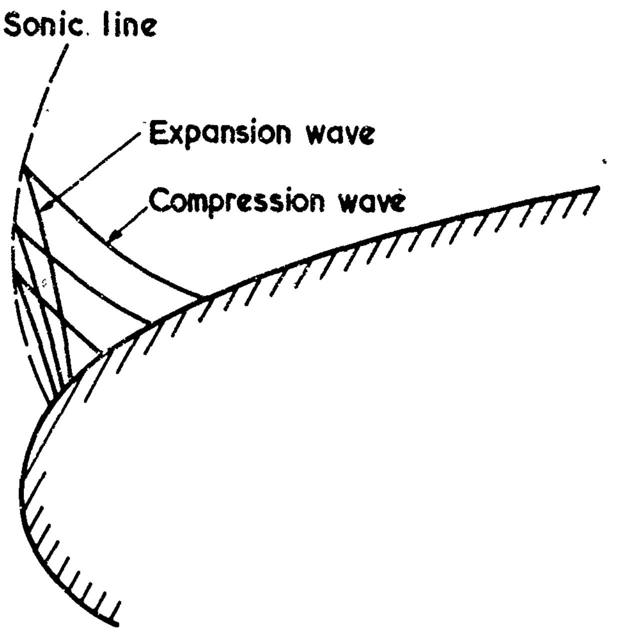

CHARACTERISTICS AT BEGINNING OF SUPERSONIC REGION ON AN AEROFOIL

Figure 1

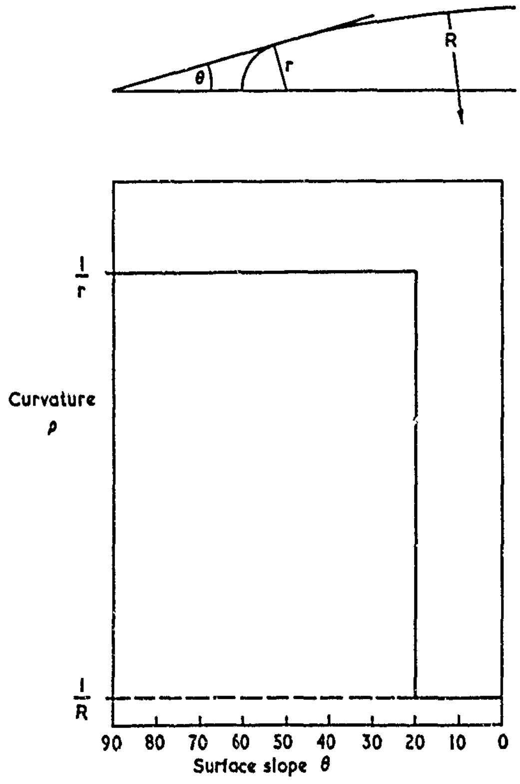

CURVATURE DISTRIBUTION FOR A CIRCULAR ARC AEROFOIL WITH CIRCULAR LEADING-EDGE

Figure 2

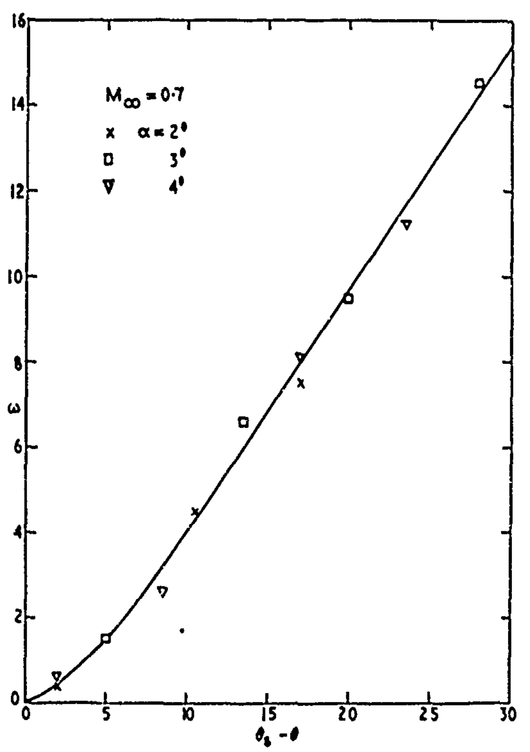

VARIATION OF PRANDTL-MEYER FUNCTION WITH TURNING ANGLE ON CIRCULAR LEADING-EDGE OF AN AEROFOIL

Figure 3

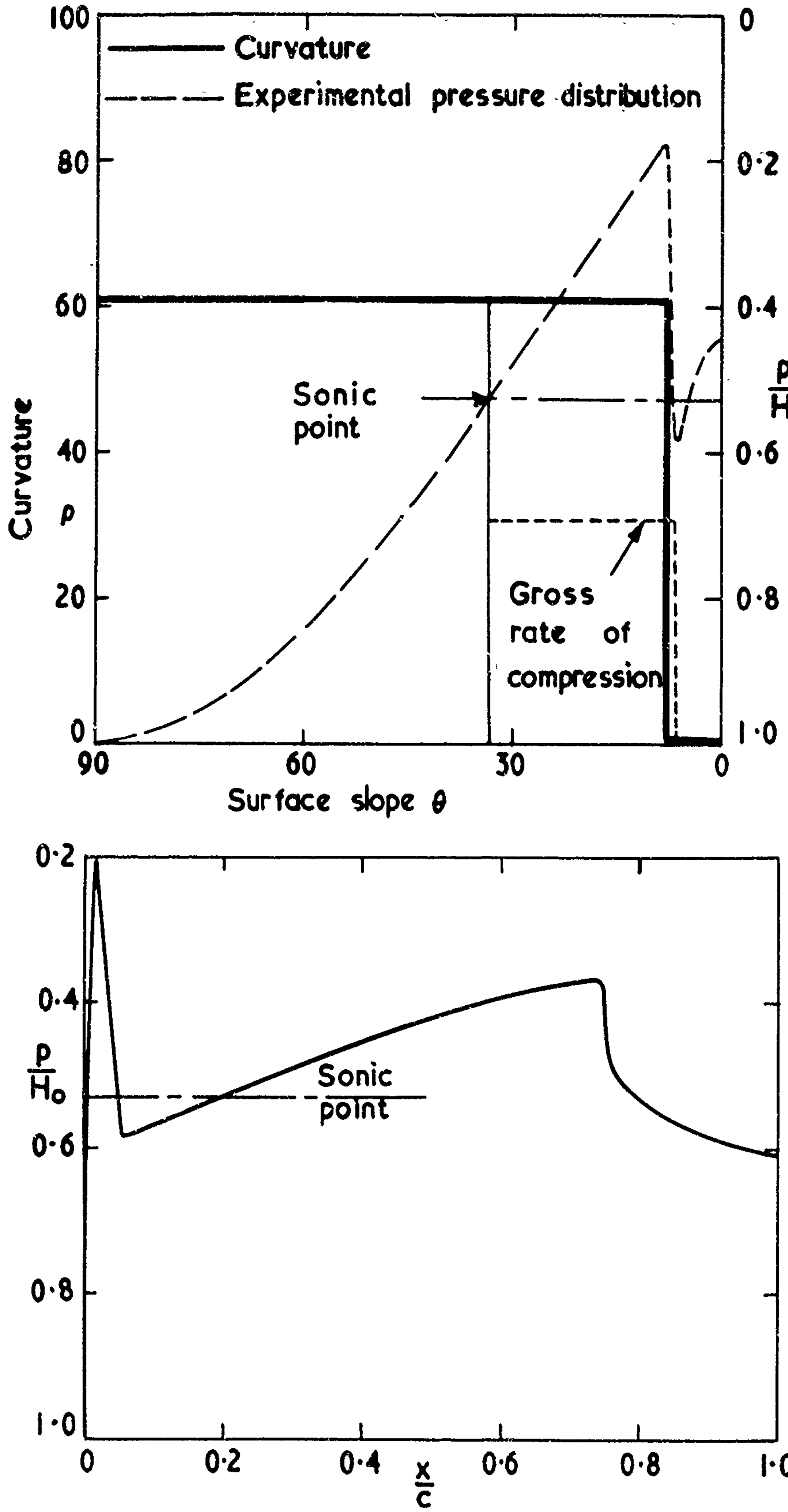

PRESSURE DISTRIBUTION ON AN AEROFOIL WITH DISCONTINUOUS CURVATURE DISTRIBUTION (NPL 9412 AT $M=0{\cdot}9$)

Figure 4

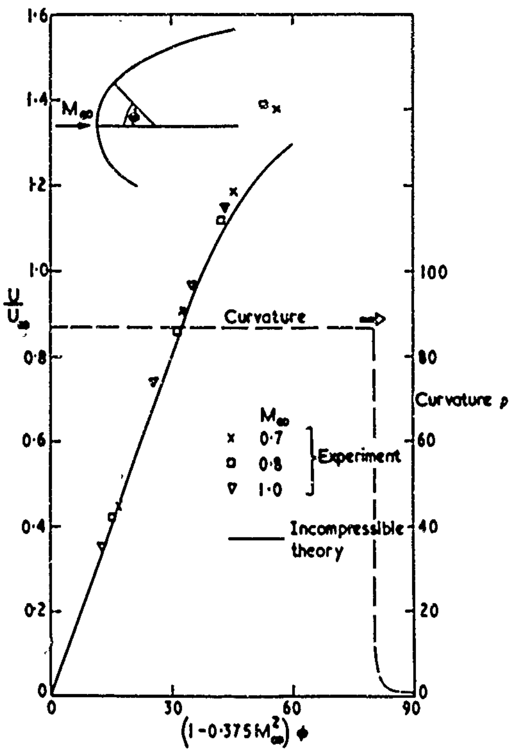

VELOCITY ON LEADING-EDGE OF NPL 9422 AT ZERO INCIDENCE

Figure 5

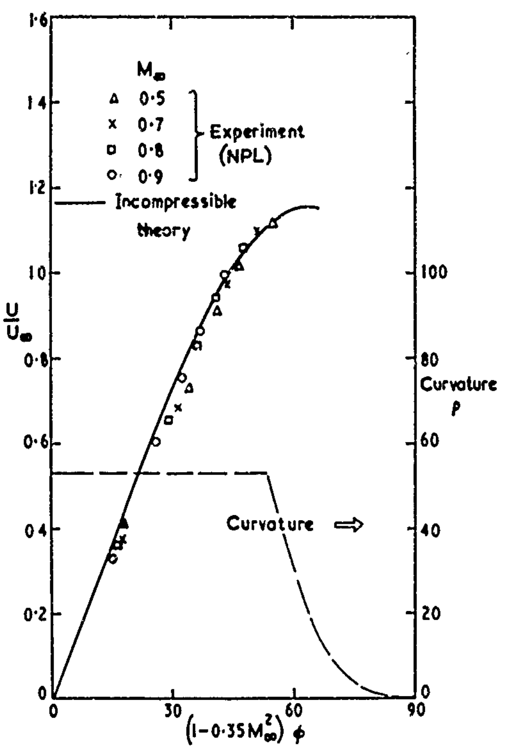

VELOCITY ON LEADING-EDGE OF NPL 9612 AT ZERO INCIDENCE

Figure 6

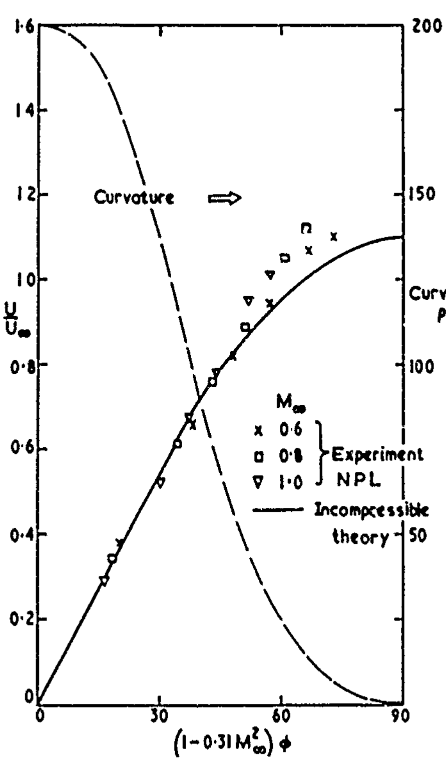

VELOCITY ON LEADING-EDGE OF NPL 9441 AT ZERO INCIDENCE

Figure 7

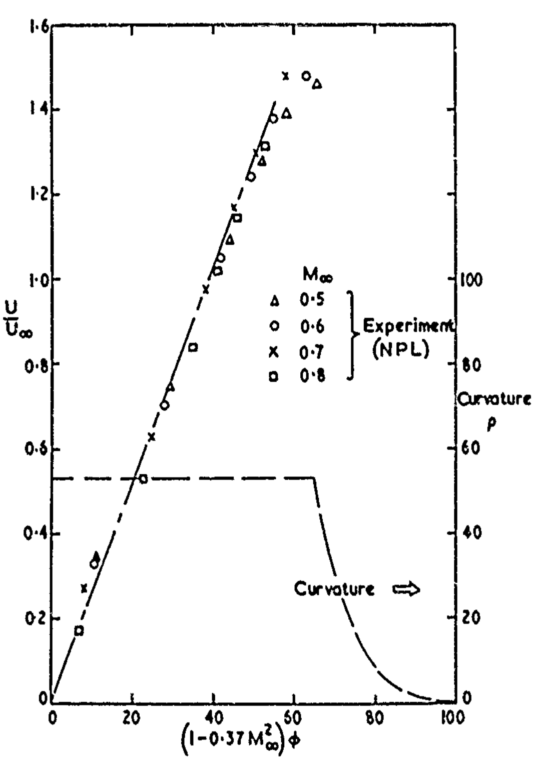

VELOCITY ON LEADING-EDGE OF NPL 9612 FOR STAGNATION POINT AT SURFACE SLOPE OF 80°

Figure 8

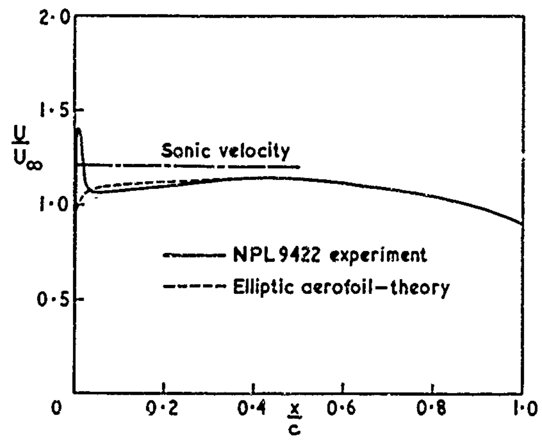

VELOCITY DISTRIBUTION ON NPL 9422 AND ELLIPTIC AEROFOIL OF SAME THICKNESS AT $M_\infty = 0{\cdot}8$

Figure 9

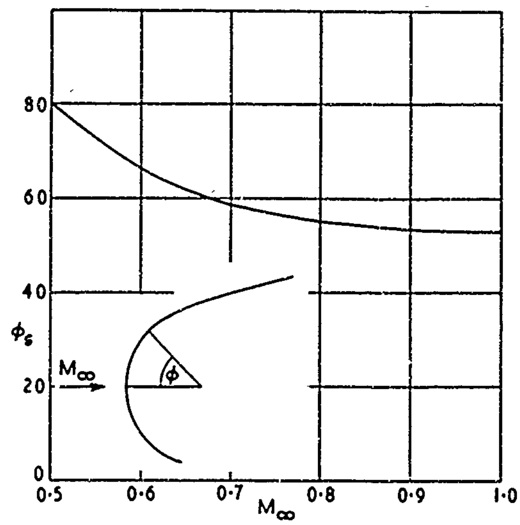

VARIATION OF SONIC POINT POSITION WITH MACH NUMBER

Figure 10

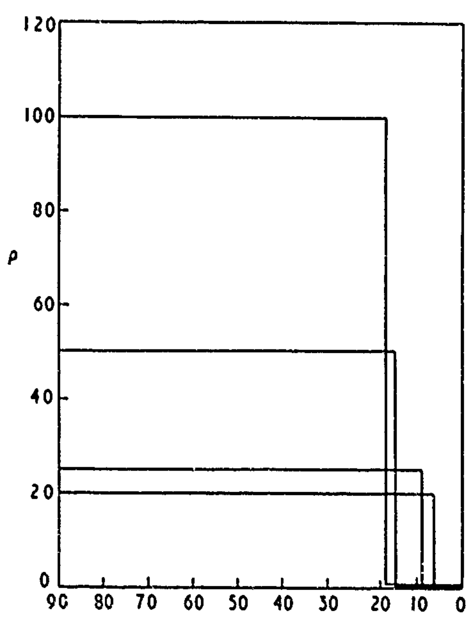

CURVATURE DISTRIBUTIONS FOR A FAMILY OF AEROFOILS WITH FIXED MAXIMUM THICKNESS

Figure 11

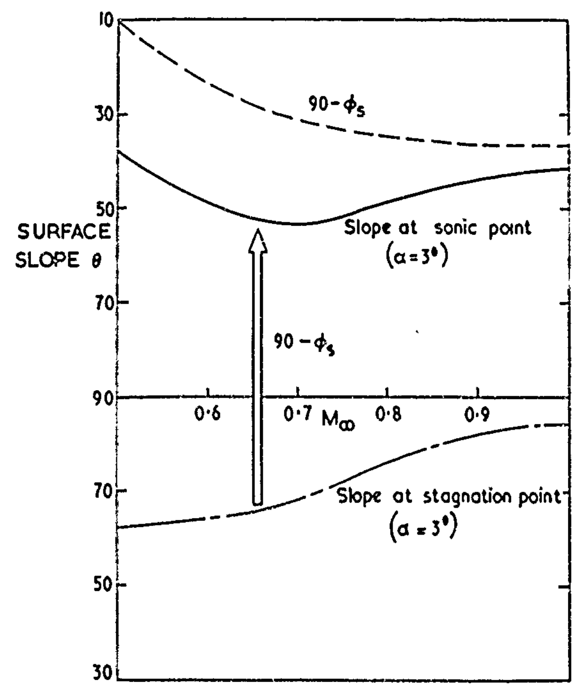

A TYPICAL VARIATION OF SONIC POINT WITH MACH NUMBER FOR AN AEROFOIL AT INCIDENCE

Figure 12

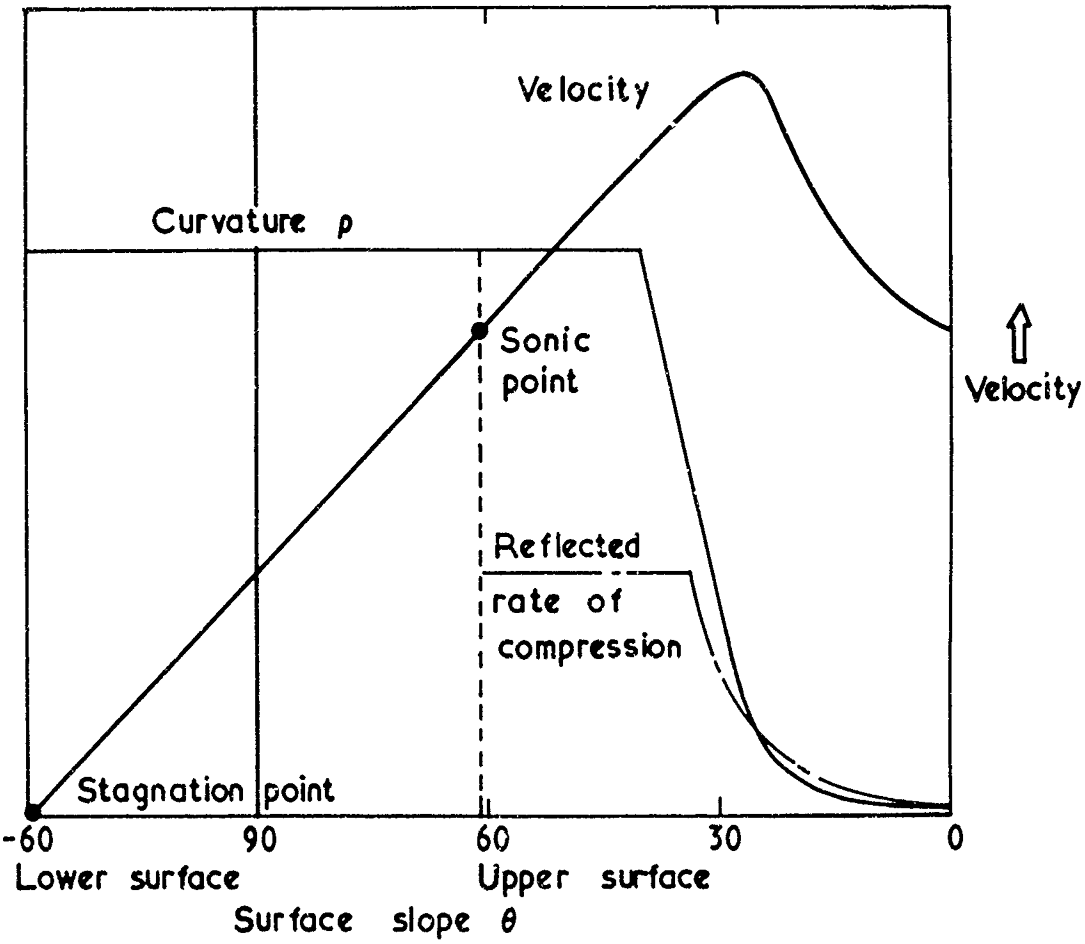

ILLUSTRATION OF CURVATURE AND VELOCITY DISTRIBUTIONS FOR IDEAL CASE OF ISENTROPIC RECOMPRESSION FROM A SUPERSONIC VELOCITY PEAK ON A LIFTING AEROFOIL

Figure 13

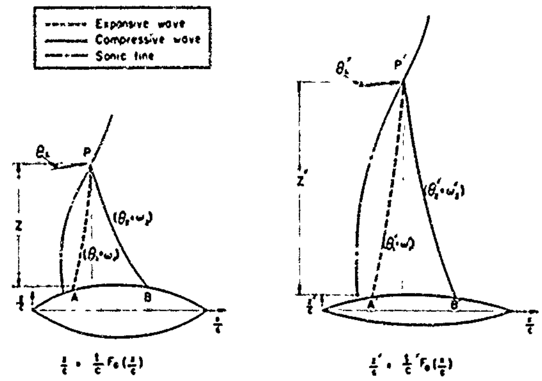

Fig. 14 The flow fields about two affinely related aerofoils in a sonic stream

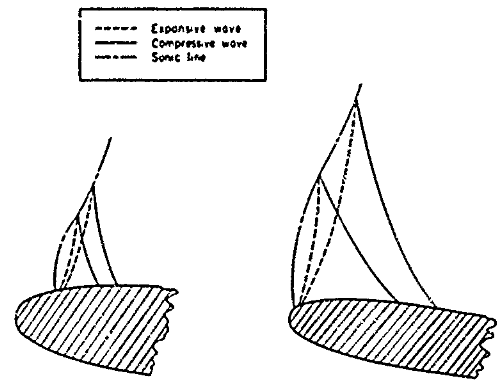

Fig. 15 Illustrations showing how an initial rapid expansion on a thin aerofoil affects the chordwise distribution of the compressive disturbance

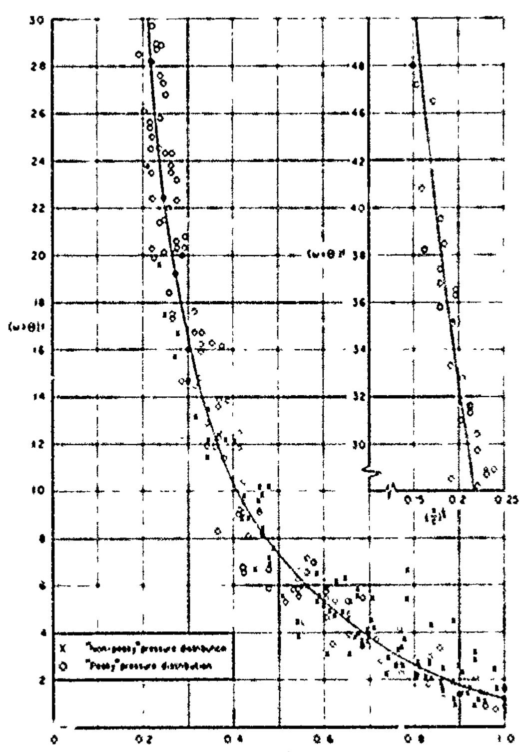

Fig. 16 Correlation of $(\omega + \Theta) f$ with $(x/c)^{1/3}$

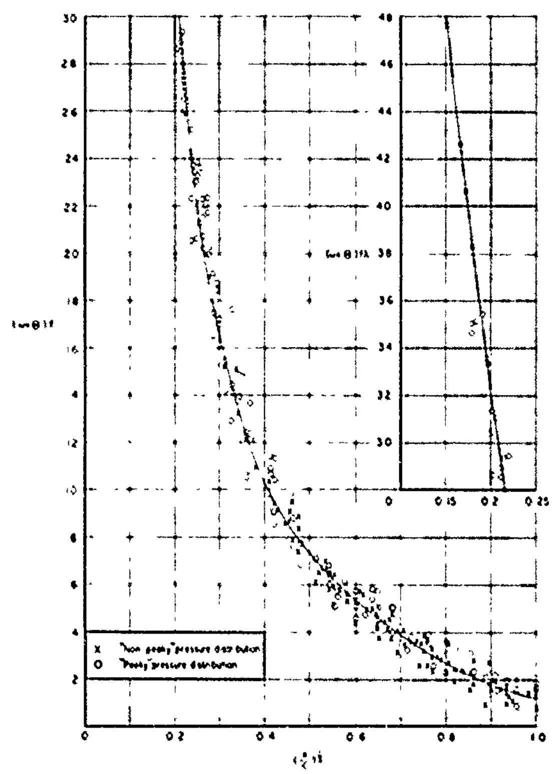

Fig. 17 Correlation of $(\omega + \Theta) f\lambda$ with $(x/c)^{1/3}$

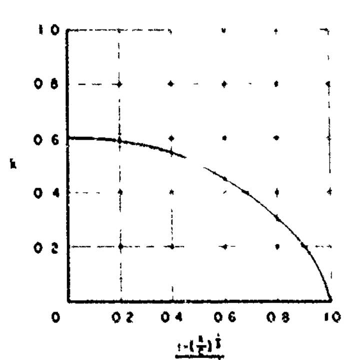

Fig. 18 Chordwise variation of the factor k when $f \geqslant 1.3$

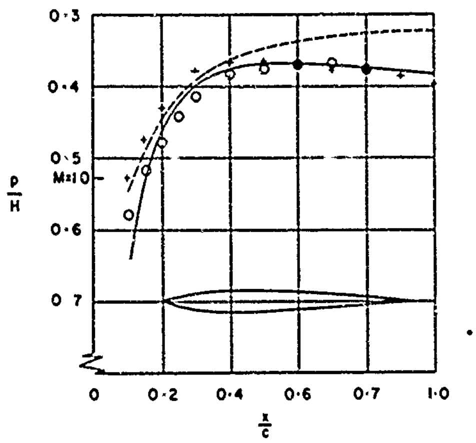

Fig.19 Max. thickness at 0.301c

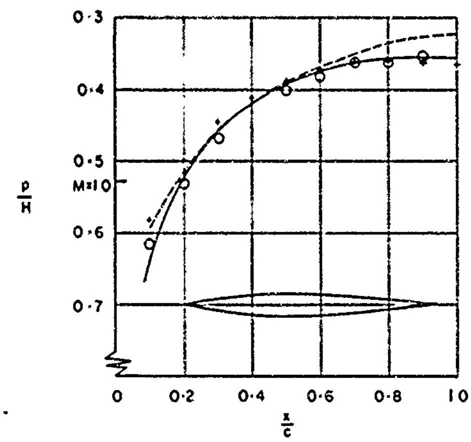

Fig.20 Max. thickness near 0.40c

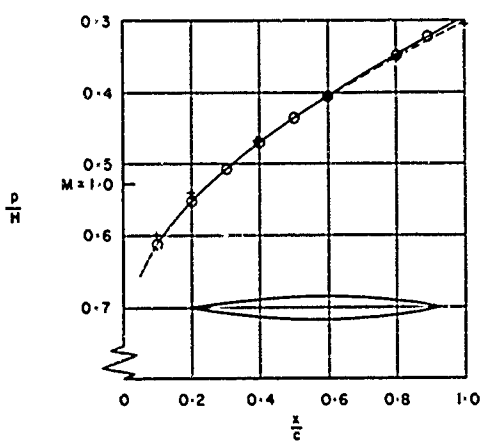

Fig.21 Max. thickness at 0.50c

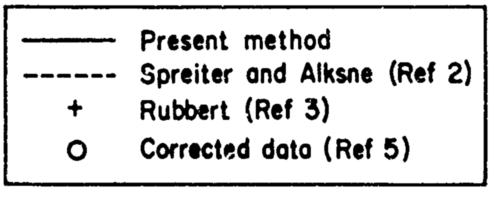

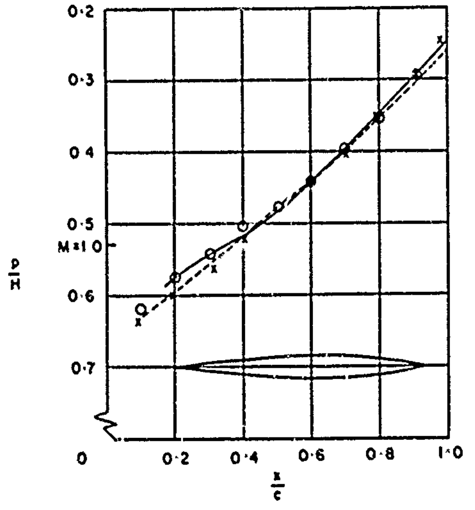

Fig.22 Max. thickness at 0.60c

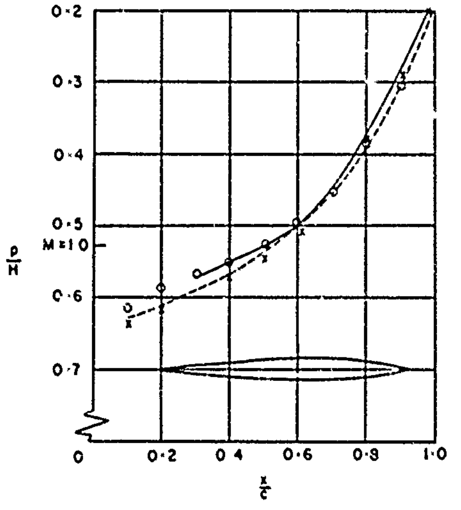

Fig.23 Max. thickness at 0.70c

Figs. 19-23 Predicted and experimental data for a family of sharp-nosed aerofoils for $\alpha = 0$ and $M_\infty = 1.0$

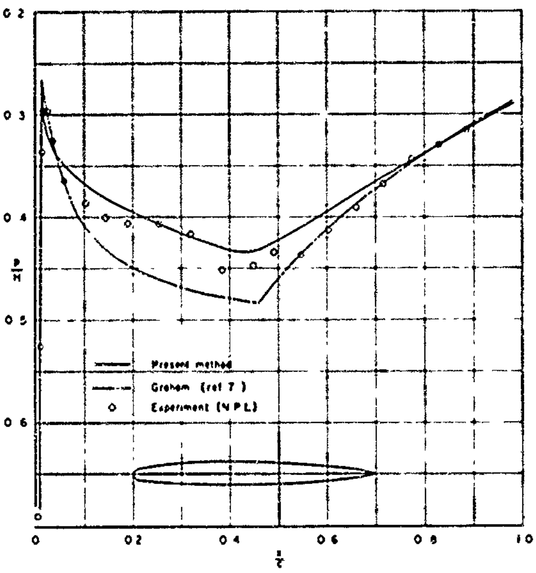

Fig.24 Predicted and experimental pressure distributions for the NPL 9431 aerofoil at $\alpha = 0$ and $M_\infty = 1.0$

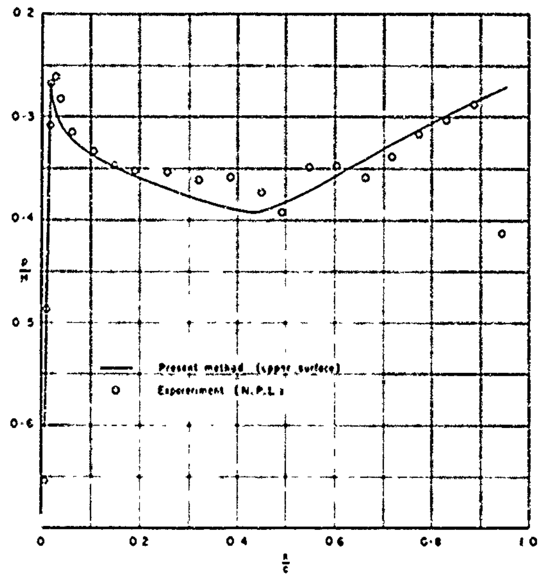

Fig.25 Predicted and experimental pressure distributions for the NPL 9431 aerofoil at $\alpha = 2^0$ and $M_\infty = 1.0$ (upper surface)

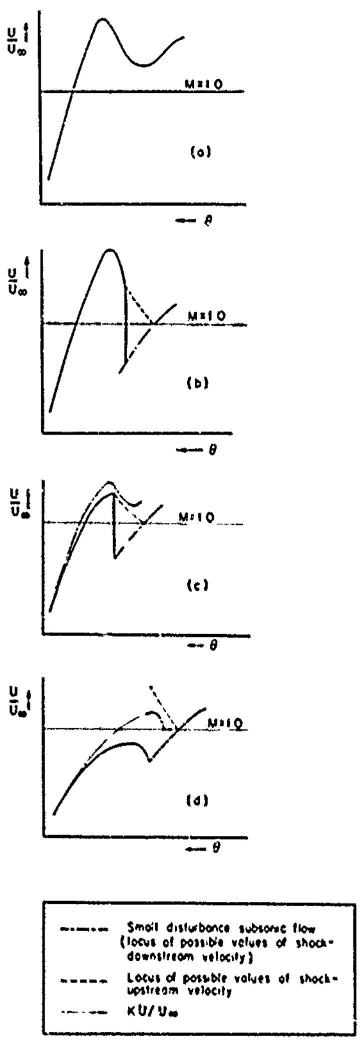

Fig.26 The various forms of leading-edge compression

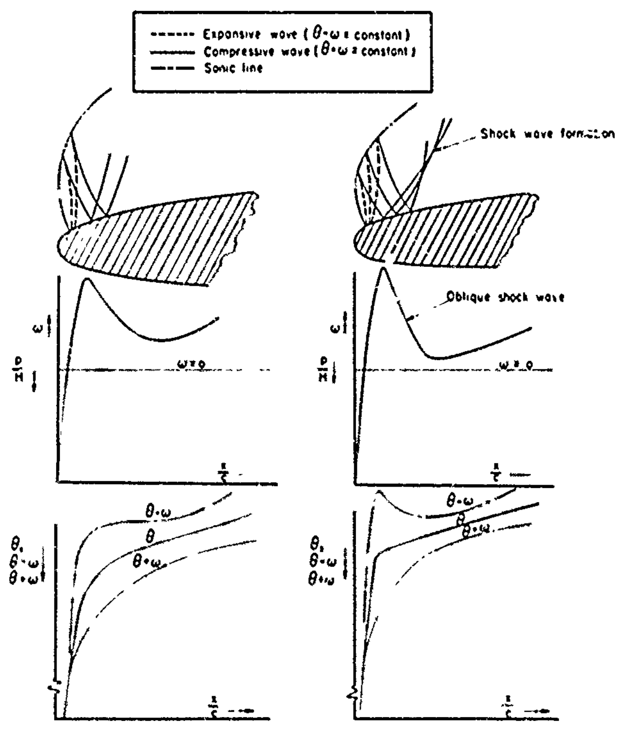

Fig.27 Illustration showing characteristics on two blunt leading-edge aerofoils

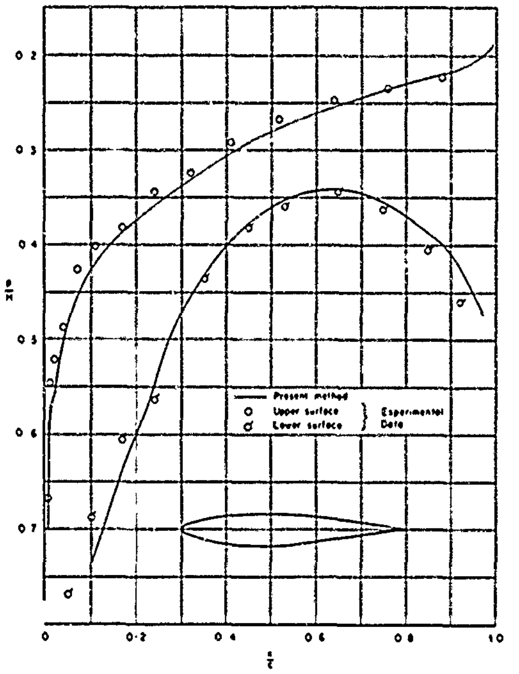

Fig.28 Predicted and experimental data for the NPL 3161 aerofoil at $\alpha = 5.2^{0}$ and $M_{\infty} = 1.0$

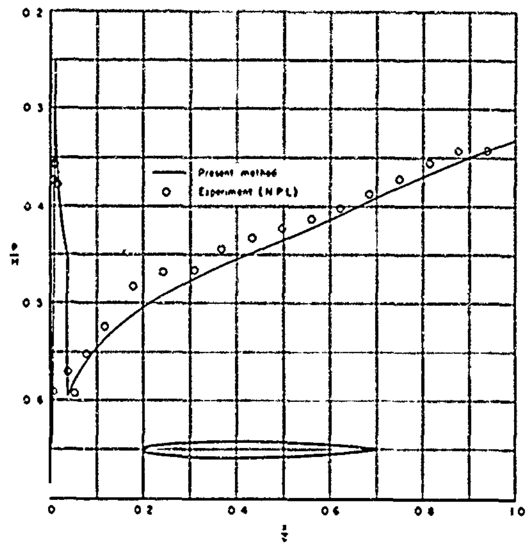

Fig.29 Predicted and experimental data for the NPL 9422 aerofoil at $\alpha = 0^{0}$ and $M_{\infty} = 1.0$

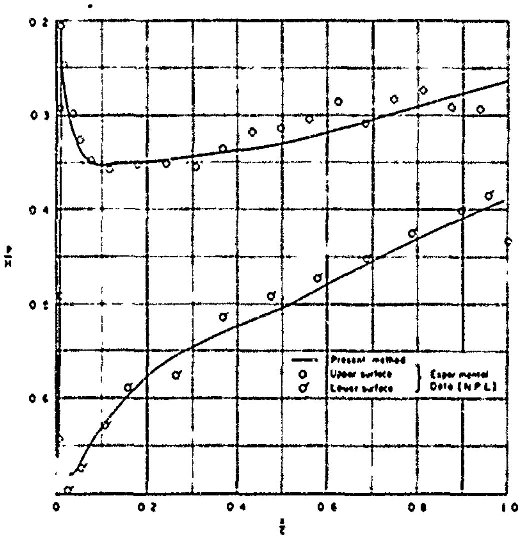

Fig.30 Predicted and experimental data for the NPL 9422 aerofoil at $\alpha = 4^{0}$ and $M_{\infty} = 1.0$

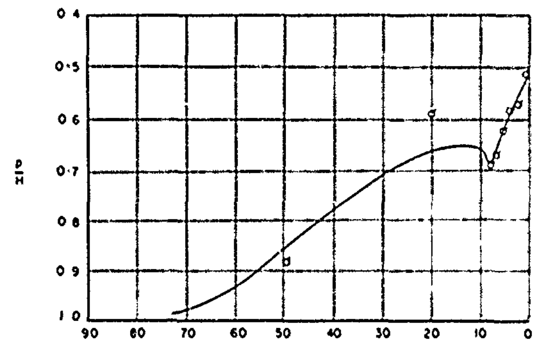

Fig.31 Predicted and experimental data for the lower surface leading-edge region of the NPL 9422 aerofoil at $\alpha = 4^{0}$ and $M_{\infty} = 1.0$

AN APPROACH TO THE DESIGN OF THE THICKNESS DISTRIBUTION NEAR THE CENTRE OF AN ISOLATED SWEPT WING AT SUBSONIC SPEED

by

M.M. Freestone

Department of Aeronautics,
The City University, London

AN APPROACH TO THE DESIGN OF THE THICKNESS DISTRIBUTION NEAR THE CENTRE OF AN ISOLATED SWEPT WING AT SUBSONIC SPEED

by
M. M. FREESTONE,
Department of Aeronautics,
The City University, London

1. Introduction

Much effort has been directed towards the design of aerofoil sections suitable for use with swept wing aircraft cruising at high subsonic Mach number. However, the aircraft application of the two-dimensional results is straightforward only when simple sweep theory is adequate. In regions near the fuselage side and towards the wing tips the three-dimensional nature of the flow is pronounced and simple sweep theory is greatly in error.

Not surprisingly, the three-dimensional theory of compressible flow is at a much less developed stage than the corresponding theory of wing sections, indeed only recently has it been practicable to calculate with reasonable accuracy the pressure distribution according to the first order theory* (linearized theory). Some improvement on the linearized theory results can be obtained if factors are applied to it to account for edge non-uniformities (the Riegels factor for example), and for local variations in Mach number. Such factors are not completely adequate, of course, nor is there any one set of factors obviously better than others which can be suggested. For these reasons, and for simplicity, all such factors are omitted in this paper.

2. General Problem

The general problem selected is that of the thickness design of the centre region of an isolated swept wing. The relevance of this problem to practical wing design can be argued quite simply; the problem, or rather its solution, is a step towards the ultimate objective of improving the overall design. To be made practical the effects of a fuselage and of adding a load distribution must be included. Concentration on the centre region also deserves some explanation. There are two reasons for this. The first is that the use of curved tip wings provided a partial solution to the tip shock problem; consequently further design of the tips is not so urgent. The second is that the centre region is thought to generate the flow features which lead, at low lift coefficients, to the formation of what has been called the 'rear shock' (Ref. 1), thus indicating that attention should be directed at the centre. It is reasonable to assume that any changes to wing tip geometry would have only a very small effect on the required centre.

3. Design Criteria

Ideally one would like to design to a very general criterion such as minimum drag under given conditions. This is not possible with aerodynamic theory in its present state, one reason being the inadequacy of drag prediction methods. The approach generally adopted has been outlined by Bagley (Ref. 2). Thus one might choose the sheared wing** pressure distribution on some basis and then determine the wing sweep which is just sufficient to make the critical Mach number equal to (say) the cruise Mach number. The design of the sheared wing section is then possible (within practical limits) by use of two-dimensional theory. This section is suitable for the mid semi-span provided the leading edge and trailing edge sweep angles are nearly equal. If the taper effect is too large then a modified approach using an effective sweep angle which varies over the chord is possible.

* The first order theory calculations presented in this paper have been made using the numerical method of Ref. 6.

** Sheared wing is used in this paper to denote a portion of the wing (probably existing only in the imagination) which is free of the effects of taper and of the proximity of the centre and tips of the wing.

The design task for the complete wing may then be stated by specifying that the complete wing (and in particular the centre region) should have a critical Mach number which is lower than the sheared wing critical Mach number by the minimum amount.

Limitations imposed by theory make this problem currently insoluble. The flow pattern on a finite wing cannot be predicted up to the onset of shock wave formation. Even if such a calculation could be made the problem of design for high critical Mach number would remain. The present approach adopts a simplified view of the two-fold problem. The first simplification has already been remarked upon, and is in the flow calculation method, the subsonic linearized theory being used in the design process. The second simplification involves the notional pressure distribution used as a basis for design in conjunction with this theory. This latter simplification takes the form of adopting certain proposed rules which, if obeyed by the notional pressure distribution should lead to shock free (or very weak shock) flows.

The simplest of these rules states that if the sheared-wing pressure distribution be maintained (in the notional pressure distribution) over the whole span then the complete wing should be as shock free as the sheared wing, for the isobars would then maintain their full sheared wing sweep throughout.

Difficulty in applying this rule lies in the observation that except perhaps for singular wing geometries (presumably of no practical interest) isobar sweep cannot possibly be maintained right into the centre*. This being so, one is left to speculate whether merely reducing the lateral extent over which loss of sweep occurs represents an improvement or not. Only experiment at present would resolve this, although intuitively one would expect an improvement to be the result.

The second rule, which has been suggested as an alternative, is that the notional pressure distribution need have full isobar sweep only in those parts of the wing where the flow is compressing in the streamwise direction. The basis for this rule derives from an interpretation of experiments in which the rear shock is believed to be formed as a result of coalescing compression waves generated inboard. Such waves should not coalesce (it is thought) if their inboard distribution is similar to that on the sheared wing.

It may be deduced that to satisfy this latter rule full sweep of the minimum pressure isobar is needed into the centre unless the peak (negative) pressure coefficient is reduced at the centre below its sheared wing value. A quantitative expression of this rule is that the Mach number component resolved in the direction normal to the local isobar direction should not exceed unity in those regions in which the flow is compressing in the streamwise direction. A variation of this rule is to relax the condition to apply only where the pressure rise is rapid. No attempt to use this variant is made here.

The conjectural nature of these rules is apparent. Their use is only justified in the absence of a more rigorous approach.

4. Selection and Solution of Particular Problems

4.1 First Problem

The problem first studied is the one suggested by the first of the rules given above, that of designing the centre region to produce the same chordwise pressure distribution as that generated by the sheared wing. The particular problem is defined once the wing planform, the sheared wing pressure distribution and the design Mach number are specified. Here it may be noted that because linearized theory is being used, a consistent change in wing thickness, i.e. a constant factor on the z-ordinates, will produce a proportional change in the perturbation velocities and also in C_p values, for the pressure coefficient is related to the streamwise velocity perturbation u by

$$C_p = -2u/U_\infty$$

(U_∞ is the free stream velocity.) Moreover, also as a result of using the simple theory, if a solution is obtained for a given wing at a certain subsonic Mach number, the same solution may be applied at any other subsonic Mach number to a different, but related, wing geometry. The relations are expressed by the subsonic similarity rule, or through the use of the analogous wing. However, the results presented in this paper will not appear to take note of these generalizations and specific thickness ratios, planforms and Mach numbers will be quoted. The advantage of this is that the practical significance of the results is more readily seen.

* On the centre line $y = 0$, $v = 0$ and $\frac{\partial v}{\partial x} = 0$. Hence, because the flow is potential, $\partial u/\partial y = 0$. Thus, isobars (identical in linearized theory with lines of constant u-velocity perturbation) must cross the centre line at right angles.

The choice of the chordwise pressure distribution for this exercise is of some significance. The following considerations guided the selection.

It may first be said that a distribution such as that produced by a sheared wing of parabolic arc section or elliptic section, although having the advantage of theoretical simplicity, would most likely be so far removed from any distribution of practical interest as to make any deduction from its study of doubtful utility.

At the other extreme any attempt to use a "peaky" pressure distribution is also likely to give spurious results. The reason in this case is that the operation of interest with these aerofoils is when there is supersonic flow over the forward part of the chord, and the subsonic theory is inadequate for such flows.

Virtually by a process of elimination therefore the choice devolves on the rooftop pressure distribution. Even here caution may be needed in passing to general conclusions from particular results for one rooftop distribution.

The basic wing chosen has been designated elsewhere as RAE Wing A. It is doubly symmetric and has the RAE 101 (9 percent thickness ratio) section throughout. It is a swept tapered wing with straight leading and trailing edges. Its aspect ratio is 6, taper ratio 1/3, and it has a mid chord sweep of 30 deg. (A sketch of the wing, together with nomenclature, is given in fig. 1.)

To appreciate the task posed by the design problem the first results give the pressure distributions of this basic wing at (free stream Mach number) $M_\infty = 0$, $M_\infty = 0.8$ and $M_\infty = 0.9$, (figs. 2 and 3). It is seen that the mid semi-span pressure is virtually the same as that on the sheared wing while the distributions at and near the centre exhibit the familiar 'centre effect'.

The problem of design formally requires a two variable singular integral equation to be solved, as does the linearized theory problem of determining the load distribution on a lifting surface. The similarity of these problems might suggest that techniques for solving the latter would be suited to the former. Thus a modification of Multhopp's method (Ref. 3) or its variants could be employed. The loading functions would be replaced by thickness distributions and the downwash velocity would be replaced by the streamwise velocity perturbation. The calculation details would naturally be quite different in the two cases.

This rather general approach to the problem is now probably feasible and might be justified. However, in view of the conjectural nature of the design criterion and the knowledge that the criterion cannot be quite satisfied, a simpler but less precise method was adopted. In this the centre section of the wing was modified according to a method due to Weber (Ref. 4). Sections outboard of the centre were defined by using straight generators from the centre to a control section positioned at a suitably chosen spanwise station. Sections outboard of this control were constant and the same as the required sheared wing section.

As expected, it was found that this simple approach would not provide quite the solution required. The centre designed by the method of Ref. 4 is strictly the section shape needed on a uniform swept wing to give the required pressure distribution at its centre. On such a wing the pressure distributions away from the centre depart markedly from the required variation. Fig. 4 shows the sheared wing pressure on a 'centre-designed' uniform wing, and compares it with the desired rooftop distribution. Clearly the centre shape has to be faired rapidly into the sheared wing section to achieve a nearly uniform spanwise distribution of pressure. Such a rapid fairing in turn leads to a reduction in the magnitude of the changes which would otherwise result at the centre.

In some respects the pressure distribution produced on a wing designed on the simple basis is acceptably near what is required, despite the above observations. Fig. 5 shows results for the design Mach number zero. One possibly important shortcoming, however, is the overshoot in negative pressure coefficient near the leading edge just outboard of the centre. Should it be necessary to remove this feature the simplest approach would be to reduce the very high leading edge radius employed in the centre section.

The choice of zero for the design Mach number in the case illustrated requires some comment. There is indeed no reason why a high subsonic Mach number should not be used except that to counteract the increase in centre effect with increase in Mach number the centre section shapes required become ever more awkward as sections to use on actual aircraft.

This fact is illustrated in fig. 6 where the centre shapes for various design Mach numbers are shown. In order to demonstrate the effect fairly the sweep angle and sheared wing section are kept constant while the design Mach number is varied. Thus, the centre is designed so as to give the same pressure distribution at the centre as is produced on a sheared wing with a 9 percent thickness ratio RAE 101 section in a flow of the same undisturbed Mach number. There are two difficulties in the sections which result. One is the marked forward trend of maximum thickness position together with a decrease in overall thickness which would make the wing torsion box structure heavier than it would otherwise need to be. The other difficulty is the 'section crossing' near the trailing edge. The theory is impractical when it produces this result and the feature must be suppressed in any practical application. The result of changing the section from what is theoretically required would probably be a lessening of the effectiveness of the centre design.

4.2 Second Problem

The results of attempting to solve the first problem suggest another approach. It is noted that to achieve the desired pressure distribution the thickness has to be concentrated towards the leading edge at the centre. This indicates that it might be beneficial to let it go in this direction by the simple expedient of extending the leading edge forward near the wing apex. Such a planform modification also seems reasonable on other grounds. It increases sweep locally near the centre just where it is needed. Whether or not the disadvantages of changing from a simple swept wing more than outweigh any advantages found in the present analysis cannot be decided at this stage. However, it may be noted that the same approach has been applied before. It must suffice here to investigate the type of pressure distribution produced by planform modifications of a fairly modest extent. The new feature is that the results of such changes can now be determined easily (albeit only for inviscid flow and even this only approximately) as a result of using three dimensional theory. Previously the preliminary design of planform variations has all very probably been done using 'composite' theories of the type outlined in Ref. 5. These are known to give poor results for cranked planforms.

Initially a rational basis for arriving at the planform changes selected for study was attempted. Subsequent results invalidated the simplified basis that was used. For this reason only the planforms and their pressure distributions are given here with no explanation for their selection.

Three planforms for which calculations have been made are shown, together with their respective centre region isobar patterns in fig. 8. Results for one case of extending the chord both forward and aft are included, the aft extension being added to see what the implications of this change are. An aft extension is often included in practical designs in order to accommodate the main undercarriage.

The sections on these modified wings were kept everywhere the same as on the basic wing (9 percent RAE 101). Consequently, the increases in chord correspond to increases in thickness near the centre, a feature of some practical significance.

An assessment of the modifications was next attempted. For this purpose a simplified form of the second of the rules given in Section 3 was employed. The method of assessment adopted was as follows.

From the calculated pressure distribution the line of peak negative pressure is identified and its sweep determined as a function of spanwise position. From this 'effective' sweep angle which, by a similar argument to that given before, must drop to zero at the centre, and the flight Mach number, the critical pressure coefficient, $C_{p_{crit}}$, is found. This is the value of pressure coefficient which makes the component of velocity resolved at right angles to the line of peak negative pressure equal to the local sonic velocity. The actual C_p calculated by the first order theory is now factored so that the 'sheared wing' is just critical at the calculation Mach number. (A value of 0.8 for this Mach number was used in the present work.) The factor needed is, of course, the factor to be applied to the original value of thickness/chord ratio used in the calculation in order to make the sheared wing just critical. The new values of minimum pressure coefficient, $C_{p_{min}}$, are next determined as a function of spanwise position. If, locally, the value of $C_{p_{crit}}$ exceeds that of $C_{p_{min}}$ then the criterion referred to is not satisfied in this region.

Fig. 9 shows that on the basis of this assessment the modifications can give a considerable improvement over the basic wing, although in none of the cases is the criterion satisfied everywhere. It is also seen that merely increasing the size of extension does not produce a consistent improvement. The reason for this is that the change in $C_{p_{crit}}$ (unlike that of $C_{p_{min}}$) does not take place in regular fashion as it depends on the sweep distribution of the minimum pressure line and this varies in a complex way.

The method of assessing the modifications is open to criticism for a number of reasons. The most obvious of these is that to achieve full use of swept wing planforms (i.e. making the sheared wing portion just critical) results in velocities which are well in excess of the local sound speed. The subsonic theory is then really inadequate.

For this and other reasons it is important to test the results produced by this approach against experimental work. It would be rather surprising, however, if at least some of the improvement shown theoretically were not reflected in the real flows.

5. Conclusions

An attempt has been made to design the centre of an isolated non-lifting swept wing on a simple basis. There are indications that improvements to the basic wing flow can be produced, although the changes which result from root section modifications are limited by the awkward shapes required, particularly at high subsonic Mach numbers. Clearly, not all the possibilities have been explored and further ideas might produce more significant advantages. Firm progress, however, depends primarily on two advances. The first is that the range of validity of the simple theory should be found, preferably when edge corrections and Mach number factors are included. Secondly, a simple but effective design criterion is needed.

REFERENCES

1. E. W. E. Rogers and I. M. Hall, An introduction to the flow about plane sweptback wings at transonic speeds.
J.Roy.Aero.Soc. (August, 1960)

2. J. A. Bagley, Aerodynamic principles for the design of swept wings
Progress in Aeronautical Sciences, Vol. 3, Pergamon Press 1962

3. H. Multhopp, Methods for calculating the lift distribution of wings
R & M 2884 January, 1950

4. J. Weber, The calculation of the pressure distribution on the surface of thick cambered wings and the design of wings with given pressure distribution
R & M 3026, 1955

5. - Transonic Data Memorandum 6312, Royal Aero. Soc. 1963

6. M. M. Freestone, Numerical evaluation of singular integrals of linearized subsonic wing theory
ARC 29729 Comp. (F.M.) 133, December, 1967

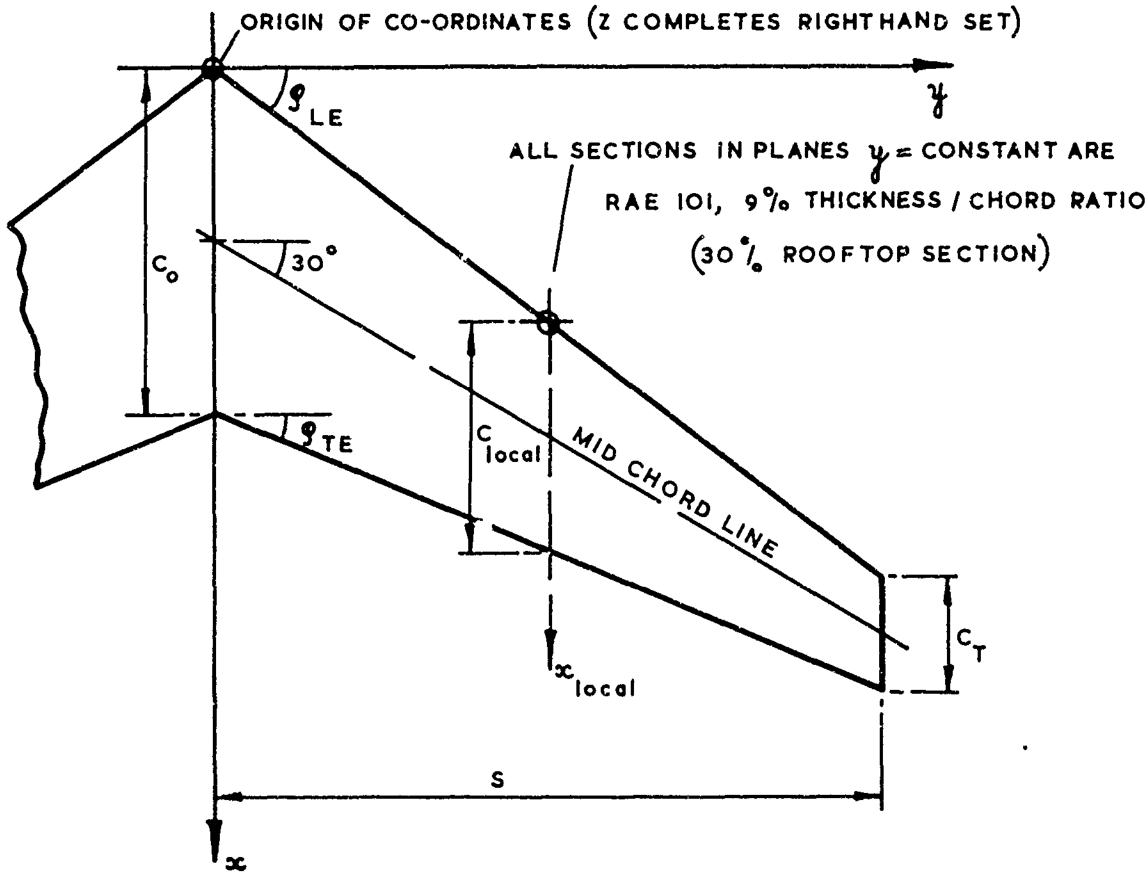

ASPECT RATIO = 6

c_T/c_o = 1/3

s/c_o = 2

FIG.1. SKETCH OF BASIC WING WITH NOMENCLATURE.

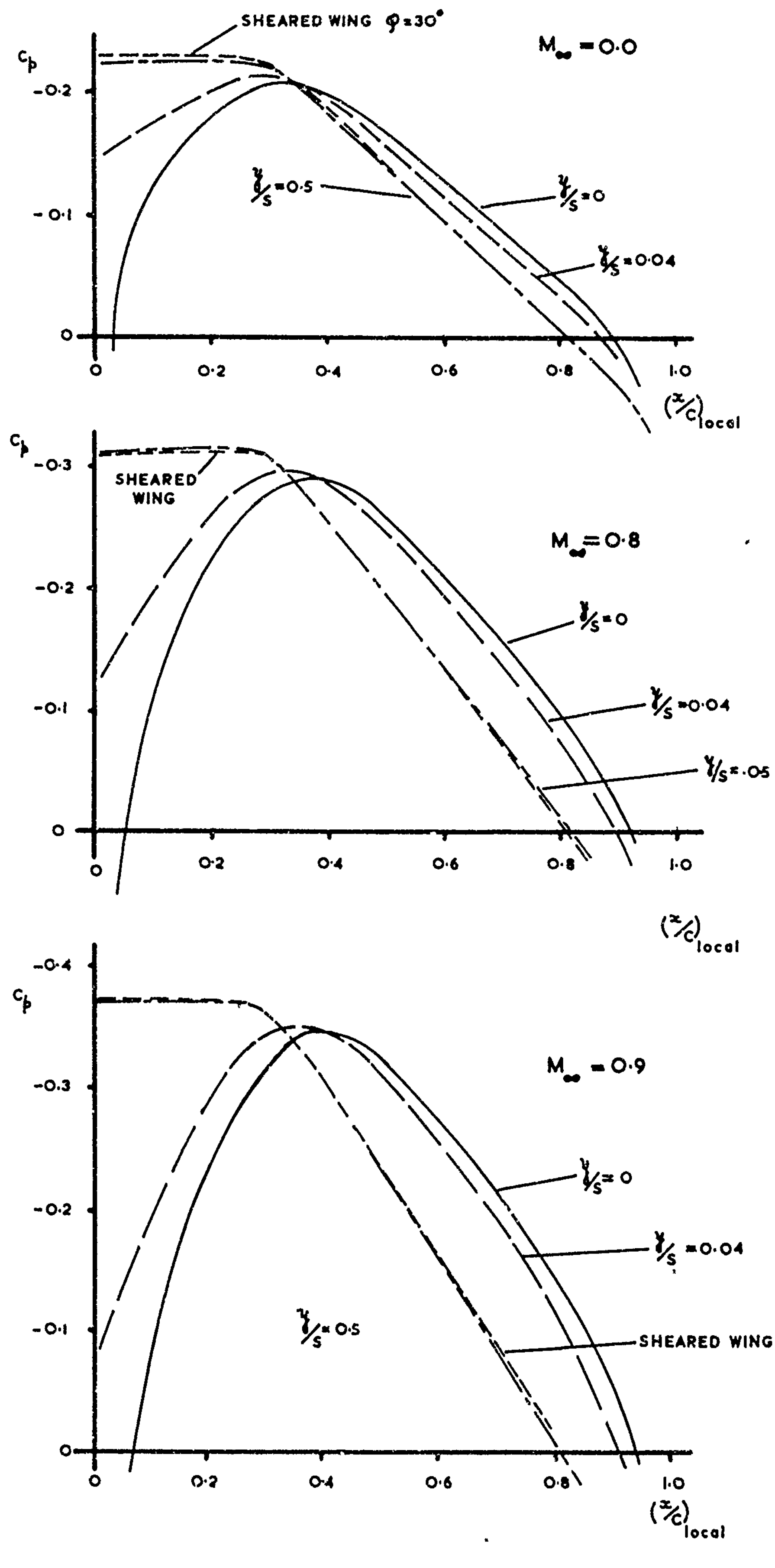

FIG. 2. CENTRE, NEAR-CENTRE, MID-SEMI-SPAN & SHEARED WING PRESSURE DISTRIBUTIONS.

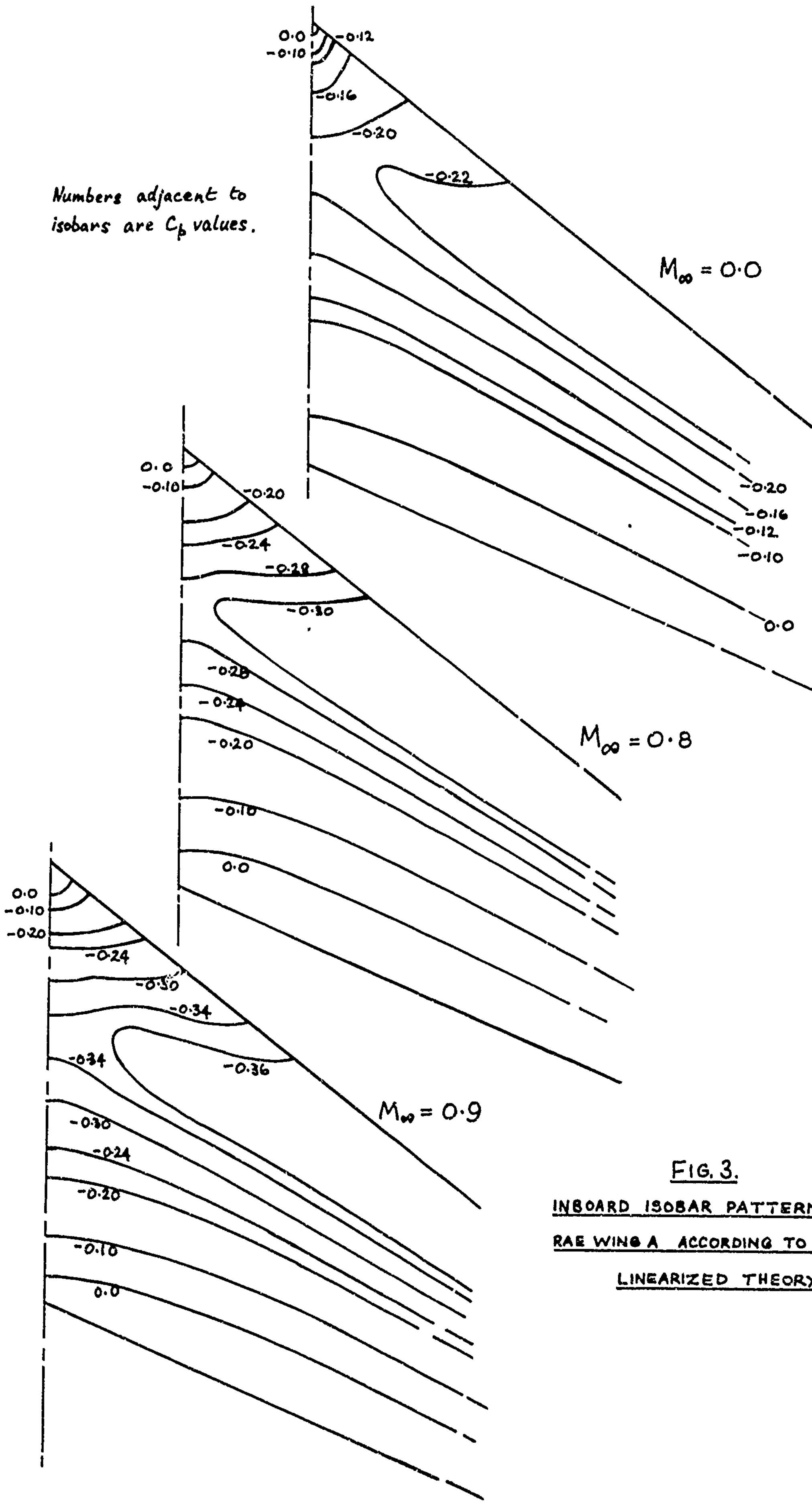

FIG. 3.

INBOARD ISOBAR PATTERNS ON THE RAE WING A ACCORDING TO SUBSONIC LINEARIZED THEORY.

FIG. 4.

SWEEP ANGLE 30°
MACH No. 0·0

CENTRE & SHEARED WING PRESSURE DISTRIBUTIONS ON A UNIFORM SWEPT WING DESIGNED TO GIVE THE REQUIRED ROOFTOP PRESSURE DISTRIBUTION AT THE CENTRE.

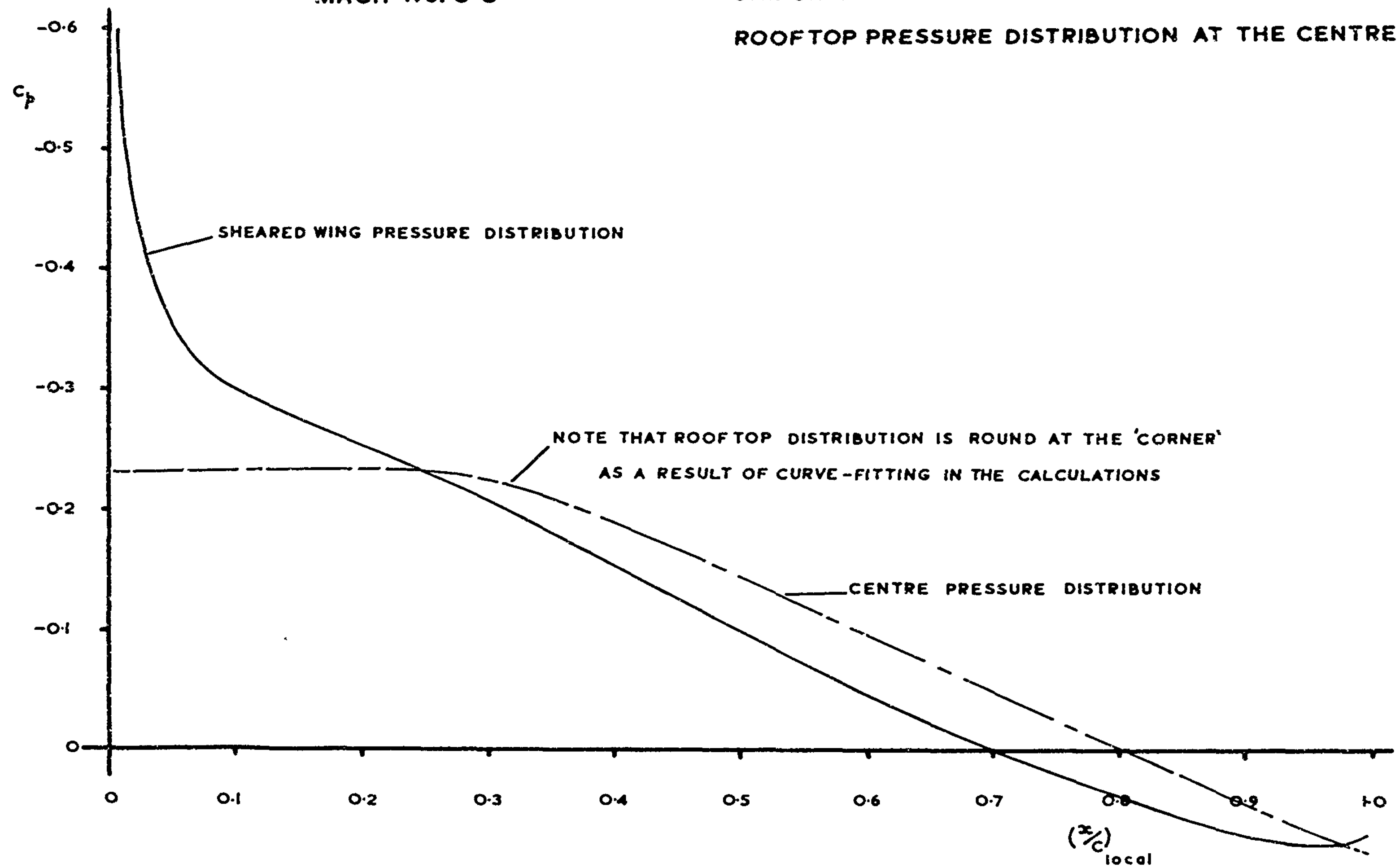

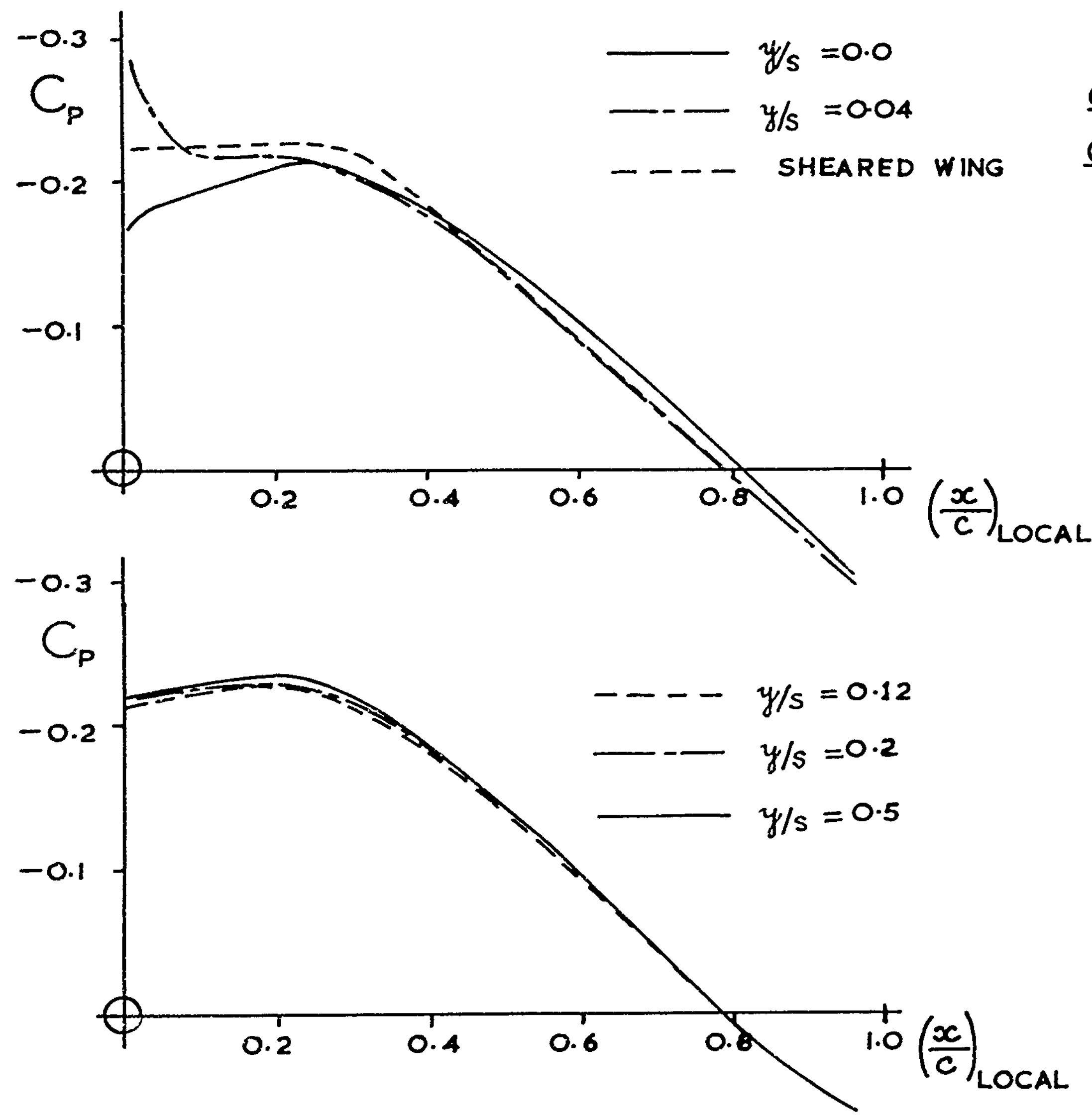

FIG. 5.

CHORDWISE PRESSURE DISTRIBUTIONS ON A DESIGNED WING.

Design Mach number 0.0
Flight Mach number 0.0
Planform as RAE Wing A
Sections : Centre, as Fig 6
Outboard of $y/s = 1/8$, 9% RAE 101
Inboard of $y/s = 1/8$, straight generators from centre to $y/s = 1/8$.

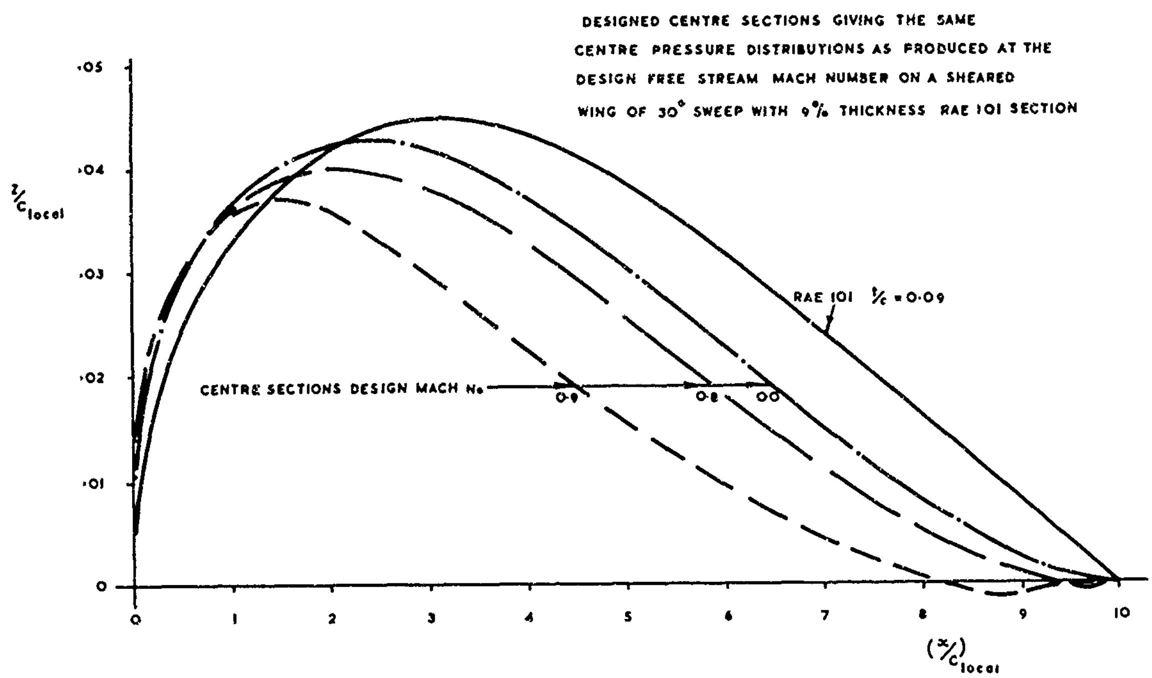

FIG.6. DESIGNED CENTRE SECTIONS.

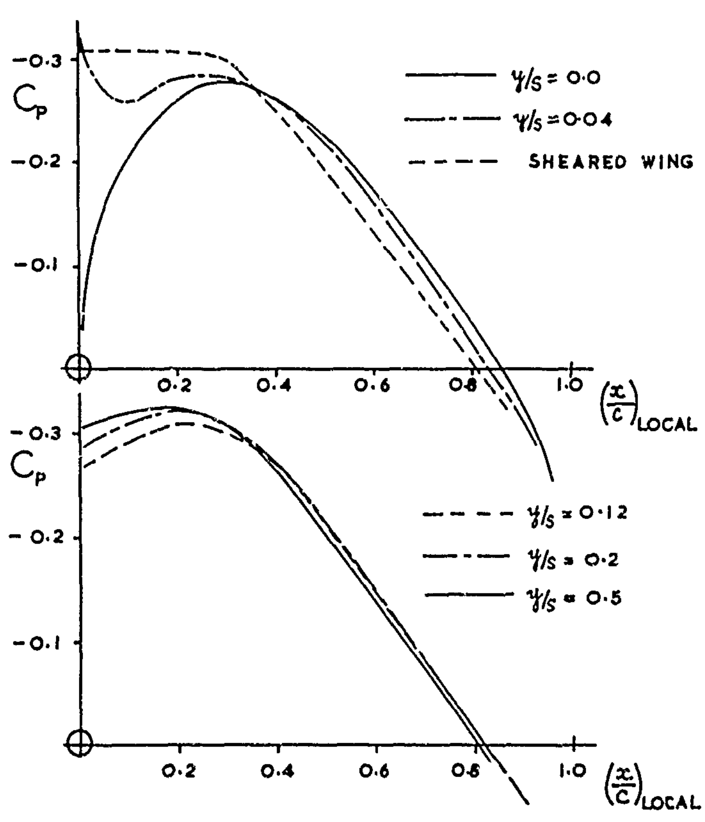

FIG. 7

CHORDWISE PRESSURE DISTRIBUTIONS ON A DESIGNED WING.

Flight Mach number 0·9
Wing as on Fig 5

FIG. 8.

ISOBAR PATTERNS ON WINGS HAVING INCREASED INBOARD SWEEP COMPARED WITH RAE WING A.

$M_\infty = 0.8$

All sections are 9% RAE 101
Spanwise limit of extensions is $y/s = 0.2$

Numbers adjacent to isobars are C_p values.

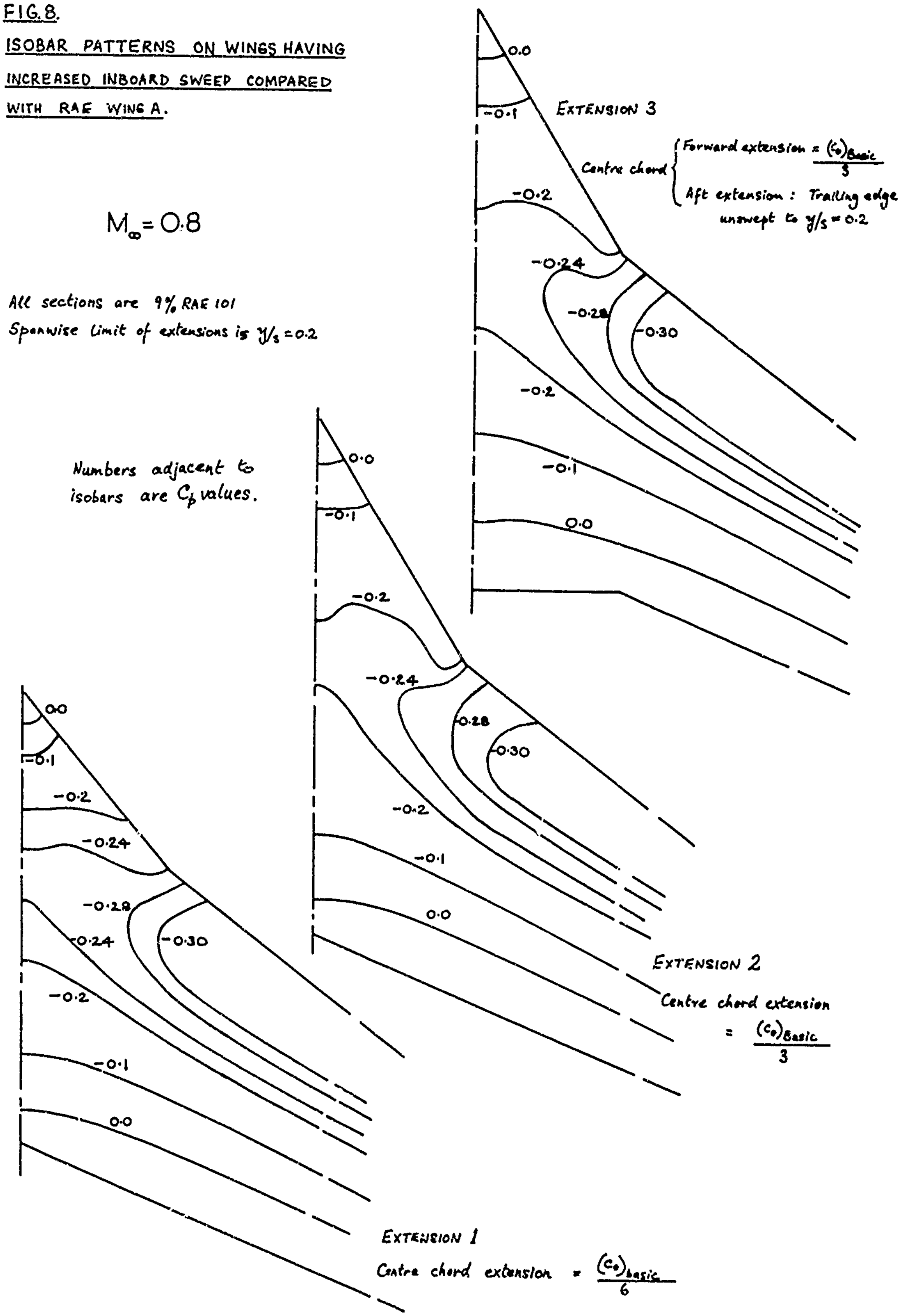

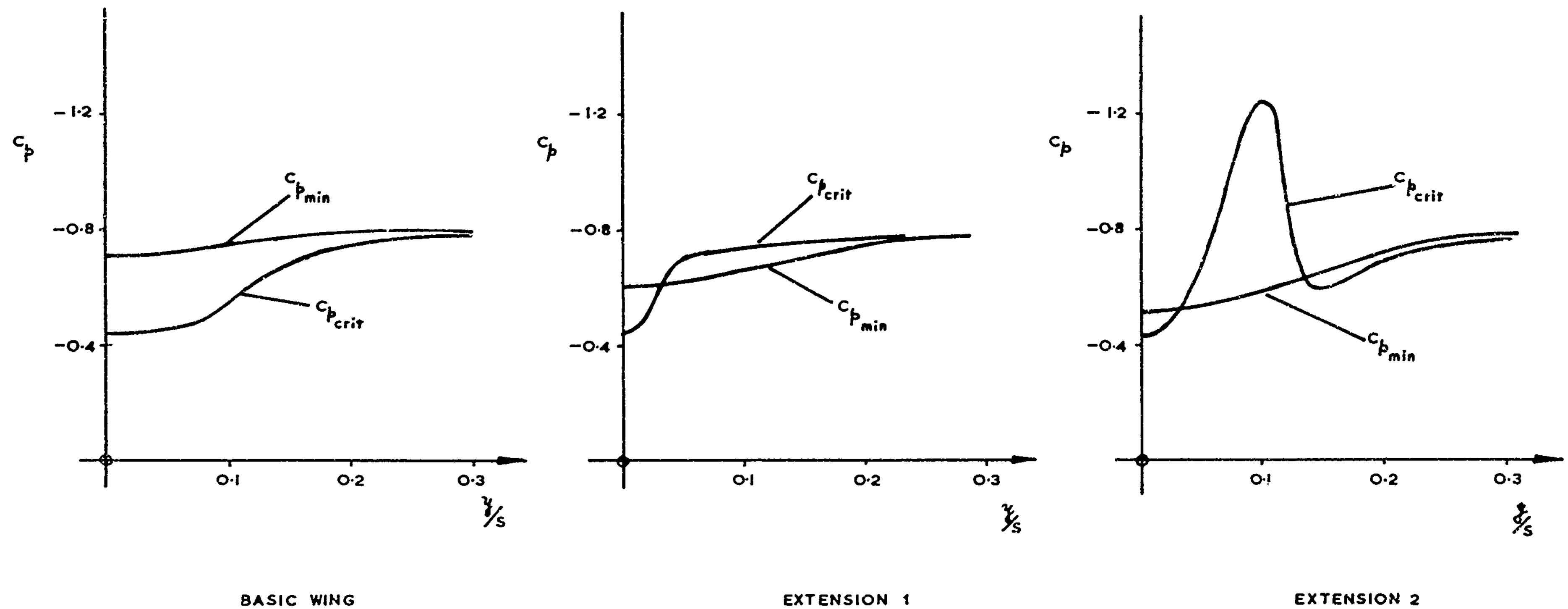

FIG.9. COMPARISON OF ASSESSMENT OF BASIC & EXTENDED WINGS.

FACTORS AFFECTING THE CHOICE OF A THREE-DIMENSIONAL SWEPT WING DESIGN FOR HIGH SUBSONIC SPEEDS

by

A.B. HAINES

Aircraft Research Association Limited,
Bedford, England

SUMMARY

The paper discusses the likely objectives for a three-dimensional sweptback wing design for operation at high subsonic speeds, and the alternatives that may be open to the designer in order to achieve these objectives. The main emphasis is on the factors that have to be borne in mind when choosing suitable target pressure distributions and isobar patterns. Results for two wings tested at A.R.A. are used in illustration. For one of these wings, the isobar pattern is relatively uniform and the shock first appears aft of the crest; for the other, the flow pattern is more complex and in particular the shock forms ahead of the crest at a Mach number well below the design cruise condition. The paper refers to some of the compromises that are often accepted to meet engineering or structural requirements, and the need for research to establish the true exchange rates involved in these compromises.

1. INTRODUCTION

The Likely "High Speed" Objectives

This paper is concerned with the aerodynamic design of three-dimensional sweptback wings for operation at high subsonic speeds. Methods of design are only mentioned incidentally; the main emphasis is on some of the factors that control and some of the problems that arise in the choice of suitable target pressure distributions and isobar patterns to meet specific design objectives. In practice, to be successful, the design of a wing for any actual aircraft project whether it be a civil transport or a military strike-fighter is essentially a matter of compromise, e.g., between aerodynamic, structural, engineering, weight and cost considerations, between low speed and high speed aerodynamic requirements etc. Even just considering the high speed aerodynamics, the wing design will often have to meet various different objectives; typical aims would be to obtain

(a) the highest possible M_D, the Mach number for the onset of the rapid increase in wave drag at a given C_L, for a given thickness/chord ratio and sweepback. This may be better expressed by saying that the aim will often be to achieve a target value of M_D with the thickest possible wing, for the sake of lower structure weight, increased fuel capacity etc. and with a modest and not too extreme sweepback for the sake of better take-off, landing and off-design characteristics,

(b) as low a drag as possible at $M = M_D$. To judge from a recent study[1] of the cruise drag of a number of subsonic transport aircraft, this particular objective should be given added prominence in the initial design stage,

(c) also, the smallest possible initial rate of increase of C_D with M beyond $M = M_D$. This point is important since the best cruise performance is usually obtained at a Mach number possibly 0.02 - 0.03 in excess of M_D and there will often be a tendency to fly as close to the buffet boundary as possible,

(d) a satisfactory M_D - C_L boundary with probably little variation in M_D with C_L. This could be particularly important for a short-range aircraft for which there were no dominant M_{cruise}, $C_{L_{cruise}}$ conditions,

(e) a satisfactory margin between the drag-rise and flow separation boundaries, both in terms of C_L at and below M_{cruise} and in terms of M above M_D at cruise C_L,

(f) a progressive flow breakdown at the stall giving not only a satisfactory useable $C_{L_{MAX}}$ but also adequate buffet warning and acceptable pitching moment characteristics.

The relative aims of these objectives will vary according to the type of wing and the type of aircraft: for example (a) - (d) would be particularly important for a transport, (f) for a fighter etc. Any single wing design considered for a particular application is unlikely to be the optimum solution for each of the above objectives; the designer will have to decide on the best compromise. The aim of the present paper is to illustrate some of the available options and some of the factors that should guide his choice.

2. CHOICE OF BASIC DESIGN PRESSURE DISTRIBUTIONS

It is probable that before starting on the detailed design of the wing to meet the objectives set out above, the aspect ratio, taper ratio, minimum acceptable thickness/chord ratio and maximum acceptable sweepback will have been defined at least approximately by other considerations. The first aim (at least for a transport) would then be to design the wing to achieve a sufficiently high M_D at the design (usually the cruise) C_L. The normal procedure starts by choosing an upper-surface pressure distribution and thickness form for the equivalent two-dimensional section. Obviously, there are many alternative options even at this stage and the thickness/chord ratio for example that will prove acceptable can depend greatly on what option is selected. This point can be illustrated quite simply by referring to the predictions in Ref.2 for the family of shapes defined in Ref.3. These sections are designed to give a roof-top upper-surface pressure distribution back to a position x_R followed by a linear pressure rise to the trailing edge, combined with a thickness distribution such that the maximum velocity due to thickness also occurs at x_R. The importance of x_R as a design variable can be seen from Fig.1. This shows that for a given M_D, extending the roof-top from $x_R = 0.3$ to $x_R = 0.6$ gives an increase of about 0.3 in C_L for a given thickness/chord ratio or alternatively, allows an increase of 0.04 - 0.05 in thickness/chord ratio for a given design C_L. These trends cannot be exploited too far since ultimately, the boundary layer may not be able to negotiate the adverse pressure gradient aft of the roof-top without separating even at full-scale Reynolds numbers. In some instances, this limit may be reached before $x_R = 0.6$. Even advancing beyond the rear-separation boundary at the best available tunnel Reynolds numbers may be considered undesirable because of the consequent difficulties in interpreting the model test data. Leaving aside this particular issue, however, this class of section design can still be rated as conservative; tests have shown that significantly higher values of M_D can be achieved for a given x_R, t/c and C_L, e.g. from extra loading at either the front or rear. Improvements could be obtained either by modifying the thickness form while still retaining the same upper surface pressure distribution or by modifying the latter. Fig.2, for example illustrates how two sections of the same thickness/chord ratio could be proposed to give the same predicted M_D at roughly the same C_L. The full-line curves in Fig.2 are for a section with $x_R = 0.5$, taken from the family just described. In this case, a shock wave would be expected to form first at a position aft of the crest ($x_{CR} = 0.35$) at a Mach number close to the predicted M_D. The other section gives a pressure distribution of the peaky-type discussed in various papers[4,5] by Pearcey and others. In this case, a local supersonic region terminated either by a shock or ideally, a largely isentropic recompression would form ahead of the crest at $M < M_D$; with increasing Mach number, the shock wave would move aft, passing over the crest, ($x_{CR} = 0.25$) at about $M = M_D$. The extra lift from the supersonic region ahead of the crest is one of the reasons why the total lift produced by the two sections is virtually the same. These two aerofoils are therefore equivalent in terms of M_D for a given t/c and C_L but even in two-dimensional flow, could well give a different C_D at M_D and a different off-design behaviour.

Other comparisons could be presented with for example, sections giving extra rear-loading but it would be wrong to suggest that the choice lies between different classes, e.g., peaky, roof-top or rear-loaded. The comparison in Fig.2 was included largely because it highlights how the choice of a two-dimensional pressure distribution can have a major effect on the problems encountered in designing the three-dimensional sweptback wing. It is fashionable - although not necessarily correct - to design the three-dimensional wing to obtain a "uniform isobar pattern" i.e. the same chordwise pressure distribution at all spanwise stations. For the roof-top type, this "merely" involves knowing how to vary the section shape across the span, how to shape the body and how to modify the planform near the tip, in order to counter the root- and tip-effects in subcritical flow. With a peaky-type distribution such as for section II in Fig.2, however, the flow at M_D is supersonic over part of the surface and therefore, retention of M_D as the design M for the three-dimensional wing implies that one can estimate how the three-dimensional root- and tip-effects are likely to affect this supercritical development. The alternative approach of designing for a lower Mach number where the flow would still be subcritical everywhere may also have its pitfalls since for a wing of say 35° sweepback, this could mean reducing the design Mach number by as much as 0.15 - 0.2. These matters are currently being investigated in a research programme at A.R.A. Experimental results are not yet available but some of the design calculations for a wing in this programme are referred to in section 5 below (Fig.6).

3. CONVERSION FROM TWO-DIMENSIONAL TO THREE-DIMENSIONAL CONDITIONS FOR WINGS (e.g.A) WITH RELATIVELY UNIFORM ISOBAR PATTERNS

For a constant-chord, infinite sweptback wing, the conversion from the equivalent two-dimensional section raises no difficulty. It has been demonstrated experimentally on several occasions[6,7] that the pressure coefficient on the swept wing at a free-stream Mach number M and lift coefficient C_L is given by

$$C_{p_{3D}} = C_{p_{2D}} \cos^2 \Lambda$$

where Λ is the angle of sweepback

and $C_{p_{2D}}$ is the pressure coefficient in two-dimensional flow at $M \cos \Lambda$, $C_L \sec^2 \Lambda$ for the section normal to the leading edge of the swept wing.

For a tapered, finite wing, however, the process is less straightforward even when merely considering the mid-semi-span region away from the immediate vicinity of the root or tip. Several possible methods can be suggested. In the past, the common design practice having chosen a suitable 2-D section, has been simply to factor the section ordinates by $\cos \Lambda_\ell$ (where Λ_ℓ is the sweepback of the lines at constant x) in order to derive the 3-D section in the free-stream direction. Wing A for which test data are presented in Figs.3, 4 is an example where this practice was followed. It is a wing with 25° sweepback on the 0.25c line, a taper ratio of 0.33 and an aspect ratio of 8.0; the local sweepback varies from 27.5° at the leading edge to 15.5° at the trailing edge. It can be described as a "relatively simple example" in that the sweepback is only modest, the chordwise pressure distributions are fairly similar at all stations across the span and the flow is subcritical everywhere almost up to M_D (0.73) at the design C_L. The section shape varies however across the span and only one "equivalent two-dimensional section" was tested. This was incorporated (with minor modifications dictated by practical considerations) in the three-dimensional design at about 0.25 x semispan. Fig.3 includes a comparison for the design C_L and at a Mach number slightly above M_D between the 3-D and 2-D data for this station, the 2-D data being converted to 3-D conditions simply on the basis of

$$C_{p_{3D}} = C_{p_{2D}} \cos^2 \Lambda_\ell \text{ at the appropriate } C_{L_{L_{3D}}} = C_{L_{L_{2D}}} \cos^2 \Lambda_{0.25}$$

It will be seen that in general, the converted 2-D and the 3-D data in Fig.3 are in fairly good agreement. This is true, for example, of the rear-loading. Clearly, however, the supercritical flow development at the rear of the (approximate) roof-top is already beginning to differ significantly. Amongst the factors responsible for this discrepancy, one can quote the following:

(i) this station at 0.25 x semispan is not far enough from the root to be unaffected by the 3-D root effects. It is believed that this is the main reason why over most of both the upper and lower surface, the pressures are lower in the 3-D case,

(ii) even leaving aside possible root and tip-effects, factoring the ordinates by cos Λ_ℓ is only to the first order, the same as aiming for $C_{p_{3D}} = C_{p_{2D}} \cos^2 \Lambda_\ell$. For example, if one considers the simple case of a symmetrical wing at zero incidence in incompressible flow, the standard formula[9] in use in the U.K. for estimating the surface pressures over a swept wing, reduces at the maximum thickness position to

$$C_{p_{3D}} = -2 \cos \Lambda_\ell \, S^{(1)} (x)$$

$$\text{where } S^{(1)} (x) = \frac{1}{\pi} \int_0^1 \left(\frac{dz_t}{dx}\right)_{x = x'} \frac{dx'}{x - x'}$$

It follows that

$$C_{p_{3D}} \neq C_{p_{2D}} \cos^2 \Lambda_\ell$$

$$\text{since } S^{(1)} (x) \neq \frac{\cos \Lambda_\ell}{\pi} \int_0^1 \left(\frac{dz_t/\cos \Lambda_\ell}{dx}\right)_{x = x'} \frac{dx'}{x - x'}$$

Similar, but quantitatively different, arguments apply in respect of the velocities due to camber. It is possible to show that accepting the above formula for $C_{p_{3D}}$ as a valid expression for a tapered wing with Λ_ℓ thus varying with x, the general result is for $C_{p_{3D}} < C_{p_{2D}} \cos^2 \Lambda_\ell$ near the leading edge and vice-versa - consistent with the comparison in Fig.3,

and finally,

(iii) even if exact equivalence between $C_{p_{3D}}$ and $C_{p_{2D}} \cos^2 \Lambda_\ell$ were obtained at subcritical speeds, this is not what is required to produce the same supercritical development. This is perhaps the most important point of the three. Suppose, for example, that the 2-D distribution is a true roof-top. The $C_{p_{3D}}$ distribution derived as above would then have a peak at the rear of the roof-top but to obtain the same initial supercritical development, one needs a peak at the front and a "sloping roof-top" distribution parallel to the variation of $C_p{*}$ with x (where $C_p{*}$ is the critical pressure coefficient in a direction normal to the lines at constant x).

This discussion may appear a little academic in relation to the 25° sweptback wing of Fig.3 but even here, it is estimated that the combined effect is to reduce the drag-rise Mach number at a given C_L by about 0.02. For a wing of higher sweepback or greater taper, the effects would be more appreciable and could well react on the choice of a suitable section/pressure distribution. In view of point (iii) above, it may be preferable to think in terms of "equivalent pressure distributions" rather than "equivalent sections", e.g., a "sloping roof-top" rather than a "roof-top" but even then, the eventual supercritical development could still differ significantly. This is because quite apart from the various 3-D factors to be discussed later in section 6, the supercritical development depends on both the pressure distribution and the surface curvature distribution.

Two consequences of adopting an "equivalent pressure distribution" approach are first, it tends to reduce the potential advantage to be expected from a rearward extension of the roof-top and second, it implies that on the tapered 3-D wing, more lift can be carried near the leading edge. With $x_R = 0.4 \sim 0.5$, increasing taper should generally tend to increase C_L for a given M_D, t/c or alternatively, M_D for a given C_L, t/c.

4. STUDY OF RESULTS FOR WING A: AT AND ABOVE "DESIGN" C_L

It has been seen that the method used for converting from 2-D to 3-D on Wing A has led to some reduction in M_D at the design C_L. For some applications, this could have been serious but in the present instance it did not conflict with the main design aims which were to obtain a high useable C_L at all Mach numbers up to the cruise value, and a satisfactory flow breakdown across the wing at the stall. Considerations such as the value of M_D at the cruise C_L were of rather less importance - always provided some minimum target figure was achieved.

The changes in pressure distribution across the span as shown in Fig.3 should also be viewed in the same light. The two main trends evident at the cruise C_L are

(i) a decrease from inner to outer wing in the suction values near the leading edge - thus leading to a stronger shock near 0.4c on the outer wing,

and (ii) a reduction particularly between 0.675 and 0.88 x semispan in the adverse pressure gradients at the rear of both the upper and lower surfaces. This is achieved by a reduction in the local thickness/chord ratio near the tip.

At the cruise C_L, (i) is clearly harmful in terms of M_D and (ii) is unnecessary but they should not be regarded as weaknesses in the design since both were aimed at improving the performance at higher C_L.

The wing design was in fact outstandingly successful in its main aim as can be seen from Fig.4 which presents the pressure distributions for $C_L = C_{L_{design}} + 0.04$ at $M = 0.71$. Features to note on Fig.4 include the following:

(a) no trailing-edge pressure divergence at any of the four stations,

(b) the shock front swept back at an angle greater than the local geometric sweepback,

(c) some isentropic recompression ahead of the shock at all four stations

and (d) a fair degree of loading at the rear, again at all four stations.

The results for this wing have shown therefore that the idea of designing for essentially a roof-top pressure distribution over the upper surface at the cruise condition and then shaping the leading edge to obtain some peaky-type development at higher C_L is an attractive concept, particularly when good results are required over a wide range of operating C_L.

5. DESIGN OF REGION NEAR THE ROOT OF A SWEPTBACK WING

To obtain a particular isobar pattern over the whole wing in the design condition one needs to be able to calculate the pressures over wings of arbitrary geometry in regions where no equivalence with two-dimensional flow can be expected. Common practice in the U.K. has been to use the method largely developed at the R.A.E. over the past 10 - 15 years and published[9] in R.Ae.S. T.D.M.6312. In its present form, the method applies to compressible, subcritical, inviscid flow. It is based on an approximation to the linear-theory solutions for both thickness and lifting effects combined in such a way as to include some of the cross-coupling terms and with corrections to allow for the principal non-linear effects particularly near the leading edge. For the thickness terms, the starting points were the exact linear-theory expressions for the velocities over an infinite yawed wing, and at the root of an infinite swept wing of constant chord and section shape. These two expressions are then linked with the aid of various approximate interpolation factors derived mostly from a study of the exact solutions for wings of relatively simple geometry but partly based as will be seen below on experience from comparisons with experimental data. Similar techniques were followed for the lifting terms except that in this case, the velocity distribution at the root due to camber was itself only known as an approximate expression having an accuracy strongly dependent on the angle of sweepback[10]. Used with due regard for the limitations imposed by the approximate nature of the interpolation factors, the absence of many of the second-order terms and of any allowance for the viscous effects, the method has proved a powerful design tool.

For applications where the drag characteristics at the cruise C_L are of paramount importance, the wing design near the root needs special care. As is well known, to maintain fully swept isobars into the root involves either appropriate body shaping and/or changes to the wing section shape such as a forward movement of the maximum thickness position. Any large local changes in the wing section geometry must tend - at least, in principle - to reduce the accuracy of the formula (or indeed, any other method) for calculating the pressure distributions. This point is illustrated by the comparison presented in Fig.5. These results are for the root section of a symmetrical, 40° sweptback wing at zero incidence; in an effort to improve the isobar sweep, the maximum thickness was brought forward to 0.15c at the root as compared with 0.42c over most of the span. The main uncertainty in calculating the pressures at the root of such a wing by the method of Ref.9 lies in deciding what values to assume for the "thickness sweep". For a wing with no change in section shape across the span, this would normally be taken as the sweep of the lines at constant x, i.e. Λ_{ℓ} as defined earlier, but Fig.5 shows that if this were done in the present case, the predicted values of $(-C_p)$ over much of the chord would be more than twice those obtained experimentally. This result was not foreseen when the wing was designed (some 14 years ago!) and as a result, the isobar pattern and wing performance were unsatisfactory as described in Ref.11. Fig.5 shows however that defining the "thickness sweep", Λ_t, at the maximum thickness position (x_t) as the sweep of the maximum thickness line and then varying tan Λ_t linearly both between $x = x_t$ and $x = 0$ and between $x = x_t$ and $x = 1$ gives results that are in fairly good agreement with the experimental data, at least back to $x = 0.5$.

It is important to realize that a suitable definition for the "thickness sweep" is only one item in a "package". Any change in other items such as the factors for planform and thickness taper or the compressibility factors, could react on what is the most suitable definition for the "thickness sweep". Earlier, for example, when some of these other factors were less soundly based, a mean of the above two definitions appeared to be the most satisfactory but now, this is no longer true! Clearly, this particular wing design is a somewhat extreme example: the sweepback of the maximum thickness line at the root is 67° as compared with a quarter-chord sweepback of only 40°. In many practical cases, the sensitivity of the results to the geometrical assumptions and the other interpolation factors would be less pronounced.

Over the years, the accuracy and range of applicability of the various factors has been steadily improved but results such as those just discussed pose the question as to whether some more radical changes to parts of the method are required. Considerable thought has been given to this point. Continuing to discuss just the thickness effects, clearly, one of the most important advances in recent years has been the method[12,13] and computer programme developed by A.M.O. Smith and his colleagues for calculating the velocities due to thickness in incompressible flow over wings and bodies of completely arbitrary shape. As a result, an exact linear-theory solution is now available against which the appropriate "block" in the formula of Ref.9 can be checked in carefully selected "test cases". Alternatively, this "block" could be actually replaced by the output data from the A.M.O. Smith programme, and this has in fact been done[14] by Loeve of N.L.R. It should prove most helpful to have this facility available for use when required but its drawback when considered as a general design tool, is that this programme would be relatively costly to use and also restricted to the larger computers. In practice, when selecting a wing shape for a given application, one would probably want to calculate the pressures over a fair number of alternative designs and at a number of different operating conditions. There will therefore continue to be a place for treating this term (velocities due to thickness: linear theory) on a less elaborate basis: either by continuing to use the present factors modified where found necessary or by adoption of a method such as that proposed in Ref.15.

One point that must be stressed is that in several important respects, the method of Ref.9 should be <u>more</u> accurate than linear-theory. It follows that in the future, improvements e.g. inclusion of further second-order terms or of allowance for viscous effects, can be introduced without departing from the essential framework of the present formula. It will thus be possible to continue the steady progressive evolution based on comparisons with other theories and experiment that has marked the previous development of this method.

This discussion has however been somewhat of a digression from the main theme of this paper, which is more concerned with the question of what are desirable target pressure distributions and isobar patterns rather than what methods one should use to find the geometry corresponding to these pressures. As noted earlier, a common aim has often been to try and obtain a "uniform isobar pattern". This is not necessarily the best solution: research over many years has shown that at least when considering the initial development of a shock, the Mach-number component normal to the isobars is the relevant parameter and hence there may be a case to strive in selected areas for an isobar sweep greater than the local geometric value. Certainly, one ought as a general rule to try and avoid any serious loss in effective sweep, e.g. through the isobars forming closed loops. This is often difficult to achieve near the root since the major 3-D root effects decay with distance from the root in a hyperbolic fashion. It follows that to obtain a perfectly uniform isobar pattern it would be necessary to have continuous surface curvature (spanwise) with very rapid local changes near the root. In practice, however, the preference has usually been for straight generation between a limited number of control stations. Up to a point, this may be acceptable but there can be little doubt that with many designs, some aerodynamic performance has been lost through the control stations being either too few in number or wrongly positioned. Some recent calculations for a 35° sweptback wing illustrate what can then happen. Pressure distributions for four stations on the inner wing are presented in Fig.6. The general aim of this design was to try and obtain similar peaky-type upper surface pressure distributions at all four stations. In the lower picture in Fig.6, stations 1 (i.e., the root) and 4 (the outermost station) are both control stations and the comparison is between results for station 3, considered alternatively as a further independent control station or with its surface geometry interpolated linearly between stations 1 and 4. The upper picture gives a similar comparison for station 2 lying between 1 and 3. The calculations assume that the flow is still subcritical at $M = M_D$; the real flow would be supercritical but with the shock lying near or ahead of the crest, provided the design is successful in its aims.

Fig.6 shows that a much closer approach to a uniform isobar pattern is achieved if all four stations are allowed to be control stations. If an intermediate station is omitted, relatively high suctions are then predicted for the intermediate region over the forward part of the chord. Alternatively, it is easy to visualise that if stations 2, 3, 4 were retained and the geometry at the root derived as an extrapolation from 2 and 3, there would then be relatively low suctions at the root and a general loss of isobar sweep inboard of station 2. Either of these alternatives <u>could</u> have particularly unfortunate consequences in the present case as it might upset not merely locally but over the whole region from 1 to 4, the desired favourable supercritical development expected on the basis of some related 2-D tests. The consequent reduction in M_D and/or increase in C_D at M_D is difficult to estimate and experimental results are not yet available. General experience based on far more than just this one example has shown that aerodynamically, 3 should be regarded as the absolute minimum number of control stations over the inner part of the wing; on engineering grounds, 3 is often thought of as a maximum number and efforts are frequently made to persuade the aerodynamicist to accept 2! This is an area where there is an outstanding need for combined aerodynamic, structural and engineering studies to establish the true exchange rates involved in such compromises.

The calculated results in Fig.6 contain some other features of general interest. For example, it will be seen that even with 4 control stations, the desired peak suction was not apparently obtained close to the leading edge at the actual wing-root section. In theory, this could have been generated either by adopting a very bluff shape or from extreme inverse droop, but probably at the expense of excess drag. Also, the suctions near 0.6c at station 4 appear somewhat high; to some extent, this is related to the wing planform with the trailing edge unswept over the inner panel. This has been a common feature of many recent subsonic transport designs, being often introduced to give an unswept hinge-line for a flap or to assist the stowage of the undercarriage. One suspects that a significant loss in performance either in terms of M_D, C_D at M_D or supercritical behaviour may often result from these planform details or from local changes in the wing thickness distributions introduced for similar reasons. Again, this could be a fruitful area for research studies to find the exchange rates and hence, improved all-round "optimum designs". Wing-root fillets and fairings on the fuselage opposite the wing could usefully form part of these studies rather than being treated in an ad-hoc fashion at a later stage or simply being designed "on past experience".

6. THREE-DIMENSIONAL INFLUENCE ON SUPERCRITICAL FLOW DEVELOPMENT INCLUDING STUDY OF RESULTS FOR WING B: AT AND ABOVE "DESIGN" M

The discussion in the preceding section was based on "subcritical" calculated pressure distributions; let us now turn to some experimental data for a wing where the flow is already supercritical at $M = M_D$ and where even at the design C_L, there is considerable non-uniformity across the span. Results for this example, wing B, are presented in Figs.7, 8.

Fig.7(a) gives a comparison between 3-D and converted 2-D data for two stations (at 0.28 (I) and 0.60 (II) x semispan) at the design C_L and $M = M_D - 0.10$. Even at this Mach number, the flow is already supercritical near the leading edge at both stations. The agreement with the converted 2-D data is reasonable at station II but at station I, it is not as good as for wing A discussed earlier. Largely, this can be explained in terms of the higher sweepback of wing B (and hence, greater root-effects), the thickness taper related to the section variations across the span and finally, the wing planform geometry which further complicates the process of deciding what is the true "equivalent 2-D section". By $M = M_D + 0.01$, Fig.7(b), the order of agreement between the 3-D and 2-D data has deteriorated further and discrepancies are now observed at both stations I and II. Over the rear of the chord, these can be explained in the same way as for the lower Mach number - the effects have merely increased in magnitude and extended further out, e.g., the higher suctions in the 3-D data near 0.4c at station II can be linked with the high suctions near 0.5 - 0.6c at station I. Differences are also evident however in the development of the local supersonic region - to some extent at II and more particularly at I. It is impossible in this brief account to comment in detail but it is worth pointing out that both the 2-D and 3-D data are very sensitive to small changes in either M or C_L. It is therefore reassuring to find that at station II at least, there is some "family resemblance" between the variation of the 2-D and 3-D data with M or C_L. At station I, however, there appears to be a more substantial difference in behaviour: whereas the 2-D data suggest a supersonic region terminated by a shock, the 3-D distributions indicate a much higher peak suction near the leading edge followed apparently by considerable isentropic recompression and no real evidence of any strong shock. This impression was confirmed by oil-flow studies. One relevant factor is that the sweepback of the isobars over the forward part of the chord near station I is much higher than the local geometric sweepback. This can be seen from the isobar patterns for $M = M_D$ and $M = M_D + 0.04$ presented in Figs.8a, b.

Comparing these two isobar patterns, the shock front near station II clearly moves rearward with increasing Mach number in this range whereas near station I, there is relatively little change. As a result, by $M = M_D + 0.04$, the sweepback of the shock front near I is near 50° rather than 35°. One would expect therefore that the rate of increase with Mach number in the wave drag associated with this shock front would be less near I than near II. At first sight, however, this is not borne out by the variation of the local section drag coefficients ΔC_{D_L} as derived from the measured pressure distributions. These are shown in Fig.8c, plotted in the form of ΔC_{D_L} vs. $(M - M_D)$ where ΔC_{D_L} is the increment in C_{D_L} compared with the value at $M = M_D$, and M_D is the drag-rise Mach number for the wing as a whole. The variation in the overall C_D is plotted below for comparison. It is clear that a spanwise integration of the values of $\frac{c}{\bar{c}} \Delta C_{D_L}$ would yield a variation with Mach number broadly similar to that obtained in the overall measurements but the changes across the span in the ΔC_{D_L} variation are somewhat unexpected. Despite what was forecast above, it is section II which appears to give the most favourable results in the range up to $(M_D + 0.04)$.

To understand this apparent anomaly, one must consider how three-dimensional effects control the development of the flow over the sweptback wing under supercritical conditions. Fig.9 helps to explain this in a diagrammatic fashion. For any sweptback wing operating at either $C_L > C_{L_{design}}$ or $M > M_{design}$, it is likely that the flow over the upper surface, leaving aside the tip region, will be characterised by a 3 (or 4)-shock system as illustrated in Fig.9. These shocks were first explained and described in detail by Hall and Rogers in several reports, e.g. Refs.16, 17, from the N.P.L. The forward shock originates from either the wing-root leading edge or the most forward point where the flow is supersonic. The mathematical condition that has to be satisfied for this shock to lie across the wing surface is given in Ref.17; its sweepback is related to the resultant Mach number of the local flow and so increases with C_L at a given M, or with M at a given C_L; typically, it is around 50°. The main significance of the forward shock is that it marks the inward boundary of the region in which the supercritical flow development can be similar to that over the corresponding two-dimensional section. Hence, in Fig.9, it is only outboard of point A that the "quasi-2D" shock bears some affinity to the 2-D behaviour. Inboard and aft of the forward shock, the flow is affected considerably by the influence of the root. Even if the inner wing sections and the body shape are such as to minimise this influence at the design condition, there can still be a considerable effect at off-design. Generally, the suction will increase over the middle part of the chord of the inner wing and this is then followed by a recompression through a series of waves which coalesce some distance out from the root to form a "rear shock". This shock intersects the forward or "quasi-2D" shocks at point B. The "outboard shock" has the combined strength of the two inner systems and frequently, therefore, the initial flow separation occurs just outboard of point B. As the Mach number is increased further beyond the design value, the general tendency will be for points A and B to come together and to move inboard but precisely what happens in any given example clearly depends on the section characteristics, wing planform, the wing-body junction shape etc.

With this very brief and simplified description, it is now possible to revert to the drag data in Fig.8c for wing-body B for which the flow pattern for $M > M_D$ is essentially of the type shown in Fig.9a. Earlier, it was noted that it was difficult to explain the fairly substantial increase in ΔC_{D_L} with $(M - M_D)$ at station I at 0.28 x semispan in terms of wave drag associated with the shock system over the forward part of the chord. Now, in terms of Fig.9a, it can be explained in terms of the development of the rear-shock. Expressed another way, the increase in drag corresponds to the increase in suction aft of the crest ahead of the rear shock. For section II, on the other hand, it is possible to interpret the small increase in ΔC_{D_L} between M_D and $(M_D + 0.04)$ by saying that the increase in wave drag has been partly offset by a reduction with Mach number in the root-influence on this section. This can be seen by comparing the pressure distributions for section 2 inset in Figs.8a, b. The relatively high suctions near 0.3 - 0.4c at $M = M_D$ were not observed in the tests on the equivalent two-dimensional section (see Fig.7b) and can probably be ascribed to root-influence. No such irregularities were observed aft of the main shock at $(M_D + 0.04)$ or in other words, this section then lies outboard of points A and B. ΔC_{D_L} can therefore be a poor indication of the wave drag associated with the main shock front; the difficulty lies in knowing how C_{D_L} would vary with Mach number in the absence of a shock wave. In the present case, the implication is that under such conditions, C_D would have decreased with Mach number at station II.

Finally, the comparison between Figs.9a, b has been included in order to illustrate that the choice of basic design pressure distribution can have a major effect on the way the 3 (or 4)- shock system develops at off-design conditions. The two pictures correspond diagrammatically with the two alternative 2-D sections considered in Fig.2. With small x_R, as in Fig.9a, the tendency is for the quasi-2D shock to link on the inner wing with the forward 3D-shock, thus leaving the rear-shock as a clearly defined separate front. With large x_R as in Fig.9b, the quasi-2D shock tends to link with the rear shock leaving the forward shock as the separate system. Obviously, these pictures and this description are grossly over-simplified but even so, certain conclusions are valid. For example, the proportion of the wing span over which the local supersonic region can develop as in two-dimensional flow is clearly greater in case (a); also, with (b), there is a greater likelihood that the supersonic region ahead of the rear shock develops in a manner completely uncontrolled by any expansion field being generated near the leading edge. It is not however the aim of this paper to pronounce in favour of (a) or (b). This would be both premature and unwise particularly as it is really misleading to think that there are just two classes of design. The distinctions have been deliberately overdrawn to simplify the discussion and to highlight the problems that are being investigated in current research.

7. GENERAL DISCUSSION AND CONCLUDING REMARKS

Examples have now been given of how the choice of basic pressure distributions and isobar patterns can affect the drag-rise Mach number (M_D) and supercritical behaviour. For a transport aircraft, another vital factor is the standard of achievement in respect of C_D at M_D and the extent to which C_D could be reduced by a change in the target pressure distributions. Indeed, it seems likely that in the past, there may have been too much stress on obtaining the best value of M_D with too little regard for C_D at M_D or for $^{dC_D}/_{dM}$ near M_D. Recent analysis has suggested[1,18] that typically, an increase of 10% or more in the wing-body drag coefficient (excluding the vortex-induced drag) can be expected between low speeds and $M = M_D$ but that the reason for this can vary widely from one design to another. The three most common reasons are:

(i) an increase in the wing profile drag with Mach number at subcritical speeds,

(ii) premature supercritical wave drag appearing as a sectional effect somewhere along the span,

and (iii) premature wave drag due to three-dimensional effects related notably to a loss in isobar sweep near the root.

A method[19] is now available for estimating (i) in two-dimensional flow; it has been shown to be reliable for a wide range of pressure distributions. Also, a criterion has been issued[20] for recognizing whether the pressure distributions are of the "triangular" type[4] - one of the main sources of (ii). Effect (iii) has already been discussed. Past experience appears to suggest that if the excess drag from any two of these sources is small, the contribution from the third item is appreciable but there is no reason why this should necessarily follow. It is merely an indication that all three effects should be considered at the initial design stage.

This paper, in its examples at least, has tended to concentrate on sweptback wings of high aspect ratio, typical of subsonic transport designs. It is however worth noting that at a design point with fully attached flow the problems encountered in designing a swept wing for a strike/fighter application are likely to be similar in principle, although differing in detail. Even though the wings would be of much lower aspect ratio, it is still possible to relate the behaviour at such a design condition with corresponding results in two-dimensional flow. Naturally, the three-dimensional root effects have a stronger influence but Ref.9 has still been used as a design method with conspicuous success.

The real differences between the two types of application arise when considering off-design conditions. For example, the stalling behaviour of swept wings of moderate aspect ratio is likely to be determined by 3-D effects such as part-span vortex sheets or a separation induced by a forward- or rear-shock rather than by an outboard quasi-2D shock. Also, for a strike/fighter, a satisfactory flow breakdown across the span at the stall in manoeuvering flight may often be the major criterion when seeking an acceptable wing design. Normally, one wants a progressive rather than a sudden flow breakdown and the choice of a uniform isobar pattern in the design condition may make it more difficult to realise this aim. Nevertheless, experience has shown that ways can be found for resolving this dilemma.

To summarise, the best possible wing design for any given application must always be a compromise. The object of research must be to find what are the major factors, to establish the exchange-rates and so help the designer to make the best choice. It is hoped that this paper has made a contribution in this respect.

Finally, the author wishes to acknowledge the help received from other members of the A.R.A. staff and from colleagues in industry, the R.A.E. and N.P.L. in the preparation of this paper. He takes full responsibility however for the opinions expressed.

REFERENCES

1.	Haines, A.B.	Subsonic Aircraft Drag: An Appreciation of Present Standards. A.R.A. Wind Tunnel Note 66, 1967. R.Ae.S. Journal pp.253-266, Vol.72, 1968.
2.		R.Ae.S. T.D.M.67008.
3.		R.Ae.S. T.D.M.67009.
4.	Pearcey, H.H.	The Aerodynamic Design of Section Shapes for Swept Wings. Paper presented at ICAS Congress, Zurich, 1960.
5.	Pearcey, H.H.	Shock-induced Separation and its Prevention by Design and Boundary Layer Control. "Boundary Layer and Flow Control", Vol.2, Part IV, Pergamon Press 1961, edited by G.V. Lachmann.
6.	Lawlor, E.F.	Wind Tunnel Tests at Mach Numbers between 0.6 and 1.4 of a 60° Swept Wing having an Aerofoil Section designed for Subcritical Flow at a Mach Number of 1.2. Part I: 9% Thick Section with "triangular" Pressure Distribution. A.R.C. C.P.582, May 1961.
7.	Rogers, E.W.E. Berry, C.J. Quincey, V.G.	Tests at Transonic Speeds on Wings with Wedge Sections and Sweep varying between 0° and 60°. A.R.C. 23,180, 1961.
8.	Lock, R.C.	The Equivalence Law Relating Three- and Two-dimensional Pressure Distributions. A.R.C.23,952, 1962.
9.		R.Ae.S. T.D.M.6312.
10.	Weber, J.	The Shape of the Centre Part of a Sweptback Wing with a required Load Distribution. A.R.C. R.& M. 3098, 1959.
11.	Haines, A.B.	Wing Section Design for Sweptback Wings at Transonic Speeds. R.Ae.S. Journal pp.238-244, Vol.61, 1957.
12.	Hess, J.L. Smith, A.M.O.	Calculation of Non-lifting Potential Flow about Arbitrary Three-dimensional Bodies. E.S.40622, 1962. - Douglas Aircraft Company.
13.	Faulkner, Sue Hess, J.L. Giesing, J.P.	Comparison of Experimental Pressure Distributions with those Calculated by the Douglas Neumann Program. LB.31831, 1964. - Douglas Aircraft Company.
14.	Labrujere, T.E. Loeve, W. Slooff, J.W.	An Approximate Method for the Determination of the Pressure Distribution on Wings in the Lower Critical Speed Range. Paper to be presented at the AGARD Specialists' Meeting on Transonic Aerodynamics, 18-20 September 1968 - Paris.
15.	Freestone, M.M.	An Approach to the Design of the Thickness Distribution near the Centre of an Isolated Swept Wing at Subsonic Speeds. Paper to be presented at the AGARD Specialists' Meeting on Transonic Aerodynamics, 18-20 September 1968 - Paris.
16.	Hall, I.M. Rogers, E.W.E.	Experiments with a Tapered Sweptback Wing of Warren 12 Planform at Mach Numbers between 0.6 and 1.6. R.& M.3271, 1960
17.	Berry, C.J. Rogers, E.W.E. Townsend, J.E.G.	A Study of the Effects of Leading-edge Modifications on the Flow over a 55° Sweptback Wing at Transonic Speeds. A.R.C.21,987, 1960.

18. Haines, A.B. — Recent Research into some Aerodynamic Design Problems of Subsonic Transport Aircraft.
Paper to be presented at ICAS Congress, Munich, 1968.

19. Nash, J.F., Osborne, J., Macdonald, A.G.J. — A Note on the Prediction of Aerofoil Profile Drag at Subsonic Speeds.
A.R.C.28,075, 1966.

20. R.Ae.S. T.D.M. 6407.

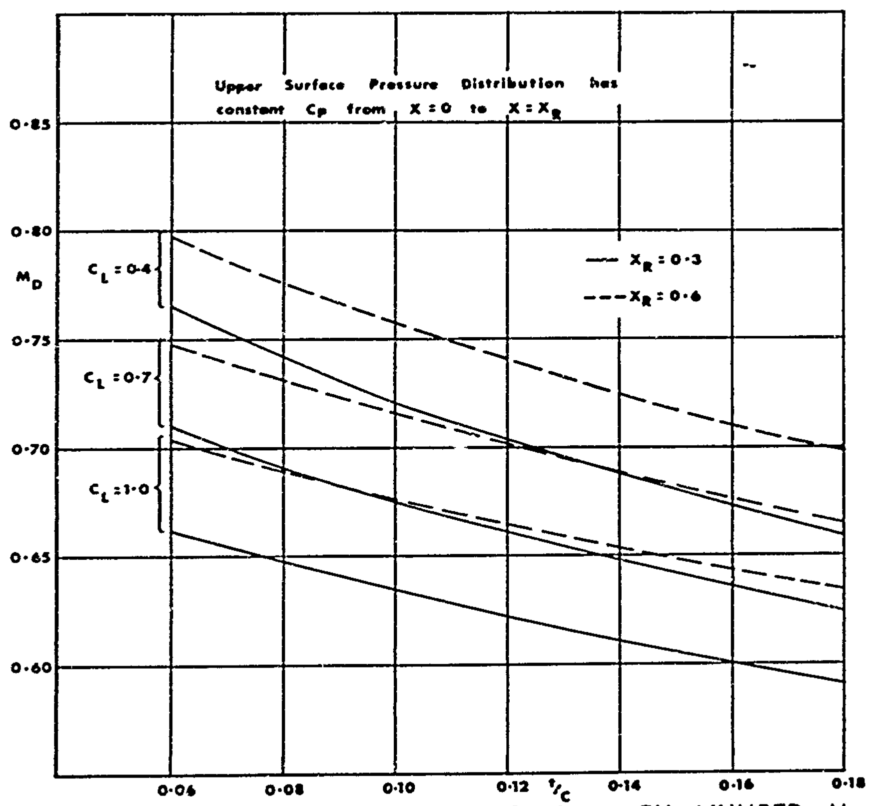

FIG.1 VARIATION OF DRAG RISE MACH NUMBER, M_D WITH DESIGN C_L, $^t/_c$ AND ROOF TOP EXTENT

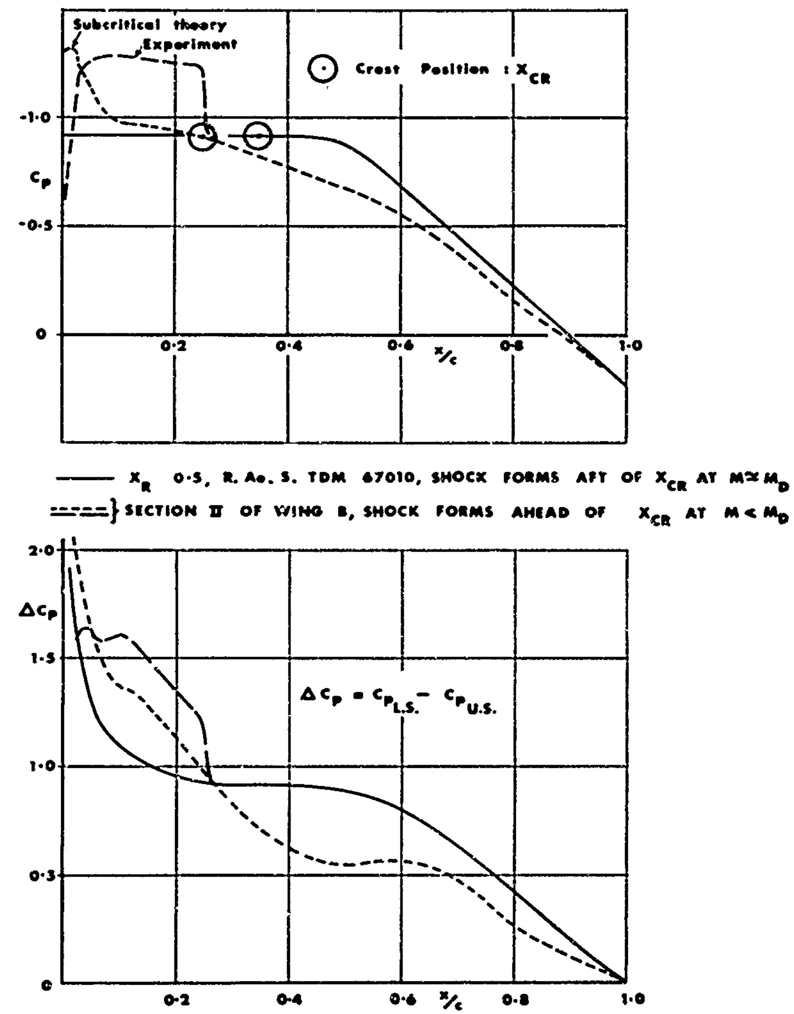

FIG.2 COMPARISON OF TWO PRESSURE DISTRIBUTIONS GIVING SIMILAR C_L AT SAME M_D AND $^t/_c$

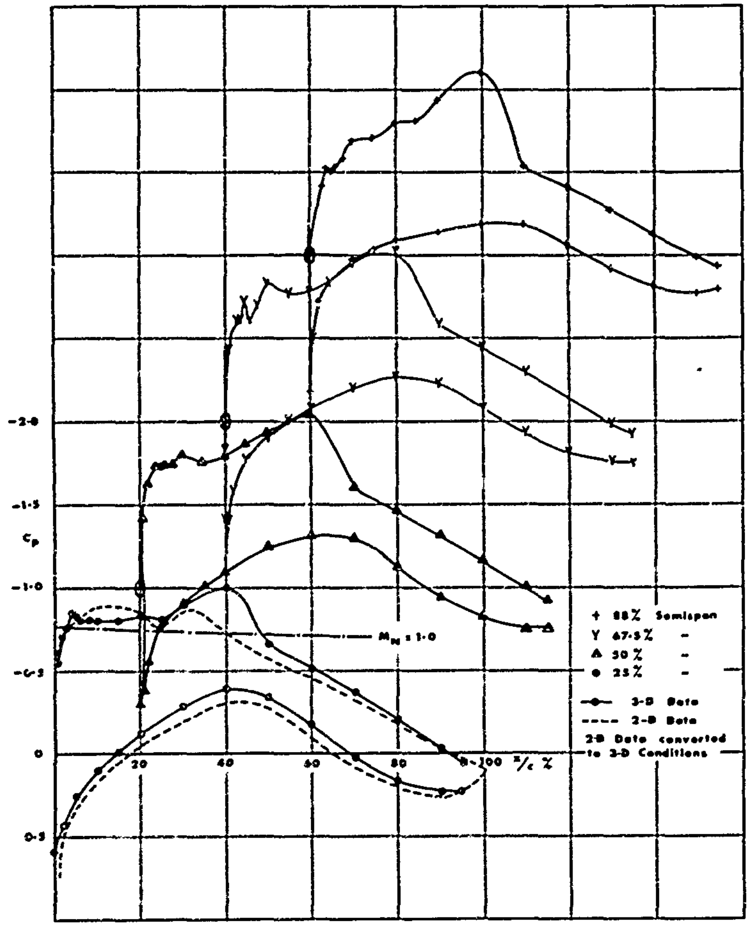

FIG.3 PRESSURE DISTRIBUTION FOR 25° SWEPTBACK WING A AT $C_{L_{DESIGN}}$; $M = 0{\cdot}74 = (M_D + 0{\cdot}01)$, $A = 8$, $\Lambda_0 = 27{\cdot}5°$, $\Lambda_{1\cdot0} = 15{\cdot}5$

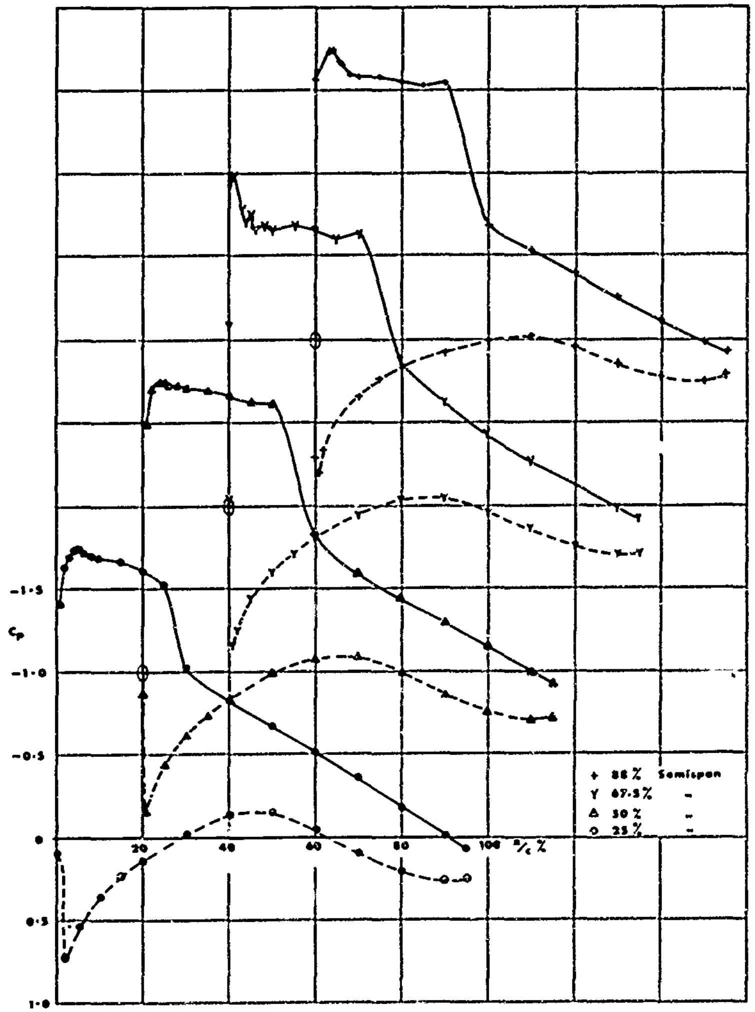

FIG.4 PRESSURE DISTRIBUTION FOR 25° SWEPTBACK WING A AT $C_L = C_{L_{DESIGN}} + 0{\cdot}4$, $M = 0{\cdot}7$

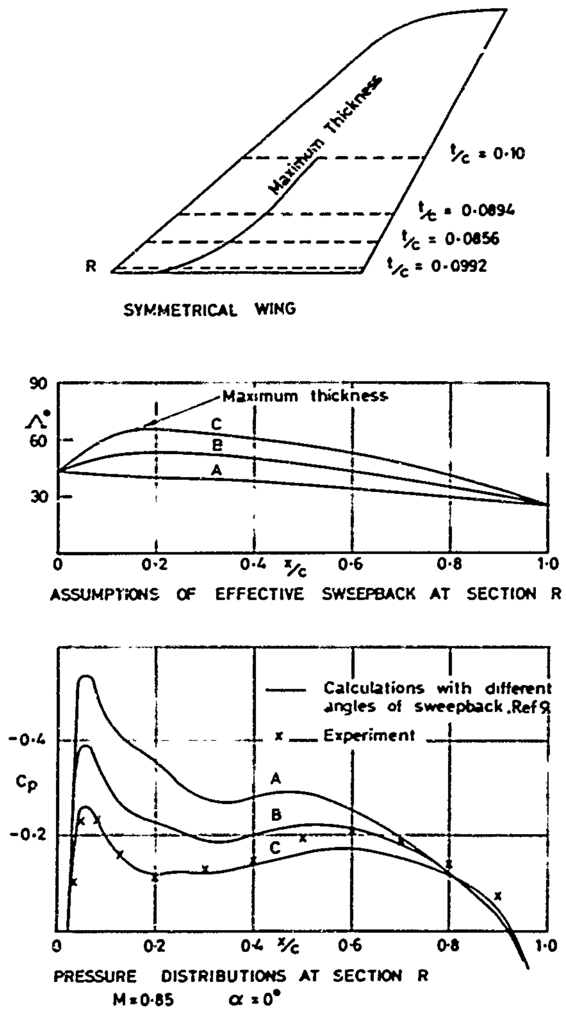

FIG. 5 EFFECT OF GEOMETRICAL ASSUMPTIONS ON CALCULATED PRESSURE DISTRIBUTIONS.

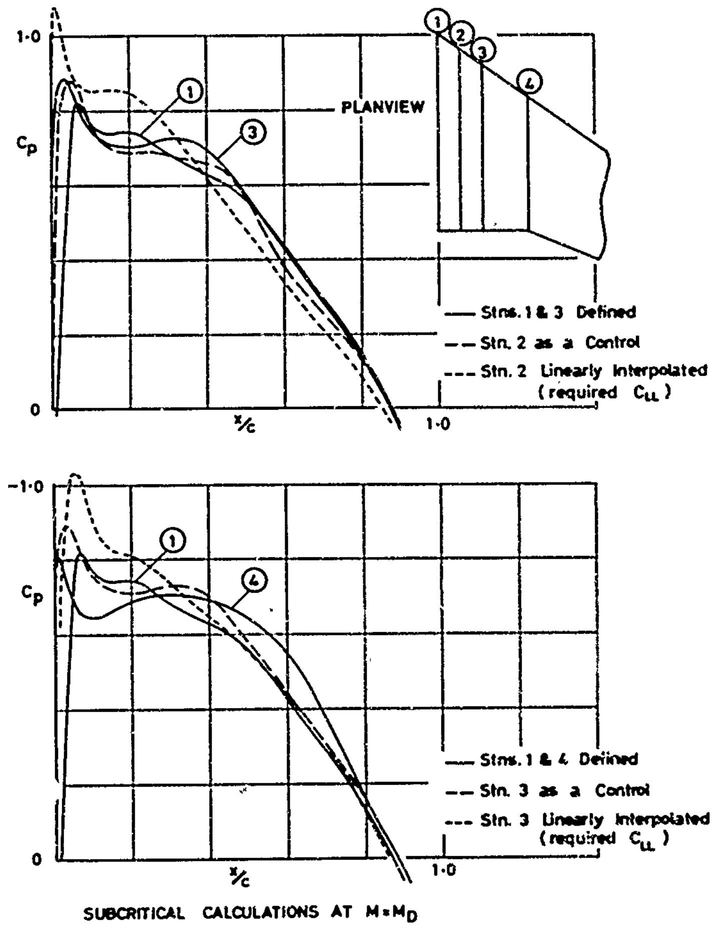

FIG. 6 EFFECT OF NUMBER OF CONTROL STATIONS ON PRESSURE DISTRIBUTIONS NEAR ROOT

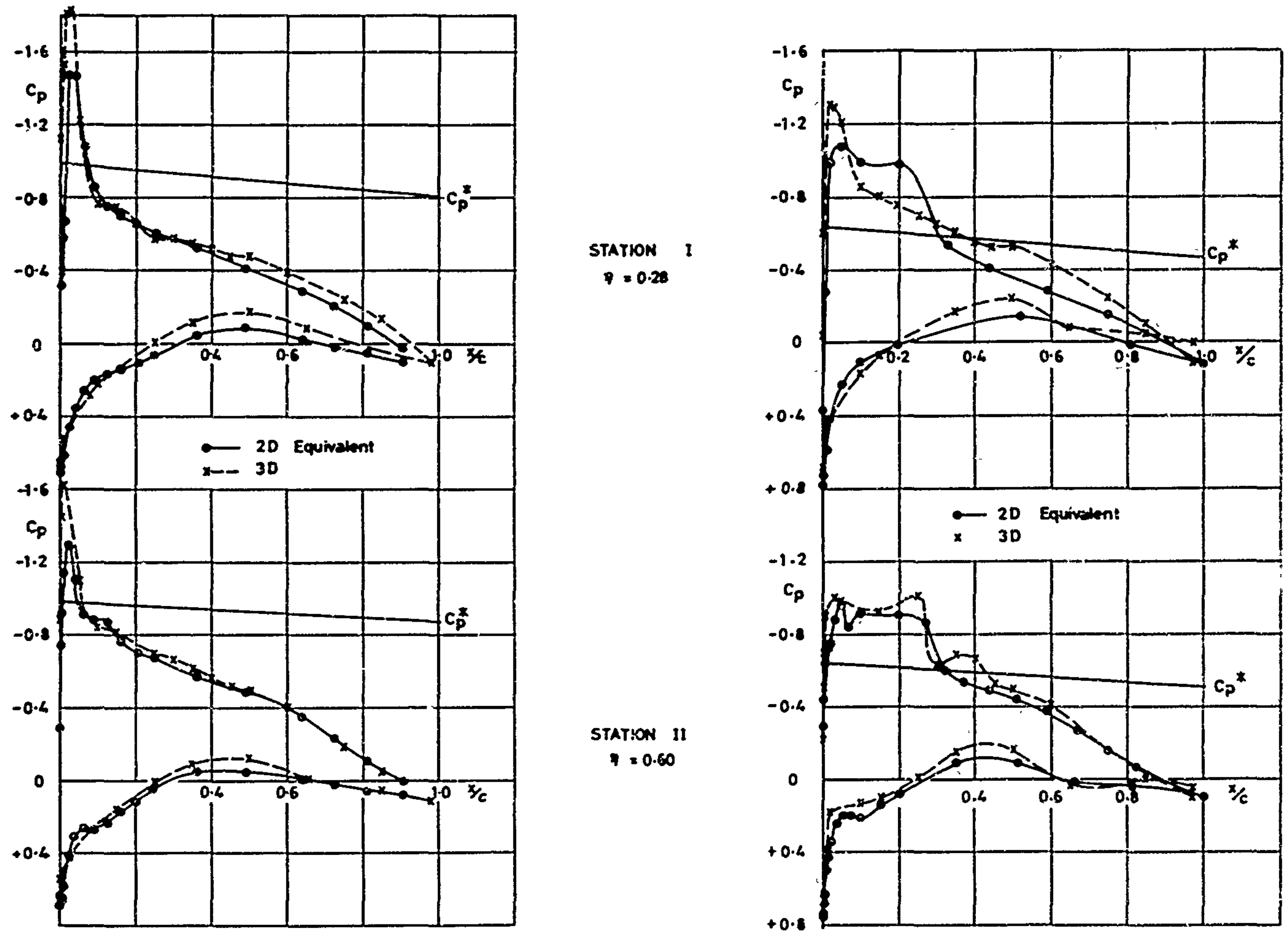

(a) SUBCRITICAL CONDITION
$M = M_D - 0{\cdot}10$
$C_L = C_{L_D}$

(b) DESIGN CONDITION (SUPERCRITICAL)
$M = M_D + 0{\cdot}01$
$C_L = C_{L_D}$

FIG. 7 COMPARISON OF 2D & 3D RESULTS FOR WING B

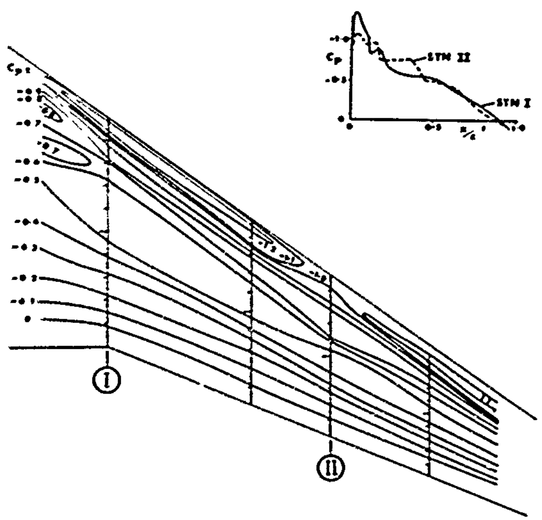

FIG.8a ISOBARS ON WING B AT $C_{L_{DESIGN}}$, $M = M_D$

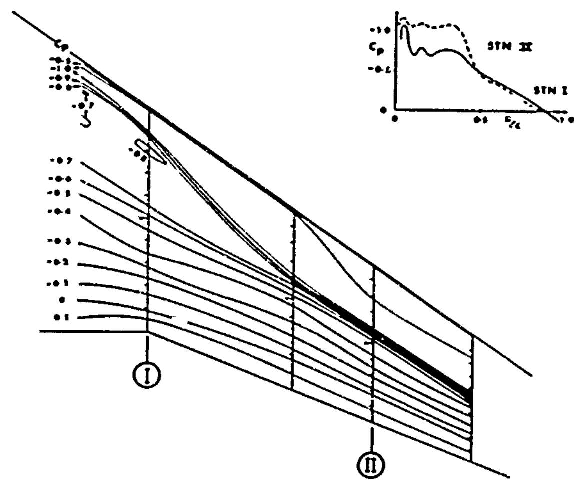

FIG.8b ISOBARS ON WING B AT $C_{L_{DESIGN}}$, $M = M_D + 0{\cdot}04$

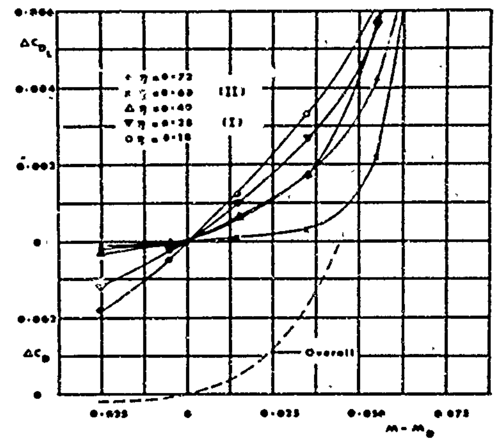

FIG. 8c VARIATION OF C_D WITH M BEYOND $M - M_D$. WING-BODY B

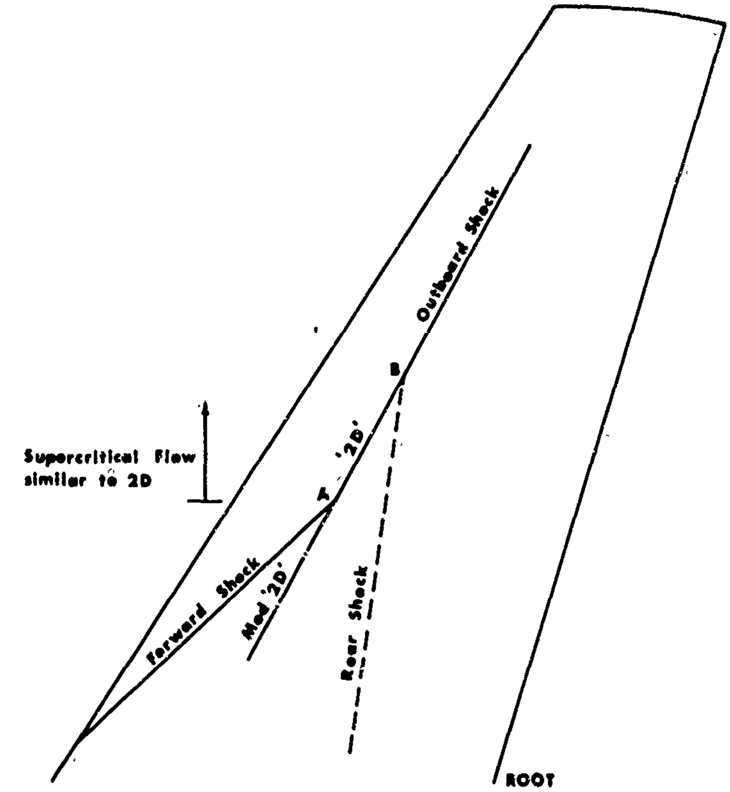

(a) FOR WING WITH 2D PRESSURES WITH SMALL X_R

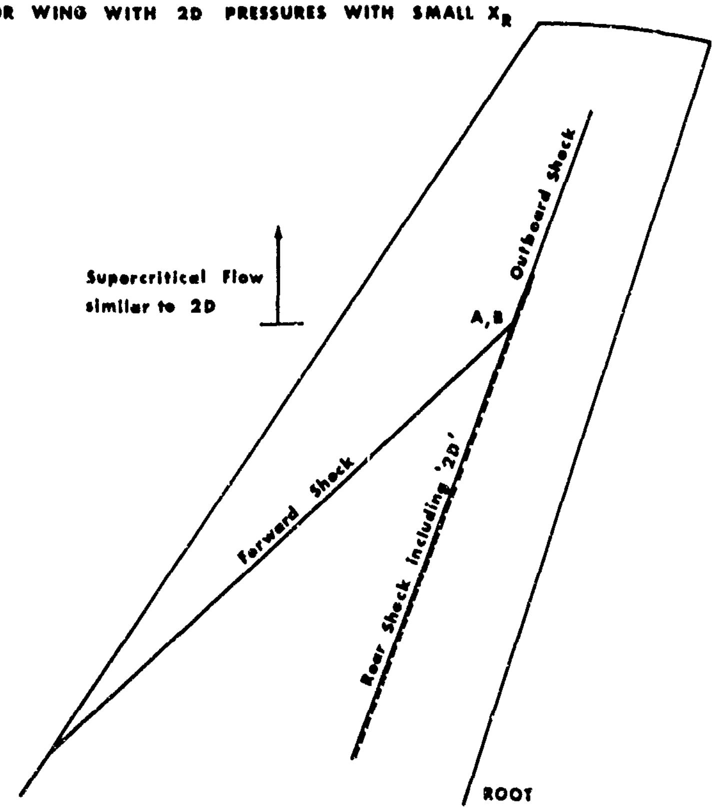

(b) FOR WING WITH 2D PRESSURES WITH LARGE X_R

FIG.9 TYPICAL SHOCK PATTERNS AT $M > M_{DESIGN}$ OR $C_L > C_{L_{DESIGN}}$

An Approximate Method for the Determination of the Pressure Distribution on Wings in the Lower Critical Speed Range

by

Th.E. Labrujere, W. Loeve and J.W. Slooff

National Aerospace Laboratory NLR, Amsterdam
Netherlands

Summary

The design of aircraft for efficient flight at high subsonic speeds demands for methods by which the pressure distributions on wings can be predicted accurately.

The present paper is concerned with an approximating method that is based on the fact that the main characteristics of subsonic flow about wings are described rather well by the linearised potential equation. In view of this, similar to Goethert's rule, the compressible flow is related to the incompressible flow around an analogous configuration which is obtained from the original one by an affine transformation. The incompressible flow is determined by means of a surface distribution of singularities and the Goethert relation is supplemented with semi-empirical factors. Viscosity effects are taken into account by applying the method to a configuration that is obtained by modifying the contour of the aerofoil for the differential growth of the boundary layer displacement thickness on the upper and lower surface.

The accuracy of the method is shown by comparison with exact results for two-dimensional flows and experimental results for two- and three-dimensional flows.

Notations

Symbols.

c	length of local chord
r	body radius
t	maximum thickness of aerofoil section
u	perturbation velocity on the surface of the aerofoil
x	chordwise coordinate
y	spanwise coordinate
z	coordinate measured normal to the reference plane of the aerofoil
B_w	compressibility factor according to Wilby (ref.2)
C_p	pressure coefficient
C_L	lift coefficient
Ma	Mach number of the onset flow
V	total velocity non-dimensionalized by the velocity of the onset flow
α	angle of attack
β	$= \left\{1 - Ma^2\right\}^{\frac{1}{2}}$
η	spanwise coordinate non-dimensionalized by the semi-span
$\left.\begin{matrix}\tau_1 \\ \varepsilon_0 \\ \Gamma\end{matrix}\right\}$	parameters defining lifting quasi-elliptical aerofoil section (ref.1)

Subscripts.

a	refers to the analogous configuration
i	refers to the incompressible flow

Superscripts.

(1)	refers to the first order approximation
$*$	refers to the critical condition

An Approximate Method for the Determination of the Pressure Distribution on Wings in the Lower Critical Speed Range

by

Th.E. Labrujere,[x)] W. Loeve[x)] and J.W. Slooff[xx)]

National Aerospace Laboratory NLR, Amsterdam
Netherlands

1 Introduction.

For flight at high-subsonic speeds special attention must be paid to the avoidance of large drag, which occur as a result of pressure losses due to viscous effects and shocks. To keep these phenomena within acceptable limits an iteration process is applied, in practice, in which use is made of both measurements in wind tunnels and aerodynamic calculations. The convergence of this process largely depends on the accuracy by which details of flow phenomena on wing-body combinations can be predicted. As exact solutions for viscous compressible flow about such configurations do not exist, only approximating methods can be applied.

Recent developments in transonic wing-design appear to lead to geometries for which in many cases existing methods are no longer satisfactory. The present paper is concerned with an approximating method which has been developed with the object to improve this situation. In doing so special attention has been paid to the prediction of compressibility effects at conditions where the velocity components normal to the isobars are near-sonic.

2 Description of the method.

2.1 General remarks.

It is well known that the main characteristics of subsonic attached flow are described rather well by the linearised potential equation. In the present method the solution of this equation is approximated in a way very similar to the Prandtl-Glauert and Goethert rules. Considering a wing-body combination in an onset flow with Mach number Ma, the compressible flow around the given configuration is related to the incompressible flow around an analogous configuration. This analogous configuration is obtained from the original one by shrinking all dimensions normal to the onset flow direction by the factor $\beta = \left\{ 1 - Ma^2 \right\}^{\frac{1}{2}}$. When applying linearised theory the incompressible flow is usually determined by means of a chord-line distribution of singularities. In the present method, however, a surface distribution is applied. Also non-linear compressibility effects are approximated semi-empirically by supplementing the Goethert rule with correction factors depending on local flow conditions. It may be emphasized that the present method has been developed in such a way that wings both with and without body may be treated.

2.2 Outline of the method for the limiting case of two-dimensional symmetric flow.

According to full linearised theory, as formulated by Goethert, the perturbation velocity u on a given aerofoil in compressible flow, is related to the perturbation velocity u_a on the analogous aerofoil in incompressible flow. Considering first order approximations, this is extablished by the well-known relation

$$u^{(1)} = \frac{1}{\beta^2} \cdot u_a^{(1)}. \qquad (1)$$

where the superscript (1) refers to first order perturbations. Non-dimensionalizing the velocities by means of the undisturbed velocity, the total velocity on the aerofoil is then determined by :

$$V = 1 + u^{(1)} \qquad (2)$$

This result is in principle only valid for thin aerofoils with cusped leading and trailing edges. In the incompressible case the first order result can be made uniformly valid for

x) Senior Research Engineer, Aerodynamics Division.

xx) Research Engineer, Aerodynamics Division.

aerofoils with round leading-edges by applying Riegels factor, viz :

$$V = \left[1 + u^{(1)} \right] . \left[1 + \left(\frac{dz}{dx}\right)^2 \right]^{-\frac{1}{2}} \tag{3}$$

where $z = \pm z\ (x)$ is the aerofoil contour in the concerning symmetric case.

For compressible flow Küchemann and Weber (ref.1) have modified this result in order to take into account non-linear effects :

$$V = \left[1 + \frac{u_a^{(1)}}{\beta B_w} \right] . \left[1 + \left(\frac{dz}{dx} / B_w\right)^2 \right]^{-\frac{1}{2}} \tag{4}$$

The compressibility factor B_w may be chosen according to the suggestion of Wilby (ref.2) viz :

$$B_w = \left\{ 1 - Ma^2 \left(1 - Ma.C_{p_i}\right) \right\}^{\frac{1}{2}} \tag{5}$$

C_{p_i} is the local pressure coefficient in incompressible flow.

Then eq.(4) represents a formula for the determination of the velocity on the aerofoil, which is adequate for aerofoils with elliptic nose shapes. Important discrepancies with exact results have been found for aerofoils with non-elliptic nose shapes. As may be expected, when applying first order approximations, this is already the case at the determination of the incompressible flow ($\beta = B_w = 1$). In principle, the approximation determined by eq.(3) may be improved by applying higher order expansions of potential theory along the lines of Imai, Van Dyke and Gretler (refs 3,4,5). However, it has been observed, when applying Gretler's approximation, that, especially in cases with rapid variation of curvature, slow convergence may cause serious errors in both incompressible and compressible solutions. An example is given in fig.1. Also, this approach is not very well suited for application to three-dimensional configurations, especially when wing-body combinations are concerned.

In the present method such difficulties are circumvented by replacing $u_a^{(1)}$ in eq.(4) by :

$$u_a = V_a \left\{ 1 + \left(\frac{dz_a}{dx}\right)^2 \right\}^{\frac{1}{2}} - 1. \tag{6}$$

Here V_a is the exact local velocity on the contour of the analogous aerofoil in incompressible flow. Then eq.(3) gives trivially the exact solution in the limiting case of incompressible flow, while in the case of compressible flow the solution is approximated by

$$V = \left[1 + \frac{V_a \left\{ 1 + \left(\frac{dz_a}{dx}\right)^2 \right\}^{\frac{1}{2}} - 1}{\beta B_w} \right] . \left[1 + \left(\frac{dz}{dx} / B_w\right)^2 \right]^{-\frac{1}{2}} \tag{7}$$

V_a is determined by applying a distribution of sources along the contour of the aerofoil.

2.3 The two-dimensional lifting case.

For the two-dimensional lifting case eq.(7) is generalized by formal substitution of the quantities for upper and lower surface respectively. The incompressible flow around the analogous profile is determined by a surface distribution of vortices.

2.4 The three-dimensional case.

The three dimensional version of the present method is obtained by generalizing the two-dimensional result. This is achieved by applying eq.(7) locally in the approximate direction of the perturbation velocity. The velocity component thus obtained, is combined with the undisturbed component of the onset flow to give the total velocity on the surface of the wing. In the case of non-lifting wings the basic solution, i.e. the perturbation velocity on the analogous wing in incompressible flow, is obtained by means of the method of Hess and Smith (ref.6).

The determination of the incompressible flow about an analogous lifting configuration is in the stage of programming. Again compressibility corrections will be applied formally in the non-lifting case.

3 Viscous effects.

When applying approximating methods for the calculation of pressure distributions on wings, it is usually assumed that the main effects of viscosity can be taken into account by determining the inviscid flow around a modified aerofoil, which is obtained when the boundary layer displacement thickness is added to the ordinates of the aerofoil contour. Due to the wake this modified aerofoil extends to infinity downstream. The modification of the aerofoil may be resolved into two main effects viz : a change of angle of attack and camber and a change of thickness.

The latter only influences the flow in the immediate vicinity of the trailing edge. It appears that for practical design purposes this effect can be neglected. Therefore, within the present method viscosity is taken into account by merely considering the effect on camber and angle of attack. This is achieved by adding to the ordinates of the contour half the difference between the displacement thickness of upper and lower surface. Then the inviscid flow around the distorted aerofoil is determined along the lines indicated above. An iterative procedure, where, alternately, the inviscid flow and the displacement thickness are determined, leads to a pressure distribution adapted to the main effect of viscosity.

4 Examples of application.

On the majority of wings, designed for high subsonic speeds, the flow near the wing surface is, up to a large extend, defined by the local geometry. Therefore, the applicability of the present method can be illustrated by means of results obtained for the limiting case of two-dimensional flow. This offers the possibility to check the accuracy of the results by comparison with exact solutions of the full potential equation. Thus, uncertainties that are present, when comparing with measurements, are avoided. Exact solutions of the full potential equation have been obtained by Nieuwland and Sells. Nieuwland (ref.7) applies an inverse hodograph method, by which the shape of a quasi-elliptical aerofoil is determined together with its pressure distribution for a given Mach number of the onset flow. Sells (ref.8) applies a direct method, which, however, can only deal with subcritical pressure distributions. x)

4.1 Non-lifting cases.

Figs. 2, 3 and 4 are concerned with three non-lifting quasi-elliptical aerofoils which have been determined for sub-critical flow. The nose shape of the aerofoil of fig. 2 is nearly elliptic. Those of figs. 3 and 4 deviate increasingly more from the elliptical shape. The pressure distributions obtained through the present method as well as the results obtained by the Von Karman-Tsien pressure rule and the Goethort rule are compared with the exact solutions. It appears that considerable improvement is achieved by the present method. Fig. 5 deals with a quasi-elliptical aerofoil which has been determined for super-critical flow. In fig. 5a the result obtained by the present method for near critical flow is compared with the results of NLR experiments. Fig. 5b provides the comparison of the present approximation with experimental results and the exact solution for the design Mach number. It may be concluded that the present method is a useful means to predict pressure distributions up to and including the lower critical Mach number. As might be expected the approximation breaks down at super-critical Mach numbers.

In fig. 6 results of the present method are given for a non-lifting wing with geometrical characteristics in the range of practical interest (aspect ratio 6, mid chord sweep 30°, thickness/chord ratio 0.09). From comparison with results obtained by means of the Goethert rule it appears that the difference between the two approximations is of the same importance as in the two-dimensional cases of figs. 2, 3 and 4.

A comparison with experimental results is given in fig. 7 for a wing of symmetrical aerofoil section attached to a body of circular cross section at zero incidence.

The agreement between the present approximation and the measurements is good. The discrepancies at the rearward part of the wing are due to a laminar separation bubble during the experiments.

---

x) The results of Sells have been obtained through the National Physical Laboratory and the Royal Aircraft Establishment.

4.2 Lifting cases.

As has been mentioned before the computer programme for the determination of the three-dimensional incompressible flow around lifting wings is not yet ready. As a consequence only two-dimensional cases are presented as examples.

In figs. 8 and 9 the results obtained by means of the present method for a lifting quasi-elliptical aerofoil and for the NPL 3111 section are compared with the exact solutions for potential flow together with the results obtained by the Von Karman-Tsien pressure rule and the Goethert rule. It appears that the differences are of the same importance as in the non-lifting cases.

Fig. 10 deals with an aerofoil which, like the aerofoil of fig. 9, has been designed for a "rooftop" type of pressure distribution. It appears that, if the influence of the boundary layer is neglected, the discrepancies between the measured and calculated pressure distribution presented in fig. 10 are larger than the comparable discrepancies between the exact and the approximate results of fig. 9. This situation is improved when viscous effects are taken into account in the way described in sect. 3. In this case the boundary layer has been calculated by means of the method of Nash and Mc Donald (ref. 9).

5 References.

1.	Küchemann, D. and J. Weber	The subsonic flow past swept wings at zero lift without and with body. R & M No.2908 (1956).
2.	Wilby, P.J.	The calculation of sub-critical pressure distributions on symmetrical aerofoils at zero incidence. NPL Aero Rep. 1208 (1967).
3.	Imai, I.	Approximation method in compressible fluid dynamics. Univ. of Maryland, Techn. Note BN-95 (1957).
4.	Van Dyke, M.D.	Second-order subsonic airfoil theory and its practical application. NACA TN 3390 (1955).
5.	Gretler, W.	Neuere Methode zur Berechnung der ebene Unterschall-strömung an dünne Profilen bei kleinen Anstellwinkeln. Acta Mech. Vol I/2, 1965
6.	Hess, J.L. and A.M.O. Smith	Calculation of potential flow about arbitrary three-dimensional bodies. Douglas Aircraft Co, Rep. ES 40622 (1962).
7.	Nieuwland, G.Y.	Transonic potential flow around a family of quasi-elliptical aerofoil sections. NLR TR T.172 (1967).
8.	Sells, C.C.L.	Plane sub-critical flow past a lifting aerofoil. RAE Rep. TR 67146 (1967).
9.	Nash, J.F. and A.G.J. MacDonald	The calculation of momentum thickness in a turbulent boundary layer at Mach numbers up to unity. NPL Aero Report 1207 (1966).

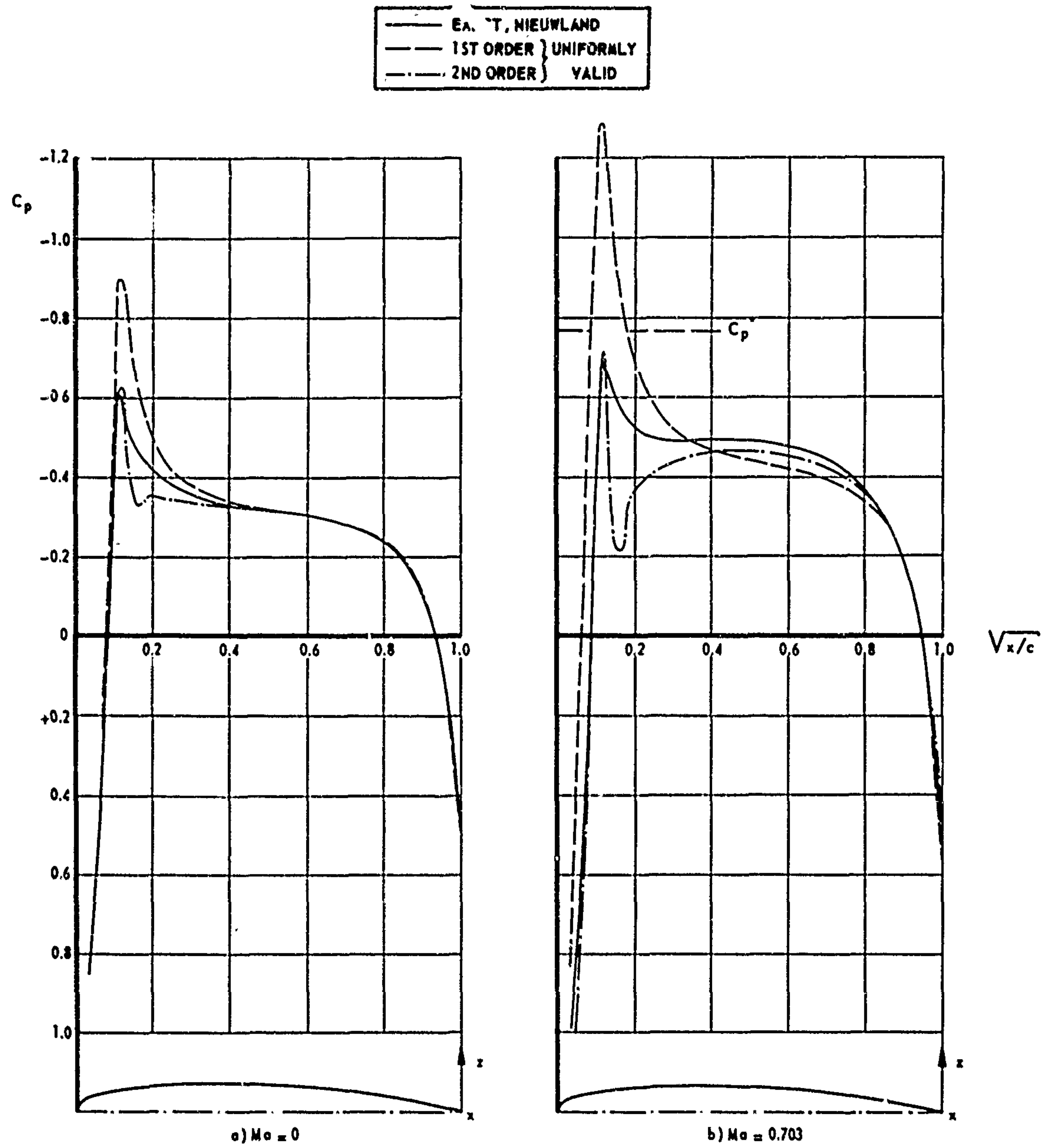

FIG. 1 EXAMPLE OF SLOW CONVERGENCE OF THIN-AEROFOIL EXPANSION SOLUTION (QUASI-ELLIPTICAL AEROFOIL 0.09-0.75-1.4).

EXACT, NIEUWLAND
PRESENT APPROXIMATION
VON KÁRMÁN – TSIEN PRESSURE RULE
GÖTHERT RULE

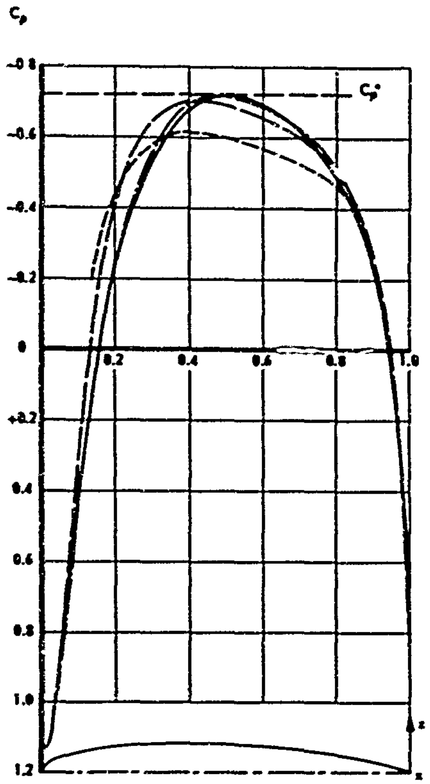

AEROFOIL 0.0925 – 0.675 – 0.95 ($t/c = 0.160$)
$M_0 = 0.774$

FIG. 2

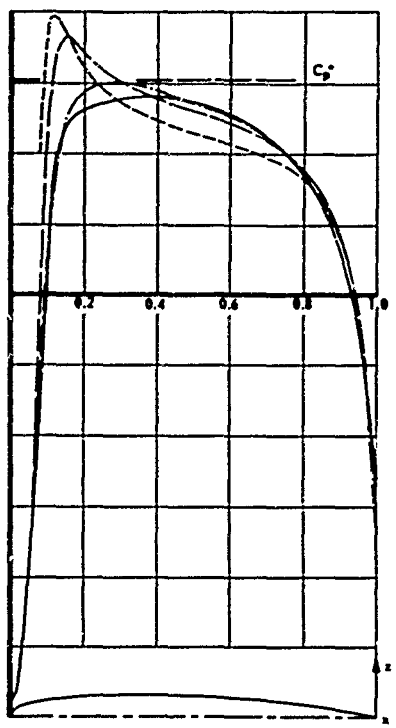

AEROFOIL 0.10 – 0.75 – 1.25 ($t/c = 0.125$)
$M_0 = 0.745$

FIG. 3

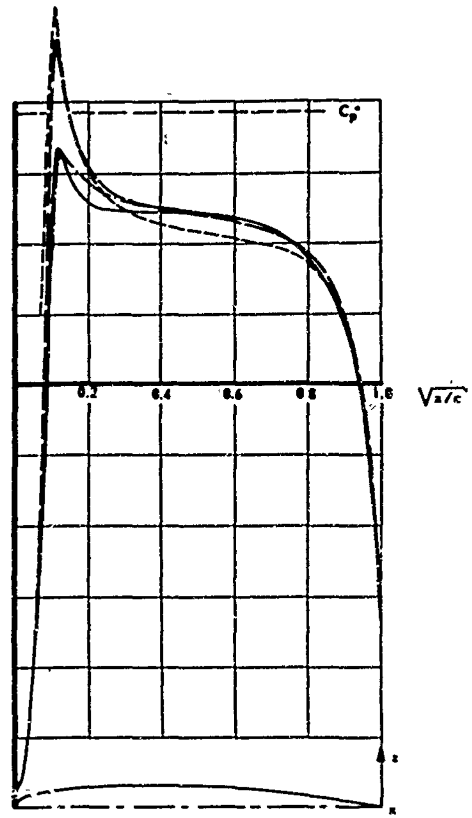

AEROFOIL 0.09 – 0.75 – 1.4 ($t/c = 0.131$)
$M_0 = 0.703$

FIG. 4

COMPARISON OF PRESSURE DISTRIBUTIONS ON NON-LIFTING QUASI-ELLIPTICAL AEROFOILS

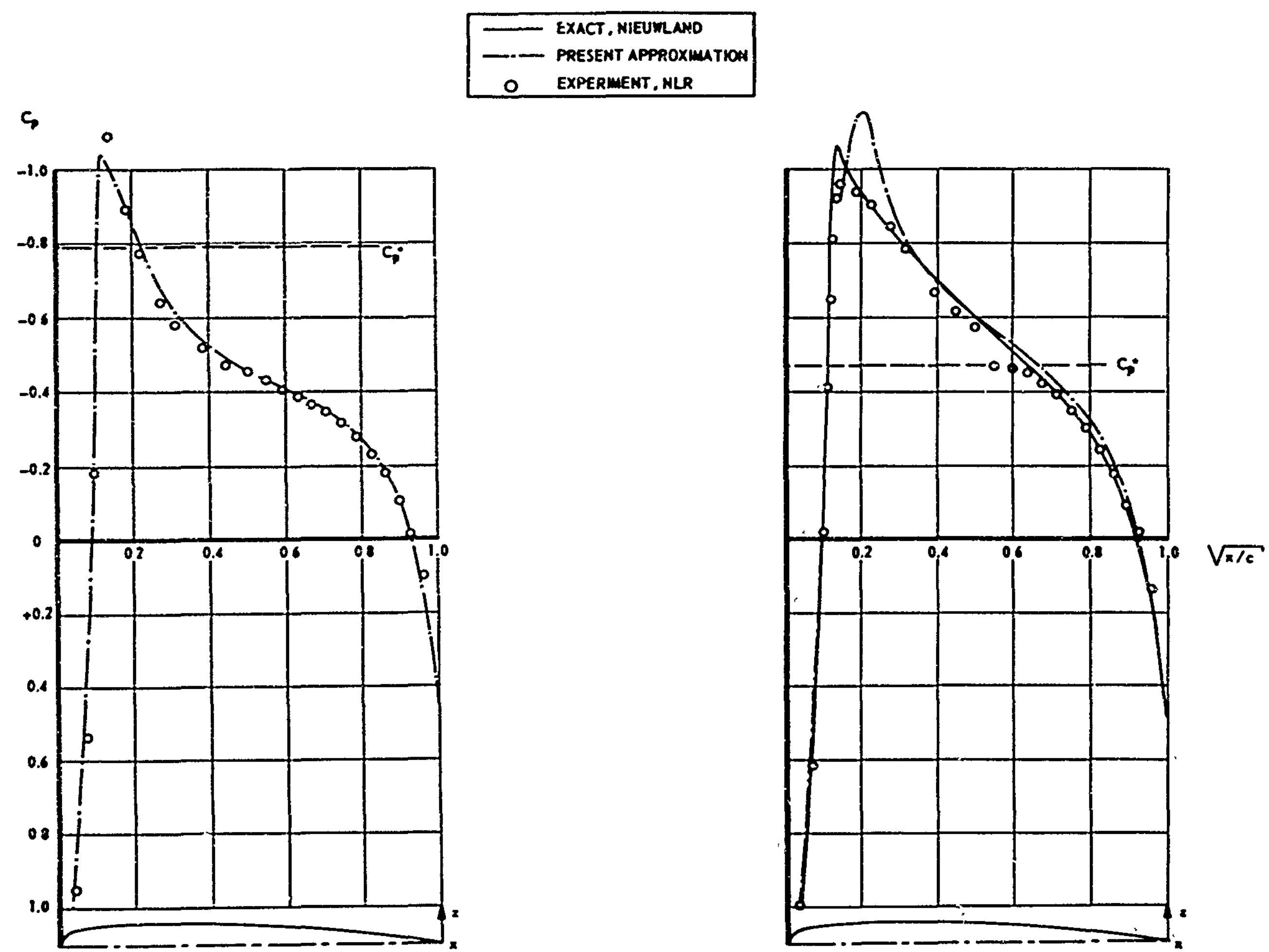

$M_\infty = 0.697$

FIG. 5a

$M_\infty = 0.786$

FIG. 5b

COMPARISON OF PRESSURE DISTRIBUTIONS ON NON-LIFTING QUASI-ELLIPTICAL AEROFOIL OF 'PEAKY' TYPE

(0.11-0.75-1.75, $t/c = 0.117$)

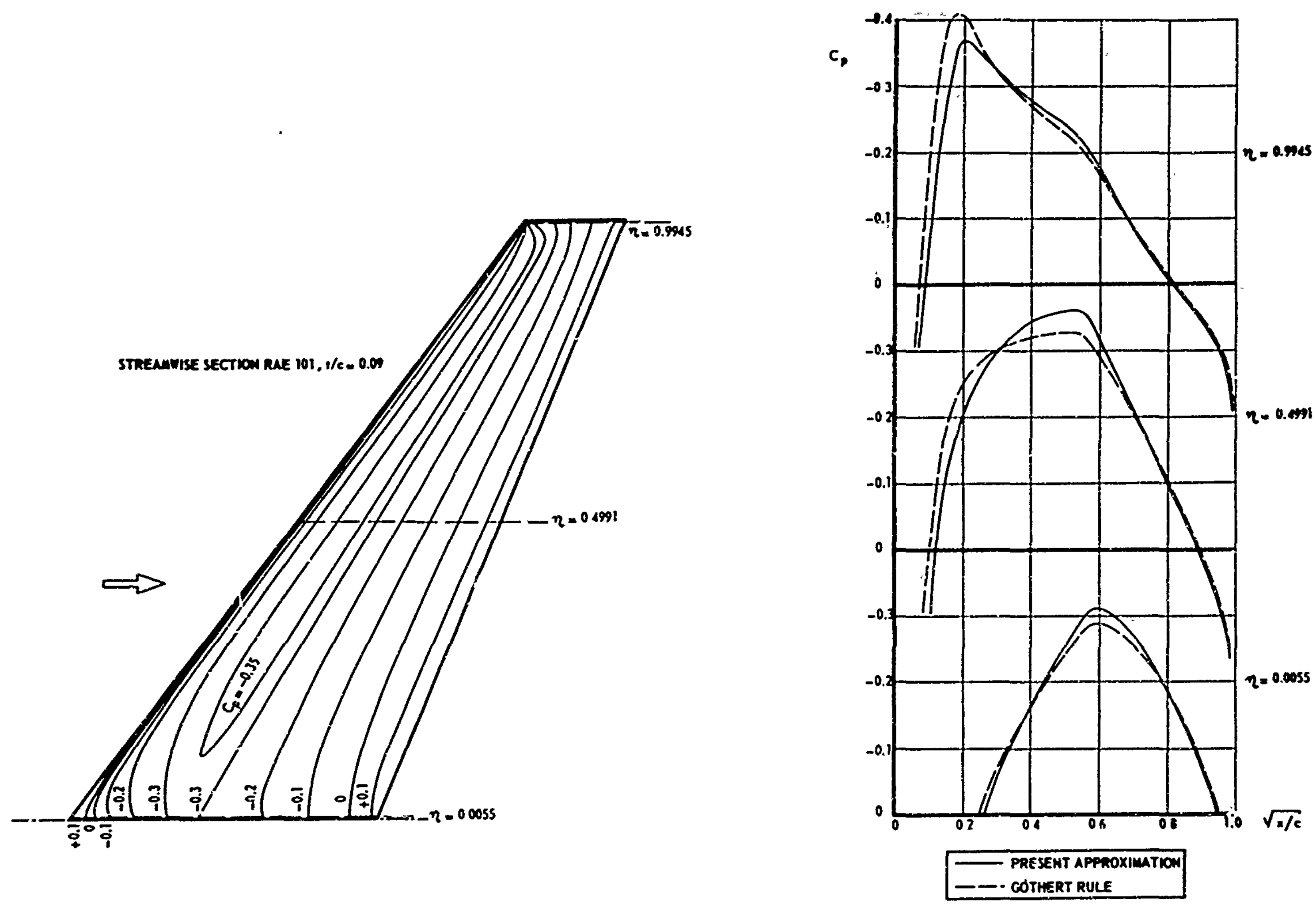

CALCULATED ISOBAR PATTERN AND CHORDWISE PRESSURE DISTRIBUTION ON A NON-LIFTING WING AT $M_\infty = 0.8$

FIG. 6

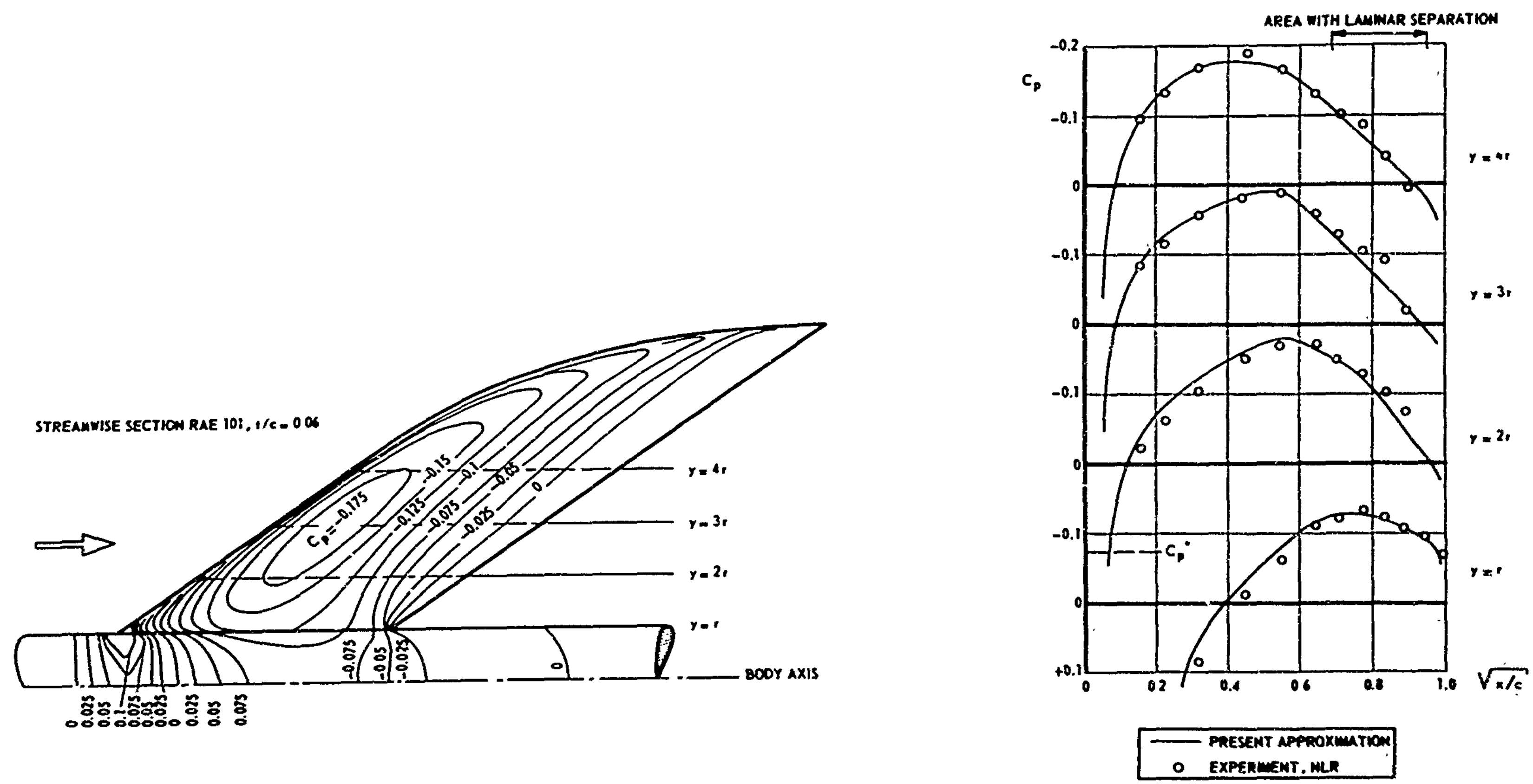

ISOBAR PATTERN AND CHORDWISE PRESSURE DISTRIBUTION FOR A NON-LIFTING WING-BODY COMBINATION, AT $M_\infty = 0.96$

FIG. 7

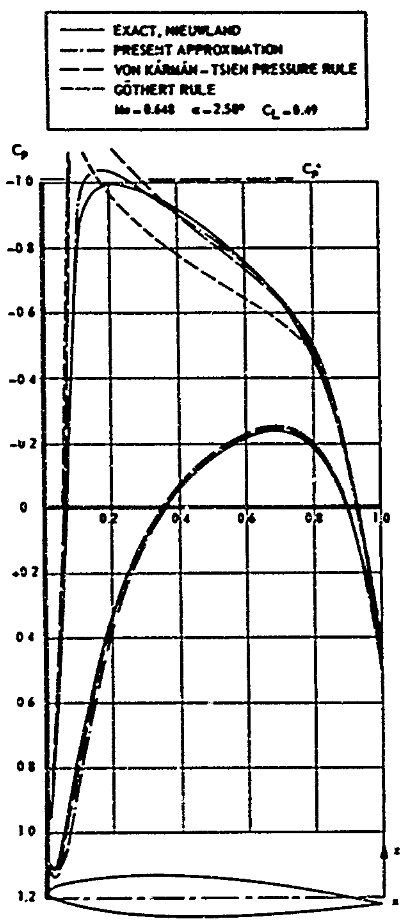

COMPARISON OF PRESSURE DISTRIBUTIONS
ON LIFTING QUASI-ELLIPTICAL AEROFOIL
($\tau_1 = 0.0775$, $\varepsilon_a = 0.71$, $\alpha = 0.845$, $\Gamma = 0.75$)

FIG. 8

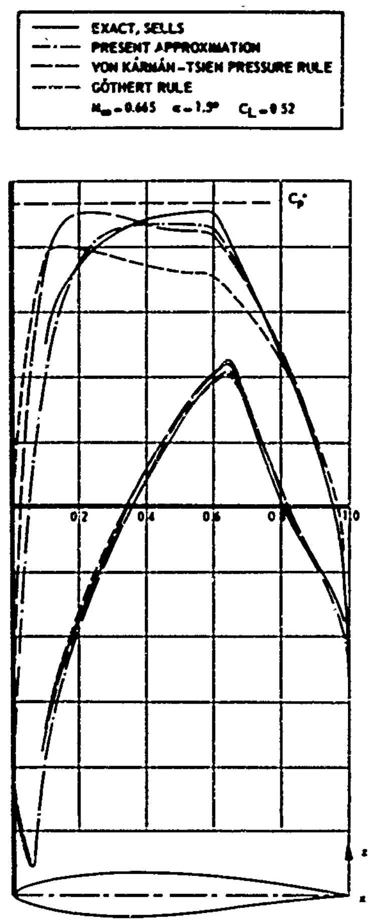

COMPARISON OF PRESSURE DISTRIBUTIONS
ON NPL 3111 AEROFOIL
($t/c = 0.14$, CAMBER RATIO 0.08)

FIG. 9

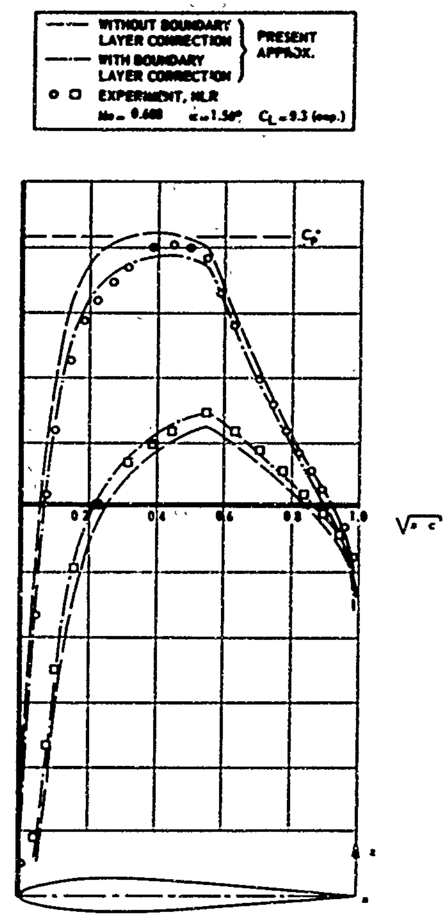

COMPARISON WITH EXPERIMENT FOR NLR
P. 2 AEROFOIL
($t/c = 0.105$, CAMBER RATIO 0.06)

FIG. 10

The Aerodynamic Design and Testing of a Lifting Swept Wing-Body Configuration with Shock Free Wing Flow at M = 1.20

by

J. Bridgewater x) (National Physical Laboratory, Teddington)

S.O.T.H. Han x) (Nationaal Lucht- en Ruimtevaartlaboratorium, Amsterdam)

H. Kramer x) (Nationaal Lucht- en Ruimtevaartlaboratorium, Amsterdam).

x) Research Engineer.

Summary

A wing-body configuration has been designed, with the intention of giving economical cruise characteristics at low supersonic speeds. The design aim was to reduce the wave drag as far as possible by designing the wing and body in such a way that boundary layer separation and shocks on the wing are avoided. A wind tunnel model was made according to this design, consisting of a 55° swept warped wing mounted on an axially symmetric waisted body.

The presentation of the wind tunnel test results has been confined to the design Mach number $M = 1.20$ and the design incidence $\alpha = 2.5^{\circ}$. The experimental pressure distributions show good agreement with the theoretical pressure distributions except for a slight overexpansion on the wing uppersurface near 30 % of the chord and a compression on the wing lower surface. Due to these pressure deviations the measured wing lift is slightly higher than the calculated value. From the test results it appears that over the main part of the wing uppersurface the flow is supercritical. In spite of this the flow suggests no indication of the presence of shock waves.

It can be concluded that the design aim of achieving a wing-body combination possessing good lift-drag characteristics at $M = 1.20$, has been fulfilled.

Notations

c	chordlength
c_o	rootchord
$\bar{c}$	aerodynamic mean chord
c_D	dragcoefficient
c_L	liftcoefficient
c_p	pressure coefficient
c_p^*	critical pressure coefficient
ℓ	wing loading
M	Mach number
$Re_{\bar{c}}$	Reynolds number based on the aerodynamic mean chord
x	streamwise coordinate
y	spanwise coordinate
z_c	camber coordinate
z_{twist}	height of wing L.E. above wing reference plane
α	angle of attack
α_{twist}	angle of wing twist
Λ	angle of sweep
η	spanwise coordinate in fractions of half wing span.

The Aerodynamic Design and Testing of a Lifting Swept Wing-Body Configuration with Shock Free Wing Flow at M = 1.20

by

J. Bridgewater x) (National Physical Laboratory, Teddington)

S.O.T.H. Han x) (Nationaal Lucht- en Ruimtevaartlaboratorium, Amsterdam)

H. Kramer x) (Nationaal Lucht- en Ruimtevaartlaboratorium, Amsterdam).

1 Introduction.

In the United Kingdom during the past decade much attention has been paid to the development of swept wing-body combinations, intended to cruise economically at low supersonic speeds (ref.1). The design aim is to reduce the wave drag as far as possible by avoiding boundary layer separation and shocks of appreciable strength on the wing. Boundary layer separation is avoided by choosing a suitable target pressure distribution, having moderate pressure gradients. Strong shocks are avoided by designing the wing and body waisting in such a way that over as much as possible of the wing the isobar pattern is similar to the straight isobar pattern on the corresponding infinite yawed wing with subcritical flow. By making use of this approach, the flow on the wing can then be related to the flow on an equivalent two-dimensional section, having the same thickness distribution as the wing in the direction normal to the isobars. Since for three-dimensional flow calculations only linearised theory can be used at present, this two-dimensional section approach enables non-linear local thickness-lift interaction effects on the wing to be included in the design.

The present paper concerns a detailed investigation of the applicability of the design procedure, which formed part of an anglo-netherlands cooperation program, and involved not only the Nationaal Lucht- en Ruimtevaartlaboratorium (NLR, Amsterdam) and the National Physical Laboratory (NPL, Teddington), but also the Royal Aircraft Establishment (RAE, Farnborough and Bedford) and the Aircraft Research Association (ARA, Bedford).

2 Detailed design procedure.

According to the above mentioned method a lifting swept wing-body has been designed to have a fully swept isobar pattern and to have a target streamwise uppersurface pressure distribution based on a "rooftop" back to 30 % of the chord just close to critical conditions at the design Mach number M = 1.20.

The overall dimensions of the wing-body design have been chosen to be similar to those of a promising preceeding design (ref.2). The configuration consists of a 55° swept wing with curved tips, uses a 6 % RAE 101 section thickness distribution in streamwise direction combined with three-dimensional camber and twist and has a waisted body (see fig.1) based on the supersonic area rule.

The wingpressure distribution due to thickness has been calculated in three dimensions using a linearised method (ref.3) in which the source strength at the wing leading edge has been corrected by means of the standard type of multiplicative Riegels factor. In this way a correction is made to the first order thickness effect for the blunt wing leading edge. In addition the body side is treated as a plane of reflection in these calculations. By adding the pressure field calculated by linearised theory due to the symmetrically waisted body, the combined pressure distribution due to thickness on the wing-body combination was then obtained. When compared with the isobar pattern on the corresponding infinite wing, these combined results show a loss of isobar sweep over the forward part of the innerwing. Attempts to straighten the isobars by a redesign of the body waisting led to inacceptable body contours from both area rule and model making points of view. Since results available from earlier tests had indicated that a gentle loss of isobar sweep in a region where the flow is accelerating could be tolerated, it was decided not to modify the body waisting in this way.

x) Research Engineer.

For the corresponding lifting surface calculation the wingwarp distribution has been designed for a given chordwise loading, invariant in the spanwise direction. This approximately gives a straight isobar pattern due to lift on the inboard part of the wing. On the outerwing, the isobar sweep increases towards the tip because of the planform shape and hence the appearance of a tipshock at the design conditions is thereby avoided.
The streamwise loading taken for this three-dimensional wing warp calculation was derived directly from the camber and incidence of the associated two-dimensional section at its design condition of $M = 0.688$ and $\alpha = 2.15^{\circ}$. This section had been designed by the Weber-Küchemann method (ref.4) to give the just critical inviscid rooftop pressure distribution shown by the curve labelled "non-linear theory" in fig.3a. Standard thin aerofoil theory was then applied to a slightly smoothed version of the camber line and the corresponding linearised loading distribution thereby obtained. This was ammended by the infinite sweep equivalence law and the resulting linearised streamwise loading used in the linearised wing warp theory assuming full reflection at the body side. Thus for the chosen design conditions of $M = 1.20$ and linearised $c_L = 0.136$, the desired wing warp shape was calculated. However, on the finite wing, the two-dimensional non-linearised loading distribution multiplied by $\cos^2 55^{\circ}$ is expected to exist rather than this linearised loading if it is assumed that the non-linear effects on the equivalent two-dimensional section and on the finite wing are similar. Details of the resulting streamwise camber lines are given in fig.2a.

The wing-body angle has been based on the experimental lift curve slope of a previous model. With the wing at its design incidence, the body has been set at a positive angle of 2.5°, so that the body upwash may help counteract the tendency for the measured load-distribution at the wing-body junction of a wing-body combination in general to be lower than the calculated loaddistribution. The wing twist distribution with the body axis in the main stream direction is given on fig.2b. At this condition, the model is at its approximate zero lift incidence at $M = 1.20$.

In order to estimate from the two-dimensional calculation what the final wing upper surface pressure distribution will be, it is assumed that for the warped wing at the design incidence, the differences between the pressure coefficientsfor the infinite yawed wing and for the actual finite wing are the same as those calculated for the symmetrical wing at zero incidence. The lower surface pressure distributions are obtained from the upper surface pressure distributions by subtraction of the calculated non-linear wing loading distribution. The kinks in the theoretical pressure distribution on the inner wing are due to the compression at the Mach-line emanating from the intersection of wing trailing edge and body. The calculated wing pressure coefficients at the design conditions $\alpha = 2.5^{\circ}$ and $M = 1.20$ are given on fig.4 and the corresponding wing loading distributions on fig.5.

3 Description of experiments.

To verify the applied design techniques, wind tunnel measurements have been made on a model of the equivalent two-dimensional section and on a model of the wing-body configuration. The presentation of the test results will be confined to the design conditions.

On the two-dimensional model pressure measurements have been made in the 0.42 m x 0.55 m pilottunnel of the NLR. The test section has closed side walls and slotted horizontal walls. The measurements have been carried out with both free and fixed boundary layer transition. Fixation of the transition has been realised by means of a roughness strip from 16.7 % to 18.4 % of the chord. The Reynolds number, based on the 0.18 m chord, was 2.1×10^6 at the design Mach number $M = .688$.

On the wing-body combination, measurements of forces, moments and surface pressures have been carried out in the transonic wind tunnel of the NLR. The 2.0 m x 1.6 m test section has solid side walls and slotted horizontal walls. All model waves reflect downstream of the modelbase for $M \geqslant 1.15$. The tests were done with both free and fixed boundary layer transition. On the wing the transition was fixed by means of a roughness strip from 5 % to 10 % of the local chord. At the design Mach number $M = 1.20$ the tests were carried out at a Reynolds number 1.16×10^6, based on the aerodynamic mean chord.

The results of the two- and three-dimensional pressure measurements with transition fixed have been corrected for the local influence of the roughness strip on the pressure distribution, making use of the transition free pressure measurements.

4 Discussion of results.

4.1 Comparison of measured and calculated results on the equivalent two-dimensional section.

On fig.2a the target inviscid rooftop pressure distribution calculated from the Weber-Küchemann method is compared with the pressure distribution measured on the equivalent two-dimensional section at the designconditions $\alpha = 2.15^{o}$ and $M = 0.688$.

The agreement between theory and experiment is good except for a supercritical over-expansion on the forward part of the uppersurface, which is not predicted by the non-linear calculation method. In spite of the appearance of this supercritical flow region, no shocks appear to occur on the section upper surface. The calculated linearisedand non-linearised loading distribution and the measured loading distribution are compared on fig.3b. On this figure, the separate effects of non-linearity, compressibility (mainly on the forward part of the section) and viscosity (mainly on the rearward part of the section) are clearly visible.

More recently, better non-linear theoretical methods (ref.5 and 6) have become available, which take into account viscosity as well as using improved compressibility terms. Even though these methods are strictly only valid for subcritical flows, some preliminary calculations made with them indicate that closer estimates can be obtained for the measured supercritical region because in this case the flow remains shock-free.

4.2 Comparison of the measured and the calulated results on the wing.

The pressure distributions on the wing, measured at the design conditions $\alpha = 2.5^{o}$ and $M = 1.20$ are given in fig.4, where they are compared with the calculated wing pressure distributions. In addition, a set of "expected" three-dimensional wing pressure distributions deduced from the two-dimensional experimental results have also been shown. To obtain these expected wing pressure distributions, the same pressure corrections with regard to the linearised thickness pressures were applied to the two-dimensional m e a s u r e d pressure distribution as had been applied previously in converting the two-dimensional t h e o r e t i c a l pressure distribution to the three-dimensional theoretical pressure distributions on the finite wing.

Before trying to interpret the pressure distributions on the wing, it is useful to recall the assymptions inherent in the method used to design the wing and to examine their consequences :

(a) the equivalence of the flow on an infinite yawed wing and the flow on an appropriate two-dimensional section is assumed to be related by $c_p \cdot \sec^2\Lambda$ and $M \cdot \cos\Lambda$, where Λ is the angle of sweep of the infinite wing. This implies that viscous effects, compressibility effects and non-linear effects are assumed to behave similarly on the equivalent two-dimensional section as on the corresponding infinite wing.

(b) the complex phenomenon of interaction effects between the waisted body and the thick lifting wing has been assumed to be taken into account by treating the fuselage side as a plane of reflection and by adding the linearised pressure field around the isolated body to the separate pressure field due to wing thickness. This rather over-simplifies the problem and as a consequence leads to only an approximate allowance for the wing-body interference.

Now the differences between the calculated and expected three-dimensional pressure distributions are directly related to the corresponding pressure differences between theory and experiment in the two-dimensional case. To eliminate these differences arising from insufficiently accurate allowances for viscosity and compressibility effects in the two-dimensional case, the comparison in the three-dimensional case will be confined to the expected and the measured wing pressure distributions. Hence, any deviations between these pressure distributions will then be due to

(a) limitations within the three-dimensional wing warp and pressure due to thickness theories,

(b) the influence of the wing-body interaction,

(c) the influence of three-dimensionality on the compressibility, non-linear and viscous effects.

Though it is not always possible to attribute exactly the pressure deviations to each of the above headings, something can be said of the general character of the pressure deviations due to the above mentioned causes. For example, the wing-body influence generated by the body, especially the waisted part, will be greatest near the root and will propagate along Mach lines in a direction determined by the local wing pressures. The influence of three-dimensionality on the compressibility and non-linear effects will be noticeable mainly on the forward part of the chord. Finally, the three-dimensional influence on the viscous effects will be most marked over the rearward part of the wing, and is likely to increase towards the tip. Differences arising from the limitations of the three-dimensional wing warp and pressure due to thickness theories are more likely to exhibit global patterns rather then the localised trends suggested above, and can be checked directly against measurement from the design calculation curves given in fig.4.

Inspection of the uppersurface pressure distributions (fig.4) shows that the supercritical overexpansion also appears in the three-dimensional measurements, but when compared with the expected wing pressure distribution, it is found to be concentrated nearer the 30 % position of the chord. The level of the measured minimum pressures increases slightly towards the tip. At the tip the agreement of the measured pressure distribution with the expected pressure distribution is unsatisfactory near the wing leading edge, but there is some evidence that the theoretical supervelocities due to thickness calculated with the basicly linearised theory method are too low, and this behaviour is also reflected in the expected wing pressure distribution. On the forward part of the innerwing somewhat higher pressures are measured than were expected. Near the wing-body junction, the local influence of the body upwash on the measured uppersurface pressure distribution is noticeable at the wing leading edge.

On the wing lower surface, comparison of the measured and expected pressure distributions shows larger deviations than on the upper surface. The deviations consist of a compression towards the rear of the most inboard section and this moves forward over the wing at stations further outboard. Undoubtly, the main part of these pressure deviations is due to body interference.

Not unexpectedly, these pressure deviations are also apparent in the wing loading distributions given on fig.5. When comparing the expected and measured wing loading distributions, it is seen that over the rear of the wing chord, the influence of three-dimensionality on the viscous effects gives a loss of loading towards the tip. This is directly associated with the spanwise drift of the three-dimensional boundary layer as the tip is approached.

The isobar pattern, corresponding to the measured wing uppersurface pressures at the design conditions, has been given in fig.6. Except at the wingroot, where deviations due to the thickness design were anticipated, the isobar pattern consists of almost straight isobars. On the forward part of the wing, the result of the increase towards the tip of the overexpansion on the direction of the isobars is noticeable. With regard to the shape of the isobar pattern good aerodynamic properties may be expected. This is confirmed by the results of the forces and moments tests. On fig.7 the experimental lift vs incidence curve is given. At the design incidence $\alpha = 2.5^{\circ}$, the measured liftcoefficient ($c_L = 0.15$) exceeds the theoretical linear liftcoefficient ($c_L = 0.136$) by about 10 %. This is due to the overexpansion on the wing uppersurface and the compression on the wing lower surface resulting mainly from the fact that the body itself is inducing extra wing lift. Fig.7 also shows the dragcoefficient c_D vs Mach number curve for the measured liftcoefficient at the design incidence and it should be noted that there is only a gentle increase in drag after the design Mach number has been reached.

5 Conclusions.

Comparison of the theoretical and experimental results on the wing shows differences which are mainly caused by an overexpansion on the wing uppersurface and by a compression on the wing lower surface. As a consequence the measured liftcoefficient exceeds the calculated liftcoefficient by about 10 %. On the wing uppersurface the pressure deviations are almost constant in the spanwise direction and this explains why the experimental uppersurface isobar pattern has straight isobars except for a small region near the wingroot. The good transonic properties of the combined RAE 101 thickness distribution and wing warp prevent the supercritical overexpansion recompressing into an undesirable strong shock formation. Thus in spite of small deviations between theory and experiment, the design aim of achieving a wing-body configuration having favourable lift-drag characteristics at $M = 1.20$ has been closely fulfilled.

To achieve closer agreement between theory and experiment for the wing pressures, it is necessary to employ improved corrections for compressibility and viscous effects in the non-linear two-dimensional design. The revised calculation methods developed at NLR and NPL (ref.5 and 6) go some way towards achieving this end.

6 References.

1. Look, R.C. and J. Bridgewater — Theory of aerodynamic design for swept-winged aircraft at transonic and supersonic speeds : Progress in Aeronautical Sciences, Vol 8, Pergamon Press, 1966.

2. Haines, A.B. and J.C.M. Jones — Transonic tunnel tests on a 6 % thick warped 55° swept back wing model : ARC Rep.& Memo 3385, 1965.

3. Haines, A.B., K. Rollins and J. Osborn — The calculation of the velocity distribution due to thickness for swept wings with subsonic edges at supersonic speeds : ARC Current Paper No 654, 1962.

4. Bagley, J.A. — Some aerodynamic principles for the design of swept wings : Progress in Aeronautical Sciences, Vol 3, Pergamon Press, 1962.

5. Labrujere, Th.E., W. Loeve and J.W. Slooff — An approximate method for the determination of the pressure distribution on wings in the lower-critical speed range : Paper 17, AGARD Specialists' Meeting on Transonic Aerodynamics, Paris, September, 1968.

6. Look, R.C., B.J. Powell, C.C. Sells and P.G. Wilby — The prediction of aerofoil pressure distributions for sub-critical viscous flows : Paper 12, AGARD Specialists' Meeting on Transonic Aerodynamics, Paris, September, 1968.

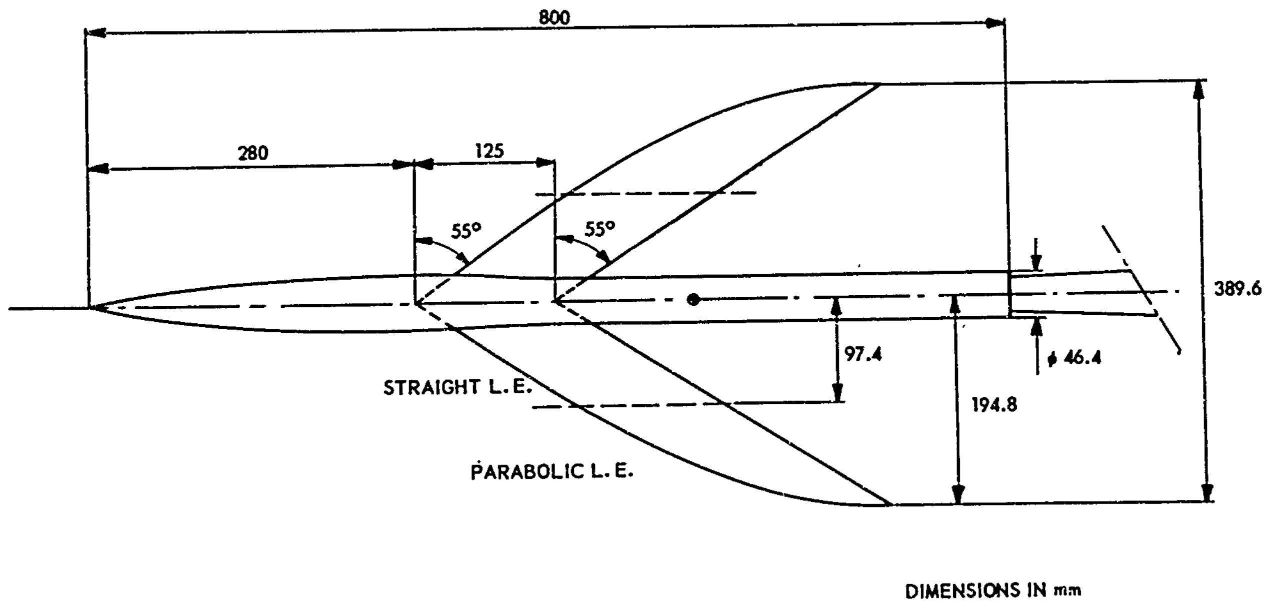

FIG. 1 GENERAL ARRANGEMENT OF THE MODEL.

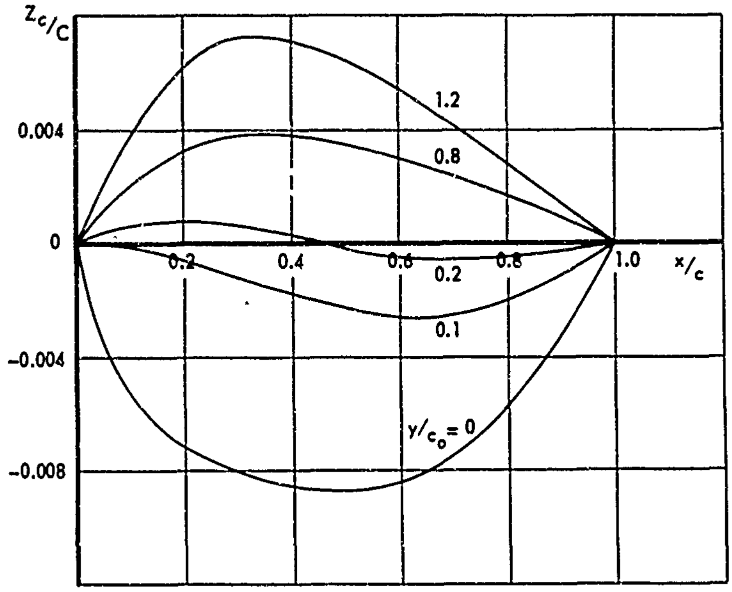

a) CAMBER DISTRIBUTION

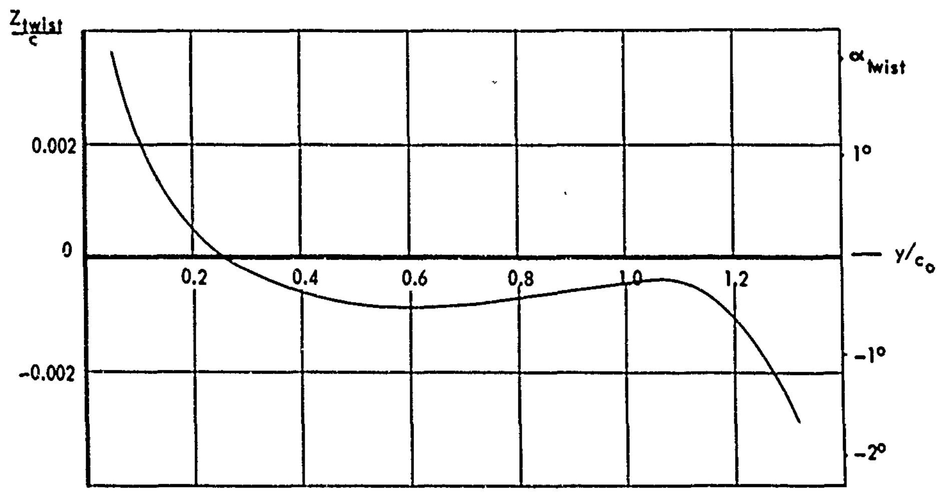

b) SPANWISE TWIST DISTRIBUTION

FIG. 2 WINGCAMBER AND TWIST DISTRIBUTION CALCULATED FOR A GIVEN CONSTANT SPANWISE LOADING DISTRIBUTION AT M = 1.20

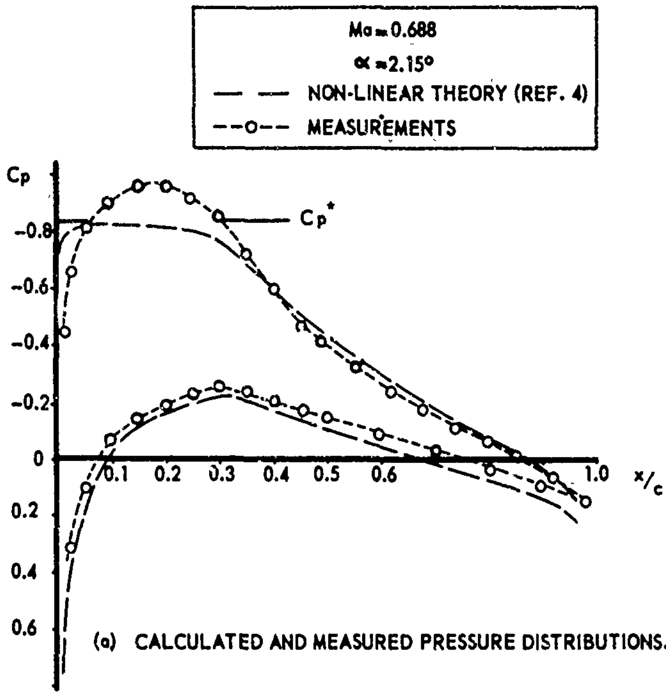

(a) CALCULATED AND MEASURED PRESSURE DISTRIBUTIONS.

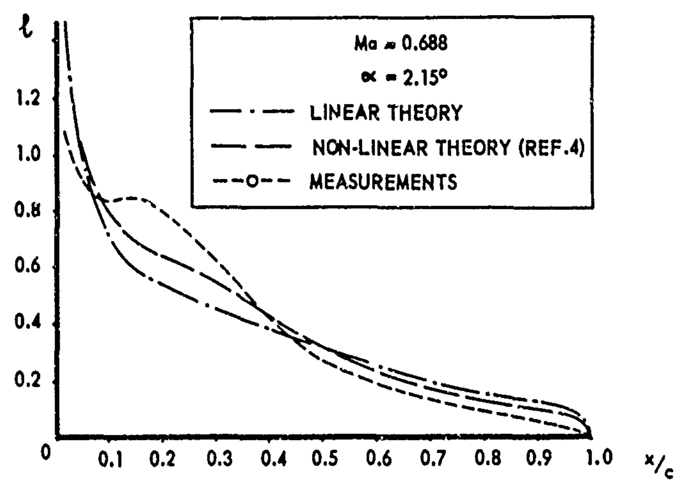

(b) CALCULATED AND MEASURED LOADING DISTRIBUTIONS.

FIG. 3 PRESSURE AND LOADING DISTRIBUTIONS ON THE EQUIVALENT TWO-DIMENSIONAL SECTION AT THE DESIGN CONDITION.

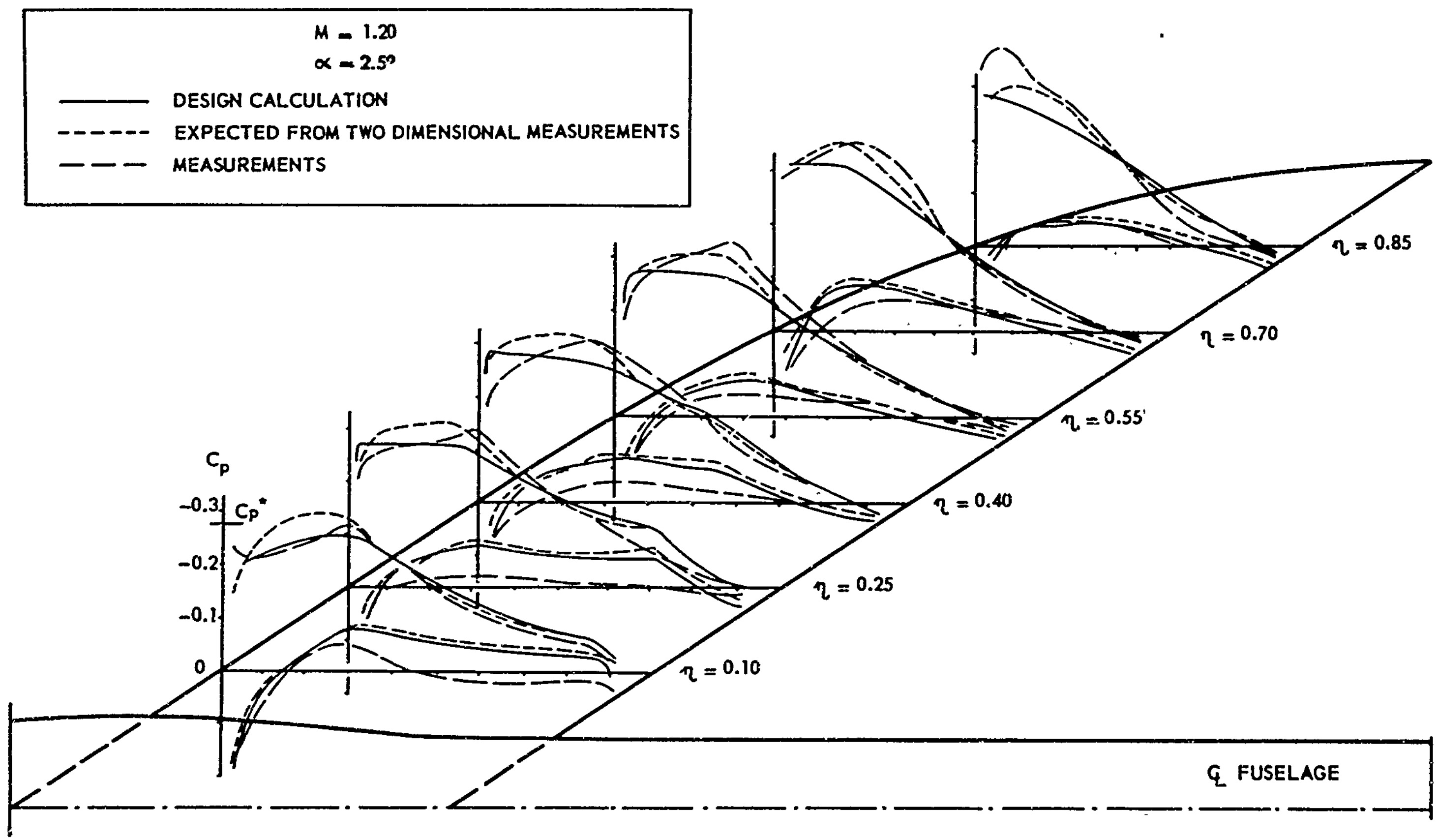

FIG. 4 CALCULATED AND MEASURED WING PRESSURE DISTRIBUTIONS AT THE DESIGN CONDITION.

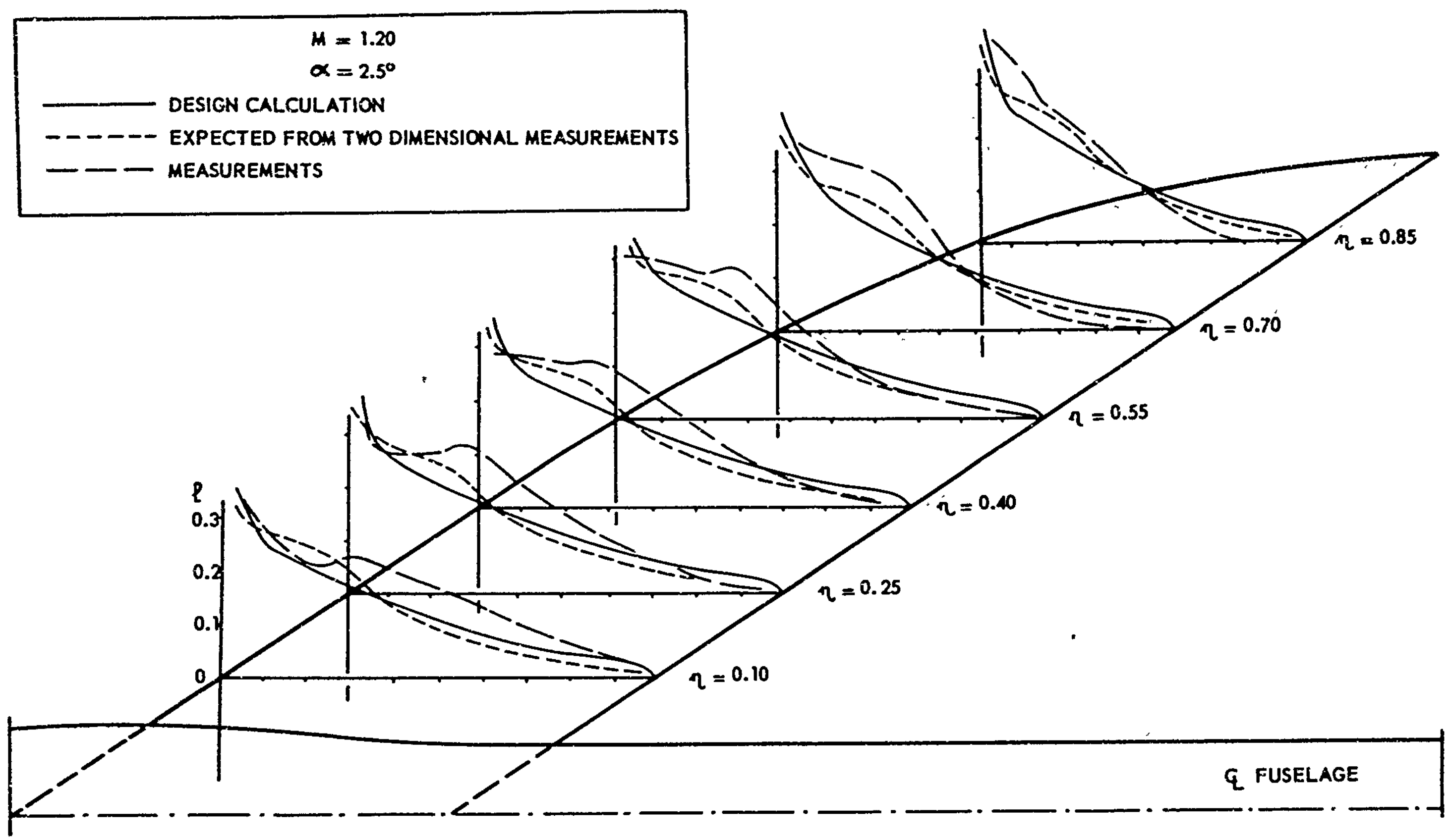

FIG. 5 CALCULATED AND MEASURED WING LOADING DISTRIBUTIONS AT THE DESIGN CONDITION.

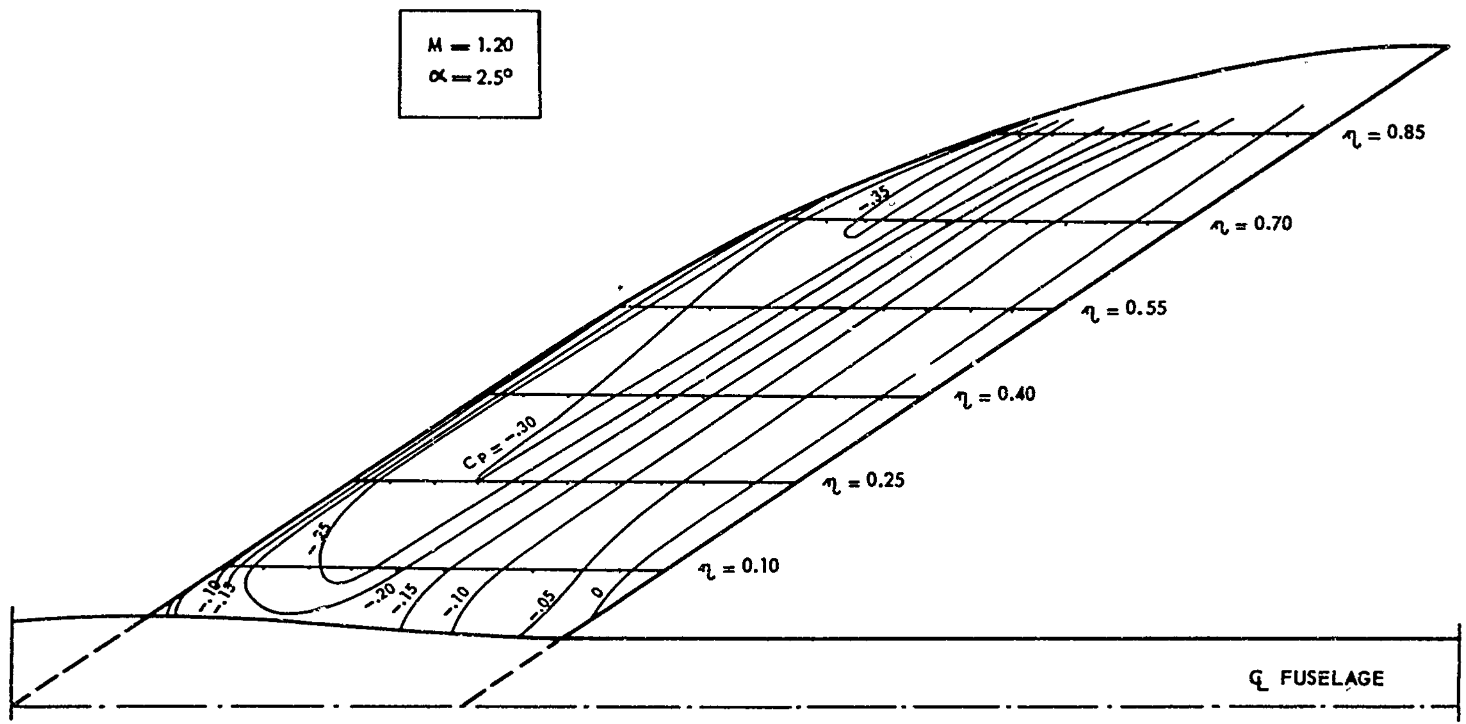

FIG. 6 EXPERIMENTAL ISOBARPATTERN AT THE DESIGN CONDITION.

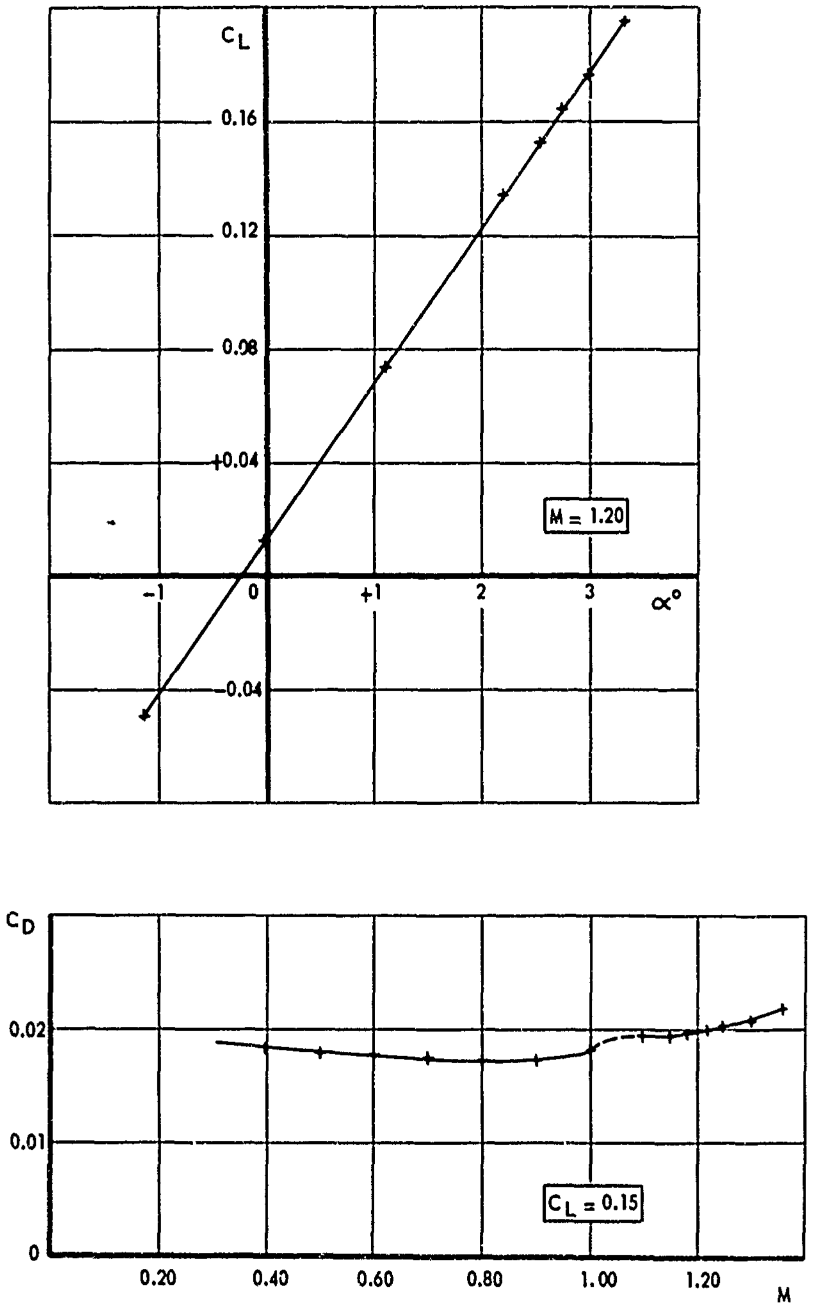

FIG. 7 C_L vs α FOR $M = 1.20$ AND C_D vs M FOR $C_L = 0.15$, $R_{e_{\bar{c}}} \approx 1.2 \times 10^6$, TRANSITION FIXED.

<u>WING-BODY INTERFERENCE AT SUPERSONIC SPEEDS</u>

by

K. Stewartson, University College London,

and

D. A. Treadgold, Aerodynamics Department,
Royal Aircraft Establishment, Farnborough.

SUMMARY

The problem considered is that of the interference between a body, consisting of an infinitely long circular cylinder aligned in the direction of motion, and a thin wing lying approximately in the diametral plane of the cylinder.

Solutions according to linearised theory are discussed for three regions typified by:-

(1) large distances from the start of the interaction,

(2) the neighbourhood of the surface bounding the initial interaction region

and, (3) the neighbourhood of the root chord of the wing excluded from (2).

The structure of the solution is presented for regions (2) and (3) where existing theoretical methods are inadequate.

Finally an illustration is given making use of the results obtained and a comparison is given of some calculated results with some experimental measurements.

1 INTRODUCTION

We consider the flow of a compressible inviscid fluid, moving with uniform speed V and at Mach number M (>1) when undisturbed, past a fixed body consisting of an infinite circular cylinder of radius a whose generators are parallel to the undisturbed direction of motion of the fluid and a thin wing lying in a diametral plane of the cylinder. This problem may be regarded as the prototype of the wing-body interference problems even though an infinite cylinder is unrealistic. In practice the cylinder would have a nose but provided, it is not bluff, its effect on the flow field near the wing is additive to the interference and can be regarded as known.

Ultimately the solution of interference problems will be achieved by fully numerical procedures, probably using the panel method and either linear or non-linear hyperbolic equations. At present however these procedures have not been developed and a significant amount of analysis is required to prepare the ground for any numerical work that is done. It is believed that such analysis is of some permanent value in that it leads to a fuller understanding of the flow and can guide the computation in particular cases.

Without any loss of generality we can take $M = \sqrt{2}$ and suppose that ε (<<1) is a characteristic measure of the flow deflection caused by the body. We also define an orthogonal set of Cartesian coordinates $Oxyz$ where O is a convenient point on the axis of the cylinder, Ox points downstream along this axis and Oy is in the plane of the wing. Then since the flow is irrotational we can write $\underline{q} = \text{grad}\,\phi^*$, $\phi^* = V(x+\varepsilon\phi)$ where $\underline{q}$ is the fluid velocity, ϕ^* is the velocity potential and, on neglecting squares of ε, the equation satisfied by ϕ is

$$\frac{\partial^2\phi}{\partial y^2} + \frac{\partial^2\phi}{\partial z^2} = \frac{\partial^2\phi}{\partial x^2} \tag{1.1}$$

The boundary conditions satisfied by ϕ, are that $\frac{\partial\phi}{\partial z}$ is prescribed on that part of the plane $z = 0$ occupied by the wing, ϕ is continuous on the remainder of the plane $z = 0$ outside the cylinder being zero upstream of the Mach lines drawn downstream from the edge of the wing and

$$\frac{\partial\phi}{\partial r} = 0 \quad \text{when} \quad r = a \tag{1.2}$$

where

$$y = r\cos\theta\,, \qquad z = r\sin\theta\,. \tag{1.3}$$

Our aim in this paper is to discuss the present state of the problem posed by (1.1)-(1.3) restricting ourselves to the exact theory of the detailed flow structure and excluding consideration of overall properties and of approximate results. The choice is made purely in view of the limited time available and in no way reflects our opinion of the relative importance of these other aspects. The exact theory may be divided into three parts - first, the asymptotic structure for x large; second, the neighbourhood of S the initial surface bounding the interaction region but excluding the neighbourhood of the root chord of the wing; and third the region near S excluded in the second part. We shall discuss these in turn.

2 THE VELOCITY FIELD FOR LARGE x

The method and principal results here are due to Nielsen (1951, 1957). We restrict attention in this section to wings symmetrically disposed to the oncoming stream or, if not, to wings with supersonic leading edges. The significance of this restriction is that it is necessary for the success of the method that $\frac{\partial\phi}{\partial z}$ is prescribed at all points of the plane $z = 0$ satisfying $|y| > a$. That being so we can take the Laplace transform of ϕ with respect to x, using $\underline{s}$ as parameter and denoting the result by $\bar{\phi}$; a differential equation for $\bar{\phi}$ is obtained with boundary conditions that can be solved, formally very simply. Suppose for example that the wings approximately occupy that part of the plane $z = 0$ defined by $|y| > a$, $x > 0$ and are at incidence ε so that the boundary condition on this plane reduces

$$\frac{\partial\phi}{\partial z} = -1 \qquad x > 0,\ |y| > a$$

$$\frac{\partial\phi}{\partial z} = 0 \qquad x < 0,\ |y| > a \tag{2.1}$$

Then $\bar{\phi}$ satisfies

$$\frac{\partial^2\bar{\phi}}{\partial y^2} + \frac{\partial^2\bar{\phi}}{\partial z^2} = s^2\bar{\phi}$$

together with

$$\frac{\partial\bar{\phi}}{\partial r} = 0 , \quad r = a , \quad \frac{\partial\bar{\phi}}{\partial z} = -\frac{1}{s} \quad \text{on } z = 0, \ |y| > a . \tag{2.2}$$

The formal solution of (2.2) is

$$\bar{\phi} = \frac{\text{sgn } z}{s^2} e^{-s|z|} + \frac{1}{s^2}\sum_{n=0}^{\infty} A_n \sin n\theta \frac{K_n(sr)}{K_n'(sa)} \tag{2.3}$$

where K_n is the Bessel function of order n, of the second kind and with imaginary argument, and where A_n are constants determined by

$$\sin\theta\, e^{-sa|\sin\theta|} = \sum_{n=0}^{\infty} A_n \sin n\theta \tag{2.4}$$

What remains to be done to determine ϕ is then the inversion of (2.3) which can be written down as a series of integrals involving W functions, defined by

$$\frac{1}{a}\int_0^{\infty} e^{-sz}\, W_n\left(\frac{x}{a}, \frac{r}{a}\right) dx = \left(\frac{a}{r}\right)^{1/2} + e^{s(r-a)} \frac{K_n(sr)}{K_n'(sa)} \ ; \tag{2.5}$$

extensive tables, but necessarily incomplete, of these functions have been prepared by Mersman (1954) and Nielsen (1957). Using these tables a number of workers [e.g. Randall (1965), Chan and Sheppard (1965)] have successfully computed pressure distributions on the body and, to some extent, on the wings. The most important region where the computation fails is the neighbourhood of S the surface separating the domain where the interference is identically zero from where it is not zero. The precise form of S in $z > 0$, $y > 0$ is

$$\left.\begin{aligned} x &= \sqrt{r^2 + a^2 - 2ra\cos\theta} && \text{if } y > a \\ x &= a\theta - a\cos^{-1}\frac{a}{r} + \sqrt{r^2 - a^2} && \text{if } 0 < y < a \end{aligned}\right\} \tag{2.6}$$

The reason is that this neighbourhood corresponds to sa large in (2.3) when the series is only slowly convergent. The elucidation of the flow near S therefore is equivalent to an elucidation of the properties of $\bar{\phi}$ when $sa \gg 1$. Before looking at this aspect however we note that Nielsen's approach cannot deal with lifting wings having subsonic edges and such interactions can at present only be dealt with in the limit case of slender wings.

3 THE NEIGHBOURHOOD OF S

The structure of $\bar{\phi}$ when $sa \gg 1$ can be determined in two ways. Either we can develop methods for summing (2.3) directly or we can revert to the basic equation (2.2) and investigate the simplifications that appear when $sa \gg 1$. Both methods are successful; indeed the first has a long history in the closely related field of short wave diffraction. The second method which is newer, while lacking somewhat in rigour, does have the advantage of being immediately applicable to arbitrary convex cylindrical bodies. The essential results are also easier to obtain and we shall concentrate on it here. For an account of the alternative approach the reader is referred to Jones (1964), who in another paper (Jones 1967) gives an alternative account of the second approach to the determination of the solution near S.

We now consider the structure of S near [but as we shall see later, not too near] $r = a$, $\theta = 0$, concentrating on wings without sweep and restricting attention to the region $z > 0$. Define Ψ by

$$\bar{\phi} = \frac{1}{s^2} e^{-sz} \Psi(y,z) \tag{3.1}$$

so that outside the interaction region $\Psi = 1$. Then in virtue of (2.2) Ψ satisfies

$$\frac{\partial^2 \Psi}{\partial r^2} + \frac{1}{r}\frac{\partial \Psi}{\partial r} + \frac{1}{r^2}\frac{\partial^2 \Psi}{\partial \theta^2} - 2s\left[\sin\theta \frac{\partial \Psi}{\partial r} + \frac{\cos\theta}{r}\frac{\partial \Psi}{\partial \theta}\right] = 0 \tag{3.2}$$

together with the boundary conditions

$$\frac{1}{r}\frac{\partial \Psi}{\partial \theta} - s\Psi = -s \qquad \theta = 0r,\ r > a \tag{3.3a}$$

$$\frac{\partial \Psi}{\partial r} - s\Psi \sin\theta = 0 \qquad r = a,\ \theta > 0 \tag{3.3b}$$

$$\Psi \to 1 \qquad \text{as } r \to \infty \tag{3.3c}$$

So far no app ximations have been made to (2.2) but now we take advantage of the fact that $sa \gg 1$. Two regions near $\theta = 0$, $r = a$ can be distinguished. The first is when $\theta \sim (sa)^{-1}$, $(r-a) \sim s^{-1}$ and here, although (3.2) simplifies, the best treatment is by cone-field theory and we shall postpone its consideration until the next section. The second region is characterised by $(r-a) \sim s^{-2/3} a^{1/3}$, $\theta \sim (sa)^{-1/3}$. In order to discuss it we write

$$R = \frac{r-a}{a}(sa)^{2/3}, \qquad \Theta = \theta(sa)^{1/3} \tag{3.4}$$

and after expressing Ψ as a function of R, Θ we let $sa \to \infty$ when (3.2), (3.3) reduce to

$$\frac{\partial^2 \Psi}{\partial R^2} - 2\Theta\frac{\partial \Psi}{\partial R} - 2\frac{\partial \Psi}{\partial \Theta} = 0$$

$$\Psi(R,0) = 1\,, \quad \frac{\partial \Psi}{\partial R} = \Theta\Psi \quad \text{when} \quad R = 0\,, \quad \Psi(\infty,\Theta) = 1 \tag{3.5}$$

The relative errors in (3.5) are all $O(sa)^{-2/3}$. The simpler problem posed by (3.5) can be solved exactly. For details the reader is referred to Stewartson (1966); the solution is

$$\Psi = \exp\left\{\Theta R - \frac{1}{6}\Theta^3\right\}\sum_{n=1}^{\infty}\frac{Ai[2^{1/3}R-\kappa_n]}{\kappa_n[Ai(-\kappa_n)]^2}e^{-2^{-1/3}\kappa_n\Theta}\int_{-\kappa_n}^{\infty}Ai(\rho)\,d\rho \qquad (3.6)$$

where Ai is the Airy function and $-\kappa_n$ are the successive zeros of $Ai'(x)$.

Having obtained this solution valid in a certain domain fairly near the intersection of S and the root chord of the wing the formal extension to the remainder of S turns out, after some rather complicated argument, to be straightforward. In the r,θ,x space the intersection of S with the cylinder is known to be the curve $r = a$, $x = a\theta$ for $0 < \theta < \frac{\pi}{2}$ [if $\theta > \frac{\pi}{2}$ S is determined by the other half of the wing approximately lying in $z = 0$, $y < -a$] . Hence for $0 < \theta < \frac{\pi}{2}$, $\bar{\phi}$ must be dominated by a factor $\exp(-as\,\theta)$ when $\theta \sim 1$ and $r \to a$. We find in fact that replacing the exponential factor outside the summation sign in (3.6) by $s^{-2}\exp(-as\,\theta)$ is sufficient to give $\bar{\phi}$ near $r = a$ for $0 < \theta < \frac{\pi}{2}$. On inverting we find that near S and $r = a$

$$\phi \sim aA\left(\frac{x-a\theta}{a}\right)^{7/4}\theta^{-9/4}\exp\left\{-\frac{1}{3}\kappa_1\theta\left[\frac{a}{2(x-a\theta)}\right]^{1/3}\right\} \qquad x > a\theta$$

provided $0 < \theta < \frac{\pi}{2}$, where A is a known constant.

The structure of ϕ at points of S not near $r = a$ can also be worked out but the results are rather complicated and are not reproduced here. A full discussion of its properties may be found in the paper already quoted. The behaviour of ϕ at points well downstream of S and neither on the body nor the wings can obviously be found from Nielsen's series taking advantage of the comparative smallness of the relevant values of as. Further, although it has not been explicitly demonstrated, it is likely that these two expansions cover a sufficiently large portion of the flow field for practical purposes. Certainly this appears to be so in the related problem of the diffraction of sound pulses by a cylinder.

Unfortunately the one part of the flow field excluded by these analysis, namely the immediate neighbourhood of the leading edge of the root chord of the wing, is of particular importance in practice and so it is necessary to develop a third procedure to handle it. Before doing so however we observe that, as with Nielsen's method, the discussion of the solution near S depends on the wings having supersonic leading edges or being symmetrically disposed to the undisturbed stream. Although it has not been investigated the extension to subsonic leading edges does not seem impossible, but it will probably be necessary to work in the x,y,z plane rather than use Laplace transform methods.

4 THE LEADING EDGE OF THE ROOT CHORD

Defining the wings, as before, by $z = 0$, $x > 0$, $|y| > a$ and the cylinder by $y^2 + z^2 = a^2$ the region we are interested in is the neighbourhood of $(0,a,0)$ and specifically when $\frac{x}{a} \ll 1$. From continuity ϕ vanishes when $x = z = 0$, $y = a$ and the value of $\frac{\partial\phi}{\partial x}$ follows by Bagley's argument (1961). The idea here is to note that the cylinder is normal to the wing on the root chord and hence to a first approximation it may be replaced by an infinite plane. Thus the value of $\frac{\partial\phi}{\partial x}$ at the leading edge is the same as if the wing were continued through the cylinder by its reflection in the infinite plane and the cylinder then removed. For the unswept wing defined above it follows that $\frac{\partial\phi}{\partial x}$ at $x = 0$ is the same whether the cylinder is there or not. For swept wings the equivalent problem is to determine $\frac{\partial\phi}{\partial x}$ at the apex of a delta wing, the solution of which is well-known.

In order to make a convincing join [graphically speaking] with the asymptotic solution when $\frac{x}{a} \gg 1$ on the root chord it is however necessary, at least, to know the value of $\frac{\partial^2\phi}{\partial x^2}$ as $x \to 0$ and this is a more formidable problem. Not, it should be emphasised, because of the difficulty of formulation, but rather the amount of manipulation and computation which seems at first sight to be necessary. The line of approach is as follows:

(a) The wing is extended by its mirror image and the cylinder neglected. An expression is derived for the velocity potential ϕ_1 at a general point of space. It is used to compute $\frac{\partial\phi_1}{\partial r}$ on $r = a$, which, to first order is equal to the value of

$$\frac{y}{a}\frac{\partial\phi_1}{\partial y} + \frac{z}{a}\frac{\partial\phi_1}{\partial z} \tag{4.1}$$

when $(y-a) = -\frac{z^2}{2a}$. After neglecting all terms $O(x^2)$ we denote the resulting form for (4.1) by

$$x\,F(\tau) \quad \text{where} \quad \tau = \frac{z}{x} : \tag{4.2}$$

(b) A new solution ϕ_2 of the potential equation is constructed to cancel the value of $\frac{\partial\phi_1}{\partial r}$ on $r = a$ given by (4.2). To order x^2 in ϕ it is sufficient that this be done on the plane $y = a$, i.e. we replace the cylinder by this plane and require

$$\frac{\partial\phi_2}{\partial y} = -x\,F(\tau) \quad \text{on} \quad y = a \tag{4.3}$$

The determination of ϕ_2 is a standard problem and solved by means of a distribution of sources of density $-x\,F(\tau)$ on $y = a$.

(c) The final step is to cancel the downwash produced by ϕ_2 on the wing without introducing a normal velocity component on the cylinder, at least to order x. If the downwash produced by ϕ_2 on the wing

$$-x\,G(\eta) + O(x^2) \tag{4.4}$$

where $\eta = \frac{y}{x}$, the new potential ϕ_3 is chosen to satisfy

$$\frac{\partial\phi_3}{\partial z} = x\,G(|\eta|) \tag{4.5}$$

on the wing and on its mirror image in the tangent plane to the cylinder at the root chord. The error in the normal velocity at the cylinder induced by ϕ_3 is $O(x^2)$ and negligible.

If the wing is unswept the value of $\frac{\partial^2\phi}{\partial x^2}$ at the leading edge of the root chord was first found by Nielsen (1951). He showed that if ϕ satisfies the boundary conditions (2.2), then as $y \to a+$, $z \to 0+$

$$\phi \to x - \frac{x^2}{3\pi a} + O(x^3) \tag{4.6}$$

If the wing is swept there are two complications. The first concerns the determination of ϕ_1 at points near the plane $y = a$. For wings with supersonic edges (i.e. the leading edge is given by $y = a + mx$, $m > 1$) it is best to work with the Laplace transform of ϕ_1, i.e.

$$\bar{\phi}_1 = m \int_{-\infty}^{\infty} \frac{d\omega \exp\{i\omega(y-a) - z\sqrt{s^2+\omega^2}\}}{(s^2+\omega^2)^{1/2}(s^2+\omega^2m^2)}, \qquad z > 0 \qquad (4.7)$$

which satisfies (2.2). On the other hand if the wing has a subsonic leading edge $(m < 1)$ and is lifting, as implied by (2.2), the two sides of the wing $(z = 0\pm)$ are not independent and the corresponding form for $\bar{\phi}_1$ is

$$\frac{m^2}{2E} \int_{-\infty}^{\infty} \frac{d\omega \exp\{i\omega(y-a) - z\sqrt{\omega^2+s^2}\}}{(s^2+\omega^2m^2)^{3/2}} \qquad (4.8)$$

where E is the complete elliptic integral of the second kind, with modulus $\sqrt{1-m^2}$ although the Laplace transform is really no further help in these cases. It is noted that if the wing is symmetric about $z = 0$ there is no need to differentiate in this way between $m < 1$ and $m > 1$.

The second complication arises in the determination of ϕ_3 when $m < 1$. This is formally a standard problem in generalised cone-field theory about which there is an extensive literature. However it was found that the primitive method of source distributions gave the necessary results in the easiest way. As a preliminary we first find a ϕ_4 such that

$$\frac{\partial \phi_4}{\partial z} = H(\eta) \qquad (4.9)$$

on the delta wing and then integrate the solution from $x = 0$ with respect to x. For a suitable choice of H and provided we add a simple standard solution of the potential equation this procedure gives ϕ_3 and completes the determination $\frac{\partial^2\phi}{\partial x^2}$ at $y = a+$, $z = 0+$, $x = 0$. The reader is referred to Stewartson (1968) for further details of the argument: considerable numerical work is needed to determine

$$B = -2a \,\mathrm{Lt}\, \frac{\partial^2\phi}{\partial x^2} \qquad \text{as } x \to 0+,\ y \to a+,\ z \to 0+$$

and the results are set out in the table below

m	B	m	B
∞	0·1061	0·966	0·0551
3·864	0·0861	0·866	0·0508
2·000	0·0732	0·707	0·0435
1·414	0·0656	0·500	0·0316
1·155	0·0606	0·259	0·0133
1·035	0·0577	0	0
1	0·0567		

Many questions remain of course and most of them will need extensive computing to answer. It would be useful however if an analytic means of joining the solution near the leading edge of the root chord, given in section 4, with the solution for the remainder of the neighbourhood of S given in section 3. One wonders whether it will also be possible to extend Nielsen's asymptotic theory to lifting wings with subsonic edges and how it fits in with slender body and not-so slender body theory. Little progress in these directions has unfortunately been made up to now.

5 ILLUSTRATION OF THE APPLICATION OF THEORY AND A COMPARISON WITH EXPERIMENT

As referred to earlier in the paper, the formal solution of the wing-body interference problem was set down by Nielsen in 1951. His method was to reduce the problem to that of numerical calculation of the sum of an infinite series of certain convolution integrals in order to find the pressure at any point in the field of the interaction. The convolution integrals involve 'W' functions, which have now been fairly extensively tabulated by Mersman (1954), and also the coefficients of the Fourier series representing the normal velocities induced at the body boundary by the velocity potential of the wing, (together with its arbitrary extension within the body) which must be cancelled by those of the interference potential.

In any practical calculation using an electronic computer, the 'W' functions may be stored as a table or, perhaps more conveniently, generated by use of the approximate functions suggested by Luke (1964). The evaluation of the Fourier coefficients is, however, a somewhat tedious task except in rather special cases where they can be determined analytically, e.g. for a wing of simple wedge section. An alternative technique which obviates the need to calculate these coefficients is possible for the symmetrical problem when the wing has straight spanwise generators, since it is possible to solve the problem by a simple superposition of the solution for wings of wedge section. Fig.1 illustrates how an arbitrary section may be built up of elementary wedge wings, QRST, for which the solution is known. Such a solution was given by Randall (1965).

For the superposition it is convenient to define an 'influence' function $F(\xi/\beta a)$, which is the difference between the pressure coefficient at any point on the wedge wing-body combination and that at the corresponding point, assuming the body side to act as a reflection plane, (i.e. that for the net wing).

$F(x/\beta a)$ is thus defined as

$$F(x/\beta a) = \frac{\beta}{\delta}\left[C_P\left(\frac{x}{\beta a}\right)\right]_{\substack{\text{wing-body}\\ \text{combination}}} - \frac{\beta}{\delta}\left[C_P\left(\frac{x}{\beta a}\right)\right]_{\text{net wing}} \tag{5.1}$$

where a = body radius

δ = wedge angle

$\beta = \sqrt{M^2-1}$

and, in general, is a function of the sweep angle Λ.

By superposition, we have for the wing-body junction, for example,

$$\beta\Delta C_{P_I} = \left[\frac{dz_w}{d\xi}\right]_{\xi=0} F\left(\frac{x}{\beta a}\right) + \int_0^x \frac{d^2 z_w}{d\xi^2} F\left(\frac{x}{\beta a} - \frac{\xi}{\beta a}\right) d\xi \tag{5.2}$$

or

$$= \int_0^x \frac{1}{\beta a}\frac{dz_w}{d\xi} F'\left(\frac{x}{\beta a} - \frac{\xi}{\beta a}\right) d\xi \qquad \text{since } F(0) = 0$$

where ΔC_{P_I} is the increment to be added to the pressure coefficient for the net wing, and the wing section is defined by $z_w = z_w(\xi)$.

Use is made of the foregoing analysis to evaluate the required forms of $F\left(\frac{x}{\beta a}\right)$ for small values of the argument which gives

$$F\left(\frac{\xi}{\beta a}\right) \approx -\frac{4m}{3\pi}\left[\frac{m\pi}{4}\left(m^2+\frac{1}{2}\right) - \frac{1}{2}m^2 - \frac{m^4}{2\sqrt{1-m^2}}\cosh^{-1}\frac{1}{m}\right]\frac{\xi}{\beta a} + O\left(\frac{\xi}{\beta a}\right)^2 \tag{5.3}$$

$(m < 1)$

for a subsonic sweep angle, and

$$F\left(\frac{\xi}{\beta a}\right) \approx -\frac{4m}{3\pi}\left[\frac{m\pi}{4}\left(m^2+\frac{1}{2}\right)-\frac{1}{2}m^2-\frac{m^4}{2\sqrt{1-m^2}}\cos^{-1}\frac{1}{m}\right]\frac{\xi}{\beta a}+0\left(\frac{\xi}{\beta a}\right)^2 \qquad (m > 1)$$

for a supersonic sweep angle; where $m = \beta \cot \Lambda$.

Fig.2 illustrates the pressure distribution at the junction of a body and a 55 degree swept wing at zero incidence and a Mach number of 1·2. The calculated results can be compared with those for the new wing. The influence of the opposite wing panel on the junction pressures is readily apparent. The figure also gives some experimental measurements made in the R.A.E. 8ft × 6ft Transonic Wind Tunnel on the model illustrated and these are seen to be in fair agreement with the calculated values.

REFERENCES

1	J.N. Nielsen	1951:	Ph.D. Thesis California Inst. of Technology
2	J.N. Nielsen	1957:	NACA Technical Note 3873
3	W.A. Mersman	1954:	Proc. Inter. Cong. Math. Amsterdam 2
4	D.G. Randall	1965:	A.R.C. Current Paper No.704
5	Y.Y. Chan and L.N. Sheppard	1965:	Australian Defence Scientific Service WRE Report HSA 18
6	D.S. Jones	1967:	Mathematika 14, 68-93
7	D.S. Jones	1964:	Theory of Electromagnetism (Pergamon Press)
8	K. Stewartson	1966:	Mathematika 13, 121-139
9	J.A. Bagley	1961:	R.A.E. Report Aero 2650
10	K. Stewartson	1968:	Aeronautical Quarterly 19, 135-148
11	Y.L. Luke	1964:	Quart. Journ. Mech and Applied Maths, Vol.XVII, Pt.1 91-103

$$\beta \Delta C_{p_I} = \left[\frac{dz_w}{d\xi}\right]_{\xi=0} F\left(\frac{x}{\beta a}\right) + \int_0^x \frac{d^2 z_w}{d\xi^2} F\left(\frac{x}{\beta a} - \frac{\xi}{\beta a}\right) d\xi$$

or

$$= \int_0^x \frac{1}{\beta a} \frac{dz_w}{d\xi} F'\left(\frac{x}{\beta a} - \frac{\xi}{\beta a}\right) d\xi$$

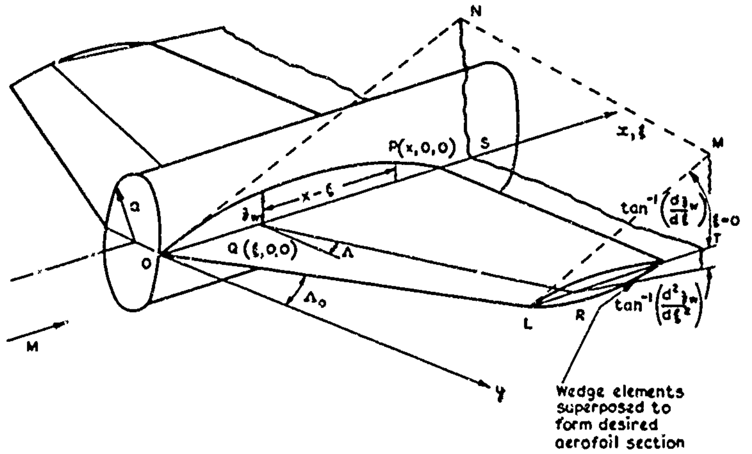

Fig.1 Superposition procedure for a symmetrical wing and body combination

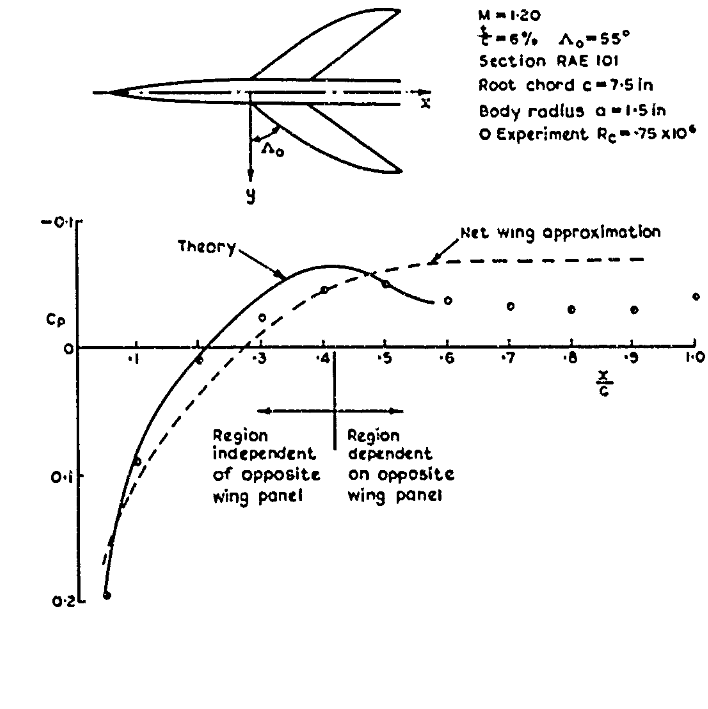

Fig.2 Pressure distribution at the junction of a body and a 55° swept wing at zero incidence and a Mach number of 1·2

EXPERIMENTAL INVESTIGATION OF WING-BODY INTERFERENCES IN THE MACH NUMBER RANGE FROM 0.5 TO 2.0

by

W. Schneider

Aerodynamische Versuchsanstalt Göttingen

Göttingen, Germany

SUMMARY

In order to investigate the effects of interference on wing-body combinations, three-component measurements were performed in the Transonic Wind Tunnel of the Aerodynamische Versuchsanstalt Göttingen in the Mach number range from 0.5 to 2.0. Three basic wings, a rectangular wing, a sweptback wing, and a delta wing with aspect ratio A between 2.3 and 2.75 were investigated alone and in combinations with two pointed cylindrical bodies of different length and diameter. For these wing-body combinations the interference effects in lift, pitching moment, wave drag, and shift of the aerodynamic center due to interferences were determined.

RESUME

Afin de rechercher l'interaction aérodynamique entre l'aile et le fuselage des measures de force ont été efféctuées avec des ailes, avec des fuselages et avec différentes combinaisons d'ailes et de fuselages dans le régime du nombre de Mach de Ma = 0,5 à Ma = 2,0. Ces measures ont été executées dans la soufflerie transonique de Aerodynamische Versuchsanstalt Göttingen. On n'a recherché que trois ailes de géométrie fondamentale : une aile rectangulaire, une aile en flèche et une aile delta d'un allongement géométrique entre 2,3 et 2,75. Ces ailes ont été combinées avec deux differents fuselages. Avec les differentes combinaisons on a recherche les effects d'interaction aérodynamiques sur la portance, sur le moment de tangage, sur la trainée due aux ondes de choc, sur les gradients de la portance et du moment de tangage et sur le déplacement du centre de poussée.

NOTATION

A	wing aspect ratio, $A = b^2/S$
a. c.	aerodynamic center of the wing
b	wing span
$c(y)$	local wing chord
$\bar{c}$	mean aerodynamic chord, $\bar{c} = \frac{1}{S}\int_{-s}^{+s} c^2(y)\,dy$
c_D	drag coefficient based on total wing plan-form area for wings and combinations
c_L	lift coefficient based on total wing plan-form area for wings and combinations and on base area for bodies
c_M	pitching moment coefficient about quarter-chord point of mean aerodynamic chord for wings and combinations, based on total wing plan-form area and mean aerodynamic chord for wings and combinations
c_r	root chord of wing
c_t	tip chord of wing
d	body diameter
$\frac{dc_L}{d\alpha}$	lift-curve slope, per radian
$\frac{dc_M}{d\alpha}$	pitching-moment-curve slope, per radian
D	drag
L	lift
M	pitching moment
Ma	Mach number
MRC	moment reference center
p	local static pressure
q_∞	free-stream dynamic pressure, $q_\infty = \frac{1}{2}\rho_\infty V_\infty^2$
qcp	local quarter-chord point
QCP	quarter-chord point of mean aerodynamic chord
Re	Reynolds number, $Re = \frac{V_\infty \bar{c}}{\nu_\infty}$
s	wing semi span
S	wing plan-form area
V_∞	free-stream velocity
x	longitudinal coordinate, measured along body axis from body nose for body alone, or measured along wing root chord from wing apex for wings and combinations, positive downstream
Δx_{ac}	distance of the aerodynamic center from MRC, positive downstream, $\Delta x_{ac} = -\left(\frac{dc_M}{dc_L}\right)_{c_L = 0} \cdot \bar{c}$
$x(y)_{qcp}$	distance of qcp from wing apex
x_{QCP}	distance of QCP from wing apex, $x_{QCP} = \frac{1}{S}\int_{-s}^{+s} x(y)_{qcp} \cdot c(y)\,dy$

y	lateral coordinate
α	angle of attack
λ	taper ratio, $\lambda = c_t/c_r$
Λ	sweep angle of wing leading edge
ν	kinematic viscosity of air
ρ	density of air

Subscripts

B	body alone
INT	interference
W	wing alone
WB	wing-body combination
∞	free-stream flow

EXPERIMENTAL INVESTIGATION OF WING-BODY INTERFERENCES IN THE MACH NUMBER RANGE FROM 0.5 TO 2.0

W. Schneider

1. INTRODUCTION

The purpose of this investigation is an experimental contribution to aerodynamics of wing-body interferences in the subsonic, transonic, and supersonic speed range. For incompressible flow the wing-body problem is discussed in some detail in Ref. [1] and [2], whereas at transonic and supersonic speeds systematic experimental investigations are scarce. Available publications are presenting mostly very special wing-body combinations, concerned with practical problems, especially the drag reduction. In this paper, in the first place the effect on lift, pitching moment, and the shift of the aerodynamic center due to interferences has been investigated. With regard to the basic character of these investigations, three wings of simple plan-form were chosen, a rectangular wing, a sweptback, and a delta wing. These wings were combined with two pointed cylindrical bodies of different diameter in order to investigate the influence of body thickness. With the chosen magnitude of aspect ratios the results may be also of some interest for modern aerodynamic applications.

2. TEST FACILITIES

The tests were performed in the 1 x 1 m^2 Transonic Wind Tunnel of the Aerodynamische Versuchsanstalt Göttingen, which has been described in Ref. [3]. This closed circuit continuously operating wind tunnel is equipped with a flexible-plate Laval nozzle for tests at supersonic speeds (Mach number from 1.25 to 2.25), and an adjacent section with four perforated walls for tests at subsonic and transonic speeds (Mach number from 0.4 to 1.2). A Reynolds number variation is achieved by changing the stagnation pressure in the tunnel from 1/10 of an atmosphere to approximately 2 atmospheres. The tunnel is equipped with strain-gauge balances for measuring aerodynamic forces on sting-supported models. Data are recorded by a system of dc-amplifiers and digital voltmeters. The measuring range of the data handling system lies between 10^{-2} and 10^{+3} volts; the accuracy is $+3 \cdot 10^{-4}$ of the measuring range.

3. MODELS

The wings (Fig. 1) used for these investigations - a rectangular wing, a sweptback wing, and a delta wing - belong to a series of wings, which was tested already in some detail in Ref. [4] and [5]. All wings had the same plan-form area of $S = 327\ cm^2$ and the same symmetrical profile NACA 65 A 005. For the wing-body combinations a second set of wings was manufactured in connexion with cylindrical bodies of $d = 60$ mm diameter. The bodies (Fig. 1) composed of a parabolic nose and a cylindrical afterbody, had fineness ratios of 10.0 and 12.0. The ratios of wing span to body diameter were 3.3 and 5.0. The wings were fixed to the bodies (Fig. 2) in such a way, that the quarter-chord points of the mean aerodynamic chords had the same distance from body apex for all combinations. The wings were located inside the Mach cones originating from body apex, so that disturbances from body nose could not reach the wings at supersonic speeds. The pitching moment reference point was the quarter-chord point of mean aerodynamic chord. For the investigation of the influence of body thickness, the cylindrical part was thickened by two shells up to $d = 90$ mm. For a body diameter of $d = 60$ mm the wing-body model had a blockage of 0.3 °/o of the test cross-section, and for $d = 90$ mm a blockage of 0.7 °/o. This means that the size of the models was in an appropriate relation to the test section of the tunnel. The models were manufactured at the AVA, all wings were made of hardened tool steel and were finished by grinding, the other parts were made of duraluminum.

4. TEST PROGRAM

The tests comprised three-component force measurements - lift, pitching moment, and drag - of wings, bodies, and wing-body combinations (Fig. 2) at the following Mach numbers, Ma = 0.50; 0.70; 0.80; 0.85; 0.90; 0.95; 1.00; 1.05; 1.10; 1.15; 1.52 and 1.97. Nominal angle of attack range was $\alpha = -5^\circ$ to $+15^\circ$. For the rectangular wing and its combinations it was not possible to keep this angle of attack range at all Mach numbers because of strong model vibrations. Near zero-incidence relatively large shifts of the center of pressure occurred on some models, caused by boundary layer effects. Thus it was necessary to repeat some tests in this incidence range ($\alpha = -5^\circ$ to $+5^\circ$) with boundary layer transition fixed. This was done by carborundum strips, 3 mm wide and 0.03 mm high, fixed on the upper and lower surface of the wing at 15 °/o chord position and on the bodies by the same strips at 15 °/o of the length of the nose.

For all tests the tunnel was running at a stagnation pressure of 1 atmosphere and a stagnation temperature of 50° C. Reynolds number per cm was $9 \cdot 10^4 < Re < 1.4 \cdot 10^5$. The permitted deviation from nominal Mach numbers was $\Delta Ma = \pm 0.005$. Angle of attack could be adjusted with an accuracy of $\Delta\alpha = \pm 0.05^\circ$.

5. RESULTS

5.1 Experimental Results

From the three-component measurements the aerodynamic coefficients, the slopes of the lift and pitching moment curve, and the aerodynamic center positions were evaluated. Reference magnitudes for the coefficients of wings and wing-body combinations are wing plan-form area and mean aerodynamic chord as given in Table 1.

Fig. 3 shows the lift-curve slopes, Fig. 4 the aerodynamic center positions versus Mach number of wings and wing-body combinations.

Wing-body interferences are defined as the differences between the aerodynamic coefficients or their derivatives of the wing-body combination and the sum of the same coefficients or derivatives of wing and body alone.

The interference effects on the wing-body combinations are defined by the following formulae

a) Total lift-interference ratio

$$\frac{c_{L_{INT}}}{c_{L_W} + c_{L_B}} = \left[\frac{c_{L_{WB}}}{c_{L_W} + c_{L_B}} - 1\right]_{\alpha = \text{const}} \tag{1}$$

see Fig. 5 to Fig. 7

b) Interference in pitching moment

$$c_{M_{INT}} = \left[c_{M_{WB}} - \left(c_{M_W} + c_{M_B}\right)\right]_{\alpha = \text{const}} \tag{2}$$

see Fig. 8 to Fig. 10

c) Wave drag interference ratio

$$\frac{\Delta c_{D_{INT}}}{\Delta c_{D_W} + \Delta c_{D_B}} = \left[\frac{\Delta c_{D_{WB}}}{\Delta c_{D_W} + \Delta c_{D_B}} - 1\right]_{\alpha = 0} \tag{3}$$

see Fig. 11

d) Lift-curve slope interference ratio

$$\frac{\left(\frac{dc_L}{d\alpha}\right)_{INT}}{\left(\frac{dc_L}{d\alpha}\right)_W + \left(\frac{dc_L}{d\alpha}\right)_B} = \left[\frac{\left(\frac{dc_L}{d\alpha}\right)_{WB}}{\left(\frac{dc_L}{d\alpha}\right)_W + \left(\frac{dc_L}{d\alpha}\right)_B} - 1\right]_{\alpha = 0} \qquad (4)$$

see Fig. 12

e) Interference in pitching moment curve slope

$$\left(\frac{dc_M}{d\alpha}\right)_{INT} = \left\{\left(\frac{dc_M}{d\alpha}\right)_{WB} - \left[\left(\frac{dc_M}{d\alpha}\right)_W + \left(\frac{dc_M}{d\alpha}\right)_B\right]\right\}_{\alpha = 0} \qquad (5)$$

see Fig. 13

f) Shift of aerodynamic center position due to interferences

$$\left(\frac{x_{ac}}{\bar{c}}\right)_{INT} = -\left[\left(\frac{dc_M}{dc_L}\right)_{WB} - \frac{d\,(c_{M_W} + c_{M_B})}{d\,(c_{L_W} + c_{L_B})}\right]_{c_L = 0} \qquad (6)$$

see Fig. 14

A representation of pitching moment interference ratio was not possible, because the pitching moments of wing and body were nearly of the same amount but of different sign at some Mach numbers.

5.2 Theoretical Results

To give an impression of the agreement with theoretical data, a few theoretical points, which could be computed without much computational effort, are shown in the diagrams. The computations were limited to lift-curve slopes and aerodynamic center positions of the wing-body combinations. For the rectangular and delta wing-body combinations the computation is based on a theory of PITTS, NIELSEN, and KAATTARI, Ref. [7]. For the sweptback wing at subsonic speeds the method of HAFER, Ref. [6], and at supersonic speeds the method of FERRARI, Ref. [8], were used. In applying the latter method to a sweptback trailing edge configuration, the wing was represented by superposition of two wings with unswept trailing edges.

6. DISCUSSION OF RESULTS

6.1 Lift-Curve Slopes (Fig. 3)

a) Rectangular wing

At subsonic speeds there is no essential difference between the lift-curve slope of the wing alone and that of the wing-body combination. For $Ma < 0.8$ the lift-curve slope of the wing is lying below those of the wing-body combinations. On the other hand at supersonic speeds the lift-curve slopes of the wing-body combinations become considerably larger than those of the wing alone. This increase in lift at supersonic speeds, as compared with that at incompressible flow, can be explained by a different loading distribution, induced by the wing on the body. At supersonic speeds the part of the body in front of the wing can not be influenced by the wing; on the other hand the part of the body downstream of the wing is strongly influenced. The contribution of the induced loading on this part of the body can be essential for the increase in lift. A comparison of experimental with theoretical values shows that the agreement is good at supersonic speeds; at subsonic speeds lift-curve slopes are somewhat overestimated by theory. The effect of a fixed boundary layer transition on lift is insignificant for the configurations of the rectangular wing.

b) Sweptback wing

For the sweptback wing the lift-curve slopes of the wing-body combinations are considerably greater at subsonic and supersonic speeds than those of the wing alone. For this particular wing the interferences are large through the whole Mach number range. Theoretical values only show the tendency of the experimental curve, but the agreement is unsatisfactory at all speeds. The effects of a fixed boundary layer transition are more pronounced than on the rectangular wing. Differences are marked at subsonic speeds and near the speed of sound.

c) Delta wing

Lift-curve slopes of the delta wing and the wing-body combinations do not differ much in the tested Mach number range. Except for $Ma = 2$, where the leading edge of the wing becomes a supersonic edge, the lift-curve slope of the combination is higher than that of the wing alone. The agreement of theory with experiment is good at subsonic speeds, but at supersonic speeds theory overestimates lift. The effect of a fixed transition is negligible.

6.2 Aerodynamic Center (Fig. 4)

a) Rectangular wing

The curves of the aerodynamic center positions are similar for both wing-body combinations. The influence of the body on the shift of aerodynamic center is significant for these configurations. For the $W_1 B_1$ combination it amounts to nearly 15 °/o of the mean aerodynamic chord and nearly to 40 °/o for the $W_1 B_2$ combination.

As it was mentioned already, considerable movements of the center of pressure occurred on the configurations at subsonic speeds. Such movements of the center of pressure are caused in the first place by boundary layer effects (separations) and are strongly dependent on Reynolds number. In wind tunnel testing it is usually not possible to reproduce the Reynolds number of a normal type of airplane. Experimental results with a fixed boundary layer transition therefore correspond more to real flow conditions. For comparison, the theoretical aerodynamic center positions were plotted in this diagram; the agreement with experiment is unsatisfactory especially at transonic speeds.

b) Sweptback wing

For the sweptback wing the shift of the aerodynamic center due to the body is smaller than for the configurations of the rectangular wing; for the $W_2 B_1$ combination it does not exceed 8 °/o of mean aerodynamic chord, and 25 °/o for the $W_2 B_1$ combinations. Differences between aerodynamic center positions with and without fixed transition are nearly twice as high as for the configurations of the rectangular wing. In the lift boundary layer effects were already noticable. With increasing sweep of the wing those effects become more marked with respect to the pitching moment behaviour, and the aerodynamic center position is strongly dependent on such effects. Theoretical and experimental values are in a fair agreement.

c) Delta wing

The curves of the aerodynamic center position of delta wing configurations are similar to those of the sweptback wing configurations. The amounts of shift of the aerodynamic centers lie between those of the rectangular and the sweptback wing configurations. On a delta wing, flow separates at the leading edge; the boundary layer of the reattached flow on the wing's upper side is largely turbulent. Boundary layer trips are, therefore, ineffective on such wings, which is shown by experiment. A peculiar feature of the aerodynamic center position of these combinations is its downstream shift at relatively low Mach numbers ($Ma < 0.7$) and its upstream shift at supersonic speeds with increasing Mach number and body diameter. Comparison of theoretical with experimental values shows good agreement.

6.3 Lift Interference Ratios

a) Rectangular wing (Fig. 5)

Near the speed of sound the experimental points of both wing-body combinations scatter increasingly with increasing angle of attack. At higher angles of attack the beginning of the scatter is displaced slightly to lower Mach numbers. This can be explained by the fact that the speed of sound is attained locally on the model at higher incidence, which evidently is connected with a change of lift distribution. The interference curves are similar for both wing-body combinations. At supersonic speeds interference ratios increase with Mach number up to an angle of attack of nearly $\alpha = 8^o$. The lift of the wing-body combination is larger in this range than the sum of lift of wing and body alone.

b) Sweptback wing (Fig. 6)

The course of lift interference ratio curves is largely similar to those of the configurations of the rectangular wing. However the amounts are larger. Thus, for angles of attack of $\alpha > 3^o$, the lift of the wing-body combination is less than the sum of lifts of wing and body alone. These losses in lift attain their highest values near $Ma = 1.5$.

c) Delta wing (Fig. 7)

For the delta wing in combination with body 2 ($W_3 B_2$) the mean losses in lift are about 10 °/o higher than for the combination with body 1 ($W_3 B_1$). These losses in lift are nearly constant for the $W_3 B_1$ combination in the range $1.2 < Ma < 1.8$, they begin only to decrease near $Ma = 2.0$. Considering in conclusion the behaviour in lift interference of the combinations of the three wings, it can be seen that the combinations of the rectangular wing show the smallest losses in lift as compared with the sum of lift of wing and body alone.

6.4 Interference in Pitching Moment

a) Rectangular wing (Fig. 8)

For both wing-body combinations the interference moment is positive in the tested range of incidence up to $Ma = 1.5$. In the transonic speed range scatter of the experimental data occurs, similar to the scatter of the lift data. Above $Ma = 1.5$ the interference moment changes its sign and tends to higher negative values with increasing Mach number. This tendency to negative values becomes stronger with increasing body diameter.

b) Sweptback wing (Fig. 9)

Here the interference-moment is of negative sign in the tested Mach number and incidence range. Tendency to higher negative values at supersonic speeds with Mach number is not so marked as for the configurations of the rectangular wing, but the negative interference moment becomes larger with increasing incidence.

c) Delta wing (Fig. 10)

Moment interference curves of the delta wing-body combinations are similar to those of sweptback wing configurations; also the values of the interference-moment agree largely. A comparison of the interferences in pitching moment of the configurations of the three wings shows a similar behaviour of the combinations of the delta and the sweptback wing. The interference-moment is of negative sign in the tested Mach number- and incidence range; for the configurations of the rectangular wing negative values occur only above $Ma = 1.5$.

6.5 Interferences in Wave Drag (Fig. 11)

A comparison of the wave drag interference of the tested wing-body combinations definitely shows the more favourable behaviour of the configurations of the delta wing to those of the rectangular and the sweptback wing. As expected, the combinations of the rectangular wing have the highest wave drag, which is only 20 °/o to 25 °/o less on the average than the sum of drag of wing and body alone. For the combinations of the sweptback wing this reduction in drag is nearly 35 °/o to 40 °/o. Influence of body diameter is insignificant, except for the sweptback wing.

6.6 Lift-Curve Slope Interference Ratios (Fig. 12)

a) Rectangular wing

The lift-curve slopes interference ratios are different for the two wing-body combinations. Near Mach number $Ma = 0.9$ the curves of both configurations show a distinct minimum, which is reduced with increasing Mach number. For $Ma > 1.2$ the amount of the lift-curve slopes of the combinations exceed the sum of amounts of wing and body alone, which is caused by additional body lift on the combination at supersonic speeds. With increasing body diameter the interference ratio of lift-curve slope is strongly reduced at subsonic and transonic speeds but increased at supersonic speeds. Test results with and without fixed transition differ only at subsonic speeds. Agreement of theory with experiment can be considered satisfactory.

b) Sweptback wing

In contrast to the rectangular wing, the configurations of the sweptback wing do not show the distinct minimum of lift-curve slope interference ratio near $Ma = 0.9$. Disregarding the scatter of interferences at transonic speeds, the curves indicate, that the differences between the interference ratios of the combinations become smaller with increasing Mach number. and nearly disappear at $Ma = 1.5$. Experimental values with and without fixed transition differ strongly at subsonic speeds. The agreement of theoretical with experimental values is unsatisfactory for these wing-body combinations.

c) Delta wing

In the tested Mach number range the lift-curve slope for the $W_3 B_1$ combination is only somewhat smaller than the sum of lift-curve slopes of wing and body alone. With increasing body diameter the lift-curve slope of the wing-body combination decreases, similar as for the combinations of the other wings. Interference ratios are of negative sign at all Mach numbers; the greatest negative values were measured near the speed of sound. At supersonic speeds losses in lift-curve slope become smaller with increasing Mach number, the differences between the interference ratios of the two combinations become smaller too. Theory and experiment agree satisfactorily at subsonic speeds, but at supersonic speeds discrepancies appear.

6.7 Moment Curve Slope Interferences (Fig. 13)

a) Rectangular wing

For the configurations of the rectangular wing interferences in pitching moment curve slope differ not much. After a slight ascent of interferences with Mach number at subsonic speeds a sudden increase occurs at $Ma = 0.9$. At the speed of sound interferences reach a maximum and drop off at supersonic speeds. Near $Ma = 1.2$ interferences disappear, for $Ma > 1.2$ they become negative. The presentation definitely shows the destabilizing effect of the interference moment of the configurations near zero incidence at transonic speeds and a stabilizing effect with increasing Mach number at supersonic speeds.

b) Sweptback wing

In the tested Mach number range pitching moment curve slope interferences are of negative sign for both combinations of the sweptback wing; the amount of interferences increases with body diameter. At supersonic speeds these interferences tend to higher negative values above $Ma = 1.5$.

Interferences in pitching moment near zero incidence are strongly dependent on Mach number for the combinations of this wing.

c) Delta wing

The interference moment near zero incidence has negative values for these configurations in the whole Mach number range; at supersonic speeds the amount is increasing with Mach number.

A comparison of pitching moment curve slope interferences between the combinations of the wings in the tested Mach number range shows interferences of negative sign on the combinations of the sweptback and the delta wing, which are increasing at supersonic speeds with Mach number and body diameter. On the combinations of the rectangular wing, negative interferences occur only at supersonic speeds, near the speed of sound the interference moment becomes strongly positive.

6.8 Shift of Aerodynamic Center Positions Due to Interferences (Fig. 14)

a) Rectangular wing

Comparing the diagram of the shift of aerodynamic center positions due to interferences with interferences in pitching moment, it can be seen, that the shift of the aerodynamic center is strongly dependent on the pitching moment. On the combinations of the rectangular wing the aerodynamic center is shifted upstream, at transonic speeds, corresponding to the destabilizing interference moment, and downstream at supersonic speeds, corresponding to the stabilizing interference moment. On the $W_1 B_2$ combinations the shift of the aerodynamic center is nearly twice as much.

b) Sweptback wing

For the combinations of the sweptback wing the shift of the aerodynamic center has positive sign in the tested Mach number range and reaches relatively high values at supersonic speeds. Body thickness has the same effect as for combinations of the rectangular wing.

c) Delta wing

Shifts of aerodynamic center are of positive sign at all Mach numbers but smaller than on the configurations of the other wings. A distinct downstream shift occurs at supersonic speeds and increases with body diameter. Shift of aerodynamic center due to interferences has positive sign on the configuration of the sweptback and the delta wing at all Mach numbers, except for the combinations of the rectangular wing, which show a shift of negative sign at transonic speeds. The strong downstream shift at supersonic speeds occurs on all configurations of the three wings.

7. CONCLUSIONS

Three-component force measurements were performed in the Transonic Wind Tunnel of the Aerodynamische Versuchsanstalt Göttingen in the Mach number range Ma = 0.5 to 2.0 on a rectangular-, a sweptback- and a delta wing and on combinations of these wings with two pointed bodies of different thickness. The main purpose of these investigations was to determine the wing-body interferences. For all wing-body combinations the interferences in lift, in pitching moment, in wave drag, in the lift-curve slope, in the moment curve slope, and the shift of the aerodynamic center due to interferences were determined and discussed. It occurred, that on all combinations these interferences are increasing with Mach number at supersonic speeds.

8. ACKNOWLEDGEMENT

The author wishes to acknowledge the proposals given to these investigation by Professor Dr.-Ing. E. TRUCKENBRODT, Technical University of Munich.

9. REFERENCES

[1] Schlichting, H., Truckenbrodt, E. — Aerodynamik des Flugzeuges, Bd. II. Springer Verlag (1960)

[2] Donovan, A. F., Lawrence, H. R. — Aerodynamic Components of Aircraft at High Speeds. Vol. VII High Speed Aerodynamics and Jet Propulsion, Princeton (1957)

[3] Ludwieg, H., Lorenz-Meyer, W., Schneider, W. — Der Transsonische Windkanal der Aerodynamischen Versuchsanstalt Göttingen. Jahrbuch der WGLR 1966, pp. 145 - 155

[4] Becker, E., Wedemeyer, E. — Untersuchungen an fünf Flügeln mit verschiedenen Umrißformen bei hohen Unterschallgeschwindigkeiten. Z. Flugwiss. 8, (1960), pp. 44 - 52

[5] Stahl, W., Mackrodt, P. A. — Dreikomponentenmessungen an symmetrischen Tragflügeln verschiedener Umrißformen in Überschallströmung. Z. Flugwiss. 11, (1963), pp. 150 - 160

[6] Hafer, X. — Untersuchungen zur Aerodynamik der Flügel-Rumpf-Anordnungen. WGLR Jb., 1957, pp. 191 - 207

[7] Pitts, E. C., Nielsen, J. N., Kaattari, G. E. — Lift and Center of Pressure of Wing-Body-Fail Combination at Subsonic, Transonic, and Supersonic Speeds. NACA Tech. Rep. 1307 (1957)

[8] Ferrari, C. — Interference between Wing and Body at Supersonic Speeds. Theory and Numerical Application. J. A. S. Vol. 15, (1948), pp. 317 - 336

[9] Ferrari, C. — Interference between Wing and Body at Supersonic Speeds. Note on Wind Tunnel Results and Abbendum to Calculation. J. A. S. Vol. 16, (1949), pp. 542 - 546

[10] Nielsen, J. N., Pitts, W. C. — Wing-Body Interference at Supersonic Speeds with an Application to Combinations with Rectangular Wings. NACA TN 2677 (1952)

Wing	W_1	W_2	W_3
Sketch	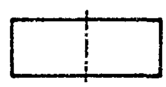	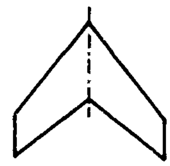	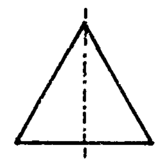
b (mm)	300	300	275
S (cm^2)	327	327	327
c_r (mm)	109	145,3	238
A	2,75	2,75	2,31
x_{QCP} (mm)	27,2	115,8	119
$\bar{c}$ (mm)	109	113	158,6
λ	1	0,5	0
Λ ($^\circ$)	0	52,8	60
Profile NACA 65 A 005			

Table 1: Geometrical Properties of Wings

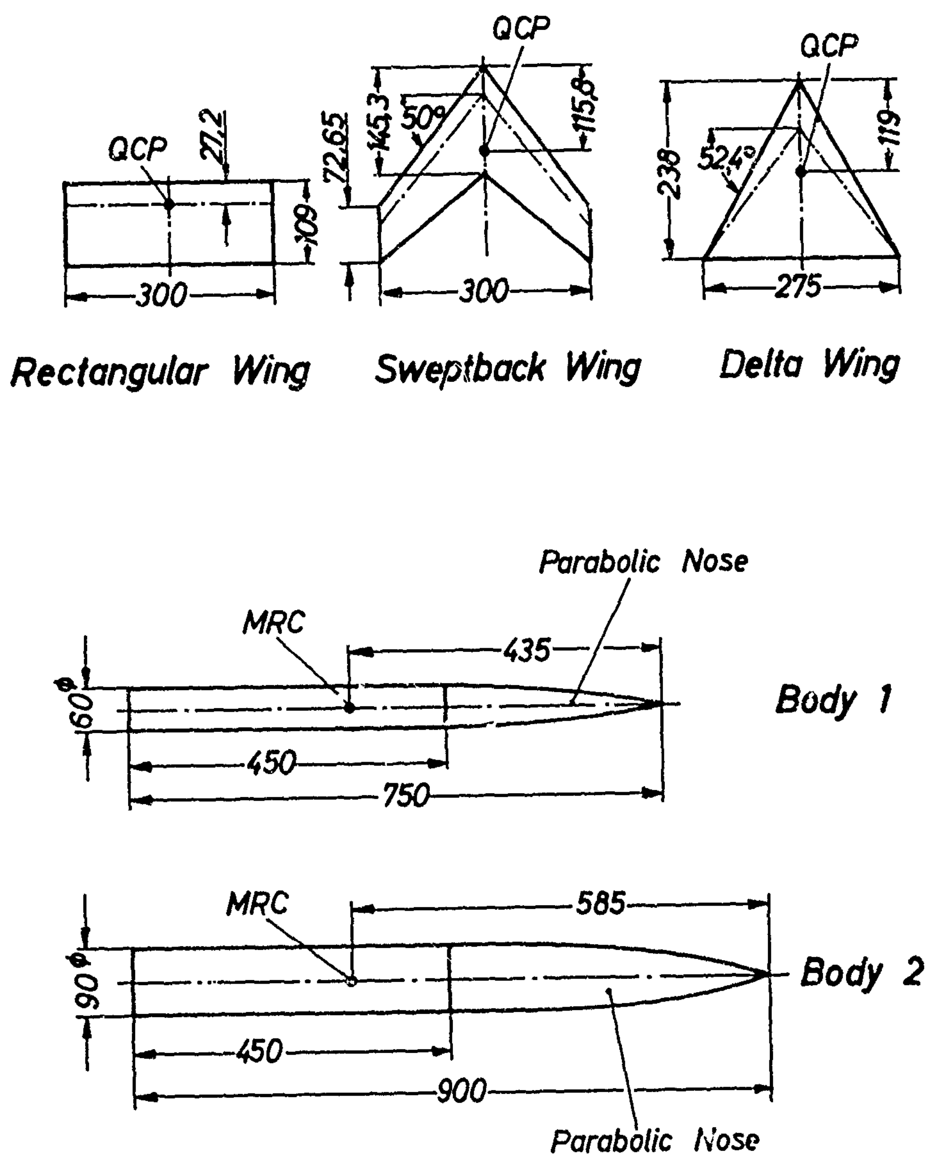

Fig. 1 Dimensions of Wings and Bodies

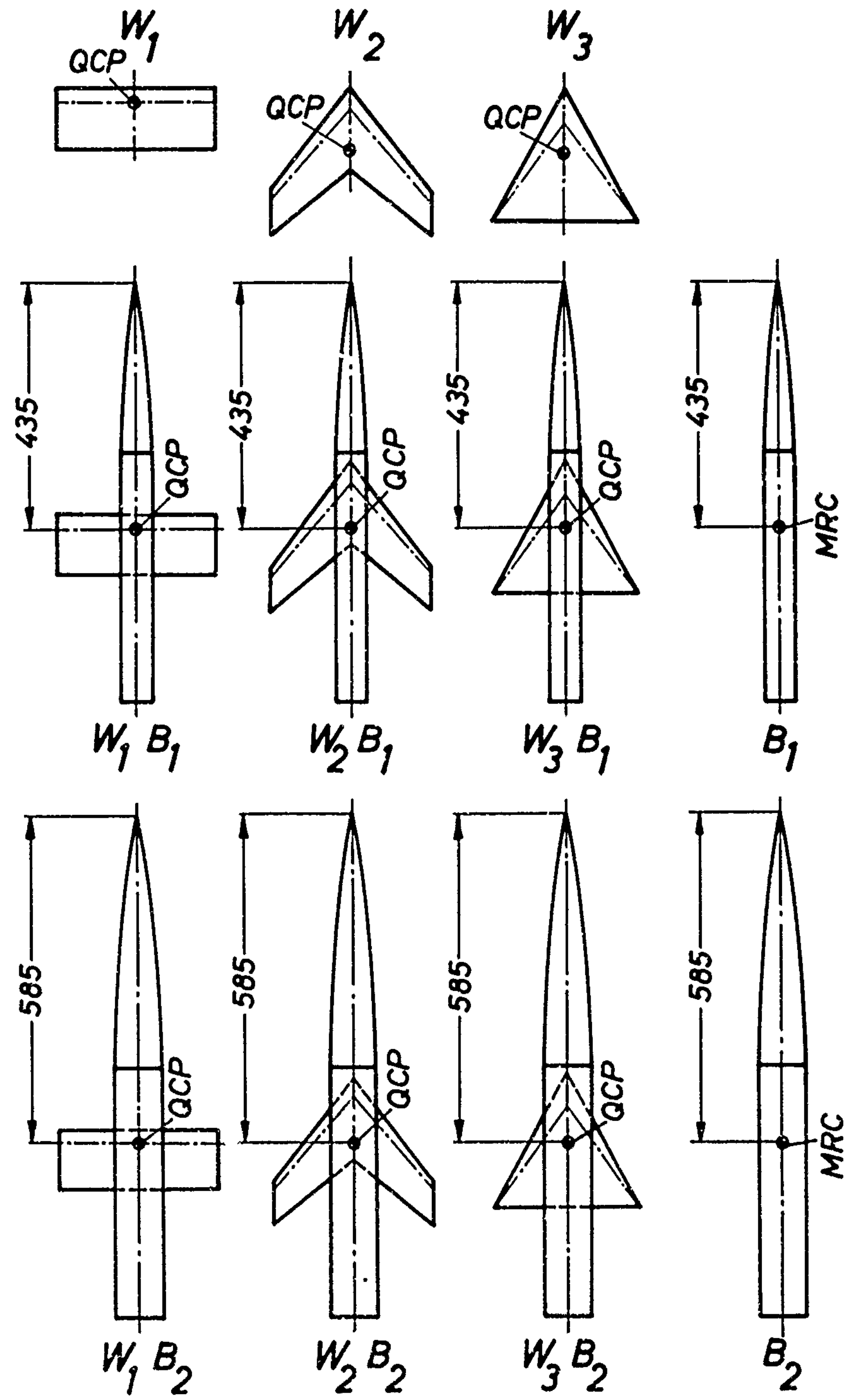

Fig. 2 Model Arrangements

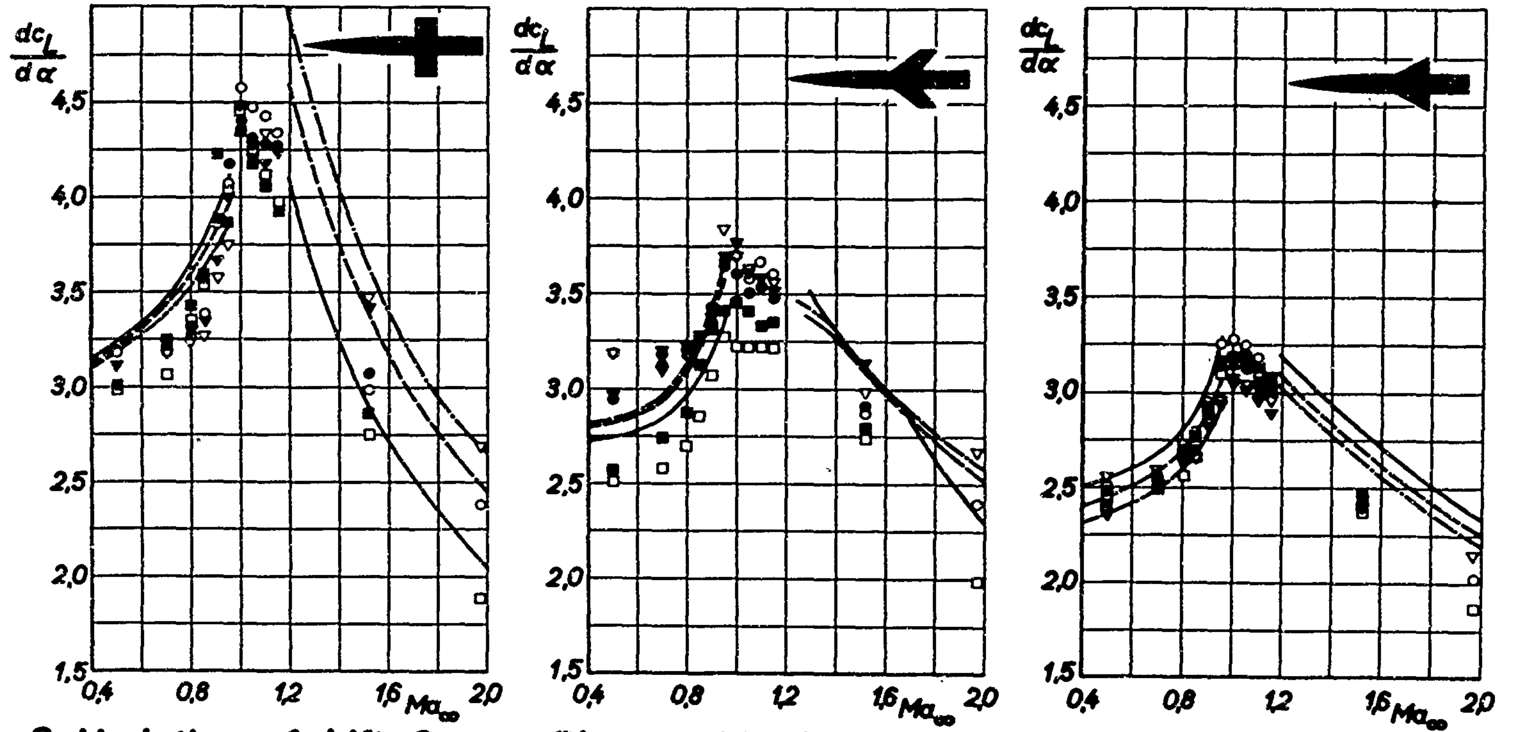

Fig. 3 Variation of Lift Curve Slope with Mach Number for Wing and Wing - Body - Combinations

□ W
■ W (Transition of B.L. fixed)
——— Theory W

○ W B_1
● W B_1 (Transition of B.L. fixed)
– – – Theory W B_1

▽ W B_2
▼ W B_2 (Transition of B.L. fixed)
—·—·— Theory W B_2

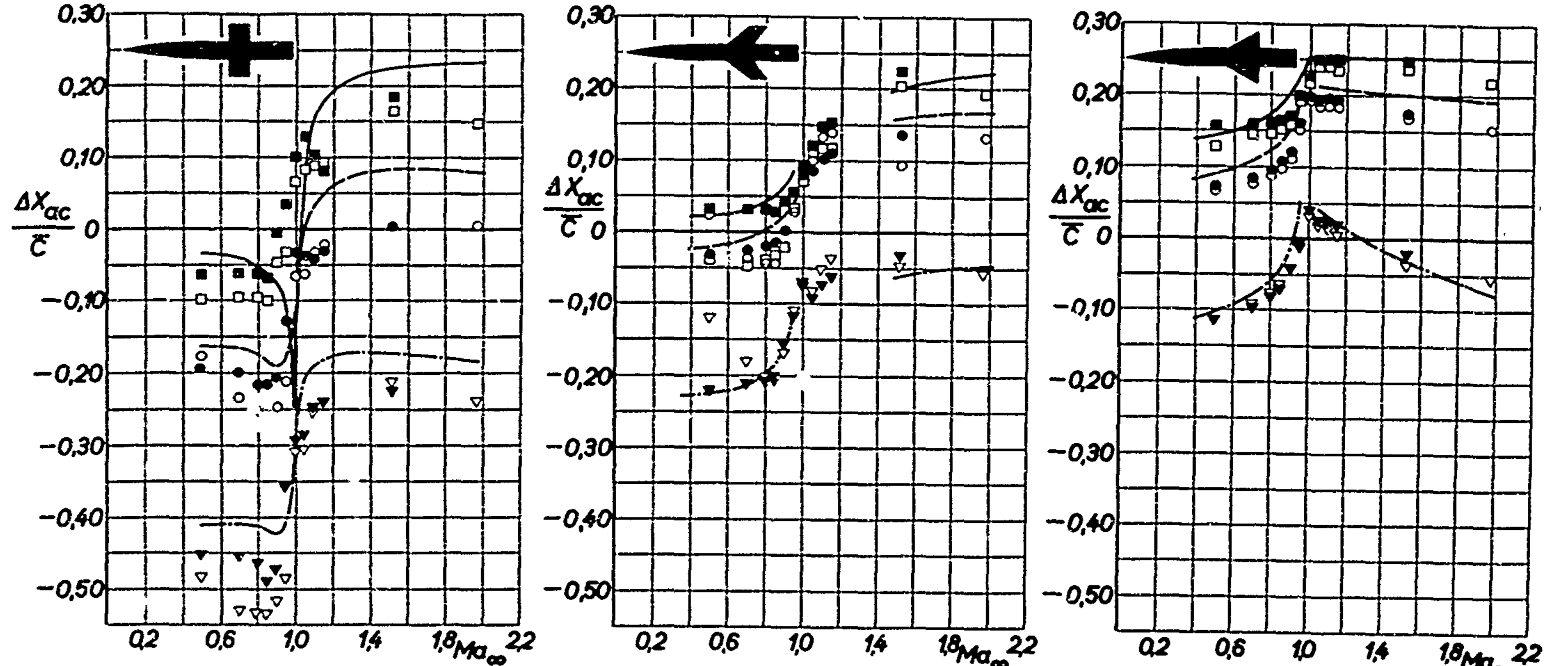

Fig. 4 Variation of Aerodynamic Center Position with Mach Number of Wing and Wing-Body Combinations

□ W
■ W (Transition of B.L. fixed)
——— Theory W

○ W B_1
● W B_1 (Transition of B.L. fixed)
– – – Theory W B_1

▽ W B_2
▼ W B_2 (Transition of B.L. fixed)
—·—·— Theory W B_2

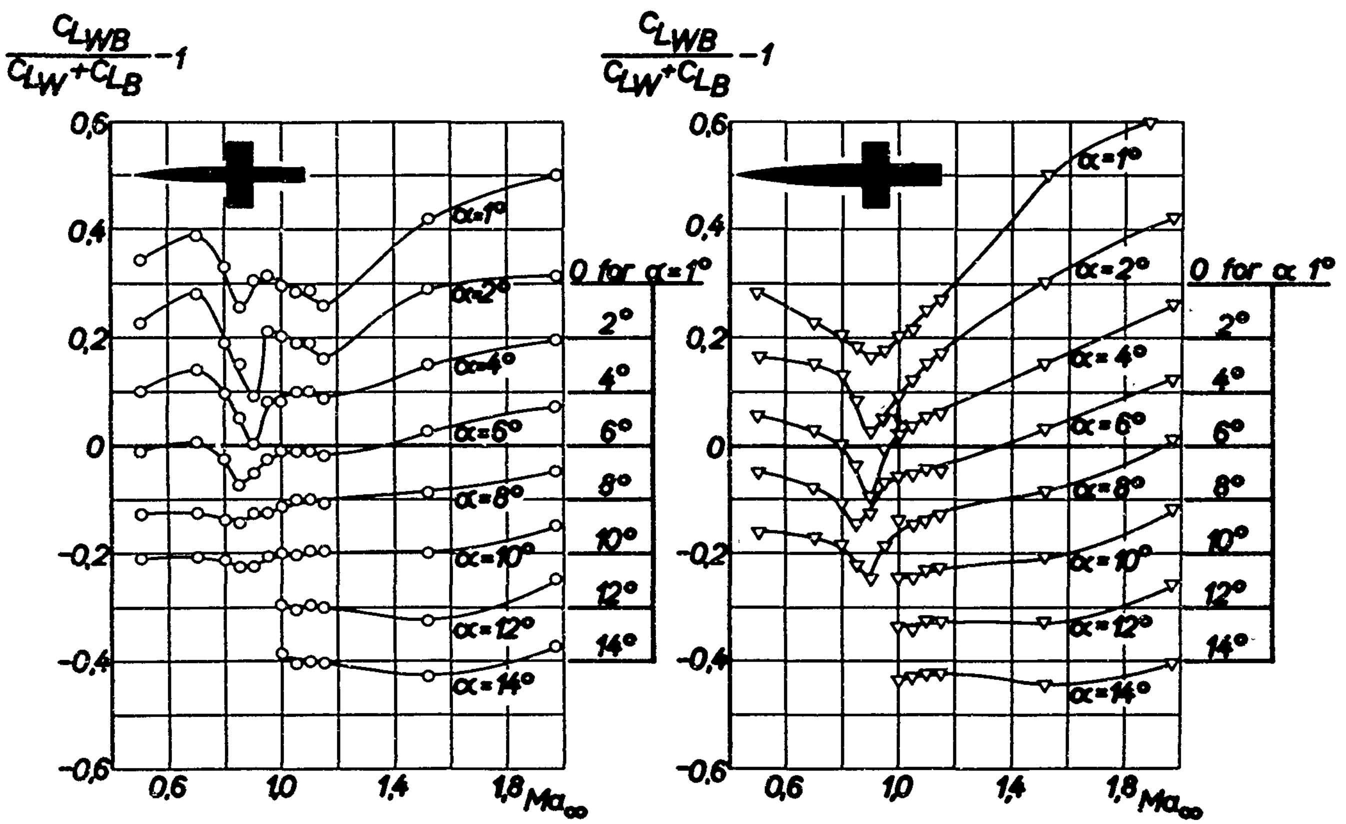

Fig. 5 ***Interference in Lift versus Mach Number for Rectangular Wing-Body-Combinations***

○ $W_1 B_1$ ▽ $W_1 B_2$

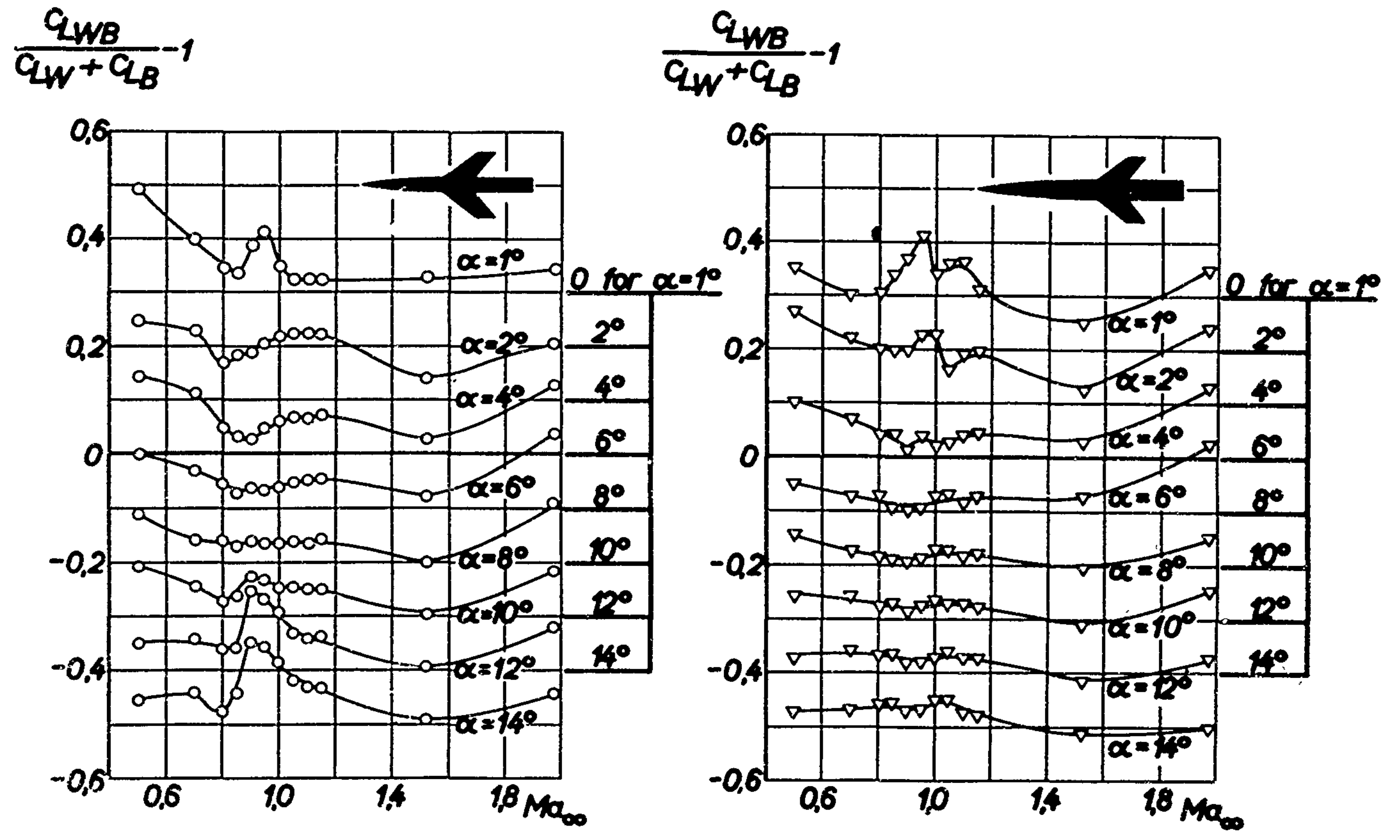

Fig. 6 Interference in Lift versus Mach Number for Sweptback Wing-Body-Combinations

○ $W_2\ B_1$ ▽ $W_2\ B_2$

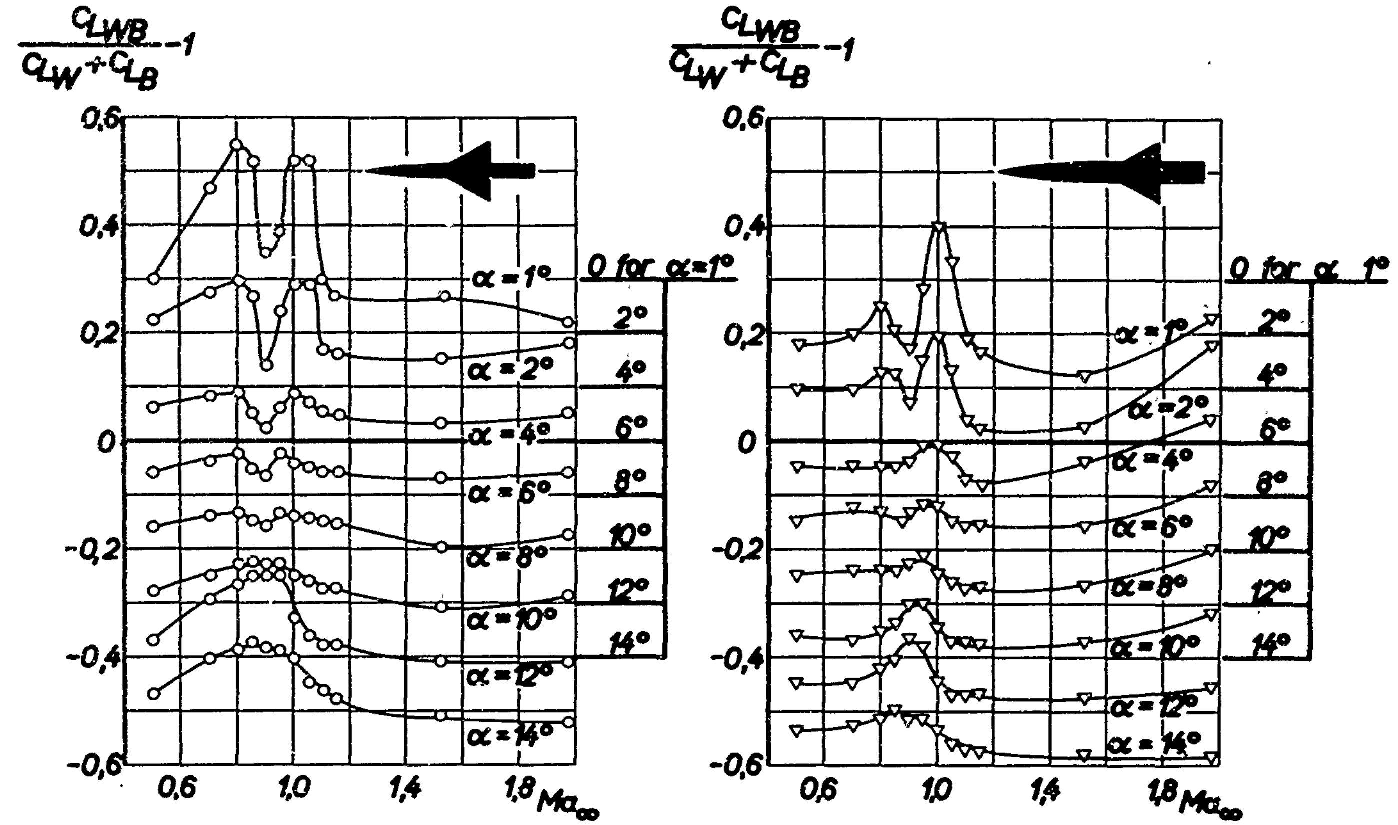

Fig. 7 ***Interference in the Lift versus Mach Number for Delta Wing-Body-Combinations***

○ W_3 B_1 ▽ W_3 B_2

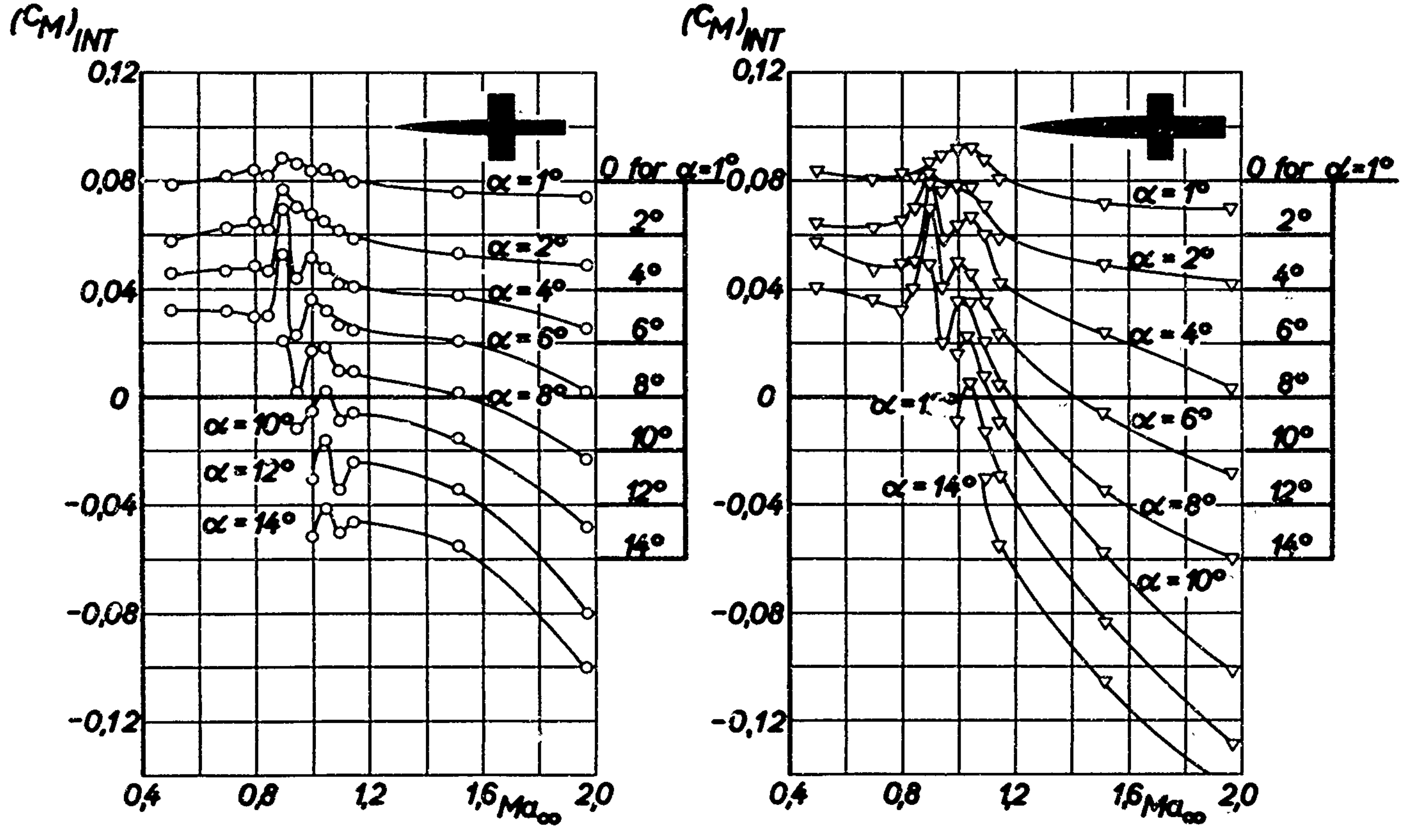

Fig. 8 Interference in the Pitching Moment versus Mach Number for Rectangular Wing-Body-Combinations

○ W_1 B_1 ▽ W_1 B_2

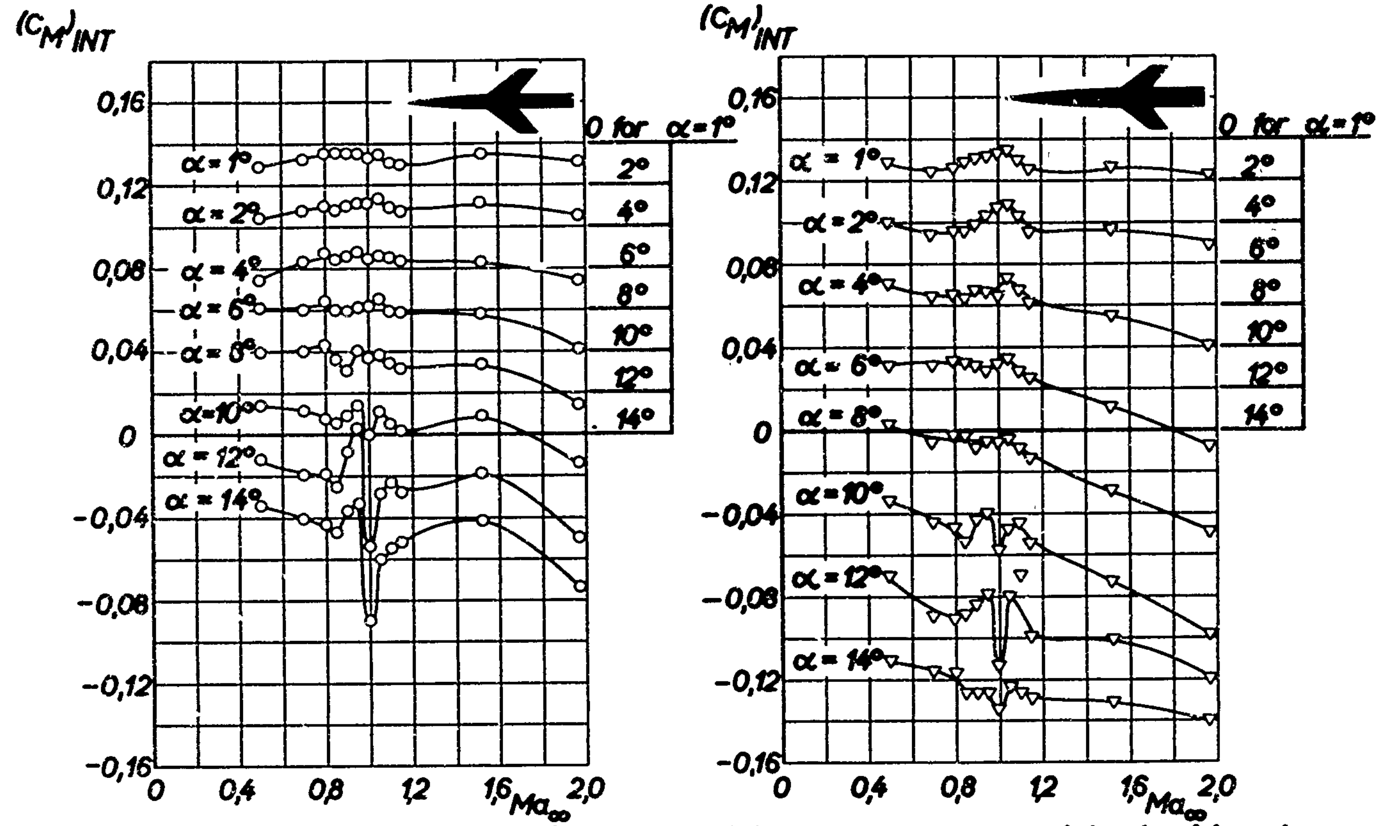

Fig. 9 Interference in the Pitching Moment versus Mach Number for Sweptback Wing-Body-Combinations

○ $W_2 B_1$ ▽ $W_2 B_2$

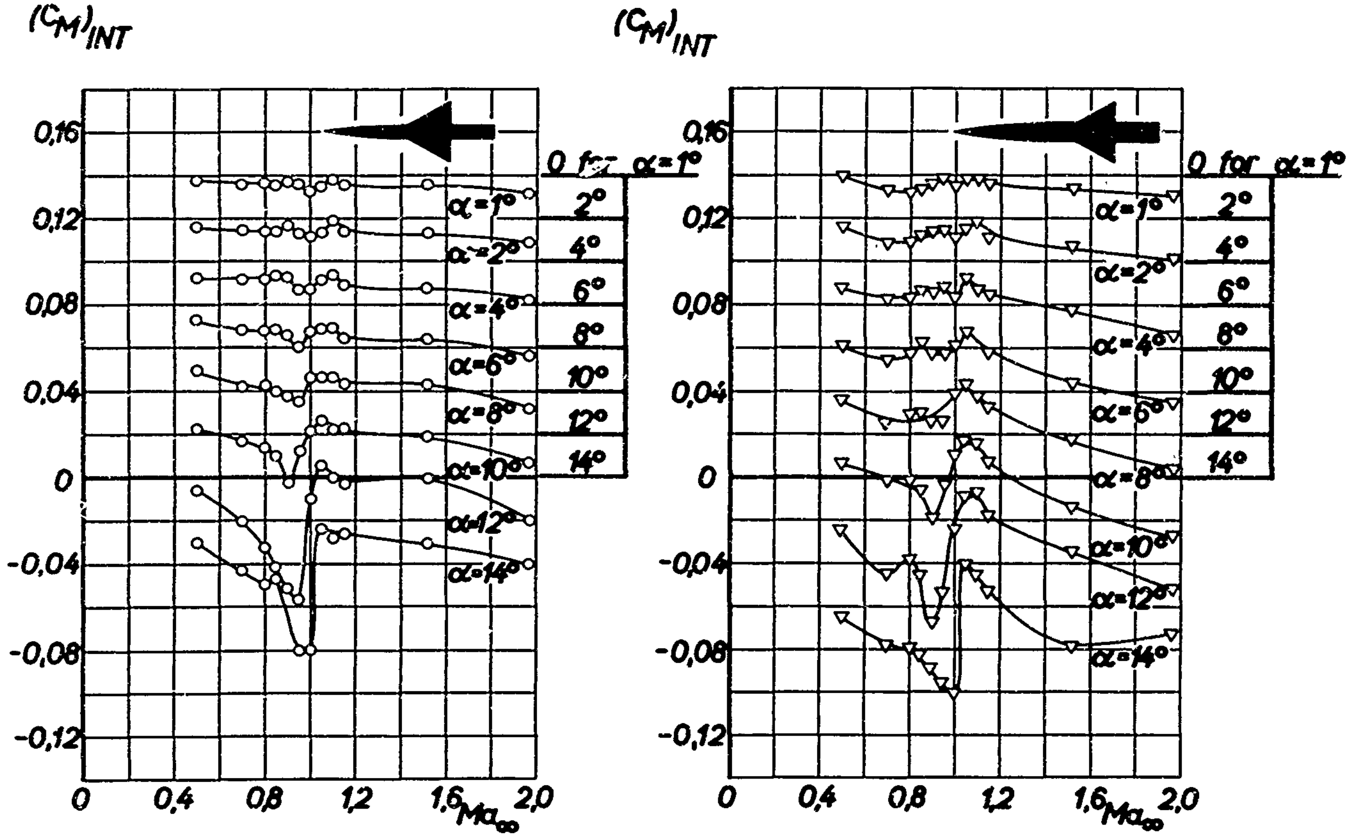

Fig. 10 Interference in Pitching Moment versus Mach Number for Delta Wing - Body - Combinations

○ W_3 B_1 ▽ W_3 B_2

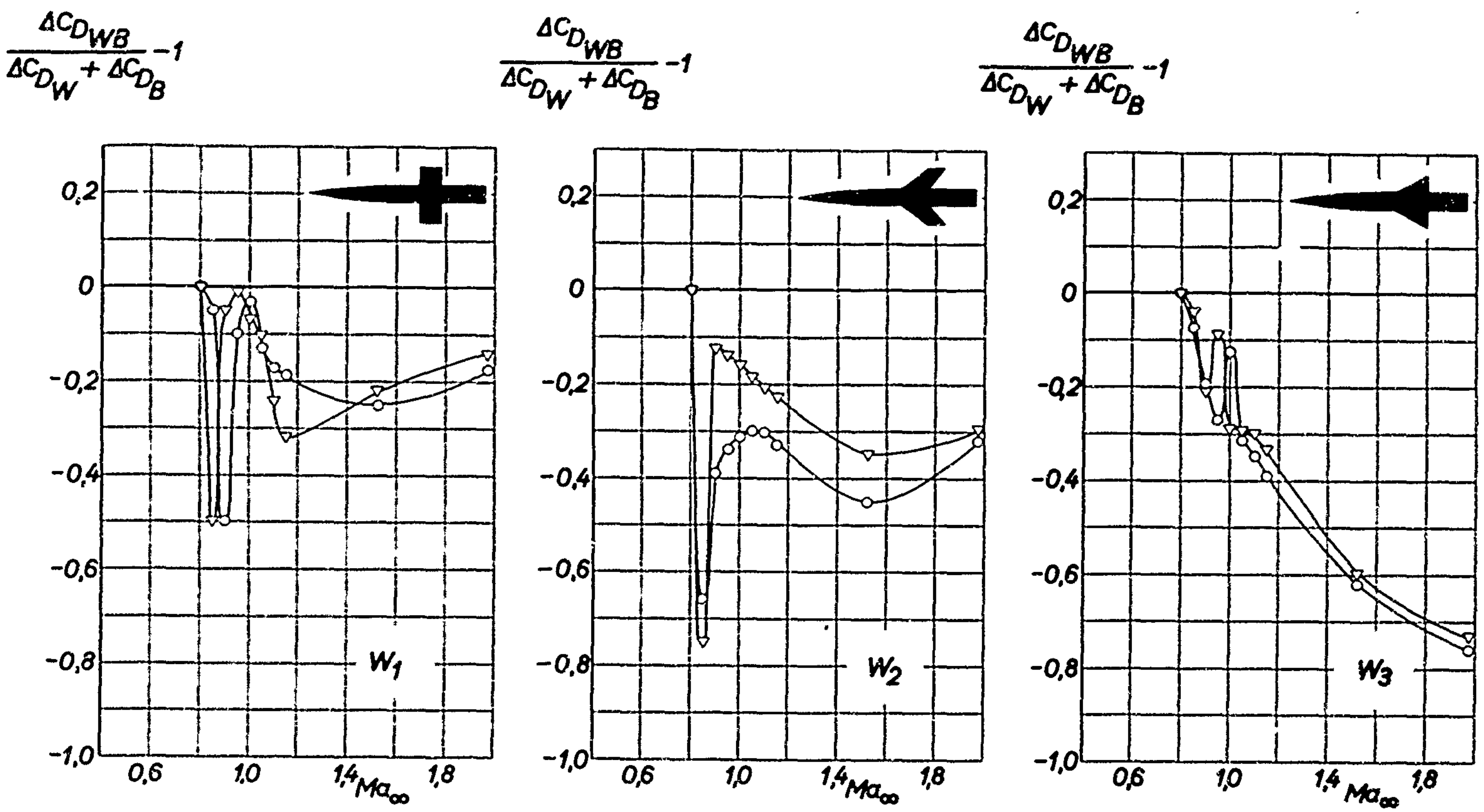

Fig. 11 Interference in the Wave Drag versus Mach Number

○ $W B_1$ ▽ $W B_2$

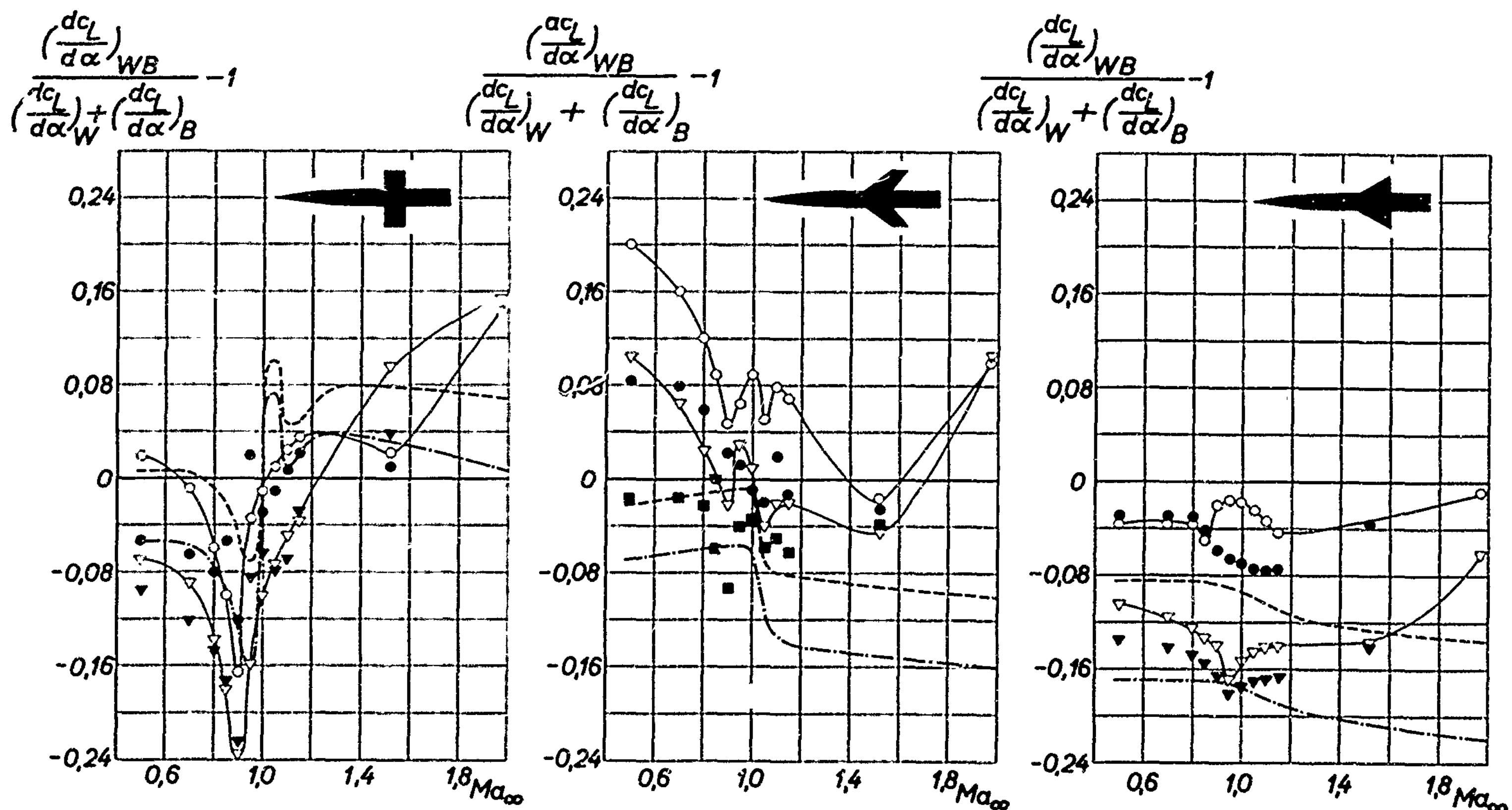

Fig. 12 Interference in the Lift Curve Slope versus Mach Number

□ W
■ W (Transition of B.L. fixed)
——— Theory W

○ W B_1
● W B_1 (Transition of B.L. fixed)
– – – – Theory W B_1

▽ W B_2
▼ W B_2 (Transition of B.L. fixed)
—·—·— Theory W B_2

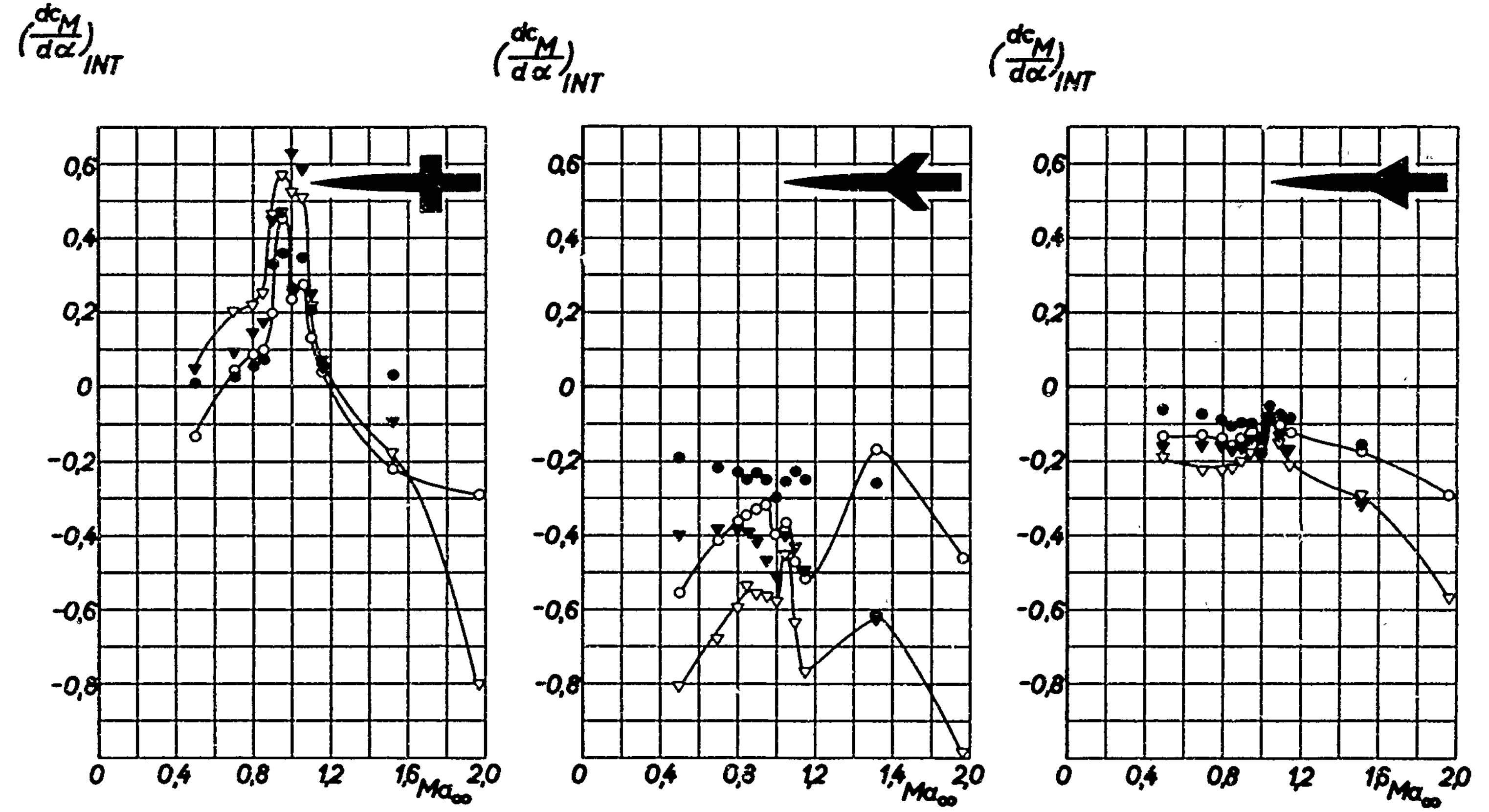

Fig. 13 Interference in the Pitching Moment Curve Slope versus Mach Number

○ W B_1

● W B_1 (Transition of B.L. fixed)

▽ W B_2

▼ W B_2 (Transition of B.L. fixed)

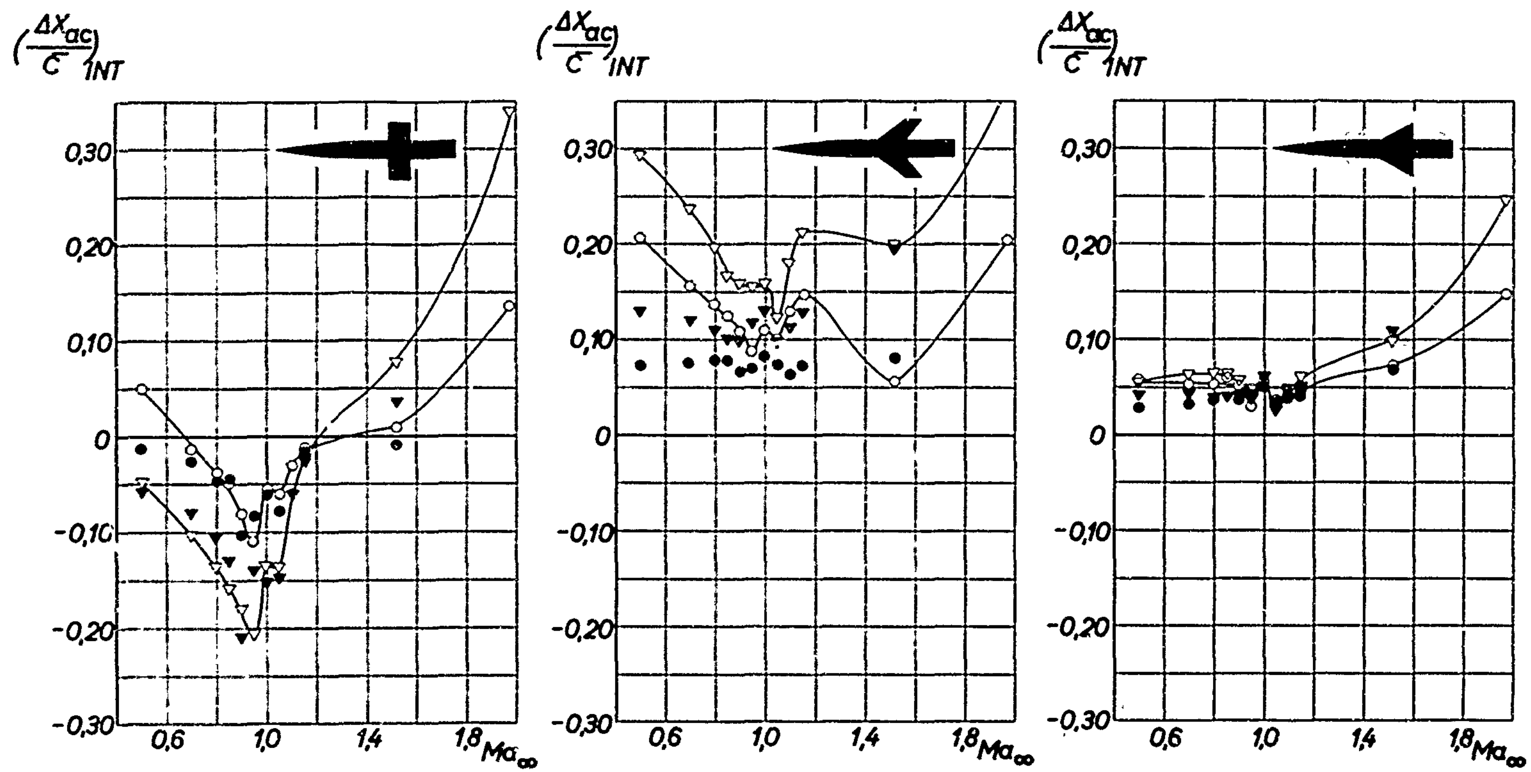

Shift of the Aerodynamic Center due to Interference versus Mach Number

○ W B_1
● W B_1 (Transition of B.L. fixed)
▽ W B_2
▼ W B_2 (Transition of B.L. fixed)

Fig. 14

EFFECT OF REYNOLDS NUMBER AND BOUNDARY-LAYER TRANSITION LOCATION ON SHOCK-INDUCED SEPARATION

By James A. Blackwell, Jr.

NASA Langley Research Center
Langley Station, Hampton, Va.

SUMMARY

A two-dimensional experimental and theoretical investigation has been conducted on an NACA 65_1-213 airfoil to determine the effect of Reynolds number and transition location on shock-induced separated flow. The experimental investigation was conducted at Mach numbers from 0.60 to 0.80, angles of attack from 0° to 4°, and Reynolds numbers from 1.5×10^6 to 16.8×10^6. Transition locations from 0.05 to 0.50 chord were utilized.

The results indicate that variation of the Reynolds number from full-scale to the usual wind-tunnel values results in substantial changes of the shock location, trailing-edge pressure recovery, and boundary-layer losses at the trailing-edge. By properly locating the boundary-layer transition point on the wind-tunnel model, full-scale results can be simulated at the usual wind-tunnel Reynolds numbers. The required location of the transition point can be predicted theoretically with acceptable accuracy by simulating the boundary-layer characteristics at the airfoil trailing-edge.

EFFECT OF REYNOLDS NUMBER AND BOUNDARY-LAYER TRANSITION LOCATION ON SHOCK-INDUCED SEPARATION

By James A. Blackwell, Jr.
NASA Langley Research Center
Langley Station, Hampton, Va.

INTRODUCTION

The correlation of data obtained at the usual wind-tunnel values of Reynolds number on wind-tunnel scale models and of data obtained during flight tests at much higher Reynolds numbers indicates that at speeds where substantial shock-induced separation is present scale effects may occur. In particular, a large Reynolds number difference may affect the shock-wave location on the model and the presence and extent of shock-induced separation. An example of the problem or a large transport airplane is shown in figure 1, reproduced from reference 1. A recent investigation into the nature of these scale effects and their minimization has resulted in a wind-tunnel technique that provides good agreement between flight and wind-tunnel data for the conditions investigated. The technique consists basically of properly locating the point of boundary-layer transition on the wind-tunnel model. This paper will discuss the results of this investigation.

The basic phenomena of scale effects at speeds where shock-induced separation is present are illustrated schematically in figure 2. In flight, at large Reynolds numbers, the boundary layer becomes turbulent near the airfoil leading edge. At transonic Mach numbers, a shock wave forms and moves rearward with increasing Mach number. When the shock is sufficiently strong, the shock induces the boundary layer to separate, hence, the term "shock-induced separation." Presently for most wind-tunnel investigations, the boundary layer is made turbulent near the leading edge of the airfoil with a boundary-layer transition trip. Since the difference in wind-tunnel and flight Reynolds numbers may be large and the relative thickness of the turbulent boundary layer varies inversely as approximately Reynolds number to the 1/5 power, the relative thickness at any given percent chord station is greater on a small-scale wind-tunnel model with transition fixed near the leading edge than on a similar full-scale wing with nautral transition near the leading edge in flight. Due to the greater thickness of the wind-tunnel boundary layer, the flow separates at a lower Mach number and is more severe than in flight. The greater displacement of the separated flow tends to push the shock farther forward than in flight.

No general procedure has been developed for correcting wind-tunnel data to flight conditions when shock-induced separation is present. Therefore, a new experimental wind-tunnel technique is desired to minimize scale effects for these conditions. The results presented in the recent paper entitled "Wind-Tunnel-Flight Correlation of Shock-Induced Separated Flow," (ref. 1) indicate that by moving the point of transition rearward on the wind-tunnel model when the flow has separated, the shock position on the model approached the same location as on the flight airplane. Based on these results, a solution to minimize scale effects in shock-induced separated flow might lie in properly locating the boundary-layer transition position on the wind-tunnel model such that the boundary layer encountered in flight is simulated on the wind-tunnel model in the region of separation.

In order to obtain a better understanding of the factors involved in minimizing the effects of Reynolds number when shock-induced separated flow is present by moving the boundary-layer transition point rearward, a comprehensive two-dimensional wind-tunnel experimental and theoretical investigation has been conducted over a wide range of Reynolds numbers with varying transition location. The results of this investigation will now be presented. It should be emphasized that the research on the concepts presented here is continuing on an intensive basis, and the present paper should be considered a status report rather than a final summation.

The author is indebted to R. T. Whitcomb who proposed the basic approach to this research, to A. A. Luoma who conducted the experiments, and to R. D. Samuels who assisted in the theoretical boundary-layer calculations, all of the Langley 8-Foot Tunnels Branch.

SYMBOLS

b	span of wing, ft (m)
c_l	section-lift coefficient
C_p	pressure coefficient, $\frac{p - p_\infty}{q_\infty}$
$C_{p,sonic}$	pressure coefficient corresponding to local Mach number of 1.0
c	chord of airfoil, in. (cm)
H	boundary-layer shape factor, δ^*/θ
M	free-stream Mach number
p	local static pressure, lb/ft^2 (newton/meter^2)

p_∞	static pressure in undisturbed stream, lb/ft^2 (newton/meter^2)
Δp_t	total-pressure loss, lb/ft^2 (newton/meter^2)
q_∞	dynamic pressure in undisturbed stream, lb/ft^2 (newton/meter^2)
R	Reynolds number
x	ordinate along airfoil reference line measured from airfoil leading edge, in. (cm)
α	geometric angle of airfoil reference line, deg
δ^*	boundary-layer displacement thickness, in. (cm)
θ	boundary-layer momentum thickness, in. (cm)

Subscripts

T	denotes boundary-layer transition location
W.T.	wind tunnel
F.S.	full scale

EXPERIMENTS

Wind Tunnel

The experiments were conducted in the Langley 8-foot transonic pressure tunnel. This facility is well suited to the investigation of the effects of Reynolds number on two-dimensional models at transonic speeds. The wind tunnel has solid side walls which act as end plates for the two-dimensional model. Also, substantially larger chord models may be tested in this facility than could otherwise be tested in tunnels designed for two-dimensional testing since the wind tunnel is approximately 7 feet (2.80 m) in height. Good results may be obtained in this facility for large chord models since the upper and lower walls are slotted, which allows a development of the flow field in the vertical direction approaching that for free flight. The slot opening at the position of the model was approximately 6.4 percent of the upper and lower surface walls. Further, the 8-foot tunnel is a variable-pressure tunnel which allows investigations to be conducted over a wide range of Reynolds numbers with the same model.

Model

The two-dimensional model investigated is shown in figure 3. The model was tested in an inverted position. The airfoil is the NACA 65_1-213 with $\alpha = 0.5$ mean line (fig. 4). This airfoil was selected for several reasons. It is the same shape as the midsemispan section of the T-33 airplane for which flight data are available (ref. 3). A sketch of the T-33 airplane is shown in figure 4. Since the T-33 wing is essentially unswept and has a high-aspect ratio, correlation with two-dimensional data at the midsemispan was expected to be good. The six-series airfoil was also selected because it represents a class of airfoils that have been recently used in high subsonic speed airplane design. The model chord was 3 feet (0.91 m) in length.

Transition Strips

Transition trips were located at the same position on both the upper and lower surfaces of the model. Results were obtained for transition strips located at 5, 20, 30, 40, and 50 percent chord. The strips were 0.1 inch (0.25 cm) wide consisting of carborundum grains set in a plastic adhesive. The size of the carborundum grains for each location was calculated using reference 4.

Measurements

The lift force acting on the airfoil was obtained from surface pressure measurements along the center line of the tunnel.

Drag forces acting on the airfoil were derived from vertical variations of the wake total and static pressures measured with the rake shown in figure 3; however, these results will not be presented in this paper.

The boundary-layer data presented herein were derived from measurements taken with a total head rake located at the trailing edge of the model. The total head tubes were flattened horizontally and closely spaced.

The total head and static pressures were measured with the use of electronically actuated pressure-scanning valves. The range of the gages in the valves was varied, depending on type of measurement and on the wind-tunnel conditions.

Corrections

The major effect of the wind-tunnel wall on the results presented herein is a substantial upflow at the position of the inverted model so that the real aerodynamic angle of attack is significantly less than the geometric angle. The mean value of this upflow at the midchord of the model, in degrees as determined by the theory of reference 2, is approximately 4.4 times the section-lift coefficient. For the design section-lift coefficient of 0.20, this angle deviation is approximately -0.88°. For the present investigation, where the lift has been obtained by surface-pressure measurements, this deviation has little effect on the validity of these results. It merely causes a change of the geometric angle of attack at which a given set of results are obtained. The angles of attack used in the results presented herein have not been corrected for this upflow.

The theory of reference 2 indicates the tunnel-wall blockage effect is small.

Range of Tests

The investigation was conducted over a Mach number range from 0.60 to 0.80. The angle of attack varied generally from about 0° to 4° in 1° increments. The Reynolds number of the investigation was varied from 1.5×10^6 which approximates the lowest values usually used for wind-tunnel investigations to 16.8 million, which is near the Reynolds number for which full-scale flight results were obtained on the T-33 airplane (ref. 3).

DISCUSSION

Wind-Tunnel Results

Flight wind-tunnel correlation.- A comparison of the wind-tunnel results and flight results from the T-33 airplane (ref. 3) are presented in figure 5 for a Mach number of 0.8. The flight data were obtained at a Reynolds number of 19 million based on the local chord, and the two-dimensional wind-tunnel results are presented at 16.8 million. The transition strip was fixed near the leading edge of the two-dimensional airfoil at 5 percent chord since this was thought to be representative of the natural transition location of the upper-surface flight results. The comparison shown in figure 5 and in other data not presented indicate generally good agreement between the flight results and the wind-tunnel results obtained at full-scale Reynolds numbers. Therefore, for the subsequent analysis, the wind-tunnel data taken at 16.8 million will be considered representative of full-scale results. It should be noted that for the condition presented, a small amount of shock-induced separation is present.

Effect of Reynolds number and transition location.- In figures 6 to 8, the effects of Reynolds number and transition location on the section aerodynamics are presented. The results shown indicate, first, the effect of increasing the Mach number at a constant angle of attack ($\alpha = 0^{\circ}$) from subcritical speeds to a condition with shock-induced separation and, second, of increasing the angle of attack so that shock-induced separation occurs. It is felt that these examples are representative of the data obtained during the investigation. The data presented include pressure distributions on the airfoil and profiles of the boundary-layer total head loss $\left(\frac{\Delta p_t}{q_\infty}\right)$. Results are presented for only the airfoil upper surface in order to simplify the analysis. The upper surface is generally the most critical as regards shock-induced separation; however, all conclusions reached regarding shock-induced separation on the airfoil upper surface will also apply to the lower surface.

For each comparison, three sets of data will be shown. The first set of data was obtained at 16.8 million with the transition located at 5 percent chord and represents what will be referred to as full-scale results. The second set of data represents data taken at the usual wind-tunnel Reynolds numbers of 3×10^6 with the transition fixed near the leading edge (0.05c). As previously indicated, this is the wind-tunnel technique presently in general use. The third set of data represents data obtained at wind-tunnel Reynolds numbers with the point of transition moved rearward of the leading edge to a location that best approximates full-scale results.

The results at subcritical speeds ($M = 0.70$) for an angle of attack of 0° are presented in figure 6. These results indicate that at the same transition location (0.05c) for full-scale and wind-tunnel Reynolds numbers, there are only small variations in the pressure distribution over the airfoil. However, it should be noted that the trailing-edge pressure recovery is less for the wind-tunnel Reynolds number. Also, as would be expected, the boundary-layer profiles indicate a thicker boundary layer at the airfoil trailing edge for the wind-tunnel Reynolds number. When the transition is moved rearward to the position for the best correlation of the trailing-edge pressure recovery for the high and low Reynolds number (40 percent chord), the boundary-layer profiles also are the same.

The effects of Reynolds number and transition location when the Mach number is increased from 0.70 to 0.80 at $\alpha = 0^{\circ}$ are shown in figure 7. For the full-scale case, boundary-layer separation has been induced by the strong shock wave. However, for the data obtained at a Reynolds number of 3×10^6 with the transition near the leading edge, the separation is substantially greater, the shock wave is farther forward on the airfoil, and the trailing-edge pressure is decreased. When the transition point is moved rearward at wind-tunnel Reynolds numbers, the trailing-edge pressure coefficients, the shock-wave location, and the trailing-edge boundary-layer profiles are all in good agreement with full-scale results for the transition location at approximately 45 percent chord. It should be noted that the data presented at $x_T/c = 0.45$ are interpolated from the data obtained at $x_T/c = 0.40$ and 0.50.

As another illustration of the effect of Reynolds number and transition location, data are shown for an increase in the angle of attack to 3° at a Mach number of 0.75 in figure 8. As in the previous example, good agreement is obtained between the data for the full-scale case and for wind-tunnel Reynolds numbers when the transition is moved rearward. For this case, the transition location for best agreement was at the 40-percent chord.

Based on the above results and other data not presented, it is concluded that for conditions at which shock-induced separation is present, good agreement can be obtained between full-scale data and results obtained at wind-tunnel Reynolds number with the proper location of the transition strip. However, the results also show that the transition point for the best agreement varies somewhat with changes of the test conditions.

Theoretical Analysis

To allow general utilization of the experimental approach to simulating full-scale shock-induced boundary-layer separation characteristics by moving the boundary-layer transition location, a method must be developed to predetermine the transition location for any airplane or flight condition without resort to experiments. This requires a more complete understanding of the fundamental factors governing the boundary-layer development. In order to provide some insight to this problem, a limited theoretical analysis was undertaken.

The experimental results (figs. 6 to 8) indicated that even with shock-induced separation present, the transition locations for best agreement between data at wind-tunnel Reynolds numbers and full-scale Reynolds numbers do not vary appreciably from the location for subcritical speeds (40 percent chord). It therefore appeared that a theoretical analysis based on subcritical pressure distributions and boundary-layer theory might be applicable. Various theories (refs. 5 to 8) were considered for the boundary-layer analysis. It was found that the results were not significantly different using the theories investigated. For the following study, the boundary-layer calculations will be based on reference 5 for the laminar portion and reference 8 for the turbulent portion.

Theoretical boundary-layer characteristics for subcritical condition.- In figure 9, theoretical boundary-layer characteristics (δ^* and H) are presented using the above-mentioned theories for the subcritical pressure distribution of figure 6. Data are presented for the conditions representing the full-scale results and the wind-tunnel results with the transition located at 5 percent and 40 percent chord, the 40-percent chord transition location being the experimental condition for best wind-tunnel-full-scale correlation of the trailing-edge pressure recovery and boundary-layer profiles. It may be seen that at the trailing edge the theory also provides a good agreement of the boundary-layer characteristics.

For the distribution of the theoretical displacement thickness over the chord, it is obvious that the δ^* distribution at the wind-tunnel Reynolds numbers with transition at 40 percent chord is a good approximation to the displacement thickness at full-scale Reynolds numbers over the critical rear portion of the airfoil. The large effect of Reynolds number and transition location on the boundary-layer characteristics is indicated by comparing the full-scale results and wind-tunnel Reynolds number results at $x_T/c = 0.40$ with the wind-tunnel Reynolds number characteristics for the transition located at 5 percent chord.

On the right side of figure 9, the theoretical boundary-layer-shape factor (H), which indicates the boundary-layer separation characteristics, is presented over the rear portion of the airfoil. With the transition located at 40 percent chord for wind-tunnel Reynolds numbers, the data indicate the full-scale separation characteristics are adequately simulated over the rear portion of the airfoil; in particular, they are matched at the airfoil trailing edge. This is significant since the oil-flow photographs taken during the investigation indicate the shock-induced boundary-layer separation originates at the airfoil trailing edge and not at the shock wave. The shape factor indicates the flow for the transition located at 5 percent for wind-tunnel Reynolds numbers to be substantially nearer separation than for the full-scale results.

Basic criteria.- Since separation does occur initially at the trailing edge experimentally, in the theoretical analysis the assumed criteria for best wind-tunnel-full-scale correlation will be to match the boundary-layer characteristics at the airfoil trailing edge. Further, since the primary interest is separation, the values of H are made equal. Throughout the following analysis this approach will be referred to as the "trailing-edge criteria."

Theoretical variation of transition location with Mach number and pressure distribution.- The transition locations obtained experimentally (figs. 6 and 7) varied as the free-stream Mach number was increased to supercritical speeds for a constant angle of attack. Therefore, it appears that the transition location for best wind-tunnel-full-scale correlation might be sensitive to the free-stream Mach number or to the change of the shape of the pressure distribution as Mach number is increased. In order to determine the sensitivity of the transition location, theoretical calculations were made for a range of pressure distributions for various Mach numbers. The pressure distributions considered are shown in figure 10. The primary variables are (1) shape of leading-edge pressure distribution, (2) trailing-edge pressure, and (3) shape of the aft end pressure recovery. The shape for the pressure distribution with the favorable gradient over the forward portion of the airfoil is typical for near-zero lift conditions such as obtained in a dive. The rooftop pressure distribution represents the conditions generally expected in flight at the higher lift conditions. The variations of the pressure distributions over the aft portion of the airfoil are similar to those noted experimentally on various types of airfoils.

Using the subcritical pressure distributions shown in figure 10, the transition locations were calculated theoretically for various Mach numbers with a full-scale Reynolds number of 16.8×10^6 and a wind-tunnel Reynolds number of 3.0×10^6. The results indicated very little effect of Mach number on transition locations (less than 1 percent). Also, the small effect of Mach number on the transition location appears to be independent of the pressure distribution, since the same conclusions as obtained for the present analysis may be reached using flat-plate theory of reference 9.

The effect of the changes in pressure-distribution shape on transition location have been calculated for a Mach number of 0.70 and are presented as vertical lines on the horizontal scale of figure 10. On the basis of this limited analysis, it can be seen that the changes in the shape of the pressure distributions over the forward part of the airfoil produce significant variations in the theoretical transition locations. However, the changes in the aft end distributions have only slight effects on these locations.

An analysis of the basic factors involved suggests that the primary influence on the theoretical transition location is the variation of the pressure gradient in the region of transition shift; that is, where the boundary layer is turbulent for the full-scale Reynolds number case and laminar [illegible] wind-tunnel Reynolds number condition. This conclusion is strengthened by the fact that flat-plate theory for momentum thickness (ref. 9) predicts generally the same transition locations (0.[illegible] chord) as that calculated for the flat or "rooftop" forward pressure distribution.

Comparison of Experimental and Calculated Results

The preceding theoretical analysis suggests that for conditions where severe shock and separation is not present, at least, correlation of experimental and calculated transition locations at wind-tunnel Reynolds numbers might be achieved when the pressure gradients over the region of transition shift are similar. For the $M = 0.70$, $\alpha = 0^\circ$ experimental case (fig. 6) the pressure gradient over the region of transition shift is similar to that for the schematic distribution of the theoretical analysis as shown by the dashed line on the left side of figure 10. The best experimentally determined transition location (0.40 chord) is the same as the calculated position.

Cases where substantial shock and separation is present will now be considered. For the $M = 0.75$, $\alpha = 3^\circ$ experimental case (fig. 8) the pressure gradient over the region of transition shift is also similar to that of the dashed line on the left side of figure 10. Again, the best experimental transition location is the same as that calculated (0.40 chord). For the $M = 0.80$, $\alpha = 0^\circ$ experimental condition (fig. 7), the pressure gradient from 0.05 to 0.45 chord is similar to that for the solid line of the theoretical analysis. Again, the experimental transition location (0.45 chord) is the same as the calculated value. In these two cases, correlation is achieved even though the nature of the actual flow is substantially different from the assumptions of the theory used for the calculations. These reasons for this agreement are not yet fully understood.

Application

The agreement of the calculated and measured transition locations for simulating full-scale characteristics suggests that the theoretical "trailing-edge criteria" is a reasonable approach to the prediction of the transition location. This agreement further indicates that in the calculations only the pressure gradient over the region of transition shift need be considered.

Effect of ratio of wind-tunnel Reynolds number to full-scale Reynolds number.- In order to indicate the variation of the theoretical transition location on the wind-tunnel model for various full-scale Reynolds numbers, figure 11 is presented based on a wind-tunnel Reynolds number of 3 million. Theoretical calculations indicate that only small variations occur (order of 1 percent) in the results shown for realistic changes in the reference wind-tunnel Reynolds number for a given Reynolds number ratio. Variations representing the two extremes of pressure gradients over the forward portion of the airfoil in figure 10 are shown. Also shown in figure 11 is the transition location curve calculated using flat-plate theory for momentum thickness (no pressure gradient).

Effect of variations of transition location from the optimum.- In conducting a wind-tunnel test, it is not always convenient or practical to change the transition location with a change of test conditions. Therefore, an attempt has been made to assess the effects of varying from the optimum transition location. An indication of the effects is provided by cross-plots of the experimental data obtained for various locations. For the cases where shock-induced separated flow is present, a change in the transition of 5 percent chord produces a movement in the shock wave of approximately 1 percent chord.

Limitations of applicability.- Certain comments as to the limitations of the applicability of the method are warranted. Since laminar flow must be maintained ahead of the transition strip, the method is limited to classes of pressure distributions that do not have severe leading-edge peaks at supercritical speeds that would result in natural boundary-layer transition ahead of the transition strip. It should also be noted that the model must be maintained absolutely smooth in front of the transition strip to prevent transition of the boundary layer.

Results of a number of investigations conducted in the 8-foot transonic pressure tunnel have indicated that, when the transition is rearward as specified by the proposed criteria and a strong adverse gradient is present ahead of the transition, more severe boundary-layer separation may be present than when the transition is in the normal location near the leading edge. For such conditions, more applicable results are obtained with the transition forward.

Results not presented indicate that when the transition strip is just ahead of the base of the shock, laminar separation occurs ahead of the transition strip. Thus, the maximum rearward movement for which applicable results can be obtained is limited. For the airfoil of the present investigation, the limit is approximately 50 percent chord.

Further Study

In addition to the results presented herein, considerable effort is being devoted to further analyzing the great body of data obtained during this investigation. Also, work is planned in two additional areas. One, the extension of the present two-dimensional method to the three-dimensional cases, and second, a study of the applicability of the technique to the proper simulation of full-scale buffet characteristics.

CONCLUDING REMARKS

A two-dimensional experimental and theoretical investigation has been conducted for an NACA 65_1-213 airfoil to determine the effect of Reynolds number and transition location on shock-induced separat ^ low. The results have led to the following conclusions:

1. Variati the Reynolds number from full-scale to the usual wind-tunnel values results in substantial chang the shock location, trailing-edge pressure recovery, and boundary-layer losses at the trailing e.

2. By properly locating the boundary-layer transition point on the wind-tunnel model, full-scale results can be simulated at the usual wind-tunnel Reynolds numbers.

3. The required location of the transition point can be predicted with acceptable accuracy by theoretically simulating the boundary-layer characteristics at the airfoil trailing edge. In this procedure, only the surface pressure gradient in the region where the boundary layer is turbulent for the full-scale Reynolds number and laminar for the wind-tunnel Reynolds number need be considered.

REFERENCES

1. Loving, Donald L.: Wind-Tunnel-Flight Correlation of Shock-Induced Separated Flow. NASA TN D-3580, 1966.

2. Davis, Don D.; and Moore, Dewey: Analytical Study of Blockage- and Lift-Interference Corrections for Slotted Tunnels Obtained by the Substitution of an Equivalent Homogeneous Boundary for the Discrete Slots. NACA RM L-53E07b, 1953.

3. Brown, Harvey H.; and Clousing, Lawrence A.: Wind Pressure-Distribution Measurements up to 0.866 Mach Numbers in Flight on a Jet-Propelled Airplane. NACA TN-1181.

4. Braslow, Albert L.; and Knox, Eugene C.: Simplified Method for Determination of Critical Height of Distributed Roughness Particles for Boundary-Layer Transition at Mach Numbers From 0 to 5. NACA TN-4363, 1958.

5. Schlichting, Hermann (J. Kestin, Trans.): Boundary-Layer Theory. McGraw-Hill Book Co., Inc., 1955, Chapter 15, pp. 355-363.

6. Bennett, J. A.; and Goradia, S. H.: Methods for Analysis of Two-Dimensional Airfoils With Subsonic and Transonic Applications. Lockheed-Georgia Company report number ER-8591, July 1966.

7. Truckenbrodt, E.: A Method of Quadrature for Calculation of the Laminar and Turbulent Boundary Layer in Case of Plane and Rotationally Symmetrical Flow. NACA TN-1379, May 1955.

8. Nash, J. F.; and Macdonald, A. G. (Miss): The Calculation of Momentum Thickness in a Turbulent Boundary Layer at Mach Numbers up to Unity. C.P. No. 963, British A.R.C., 1967.

9. Sommer, Simon C.; and Short, Barbara J.: Free-Flight Measurements of Turbulent-Boundary-Layer Skin Friction in the Presence of Severe Aerodynamic Heating at Mach Numbers From 2.8 to 7.0. NACA TN-3991, 1955.

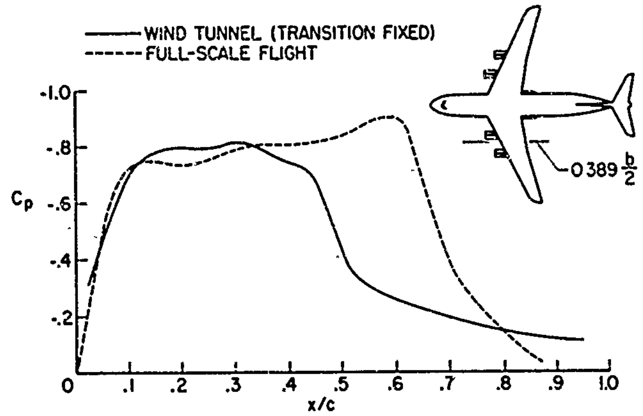

Figure 1.- Supercritical pressure distribution. $M = 0.85$; $\alpha_r \approx 0^{\circ}$.

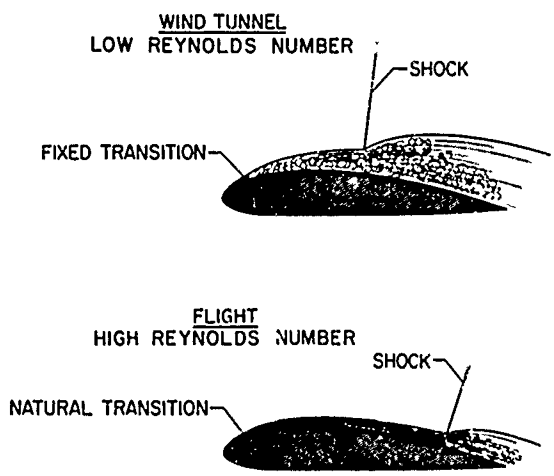

Figure 2.- Effect of boundary layer on shock-induced separation.

Figure 3.- Wind-tunnel installation of two-dimensional model.

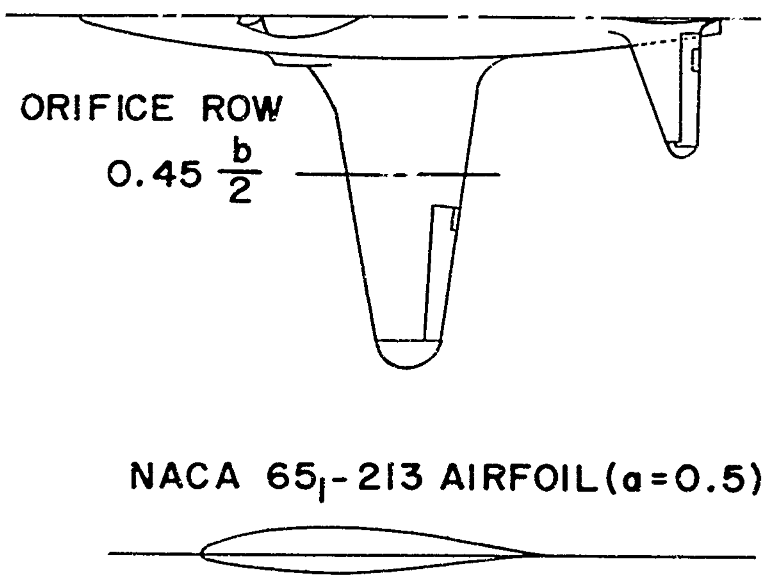

Figure 4.- Flight configuration.

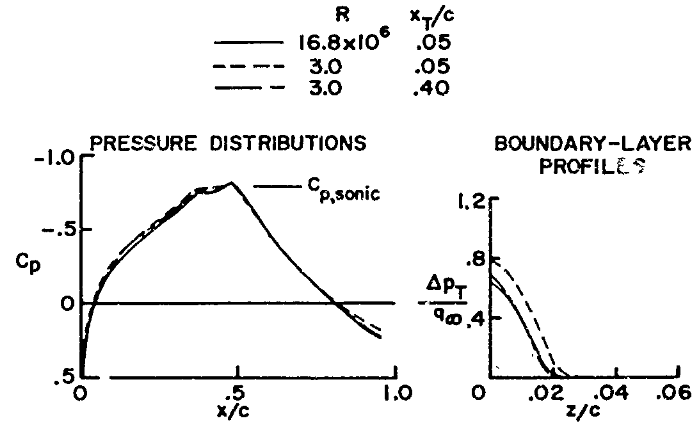

Figure 6.- Effect of R and transition location. $M = 0.70$; $\alpha = 0^{\circ}$.

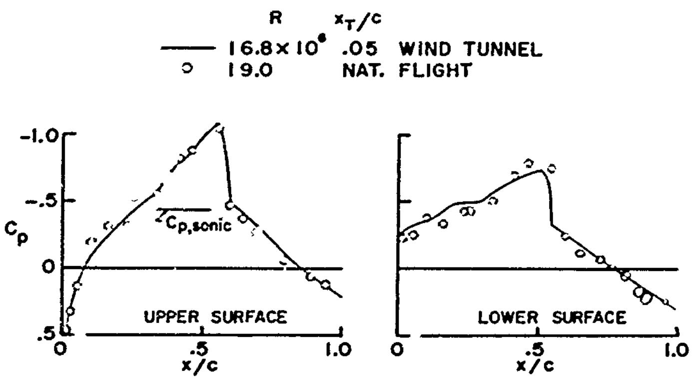

Figure 5.- Correlation of wind-tunnel-flight results. $M \approx 0.80$; $c_l = 0.056$.

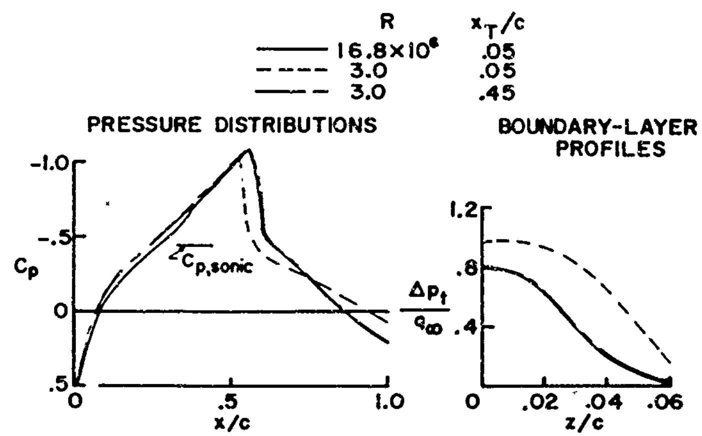

Figure 7.- Effect of R and transition location. $M = 0.80$; $\alpha = 0^{\circ}$.

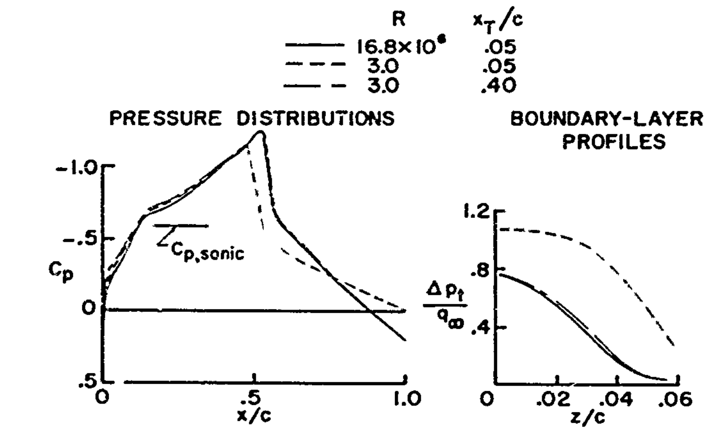

Figure 8.- Effect of R and transition location. M = 0.75; $\alpha = 3^{\circ}$.

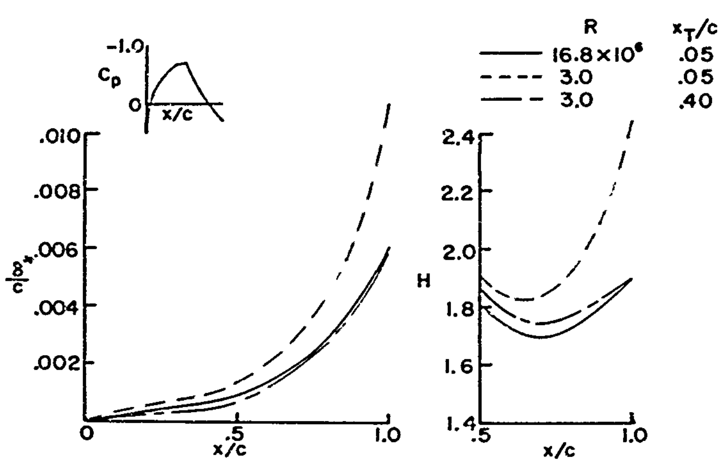

Figure 9.- Theoretical boundary-layer characteristics. M = 0.70; $\alpha = 0^{\circ}$.

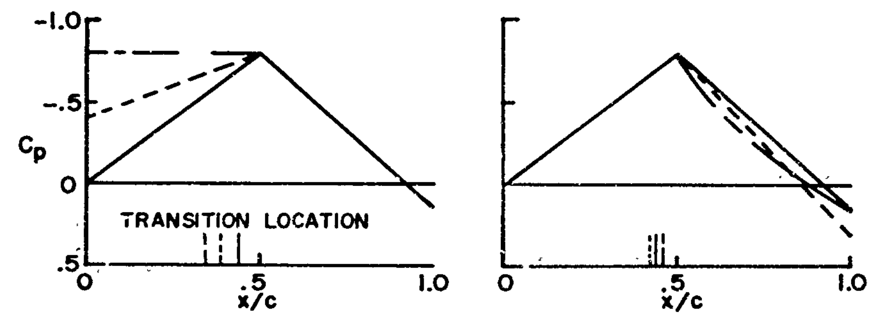

Figure 10.- Effect of pressure distribution on theoretical transition location. M = 0.70.

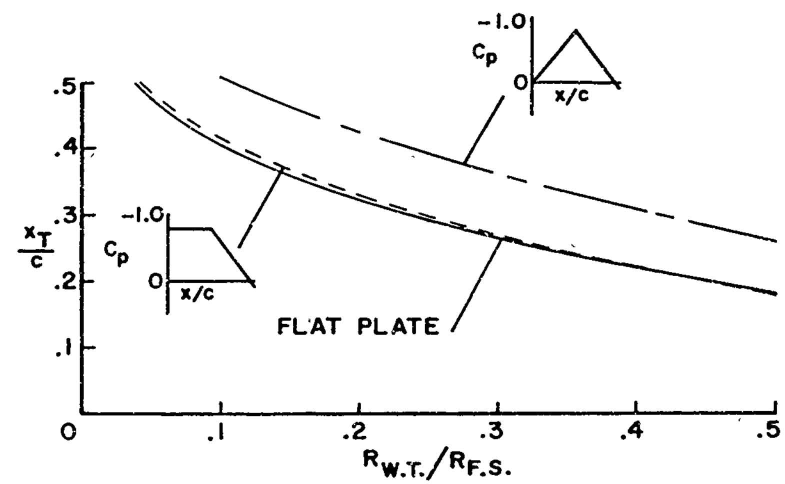

Figure 11.- Effect of Reynolds number on theoretical transition location. M = 0.70; $R_{W.T.} = 3 \times 10^6$.

WIND TUNNEL EXPERIMENTS ON THE INTERFERENCE BETWEEN A JET AND A WING AT SUBSONIC SPEEDS

by

J. A. Bagley

Royal Aircraft Establishment, Farnborough

In most wind-tunnel experiments on complete aircraft models it is not possible to represent the engine jet flow. A series of experiments are reported in this note in which the influence of a blown jet, simulating the exhaust stream of a fan-jet engine, on the pressure distribution on an adjacent wing has been measured. A brief survey is given of the effects of flight Mach number, jet pressure ratio, vertical and horizontal spacing between engine nacelle and wing, and shape of the nacelle, on the incremental wing pressures due to the jet. The possibility of representing the blown jet by a solid body extending behind the nacelle is also discussed.

1 INTRODUCTION

Many current design proposals for large transport aircraft have large engines of high bypass ratio mounted on short pylons beneath wings of about 25° or 30° sweepback. The engines have a front fan, and the annular fan nozzle is fairly close to the wing leading edge. With such an arrangement, it is possible that the jet flow passing close to the wing has a significant influence on the wing pressure distribution, and on the lift and drag. To measure such effects on a complete model of the aircraft at high subsonic speeds is very difficult, and most wind-tunnel tests are therefore made with the engines represented by simple open "flow nacelles", in which only the external geometry of the engine nacelle is represented and no attempt is made to simulate the jet flow.

The experiments described in this paper were an attempt to find out, using a simpler apparatus, whether jet interference effects are likely to be large for an engine installation similar to that on current large subsonic transport aeroplanes, or whether the conventional wind-tunnel model without jet will still give a satisfactory representation.

An aircraft of this type will normally be designed to have a subsonic type of flow over the wing, with straight isobars and a chordwise pressure distribution of the type shown in Fig.1. This has a "roof-top" shape, with a flat plateau over the front part of the section with near-sonic local velocities and a fairly steep pressure recovery behind it. A fairly thick section is normally used, and the lower surface velocities are likely to have a fairly high peak around mid-chord, as shown. There are three places where any alteration of this pressure distribution in the presence of the jet may lead to particular problems:

(1) around the nose, which has been carefully shaped to develop a favourable supersonic peak as incidence or speed increases,

(2) around mid-chord on the lower surface, where any further increase in local velocities may well lead to the formation of shocks;

(3) towards the rear of the lower surface, where any increase in the adverse pressure gradient may lead to flow separation.

2 FIRST SERIES OF EXPERIMENTS

All these problems could be investigated using an unswept wing, and the model shown in Figs.2 and 3 was therefore constructed. For the majority of the tests, a wing of 10 inches span and 5 inches chord was used which had been tested in a smaller tunnel at N.P.L. This was mounted between end plates as shown, and carried on a box framework from the traversing gear of the 2½ft X 1½ft Transonic Tunnel The pressure holes on this wing were distributed across the middle 4 inches of the span, so it was necessary to traverse the wing past the jet to obtain a complete chordwise pressure distribution. Tests were made at a Reynolds number of about one million (based on chord length) over a range of Mach numbers from 0.6 to 0.74.

The engine nacelle and jet were represented in these tests by the pipe shown, coming from the settling chamber of the tunnel and terminating in a double nozzle simulating the two nozzles of a bypass engine. A fairly thick boundary layer develops along the jet tube, and this is reduced in thickness by applying suction through the slots shown. Both nozzles were supplied by a common air supply, as shown in Fig.4, and were arranged to choke at the exit, so the flow from the nozzles exhibits the characteristic pattern of alternating expansion waves and shocks shown in Fig.5. Note here that the flow pattern expands with increasing jet pressure ratio in the usual way. The jet pipe and wing were mounted quite separately in the tunnel, and no attempt was made to represent a pylon.

The displacement flow around the jet pipe itself modifies the wing pressures, so the influence of the jet is measured by comparing pressures measured on the wing when the jet is blown at a prescribed pressure ratio (appropriate to the type of engine being simulated) with the pressures measured when the jet total head is equal to that of the free stream. This latter condition corresponds to that obtained with a free flow nacelle in a conventional model test.

A typical experimental result* is shown in Fig.6, at a jet pressure ratio of 2.4 (corresponding to an engine of bypass ratio about 5) and for a wing-nacelle spacing appropriate to an airbus type of aeroplane with short fan cowls. The Mach number $M_0 = 0.7$ gives approximately local sonic velocity at the peak velocity on the upper surface, so corresponds essentially to the design condition at higher Mach number on a swept wing. (As will be seen later, the phenomena under discussion do not seem to change significantly over a fairly wide range of subsonic Mach numbers.)

It is immediately obvious that the jet has had very little influence on the upper surface pressures, although the presence of the jet pipe has changed them somewhat This conclusion, that there is virtually no jet interference on upper surface pressures, was confirmed throughout the whole range of configurations tested, so the upper surface will not be mentioned again.

Turning to the lower surface, it is clear that in this case there is no significant increase in the peak suction and little if any change in the adverse pressure gradient over the rear part of the section. The peak has been moved forward by the combined effects of the jet and the displacement flow around the jet pipe, and on a swept wing this would imply some change in isobar sweepback, but for this case no serious problems would be anticipated. The pressure increments due to the jet flow do not exceed $\Delta C_p = \pm 0.1$, and the change in sectional lift coefficient is only about $\Delta C_L = 0.02$.

The results of this first test are rather comforting to the wind-tunnel engineer, suggesting that the use of free-flow nacelles on his complete models should not give misleading answers (at least in this context), but it seems desirable to explore the influence of various changes. In the next few figures we show ΔC_{pj} - the difference in lower surface pressures when the jet is blown at the prescribed pressure ratio and those when its total head is equal to the free-stream. Fig.7 shows the results for the datum configuration (with $Y/D_e = 0.44$, $Z/D_c = 0.29$) at several free-stream Mach numbers, and it is clear that there is only a small increase in ΔC_{pj} over this range of free-stream Mach numbers, although the local Mach number at the peak varies from $M_\ell = 0.85$ to 1.2

Fig 8 shows the effect of moving the nacelle vertically closer to the wing, and as might be expected there is a change in magnitude of ΔC_{pj}, but a remarkably constant shape of curve is obtained For the closest position, the peak again represents a locally sonic

*The experimental results are more fully reported in Ref.1

velocity, and it would hardly be possible to ignore this amount of jet interference. However, this position seems to be closer to the wing than any aircraft design published so far.

Fig.9 shows the influence of increasing the jet pressure ratio, and exactly the same pattern appears as in Fig.8. As jet pressure increases, the magnitude of ΔC_{pj} increases, but the shape of the curve remains virtually constant until at $H_j/p_o = 4$ the rear peak seems to be somewhat broader. This seems a rather surprising result – the pattern of alternate compression and expansion waves in the jet lengthens as jet pressure ratio increases, and it might be expected that this would be shown up by an expanding pattern of peaks and troughs in ΔC_{pj} on the wing.

For the wing-nacelle configurations so far considered, the first peak in ΔC_{pj} falls on a part of the wing chord where the velocities on the isolated wing are no higher than the free-stream velocity. In Fig.10 is shown an example where the peak suction of the interference field falls on a part of the wing where the velocity is already high, and the interference effects are thereby magnified. The nacelle was moved back by about 25% chord, so that the annular fan nozzle now lies behind the wing leading edge (probably a rather unlikely position in practice). The peak suction of the interference field has moved back (but only about half as much as the nacelle movement) and now falls on top of the suction peak of the basic wing pressure distribution. The interference is magnified considerably, and might now be a serious problem to the aircraft designer.

Before discussing some further work which was done in the search for an explanation of these observations, it is worth mentioning one technique which has been used in some wind-tunnel experiments to simulate the effects of a blown jet. The jet is represented by a solid extension of the nacelle, in the hope that the displacement flow about a suitable solid body will be similar to the displacement flow around the jet. To check this point, in one test the blown jet was replaced by a solid body extending some distance behind the wing trailing edge, as shown in Fig.4. Measurements showed that the jet from the annular nozzle followed closely the contour of the centre body, and expanded at only about 1° behind this (confirmed by Lawrence's measurements[3] of the expansion of a similar flow with cylindrical afterbody), so the shape of the solid body was made to represent a constant area jet. The "jet interference" on the wing with this solid body is shown in Fig.11 for two cases, compared with ΔC_{pj} due to the real jet. It is obvious that there is little or no resemblance between the two curves, and it seems very doubtful whether this technique of jet simulation has any validity.

3 SECOND SERIES OF EXPERIMENTS

With the experimental rig shown in Figs.2 and 3, it was impossible to make schlieren or shadowgraph observations of the flow. These seemed to be desirable, so a new wing was made to span the width (30 inches) of the tunnel. For this purpose the slotted sidewalls were replaced by solid glass walls. The wing section chosen was slightly different to the previous one, and for various reasons the wing chord was increased from 5 to 6 inches. The jet tube was unchanged.

Fig.12 shows a comparison of ΔC_{pj} for the new configuration and the previous one. The horizontal coordinate has been measured in terms of the fan nozzle diameter (which remained constant) rather than wing chord. It is seen that there is considerable similarity in the shape of the interference curve and in the magnitude of the front peak; the rearward peak is somewhat smaller. Fig.13 shows the corresponding schlieren picture of the flow at $H_j/p_o = 2.4$, whilst Fig.14 shows the flow pattern at $H_j/p_o = 2.9$. These begin to show why in the earlier tests there was little change in the shape of the interference curve: although the pattern of shocks in the jet on the far side of the nozzle expands with increasing jet pressure ratio in the conventional way, on the side of the jet near the wing the shocks are apparently "fixed" by the influence of the wing. This leads to a lack of symmetry in the jet behind the second nozzle, which is evident in Fig.13.

Fig.15 shows the values of ΔC_{pj} obtained for this nozzle position, compared with those obtained for a much closer position. In the second case the pressure increments increase considerably with increasing jet pressure ratio, and the peaks tend to move rearwards at the same time. Here it seems that the pattern of shocks and expansions in the jet is directly influencing the wing pressure distribution Although the wing is not fully immersed in the jet (as schlieren photographs show), the jet interference seems to be different in character from that in the earlier examples. It is suggested that there may well be a critical spacing between wing and nacelle, below which the jet directly influences the wing, as here; this minimum spacing may be larger at higher jet pressure ratios.

At this point of the investigation, it seemed likely that the shape of the nacelle afterbody might have a controlling influence on the shape of the jet interference curve – the main suction peak in ΔC_{pj} seemed to occur just behind the narrowest part of the gap between the wing and nacelle, for example. As the latest trend in engine design is towards longer fan cowls and correspondingly short afterbodies, the centre-body of the jet nozzle was shortened as shown in Fig.16. The fan nozzle is unchanged, and is in the same position relative to the wing.

As anticipated, this change makes a very marked alteration in the interference pressure curve, Fig.17. The main suction peak now appears further back, and is a little higher than with the previous nozzle. There is the same effect with increasing jet pressure ratio that the shape of the curve is almost constant but the magnitude of ΔC_{pj} increases, this seems even more surprising in the present case For the datum jet pressure ratio $H_j/p_o = 2.4$ the peak value of ΔC_{pj} is only a little higher than it was in Fig.15, but because this is superimposed on the suction peak of the wing field there is a "magnification" of the pressure increment with increasing jet pressure ratio as occurred in earlier cases when the two suction peaks coincided.

4 CONCLUSIONS

The investigation reported here has been rather limited in scope, and general conclusions must be rather tentative. Fuller details of the experiments are reported in Refs.1 and 2, these results have been taken into account in reaching the conclusions listed below. All these points refer specifically to aircraft of small or moderate sweepback operating at subcritical Mach numbers and with engines of fairly high bypass ratio for which the ratio of engine diameter to wing chord is around $^1/_3$.

(1) Except when the jet is very close to the wing, it has no significant effect on the pressures on the upper surface.

(2) When the vertical spacing between the fan jet nozzle and the wing leading edge is less than about one-fifth of the nozzle diameter, the jet-induced pressures on the wing are markedly dependent on jet pressure ratio, and the wing can be regarded as being immersed in the jet. This limiting spacing increases with increasing jet pressure ratio.

(3) When the vertical spacing between wing and jet is greater than this limit, the shape of the incremental pressure distribution on the wing, ΔC_{pj}, is characteristic for a particular nozzle and afterbody configuration and fore-and-aft location relative to the wing. The magnitude of ΔC_{pj} increases as the jet is brought closer to the wing and as the jet pressure ratio increases, but increases only slightly as free-stream Mach number is raised.

(4) The dominant feature of the jet interference curve, ΔC_{pj}, is a velocity peak, which may be followed by a subsidiary peak further downstream. For a range of configurations which appear to be of practical interest, the maximum suction increment is $-\Delta C_{pj} < 0.15$ at $H_j/p_o = 2.4$; this is unlikely to lead to a large change in overall wing characteristics. If the suction peak due to jet interference falls close to the suction peak on the wing in the presence of the nacelle without jet, the values of ΔC_{pj} increase rapidly with increasing jet pressure ratio, and might be of major practical significance in some cases.

ACKNOWLEDGEMENTS

The bulk of the experimental work reported here was undertaken by my colleagues D.J. Raney, A.G. Kurn and C. Young, to whom my thanks are due.

REFERENCES

1 D.J. Raney, A.G Kurn, J.A. Bagley. Wind tunnel investigation of jet interference for underwing installation of high bypass ratio engines. R.A.E. Technical Report 68049, March 1968

2 A.G. Kurn. R.A.E. Report in preparation

3 R.L. Lawrence Afterbody flow fields and skin friction on short duct fan nacelles. Journal of Aircraft Vol.2, pp.318-327, July 1965

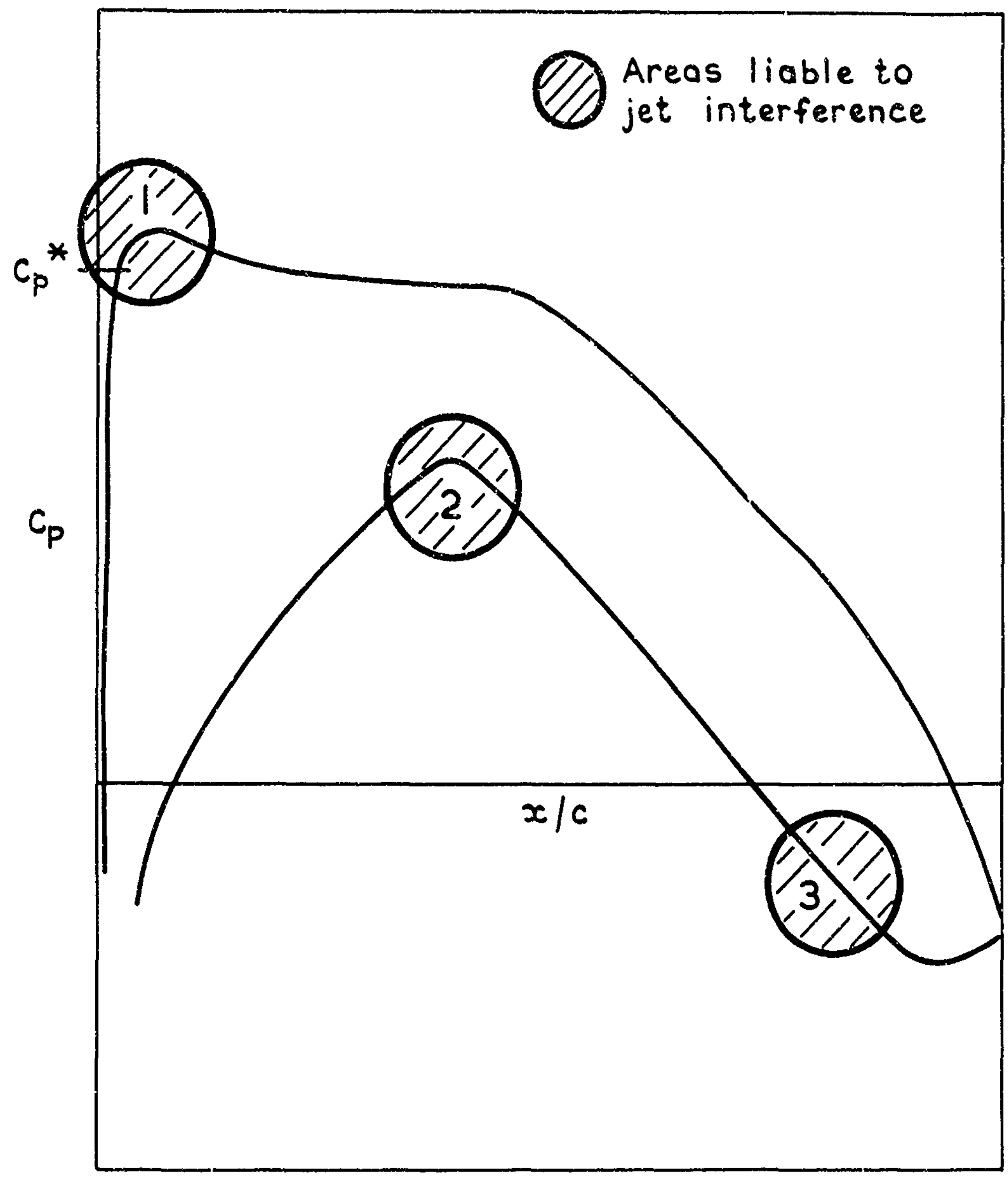

Fig.1 Typical modern aerofoil design pressure distribution

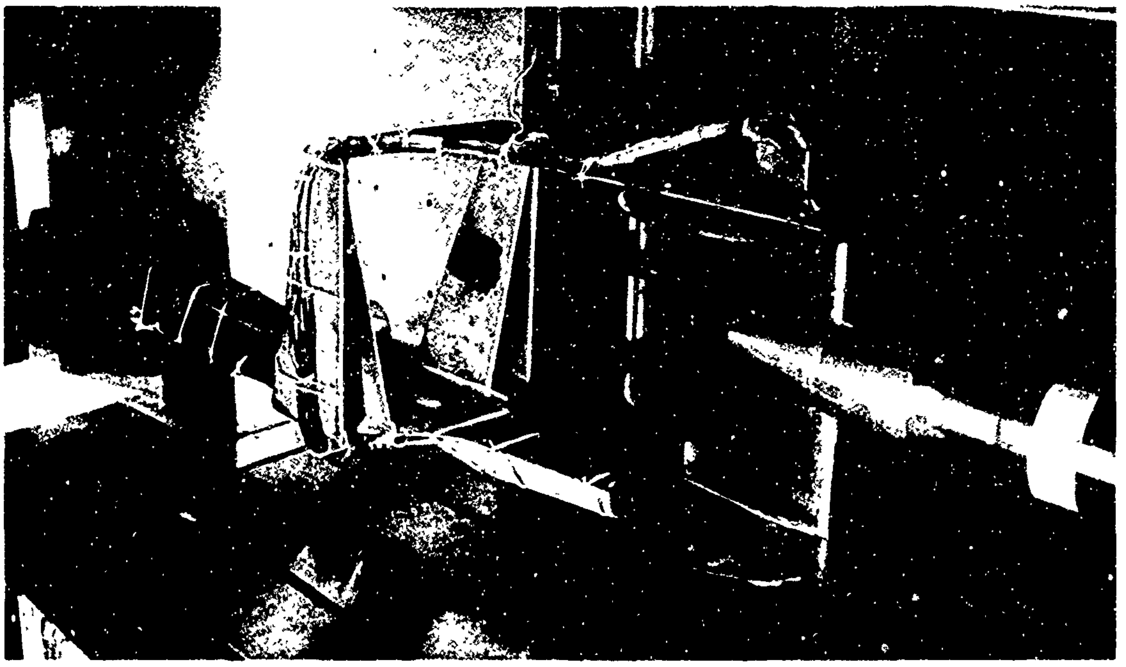

Fig.2 Wing and jet nozzle in tunnel

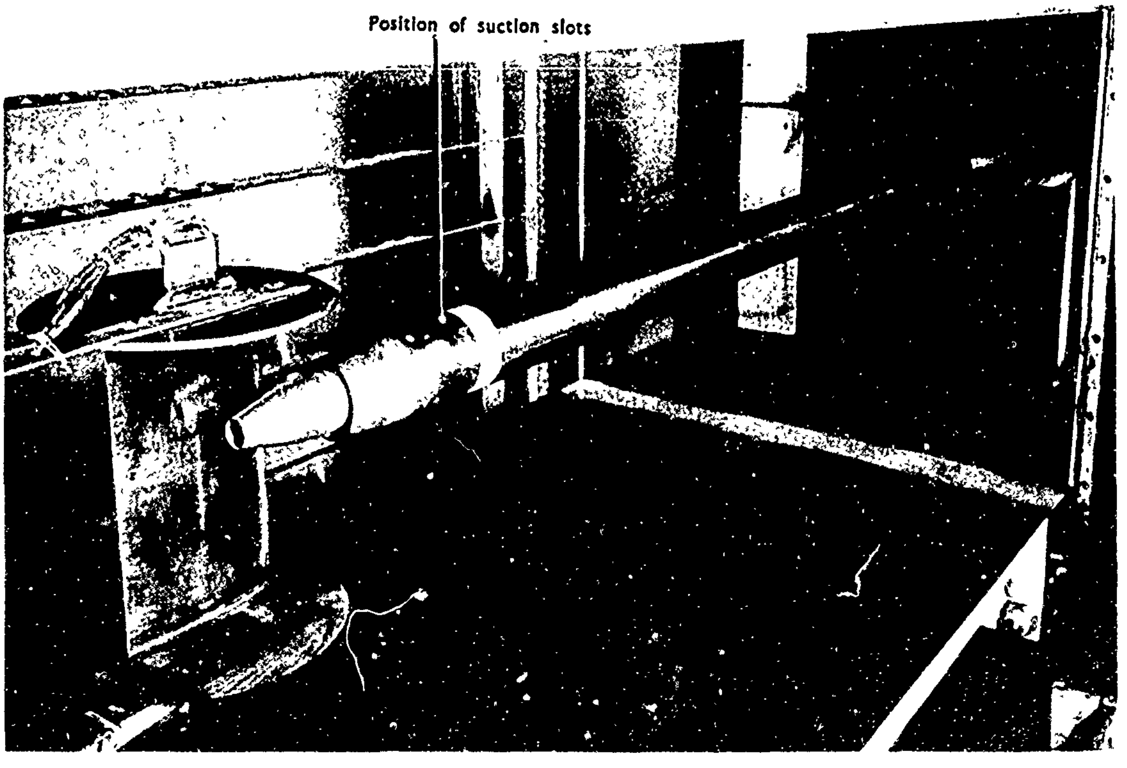

Fig.3 Wing and jet nozzle in tunnel

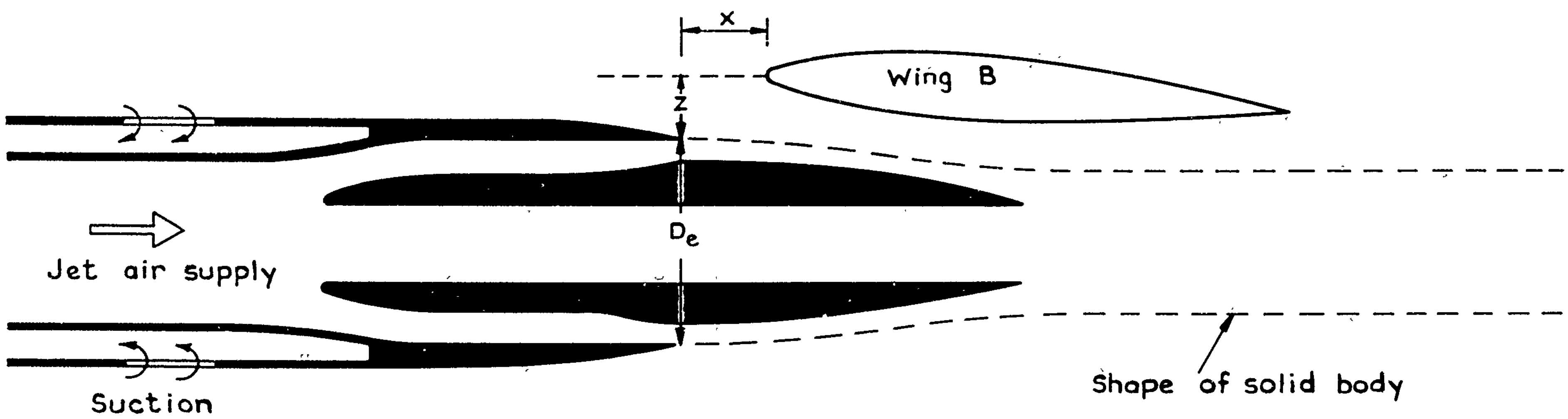

Fig.4 Nozzle and wing in datum position
$(X/D_e = 0{\cdot}44 \, , \, Z/D_e = 0{\cdot}29)$

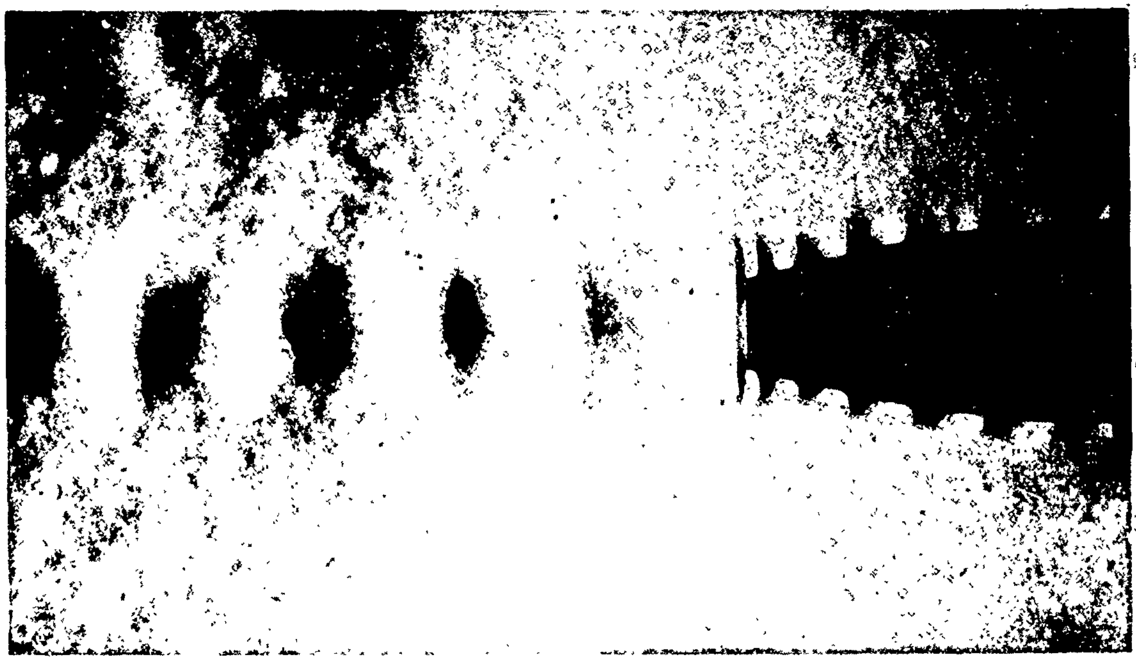

a M_o = 0.7 H_j/p_o = 2.4

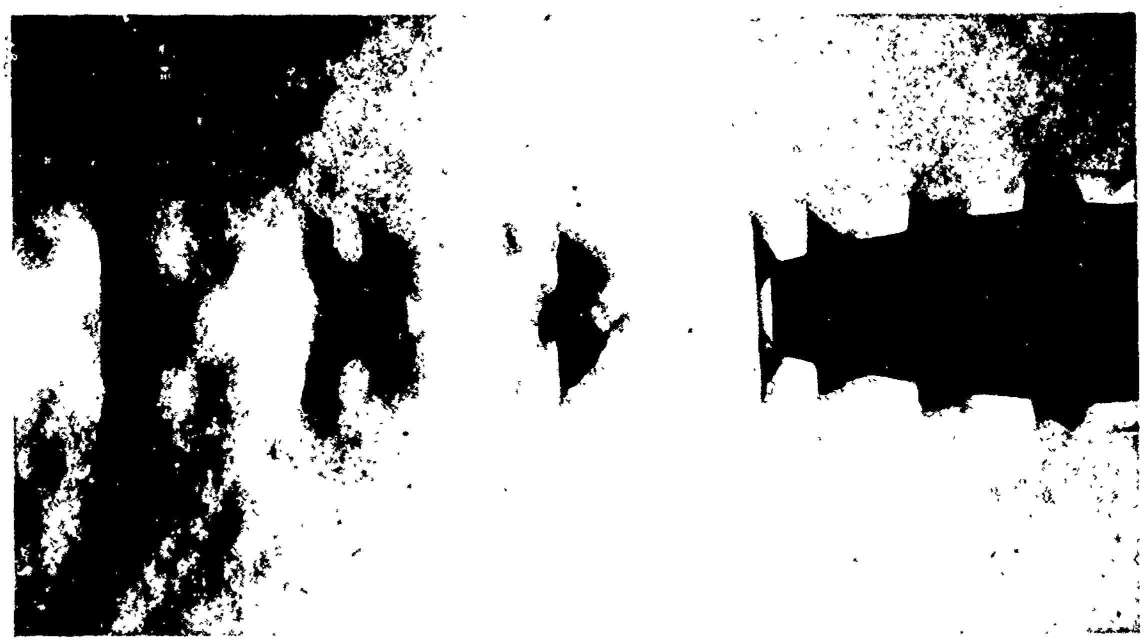

b M_o = 0.7 H_j/p_o = 3.0

Fig.5 Schlieren photographs of flow from bypass nozzle

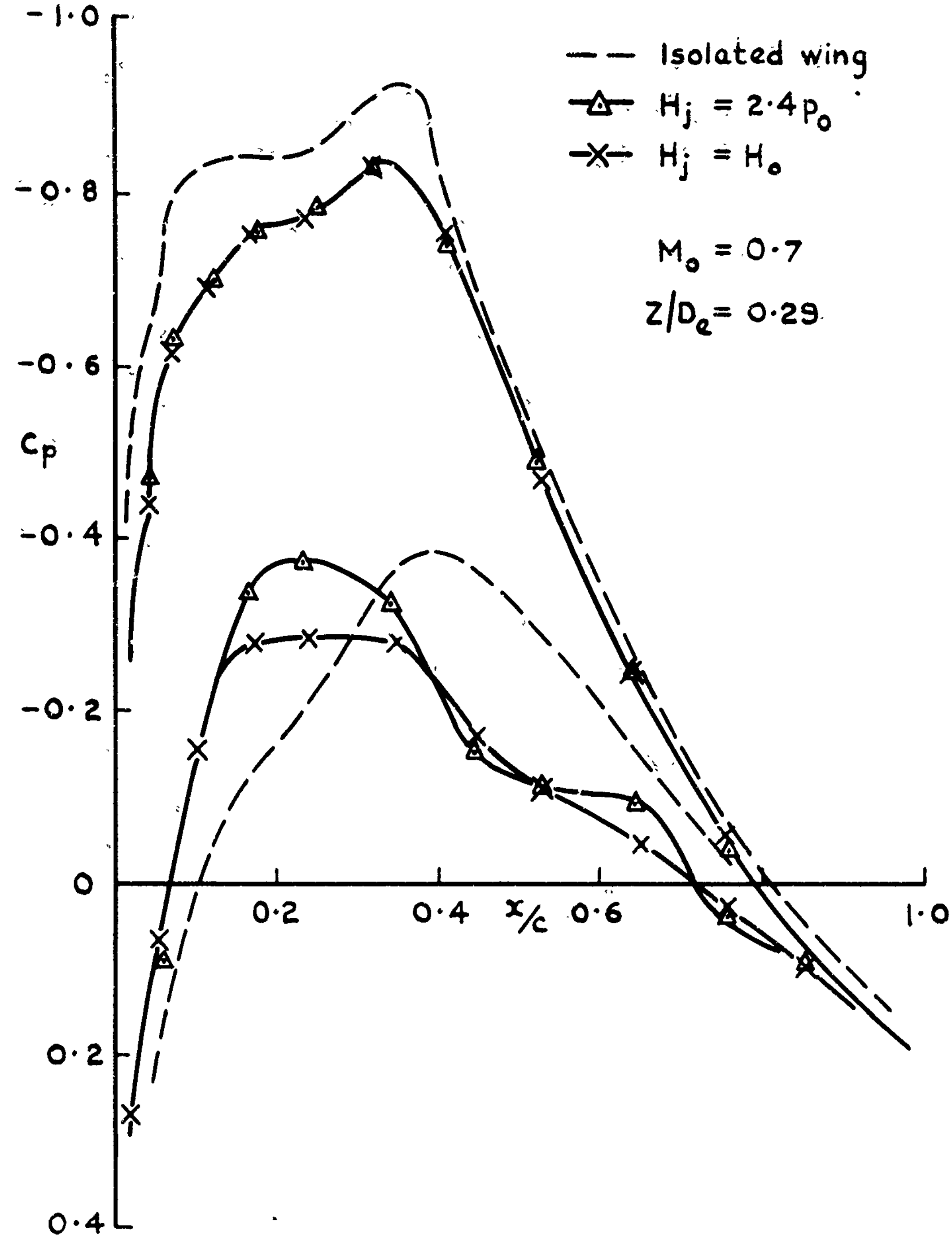

Fig. 6 Wing pressures with and without jet blowing

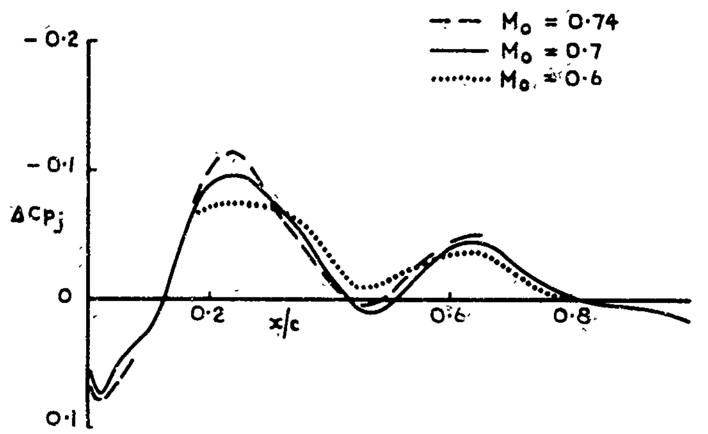

Fig. 7 Effect of Mach number

$H_j/p_o = 2{\cdot}4$, $Z/D_e = 0{\cdot}29$, $X/D_e = 0{\cdot}44$

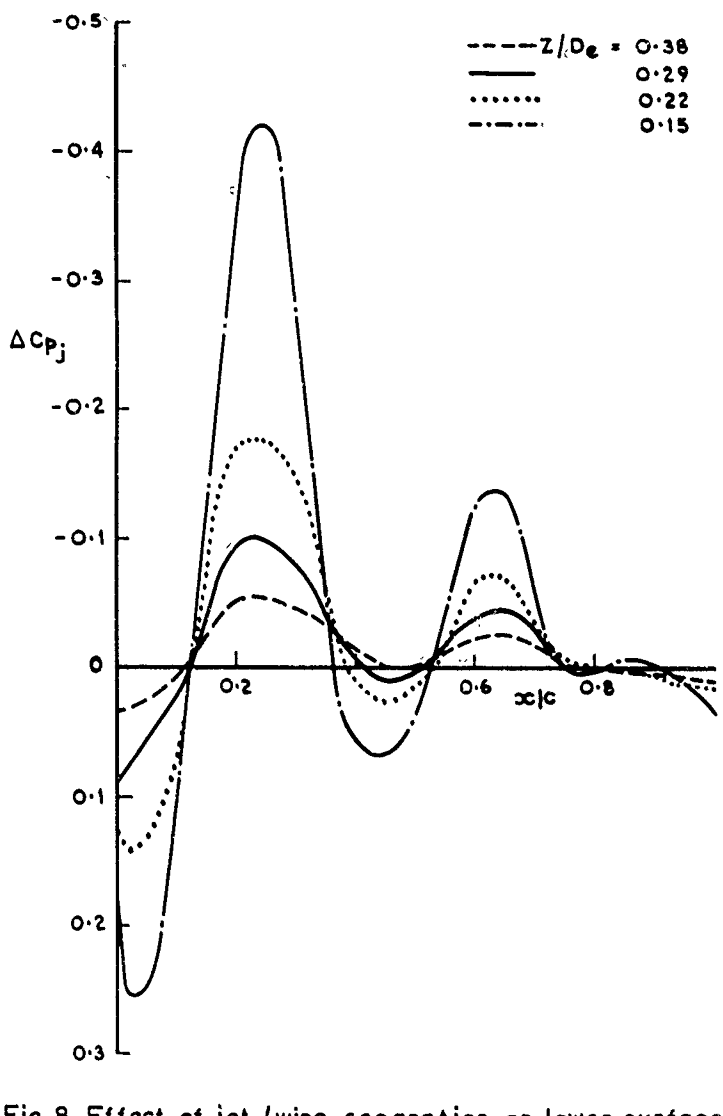

Fig. 8 Effect of jet/wing separation on lower surface pressure increment due to jet blowing

$H_j = 2{\cdot}4\,p_o$, $M_o = 0{\cdot}7$, $X/D_e = 0{\cdot}44$

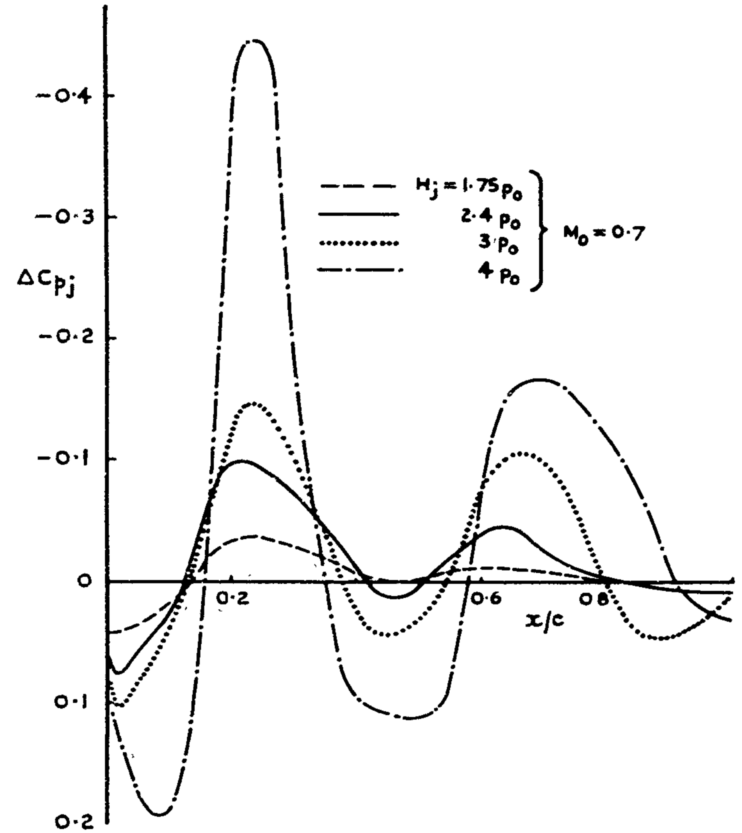

Fig.9 Lower surface pressure increment in plane of jet, due to jet blowing. Datum wing/nacelle configuration $X/D_e = 0·44$, $Z/D_e = 0·29$ $M_o = 0·7$

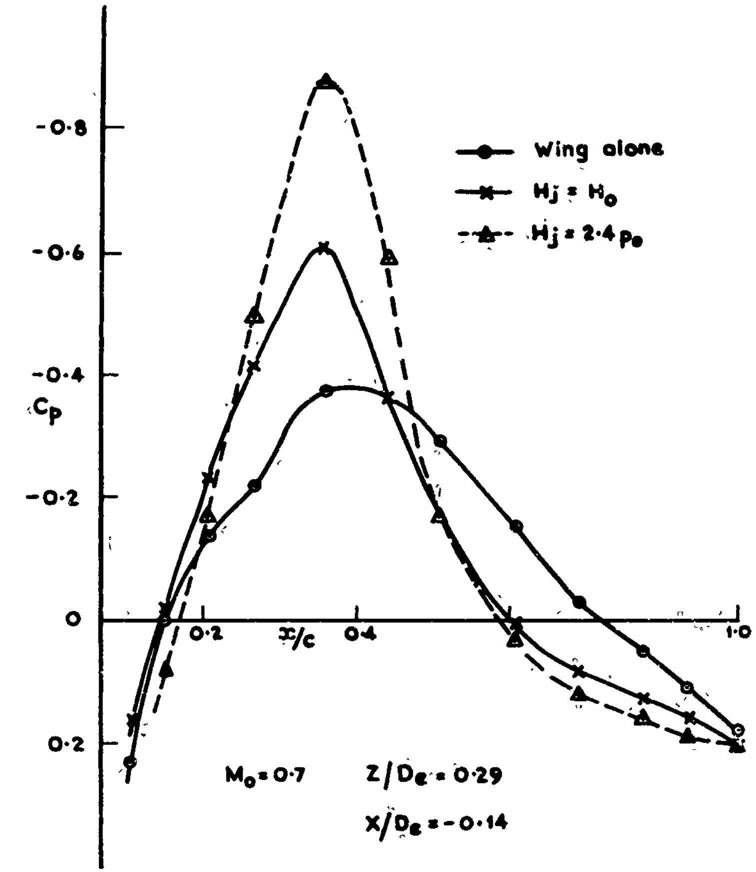

Fig.10 Pressures on lower surface of wing: rearward nacelle position

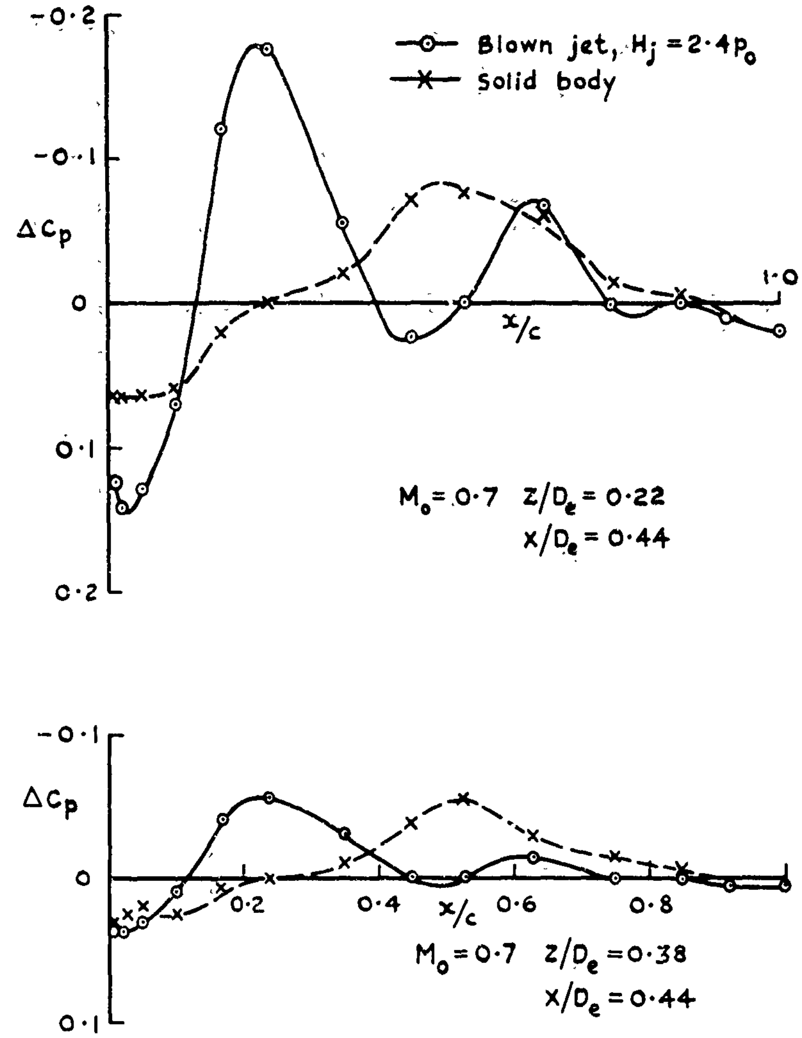

Fig. 11 Pressure increments due to jet and to solid body of similar shape

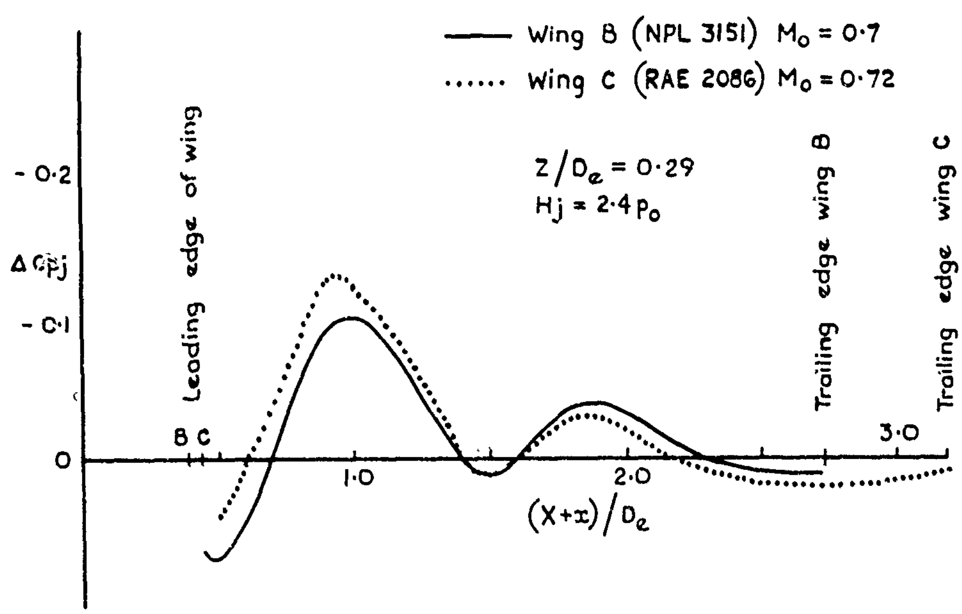

Fig. 12 Jet interference on two wings

Fig.13 Schlieren picture of flow

X/D_e = 0.38, Z/D_e = 0.29, M_0 = 0.72, H_j/p_0 = 2.4

Fig.14 Schlieren picture of flow

X/D_e = 0.38, Z/D_e = 0.29, M_0 = 0.72, H_j/p_0 = 2.9

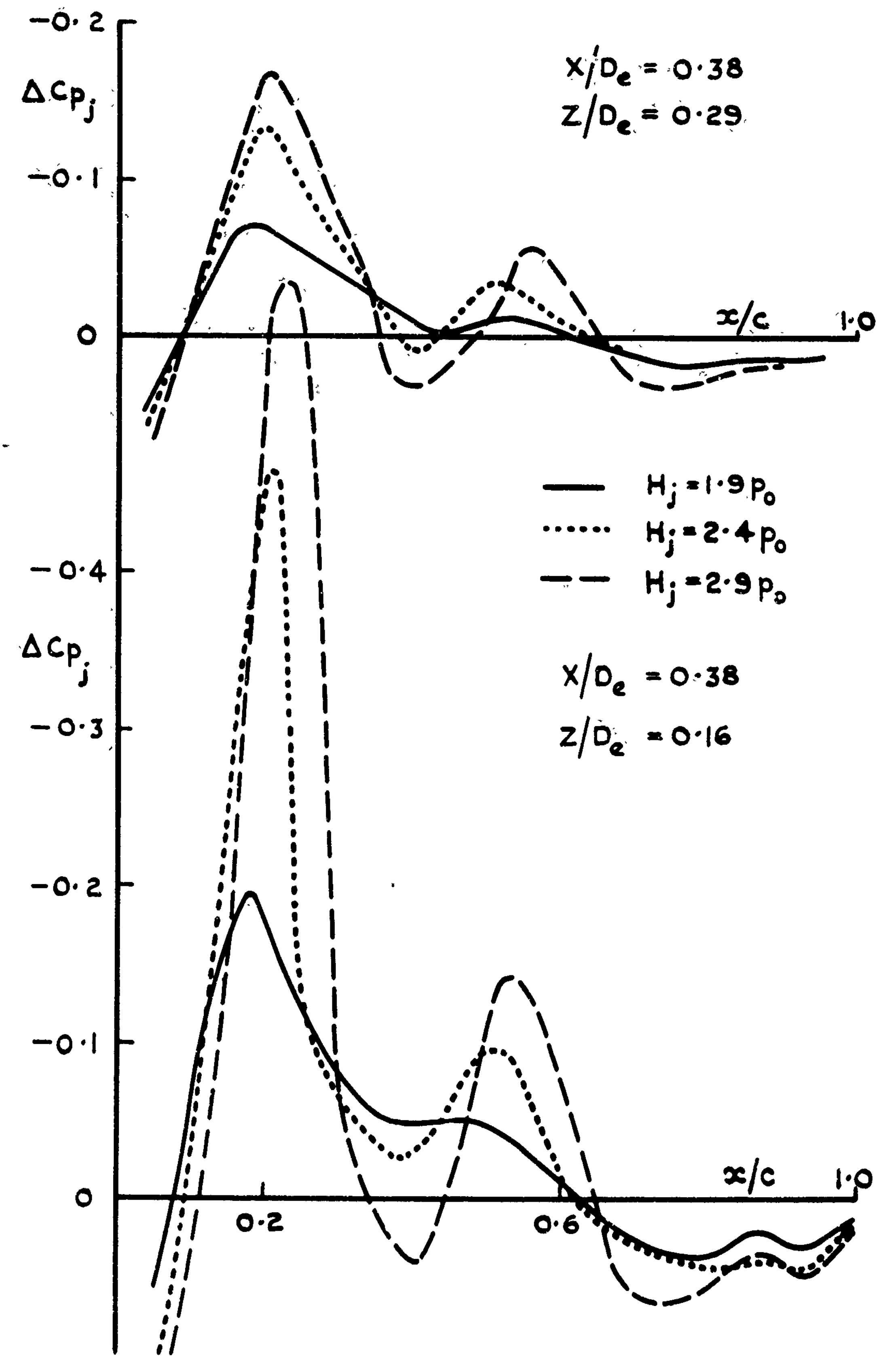

Fig. 15 Jet interference for two vertical spacings of nacelle and wing C

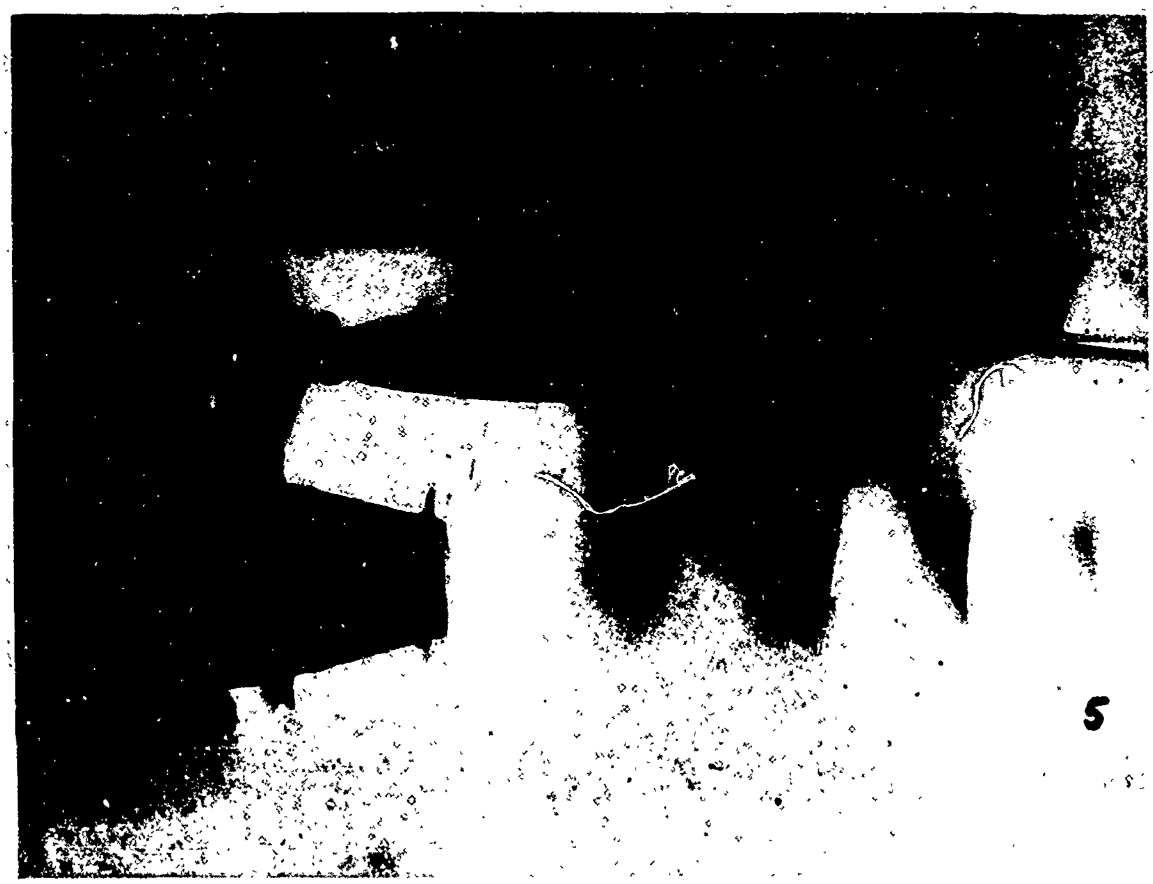

Fig.16 Schlieren picture of flow with long-cowl nacelle
$X/D_e = 0.38$, $Z/D_e = 0.29$, $M_o = 0.72$, $H_j/p_o = 2.4$

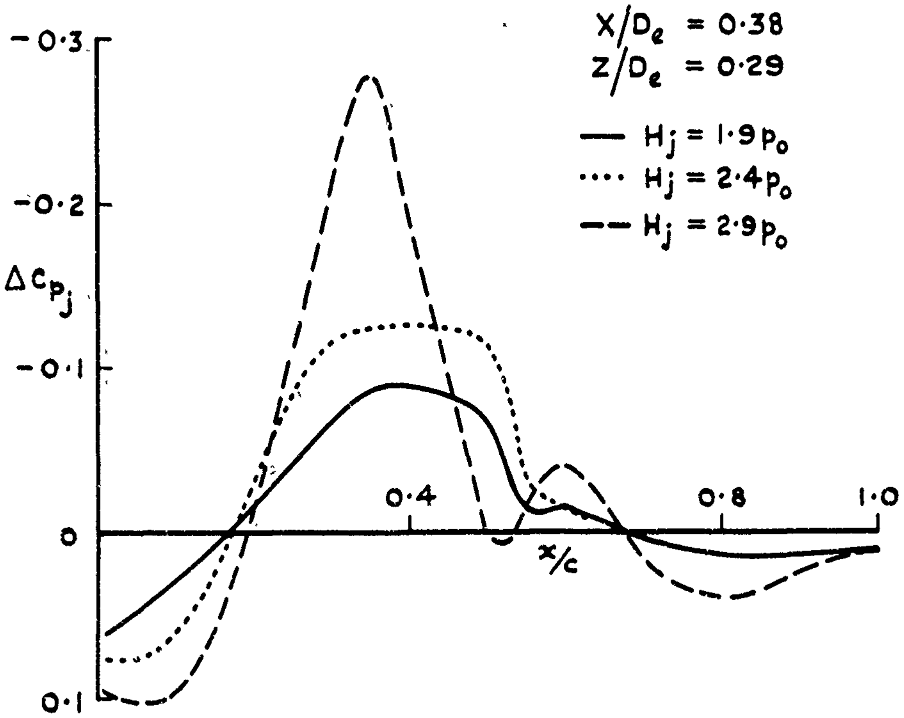

Fig.17 Jet interference for nacelle with short afterbody

QUELQUES PROBLEMES TRANSSONIQUES DU FUSEAU MOTEUR

D'UN AVION DU TYPE "AIRBUS"

par

J. LEYNAERT*

G. MEAUZE**

O.N.E.R.A. (92 - Châtillon - FRANCE)

* Chef de Groupe de Recherches

** Ingénieur de Recherches

S O M M A I R E

Le développement des avions de transport subsoniques à grande capacité a conduit au choix de gros turbo-réacteurs à double flux ayant un taux de dilution élevé : il en résulte des problèmes aérodynamiques nouveaux, liés à l'importance des débits captés par la prise d'air et aux effets de l'interaction du jet froid du "fan" sur l'écoulement extérieur lorsque le réacteur est suspendu sous la voilure.

En ce qui concerne la prise d'air, on doit rechercher un compromis assurant un écoulement sans décollement interne au décollage et sans survitesse prohibitive sur la carène en régime de croisière.

La forme d'un profil réalisant ce compromis a été recherchée à l'aide de la méthode des analogies électriques, dont les résultats valables pour un écoulement de révolution incompressible ont été affectés des corrections classiques pour la transposition au régime compressible de croisière.

Le fonctionnement aux très faibles vitesses et notamment au point fixe fait apparaître une distorsion non négligeable de l'écoulement interne, imputable au régime transsonique qui s'établit au contournement du bord d'attaque et aux décollements qui en résultent.

Les résultats expérimentaux correspondants sont présentés et discutés.

Une étude en soufflerie de la confluence du jet primaire et de l'écoulement extérieur transsonique au voisinage de la sortie du jet est également présentée, pour mettre en évidence l'influence du régime du moteur sur la structure de cet écoulement.

SOME PROBLEMS OF TRANSONIC FLOW FOR ENGINE NACELLES OF AIRBUS TYPE AIRCRAFT

S U M M A R Y

High by pass ratio turbofans used for large subsonic transport aircraft envolve new aerodynamic problems due to the importance of the mass flow both at the intake and at the exhaust.

For the intake lip problem, a compromise must be found to obtain a flow without internal separation at take-off, and without excessive external super velocities during cruise.

Electrical analogy has made possible the study of various forms of lip profiles, by an incompressible flow simulation corrected for compressibility effect, and the solution of the problem to a first approximation.

At very low speed, however, and in particular in the static case, transonic flow and shock waves at the leading edge may cause local flow separation internally, and distorsion of the total pressure profile.

Experimental studies of these phenomena are presented.

For the exhaust problem and engine nacelle boattail drag, some transonic wind tunnel pressure measurements on representative models are also discussed.

L'AVENEMENT DES NOUVEAUX MOTEURS DOUBLE FLUX à taux de dilution élevé conduit à considérer avec plus d'attention l'aérodynamique des nacelles dont l'importance relative par rapport aux dimensions générales de l'avion est fortement accrue. La traînée de motorisation en vol de croisière atteint 7 à 8% de la traînée totale de l'avion, et l'enjeu d'une étude d'optimisation de l'ensemble à partir d'une configuration définie en vertu de quelques règles empiriques approchées peut être de 1/2% de la poussée.

L'un des buts de cette étude préliminaire a été de définir un carénage évitant les survitesses transsoniques sur les profils externes en vol de croisière, et la traînée qui en résulte par ondes de choc éventuelles et frottement accru. S'il s'avérait toutefois nécessaire d'accepter de telles survitesses, des profils de moindre traînée type "peaky" [1] [2] seraient à considérer.

La première phase consiste à étudier le fuseau seul et à en rechercher une forme optimale qui servira de point de départ pour l'optimisation de l'ensemble nacelle-avion [3 à 7]. Une solution type de ce problème est représentée figure 1. Les répartitions de pression sur les profils de carène et d'arrière corps traduisent les caractéristiques suivantes : sur le profil externe de la prise d'air, une survitesse subcritique à peu près constante jusqu'au delà du maître-couple ; de même sur le profil interne du diffuseur, une plage de survitesses subcritiques. Un bord d'attaque moins épais permettrait d'atténuer ces survitesses, mais les performances au décollage seraient pénalisées, comme nous le verrons. Sur le rétreint de la carène, on observe vers l'arrière une recompression régulière de l'écoulement. Sur le corps central, le jet du "Fan" se détend à une pression voisine de la pression ambiante, donnant naissance à une succession d'ondes de détente et de compression très atténuées.

Ces différents éléments vont être maintenant examinés plus en détail, en considérant successivement sous leurs aspects transsoniques le problème de la prise d'air au décollage et en croisière, celui de la prise d'air au point fixe et aux très basses vitesses, et le problème du rétreint de la carène et du corps central en vol de croisière.

OPTIMISATION DE LA PRISE D'AIR AU DECOLLAGE ($M_\infty = 0,2$) ET EN VOL DE CROISIERE ($M_\infty = 0,85$)

Un processus très élémentaire a été suivi pour rechercher cette optimisation : une certaine forme de carénage de la prise d'air étant définie a priori, le champ de l'écoulement de révolution autour de cette carène est déterminé en incompressible. A cet effet, on utilise la méthode d'analogie électrique des écoulements de révolution [8] dans une cuve à fond incliné où est disposé un secteur de la maquette de la prise d'air, en matériau léger isolant (fig. 2). Le relevé du champ aérodynamique fait apparaître les zones de survitesses à corriger, et permet d'orienter la recherche d'une nouvelle forme améliorée. Par des essais successifs, on aboutit ainsi très rapidement au choix d'une configuration dont l'essai en soufflerie donne une évaluation précise des performances. A partir de ce résultat, un nouvel ajustement peut être recherché en s'appuyant à nouveau sur le sens des indications recueillies dans l'analogie incompressible.

Un certain nombre de règles empiriques ont été dégagées par différents auteurs pour définir la forme initiale de la carène et du fuseau moteur [9 à 12]. Un calcul numérique en régime incompressible est utilisé par d'autres auteurs [13], mais il n'existe pas encore, à notre connaissance, de méthode de calcul pour l'écoulement compressible. Une telle méthode est en cours de développement à l'O.N.E.R.A. [14]. La méthode suivie a donc consisté à procéder à une correction des résultats obtenus en incompressible par la formule de KARMAN-TSIEN, considérée comme donnant une approximation grossière, mais suffisante pour guider le choix d'un profil.

Les figures 3 et 4 présentent deux étapes successives de la définition de la forme de la prise d'air. Ces figures donnent les distributions de pression calculées comme il vient d'être dit, pour les nombres de Mach de vol $M_\infty = 0,85$ et $M_\infty = 0,2$. Lorsque ce calcul fait apparaître des zones supercritiques (rapport de la pression à la pression génératrice $p/p_{i\infty}$ inférieur à 0,528), il perd évidemment toute précision mais avertit seulement que la vitesse critique sera certainement franchie. Ainsi, le profil initial "A" de la figure 3 fait prévoir d'une part une forte survitesse sur la carène externe à $M_\infty = 0,85$ consécutive à une courbure locale trop accentuée du profil. D'autre part, à $M_\infty = 0,85$ comme à $M_\infty = 0,2$, une survitesse apparaît également sur le profil du diffuseur interne, au voisinage de l'entrée : sachant par analogie avec les bords d'attaque de voilure qu'en redressant son squelette, on pourra atténuer ces survitesses internes, on a défini la solution "B". Dans cette solution, les survitesses internes sont effectivement ramenées à un niveau acceptable, mais, à l'"extrados" (profil externe de la carène), la faible diminution de courbure donnée au profil n'a pas compensé l'accélération de l'écoulement due à l'augmentation de l'"incidence", et la survitesse est devenue supérieure à ce qu'elle était antérieurement. On observe toutefois qu'au voisinage immédiat du bord d'attaque, les vitesses externes sont faibles, et il sera par conséquent admissible de les accroître en adoptant un profil de plus forte courbure locale. Cette disposition permettra en même temps de réduire la courbure plus en aval, dans la région où elle est trop accentuée. Le profil "C" comparé au profil "B" (figure 4) répond à ces conditions. La répartition de pression sur la carène externe est presque uniforme, à un nombre de Mach subsonique constamment voisin de 1. Au même nombre de Mach $M_\infty = 0,85$, les pressions sur le profil interne de la carène sont pratiquement inchangées et restent satisfaisantes ; à $M_\infty = 0,2$, on observe toutefois un accroissement de la survitesse au contournement du bord d'attaque, consécutive à l'augmentation de courbure. Cette survitesse dépasse la valeur critique, mais pourra sans doute être atténuée par une légère modification de la répartition des courbures du profil interne à l'entrée.

L'obtention à $M_\infty = 0{,}85$ d'une vitesse critique quasi-constante sur tout l'extrados indique que l'on est proche d'une configuration optimale.

Une première série d'essais a été entreprise sur la configuration "C" dans une soufflerie à basse vitesse pour vérifier son comportement interne au régime de décollage et aux très basses vitesses où des troubles transsoniques sont à craindre au voisinage du bord d'attaque.

La figure 5 représente le montage utilisé dans la soufflerie S3 de Chalais Meudon. Le débit de la prise d'air est assuré par une trompe d'extraction disposée à la suite d'un débitmètre venturi. La carène de la prise d'air, d'un diamètre de 165 mm au plan d'entrée du moteur, est équipée de prises de pression statique le long d'une génératrice. Un peigne de pressions d'arrêt permet de relever le profil de l'écoulement au plan d'entrée du moteur. La vitesse de la soufflerie est limitée à 100 m/s. Les résultats obtenus à $M_\infty = 0{,}2$ sont reportés figure 6.

L'allure de la répartition des pressions autour du bord d'attaque est correctement prévue par le calcul, mais la survitesse interne au bord d'attaque est inférieure à la valeur prédite. La différence provient en partie du fait que le calcul est effectué en incompressible, mais aussi en partie du fait que l'on s'est contenté de mesures approchées dans la cuve d'analogie électrique.

Les résultats montrent l'absence de phénomènes transsoniques parasites autour du bord d'attaque au décollage à $M_\infty = 0{,}2$, selon l'objectif du calcul d'optimisation. Il n'en est toutefois pas de même au point fixe et à très basse vitesse.

PRISE D'AIR AU POINT FIXE ET A TRES BASSE VITESSE

La figure 7 montre l'évolution de l'écoulement autour du bord d'attaque à l'entrée de la prise d'air lorsque le nombre de Mach de vol passe de $M_\infty = 0{,}3$ à $M_\infty = 0$, le moteur étant au régime maximum. Le contournement du bord d'attaque étant de plus en plus accentué, on observe d'abord une survitesse croissante, localement supersonique à $M_\infty = 0{,}1$, suivie d'une recompression très brutale de l'écoulement. Lorsque le nombre de Mach est réduit à 0,08, la couche limite au bord d'attaque décolle ; le phénomène se manifeste sur le profil des pressions par l'établissement d'une plage isobare remplaçant la pointe de survitesse. Cette plage de décollement s'étend, lorsque M_∞ décroît jusqu'à 0.

La dégradation des profils de pression d'arrêt dans le plan d'entrée du "fan" reportés figure 8 traduit l'effet du décollement. L'efficacité, rapport de la pression génératrice moyenne dans le plan d'entrée du moteur, p_{iF}, à la pression génératrice amont $p_{i\infty}$, accuse également l'apparition du décollement comme le montre la courbe reportée figure 8.

Pour vérifier le rôle du nombre de Reynolds dans ces phénomènes, des essais en "transition déclanchée" au bord d'attaque ont été réalisés. La transition a été assumée par des fils longitudinaux collés sur le bord d'attaque, dans des plans méridiens régulièrement espacés (figure 9). Par ce procédé, la diffusion transversale de la turbulence émise le long des fils assure la transition de la couche limite sans provoquer de perturbation locale, indépendamment de la position du point d'arrêt au bord d'attaque, et en limitant au mieux l'épaississement initial de la couche limite [15]. L'effet de la transition ainsi déclanchée est très important, comme le montre les répartitions de pressions comparées figure 9 : à $M_\infty = 0{,}08$, la couche limite maintenant turbulente n'est pas décollée, contrairement à l'essai en transition naturelle. A $M_\infty = 0$, l'étendue du décollement est sensiblement réduite. Les pressions d'arrêt dans le plan du compresseur ainsi que l'efficacité globale (figure 10) reproduisent les mêmes effets. Les perturbations transsoniques de contournement du bord d'attaque peuvent être évitées, si besoin est, par l'aménagement de portes auxiliaires dans la prise d'air, mais ceci est un autre sujet.

ETUDE DE LA PARTIE ARRIERE DE LA NACELLE

L'installation d'essai de la partie arrière du fuseau moteur est présentée figure 11. Les parois haut et bas de la veine ont une perméabilité de 8%. La dimension de la maquette permet un équipement des profils en prises de pression.

La figure 12 montre les répartitions de pression sur le rétreint de la carène et sur l'arrière corps aux conditions nominales de la croisière. Sur le rétreint de la carène s'exerce vers l'arrière une recompression subsonique régulière, sans choc ni décollement. Le jet supersonique du "fan" est à peu près isobare à la pression ambiante ; sa structure est néanmoins marquée par une succession d'ondes de détente et de compression de faible intensité, comme le montre la visualisation strioscopique, mais que décèle à peine la répartition des pressions.

La figure 13 montre l'effet d'une variation du nombre de Mach pour un rapport constant de la pression génératrice du jet, p_{iJF}, à la pression génératrice de l'écoulement, $p_{i\infty}$. La recompression sur la carène reste régulière à $M = 0{,}9$, tandis que l'accroissement du taux de détente p_{iJF}/p_∞, avec le nombre de Mach fait apparaître une sinuosité plus marquée de la pression sur l'arrière corps due à l'intensification de l'onde de détente initiale, à la confluence des deux écoulements. Cet effet se retrouve, plus accentué, figure 14, où est donné l'effet d'une variation du rapport p_{iJF}/p_∞ à M_∞ donné.

Les pressions sur la carène ne sont pas affectées par la variation du taux de détente, dans les limites étudiées, mais les ondes de détente et de compression du jet s'intensifient fortement avec le rapport de pression.

Cet ensemble de résultats montre que l'écoulement autour des formes choisies pour la partie arrière du fuseau moteur est très régulier, au régime normal de vol de croisière. Le principe même du montage d'essai se prête toutefois à quelques critiques. C'est ainsi par exemple que la non-représentation du bord d'attaque de la prise d'air conduit à des survitesses au maître-couple vraisemblablement moins élevées que les survitesses réelles. Par ailleurs, la présence d'une couche limite sur le rétreint de la carène relativement plus importante que sur l'avion peut modifier légèrement les conditions locales de confluence des écoulements externe et interne à la sortie du "fan", et la structure du jet qui en résulte [16]. A cet égard, des essais avec aspiration de la couche limite en amont du carénage peuvent être envisagés [17].

CONCLUSION

Quelques exemples de phénomènes transsoniques rencontrés dans l'étude des carénages d'un moteur double flux à taux de dilution élevé ont été présentés. Les méthodes de calcul en incompressible actuellement encore utilisées, ne permettent de prévoir ces phénomènes qu'en première approximation, mais sont cependant un guide utile pour orienter la recherche d'une solution appropriée.

Les décollements de la couche limite au bord d'attaque, rencontrés dans certaines configurations, sont évidemment tributaires du nombre de Reynolds, et la plus grande attention doit être apportée à l'effet de ce paramètre, et au déclanchement naturel ou forcé de la transition de la couche limite.

REFERENCES

[1] H.H. PEARCEY

The aerodynamic design of section shapes for swept wings
Advances in Aeronautical Sciences, Vol. 3, pp. 277 - 322

[2] M. VINCENT DE PAUL

Recherches expérimentales sur les profils d'aile supercritiques
A.G.A.R.D. "Aérodynamique transsonique" - Paris (septembre 1968)

[3] W.C. SWAN

A discussion of selected aerodynamic problems on integration of propulsion systems with airframe on transport aircraft
AGARDograph 103, "Aerodynamic of power plant installation" (octobre 1965)

[4] J. SEDDON

Factors determining engine installation drag on subsonic and supersonic long-range aircraft
A.G.A.R.D. CP n° 9, part. I - Gaz turbine (1966)

[5] J.T. KUTNEY

High bypass versus low bypass engine installation considerations
S.A.E. paper 660735 (Octobre 1966)

[6] J.H. PATERSON

Aerodynamic design features of the C 5A
Aircraft engineering (June 1968)

[7] Ph. POISSON-QUINTON et M. VINCENT DE PAUL

Contribution à l'étude aérodynamique d'un avion de type "AIRBUS"
6ème Congrès I.C.A.S. - Munich (Septembre 1968)

[8] L.C. MALAVARD

L'emploi des analogies rhéoélectriques en aérodynamique
AGARDograph 18 (Août 1956)

[9] W.M. DOUGLASS

Aerodynamic installation of high-bypass ratio fan engines
S.A.E. paper 660732 (Octobre 1966)

[10] G.T. FRAZIER

Aerodynamic considerations for engine exhaust design for subsonic high-bypass fan engines
S.A.E. paper 660734 (Octobre 1966)

[11] W.S. VIALL

Aerodynamic considerations for engine inlet design for subsonic high-bypass fan engines
S.A.E. paper 660733 (Octobre 1966)

[12] R. SCHERRER and W.E. ANDERSON

Preliminary investigation of a family of diffusers designed for near sonic inlet velocities
N.A.C.A. T.N. 3668 (Février 1956)

[13] J.L. HESS and A.M.O. SMITH

A general method for calculating low speed flow about inlets
AGARDograph 103 - "Aerodynamic of power plant installation (Octobre 1965)

[14] P. CARRIERE et C. CAPELIER

Application de la méthode des caractéristiques instationnaires au calcul numérique d'un écoulement permanent compressible
A.G.A.R.D. "Aérodynamique transsonique" - Paris (Septembre 1968)

[15] R. MICHEL et M. SIRIEIX

Déclenchement de la transition par fils longitudinaux ceinturant la maquette
La Recherche Aéronautique n° 52 (1956)

[16] P. CARRIERE

Effets de l'écoulement interne sur le comportement aérodynamique d'un avion à réaction
I.C.A.S. - Munich (Septembre 1968)

[17] D.J. RANEY, AG. KURN, J.A. BAGLEY

Wind tunnel investigation of jet interference for underwing installation of high-bypass ratio engines
R.A.E. TR 68049 (1968)

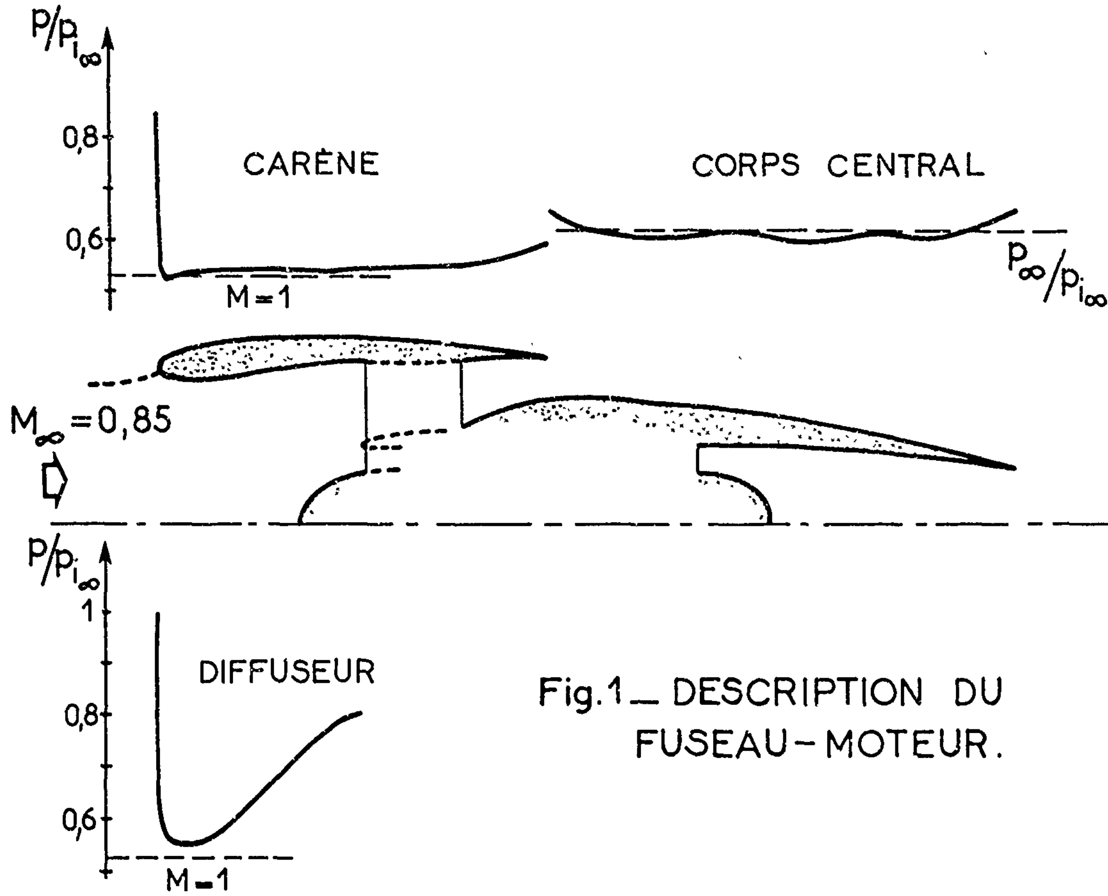

Fig.1 _ DESCRIPTION DU FUSEAU-MOTEUR.

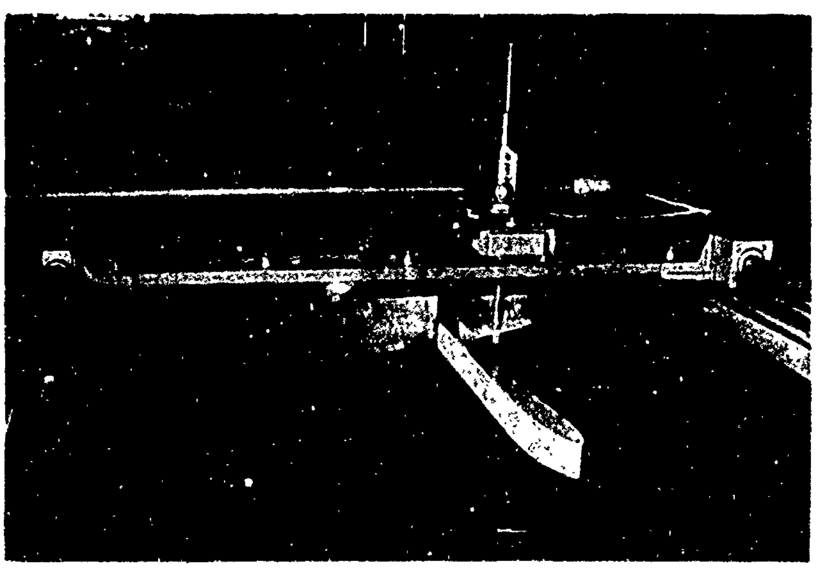

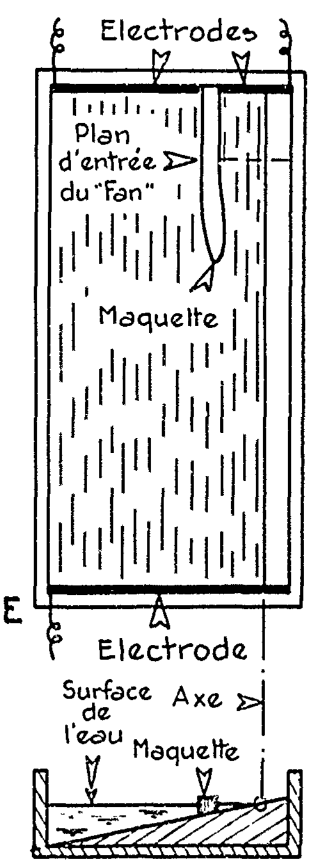

Fig. 2 CUVE D'ANALOGIE RHÉOÉLECTRIQUE

SIMULATION DE L'ÉCOULEMENT DE RÉVOLUTION AUTOUR DE LA CARÈNE EN INCOMPRESSIBLE

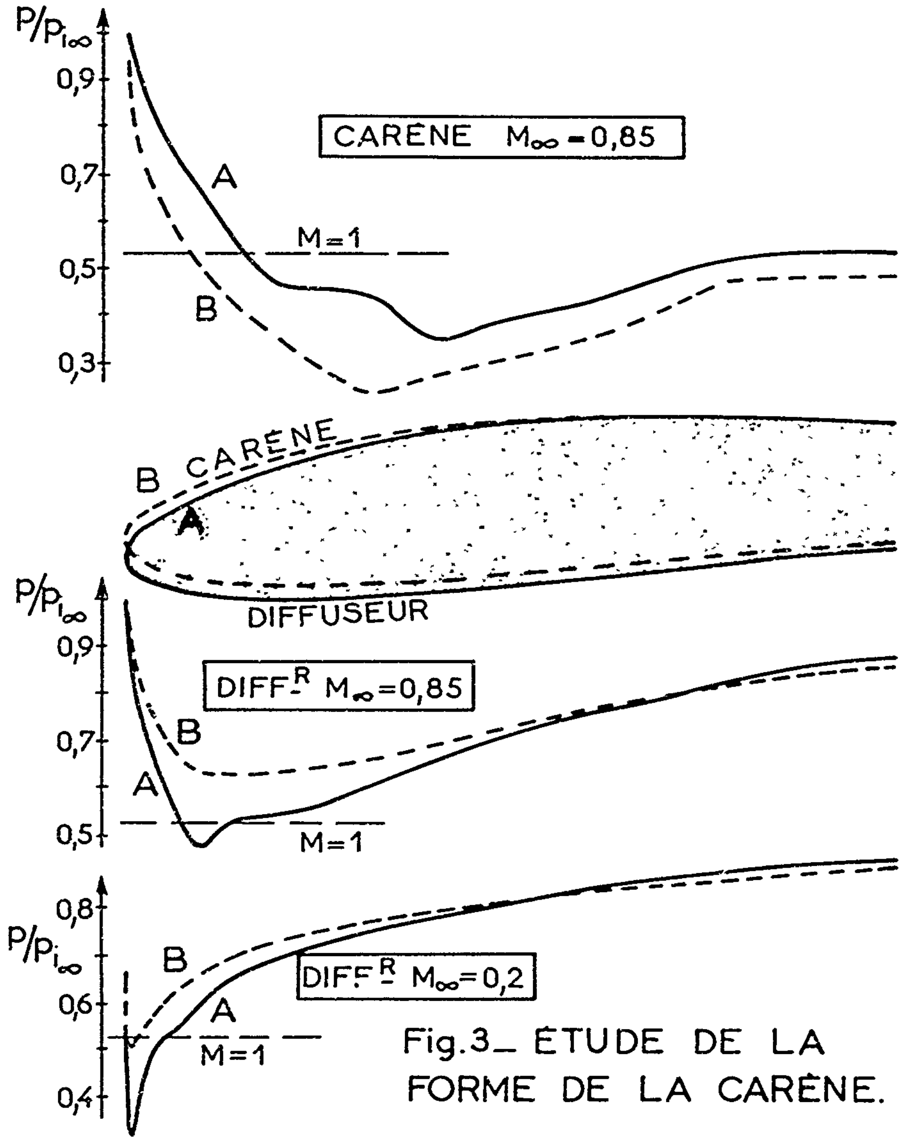

Fig.3_ ÉTUDE DE LA FORME DE LA CARÈNE.

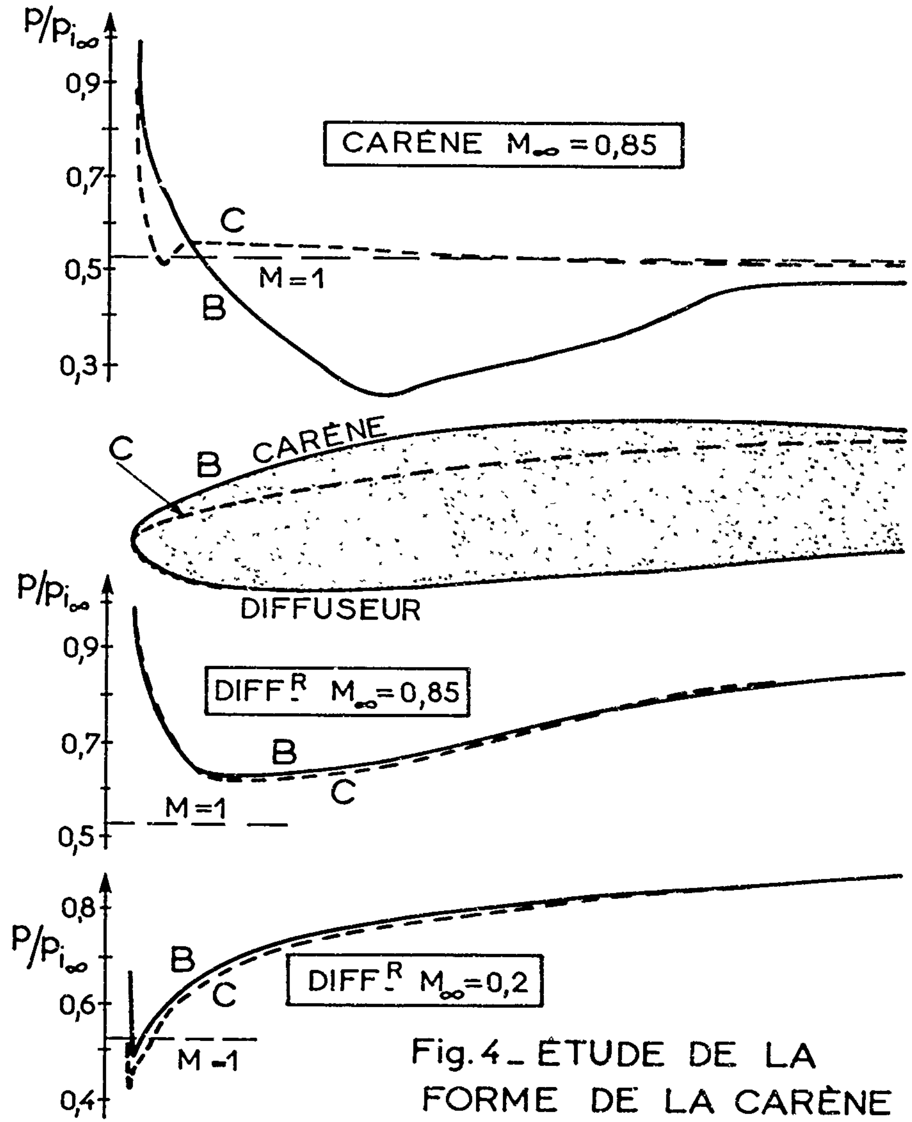

Fig. 4_ ÉTUDE DE LA FORME DE LA CARÈNE

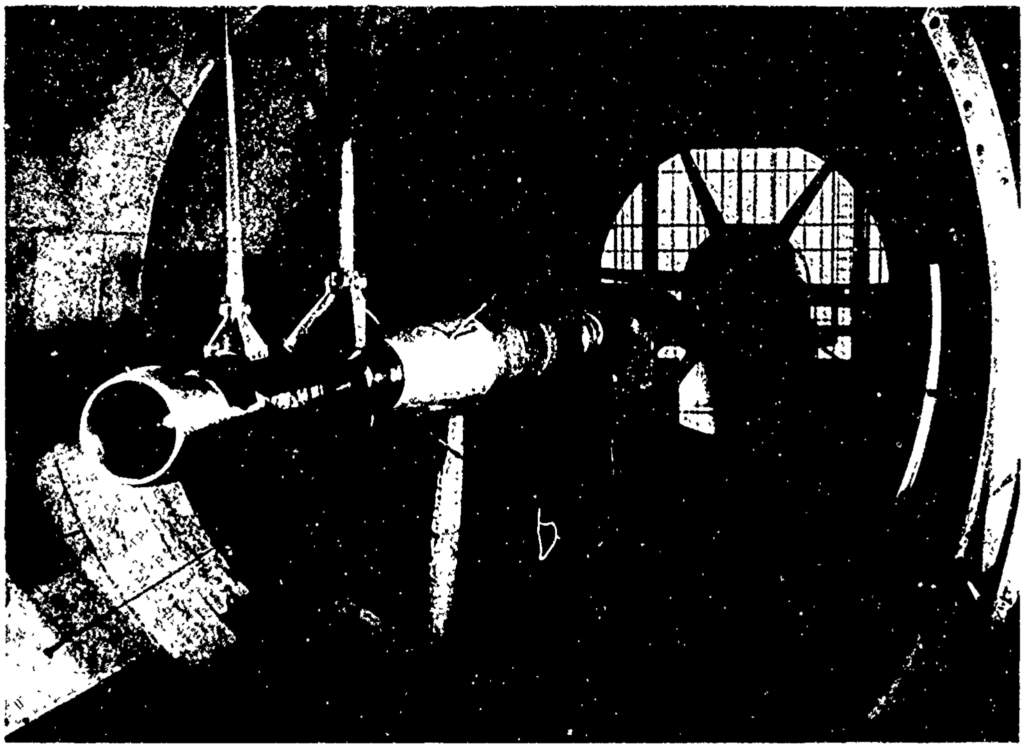

Fig. 5

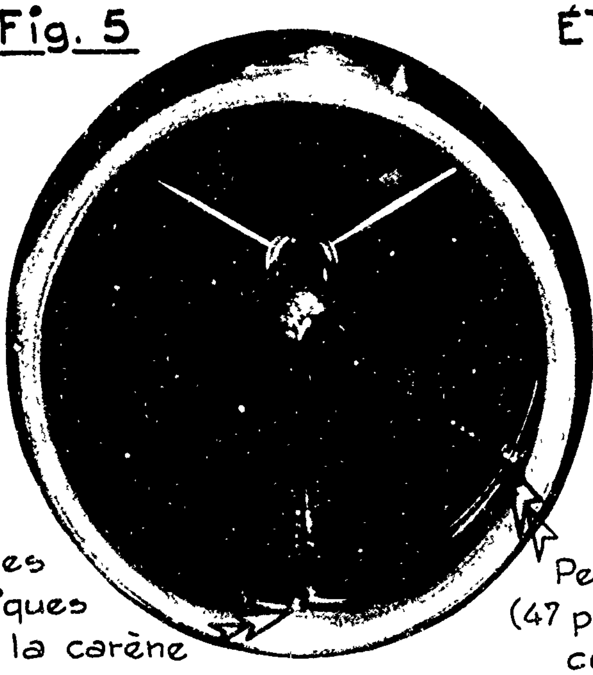

ÉTUDE DE LA PRISE D'AIR AIRBUS à S_2 Chalais

($D = 3\,m$; $V_0 \leq 100\,m/s$)

Aspiration par trompe à induction ($Q = 4\,kg/s$)

Diamètre intérieur de la prise d'air : 0,152m

36 prises statiques sur la carène

Peigne de pression d'arrêt (47 prises) dans le plan du compresseur.

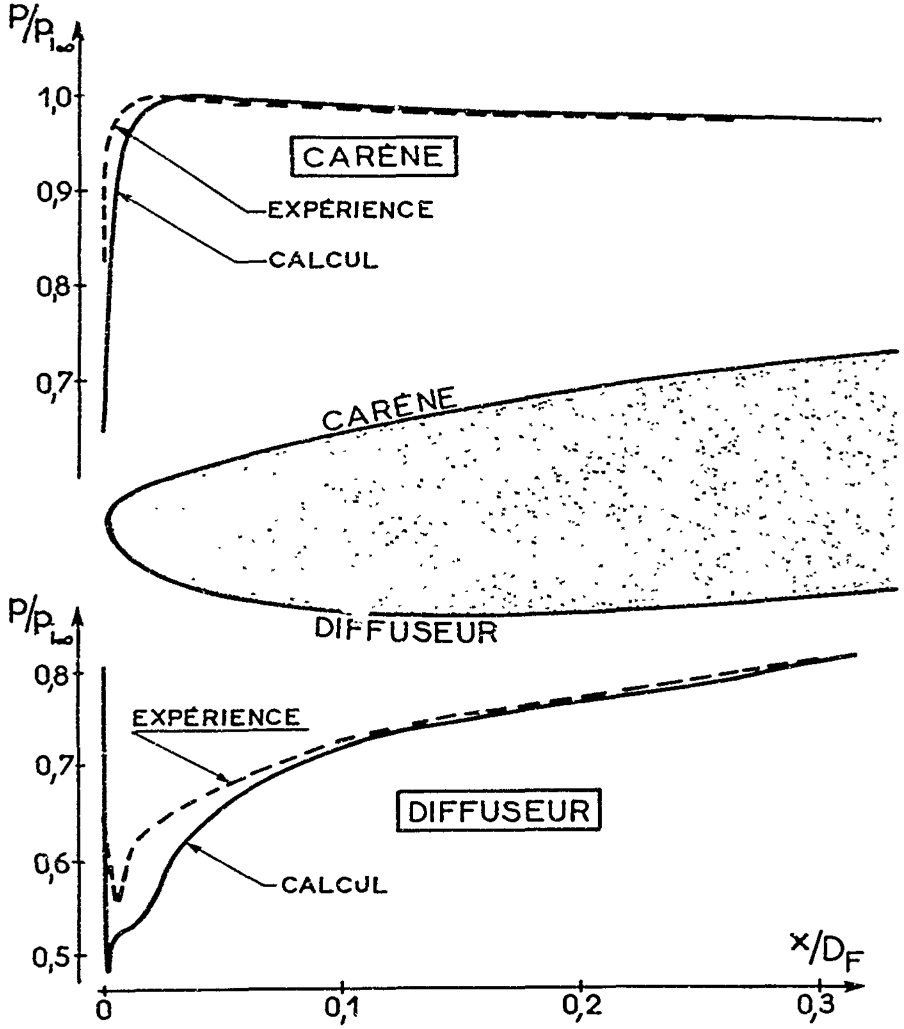

Fig. 6_ COMPARAISON THÉORIE EXPÉRIENCE CALCUL INCOMPRESSIBLE. ESSAI $M_o = 0,2$.

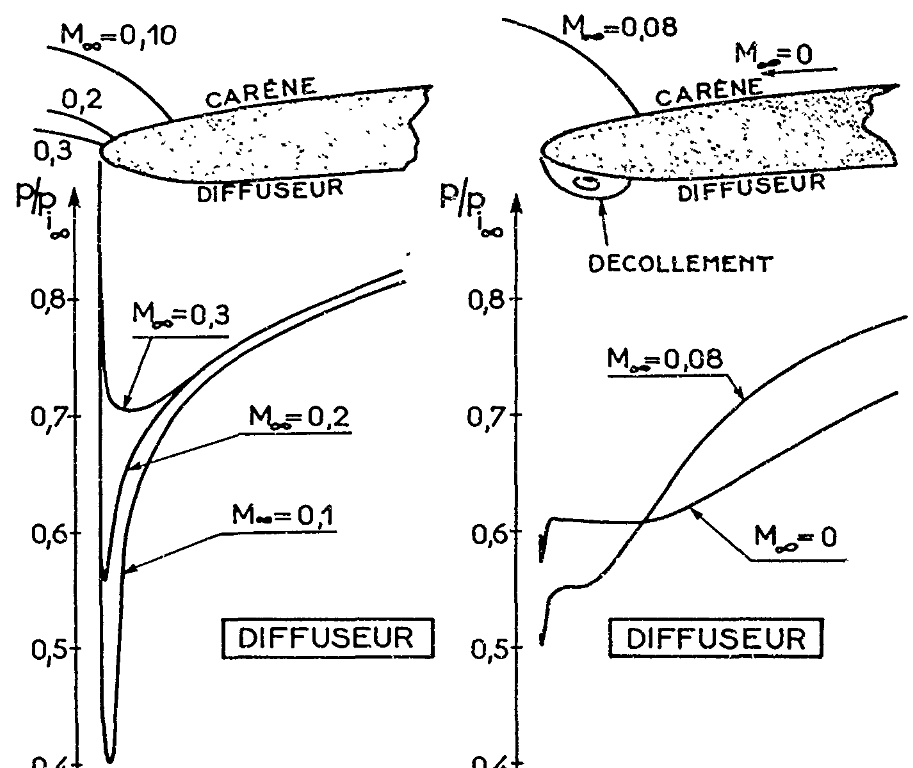

Fig. 7_ CONTOURNEMENT DU BORD D'ATTAQUE AU POINT FIXE ET AU DECOLLAGE. (Débit réduit constant)

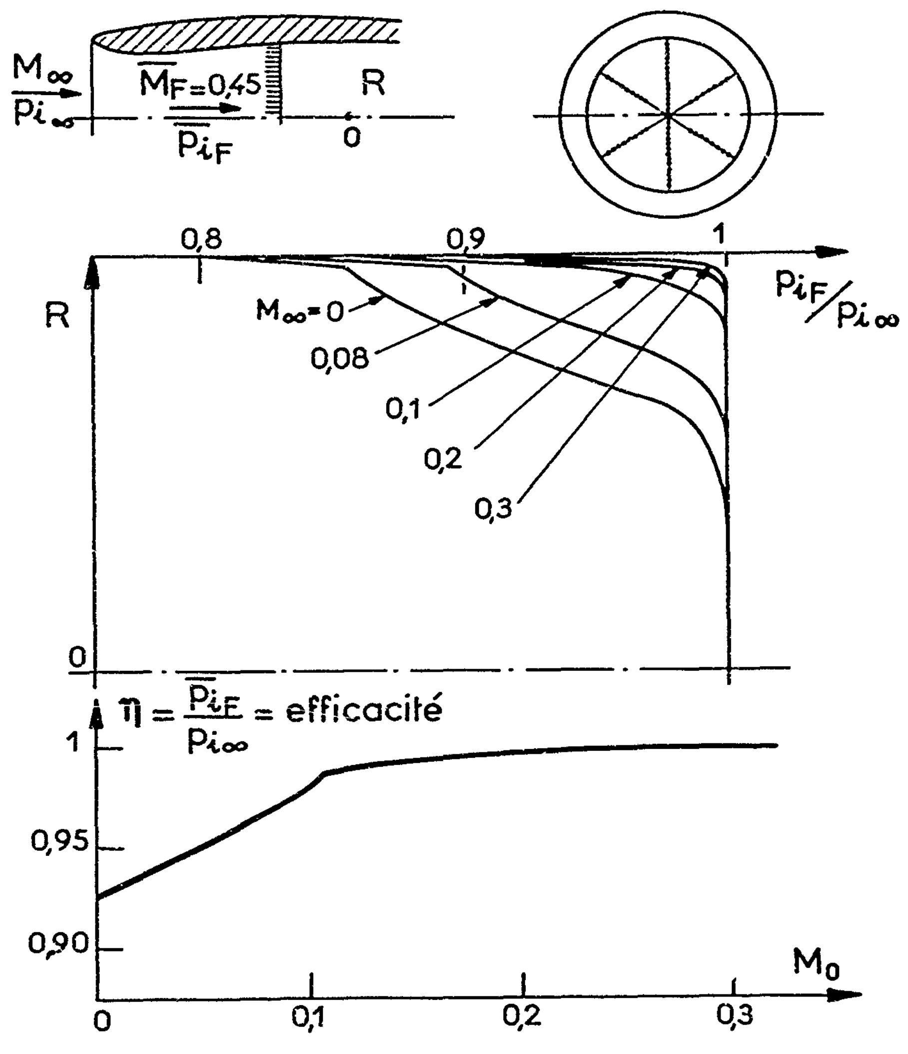

Fig.8_ PROFILS DES PRESSIONS D'ARRET ET EFFICACITÉ AU DÉCOLLAGE

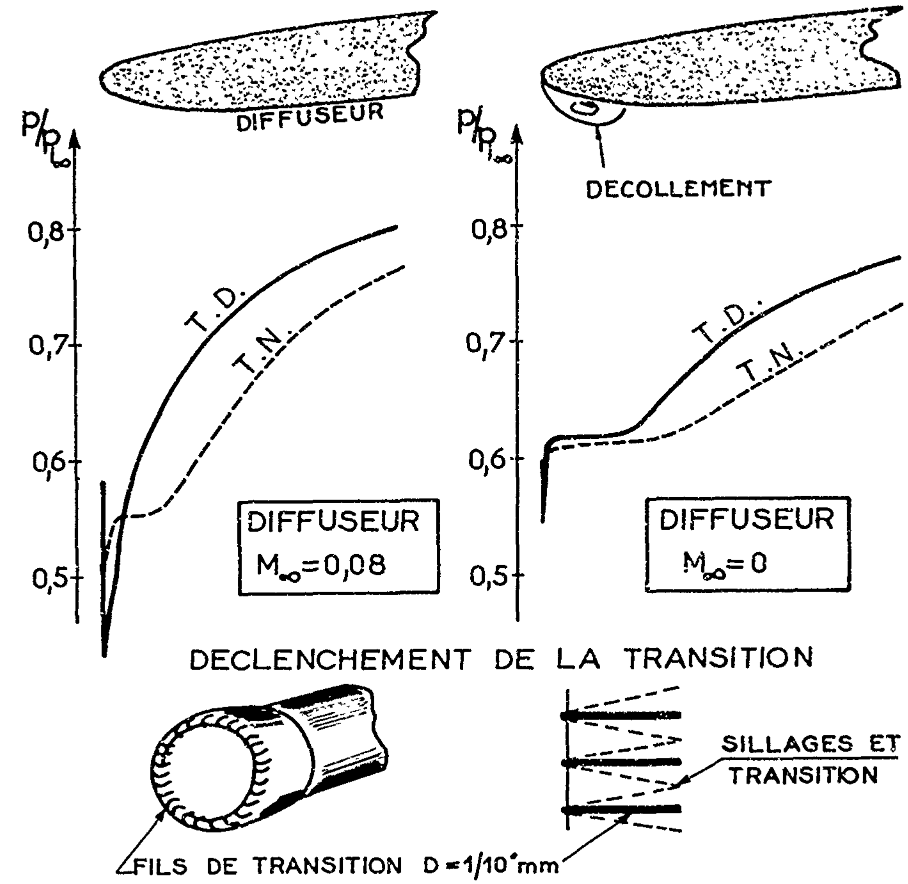

Fig.9_EFFET DU DÉCLENCHEMENT DE LA TRANSITION AU BORD D'ATTAQUE.
ESSAIS A $R_{D\ \text{entrée}} = 2{,}3.10^6$_ DEBIT REDUIT CONSTANT

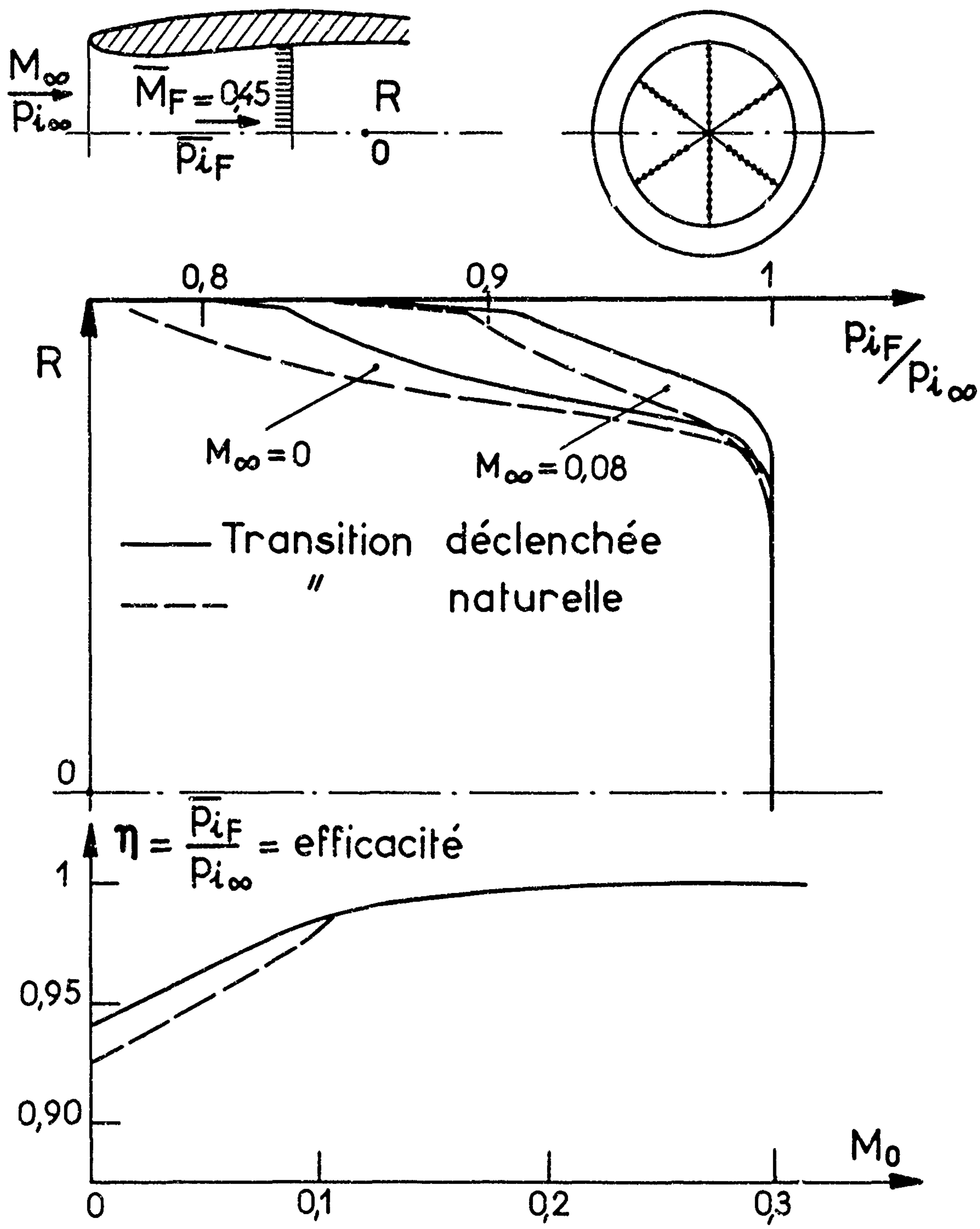

Fig.10_ EFFET DU DÉCLENCHEMENT DE LA TRANSITION AU BORD D'ATTAQUE

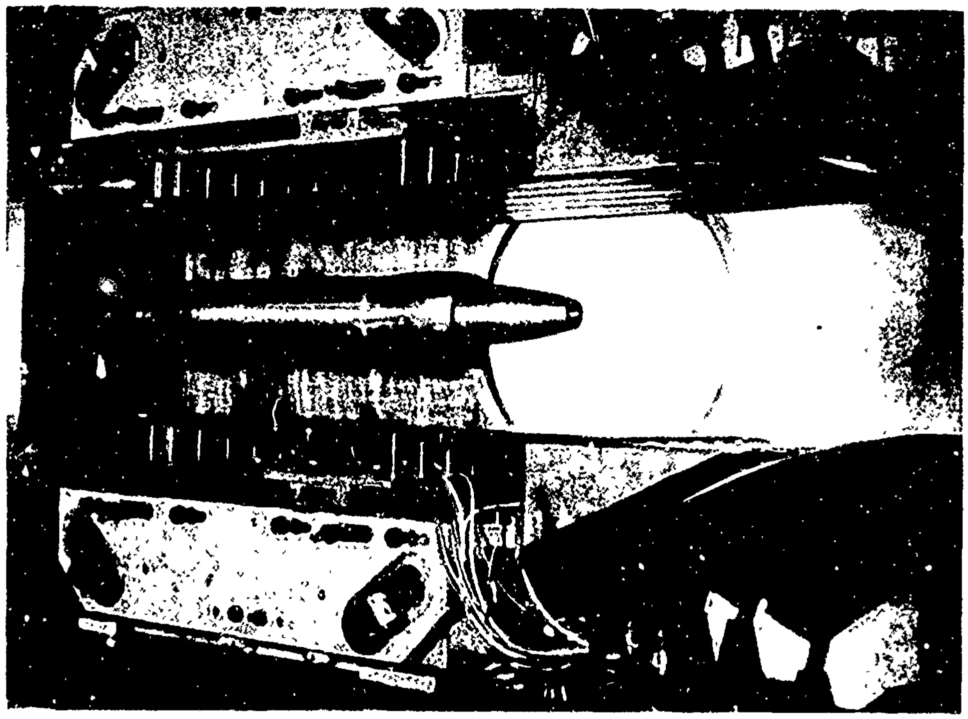

Fig. 11. S_5 Chalais. MONTAGE DOUBLE-FLUX POUR ÉTUDE DE L'ARRIÈRE-CORPS EN TRANSSONIQUE.

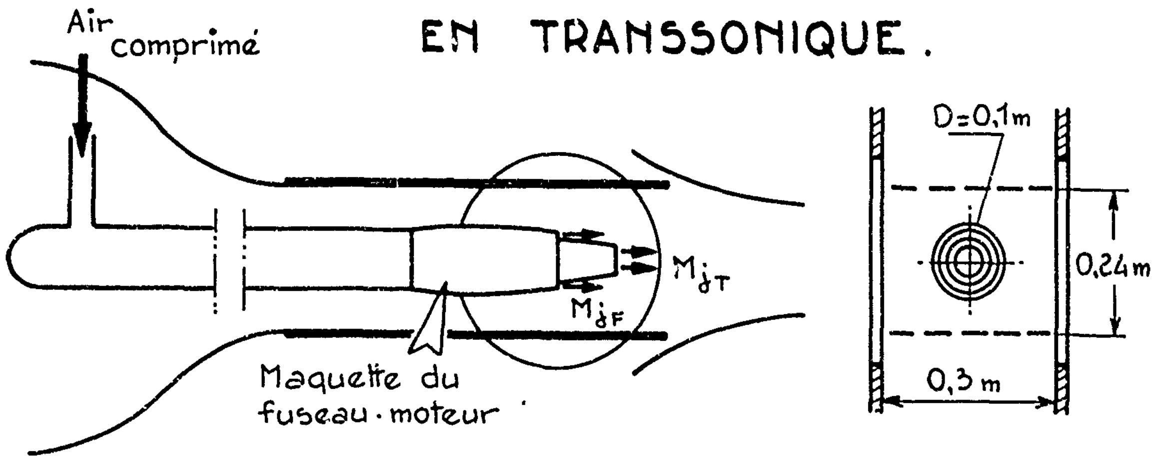

SIMULATION { Nombre de Mach et vitesse du jet "Fan", M_{jF}, V_{jF}.
Nombre de Mach du jet central, M_{jT}.

Fig. 12 . PRESSIONS SUR LA CARÈNE ET SUR LE CORPS CENTRAL

$M_\infty = 0,85$

$Re_D = 0,5 \times 10^6$

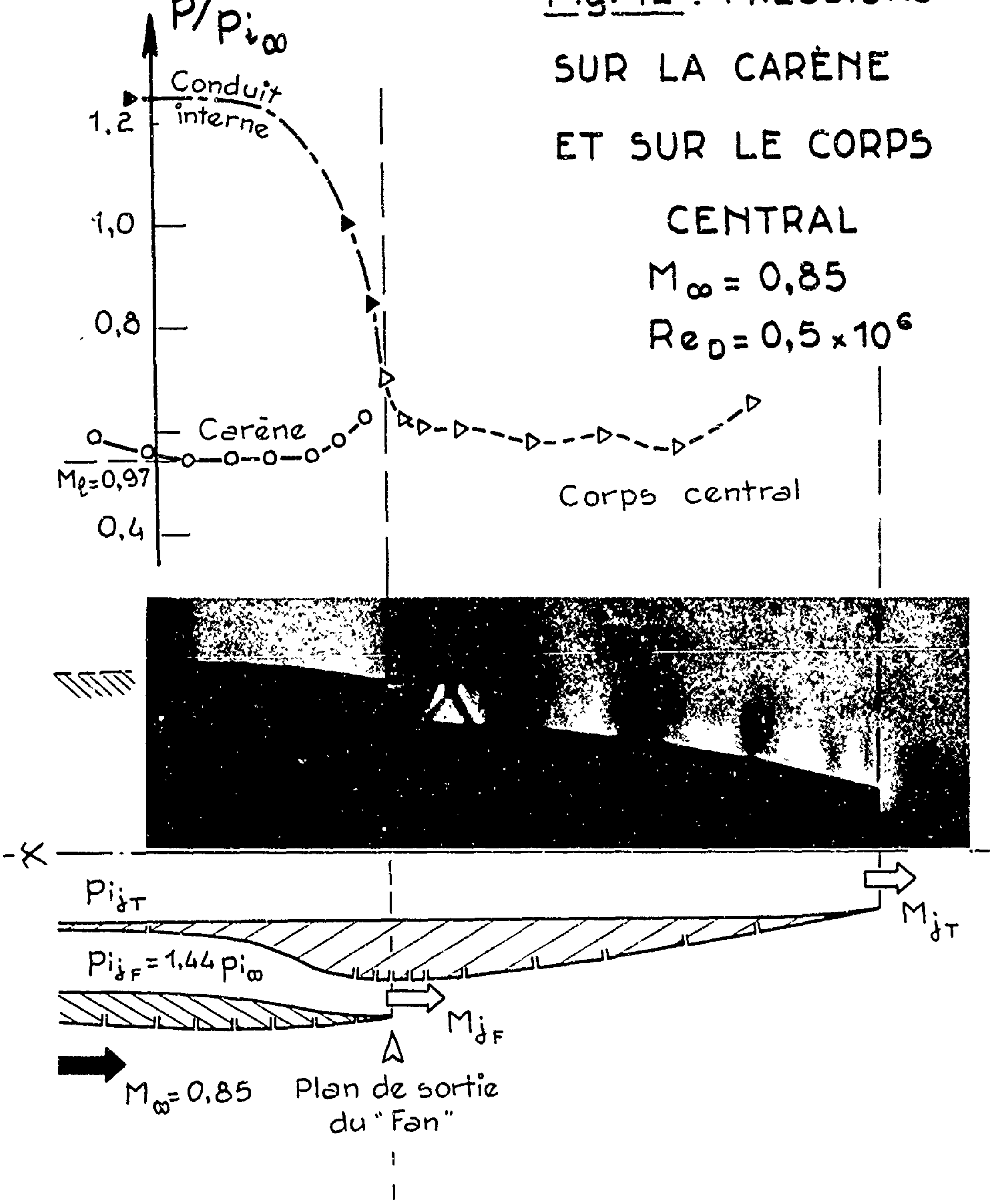

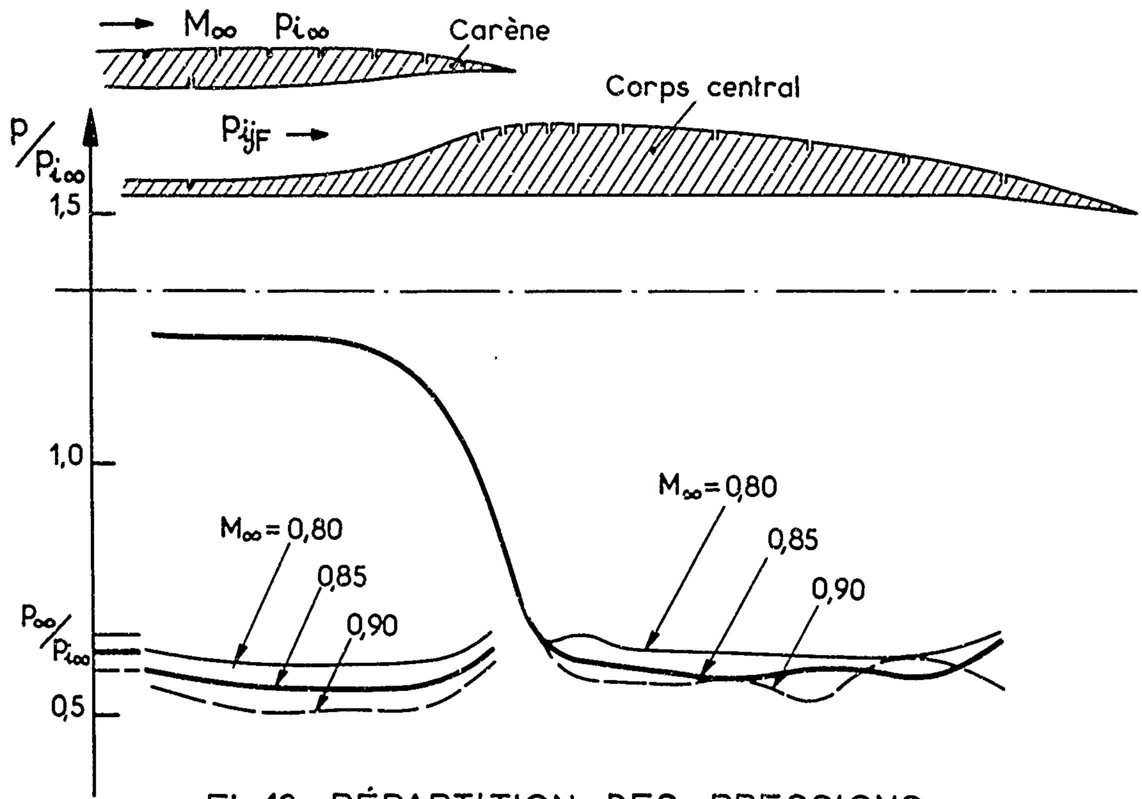

Fig.13_ RÉPARTITION DES PRESSIONS
$p_{ij_F}/p_{i\infty} = 1{,}44$ $M_\infty = 0{,}80,\ 0{,}85,\ 0{,}90$

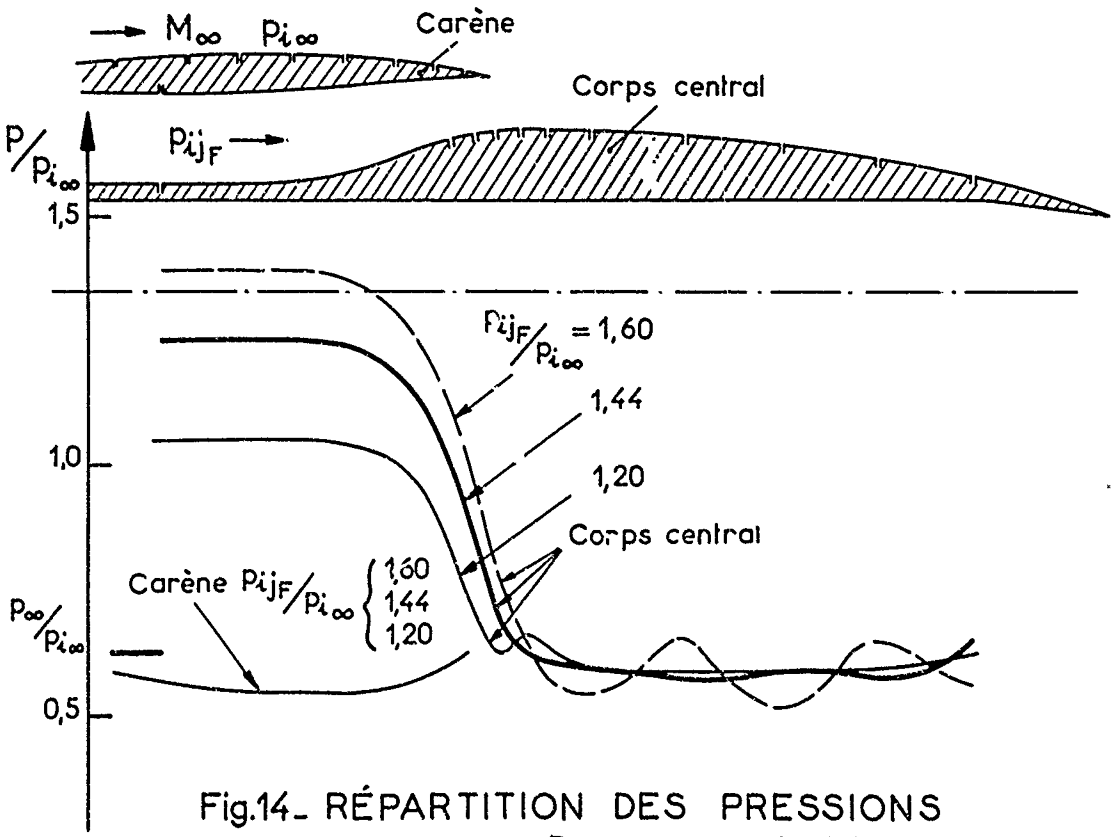

Fig.14_ RÉPARTITION DES PRESSIONS
$M_\infty = 0{,}85$ $p_{ij_F}/p_{i\infty} = 1{,}20 \,.\, 1{,}44 \,.\, 1{,}60$

NEW RESULTS ON STEADY, TWO-DIMENSIONAL TRANSONIC FLOW

by

K. Oswatitsch

Institut für Theoretische Gasdynamik der DVL
Aachen, Germany

New Results on Steady, Two-dimensional Transonic Flow

By K. Oswatitsch +)

Institut für Theoretische Gasdynamik der DVL, Aachen, Germany

Abstract

A brief report on the doctoral research of two students is presented. The contribution of H. Sobieczky is concerned with the construction and discussion of two-dimensional transonic flow patterns. In the thesis of H. Nörstrud the integral equation method is used to treat transonic flows past lifting airfoils.

1. Introduction

My present paper informs you about the doctoral research of two of my students. One has finished his thesis, the other is still working on it. Both investigations are concerned with two-dimensional, transonic flow. This type of flow is a rather crude approximation of the actual transonic flow about an aircraft. The two papers under consideration are theoretical. I know that an engineer does not appreciate highly theoretical work. Nevertheless, I hope that my informations will prove useful to you, because two-dimensional transonic flow is basic for the understanding of three-dimensional transonic flow. Furthermore, the theoretical treatment I am going to present is relatively simple,an engineer may find it not too difficult.

2. Basic Equations

Two-dimensional irrotational transonic flow is described by the well-known gasdynamic equation and the equation of irrotationality. In what follows we assume small disturbances in the vicinity of the sound speed $W = c^*$. The two basic equations mentioned can then be written

$$(\varkappa+1)(1-W/c^*)\frac{\partial}{\partial x}(1-W/c^*)-\frac{\partial \vartheta}{\partial y}=0. \quad (1)$$

$$\frac{\partial}{\partial y}(1-W/c^*)-\frac{\partial \vartheta}{\partial y}=0. \quad (2)$$

W, ϑ, $\varkappa$ and c^* are, respectively, the absolute value of the velocity, the flow angle, the ratio of the specific heats and the critical sound speed. Let the positive x-direction be parallel to the oncoming stream. Thus, we have to fulfil the boundary con-

+) Professor of fluid mechanics, head of the DVL-Institut für Theoretische Gasdynamik ditions

$$\sqrt{x^2+y^2} \longrightarrow \infty\,;\; W = W_\infty\,;\; \vartheta = 0\,. \quad (3)$$

3. Transonic Flow, Subsonic Domain

The paper of Helmut Sobieczky [1] is mainly concerned with the subsonic domain of flows with free stream Mach number one. However, the calculation can be continued across the sonic line. It is well-known that the system (1), (2) can be linearized without loss in generality using transformations similar to those already used by Timman [2] and M.Schäfer [3]. Now let us introduce a new dependent variable

$$q = -\frac{2}{3}\sqrt{\varkappa+1}\,\left(1 - W/c^*\right)^{3/2} \qquad (4)$$

one can choose new independent variables s, t so that the following Cauchy-Riemann equations hold

$$-\frac{\partial q}{\partial s} + \frac{\partial \vartheta}{\partial t} = 0\,; \qquad \frac{\partial q}{\partial t} + \frac{\partial \vartheta}{\partial s} = 0\,. \quad (5)$$

x and y must satisfy the Beltrami differential equations

$$\frac{\partial x}{\partial s} = -K(s,t)\frac{\partial y}{\partial t}\;;\quad \frac{\partial x}{\partial t} = +K(s,t)\frac{\partial y}{\partial s} \quad (6)$$

K is a function of q only

$$\begin{aligned} K(s,t) &= \left|\sqrt{(\varkappa+1)(1-W/c^*)}\right| = \\ &= \left[-\frac{3}{2}(\varkappa+1)\,q\right]^{1/3} = A q^{1/3} \end{aligned} \qquad (7)$$

All quantities in the latter equation are taken real. It then follows from equation (4) that $W < c^*$ and we have $K(s,t) \geq 0$ because of $A < 0$ and $q \leq 0$.

In the direct method $1 - W/c^*$ and ϑ are sought as functions of x and y and in the hodograph method x and y must be determined as functions of W and ϑ. However, in the system (5), (6) both q, ϑ and x, y are functions of s and t. It is possible to assign a linear system of Beltrami equations to any solution of equation (5), in particular to any analytic function

$$E(s+it) = q(s,t) + i\vartheta(s,t)\,. \qquad (8)$$

Although the Beltrami equations are linear their solution is the main problem, because the system (6) has variable coefficients. I continue with some remarks concerning this situation.

Let us focus our attention to the system (6). In case of an incompressible flow we would have K = 1 and -q, ϑ could be interpreted as components of a velocity disturbance. x, y satisfy Cauchy-Riemann differential equations and the system (5) is mapped onto itself by a conformal transformation of the coordinates. Now we recognize that a particular solution of (5), for instance

$$q = s\;; \qquad \vartheta = t\,. \qquad (9)$$

can lead to different flows, if we assign different solutions of the Beltrami equations (6) to (9).

Furthermore, the solution of the Beltrami equations (6) and the corresponding Cauchy-Riemann equations (with K = 1) differ qualitatively only slightly. This is due to the fact that K depends on the cubic root of q only (picture 1).

x, y are orthogonal coordinates in both cases. The solutions of the Beltrami equations end at the sonic line q = K = 0. But one can always find solutions for $K = Aq^{1/3}$ and K = 1 which differ only slightly from each other. This is very helpful in finding a desired flow pattern.

Restricting the Beltrami equations (6) to the subsonic domain means that the solution ends at the sonic line. It does not necessarily mean that the flow ends at the line $W = c^*$, q = 0 and a limit line occurs there. The acceleration of the flow in the physical plane has to be regular at the sonic line. We can then continue the flow in the supersonic domain using the method of characteristics. Such a requirement does not lead to additional difficulties.

In picture 2 the vicinity of the sonic line in the s,t-plane and the x,y-plane are compared. In the s,t-plane the lines x = const and y = const are quite similar to the lines s = const and t = const. The curves ϑ = const, which are orthogonal to the sonic line in the s,t-plane have a perpendicular tangent in the x,y-plane because of $W = c^*$. This follows from equation (1). ($W = c^*$, $d\vartheta/dy = 0$). Nevertheless, the streamlines are smooth at the sonic line.

4. Particular Solutions

All subsequent solutions are based upon the solution (9). The Beltrami equations (6) then take the form

$$\frac{\partial x}{\partial s} = -A s^{1/3} \frac{\partial y}{\partial t} \; ; \quad \frac{\partial x}{\partial t} = +A s^{1/3} \frac{\partial y}{\partial s} \; . \qquad (10)$$

We now proceed to discuss some particular solutions of this system. (Picture 3).

$$x = A\left(C_1 t - \frac{3}{4} C_2 s^{4/3}\right);$$
$$y = C_2 t + \frac{3}{2} C_1 s^{2/3} \; . \qquad (11)$$

represents the flow in the vicinity of the sonic line in a curved duct. (Picture 4).

$$x = A\left(C_1 t - \frac{3}{2} C_2 s^{4/3} t\right);$$
$$y = \frac{3}{2} C_1 s^{2/3} - \frac{3}{4} C_2 s^2 + C_2 t^2 \; . \qquad (12)$$

is the local supersonic domain corresponding to the Ringleb solution.

In the further discussion we make use of polar coordinates

$$r = \sqrt{s^2 + t^2} \; ; \qquad tg\,\varphi = t/s$$

The solution

$$x = -C A \cdot \frac{1}{2} r^{2/3}\left[(1+\sin\varphi)^{2/3} + (1-\sin\varphi)^{2/3}\right],$$
$$y = C r^{1/3}\left[(1+\sin\varphi)^{1/3} - (1-\sin\varphi)^{1/3}\right] . \qquad (13)$$

describes the flow through a Laval nozzle in the vicinity of the sonic line which is shown in picture 5.

Another particular solution reads

$$x = C \cdot A \cdot r^{-1/3}\left[(1+\sin\varphi)^{2/3} + (1-\sin\varphi)^{2/3}\right],$$
$$y = C r^{-2/3}\left[(1+\sin\varphi)^{1/3} - (1-\sin\varphi)^{1/3}\right] \qquad (14)$$

Equation (14) describes the behavior of a flow with free stream Mach number one in the vicinity of a stagnation point. This behavior is illustrated in picture 6.

Müller-Matschat [4] found an asymptotic solution for the two-dimensional flow about an airfoil at $W = c^*$ (picture 7). This solution is given by

$$x = C \cdot A \cdot r^{-4/3}\left[(1+\sin\varphi)^{2/3}(2 - 3\sin\varphi) + (1-\sin\varphi)^{2/3}(2 + 3\sin\varphi)\right] , \qquad (15)$$
$$y = -C r^{-5/3}\left[(1+\sin\varphi)^{1/3}(1 - 3\sin\varphi) - (1-\sin\varphi)^{1/3}(1 + 3\sin\varphi)\right] .$$

It is worth noting that the various examples are exact solutions. A variation of the arbitrary constant C_1 is equivalent to applying the transonic similarity rules. A portion of the discussed solutions is already known. In a recent paper Zierep [5] gives a representation of the flow about the so-called Guderley profile in the physical plane. Sobieczky obtains the Guderley solution by superposing the nozzle flow equation (14) and the asymptotic solution (15) (picture 8).

All results mentioned are based upon the same linear Beltrami system. Consequently, one can superpose all solutions mentioned.

I give you an example. The combined solution (11) + (14) + (15) represents the sonic flow about a curved profile which seems to be a new result.

5. General Solutions

The variety of solutions is not reduced essentially by the solution (9). This has already been pointed out and is in accordance with what we found in the foregoing discussions. The Beltrami equations (10) belonging to equation (9) can be written as second order differential equations for x and y

$$x_{ss} + x_{tt} - \frac{1}{3}\cdot\frac{1}{s}\, x_s = 0\,;$$
$$y_{ss} + y_{tt} + \frac{1}{3}\cdot\frac{1}{s}\, y_s = 0\,. \qquad (16)$$

The homogeneous solutions of these equations (ν = integer)

$$x = r^{\frac{2}{3}+\nu}\cdot F(\varphi);\quad y = r^{\frac{4}{3}+\nu}\cdot G(\varphi) \qquad (17)$$

are hypergeometric functions of a simple kind. This feature is characterized by the fact that $F(\varphi)$ and $G(\varphi)$ can be written as a finite sum of functions of an angle. The usual nozzle solution (14) and the Müller-Matschat solution (15) are the special cases $\nu = 0$ and $\nu = -2$ of eqs. (17). The solution $\nu = -1$ (i.e. the solution (13), picture 5) which seems to be a new result might also be of particular interest. Using further solutions $\nu > 0$ one can compile a whole table of sonic flows about cusp-nosed airfoils. It seems that this table widens the possibilities of theoretical treatment and makes the treatment itself easier.

6. Integral Equation for Cambered Profiles at Angle of Attack

H. Nörstrud [6] uses the integral equation method to treat the flow about cambered profiles at angle of attack. First of all, let us introduce reduced quantities

$$U = \frac{W - W_\infty}{c^*}\,\tau^{-2/3}(\varkappa+1)^{1/3}\,;\quad V = \frac{\vartheta - \vartheta_\infty}{\tau}\,;$$
$$X = x\,;\qquad Y = \tau^{1/3}(\varkappa+1)^{1/3}\,y\,; \qquad (18)$$
$$\lambda = 1 - (1 - M_\infty^2)\,\tau^{-2/3}\,(\varkappa+1)^{-2/3}\,.$$

τ denotes the thickness ratio and λ is a transonic similarity parameter which takes the value $\lambda = 1$ for $M_\infty = 1$. Eqs. (18) give one of various possible reductions in the transonic régime.

With the aid of eqs. (18) the system 1, 2 can be rewritten to give

$$\frac{\partial U}{\partial X} + \frac{\partial V}{\partial Y} = (\lambda + U)\,\frac{\partial U}{\partial X}\;; \qquad (19)$$

$$\frac{\partial U}{\partial Y} - \frac{\partial V}{\partial X} = 0\;; \qquad (20)$$

From equation (20) it follows that a velocity potential exists:

$$\varphi_X = U\;;\qquad \varphi_Y = V\,. \qquad (21)$$

Let the subscript L refer to the solution of the linear system, i. e. the system in which the right hand side of equation (20) vanishes. We can use the linear solutions in order to satisfy the boundary conditions at the body. The complete solution can be written as a set of nonlinear integral equations

$$\left.\begin{aligned}\varphi_X &= \varphi_{LX} + \frac{1}{2\pi}\iint[\lambda+\varphi_\xi]\,\varphi_{\xi\xi}\,\frac{\partial}{\partial\xi}\ln r\; d\xi\, d\eta\,;\\ \varphi_Y &= \varphi_{LY} + \frac{1}{2\pi}\iint[\lambda+\varphi_\xi]\,\varphi_{\xi\xi}\,\frac{\partial}{\partial\eta}\ln r\; d\xi\, d\eta\end{aligned}\right\} \qquad (22)$$

with $\quad r = \sqrt{(X-\xi)^2 + (Y-\eta)^2}\,,$

$$\frac{\partial}{\partial\xi}\ln r = \frac{X-\xi}{(X-\xi)^2+(Y-\eta)^2}\;;$$

$$\frac{\partial}{\partial\eta}\ln r = \frac{Y-\eta}{(X-\xi)^2+(Y-\eta)^2} \qquad (23)$$

In the integral equation method the two-dimensional integrals in (22) are approximated by one-dimensional integrals. In this way one obtains one-dimensional, non-linear integral equations. The main problem is to solve these integral equations.

The approximations just mentioned do not play an essential role in the subsequent considerations and will therefore not be discussed in more details.

Let us focus our attention to the solution of the nonlinear integral equations. With regard to the large possibilities which electronic computers offer one can proceed as follows. Starting with a known subcritical flow with $\lambda_{krit} < \lambda$ we proceed step by step taking a new value for λ in each step. It is permitted in each step to linearize the equations for the disturbances of the unknown quantities. Thus, each step results in solving a system of linear equations. This method of solution is closely related to the method of parametric differentiation developed by Rubbert and Landahl [7] for a very general case.

The integral equation method has been used several times in the case of a non-lifting symmetric airfoil. In this case only the first equation (22) is needed. It turns out that the method of parametric differentiation fails soon after increasing the free stream Mach number above its critical value. The reason for this failure is the occurrance of both compression and rarefaction shocks in the solution obtained by the method of parametric differentiation. Such a solution is useless from the physical point of view.

7. Decomposition of the Solution

Given the velocity potential of a flow about an inclined or cambered profile of finite thickness. This potential can be decomposed into a symmetric and antisymmetric part with respect to Y.

$$\varphi(X,Y) = \varphi^+(X,Y) + \varphi^-(X,Y) \qquad (24)$$

with

$$\varphi^+(X,Y) = \varphi^+(X,-Y)\,; \quad \varphi^-(X,Y) = -\varphi^-(X,-Y)\,;$$

$$U^+(X,Y) = U^+(X,-Y)\,; \quad U^-(X,Y) = -U^-(X,-Y)\,; \qquad (25)$$

$$V^+(X,Y) = -V^+(X,-Y)\,; \quad V^-(X,Y) = V^-(X,-Y)\,.$$

Observe that V does not have the same sign as φ and U because of equation (21). Equations similar to equation (25) hold for the linear solutions. Let the subscript L refer to these linear solutions. φ_L^+ can always be represented by a source distribution on the x-axis and φ_L^- can be represented by a vortex distribution on the x-axis. Thus, in determining φ_L^+ one encounters a linear problem associated with a symmetric non-lifting airfoil of finite thickness. The determination of φ_L^- leads to a linear problem associated with a lifting profile of zero thickness. We shall see that the calculation of φ^+ leads again to a problem associated with a non-lifting profile of finite thickness. However, φ^- does not describe a flow about a lifting airfoil of zero thickness in the non-linear case. The latter remarks are not relevant for our conclusions.

In case of an inclined or cambered profile all calculations are based on distributions on the x-axis. We therefore specialize the subsequent equations taking Y = 0. Numerous terms then cancel each other. Carrying through the decomposition we obtain

$$y = +0:$$

$$U^+ = U_L^+ + \frac{1}{2\pi}\iint\Big[\lambda\frac{\partial U^+}{\partial\xi} + U^+\frac{\partial U^+}{\partial\xi} + U^-\frac{\partial U^-}{\partial\xi}\Big]\frac{X-\xi}{(X-\xi)^2+\eta^2}\,d\xi\,d\eta$$

$$V^+ = V_L^+\,; \quad U^- = U_L^- \qquad (26)$$

$$V^- = V_L^- - \frac{1}{2\pi}\iint\Big[\lambda\frac{\partial U^-}{\partial\xi} + U^+\frac{\partial U^-}{\partial\xi} + U^-\frac{\partial U^+}{\partial\xi}\Big]\frac{\eta}{(X-\xi)^2+\eta^2}\,d\xi\,d\eta$$

Clearly, we have $U^- = V^- = 0$ for $U_L^- = V_L^- = 0$. However, $U^+ \neq 0$ for $U_L^+ = V_L^+ = 0$. This is not necessary, if the effect due to inclination and camber are small in comparison with the effects due to thickness. This condition was assumed to be true in an earlier paper by T. Gullstrand [8] . In the paper by H. Nörstrud however, the disturbances due to thickness are assumed to be of the same order of magnitude as those due to lift.

8. Results

The method of parametric differentiation can also be applied to flows about lifting profiles of finite thickness. One of Nörstrud's results is presented in picture 9. His calculations show that the method of parametric differentiation does not lead to difficulties and provides smooth solutions as long as the partial solutions U^+ and U^- remain subcritical. This result as such does not seem to be very surprising.

A supercritical solution can be composed of two subcritical solutions without difficulties. In this way one obtains supercritical solutions for the lifting profiles without a compression shock and consequently without drag. This statement obtained from an approximate method seems to be quite plausible. Increasing the Mach number above its subcritical value does not at once lead to drag in case of a non-lifting profile. The shifting of the suction downstream the maximum thickness occurs when the mass flow density at the maximum thickness reaches about the value of the mass flow density of the oncoming stream. In this situation there is no longer sufficient space for the flow at such high velocities in the plane through the maximum wing section. In case of a lifting airfoil there is sufficient space for the air on the pressure side to flow past the airfoil. Lack of space on the suction side can therefore be compensated.

Observing H. Nörstrud's results one may doubt whether intensive :earch on transonic flows past non-lift g airfoils is reasonable. In practice one is of course mainly interested in lifting airfoils. Being aware of the fact that the conclusions concerning lifting airfoils are based upon an approximate method we must expect that the lifting and non-lifting airfoil in transonic flow are essentially different problems.

References

[1] Sobieczky, H.E., "Exakte Lösungen der schallnahen gasdynamischen Gleichung", Dissertation, T.H. Wien, in preparation

[2] Timman, Proc. Seventh Int. Congress Appl. Mech. 4 (1948) S.28 - 48

[3] Schäfer, M., "Eine einheitliche Charakteristikenmethode zur Behandlung gemischter Unterschall- Überschallströmungen", (1953) Mech. and Analy., Vol. 2 Nr. 3

[4] Müller, E.A., Matschat, K., "Ähnlichkeitslösungen der transsonischen Gleichungen bei der Anströmmachzahl 1", Sonderdruck Applied Mechanics, Proceedings of the Eleventh International Congress of Appl. Mechanics, Munich 1964

[5] Zierep, J., "Schallnahe und Hyperschallströmungen", G.Braun Karlsruhe 1966

[6] Nörstrud, H., "Numerische Lösungen von schallnahen Strömungen um ebene Profile", Dissertation, T.H. Wien, 1968

[7] Rubbert, P.E. and Landahl, M.T., "Solution of the Transonic Airfoil Problem through Parametric Differentiation", AIAA J. 5, March 1967, 470 - 479

[8] Gullstrand, T.R., "The Flow over two-dimensional aerfoils at incidence in the transonic speed range", KTH-Aero TN 27, Stockholm, 1952

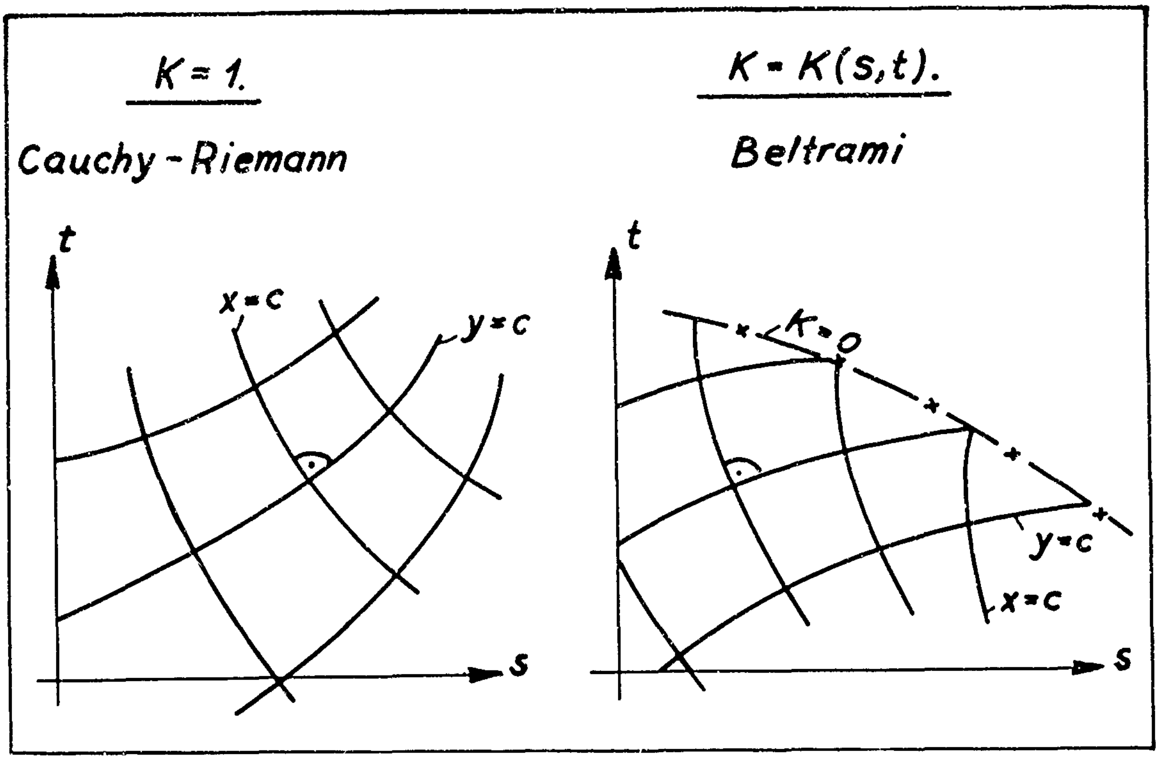

Fig. 1. Beltrami differential equations

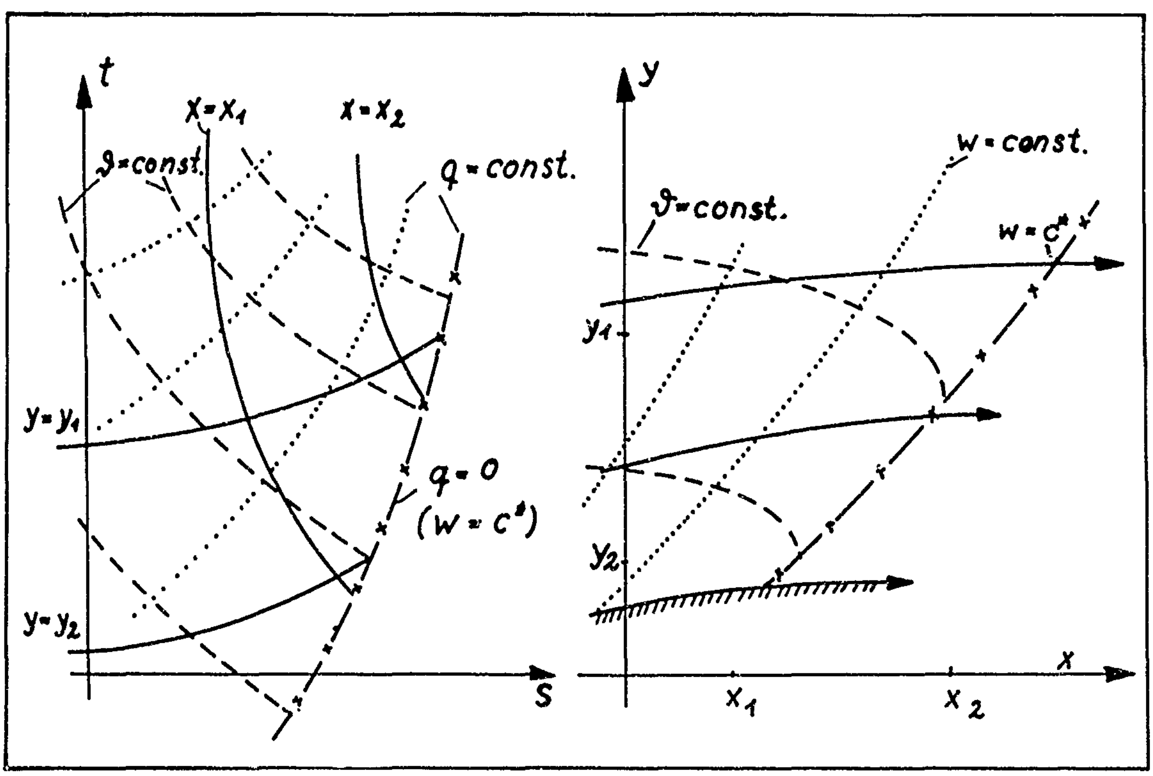

Fig. 2. s,t-plane and x,y-plane

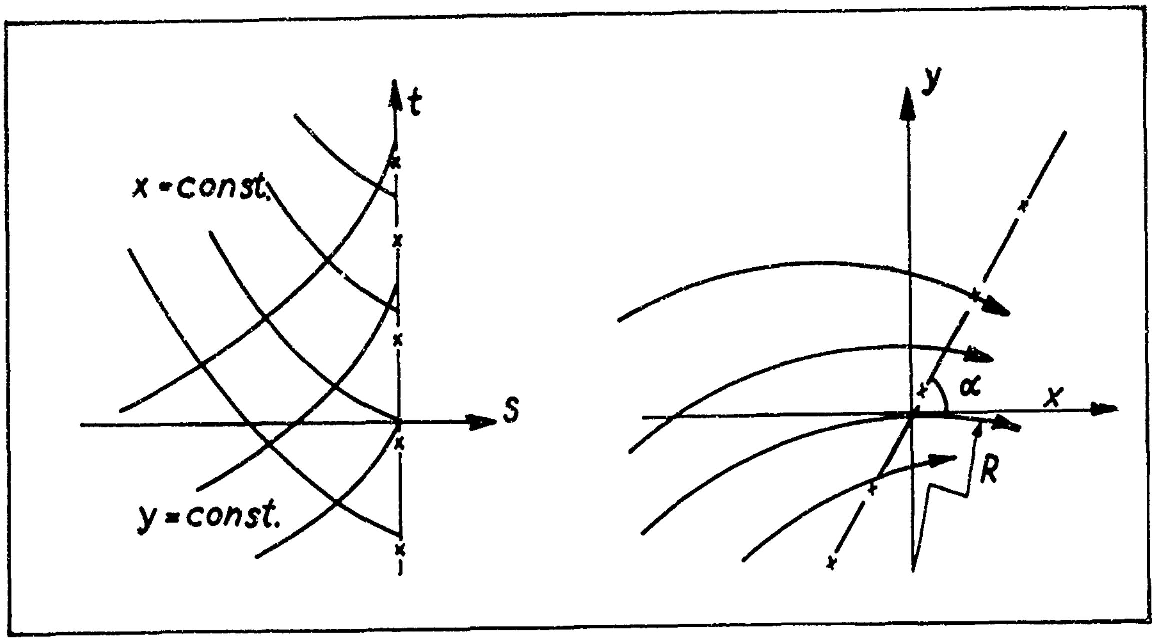

Fig. 3. Slope of the sonic line and streamline curvature

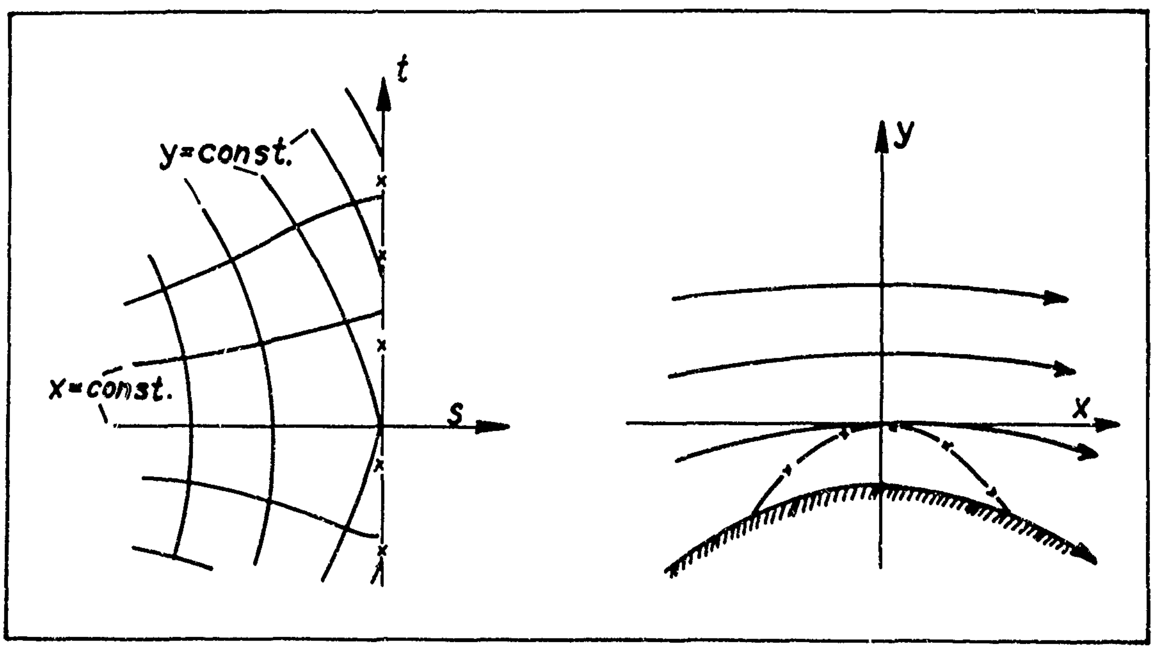

Fig. 4. Local supersonic domain

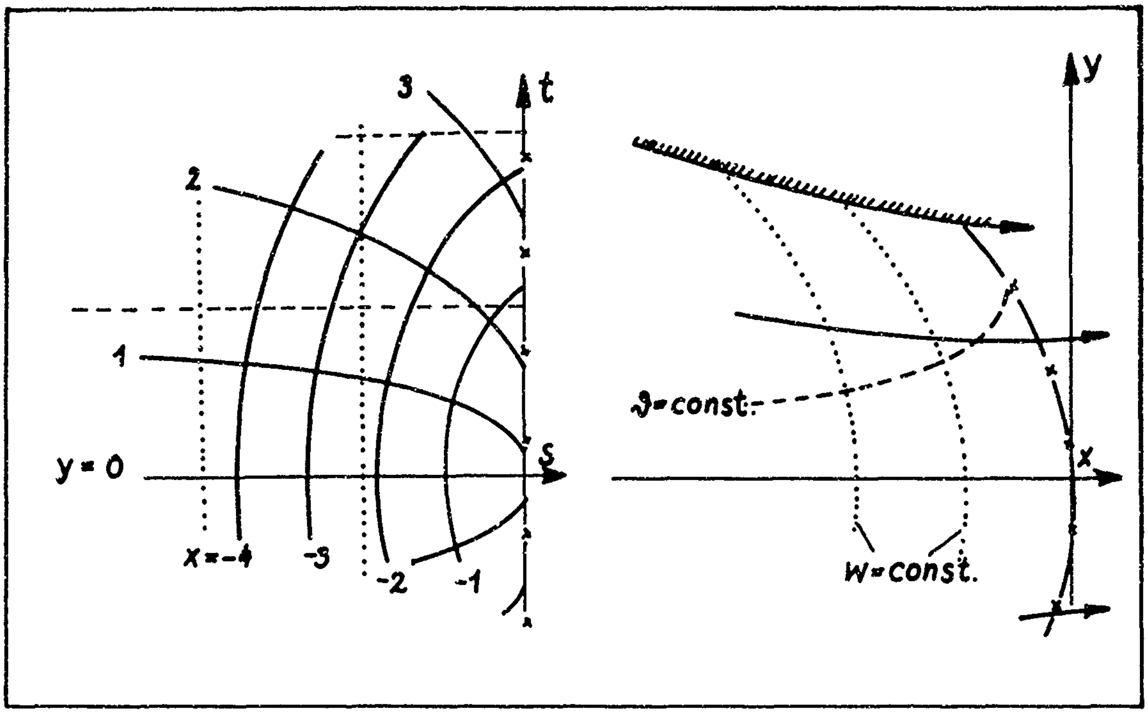

Fig. 5. Nozzle flow with acceleration

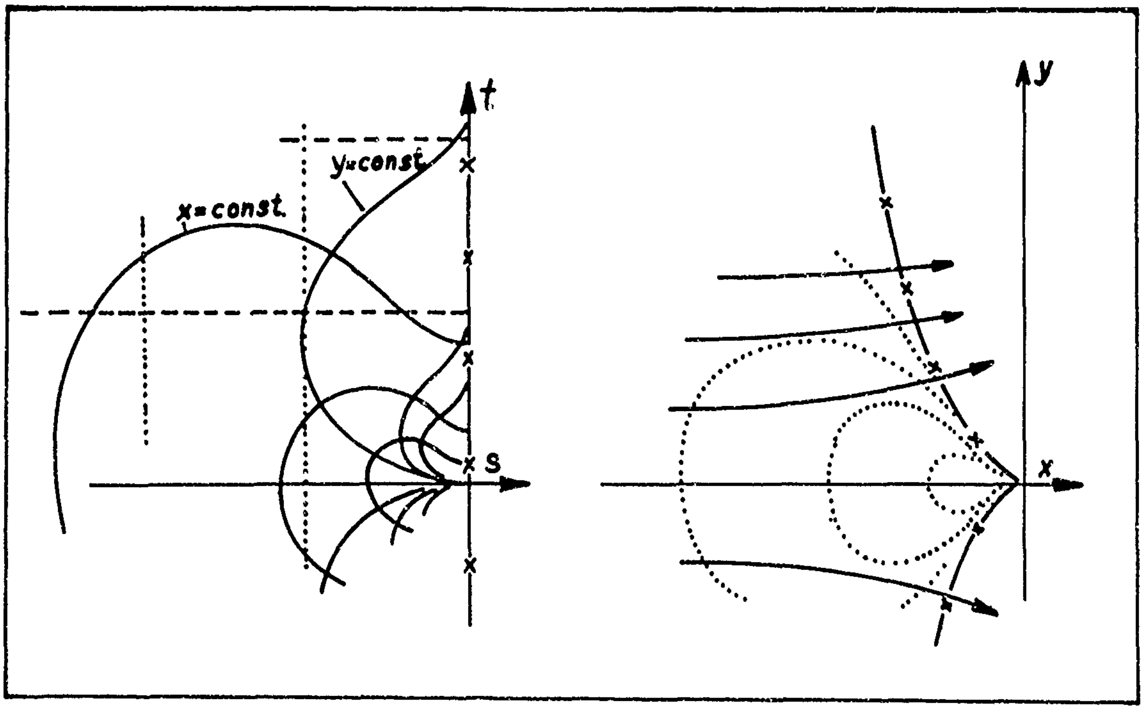

Fig. 6. Stagnation point

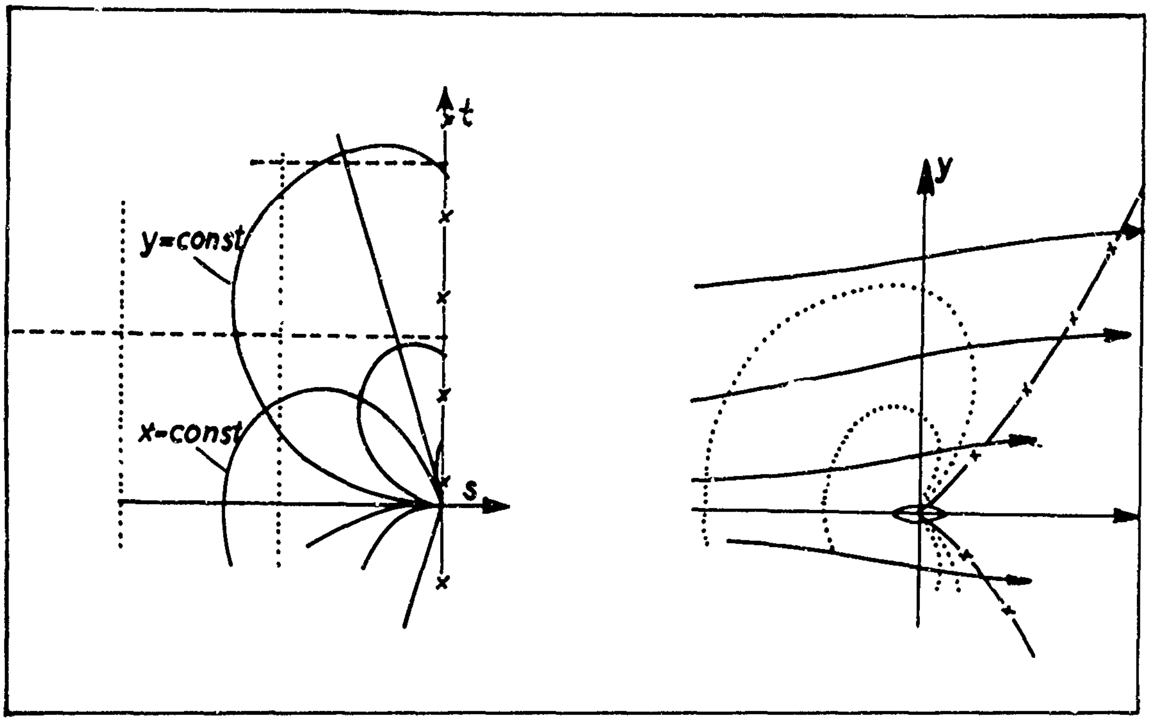

Fig. 7. Asymptotic flow about an airfoil

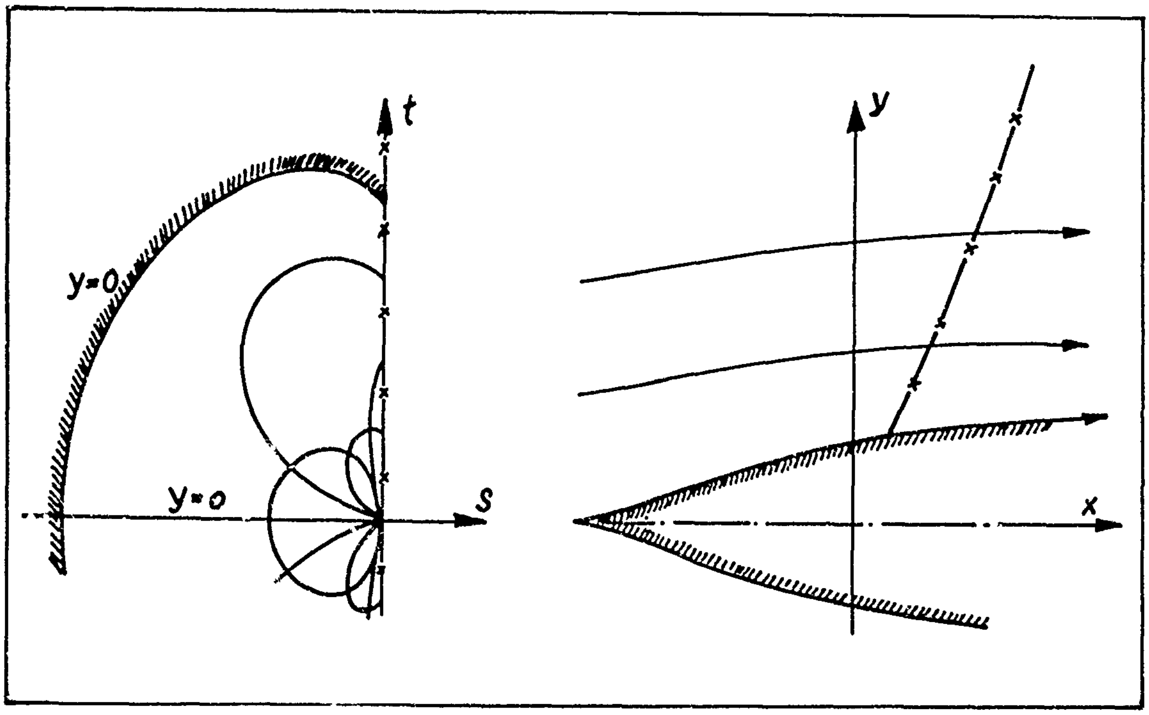

Fig. 8. Transonic flow about an airfoil

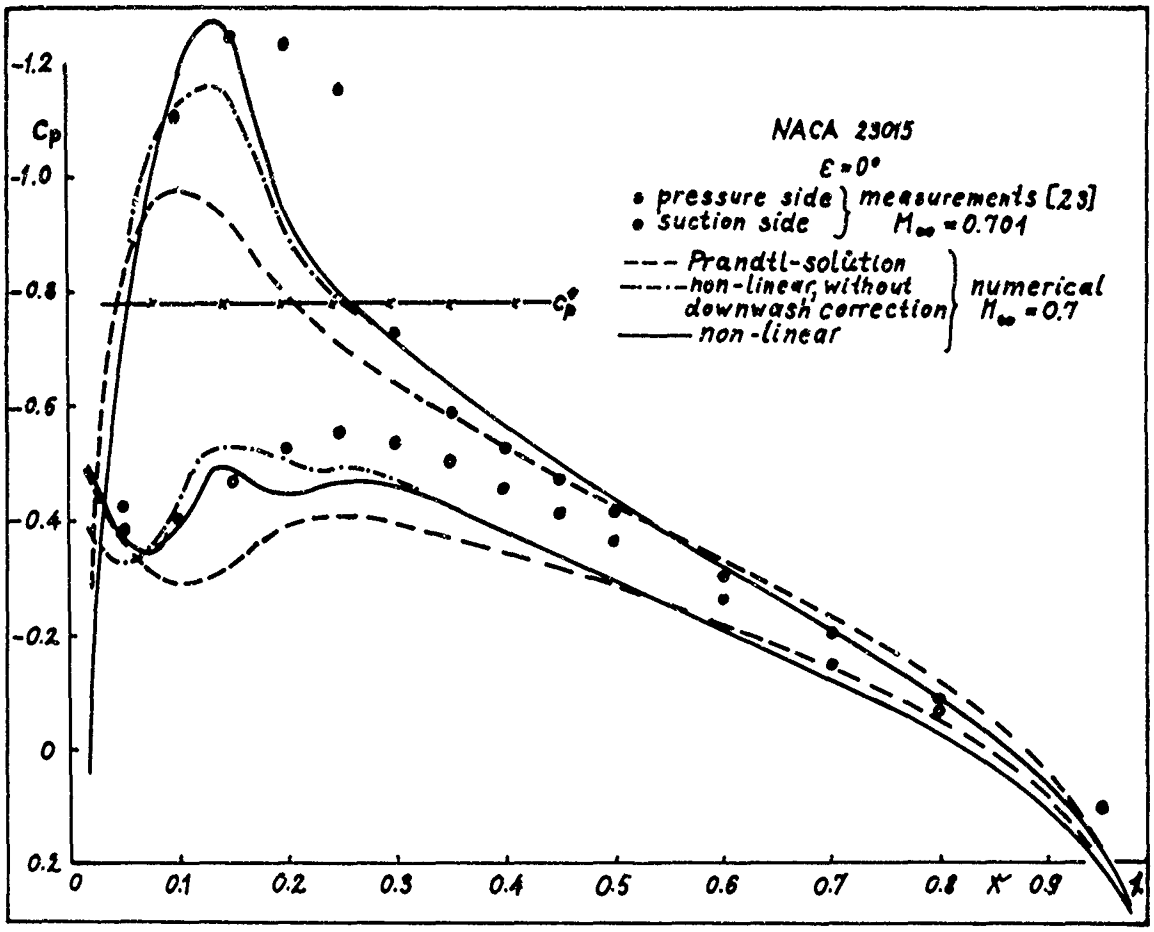

Fig. 9. NACA 23o15 profile at zero incidence

Information regarding the availability of further copies of AGARD publications may be obtained from

The Scientific Publications Officer,
Advisory Group for Aerospace Research and Development,
7, rue Ancelle,
92 Neuilly-sur-Seine,
France.